UFR Sciences et Techniques des Matériaux et des Procédés.
Département de Formation Doctorale :
Chimie et Physico-Chimie Moléculaire et Théorique

Thèse

présentée pour l'obtention du titre de

Docteur de l'Université Henri Poincaré, Nancy-I
en Chimie Informatique et Théorique

par **Vincent GOTTE**

ETUDES STRUCTURALES PAR SPECTROSCOPIE D'ABSORPTION DES RAYONS X POLARISÉS

Soutenue le 9 Novembre 1999

Membres du Jury :

Président :	Pr. J.L. RIVAIL	Université Henri Poincaré de Nancy I.
Rapporteurs :	Pr. R. GUILARD	Université de Bourgogne, Directeur du LIMSAG (UMR 5633).
	Dr. C. BROUDER	Directeur de Recherche au CNRS, Universités de ParisVI et Paris VII.
Examinateurs :	Pr. C. LECOMTE	Université Henri Poincaré de Nancy I.
Invité	Dr. H. LEDON	Responsable du domaine des bioressources, Air-Liquide, Paris.
	Dr. J. GOULON	Directeur de Thèse, Directeur de Recherche au CNRS.

Table des matières

Introduction générale

Le travail présenté dans ce mémoire a été effectué à l'Installation Européenne de Rayonnement Synchrotron de Grenoble (European Synchrotron Radiation Facility) dans le groupe de Spectroscopie d'Absorption X dirigé par J. Goulon et en collaboration avec l'Unité Mixte de Recherche 5633 CNRS-Air Liquide, dirigée par le Profeseur R. Guilard, dans le cadre d'une Bourse de Thèse co-financée pour moitié par ESRF et par Air-Liquide.

Le projet de recherche portait sur l'utilisation des spectroscopies d'absorption X dans le but d'accéder aux informations structurales sur les complexes formés, d'une part, au cours de l'activation de l'ozone par des dérivés porphyriniques du manganèse, et d'autre part, lors de la solubilisation des gaz rares (argon, xénon) en solution.

Les spectres présentés dans cette thèse ont été enregistrés sur la ligne de lumière ID-12A, plus spécifiquement dédiée aux études d'absorption X sous faisceau polarisé. La source de lumière Helios-II est un onduleur qui fonctionne dans la gamme d'énergie 2 keV- 15 keV et qui a été optimisé pour délivrer, à la demande, une lumière polarisée circulairement (droite ou gauche) ou linéairement. Cette particularité indispensable pour réaliser les expériences de dichroisme explique pourquoi nous avons participé aussi aux projets du groupe se rapportant à la mise en évidence de l'existence du dichroisme circulaire "naturel" dans le domaine des rayons X, en plus des études liées à notre contrat avec l'UMR 5633.

A ce niveau, notre contribution personnelle se situe dans le développement de logiciels destinés à l'analyse des spectres enregistrés: notre première tâche a été la remise à jour des codes X0, X1, X2 précédemment mis au point par J. Goulon et ses collaborateurs pour l'analyse des spectres EXAFS[1]. Ces codes sont également utilisables pour l'analyse des spectres d'EXAFS magnétique. De nouveaux codes DICHRO, CRYSTAL ont aussi été écrits et sont désormais opérationnels pour l'analyse des données de dichroisme circulaire naturel ou magnétique. Enfin, l'interfaçage des codes MSXAS et CONTINUUM permet de conduire les simulations *ab initio* des spectres expérimentaux.

Toutes les études que nous avons menées ou auxquelles nous avons été associé ont été publiées ou sont actuellement en cours de publication. C'est pourquoi, nous avons choisi de rassembler dans notre mémoire, les textes de ces publications précédés d'un court résumé. Le plan adopté est le suivant:

La première partie est une présentation générale des spectroscopies d'absorption X et de leur intérêt pour l'étude structurale des complexes porphyriniques. Elle reproduit les paragraphes I, II et III du chapitre 49 intitulé "X-ray Absorption Spectroscopy Applied to Porphyrin Chemistry" (par J. Goulon, C. Goulon-Ginet et V. Gotte), dans le Volume 9 de la série "The Porphyrin Handbook" édité par K.M. Kadish, K.M. Smith et R. Guilard. La publication des 10 volumes de cet ouvrage par Academic Press est prévue pour octobre-novembre prochain.

[1] EXAFS: Extended X-ray Absorption Fine Structures.

La deuxième partie, constituée de deux chapitres, est consacrée aux études entreprises dans le cadre du contrat avec l'UMR 5633 et Air-Liquide. Le travail le plus important a été réalisé sur les complexes entre l'ozone et les dérivés halogénés de porphyrines de manganèse. Le but de cette étude était de caractériser les intermédiaires formés au cours de la réaction, en utilisant les spectres XANES[2], EXAFS et XMCD[3] et en mettant en oeuvre les méthodes différentielles d'analyse des spectres EXAFS particulièrement bien adaptées à ces études, comme nous le soulignons dans le chapitre I. L'ensemble de ce travail est détaillé dans le texte actuellement soumis pour publication au Journal of Physical Chemistry , les résultats préliminaires ayant déjà fait l'objet d'une publication au Journal de Physique lors de la conférence XAFS IX de Grenoble. Le deuxième chapitre, très court, est le rapport des expériences réalisées sur ID-12A pour tenter de caractériser les complexes d'inclusion de l'argon avec le cryptophane A et le kryptofix(222) dans des solvants organiques. Nous y précisons les difficultés expérimentales que nous avons rencontrées et qui nous ont contraint à abandonner ce projet pour lequel la spectroscopie d'absorption X ne s'est pas révélée l'outil le plus approprié.

La troisième partie rassemble les publications sur les premières mesures faites sur ID-12A en 1997 qui ont permis de mettre en évidence, de manière indiscutable, le dichroïsme circulaire "naturel" dans le domaine des rayons X. Rappelons que les expériences de dichroïsme circulaire consistent à mesurer les différences entre les spectres d'absorption enregistrés successivement avec un faisceau X polarisé circulairement à droite et à gauche. Notre équipe a pu démontrer que, dans le domaine des rayons X, l'existence de dichroïsme circulaire a pour origine les interactions de type dipole électrique-quadripole électrique alors que le terme d'interférence dipole électrique-dipole magnétique qui régit ce phénomène dans le domaine UV-visible, est inexistant. C'est pourquoi, l'observation du dichroïsme naturel ne peut être faite que sur des cristaux gyrotropes appartenant à des groupes cristallographiques bien spécifiques. La première publication se rapporte aux premières expériences effectuées sur le monocristal uniaxial de iodate de lithium aux seuils L_1, L_2 et L_3 de l'iode. Dans la deuxième publication, nous montrons que le phénomène XNCD[4] est beaucoup plus difficile à mettre en évidence sur des cristaux biaxiaux où les signaux de dichroïsme circulaire peuvent être masqués par la biréfringence et le dichroïsme linéaire. La troisième publication est une analyse complète des modifications de l'état de polarisation d'un faisceau X à la traversée d'un cristal biaxial.

La quatrième et dernière partie ne sera commentée que brièvement car elle reproduit quatre courtes publications sur des travaux auxquels nous avons été associés pour notre participation à l'analyse des spectres. Elle ne constitue donc qu'une partie annexe de notre travail. Il s'agit:

(i) d'expériences faites lors de la mise au point de la technique dite "gap-scan" qui permet d'enregistrer les spectres EXAFS sur un domaine d'énergie suffisant, même avec un onduleur ,

---

[2] XANES: X-ray Absorption Near Edge Structure.
[3] XMCD: X-ray Magnetic Circular Dichroism
[4] XNCD: X-ray Natural Circular Dichroism

(ii) d'analyses de spectres XANES et EXAFS enregistrés au seuil K du soufre pour caractériser des caoutchoucs vulcanisés ou encore des bitumes et asphaltènes,

(iii) d'une étude de dichroïsme circulaire magnétique du sulfure d'europium pour mettre en évidence les signaux EXAFS polarisés en spin.

Dans la conclusion, nous ne manquerons pas de souligner les apports des nouvelles sources de rayonnement de troisième génération: flexibilité dans le contrôle de la polarisation, grande brillance, haute stabilité. Sans ces avantages, les premiers signaux de dichroisme circulaire naturel dans le domaine des rayons X n'auraient pas pu être obtenus.

Première partie

Présentation générale de la spectroscopie d'absorption X. Intérêt pour l'étude structurale des complexes porphyriniques.

1.1 Introduction

1.1.1 La spectroscopie d'absorption des rayons X

Depuis les années 70, la spectroscopie d'absorption des rayons X s'est progressivement imposée comme une technique puissante de caractérisation des propriétés structurales et électroniques de la matière. Grâce à l'apparition de sources intenses de rayonnement synchrotron, ses domaines d'applications se sont multipliés: chimie inorganique et organométallique, biochimie, géochimie, catalyse...etc...

Cette spectroscopie, qui met en jeu des transitions électroniques à partir d'un niveau de coeur vers des niveaux électroniques vides puis, après le seuil de photoionisation, vers le continuum d'états électroniques, est présentée de manière détaillée, avec ses fondements théoriques, dans les paragraphes I et II de la publication reproduite ci-après. Nous nous contenterons ici d'en rappeler les caractéristiques principales.

On distingue généralement, deux types d'études :

1) L'étude du détail des seuils de photoionisation d'une couche électronique profonde sur un court domaine d'énergie (environ 50 eV) est aujourd'hui désignée par l'acronyme anglo-saxon XANES (X-ray Absorption Near Edge Structure). La zone XANES comprend les processus d'excitation électronique vers des états liés ainsi que les processus qui ont lieu tout de suite après le seuil de photoionisation appelés "régime de diffusion multiple résonnant dans le continuum". Elle est sensible à la structure électronique locale de l'atome cible, et à l'organisation des atomes jusqu'à moyenne distance autour de l'atome absorbant. Le volume d'espace exploré est gouverné par le libre parcours moyen du photoélectron, qui peut atteindre quelques dizaines d'angströms dans cette région. Lorsque l'onde du photoélectron se propage à travers le matériau, elle est diffusée élastiquement et de façon multiple par les potentiels atomiques des atomes environnants. Chacun des ces événements introduit pour cette onde un déphasage qui dépend de l'énergie. Des interférences constructives ou destructives peuvent alors se produire, donnant naissance à des pics ou des creux sur le spectre XANES.
Les spectres XANES des monocristaux et des échantillons orientés sont sensibles à l'orientation du cristal par rapport à la direction du vecteur de polarisation. Cette dépendance angulaire est la caractéristique d'un effet plus général nommé dichroisme linéaire X (**X**-ray **L**inear **D**ichroism). L'apparition de sources intenses de rayons X polarisés circulairement a permis, en 1987, la mesure du dichroisme circulaire magnétique, XMCD (**X**-ray **M**agnetic **C**ircular **D**ichroism) et dix années plus tard, la mesure du dichroisme circulaire naturel XNCD (**X**-ray **N**atural **C**ircular **D**ichroism). Les mesures XMCD intéressent les matériaux ferromagnétiques et se rapportent, pour un échantillon placé dans un champ magnétique externe orienté suivant la direction de propagation du rayonnement incident, à la différence existant entre les sections efficaces d'absorption des rayons X polarisés circulairement à gauche ou à droite. Cet effet est plus intense aux seuils L des métaux de transition, qu'au seuil K. Cette technique permet, en utilisant les règles de somme magnéto-optique, de séparer les contributions des moments orbital et de spin de l'atome absorbeur.

Les signaux XNCD, plus faibles que les signaux XMCD, sont obtenus, eux aussi, en mesurant la différence entre les sections efficaces d'absorption des rayons X polarisés circulairement à gauche et à droite. Cet effet, qui a été mis en évidence pour le première fois en 1997 par J.Goulon et coll. sur des cristaux gyrotropes, est sensible à la configuration absolue d'un site absorbant chiral (cf. Troisième partie de ce mémoire).

D'une manière générale, il est nécessaire de conduire des modélisations *ab initio* afin de pouvoir extraire des informations quantitatives des spectres XANES, XMCD ou XNCD.

2) L'étude des oscillations de Kronig[1], découvertes au début de ce siècle, qui perturbent les spectres d'absorption sur plus de 1000 eV au-delà du seuil de photoionisation d'une couche profonde, est connue maintenant sous l'acronyme EXAFS (Extended X-ray Absorption Fine Structures). La zone de l'EXAFS comprend essentiellement des processus de diffusion simple. Stern et coll.[2] ont montré qu'il est possible d'extraire de ces oscillations, la distribution radiale des atomes constituant le proche environnement de l'atome absorbeur, et de mesurer avec une précision de l'ordre de 0.02 Å les premières distances inter-atomiques. L'atome absorbeur joue le rôle de sonde structurale locale très sélective puisque les seuils de photoionisation des éléments du tableau périodique sont caractéristiques d'un élément donné. L'énergie cinétique du photoélectron étant plus grande que dans la region du seuil et son libre parcours moyen est plus faible[3]. En effet, il n'excède pas 50 Å pour une valeur de l'énergie cinétique du photoélectron comprise entre 10 et 1000 eV. Ainsi les oscillations d'un spectre EXAFS résultent principalement de la diffusion simple de l'onde du photoélectron sur les atomes voisins.

L'EXAFS est devenu une technique très populaire car il ne nécessite pas la préparation de monocristaux stables. En fait, on peut enregistrer le spectre EXAFS d'un échantillon se présentant sous la forme d'une solution ou d'une poudre.

L'excitation d'un électron d'une couche de coeur se solde par la création d'une lacune électronique profonde: une telle configuration électronique est très instable et va relaxer vers un état d'équilibre par des mécanismes secondaires, qui peuvent être soit radiatifs (fluorescence des rayons X), soit non radiatifs (Auger, Coster-Kronig).
L'émission de fluorescence X permet de transférer la lacune d'une couche de coeur vers une couche moins profonde, puis en cascade vers les niveaux de valence, avec émission d'un photon de fluorescence.
Les transitions bi-électroniques de type Auger ou Coster-Kronig consistent à substituer deux lacunes moins profondes à la lacune initiale, et s'accompagnent de l'éjection d'un électron des couches externes.

Tous les spectres présentés dans le cadre de ce mémoire ont été enregistrés sur la ligne de lumière ID-12A par détection de l'émission secondaire de fluorescence X. En effet,

---

[1] Kronig, R. de L.; *Zs. f. Phys.*, **1931**, *75*, 317
[2] Stern, E.A.; *Phys. Rev. B* **1974**, *10*, 3027.
[3] La variation du libre parcours moyen en fonction de l'énergie est donnée par: $\lambda(E) = 2\hbar\ (2E/m)^{1/2}/\Gamma(E)$, $\Gamma(E)$ étant la largeur du trou profond (d'autant plus faible que l'élément considéré est léger).

cette technique de détection offre un gain spectaculaire de sensibilité pour étudier des échantillons dans lesquels l'élément absorbeur est dilué dans une matrice d'éléments légers ou de solvant, par rapport aux expériences de transmission conventionnelles, ou pour détecter les signaux très faibles de dichroisme circulaire naturel. Notons aussi que cette technique de détection s'est révelée fondamentale pour les investigations structurales des échantillons biologiques.

Il est important de souligner que la sensibilité de détection par fluorescence X des spectres d'excitation X n'est pas uniforme pour tous les seuils. Le rendement quantique de fluorescence varie. En effet, pour les éléments légers, l'émission de fluorescence X ne constitue pas le mécanisme de relaxation prépondérant, d'autre part en dessous de 4 keV, l'absorption propre de la matrice devient très importante et réduit d'autant l'intensité du signal de fluorescence. C'est pourquoi, il est nécessaire d'appliquer systématiquement à tous les spectres la correction homographique de fluorescence proposée par J. Goulon[4] afin de pallier à ces inconvénients.

1.1.2 La ligne de lumière ID-12A

Un schéma général de la ligne de lumière ID-12A est représenté ci-dessous :

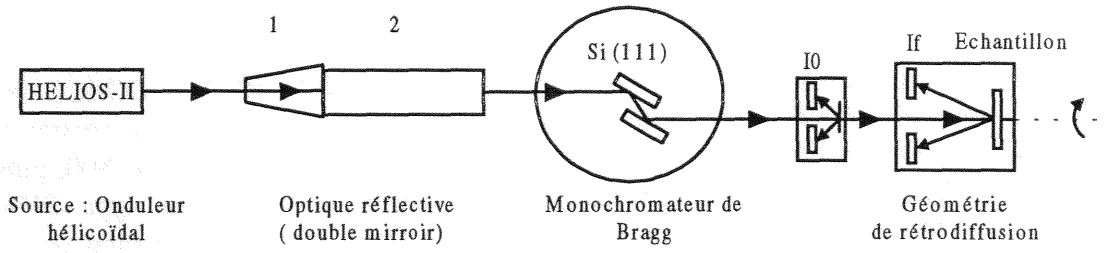

C'est une ligne de lumière opérant sans fenêtre, sous ultra-haut-vide. Elle a été conçue pour enregistrer des spectres d'absorption de rayons X de haute qualité. Elle est constituée de :

- La source de lumière Helios-II qui est un onduleur hélicoidal qui fonctionne dans la gamme d'énergie 2 keV-15 keV. Il délivre une lumière polarisée circulairement (droite ou gauche) ou linéairement.
- Un dispositif d'optique réflective utilisée pour réduire l'amplitude des harmoniques d'un facteur 5 par rapport à la fondamentale, et pour diminuer la charge thermique sur le monochromateur.
- Le monochromateur à sortie fixe est équipé d'une paire de cristaux Si (111) refroidis à 152K pour minimiser la déformation thermomécanique du premier cristal.
- Les spectres sont enregistrés dans le mode fluorescence. Les détecteurs utilisés pour mesurer les intensités I0 (référence) et If (fluorescence de l'échantillon) sont des photodiodes de silicium (P+NN+), opérant en mode photovoltaïque et en géométrie de rétrodiffusion, et disposées symétriquement par rapport au plan vertical. Pour améliorer les performances, le nombre des détecteurs de la chambre de fluorescence a été porté de quatre à huit. Les programmes de traitement des données tiennent compte de cette évolution. La détection de fluorescence dans

[4] Goulon,J; Goulon-Ginet, Ch.; Cortès, R.; Dubois, J-M; *J. Phys. France* **1982**, *43*, 539-548.

l'aimant supraconducteur de 7 T utilisé pour les expériences de XMCD, est réalisée par une seule photodiode de silicium en raison du peu d'espace disponible à l'intérieur de cet aimant.

1.1.3 Traitement des données

Le paragraphe III de la publication 1.2 rappelle quelles sont les techniques numériques que l'on peut mettre en oeuvre pour extraire des spectres EXAFS ou XANES, les informations structurales recherchées: transformée de Fourier, maximisation d'entropie, ...etc... Les exemples qui illustrent ce paragraphe ont été choisis dans la chimie des porphyrines. Les méthodes d'analyse différentielle dont nous avons fait grand usage pour étudier les interactions entre l'ozone et les dérivés porphyriniques de manganèse (cf. Deuxième partie de ce mémoire) y sont présentées et discutées.

C'est au niveau de l'analyse des données que se situe notre contribution personnelle aux autres projets auxquels nous avons été associés et qui sont présentés dans les parties III et IV du manuscrit. C'est pourquoi nous allons décrire succinctement les codes que nous avons été amené à modifier ou à développer.

Les programmes utilisés pour analyser les spectres XANES, EXAFS, XMCD ou XNCD sont écrits en FORTRAN77, norme ISO 1539:1980. Une première version a été réalisée pour être utilisée sur une station de travail de type HP9000 série 800, puis a été modifiée pour être exploitable sur une station de travail de type SUN ENTERPRISE E-450. Ils sont tous dotés d'une interface graphique. Certains codes tels que X1, X2 et X6 développés par J. Goulon et coll. depuis 1976 ont été adaptés aux systèmes d'exploitation actuels.

- X1 : Il regroupe les fonctions de préparations des données (normation, correction homographique de fluorescence), d'extraction des oscillations EXAFS, et permet d'en calculer la transformée de Fourier optique corrigée des déphasages et amplitudes de rétrodiffusion pour la première couche.

- X0 : Ce code a été conçu pour analyser les spectres EXAFS en utilisant la méthode de maximisation d'entropie. Il reprend les fonctions de préparation des données et d'extraction des oscillations EXAFS du code X1. Il permet de corriger ces oscillations des déphasages et amplitudes de rétrodiffusion. A ce point il permet, soit de calculer la transformée de Fourier optique comme le fait le code X1, soit de calculer la fonction d'autocorrélation et d'en calculer la transformée de Fourier pour obtenir le spectre de puissance de la densité spectrale autocorrélée, ou d'analyser le spectre d'autocorrélation avec la méthode de maximisation d'entropie. En effet, les oscillations EXAFS sont, le plus souvent, analysées comme un signal déterministe noyé dans un bruit qui est considéré comme stationnaire et ergodique. Selon Wold[5], un signal déterministe peut être transformé en un processus

[5] Wold,H. *A study in the analysis of stationary time series*, Ph. D. Thèse de l'université de Stockholm (2nd edition par Almqvist et Wiksell: Uppsala, 1954).

stationnaire en le convoluant avec un bruit blanc d'une unité de densité spectrale. Le but prioritaire étant d'extraire des oscillations EXAFS, la distribution radiale des atomes diffuseurs, nous devons donc transformer les oscillations EXAFS en un processus quasi-stationnaire dans l'espace des moments de transfert. Cela est fait en corrigeant les oscillations EXAFS des déphasages et amplitudes de rétrodiffusion. Nous pouvons accéder à la fonction d'autocorrélation, ainsi qu'à sa transformée de Fourier, après avoir introduit une fenêtre de Kaiser-Bessel afin de minimiser les lobes secondaires dans l'espace des distances (R). La transformée de Fourier des oscillations EXAFS et la transformée de Fourier de la fonction d'autocorrélation sont reliées par le théorème de Wiener-Khinchin. Le spectre de puissance de la densité spectrale autocorrélée permet (i) d'avoir une meilleure résolution que le spectre de puissance de la transformée de Fourier, (ii) de détecter plus facilement toute décomposition de l'échantillon car dans ce cas le processus n'est plus stationnaire, et le spectre de puissance de la densité spectrale autocorrélée montre de grandes distorsions, (iii) de détecter la présence de diffuseurs lourds car dans ce cas encore, la condition stationnaire n'est plus valide. Un signal stationnaire peut être analysé avec les ressources du filtrage linéaire par les 'Méthodes de Maximisation d'Entropie'. Ces méthodes sont séduisantes car elles permettent d'avoir des pics extrêmement fins qui ne sont plus contaminés par la présence de lobes secondaires comme dans le cas des spectres de transformée de Fourier avec fenêtre. Les limitations de cette méthode sont les suivantes : (i) il n'existe pas de critère général pour choisir la longueur du filtre de prédiction d'erreur, (ii) un découplage ou un déplacement artificiel des pics peut être observé dans le cas de données bruyantes si le filtre de prédiction d'erreur est sur-dimensionné.

- X6 : Ce code est utilisé pour affiner les analyses EXAFS, notamment pour déterminer la longueur du chemin de diffusion, le nombre d'atomes d'une couche, et pour en caractériser le désordre structural. Principalement, il se compose de la bibliothèque de fonctions d'optimisation MINUIT[6] développée par le CERN.

- X2 : C'est le code utilisé pour réaliser les analyses différentielles des spectres EXAFS. La partie du programme consacrée à l'analyse différentielle avec perturbations structurales a été intensivement utilisée lors de l'étude des métallo-porphyrines. En effet, dans le cas idéal, les signatures caractéristiques du macrocycle des porphyrines peuvent être éliminées et le spectre de différence est alors dominé par la contribution des ligands axiaux. On peut alors simuler les signatures des ligands axiaux, avec une réduction considérable du nombre de paramètres et de corrélations. De plus, dans l'analyse différentielle avec perturbation structurale, le déplacemant axial du ligand n'est pas calculé par triangulation mais résulte de transformations géométriques optimisées qui affectent tous les atomes du macrocycle. Cette méthode permet d'identifier les ligands axiaux et de détecter des distortions structurelles significatives du macrocycle. Néanmoins, cette méthode ne peut s'appliquer que lorsque deux composés sont constitués d'au moins une partie identique contribuant au champ de ligand, et ne peut être utilisée pour une étude *ex nihilo*. La pureté et la stabilité chimique du composé modèle est aussi un point à ne pas négliger. D'autre part, les procédures d'extraction du fond

---

[6] James, F.;Roos,M.; *MINUIT: A system for minimizing a function of n parameters and computing the errors and correlations*; CERN computer center program library: Genova, **1974**, D506-516.

continu et de pré-normalisation sont aussi des points critiques, tout autant que le rapport signal sur bruit des données expérimentales.

- DICHRO : Les résonances de pré-seuil ont une mauvaise résolution en énergie à cause de l'élargissement dû (i) à la courte durée de vie du trou profond, (ii) à la résolution du monochromateur. De ce fait, il est difficile de quantifier la séparation en énergie des états liés. Afin d'améliorer la résolution en énergie du spectre XANES, il est nécessaire de le déconvoluer par un profil de Voigt. Le logiciel DICHRO déconvolue les spectres XANES en utilisant une approximation numérique du profil de Fano-Voigt proposée par Teodorescu[7] et coll.. En outre, il permet de caractériser les résonances de pré-seuil en donnant leurs positions en énergie, leurs largeurs à mi-hauteur, et leurs amplitudes en simulant ces signatures. La simulation utilise la bibliothèque de fonctions MINUIT. Ce logiciel permet aussi de normer les spectres et d'appliquer la correction homographique de fluorescence. Ce programme est aussi utilisé pour analyser les spectres XMCD.

- CRYSTAL : Il est utilisé pour analyser les spectres de cristaux biaxiaux enregistrés en rotation axiale (rotation autour de son axe optique) pour des valeurs discrètes de l'énergie ou, à l'inverse, pour analyser les spectres de cristaux biaxiaux enregistrés par balayage du domaine d'énergie pour une position fixe du cristal. Avant tout traitement, les spectres sont normés et on applique la correction homographique de fluorescence. Il permet de calculer les moments spectraux à l'aide des coefficients de Fourier pour l'analyse des spectres XNCD et XNLD. Des procédures spécialisées ont été écrites afin de normer, lisser et accumuler les spectres de dichroïsme enregistrés, pour un même échantillon, lors d'expériences différentes que l'on souhaite additionner pour améliorer le rapport signal sur bruit.

En plus de ces programmes d'analyse de données, nous avons utilisé le programme CONTINUUM. Ce programme a été développé par Natoli et coll.[8], au début des années 80 pour calculer les spectres d'absorption théoriques de rayons X dans la région proche du seuil. La méthode utilisée est basée sur la théorie de la diffusion multiple totale (paragraphe II de la publication 1.2) .Voici une présentation succincte de la méthode retenue pour effectuer une simulation de spectre XANES :
Avant de résoudre les équations de la diffusion multiple, il faut construire le potentiel moléculaire qui rend compte du cluster d'atomes, en suivant les prescriptions de Mattheiss[9]. A partir des fonctions d'ondes atomiques autocohérentes d'atomes neutres tabulées, on calcule les densités de charges atomiques. Ensuite, la résolution de l'équation de Poisson conduit au potentiel électrostatique de chaque atome. Le potentiel moléculaire résulte de la superposition de ces derniers dans tout l'espace. Les densités de charge et les potentiels sont limités dans des sphères atomiques dont les rayons ("rayons de muffin-tin") sont déterminés par le critère de Norman[10]. Enfin, pour rendre compte des interactions multiélectroniques, on ajoute au potentiel moléculaire

---

[7] Teodorescu, C.M.;Esteva, J.M.;Karnatak, R.C.;El Alif, A. *Nucl. Instr. Meth. Phys. Res. A* **1994**, 345, 141-147.
[8] Natoli C.R.; Misemer D.K.; Doniach S.;Kutzler, F.W. *Phys. Rev.* **1980**, A22,1104.
[9] Mattheiss, L. F.; *Phys Rev.* **1964**, *133*, A1399-A1403; *ibid.* **1964**, *134*, A970-A973.
[10] Norman, J.G.; *J. Mol. Phys.* **1976**, *31*, 1191-1198.

un terme d'échange et de corrélation, qui peut être de type Xα[11], de type Dirac-Hara[12] ou de type Hedin-Lundqvist[13]. Dans notre cas, nous avons utilisé le terme d'échange et de corrélation Xα. Le potentiel étant déterminé, le programme calcule la section efficace d'absorption pour chaque énergie des photons incidents. C'est cette approche dite *extended continuum MSW-Xα* qui a été utilisée afin de simuler les spectres XANES des métalloporphyrines.

Nous avons aussi utilisé le programme MSXAS[14], développé au sein du laboratoire de Chimie Théorique de Nancy, par M.F. Ruiz-Lopez et F. Bohr. Ce logiciel est un ensemble de programmes pour le calcul théorique des spectres d'absorption EXAFS. Il est principalement basé sur le modèle Xα en onde diffuse de Slater, mais il peut utiliser plusieurs approximations locales pour le potentiel d'échange-corrélation. Il calcule d'abord le potentiel moléculaire et les matrices de déphasages atomiques, pour l'ensemble des atomes du cluster en tenant compte des propriétés de symétrie moléculaire. Les "rayons de muffin-tin" sont déterminés grâce au critère de Norman, et en outre ce programme réserve le choix entre trois potentiels d'échange-corrélation (Xα, Hedin-Lundqvist, Dirac-Hara). Ensuite, le coefficient d'absorption pour un seuil donné est calculé avec l'approche de diffusion multiple. Les contributions des chemins de diffusion du photoélectron au spectre EXAFS peuvent être calculées pour tout ordre et pour tout arrangement atomique, mais des algorithmes spécifiques sont utilisés afin d'accélérer le calcul[15]. Ce programme a déjà permis de simuler le spectre EXAFS de porphyrines de fer; c'est pourquoi, il nous a semblé adapté à notre problème.

En résumé, nous dirons que l'analyse des spectres XANES a pu être faite grâce aux logiciels DICHRO et CONTINUUM, et que l'analyse des spectres EXAFS a requis l'utilisation les codes X0, X1, X2, X6 et MSXAS. Les spectres XNCD et XNLD ont été analysés avec le logiciel CRYSTAL.

1.2 Publication

---

[11] Slater, J.C.; *The self-consistent field for molecules and solids*, vol. IV, Mc Graw-Hill, New-York, **1974**.

[12] Hara, S.;*J. Phys. Soc. Japan.*, **1967**, *22*,710.

[13] Hedin, L.; Lundqvist, B.I.; *J.Phys. C: Solid State Phys.*, **1971**, *4*, 2064.

[14] Ruiz-Lopez, M.F.; Bohr, F.; Filiponi, A.; Di Cicco, A.; Tyson, T.; Benfatto, M.; Natoli, C.R.; *MSXAS: A system of programs for X-ray Absorption Spectra Calculations Using the Multiple Scattering Approach*, in: *X-ray Absorption Fine Structure VII*; Hasnain, S.S.; Ed., Ellis-Horwood,; **1991**,p 75-77.

[15] Bohr, F.; Ruiz-Lopez, M.-F.; *Chem. Phys.*, **1991**, *156*, 55

X-RAY ABSORPTION SPECTROSCOPY APPLIED TO PORPHYRIN CHEMISTRY

José GOULON , Chantal GOULON-GINET[1]
and Vincent GOTTE
European Synchrotron Radiation Facility,
F-38043 Grenoble Cedex,

[1]Also: Faculté de Pharmacie, Université de Grenoble, Domaine de La Merci, F-38700 La Tronche

Contents

I. SCOPE OF XAS *TODAY*

X-Ray Absorption Spectroscopy (XAS) is concerned with the excitation of electronic transitions from atomic deep core states (K shell for $1s$ electrons, L shells for $2s, 2p$ electrons...)[1] Typically, X-ray absorption spectra exhibit a series of well separated (K, L...) absorption edge singularities at energies which are characteristic of a given element: this is this *element specificity* which makes XAS such an attractive tool in structural chemical physics. For many years, XAS has been a rather obscure field of research which had a marginal impact on materials science compared to X-ray diffraction techniques. With the availability of intense synchrotron radiation sources, the past decades have seen a rebirth of the interest in XAS and an exponentially growing list of applications in inorganic and organometallic chemistry, biochemistry and geochemistry, catalysis and surface sciences, magnetism and crystal optics. Several of these subjects have already been covered by recent books[2–4] but new methods are still emerging which should allow one to extract more and more information out of X-ray absorption spectra: this is opening enough space for the present review in which we want to emphasize the important developments associated with the construction of new X-ray sources of unprecedented spectral brilliance and which offer the advantages of an improved overall stability, a full control of the polarization of the emitted photons and a clean time structure.

A. XANES and Polarization Effects

In the very close vicinity of the edge singularity, one may often observe a series of poorly resolved *resonant structures* which are called *X-ray Absorption Near Edge Structures* (XANES).[5–7] As a matter of illustration, we have reproduced in **Figure 1** the chlorine K-edge and the tin L-edge XANES spectra of (OEP)$SnCl_2$, *i.e.* the dichlorotin (IV) complex of the 2,3,7,8,12,13,17,18-octaethylporphyrinato dianion hereafter denoted (OEP).

Some of these resonances may be quite sharp and intense, especially in the soft x-ray range. This explains why they are still often called "*white lines*" by reference to the early days of XAS, *i.e.* when the spectra were recorded on photographic plates.[8] XANES are sensitive finger prints of the local electronic

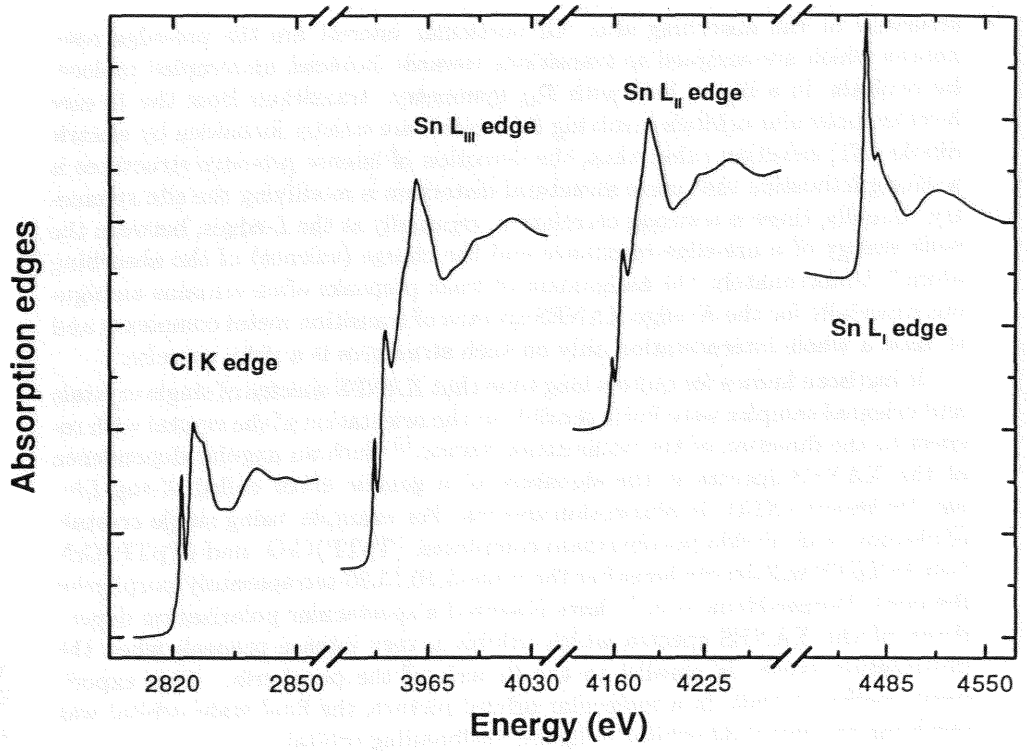

Figure 1: Multi-edge XANES spectra of (OEP)$SnCl_2$

structure at the absorbing site. Of particular interest are the pre-edge resonances which are assigned to transitions towards *localized*, unoccupied molecular orbitals. In a ligand field with $\mathcal{D}_{4h}$ symmetry, transitions from the $1s$ core level to molecular orbitals involving $3d$ orbitals are strictly forbidden by electric dipole ($E1$) selection rules: thus, the detection of intense pre-edge structures is a strong indication that some structural distortion is modifying the site symmetry. Usually, there is a strong correlation, especially at the L-edges, between the peak energy of a pre-edge resonance and the charge (valence) of the absorbing atom.[9] Unfortunately, the assignment of weak prepeaks often remains ambiguous especially for the K-edge XANES spectra of transition metal complexes and to base a whole interpretation only on such structures is a risky exercise.

It has been known for quite a long time that XANES spectra of single crystals and oriented samples were fairly sensible to the orientation of the crystal with respect to the direction of the polarization vector.[10] Such an angular dependence of the XANES spectra is the signature of a generic effect called *X-ray Linear Dichroism* (XLD) in absorption spectra. For example, using single crystals of chromyl and nitrido porphyrinato complexes: (TpTP)CrO and (TpTP)CrN (where TpTP will denote hereafter the *meso*-5,10,15,20-tetraparatolylporphyrinato dianion), Penner-Hahn *et al.*[11] have observed a spectacular polarization dependence of the XANES spectra which exhibit a very intense prepeak when the polarization vector is parallel to the $\mathcal{C}_4$ axis of the porphyrin. This experiment confirmed that, in a molecular orbital picture, the final state orbital was involving the metal $3d$ orbital + ligand antibonding orbital.

With the recent availability of intense sources of circularly polarized X-rays, *circular dichroism* (CD) has also been detected:

- The story started in 1987 with the discovery of a very weak *X-ray Magnetic Circular Dichroism* (XMCD) at the K-edge of iron metal.[12] Shortly later, it was observed that XMCD could be quite strong at the L-edges of ferromagnetic transition metals.[13,14] This new technique attracted much attention when it was realized that, using *magneto-optical sum rules*, one could disentangle the respective contributions of the *orbital* and *spin* moments carried by the absorbing atom.[15,16] Materials which have a large magnetic anisotropy and in which one expects a large orbital moment are obviously the best candidates for such studies:[17,18] this should be the case of molecular magnets based on organometallic complexes. For what concerns $3d$ transition metal complexes, L-edge XMCD has already been a very valuable source of information on the interplay between the ligand field splitting ($10Dq$) and the metal spin-orbit coupling parameters in the $2p$ or $3d$ states.[19,20] It is noteworthy that L-edge XMCD has even been detected in the magnetically aligned paramagnetic phase of metalloproteins such as *Pyrococcus furiosus* rubredoxin[21] or ferredoxin[22] and related complexes.[23]

- X-ray *Natural* Circular Dichroism (XNCD) was reported for the first time in 1998 by Goulon *et al.*[24] It has been firmly established that this effect was due to the $E1.E2$ rotatory strength involving cross terms between electric dipole ($E1$) and electric quadrupole ($E2$) transition matrix elements. This is different from what is observed in the UV-visible spectral range where CD is primarily caused by the Rosenfeld-Condon rotatory strength

$E1.M1$ which is coupling the electric and the magnetic dipole ($M1$) transition matrix elements. Unfortunately, the origin of XNCD implies that it can only be detected in gyrotropic *single crystals* or at least in systems featuring some *partial orientational order*. Whenever it is observed, XNCD is sensitive to the *absolute configuration* of a chiral absorbing site and also carries element specific information on the *mixing of orbitals of even and odd parity* at this site.[25]

Let us make clear that XNCD has not yet been detected in any chiral metalloporphyrin complex. To the best of our knowledge, there are still very few XMCD studies concerned with metalloporphyrins. This is not too surprising because porphyrinic complexes of $3d$ transition metals suffer from a triple handicap: (*i*) high quality L-edge spectra are not easy to obtain in the soft x-ray range because the ligand contributes to a strong background absorption and long data acquisition times are hardly compatible with the severe radiation damages most often experienced by organometallic complexes in the soft x-ray range; (*ii*) XMCD signals are very weak at the K-edge due to the lack of spin-orbit coupling in the core state; (*iii*) the spin ordered low temperature phases are often *antiferromagnetic* so that the XMCD signal vanishes. Rare earth compounds but also $4d$ or $5d$ transition metal complexes are definitely more propitious systems to detect XMCD. As an illustration, we have reproduced in **Figures 2** the $L_{II,III}$ edge XANES and XMCD spectra of a bimetallic porphyrin complex of gadolinium. In this complex formally denoted (DPA)[Gd(OH)]$_2$, the dimeric moiety [Gd(OH)]$_2$ is expected to be trapped by a *cofacial* bis-porphyrin ligand denoted for shortness DPA where DPA^{4-} = 1,8-bis[5-(2,8,13,17-tetraethyl-3,7,12,18-tetramethyl)porphyrin] anthracene. The synthesis and the characterization of the porphyrin free base has been described elsewhere.[26] It was postulated that the latter bis-gadolinium complex had some structural analogy with the bis-lutetium dimer for which a crystal structure is known.[27] Note that the XANES and XMCD spectra reproduced in **Figures 2** were recorded in the low temperature paramagnetic phase (T = 10 K) under a strong magnetic field ($B \geq 5$ T). As illustrated by **Figures 2**, the normalized intensity of the XMCD signal exceeds 14% (peak-to-peak) at the L_{II} edge and confirms that spin-dependent effects are not marginal in XAS as thought still a few years ago. We will show in section II.D.4 that this large effect is related, to some extent, to the spin polarization of the $5d$ orbitals and $2p$ inner shell orbitals of gadolinium by the valence $4f$ electrons while superexchange may also imply the spin polarization of the orbitals of the hydroxy groups.

In general, XANES and XMCD suffer from a common handicap: *quantitative* information can hardly be extracted without conducting *ab initio* modellizations. We expect such analyses to be routinely performed in the forthcoming years 2000.

B. EXAFS, MEXAFS

On the high energy side of an absorption edge singularity, one may observe *damped* oscillatory structures now commonly referred to as "*Extended X-ray Absorption Fine Structures*" (EXAFS).[8] These structures were discovered by R. de L. Kronig early in this century[28] but their potentiality as a structural tool was recognized only 25 years ago by Stern and his colleagues.[29,30] EXAFS have

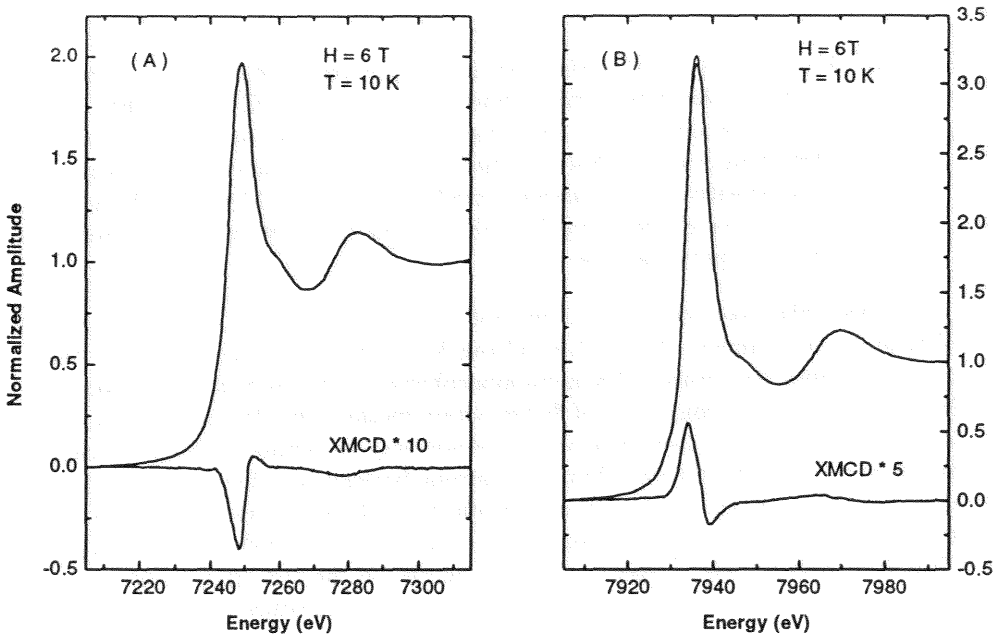

Figures 2: Gadolinium L-edge XANES and XMCD spectra of the bimetallic complex $(DPA)[Gd(OH)]_2$.

Figure 2A : L_{III}-edge XANES and XMCD spectra.

Figure 2B : L_{II}-edge XANES and XMCD spectra.

a simple origin: the photoionization of a core state produces a photoelectron represented as an *outgoing spherical wave* interfering with the *backscattered* waves resulting from the interaction of the photoelectron with the surrounding atoms. A "*standing wave system*" is developing which depends on the magnitude of the photoelectron wavevector **k** (*i.e.* on the fraction of the absorbed energy which is converted into kinetic energy transferred to the photoelectron) and on the interatomic distance R_j. Increasing the energy of the incident X-ray photon will change k and thus will perturb the photoelectron standing wave system: this causes oscillations of the absorption cross section which varies as a sinus function of the argument kR_j. A Fourier analysis of the EXAFS oscillations in the momentum space can then probe the radial distribution of the atoms surrounding the absorbing center: this is precisely the basis of modern EXAFS studies as pioneered by Stern *et al.*[30] There is some analogy between EXAFS and *electron scattering,* the main difference being that, in EXAFS, the electrons are generated *in situ* by photoionization of a core level. Comparing EXAFS with photoelectron diffraction would reveal a major simplification: in EXAFS one is concerned only with *closed scattering paths* beginning from, and ending at the photoabsorbing site (o) because one is measuring the X-ray absorption cross section with the initial state *fully localized* at site (o). This is precisely this peculiarity which entails the remarkable site specificity of EXAFS.[31]

In the case of metalloporphyrins, EXAFS oscillations may be detected (in favorable cases) up to 2000 eV above the metal edge. Their relative magnitude, however, never exceeds a few percent of the pure atomic background absorption. As a matter of illustration we have reproduced in **Figure 3** the vanadium K-edge EXAFS spectrum of (TPP)VO, *i.e.* the vanadyl *meso*-5,10,15,20-tetraphenylporphyrinato complex. The latter spectrum was recorded at low temperature (T=10 K) for reasons which will become clear later. EXAFS oscillations are unambiguously detectable over a momentum range as large as $\Delta k = 21$ Å^{-1}. We will show in section III.A.2 that extremely accurate interatomic distances can be extracted from such spectra. What contributed to make EXAFS a popular technique is certainly the fact that *no single crystal is required* and that *basic* EXAFS spectra can be recorded in solution as well as in powdered samples.

For single crystals, aligned Langmuir-Blodgett films, or any type of oriented samples, more information can be obtained because the EXAFS spectra are sensible to the orientation of the sample with respect to the direction of the polarization vector.[10] As regards oriented metalloporphyrins, *Linear Dichroism* in EXAFS spectra can be exploited to better identify the signatures of the axial ligands which, very often, interfere with the signatures of the four nitrogen atoms of the macrocyclic ligand. Similarly, X-ray magnetic circular dichroism can extend as well as Linear Dichroism in the EXAFS regime, at least for ferromagnetic materials. To date, we are not aware of any paper reporting a successful *Magnetic-EXAFS* (MEXAFS) study on a metalloporphyrin complex. In the case of the aforementioned binuclear gadolinium DPA complex, a very weak MEXAFS signal was detected which seems to support the initial guess that the complex was dimeric with a Gd...Gd intramolecular distance of the order of 4.2 Å.[32] Severe radiation damages, unfortunately, prevented us to refine the MEXAFS spectra over long data acquisition times. This very preliminary experience suggests that, with improved instrumentation resulting in shorter

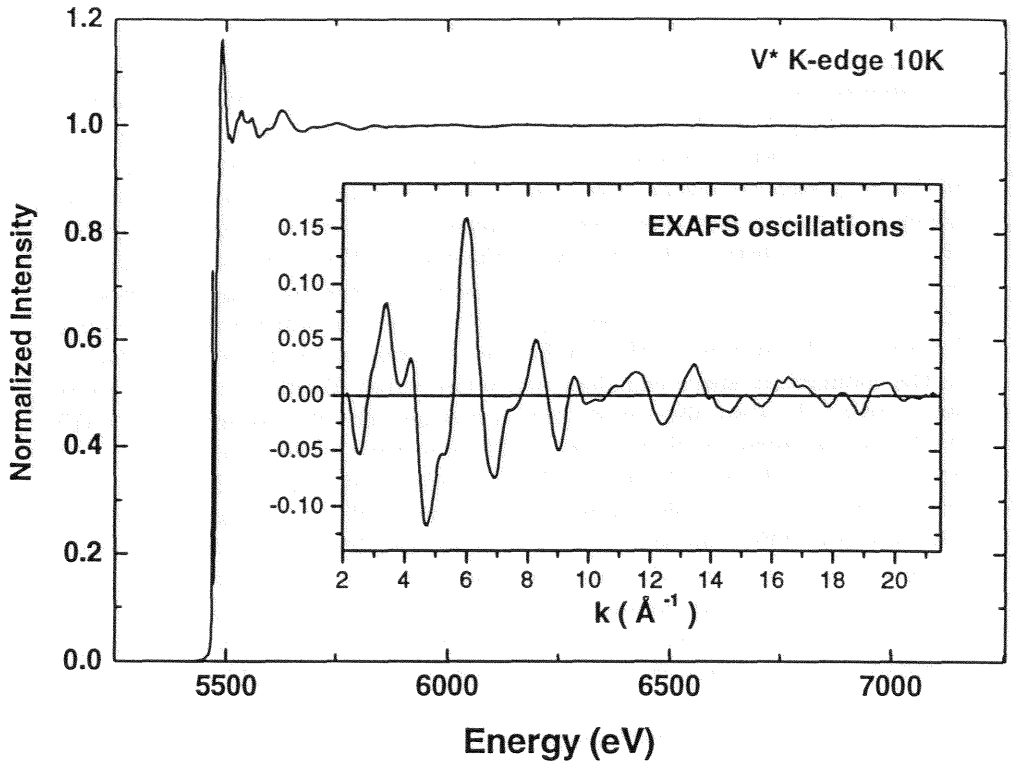

Figure 3: Vanadium K-edge EXAFS spectrum of (TPP)VO . The experimental data were collected at the ESRF from a powdered sample kept at low temperature (T = 10 K).

data acquisition times, one should be able to record useful MEXAFS spectra of organometallic systems in their paramagnetic phase.

C. Fluorescence Detected X-ray Excitation Spectra

There is an essential by-product in the photoionization of a core state: a deep core hole is created which will relax either by *radiative* (X-ray fluorescence) or *non-radiative* (Auger, Coster-Kronig or super Coster-Kronig) decay channels. In the former case, the inner core hole is filled with an electron of an outer shell with the spontaneous emission of an X-ray fluorescence photon. In the alternative option, the inner core hole is still filled with an electron of a higher shell (Auger process) or of another subshell (Coster-Kronig process), but the excess energy is now released by ejecting another electron from an outer shell. In this chapter which is concerned with applications of XAS to metalloporphyrin chemistry, we will concentrate exclusively on the radiative process. What is most easily measured is the *total fluorescence yield*, *i.e.* the total intensity integrated over the whole emission spectrum. As far as one admits that the quantum yield of fluorescence does not vary with the energy of the exciting photons, monitoring the total fluorescence yield as a function of the energy of the exciting photons is an indirect way of measuring the absorption cross section since what is measured is *the probability of creating an inner core hole*. There is, however, a tremendous advantage in measuring "*Fluorescence Detected*" XANES or EXAFS spectra in the case of *dilute samples*: since there is no detectable fluorescence emission associated with the absorption by the solvent or by any low-Z matrix element, there is a spectacular gain in the signal-to-noise ratio compared to conventional transmission experiments where the spectra are primarily dominated by the strong background absorption of the solvent and low-Z elements.[33,34] This technique has proved to be of fundamental importance for structural investigations of biological samples such as hemoproteins in solutions or for the structural characterization of trace amounts of nickel or vanadyl porphyrins in heavy crude oils as discussed in section IV.

D. Resonant X-ray Emission Spectroscopy

With the recent availability of powerful third generation synchrotron radiation sources, even more ambitious experiments became feasible, at least on concentrated metalloporphyrin samples. Instead of measuring the total fluorescence yield, one may try to use a crystal analyzer to resolve in energy the fluorescence emission and record "*Resonant X-ray Emission Spectra*" (RXES) with a high energy resolution.[35–38] Obviously, such experiments require high brilliance X-ray sources because:

- the primary monochromatic X-ray beam has to be refocused on a small spot at the sample in order to optimize the energy resolution of the crystal analyzer;
- the counting rate in the monochromatic emission channel is usually very low because the angular acceptance of the analyzer is extremely small.

In this experimental configuration, the Kramers-Heisenberg inelastic scattering picture of "*one photon-in, one photon-out* " is getting more appropriate to describe the complex spectroscopic process that is developing. The initial state consists of an absorbing atom in state $|a\rangle$ and an incoming X-ray photon $|\mathbf{e}_1, \mathbf{q}_1\rangle$ with energy $\hbar\omega_1$; the final state is to be described with the same atom in state $|b\rangle$ and an outgoing X-ray photon $|\mathbf{e}_2, \mathbf{q}_2\rangle$ with energy $\hbar\omega_2$. New effects are expected to take place in the "*Resonant Inelastic X-ray Scattering*" (RIXS) regime alternatively called "*X-ray Resonant Raman*" (XRR) regime: when $|\omega_1 - \omega_2|$ is getting "*small enough*" and when the final state is still an excited bound state, varying the excitation energy $\hbar\omega_1$ will make it possible to record pre-edge resonant structures *with an enhanced resolution* compared to what is measured in conventional XANES spectra.[39] In these recent years, this new technique has attracted much interest with the hope that it could help in refining the assignment of the pre-edge resonances observed in the XANES spectra. It was soon realized that the interpretation of XRR spectra was not as straightforward as anticipated by the promoters of this technique which, nevertheless, can yield extremely useful additional information. Most exciting, in our opinion, is the exploitation of the well resolved $K_{\beta'}$ satellite of the $K_{\beta 1,3}$ fluorescence lines in high-spin manganese or iron compounds.[40,41] The existence of a strong $K_{\beta'}$ satellite in high-spin complexes is currently explained as resulting from the *spin polarization* of the $3p$ electrons by exchange-correlation with the valence $3d$ electrons.[42] *Ligand Field Multiplet* calculations together with photoemission experiments have suggested that the $K_{\beta'}$ satellite should be exclusively associated with transitions filling a *spin-up* $1s$ hole whereas the $K_{\beta 1,3}$ fluorescence peak would be associated *primarily* with transitions filling a *spin-down* $1s$ hole with respect to the majority spin of the $3d$ electrons. If this can be more firmly established, this would have the important practical consequence that *spin selective* XANES[43,44] and, perhaps, *spin selective* EXAFS[45] excitation spectra could be recorded by tuning the fluorescence analyzer either at the maximum intensity of the $K_{\beta 1,3}$ fluorescence line or of its satellite. As a matter of illustration, we have reproduced in **Figure 4A** the high resolution emission spectrum of the μ-oxo di-iron TPP complex $[(TPP)Fe]_2O$ recorded at a fixed excitation energy selected well above the absorption edge. The iron $K_{\beta 1,3}$ fluorescence line and its $K_{\beta'}$ satellite are well apparent from this typical emission spectrum. We have reproduced in **Figure 4B** the spin polarized XRR excitation spectra recorded with the crystal analyzer tuned to the maximum intensity of either the iron $K_{\beta 1,3}$ fluorescence line or its $K_{\beta'}$ satellite. For the sake of comparison, we have added on the same figure the XANES spectrum of $[(TPP)Fe]_2O$ recorded by monitoring the total fluorescence yield. As expected, the differences are most spectacular in the pre-edge region where transitions to bound states take place. Some differences were also detected in the EXAFS spectra but it remains still to be proved that these differences are unambiguously related to the spin polarization of the ejected photoelectron.[46] The theory of spin-polarized XRR spectra may deserve much more attention but this method, which does not require any ordering of the magnetic moments in a magnetic field, seems to have a potentiality even greater than XMCD for the investigation of the magnetic properties of organometallic complexes with $3d$ transition metals.

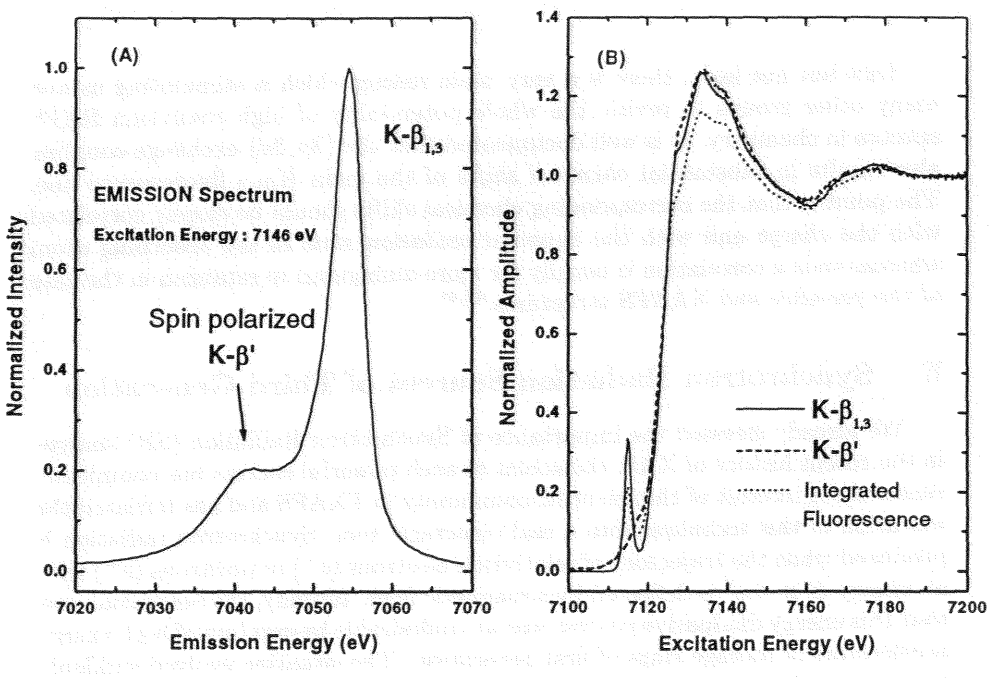

Figures 4: High resolution X-ray fluorescence and X-ray Resonant Raman (XRR) spectra of $[(TPP)Fe]_2O$

Figure 4A: High resolution emission spectrum\ of the $K_{\beta 1,3}$ fluorescence line and its $K_{\beta'}$ satellite.

Figure 4B: XRR excitation spectra recorded by tuning the crystal analyzer to the maximum intensity of either the $K_{\beta 1,3}$ fluorescence line or its $K_{\beta'}$ satellite *(dot-dashed line)*. Note the fairly different intensity and location of the pre-edge structures. For the sake of comparison the fluorescence-integrated XANES spectrum is also reproduced *(dotted line)*.

Last but not least, there is a very basic reason which is stimulating us and many other groups to revisit the whole potentiality of high resolution RXES spectra in chemistry. It is well documented that the $\{3p, 3d\}$ exchange coupling also results in substantial *chemical shifts* of the main $K_{\beta 1,3}$ fluorescence line. The point is that the corresponding chemical shifts should be closely correlated with the *charge* and with the *apparent oxidation state* of the absorbing atom whereas such a correlation is usually far more ambiguous to establish in the case of the pre-edge and XANES structures.[47,48]

E. Synchrotron Radiation Sources of Third Generation

We already stressed the importance of Synchrotron Radiation (SR) sources in the recent history of XAS: the access to such powerful sources has completely renewed the interest of the scientific community in EXAFS and has initiated the mutation of this technique into a real structural tool. Synchrotron radiation is produced when the trajectory of relativistic electrons (e^-) or positrons (e^+) with an energy $E \gg mc^2$ is deflected by a magnetic field. Initially, the perception was that this energy dissipative process was an undesirable by-product of high energy accelerators or storage rings of first generation. The situation evolved suddenly in the seventies when it was realized that SR could be a very intense and wide-band source of photons in the VUV and X-ray spectral ranges where lasers can hardly be competitive. This led to the construction of machines optimized to deliver intense fluxes of synchrotron radiation at several X-ray beamlines operated in parallel.[49] In the second generation of storage rings, synchrotron radiation was still produced mainly by dipolar bending magnets. It was rapidly found that even higher fluxes could be generated if the relativistic electrons (or positrons) were allowed to travel through *periodic* magnetic structures called Insertion Devices (ID) which force the electron beam to move on a sinusoidal or an helical trajectory with a large number of magnetic periods. One has now to make a distinction between two different regimes:

- in the *"wiggler regime"* all radiations emitted by the successive magnetic periods *add incoherently* to produce fairly intense wide-band X-ray sources;
- in the *"undulator regime"* constructive interferences develop between the radiation emitted along the N periods of the insertion device.[50] The emission spectrum of an undulator is typically characterized by a series of discrete, very sharp peaks of unprecedented optical brilliance in a narrow bandwidth. Moreover, the polarization of the emitted undulator radiation can be controlled by forcing the electrons to move either on a *planar* trajectory to emit *linearly* polarized X-ray photons, or on an *helical* trajectory to emit *circularly* polarized X-ray photons.

An important parameter characterizing the electron motion is the so-called *deflection parameter*: $K_g \simeq 0.934 \lambda_u B_g$ where $\lambda_u\,[cm]$ is the length of the magnetic period and $B_g\,[T]$ is the maximum amplitude of the magnetic field experienced by the electrons for a given undulator geometry, *i.e.* for a given magnetic gap g_p. Typically, the undulator regime is obtained for $K \leq 1$ whereas the wiggler regime is observed for $K \gg 1$. There are a number of prerequisites which

need to be satisfied in order to run an insertion device in the true undulator regime in the X-ray range: these requirements led to the construction of *high energy* synchrotron radiation sources of third generation in Europe (ESRF: 6 GeV machine), in the U.S.A. (APS: 7 GeV machine) and in Japan (SPring-8: 8 GeV machine), all of them having long straight sections to accommodate powerful X-ray undulators. Several XAS beamlines are now routinely operated at the ESRF with different types of undulator sources.[51] The availability of helical undulators delivering huge fluxes of circularly polarized photons made it possible to detect for the first time XNCD and also has stimulated much interest in XMCD and MEXAFS studies. The design of the beamlines and the instrumentation had to evolve in order to keep the full advantage of the brilliance and of the polarization characteristics of the undulator sources.[52–55] There is a problem arising from the fact that the undulator radiation is inherently emitted in a very narrow energy bandwidth. For instance, the measured Full Width at Half Maximum (FWHM) of the radiation emitted by the ESRF undulator Helios-II is typically $\Delta E_{FWHM} \simeq 90\ eV$ for the first spectral harmonic ($n = 1$). One might be tempted to conclude that undulator sources are inappropriate for recording EXAFS spectra over 1000 eV or more: fortunately, this is not true because undulators are *tunable* over a limited but still appreciable energy range which depends on the maximum amplitude B_0 of their magnetic field. In fact, the magnetic field B_g^n acting on the electron (positron) beam is related to the magnetic gap g_p of the undulator by a rather simple equation:

$$B_g^n = B_0 \exp\left[-\frac{n\pi g_p}{\lambda_u}\right] \tag{1}$$

where λ_u/n is the period of the Fourier component of order n of the oscillating magnetic field along the direction of propagation of the relativistic electrons (positrons). Since the peak energy is given by the equation:

$$E_{peak}\,[keV] \simeq 0.95 \frac{n\,[E_{beam}]^2}{\lambda_u\left[1 + (K_g)^2/2\right]} \tag{2}$$

where $E_{beam}\,[GeV]$ is the energy of the relativistic electron beam, it becomes clear that a small increase of the magnetic gap will result in a reduction of the deflection parameter K_g and will cause a subsequent shift of E_{peak} towards higher energy. This led Rogalev *et al.*[56] to develop at the ESRF the so-called "*Gap-scan*" technique which is now getting standard: it consists in varying in a correlated way the energy of the monochromator *and* the magnetic gap of the undulator in order to record the whole EXAFS spectrum under ideal conditions of brightness and polarization control .

As far as metalloporphyrins are concerned, EXAFS or XANES spectra reported hitherto in the literature were recorded in most cases using spectrometers exploiting the wide band emission of dipolar *bending magnets* at first or second generation storage rings. In this chapter, we wish to highlight some exciting new perspectives associated with the use of undulators which can be operated as versatile x-ray sources with very high spectral brilliance and a full control of the polarization state of the emitted x-ray photons: such sources already pushed the ultimate detection limits of EXAFS in the ppm range for dilute solutions of metalloporphyrins or metalloproteins but should also boost the development of

time-resolved XAS studies with time scales ranging from a few seconds down to a few nanoseconds. At such short time scales, it is most convenient to exploit the time structure of the synchrotron radiation which consists of short pulses with a duration of 100 ps or less. For sure, the applications of polarization dependent studies such as XLD, XMCD and XNCD are also expected to grow and should give us a deeper insight in the electronic and magnetic structure of organometallic complexes.

F. Outline of the Chapter

The outline of the chapter is as follows. **Section II** will recast XANES /XMCD and EXAFS/MEXAFS in the unified framework of the Multiple Scattered Wave (MSW) theory which is, in our opinion, the key to modern analyses of X-ray absorption spectra. What makes the MSW theory superior to any other approach is its remarkable capacity to embody all new developments such as XMCD[31] or XNCD.[25] The aim of this section is to clarify where are the present limitations in *ab initio* modellizations of the X-ray absorption spectra. Over the recent years, calculations from first principles of EXAFS spectra including multiple scattering paths have become commonplace since well established codes are now available. The simulation of XANES spectra is also possible but still remains a much more delicate exercise because one has to pay the full price for the approximations which are made, especially for the use of spherical potentials and for the neglect of multiexcitation channels. The simulation of XMCD and MEXAFS spectra appears far more complicated and has not reached yet the same level of maturity: the comparison between theory and experiments has been restricted for a long time to ferromagnetic gadolinium or iron metals and the interest of theoreticians in paramagnetic organometallic systems is at best embryonic. Nevertheless, anticipating over future needs, we found desirable to review the existing MSW theories of spin dependent effects in XAS. Due to space and time limitations, we have renounced to include a presentation of the *Ligand Field Multiplet* theory which proved itself to be the best alternative to MSW calculations for XMCD analyses in the soft X-ray range.

Section III is dedicated to more practical questions such as how to extract reliable structural information from experimental EXAFS spectra of metalloporphyrins. Classical analyses exploiting Fourier Transform and curve fitting techniques will be briefly reviewed but less classical methods based on regularization algorithms, on autocorrelation power spectral densities or Maximum Entropy Spectral Analyses (MESA) will also be introduced because they offer interesting, unexploited potentialities. As far as porphyrin chemistry is concerned, we will show that *Difference Analyses* are often much more powerful than direct analyses and are particularly helpful to identify the axial ligands. How to extract more information from the XANES spectra will be discussed. Finally, we like to give a quick introduction to practical problems associated with time-resolved experiments and polarization dependent studies which are expected to develop at third generation SR sources.

Section IV will give an overview of the abundant literature reporting XAS studies on metalloporphyrins and hemoproteins. There have been, unfortunately, a few conflictive reports concerned mostly with structural studies of dilute hemoproteins. This points out to the danger of *overinterpreted* XAS ex-

periments which can cause the unmerited disqualification of a technique that has, like any other spectroscopy, strengths but also limitations. One should always keep in mind that the information content of X-ray Absorption Spectra is very poor compared to what can be learned from a well resolved crystal structure: only well-posed structural problems have any chance to be solved by XAS. Therefore, emphasis will be laid only to those applications where XAS has yield unambiguous conclusions which allowed the authors to discriminate between different structural or electronic models.

II. FORMAL THEORIES OF XAS

A. MSW Formalisms

In this section, we wish to link in a rational way well established physical concepts in order to trace back where the various equations or approximations used in the analyses of XAS are coming from. As far as possible, we tried to keep hidden the details of the mathematical derivations: readers in search of more rigorous derivations are invited to refer to the original papers or to specialized review articles cited in the references. The ultimate goal is to identify where more advanced theories are needed to push the limits of the current analyses.

1. Wavefunctions or Green Functions ?

Starting from Fermi's golden rule, the x-ray absorption cross section can be written:[10]

$$\sigma_D = 4\pi^2 \alpha_0 \hbar\omega \sum_f \left| \langle \psi_f | \, \widehat{\boldsymbol{\varepsilon}}.\mathbf{r} \, | \psi_{in}^c \rangle \right|^2 \delta \left(\hbar\omega - E_f + E_{in} \right) \tag{3}$$

where $\hbar\omega$ is the photon energy, $\widehat{\boldsymbol{\varepsilon}}.\mathbf{r}$ is the radiation-matter interaction hamiltonian in the simplified electric dipole (E1) approximation, $\alpha_0 \simeq \frac{1}{137}$ is the Sommerfeld fine structure constant, ψ_f refers to a final state of energy E_f whereas the initial core state ψ_{in}^c has the energy E_{in}. Higher order terms such as the absorption cross section for the electric quadrupole terms (σ_Q) are disregarded here for the sake of simplicity. The calculation of ψ_{in}^c which is a pure atomic state does not represent a major problem: there are sophisticated codes available to solve the relativistic Dirac equation for a core electron. Our problem is indeed to calculate ψ_f and one may envisage three options:[57,58]

(*i*) the *real space, Scattered Wave* (SW) approach which consists in representing ψ_f as the *time-reversed* wave function ψ_E^- of a photoelectron scattered by a cluster of atoms;[59]

(*ii*) the *band structure* approach which requires periodic systems (crystals) in which the scattered waves can be replaced by Bloch states: as observed by Vedrinskii and Novakovich,[60] this is basically an alternative formulation *in the reciprocal space* of the previous multiple scattering model;

(*iii*) the *Green operator* approach in which one is building with appropriate boundary conditions the solution of a *symbolic* equation: $(E - H)\, G = I$ replacing the Schrödinger equation: $(E - H)\, |\Psi\rangle = 0$.[61]

Formally, all three approaches are strictly equivalent (to the same order of approximation) as a consequence of the *optical theorem* extended by Lloyd and Smith,[62] and by Natoli *et al.*[58] in the case of a cluster of atoms. In practice, each method has different limitations. For instance, band structure calculations suffer from the requirement of translational symmetry (which is hardly compatible with the creation of a core hole in the absorbing atom) whereas the energy range accessible is dramatically restricted to 30-50 eV due to limited basis set problems: such handicaps do not exist in real space multiple scattering calculations. Option (*i*) usually appears more natural to newcomers in the field and, at this stage, is perhaps more pedagogical: those who want to stick with this classical approach are invited to jump directly to section II.A.3.

Wave function calculations become rapidly involving for very large molecules or giant clusters in solid state physics: the problem is then to calculate *densities of states.* This is precisely where Green functions become attractive since equation (3) can be rewritten:

$$\begin{aligned} \sigma_D &= 4\pi^2\alpha_0\hbar\omega \sum_f \langle\psi_{in}^c|\ \widehat{\boldsymbol{\varepsilon}}^*.\mathbf{r}\ |\psi_f\rangle\, \delta\left(\hbar\omega + E_{in} - E_f\right) \langle\psi_f|\ \widehat{\boldsymbol{\varepsilon}}.\mathbf{r}\ |\psi_{in}^c\rangle \quad (4) \\ &= \mp 4\pi\alpha_0\hbar\omega\, \langle\psi_{in}^c|\ \widehat{\boldsymbol{\varepsilon}}^*.\mathbf{r}'\ \mathrm{Im}\left[G^{\pm}\left(E\right)\right]\ \widehat{\boldsymbol{\varepsilon}}.\mathbf{r}\ |\psi_{in}^c\rangle \end{aligned}$$

The latter formulation can be easily established by introducing the *Cauchy Principal Part operator PP* which may be defined by the *symbolic* operator-equation:

$$PP\frac{1}{x - x_0} = \frac{1}{x - x_0 \pm i\epsilon} \pm i\pi\delta\left(x - x_0\right) \qquad \text{with } \epsilon \to 0 \qquad (5)$$

that has a meaning only for integration kernels. Identifying E with $\hbar\omega + E_{in}$, the Green operator is defined as:[63]

$$G^{\pm}\left(E\right) = PP\frac{1}{E - H} \mp i\pi\delta\left(E - H\right) \qquad (6)$$

Keeping in mind that $H\psi_f = E_f\psi_f$ and using the closure relation:

$$\sum_f |\psi_f\rangle\langle\psi_f| = 1 \qquad (7)$$

one is led to equation (4). One should not confuse Green *operators* $G^{\pm}\left(E\right)$ with their real space representations, *i.e.* with the *matrix elements*: $G^{\pm}\left(\mathbf{r},\mathbf{r}',E\right) = \langle\mathbf{r}|\ G^{\pm}\left(E\right)|\mathbf{r}'\rangle$. The latter quantities are termed *Green functions* and are solutions of the Schrödinger equation for $\mathbf{r} \neq \mathbf{r}'$. We want to list briefly below some important properties of these functions. It is first interesting to decompose the Green functions on a basis set made of the orthogonal eigenfunctions of the Hamiltonian H:[64]

$$G^{\pm}\left(\mathbf{r},\mathbf{r}',E\right) = \sum_f \frac{\langle\,\psi_f\left(\mathbf{r}'\right)|\psi_f\left(\mathbf{r}\right)\rangle}{E - E_f \pm i\epsilon} \qquad (8)$$

with the additional condition:

$$\sum_f \langle\psi_f\left(\mathbf{r}'\right)|\psi_f\left(\mathbf{r}\right)\rangle = \delta\left(\mathbf{r} - \mathbf{r}'\right) \qquad (9)$$

On the other hand, defining the *charge density* matrix as: $\varrho(\mathbf{r},\mathbf{r}',E) = \sum_f \langle \psi_f(\mathbf{r}') | \psi_f(\mathbf{r}) \rangle \delta(E - E_f)$, one would show that:

$$\varrho(\mathbf{r},E) = \varrho(\mathbf{r},\mathbf{r},E) = \frac{1}{2\pi} \mathrm{Im}\left[G^+(\mathbf{r},\mathbf{r},E) - G^-(\mathbf{r},\mathbf{r},E)\right] \tag{10}$$

We have reproduced the latter equations essentially to emphasize that the Green functions give access to the practical calculation of most physical *observables.*

Those who are not familiar with the Green functions may have the fallacious perception that the Green functions have no physical meaning and that we have played some elegant mathematical game. This is not true and the physical meaning of the Green functions will become more transparent if we Fourier Transform them *back into the time domain*[64]*:*

$$\begin{aligned} \widetilde{G}^+(\mathbf{r},\mathbf{r}',t-t') &= \sum_f \langle \psi_f(\mathbf{r}',t') | \psi_f(\mathbf{r},t) \rangle \\ &= -i \sum_f \langle \psi_f(\mathbf{r}') | \psi_f(\mathbf{r}) \rangle \exp\left[-i\hbar^{-1} E_f (t-t')\right] \vartheta(t-t') \end{aligned} \tag{11}$$

$\widetilde{G}^+(\mathbf{r},\mathbf{r}',t-t')$ and $\widetilde{G}^-(\mathbf{r},\mathbf{r}',t-t')$ can then be identified with time-ordered *autocorrelation functions* of the wavefunction for $t > t'$ and $t < t'$ respectively. Note that $\vartheta(t-t')$ is a common notation for the Heaviside step function. Equation (11) justifies why $G^+(\mathbf{r},\mathbf{r}',E)$ and $G^-(\mathbf{r},\mathbf{r}',E)$ are called time- (R)*etarded* and (A)*dvanced* Green *propagators.* Suppose that we know a given eigenfunction of H at a particular space-time variable $(\mathbf{r}'t')$, then we can deduce the wavefunction at a later time t from a very general *causal transformation*:

$$\Psi(\mathbf{r},t) = i \int \widetilde{G}^+(\mathbf{r},\mathbf{r}',t-t') \Psi(\mathbf{r}',t') \vartheta(t-t') \, d\mathbf{r}' \tag{12}$$

We are still missing the key application of the Green operators: the capability to build up solutions of the *inhomogeneous* Schrödinger (or Dirac) equations in the presence of the potential $V(\mathbf{r})$. This stems from a *mathematical property* of the Green operators known as the *resolvent identities*:

$$G(E) = G_0(E) + G_0(E) V G(E) = G_0(E) + G(E) V G_0(E) \tag{13}$$

in which $G(E) = G^{\pm}(E)$ whereas $G_0(E)$ stands for the *perturbation free* Green operator. Let us make it clear that all products of operators that appear in the latter equation have to be understood as integrals over space variables, *e.g.* $G_0(E) V = \int d^3r' \, G_0(\mathbf{r},\mathbf{r}',E) V(\mathbf{r}')$. The integral formulation of equation (13) is precisely termed the *Dyson equations for Green functions.* A link between equation (13) and the Wigner-Brillouin perturbation theory can be found in the series expansion:[64]

$$\begin{aligned} G(E) &= G_0(E) + G_0(E) V G_0(E) + G_0(E) V G_0(E) V G_0(E) + \ldots \\ &= G_0(E) \left[1 - V G_0(E)\right]^{-1} = \left[1 - G_0(E) V\right]^{-1} G_0(E) \end{aligned} \tag{14}$$

By identification with the results of the perturbation theory, one would easily check that the wavefunction solution to the inhomogeneous Schrödinger equation $\Psi(\mathbf{r})$ can be written in a formal way:

$$\Psi^{\pm}(\mathbf{r}) = \Phi_0(\mathbf{r}) + G^{\pm}(E)\, V\Psi^{\pm}(\mathbf{r}) \tag{15}$$

where the first term $\Phi_0(\mathbf{r})$ is the solution of the *homogeneous* Schrödinger equation. The integral formulation of equation (15) is known as the *Lippmann-Schwinger* equation. It also suggests an alternative way of exploiting the Green's functions to calculate σ_D using directly equation (3).We will show in the next subsection that the Green's operators are extremely powerful tools to describe *multiple scattering* events.[65,66] A stringent argument for introducing Green's functions is that, even when the concept of *single particle* wavefunctions has lost any meaning in many-body problems, the Green's functions can still be calculated and will retain most of their remarkable properties.[64]

2. Scattering Path Operators

It is essential to discern the different nature of the $\Psi^{+}(\mathbf{r})$ and $\Psi^{-}(\mathbf{r})$ states:[63] in the time-domain, they refer to the states of the system "*before*" and "*after*" a collision takes place; in the energy domain, one may think of the "*incoming*" and "*outgoing*" states of a collision process. In the formal theory of collision phenomena, a collision is precisely described by the symbolic equation: $\Psi^{-}(\mathbf{r}) = S\ \Psi^{+}(\mathbf{r})$ where S is the *scattering* operator commonly rewritten as: $S = \exp(2i\Delta)$ where the *phase-shift* matrix Δ is Hermitian. For spherical waves, often called *partial waves,* Δ is diagonal with eigenvalues $S_\ell = \delta_\ell$. Note that these phase-shifts $[\delta_\ell]$ will play a central role in the theory as well as in the practice of XAS. By analogy with the scattered wave picture, it is more convenient to decompose the outgoing state as a sum of two terms:[63]

$$\Psi^{-}(\mathbf{r}) = \Psi^{+}(\mathbf{r}) + \Psi^{Scatt}(\mathbf{r}) = [1+T]\,\Psi^{+}(\mathbf{r}) \tag{16}$$

The latter equation defines the so-called T *(transition)* operator which should not be confused with the scattering operator S. Suppose that $\Phi_0(\mathbf{r})$ is a known set of solutions of the *homogeneous* Schrödinger equation for a *free* electron: the projection $\langle \Phi_0(\mathbf{r}) | V\Psi^{+}(\mathbf{r}) \rangle$ will then *measure the amplitude scattered* by the potential V. The operator associated with that projection is precisely the T operator *(*or *transition* matrix). It is related to the S operator and, using a partial wave expansion, one would easily check that:[63] $T_\ell = \frac{1}{2ik}\left[S_\ell - 1\right]$. What makes the T operator more attractive is a straightforward connection with the Green's operator introduced in the previous section. From a direct identification with the *Lippmann-Schwinger* equations one finds:

$$T(E) = V + VG^{+}(E)\, V \tag{17}$$

From the resolvent identities of the Green operators,[65] one would also check that: $VG^{+}(E) = T(E)G_0^{+}(E)$ and therefore:

$$T(E) = V + T(E)\, G_0^{+}(E)\, V = V\left[1 - G_0^{+}V\right]^{-1} \tag{18}$$

Let us explicit now the *free* Green function $G_0(\mathbf{r}, \mathbf{r}', E)$. This is also known in mathematics as *the Helmholtz problem.* For an outgoing wave, and assuming that $\mathbf{r}$ and $\mathbf{r}'$ refer to *the same origin o*, $G_0(\mathbf{r}, \mathbf{r}', E)$ can be expanded in terms of spherical harmonics commonly written $Y_L = Y_\ell^m(\widehat{\mathbf{r}})$; $Y_{-L} = (-1)^m\, Y_\ell^{-m}(\widehat{\mathbf{r}}) = Y_L^{*}$ in which $\widehat{\mathbf{r}}$ denotes the unit vector along $\mathbf{r}$:

$$G_0(\mathbf{r},\mathbf{r}',E) = -\frac{\exp(i\kappa|\mathbf{r}-\mathbf{r}'|)}{4\pi|\mathbf{r}-\mathbf{r}'|} = -i\kappa\sum_L [j_\ell(\kappa r_<) Y_L(\widehat{\mathbf{r}_<})]\left[h_\ell^+(\kappa r_>) Y_{-L}(\widehat{\mathbf{r}_>})\right] \tag{19}$$

where $\kappa^2 = 2mE\hbar^{-2}$. Moreover: $r_< = r$ and $r_> = r'$ if $r \leq r'$; $r_< = r'$ and $r_> = r$ if $r \geq r'$. In equation (19), $j_\ell(\kappa r)$ is the ordinary Bessel function and $h_\ell^+(\kappa r)$ is a spherical Hankel function:

$$h_\ell^+(z) = (-i)^{\ell+1}\frac{\exp(iz)}{z}\sum_{k=0}^{\ell}\frac{(\ell+k)!}{k!\,(\ell-k)!}\left(\frac{i}{2z}\right)^k \tag{20}$$

Let us now assume that the molecular potential can be decomposed as: $V(\mathbf{r}) = \sum_j V_j(\mathbf{r}-\mathbf{R}_j) = \sum_j V_j(\mathbf{r}_j)$ where the sum is over a finite number of atomic sites j centered at $\mathbf{R}_j$. It becomes then possible to extend equation (17) for a cluster of atoms, *i.e.* for a molecule:[65]

$$T = V + VG^+(E)V = \sum_{ij} T^{ij} = \sum_{ij} V_i\delta_{ij} + V_iG^+(E)V_j \tag{21}$$

and simple algebra would allow us to rewrite T^{ij} as:

$$T^{ij} = T^i\delta_{ij} + \sum_{k\neq i} T^iG_0(E)T^{kj} \tag{22}$$

The real space representation $T^{ij}(\mathbf{r},\mathbf{r}',E)$ is non-zero only if $\mathbf{r}$ belongs to the local cell $\Omega_i(V_i)$ and $\mathbf{r}'$ belongs to the local cell $\Omega_j(V_j)$. This implies that the Green function $G_0(\mathbf{r},\mathbf{r}',E)$ should be preferably expressed as functions of $\mathbf{r}_i$ and $\mathbf{r}'_j$: this is a pure mathematical problem the solution of which is known as the *re-expansion theorems* for Green functions. For $r_i + r_j < R_{ij}$ and for non-overlapping spherical domains, one obtains:[66]

$$G_0(\mathbf{r}_i,\mathbf{r}'_j,E) = \kappa\sum_{L,L'}[j_\ell(\kappa r_i) Y_L(\widehat{\mathbf{r}_i})]\left[H^{ij}_{LL'}\right]\left[j_{\ell'}(\kappa r'_j) Y_{-L'}\left(\widehat{\mathbf{r}'_j}\right)\right] \tag{23}$$

where the matrix element $[H]^{ij}_{LL'}$ is entirely defined by the cluster geometry, *i.e.* by the vectors $\mathbf{R}_{ij}$:

$$[H]^{ij}_{LL'} = -4\pi i\sum_{L''} i^{(\ell''+\ell'-\ell)}\mathbb{C}^{L'}_{LL''}h^+_{\ell''}(\kappa R_{ij}) Y_{L''}\left(\widehat{\mathbf{R}}_{ij}\right) \tag{24}$$

In the latter expression, the $\mathbb{C}^{L'}_{LL''}$ are the Gaunt coefficients which appear in the calculation of the product of three spherical harmonics. They can be expressed either in terms of the Wigner $(3j)$ symbols:

$$\begin{aligned}\mathbb{C}^{L'}_{LL''} &= \left[\frac{(2\ell+1)(2\ell'+1)(2\ell''+1)}{4\pi}\right]^{1/2}\cdot(-1)^{m'} \\ &\times\begin{pmatrix}\ell & \ell' & \ell''\\ 0 & 0 & 0\end{pmatrix}\begin{pmatrix}\ell & \ell' & \ell''\\ m & -m' & m''\end{pmatrix}\end{aligned} \tag{25}$$

or in terms of the Clebsch-Gordan coefficients:

$$\mathbb{C}_{LL''}^{L'} = \left[\frac{(2\ell+1)(2\ell''+1)}{4\pi(2\ell'+1)}\right]^{1/2} (\ell 0\ \ell'' 0|\,\ell' 0)\,(\ell m\ \ell'' m''|\,\ell' m') \tag{26}$$

One has now all the ingredients to calculate the real space matrix representation of the operator $T^{ij}(E)$, *i.e.* the functions $T^{ij}(\mathbf{r},\mathbf{r}',E)$ and, even more interesting, to expand the latter on the basis of the free space wavefunctions. What comes out (after implicit integration over $\mathbf{r}_i$ and $\mathbf{r}_j$ and any relevant intermediate variable) is a number of matrix components:

$$\boldsymbol{\tau}_{LL'}^{ij} = [T]_{LL'}^{i}\,\delta_{ij} + \kappa \sum_{k\neq i}\sum_{\Lambda\Lambda'} [T]_{L\Lambda}^{i}\,[H]_{\Lambda\Lambda'}^{ik}\,[T]_{\Lambda' L'}^{kj} \tag{27}$$

The *super matrix* $\boldsymbol{\tau}^{ij}$ is called a *scattering path operator* or a *multiple scattering operator*.[67,68] The key ingredients entering in the construction of $\boldsymbol{\tau}^{ij}$ are the photoelectron propagation matrices H^{ij} and the site-specific scattering matrices T^{i}. At this stage, it is desirable to relate $\left[T^{i}\right]$ either to the diagonal t-matrices t_ℓ^i or to the *scattering phase-shifts* δ_ℓ^i according to:

$$\left[T^{i}\right]_{LL'} = -\left(\frac{1}{\kappa}\right)\delta_{LL'} t_\ell^i = -\left(\frac{1}{\kappa}\right)\delta_{LL'}\exp\left(i\delta_\ell^i\right)\sin\delta_\ell^i \tag{28}$$

We like to stress here that t_ℓ^i and δ_ℓ^i are entirely defined by the *local scattering potential* V_i. Our next step is to explicit the *multiple scattering* Green function $G^{+}(\mathbf{r},\mathbf{r}';E)$. Simple algebra would allow us to rewrite the resolvent identity as:[65]

$$G^{+}(E) = G_0^{+}(E) + G_0^{+}(E)\,T(E)\,G_0^{+}(E) \tag{29}$$

In order to preclude unwanted divergences, one should avoid situations where both arguments $\mathbf{r}$ and $\mathbf{r}'$ belong to the same atomic cell. A safe strategy recommended by Gyorffy and Stott[68] or Brouder[65] is to include the potential V_i in some "*unperturbed* " Hamiltonian H_0' so that the resolvent identity now becomes:

$$G^{+}(E) = G_i^{+}(E) + \sum_{a\neq i}\sum_{b\neq i} G_i^{+}(E)\,T^{ab}G_i^{+}(E) \tag{30}$$

with: $G_i^{+}(\mathbf{r},\mathbf{s}\,;E) = -i\kappa\sum_L \psi_L(\mathbf{r}_i)\,h_\ell^{+}(\kappa s)\,Y_{-L}(\widehat{\mathbf{s}})$ where $\mathbf{r}\in\Omega_i$ but $\mathbf{s}\notin\Omega_i$. In the latter expression, $\psi_L(\mathbf{r}_i) = t_\ell^i(V_i,E)\,R_\ell^i(\mathbf{r}_i,E)\,Y_L$ is the *regular* wavefunction associated with the local potential V_i. The full multiple scattering Green function in the neighborhood of the absorbing site i can be finally written:[65]

$$\begin{aligned} G^{+}(\mathbf{r}_i,\mathbf{r}_i'\,;E) \;=\; & G_i^{+}(\mathbf{r}_i,\mathbf{r}_i'\,;E) \\ & + \sum_{LL'}\psi_L(\mathbf{r}_i)\left[\left[T^{i}\right]^{-1}\boldsymbol{\tau}^{ii}\left[T^{i}\right]^{-1} - \left[T^{i}\right]^{-1}\right]_{LL'}\psi_{-L'}(\mathbf{r}_i') \end{aligned} \tag{31}$$

Equation (31) shows that $G^{+}(\mathbf{r}_i,\mathbf{r}_i'\,;E)$ is the sum of the Green function for the *isolated* cell i, plus another term describing how the rest of the cluster (molecule) modifies the density of states in cell i. The second term which depends on $\boldsymbol{\tau}^{00} = \boldsymbol{\tau}^{ii}$ is essential to describe EXAFS and XANES spectra. We will skip here the last mathematical step which would be to separate the real and the imaginary parts of $G^{+}(\mathbf{r},\mathbf{r}_i';E)$.

3. Wavefunction Approach and Optical Theorem

In this section, we want to establish a link between the *scattering path operator* formalism and the more common wavefunction approach.[69] Since the early work of Dill and Dehmer,[70] it is a common practice to adopt the space partition illustrated by **Figure 5**:

- zone (I) refers to spherical portions of space (of radius b_j) where the local atomic potentials V_j dominate and can be spherically averaged;
- zone (II) refers to the interstitial portion of space not covered by the atomic potentials of section (I): classically, one assumes that the whole cluster is embedded in a *constant average potential* $\overline{V}_{int}$.
- zone (III) refers to the "extramolecular potential" which is essential to warrant a correct asymptotic behavior of the wavefunctions: in practice one will define an "outersphere" potential which is centered on origin and has again a spherical symmetry.

Inside each "atomic" area of type (I), the wavefunction can be decomposed on the spherical harmonics basis $Y_L(r)$:

$$\psi^j_{(I)}(r_j = r - R_j) = \sum_L C^j_L R^j_\ell(E; r_j) Y_L(r_j) \; with: \; 0 < r_j \leq b_j \qquad (32)$$

the functions $R^j_\ell(E;r)$ being solutions of the radial part of the Schrödinger equation which can be separated from the angular part *only* for a spherical potential $V_j(r)$. In the "extramolecular" outersphere region (III) of radius b_0, the wavefunction can be expanded in the same way since we have again a spherical potential:

$$\psi_{(III)}(r) = \sum_L C^0_L R^0_\ell(E; r) Y_L(r) \quad \text{with:} \quad r \geq b_0 \qquad (33)$$

The situation is more complicate in the interstitial region (II) but the wavefunction can basically be decomposed as a sum of multicentric partial waves entering into region (II). The mathematics require us to distinguish between: (*i*) $E < \overline{V}_{int}$ (*quasi*-bound states of the photoelectron); (*ii*) $E > \overline{V}_{int}$ (true continuum states):

For: $E < \overline{V}_{int}$ and $\hbar\kappa = \left[2m\left(\overline{V}_{int} - E\right)\right]^{1/2}$

$$\psi_{(II)}(r) = \sum_j \sum_L A^j_L k^{(1)}_\ell(\kappa r_j) Y_L(r_j) + \sum_L A^0_L i_\ell(\kappa r_0) Y_L(r_0) \qquad (34)$$

For: $E > \overline{V}_{int}$ and $\hbar\kappa = \left[2m\left(E - \overline{V}_{int}\right)\right]^{1/2}$

$$\psi_{(II)}(r) = \sum_j \sum_L A^j_L n_\ell(\kappa r_j) Y_L(r_j) + \sum_L A^0_L j_\ell(\kappa r_0) Y_L(r_0) \qquad (35)$$

where the first term is to be interpreted as a sum of outgoing spherical waves dispersed by all atomic potentials V_j, whereas the second term is an incoming wave directed towards the center of the molecule and scattered by the extramolecular

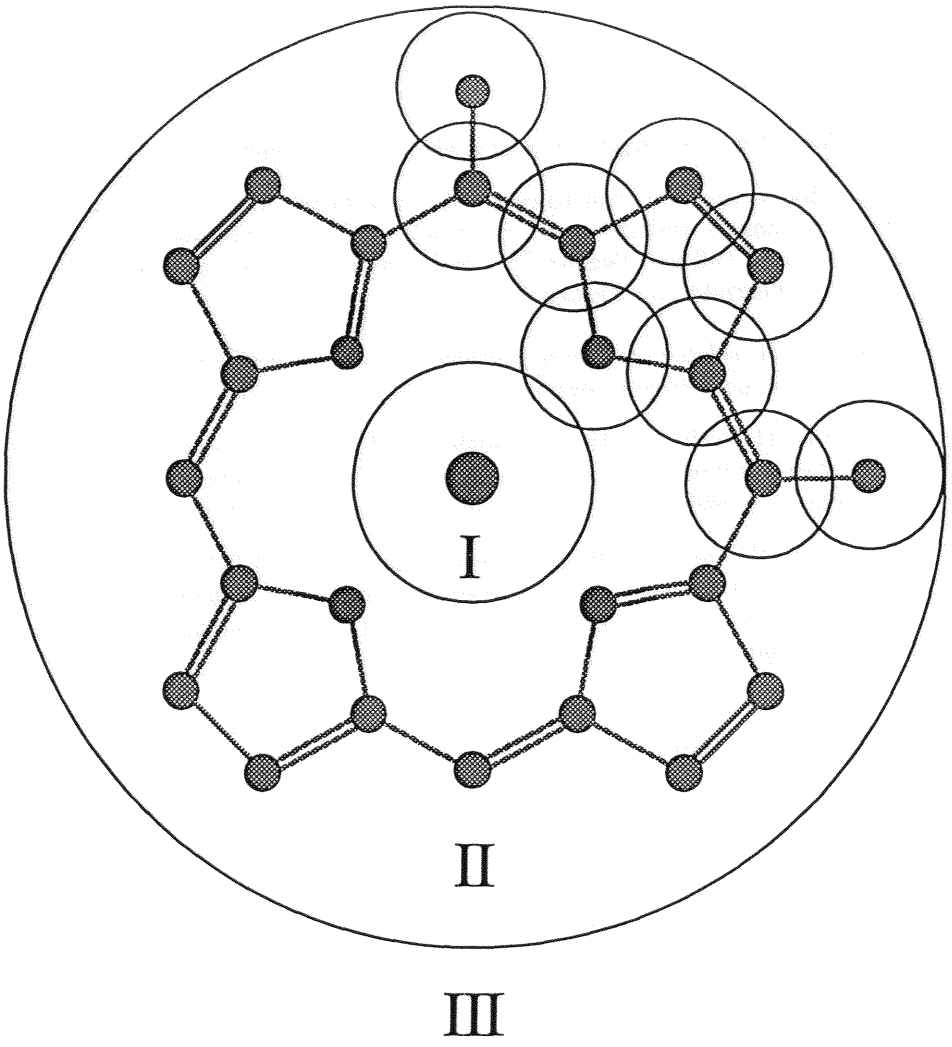

Figure 5: Space partition used for multiple scattering calculations. The absorbing center is the metal located at the origin of the coordinate system.

potential. At the interface between the interstitial region (II) and the atomic sphere (I) associated with every atom j, we can also describe the wavefunction as the sum of an *incoming wave* directed towards atom j and a scattered wave: $\psi_{(II)_j}(r) = \psi^{inc}_{(II)_j}(r) + \psi^{sca}_{(II)_j}(r)$ with:

$$\psi_{(II)_j}(r) = \sum_L B^j_L i_\ell(\kappa r_j) Y_L(r_j) + \sum_L A^j_L k^{(1)}_\ell(\kappa r_j) Y_L(r_j) \quad (for: E < \overline{V}_{int}) \tag{36}$$

$$\psi_{(II)_j}(r) = \sum_L B^j_L j_\ell(\kappa r_j) Y_L(r_j) + \sum_L A^j_L n_\ell(\kappa r_j) Y_L(r_j) \quad (for: E > \overline{V}_{int}) \tag{37}$$

where the first term includes all wave components scattered by the other atoms $j' \neq j$. In equations (34) up to (37), we kept standard notations:

- $i_\ell(z)$ is a modified spherical Bessel function related to the ordinary Bessel function $j_\ell(z)$ by: $i_\ell(z) = i^{-\ell} j_\ell(iz)$;
- $k^{(1)}_\ell = (-i)^{-\ell} h_\ell(iz)$ denotes a modified spherical Hankel function of the first type;
- $n_\ell(z)$ is the spherical Neumann function.

Continuity requires that locally: $\psi_{(II)}(r) = \psi_{(II)_j}(r)$ the latter identification resulting finally in the familiar *secular equations*[69]*:*

$$\begin{aligned} \sum_{j' \neq j} \sum_{L'} \left[T^{-1}(E)\right]^{jj'}_{LL'} A^{j'}_{L'} - \sum_{L'} S^{j0}_{LL'}(E) A^0_{L'} &= 0 \\ \sum_{j' \neq j} \sum_{L'} S^{jj'}_{LL'}(E) A^{j'}_{L'} - \sum_{L'} \delta_{LL'} \left[t^0_\ell(E)\right] A^0_{L'} &= 0 \end{aligned} \tag{38}$$

where:

$$S^{j0}_{LL'}(E) = 4\pi (-1)^{\ell+\ell'} \sum_{L''} \mathbb{C}^{L'}_{LL''} \left[i j_{\ell''}(\kappa R_{j0})\right] Y_{L''}\left(\widehat{R}_{j0}\right) \tag{39}$$

$ij_\ell(z) = i_\ell(z)$ if $E < \overline{V}_{int}$ or $ij_\ell(z) = j_\ell(z)$ if $E > \overline{V}_{int}$. The Gaunt coefficients $\mathbb{C}^{L'}_{LL''}$ as well as the scattering matrices $[T(E)]^{ij}_{LL'}$ were already made explicit in the previous section and we refer to equations (25) and (28) for their definition. We have now the basic ingredients that are necessary to calculate ψ_f and the absorption cross section. At the interface of the interstitial region (II) with the sphere (I) associated with the absorbing atom $j = 0$, the wavefunction ψ_f can be represented by equation (32) but also by equation (34) if $E < \overline{V}_{int}$ or by equation (35) if $E > \overline{V}_{int}$. Again, continuity will require that the right handsides of the two equations are identical so that the coefficients C^j_L can be expressed as functions of the coefficients A^j_L and A^0_L which are solutions of the secular equations. The absorption cross section can finally be written in the matrix form:

$$\sigma = 4\pi\alpha_0\kappa\hbar\omega \sum_{LL'} M_L M^*_{L'} \sum_{L''} Q^0_{LL''} Q^0_{L'L''} \tag{40}$$

where: $M_L = \langle R_L Y_L | \widehat{\varepsilon}.\mathbf{r} | \psi^c_{in} \rangle$ in which R_L is solution of the *radial part* of the Schrödinger equation for the photoelectron. The generalized *optical theorem* states that the right handside can also be rewritten:[57,58]

$$\sigma = -4\pi\alpha\kappa\hbar\omega \sum_{LL'} M_L M^*_{L'} \, \mathrm{Im}\left\{\kappa \boldsymbol{\tau}^{00}_{LL'}\right\} \tag{41}$$

Thus, the optical theorem is the link between the two formalisms which the physicists and the theoretical chemists are using. In the single electron excitation picture, equation (41) is the most general formulation for X-ray absorption cross sections in the electric dipole approximation: it is valid for XANES as well as for EXAFS and it will be the starting point for the calculation of XMCD spectra. Indeed, $\boldsymbol{\tau}$ is the same "*scattering path operator* " as defined in the previous section:

$$\boldsymbol{\tau} = \frac{[T]}{[1] - \kappa\,[T]\,[H]} = \left[[T]^{-1} - \kappa\,[H]\right]^{-1} \tag{42}$$

Once again, $[T]$ refers to the atomic t-matrices which depend only on the *nature* of the scattering atoms, whereas $[H]$ contains the whole information on the *stereogeometry* of the cluster as indicated by equation (24). The scattering path operators $\boldsymbol{\tau}^{ij}$ are symbolic super-matrices describing the whole set of scattering paths that *begin at atom i and terminate at atom j*, possibly visiting other sites at intermediate steps. Thus, as expected, $\boldsymbol{\tau}^{00}$ embodies *all* scattering paths that begin and end at the *absorbing atom.* A formal separation between atomic and cluster effects is possible if one decomposes the scattering path operator as: $\boldsymbol{\tau} = \mathbf{T}_0\,[\mathbf{I} + \mathbf{X}]$ where $\mathbf{X}$ would be the ‹cluster› operator as opposed to $\mathbf{T}_0$ which would characterize the scattering process by the absorbing atom. For both numerical and physical reasons, Brouder has proposed to exploit a symmetrized operator:[71] $\widetilde{\mathbf{X}} = \left[\mathbf{I} - \kappa\,[T]^{1/2}\,[H]\,[T]^{1/2}\right]^{-1} - \mathbf{I}$. Under proper convergence conditions, the inverted matrices that appear in the formulation of $\boldsymbol{\tau}$ or $\widetilde{\mathbf{X}}$ can be expanded in series. We want to show now that such series expansions have a physical interpretation in terms of scattering paths. For instance:

$$\begin{aligned} \widetilde{\mathbf{X}} \;=\; & \kappa\left[T^0\right]^{1/2}\left[H^{00}\right]\left[T^0\right]^{1/2} + \sum_{j\neq 0} \kappa^2 \left[T^0\right]^{1/2}\left[H^{0j}\right]\left[T^j\right]\left[H^{j0}\right]\left[T^0\right]^{1/2} \\ & + \sum_{j\neq k\neq 0} \kappa^3 \left[T^0\right]^{1/2}\left[H^{0j}\right]\left[T^j\right]\left[H^{jk}\right]\left[T^k\right]\left[H^{k0}\right]\left[T^0\right]^{1/2} + \ldots \end{aligned} \tag{43}$$

but it results from its definition that: $\left[H^{00}\right] \equiv 0$. Thus, the first term which is non-zero is the second term of the left handside, which we will denote $\widetilde{\mathbf{X}}_{(2)}$. It clearly describes a sum of scattering processes which start at the absorbing atom: $\left[H^{0j}\right]$ propagates first the photoelectron towards atom j where it is scattered according to matrix $\left[T^j\right]$; then $\left[H^{j0}\right]$ is propagating the photoelectron back to the absorbing site. Similarly, the third term in equation (43) is describing *multiple scattering paths* since $\left[H^{jk}\right]$ is propagating the photoelectron to site

k where it is scattered according to $\left[T^k\right]$ before returning to the absorbing atom as described by matrix $\left[H^{k0}\right]$. This illustrates how elegant and concise is the symbolic formalism of multiple path operators. We will see later that $\widetilde{\mathbf{X}}$ could be identified with some ‹exafs› operator with the restriction that the experimentalist, unlike the theoretician, is not able to "*remove*" from his data the central atom phase-shift together with the unwanted atomic background.

4. Polarization and X-ray Linear Dichroism

In this section, we want to explicit the polarization and angular dependences of the absorption cross section $\sigma\left(\widehat{\boldsymbol{\varepsilon}}\right)$. This can be made in a concise way if we exploit the remarkable properties of the spherical harmonics $\mathbf{Y}_\ell^m\left(\widehat{\mathbf{r}}\right)$.[72] Note that the integrals M_L and $M_{L'}$ which appear in equation (41) depend on the polarization vector $\widehat{\boldsymbol{\varepsilon}}$ throughout the electric dipole operator $\widehat{\boldsymbol{\varepsilon}}.\mathbf{r}$. Let us temporarily forget about the case of circularly polarized X-ray photons which will be considered in section II.D which is dedicated to spin dependent effects. On expanding the electric dipole operator $E1 = \widehat{\boldsymbol{\varepsilon}}.\mathbf{r}$ on spherical harmonics, one obtains a classical result:

$$\widehat{\boldsymbol{\varepsilon}}.\mathbf{r} = \frac{4\pi}{3} r \sum_\mu (-1)^\mu \, \mathbf{Y}_1^{-\mu}\left(\widehat{\boldsymbol{\varepsilon}}\right) \mathbf{Y}_1^\mu\left(\widehat{\mathbf{r}}\right) \tag{44}$$

It is most convenient to extract the radial integrals $M_{\ell_0,\ell}^{E1}$ and $M_{\ell_0,\ell'}^{E1}$ from M_L and $M_{L'}$ and to combine the angular parts $\mathbf{Y}_\ell^m\left(\widehat{\mathbf{r}}\right)$ and $\mathbf{Y}_{\ell'}^{m'}\left(\widehat{\mathbf{r}}'\right)$ in the spherical matrix elements:

$$\left\langle \mathbf{Y}_L\left(\widehat{\mathbf{r}}\right) \middle| \boldsymbol{\tau}^{00} \middle| \mathbf{Y}_{L'}\left(\widehat{\mathbf{r}}'\right) \right\rangle = \sum_{c\gamma} (-1)^{(\ell - m)} \left(\ell - m; \ell' m' \middle| c\gamma\right) \boldsymbol{\tau}^{00}\left(\ell, \ell'; c\gamma\right) \tag{45}$$

Here $\left(a\alpha; b\beta \middle| c\gamma\right)$ is a standard notation for the Clebsch-Gordan coefficients which would allow us to develop $\mathbf{Y}_a^\alpha \mathbf{Y}_b^\beta$ on a basis of spherical harmonics $\mathbf{Y}_c^\gamma$. By analogy with equation (45), one would define in the same way the spherical matrix elements $\widetilde{\mathbf{X}}_{(n)}\left(\ell, \ell'; c\gamma\right)$ associated with the ‹exafs› operator $\widetilde{\mathbf{X}}$. Such decompositions are the mathematical transcription of the rotational transformation of both operators which are also invariant in any other operation of the group of symmetry to which the molecule belongs: the latter property, which we are not going to discuss any longer here, is exploited as well to reduce the number of matrix elements to be calculated by the computer. After some algebra, the absorption cross section can be rewritten:[72]

$$\begin{aligned} \sigma\left(\widehat{\boldsymbol{\varepsilon}}\right) &= 4\pi\hbar\omega\kappa\left(2m/\hbar^2\right)\frac{1}{3}\left(2\ell_0 + 1\right) \\ &\quad \times \sum_{\ell,\ell'} M_{\ell_0,\ell}^{E1} M_{\ell_0,\ell'}^{E1} \left(\ell_0 0; 10 \middle| \ell 0\right)\left(\ell_0 0; 10 \middle| \ell 0\right) \chi_{\ell\ell'}\left(\widehat{\boldsymbol{\varepsilon}}\right) \end{aligned} \tag{46}$$

where $\delta_{\ell\ell'}\chi_{\ell\ell'}\left(\widehat{\boldsymbol{\varepsilon}}\right)$ is the EXAFS function $\chi^\ell\left(\kappa\right)$ where $\ell = \ell_0 \pm 1$ is the angular momentum in the final state, ℓ_0 being the angular momentum in the initial core state. It has been shown elsewhere that:

$$\chi_{\ell\ell'}\left(\widehat{\boldsymbol{\varepsilon}}\right) = \frac{4\pi\kappa}{\sin\delta_\ell^0 \sin\delta_{\ell'}^0} \sum_{c\gamma} W\left(1 \; \ell_0 \; c \; \ell; \; \ell \; 1\right) \left\langle c \middle| \middle| 1 \middle| \middle| 1 \right\rangle \tag{47}$$

$$\times \mathrm{Im}\left[(-1)^{\gamma}\,\boldsymbol{\tau}^{00}\left(\ell,\ell';c\gamma\right)\mathbf{Y}_{c}^{-\gamma}\left(\widehat{\boldsymbol{\varepsilon}}\right)\right]$$

The factor $W\left(abcd;ef\right) = (-1)^{(a+b+c+d)}\left\{\begin{array}{ccc} a & b & e \\ d & c & f \end{array}\right\}$ is the Racah W function. More about the algebra of Racah coefficients could be found in any textbook discussing the mathematical problem of the coupling of three angular momenta. Most important to us is the *availability of analytical expressions* to compute the Racah coefficients as easily as the Clebsch-Gordan coefficients. The *reduced matrix* $\langle a|\,|b|\,|c\rangle$ is defined by the identity:

$$\langle c|\,|b|\,|a\rangle \equiv \left[\frac{(2a+1)\,(2b+1)}{4\pi\,(2c+1)}\right]^{1/2}(b0;\,a0|\,c0) \tag{48}$$

One would check that $\langle c|\,|1|\,|1\rangle = 0$ unless $c = 0, 2$. Looking now at equation (47), it is easily deduced that the $c = 0$ term yields the *polarization-averaged absorption cross section* (*e.g.* for powdered samples) whereas the $c = 2$ terms contain the whole angular dependence on polarization. Every reader familiar with spectroscopy will have noticed that the electric dipole selection rule $\Delta\ell = \pm 1$ is the condition required for the Clebsch-Gordan coefficient $(\ell_0 0;\,10|\,\ell 0)$ to be non-zero. Thus, in the electric dipole approximation and over the whole energy range of EXAFS and XANES, the X-ray absorption cross section is given by the fairly general equation:[10]

$$\sigma^{E1}\left(\widehat{\boldsymbol{\varepsilon}}\right) = \sigma^{E1}\left(c,\gamma\right) = \sigma^{E1}\left(0,0\right) - \sqrt{\frac{8\pi}{5}}\sum_{\gamma=-2}^{2}(-1)^{\gamma}\,\sigma^{E1}\left(2,\gamma\right)\mathbf{Y}_{2}^{-\gamma}\left(\widehat{\boldsymbol{\varepsilon}}\right) \tag{49}$$

which is the foundation of all applications of X-ray *Linear Dichroism*. For metalloporphyrins which often belong to point groups which have a C_4 rotation axis (*e.g.* C_{4v} or D_{4h}), one has $\sigma^{E1}\left(2,\gamma\right) = 0$ for $\gamma \neq 0$ and one is left with a simplified formula:

$$\sigma^{E1}\left(\widehat{\boldsymbol{\varepsilon}}\right) = \sigma^{E1}\left(0,0\right) - \frac{1}{\sqrt{2}}\left(3\cos^{2}\theta - 1\right)\sigma^{E1}\left(2,0\right) \tag{50}$$

where θ is the angle between the polarization vector and the symmetry axis C_4.

We still need to investigate what happens if we replace the multiple scattering path operator by the Born series expansion. The first term of the series, *i.e.* $\boldsymbol{\tau}_{(0)}^{00}\left(\ell,\ell';c\gamma\right) = -\left(1/\kappa\right)\left(2\ell+1\right)^{1/2}\delta_{c0}\delta_{\gamma 0}\delta_{\ell\ell'}t_{\ell}^{0}$ is obviously polarization independent and finally results in $\chi_{\ell\ell'} = \delta_{\ell\ell'}$: it is associated with the atomic background absorption $\sigma_{0}^{E1}\left(0,0\right)$. Let us develop next $\left[H^{ij}\right]_{LL'}$ also on spherical harmonics:

$$\left[H^{ij}\right]_{LL'} = \sum_{a}\mathcal{H}_{\ell\ell'}^{+a}\left(\kappa R_{ij}\right)\sum_{a,\alpha}(-1)^{(\ell-m)}\left(\ell,-m;\,\ell'm'|\,a\alpha\right)\mathbf{Y}_{a}^{\alpha}\left(\widehat{\mathbf{R}}_{ij}\right) \tag{51}$$

In practice, it is more convenient to introduce the spherical tensor: $\Xi_{(n)}\left(\ell,\ell';c\gamma\right)$ that is related to $\boldsymbol{\tau}_{(n)}^{00}\left(\ell,\ell';c\gamma\right)$ or $\widetilde{\mathbf{X}}_{(n)}\left(\ell,\ell';c\gamma\right)$ by the following identities:

$$\boldsymbol{\tau}_{(n)}^{00}\left(\ell,\ell';c\gamma\right) = (-1)^{n+1}\left(1/\kappa\right)t_{\ell}^{0}t_{\ell'}^{0}\;\;\Xi_{(n)}\left(\ell,\ell';c\gamma\right) \tag{52}$$

$$\widetilde{\mathbf{X}}_{(n)}\left(\ell,\ell';c\gamma\right) = (-1)^{n+1}\left(1/\kappa\right)\left[t_{\ell}^{0}\right]^{1/2}\;\Xi_{(n)}\left(\ell,\ell';c\gamma\right)\left[t_{\ell'}^{0}\right]^{1/2} \tag{53}$$

Let us explicit the single scattering ‹exafs› matrix element $\widetilde{\mathbf{X}}^{j}_{(2)}(\ell,\ell';c\gamma)$ for the single shell j:

$$\begin{aligned}\widetilde{\mathbf{X}}^{j}_{(2)}(\ell,\ell';c\gamma) &= \sum_{ab}\sum_{\ell''}\left[t^{0}_{\ell}\right]^{1/2}\mathcal{H}^{+a}_{\ell\ell''}(\kappa R_{0j})\; t^{j}_{\ell''}\; \mathcal{H}^{+b}_{\ell''\ell'}(\kappa R_{j0})\left[t^{0}_{\ell'}\right]^{1/2} \\ &\times(-1)^{a+b}\left[(2a+1)(2b+1)\right]^{1/2}(-1)^{c}W(\ell a,\ell' b;\ell'' c) \\ &\times\sum_{\alpha\beta}(a\alpha\; b\beta|\,c\gamma)\mathbf{Y}^{\alpha}_{a}\left(\widehat{\mathbf{R}}_{0j}\right)\mathbf{Y}^{\beta}_{b}\left(\widehat{\mathbf{R}}_{j0}\right)\end{aligned} \tag{54}$$

and the single scattering EXAFS function becomes:[72]

$$\chi^{(2)}_{\ell\ell'}(\widehat{\boldsymbol{\varepsilon}}) = \mathrm{Im}\left[\begin{array}{l}\exp\left(i\delta^{0}_{\ell}+i\delta^{0}_{\ell'}\right)\sum_{j}\sum_{ab}\sum_{\ell''}\mathcal{H}^{+a}_{\ell\ell''}(\kappa R_{0j})\,t^{j}_{\ell''}\mathcal{H}^{+b}_{\ell''\ell'}(\kappa R_{j0}) \\ \times(-1)^{a+b}\left[(2a+1)(2b+1)\right]^{1/2}\sum_{c}(-1)^{c}W(\ell a,\ell' b;\ell'' c) \\ \times\langle c||a||b\rangle\langle c||1||1\rangle W(1\;\ell_0,c\;\ell';\ell\;1)(2c+1)\,P_c\left(\widehat{\boldsymbol{\varepsilon}}.\widehat{\mathbf{R}}_{0j}\right)\end{array}\right] \tag{55}$$

where $P_c\left(\widehat{\boldsymbol{\varepsilon}}.\widehat{\mathbf{R}}_{0j}\right)$ is the Legendre polynomial of order c.

- For $c=0$, $P_0\left(\widehat{\boldsymbol{\varepsilon}}.\widehat{\mathbf{R}}_{0j}\right)\equiv 1$ and there is no polarization dependence.
- For $c=2$, $P_2\left(\widehat{\boldsymbol{\varepsilon}}.\widehat{\mathbf{R}}_{0j}\right)=\left[3\cos^2\theta_j-1\right]/2$ and there will be no EXAFS contribution of any scattering atom j for which the angle θ_j between the unit vectors $\widehat{\boldsymbol{\varepsilon}}$ and $\widehat{\mathbf{R}}_{0j}$ is the so-called magic angle (57°). Atom j will have its maximum contribution to the EXAFS spectrum if the two vectors are parallel. Since $P_2\left(\widehat{\boldsymbol{\varepsilon}}.\widehat{\mathbf{R}}_{0j}\right)$ averages out to zero, the $c=2$ terms vanish for a disordered powder.

The best strategy to calculate the higher order terms $\chi^{(n)}_{\ell\ell'}(\widehat{\boldsymbol{\varepsilon}})$ is to exploit the *recursion relation*:[72]

$$\begin{aligned}\Xi_{(n+1)}(\ell,\ell';c\gamma) &= \sum_{A,B,\ell''}\Xi_{(n)}(\ell,\ell'';a\alpha)\,t^{j+1}_{\ell''}\mathcal{H}^{+a}_{\ell''\ell'}(\kappa R_{jj+1}) \\ &\times(-1)^{a+b}\left[(2a+1)(2b+1)\right]^{1/2}(-1)^{c}W(\ell a,\ell' b;\ell'' c) \\ &\times(a\alpha\; b\beta|c\gamma)\mathbf{Y}^{\beta}_{b}\left(\widehat{\mathbf{R}}_{jj+1}\right)\end{aligned} \tag{56}$$

where $A=(a,\alpha)$ and $B=(b,\beta)$. We have already mentioned that $\boldsymbol{\tau}^{00}_{(1)}=\widetilde{\mathbf{X}}^{00}_{(1)}=\Xi^{00}_{(1)}\equiv 0$ due to the intrinsic definition of the propagator $[H]^{00}$ but one should not confuse $[H]^{00}$ with $[H]^{0j}$ which leads to:

$$\Xi^{0j}_{(1)}(\ell,\ell';a\alpha)=(-1)^{a}\,\Xi^{j0}_{(1)}(\ell,\ell';a\alpha)=\mathcal{H}^{+a}_{\ell\ell''}(\kappa R_{0j})\left[(2a+1)/4\pi\right]^{1/2}\delta_{\alpha 0} \tag{57}$$

All successive terms of the multiple scattering series can be obtained to any order by recursion and their polarization dependence can be also determined. The corresponding expressions may look formidable but they are perfectly manageable by a computer. In the next section, we will simplify the formulation of the EXAFS series for "*pedestrian*" applications. There is, however, no black magic: such simpler formulations are useless for *ab initio* computations. The present formulation[72] is fairly general but alternative expressions restricted to the first few terms of the Born series can be used as well and are detailed in references.[73–77]

B. XANES and EXAFS Regimes

1. Shape Resonances, Pre-edge Resonances

Shape resonances[3,78] are nothing more than the analogues, for a cluster of atoms, of the scattering resonances of atomic physics:[79] any repulsive potential barrier ($\Delta V > 0$) creates a sort of "*cage*" that traps the final state electron in a *quasi*-bound state decaying away with a life-time: $\tau_r = \hbar\Gamma_r^{-1}$connected with the tunneling probability through the potential barrier. A classical example taken from atomic physics is the centrifugal barrier whose height $\simeq \ell(\ell+1)/R^2$ gives rise to strong resonances for $\ell \geq 3$.[63,80] In the cluster case, resonances are to be expected from (42) for all singularities of the scattering path operator which we may rewrite for more convenience:[79] $\boldsymbol{\tau} = [M - i\Delta]^{-1}$where M and Δ are now real matrices. Mathematics immediately tell us that a resonance will be observed for $k = k_r$ every time the condition: $Det\,\|M\| = 0$ will be satisfied. This condition can be turned into a functional form: $F\left[\cot\left(\delta_\ell^j\right);\ k_r R_j;\ \widehat{\mathbf{R}}_j\right] = 0$ which, unfortunately, is most often intractable in practice. Nevertheless, if one wishes to compare the XANES of some unknown metalloporphyrin (or the edge spectrum of any uncharacterized hemoprotein) with the XANES of a model compound which is expected to have the same basic coordination polyhedron (*i.e.* with the stereogeometrical constraint that $\widehat{\mathbf{R}}_j$ is roughly invariant), then, under the further restriction that the phase-shifts are transferable (*i.e.* the δ_ℓ^j are also invariant), one may exploit an interesting rule proposed by Natoli:[81]

$$[k_r.R_j]^{\text{unknown}} = \left[k'_r.R'_j\right]^{\text{model compound}} \tag{58}$$

which is most often reformulated in a way that is more appropriate for direct experimental verifications: $\Delta E.R^2 = Cst$ where ΔE is the measured energy difference between a shape resonance in the continuum and a signature as close as possible to the Fermi level, typically a characteristic pre-edge resonance or simply the threshold energy. This is a quick, but very reliable way to detect variations in the interatomic distances R_j within series of compounds that can be compared. In the early days of XAS studies with synchrotron radiation, Natoli's rule has found numerous applications in XANES studies of dilute solutions of hemoproteins for which EXAFS spectra could not be collected with a good enough signal-to-noise ratio. There is an abundant literature concerning the extension of this rule by Sette *et al.*[82] who established a correlation between the K-edge σ^* resonance positions of low Z elements as a function of molecular bond lengths for various classes of molecules for which the sum of atomic numbers of bonded atoms Z_B is identical. In soft XAS, this is still referred to as a method to measure "*bond lengths with a ruler*".[3,83]

As far as biochemistry is concerned, the danger is, however, to forget that the validity of Natoli's rule is subject to strict requirements. With third generation sources, EXAFS spectra can now be recorded on ultra dilute systems and Natoli's rule is getting less used. Another way of using the same condition $Det\,\|M\| = 0$ is to turn back to the secular equations (38) and to solve the equation:

$$Det \left\| \begin{array}{cc} \left[T^{-1}(E)\right]_{LL'}^{jj'} & -S_{LL'}^{j0}(E) \\ S_{LL'}^{0j'}(E) & -\delta_{LL'}\left[t_\ell^0(E)\right]^{-1} \end{array} \right\| = 0 \tag{59}$$

which for $V < \overline{V}_{int}$ gives the energies of the molecular orbitals of the clusters. Equation (59) is the basis of the so-called "*Extended Continuum*" technique which has been used by Penner-Hahn *et al.*[11] to assign the intense pre-edge resonances observed in high oxidation state Cr porphyrins to transitions towards *quasi*-bound excited states which have been shown to have a strong metal character. Quite similar calculations have also been performed in our group by Ruiz-Lopez *et al.* on vanadyl porphyrins.[84,85]

2. Multiple Scattering Regime of EXAFS

This regime corresponds to the case where the Born series expansion of the multiple scattering path operator is convergent. From the mathematical point of view, this requires that the convergence radius of the series is less than unity: $\rho\left[\kappa\sqrt{T}H\sqrt{T}\right] < 1$ where $\rho[M]$ denotes the highest eigenvalue of matrix M. From a more practical point of view, one may start from results established in sections II.A.3-4 which show that the EXAFS function is the sum of a series of terms starting with the order $n \geq 2$:

$$\chi^{\ell}(\kappa) = \sum_{n=2}^{\infty} \chi^{\ell}_{(n)}(\kappa) \tag{60}$$

where the superscript ℓ refers to the selected final state. In real spectra, the single scattering terms ($n = 2$) are largely dominant and we have already pointed out that they yield information only about the radial distribution of the surrounding scatterers whereas more complete information about the stereogeometry of the whole cluster could be extracted, in principle, from the higher order correlation terms $\chi^{\ell}_{(3)}(\kappa)$, $\chi^{\ell}_{(4)}(\kappa)$... This is the point here at which to introduce a more classical expression of $\chi^{\ell}_{(n)}(k)$:

$$\chi^{\ell}_{(n)}(\kappa) = \sum_{p} \left|A^{\ell}_{(n)}\left(\kappa, R^{p}_{(n)}, \widehat{\mathbf{R}}_{ij}\right)\right| \sin\left[\kappa R^{p}_{(n)} + 2\delta^{\ell}_{0} + \varphi^{\ell}_{(n)}\left(\kappa, R^{p}_{(n)}, \widehat{\mathbf{R}}_{ij}\right)\right] \tag{61}$$

where $A^{\ell}_{(n)}$ and $\varphi^{\ell}_{(n)}$ are the scattering amplitude and the scattering phase-shift for a given scattering path $R^{p}_{(n)}$. Remember that both $A^{\ell}_{(n)}$ and $\varphi^{\ell}_{(n)}$ are not simply function of κ but also depend implicitly on the whole stereogeometry (including bond angles) of the cluster. There are a few points which we want to make clear:

- Far above the edge, *i.e.* for large κ values, the scattering amplitudes decay rapidly and multiple scattering processes of high order should have only very weak contributions: their detection requires therefore an excellent signal-to-noise ratio.

- One has to take into account not only the finite experimental energy resolution ($\Gamma_{\text{exp}} \simeq 1$ eV) but also the life-time of the core hole ($\Gamma_h \geq 0.5\ eV$) and the life-time of the photoelectron itself. The latter is usually taken into account when the self energy has an imaginary part as this is the case with the Hedin & Lundqvist effective potential[86,87] discussed in section II.C. The practical consequence is that both long multiple scattering

paths and distant single scattering produce no structure that survives such a severe energy broadening. Under the simplest approximations the damping function can be written:[88]

$$D^{\ell}_{(n)}(\Gamma_t;k) = \exp\left\{-\frac{\Gamma_t}{2k}\left(2m\hbar^{-2}\right)\left[R^{p}_{(n)} + \Delta^{\ell}_{(n)}(k)\right] - g\right\} \qquad (62)$$

$$\text{where} : \quad \Gamma_t(eV) = \Gamma_{\exp} + \Gamma_h \quad (\textit{is converted into } \text{Å}^{-2})$$

$$R_{(n)} = \sum_{i=0}^{n-1} R_{i,(i+1)} \quad \text{and} : \quad \Delta^{\ell}_{(n)} = \frac{\partial}{\partial k}\left[2\delta_0(k) + \phi^{\ell}_{(n)}(k)\right]$$

with $\Delta < 0$. Note that the additional factor $\exp[-g]$ is the probability for no "*intrinsic losses*" caused by the excitation of inelastic channels.

- The angular dependence of a multiple scattering path $R^{p}_{(n)}$ is often determinant. For instance, $\chi^{\ell}_{(3)}(k)$ can be expanded in a series of terms $\sum_{\lambda} f_{\lambda} P_{\lambda}\left(\widehat{\mathbf{R}}_i.\widehat{\mathbf{R}}_j\right)$ in which only the first order term $\lambda = 1$ will vanish if $\widehat{\mathbf{R}}_i$ and $\widehat{\mathbf{R}}_j$ are orthogonal. One may expect, then, $\chi^{\ell}_{(3)}(k)$ to be certainly weaker (but not zero) if $\widehat{\mathbf{R}}_i$ and $\widehat{\mathbf{R}}_j$ are (nearly) orthogonal. Concretely, this implies that in the case of a metalloporphyrin, the third order correlation involving the 4 nitrogen atoms and the axial ligands should be rather weak, as confirmed by all the experiments reported so far.

- On the other hand, it has been known for a long time that any colinear or slightly bent arrangement of the absorber + two (or more) scatterers will result in a so-called "*shadowing effect*" that enhances the contribution of the most distant scatterers.[59,61,75] There are two reasons to expect large effects:

  (*i*) *forward* scattering is systematically more intense than *backward* scattering;[89]

  (*ii*) the $\chi^{\ell}_{(2)}(k)$, $\chi^{\ell}_{(3)}(k)$, $\chi^{\ell}_{(4)}(k)$ contributions relative to the most distant atom are overlapping and are possibly interfering : they can hardly be resolved. We like to draw attention on the necessity to have not only excellent phase-shifts *but also excellent amplitudes* (...which is more difficult) for modelling the interferences of those three signals.[90–93]

In coordination chemistry, there are several ligands which are known to give very strong *shadowing* or focusing effects: $-CO$, $-CS$, $-NO$, CN^{-}, SCN^{-}.[94–96] It is now well documented that histidine and imidazole ligands which are essential in biology also contribute to intense multiple scattering paths due to the focusing effects caused by the strong forward scattering from the nearest neighbor atoms:[97,98] this is, in fact, a general property which is shared by most aromatic five or six atom rings. For what concerns the porphyrin macrocycle itself, multiple scattering effects are less spectacular but are quite real and cannot be neglected anymore in refined analyses. The shortest multiple scattering paths that are expected to contribute to the EXAFS spectrum of a metalloporphyrin are illustrated by **Figure 6**:

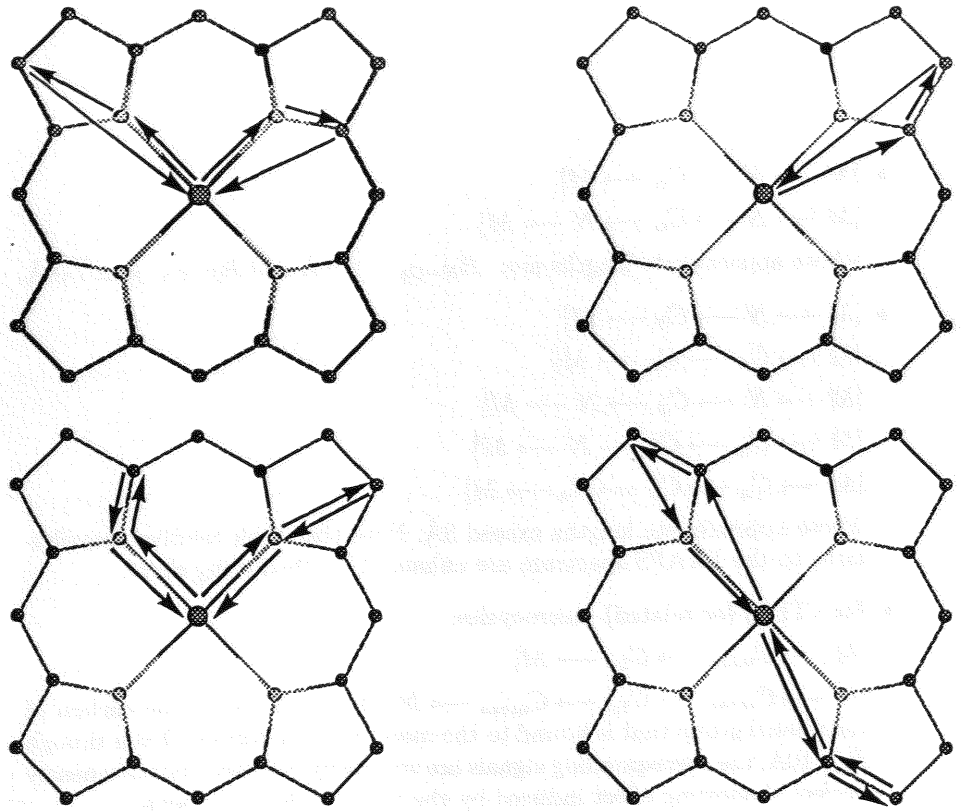

Figure 6: Main multiple scattering paths contributing to the calculation of the EXAFS signal in the case of a metalloporphyrin.

- $[M \longrightarrow N \longrightarrow C_\alpha \longrightarrow M]$
  $[M \longrightarrow N \longrightarrow C_\alpha \longrightarrow N \longrightarrow M]$
  whose approximate lengths are: $R_{N-Ca} \simeq 6.6$ Å and $R_{N-Ca-N} \simeq 7.0$ Å.
- $[M \longrightarrow N \longrightarrow C_\beta \longrightarrow M]$
  $[M \longrightarrow C_\alpha \longrightarrow C_\beta \longrightarrow M]$
  $[M \longrightarrow N \longrightarrow C_\beta \longrightarrow N \longrightarrow M]$
  $[M \longrightarrow C_\alpha \longrightarrow C_\beta \longrightarrow N \longrightarrow M]$
  $[M \longrightarrow C_\alpha \longrightarrow C_\beta \longrightarrow C_\alpha \longrightarrow M]$
  whose approximate lengths exceed 8Å. Note that their relative contributions to the EXAFS spectrum are enhanced by shadowing effect.
- For (TPP) (or related) macrocycles:
  $[M \longrightarrow C_{meso} \longrightarrow C_{1\phi} \longrightarrow M]$
  $[M \longrightarrow C_{meso} \longrightarrow C_{1\phi} \longrightarrow C_{meso} \longrightarrow M]$ in which $C_{1\phi}$ is the carbon of the phenyl group that is bound to the *meso* bridging carbon. Even though $R \geq 10$Å, the corresponding signals are still easily detected due to a nearly perfect shadowing effect induced by the *meso* bridging carbons.

3. Fast Spherical Wave and Other Approximations

For practical applications, one has to explicit $\chi^{\ell}_{(n)}(k)$ in a more tractable form. We will restrict ourself to the simplest case of unpolarized EXAFS, *i.e.* $c = \gamma = 0$. We have the very general formulation:[72]

$$\chi^{\ell}_{(n)}(k) = \frac{(-1)^n}{(2\ell+1)^{1/2}} \operatorname{Im}\left[\exp\left(2i\delta^0_\ell\right) \sum_{ij} \Xi^{ij}_{(n)}(\ell,\ell;00)\right] \tag{63}$$

Starting with the single scattering contribution, the following formula holds true at any edge:

$$\chi^{\ell}_{(2)}(k) = -\operatorname{Im}\left[\begin{array}{c}\exp\left(2i\delta^0_\ell\right) \sum_j \sum_{\ell'} (2\ell'+1)\ t^j_{\ell'} \\ \times \sum_a (\ell 0,\ell' 0|\, a0)^2 \left[h^+_a(kR_j)\right]^2\end{array}\right] \tag{64}$$

For the third and fourth order terms, recurrent formula are more appropriate:

$$\chi^{\ell}_{(3)}(k) = -\frac{1}{(2\ell+1)} \operatorname{Im}\left[\begin{array}{c}\exp\left(2i\delta^0_\ell\right) \sum_{ij} \sum_{\ell',a\alpha} \Xi^{0ij}_{(2)}(\ell,\ell';a\alpha)\ t^j_{\ell'} \\ \times \Xi^{j0}_{(1)}(\ell',\ell;a-\alpha)\,(-1)^{\ell-\ell'-\alpha}\end{array}\right] \tag{65}$$

$$\chi^{\ell}_{(4)}(k) = +\frac{1}{(2\ell+1)} \operatorname{Im}\left[\begin{array}{c}\exp\left(2i\delta^0_\ell\right) \sum_{ij} \sum_{\ell',a\alpha} \Xi^{0ij}_{(2)}(\ell,\ell';a\alpha)\ t^j_{\ell'} \\ \times \Xi^{jk0}_{(2)}(\ell',\ell;a-\alpha)\,(-1)^{\ell-\ell'-\alpha}\end{array}\right] \tag{66}$$

and one may appreciate that the recurrent formula are very efficient for practical calculations since the quantities $\Xi^{0i}_{(1)}$ and $\Xi^{0ij}_{(2)}$ are calculated only once for every energy and then are combined differently to yield $\chi^{\ell}_{(2)}(k)$, $\chi^{\ell}_{(3)}(k)$ ...up to

$\chi^{\ell}_{(6)}(k)$.[72] Note that the computing codes MSXAS[99] or GNXAS[100] which are often cited in the recent literature are based on such recurrent calculations.

In practice, one needs to calculate a large number of products of modified Hankel functions $\left[h^{+}_{\ell}(kR_i)\right]^{p}\left[h^{+}_{\ell}(kR_j)\right]^{q}$. Much computing time can be saved by exploiting useful approximations:

- the plane-wave (PW) approximation:

$$h^{+}_{\ell}(kR) = (-i)^{\ell+1}\,\underline{h}^{+}_{\ell}(kR)\left[\exp(ikR)\right]/kR \;\; with \;\; \underline{h}^{+}_{\ell}(kR) \simeq 1$$

- the fast spherical wave (FSW) approximation (Rehr *et al.*,[101] Gurman *et al.*[75]):

$$\underline{h}^{+}_{\ell}(kR) \longrightarrow \exp\left[i\ell(\ell+1)/2kR\right]\left[1+\ell(\ell+1)/2(kR)^2\right]^2 \;\; if \;\; (kR) \longrightarrow \infty$$

Clearly, a major advantage of the PW approximation is that both the scattering amplitude and the phase-shift *become independent of the dimensionless variable* kR and can be tabulated. This approximation becomes more acceptable at large values of kR which are usually heavily weighted in standard numerical analyses such as the Fourier Transform (FT) analyses discussed in section III.A.2. Unfortunately, detailed numerical calculations have clearly established that the PW approximation introduces at low/medium k values quite severe distortions of $\chi^{\ell}_{(2)}(k)$ while the real signal is well reproduced both in phase and amplitude by the fast spherical FSW approximation. As pointed out by Natoli and Benfatto,[57] the PW approximation is not satisfactory for the high order correlations $\chi^{\ell}_{(3)}(k)$, $\chi^{\ell}_{(4)}(k)$,... and should be definitely abandoned. In our experience, even the FSW approximation may fail to reproduce the amplitudes correctly.

Even though the PW approximation is not to be recommended for refined calculations, it remains useful to elaborate and justify approximations of higher orders. This is nicely illustrated by another useful recipe that has been proposed by Rehr and Albers[102] in order to speed up the calculation of the Green function in the typical case one wishes to include a large number of high order scattering paths. Their starting point was the remark that, within the PW approximation, the Green function of a multiple scattering path results in a simple factorization of scattering amplitudes $A_{(N-1)}(\theta_{N-1})\,A_{(N-2)}(\theta_{N-2})\,A_{(N-3)}(\theta_{N-3})$ $...A_{(1)}(\theta_1)$, in which the summation over angular momenta that is carried out at each site combines with the $t-$matrix:

$$\chi_{(N-1)}(\kappa) = \mathrm{Im}\left\{ \begin{array}{c} A_{(N-1)}(\theta_{N-1})\,A_{(N-2)}(\theta_{N-2})...A_{(1)}(\theta_1)\,(\widehat{\boldsymbol{\rho}}_1\cdot\widehat{\boldsymbol{\rho}}_N) \\ \times \exp\left[i\rho_1 + i\rho_2 + ...i\rho_N + 2i\delta_0\right]/\rho_1\rho_2...\rho_N \end{array} \right\} \quad (67)$$

where: $\boldsymbol{\rho}_i = \kappa\left(\mathbf{R}_{(i+1)} - \mathbf{R}_{(i+1)}\right)$ is a dimensionless scattering path vector. The strategy of Rehr and Albers was then to study under which conditions a factorization of the Green function could still be preserved while abandoning the crude PW approximation. They started from a *factorized* formulation of the two center Green functions:

$$G(\mathbf{r},\mathbf{r}',E) = \sum_{LL'} j_L(\mathbf{r}-\mathbf{R})\,j_{L'}(\mathbf{r}'-\mathbf{R}')\,G_{LL'}(\boldsymbol{\rho}) \quad (68)$$

with:

$$G_{LL'}(\boldsymbol{\rho}) = \frac{\exp[i\rho]}{\rho} \sum_{\Lambda} \widetilde{\Gamma}^{L}_{\Lambda}(\boldsymbol{\rho})\, \Gamma^{L'}_{\Lambda}(\boldsymbol{\rho}) \tag{69}$$

where the exact functions $\widetilde{\Gamma}^{L}_{\Lambda}$ and $\Gamma^{L'}_{\Lambda}$ can be replaced by their series expansion. The first term which is first order with respect to $1/\rho$ can be indeed identified with the PW approximation: it yields a (3×3) matrix with respect to the combined indices $\Lambda = (\mu, \nu) = (0,0)\,;(0,\pm 1)$. Rehr and Albers have suggested[102] that, in practice, a truncation of the series preserving only the first and the second order terms with respect to $1/\rho$ should be enough. This reduces the problem to the calculation of a (6×6) matrix restricted to the following indices: $\Lambda = (\mu, \nu) = (0,0)\,;(0,\pm 1)\,;(0,\pm 2)\,;(1,0)$. One will get immediately a good idea on how much this approximation speeds up the calculation if one realizes that a true multiple scattering calculation would involve the multiplication of $2\ell^2_{\mathbf{max}}$x$2\ell^2_{\mathbf{max}}$ matrices whereas the fast algorithm of Rehr and Albers involves the multiplication of only (6×6) matrices. One should keep in mind that in the simulation of EXAFS spectra there is the rule of thumb that: $\ell_{\mathbf{max}} \sim ka_0$ (where a_0 is the muffin-tin radius of the absorbing atom) so that, in practice,: $\ell_{\mathbf{max}}$ ~25-30. This algorithm contributed to make very fast the codes FEFF3-FEFF7 developed by Rehr and his coworkers.[103-108] It is also used in the most recent version of the code EXCURVE98 developed in Daresbury (U.K.). For the sake of completeness, we wish still to give the general formulation of the factorized Green function of Rehr and Albers for multiple scattering paths of order (n):

$$G^{(n)}_{L_N L_0}(\mathbf{R}_1, ...\mathbf{R}_N) = \frac{\exp[i\rho_1 + ...i\rho_N]}{\rho_1 \rho_2 ... \rho_N} \sum_{\Lambda_i \Lambda_j} B^{L_0 L_N}_{\Lambda_1 \Lambda_N}\, \Pi^{N-1}_{A} \tag{70}$$

where Π^{N-1}_{A} is the product of the local scattering amplitudes :

$$\Pi^{N-1}_{A} = A^{N-1}_{\Lambda_N \Lambda_{N-1}}(\boldsymbol{\rho}_N\ ,\ \boldsymbol{\rho}_{N-1}) ... A^{1}_{\Lambda_2 \Lambda_1}(\boldsymbol{\rho}_2,\ \boldsymbol{\rho}_1) \tag{71}$$

with:

$$A^{i}_{\Lambda\Lambda'}(\boldsymbol{\rho},\ \boldsymbol{\rho}') = \sum_{L} t^{i}_{\ell}\, \Gamma^{L}_{\Lambda}(\boldsymbol{\rho})\, \Gamma^{L'}_{\Lambda'}(\boldsymbol{\rho}') \tag{72}$$

whereas the so-called *termination matrix* $B^{L_0 L_N}_{\Lambda_1 \Lambda_N}$ is defined by:

$$B^{L_0 L_N}_{\Lambda_1 \Lambda_N} = \Gamma^{L_0}_{\Lambda_0}(\boldsymbol{\rho}_1)\, \Gamma^{L_N}_{\Lambda_N}(\boldsymbol{\rho}_N) \tag{73}$$

This formulation proved itself to be reliable in several applications. It seems, however, that its extension to the case of fully relativistic systems is not completely straightforward and deserves more attention.

4. Configuration Average and Debye-Waller Damping Factor

As a consequence of static and vibrational disorders affecting the whole cluster, what is actually measured in EXAFS is never $\chi^{\ell}_{(n)}(k)$ but rather some configurational average $\left\langle \chi^{\ell}_{(n)}(k) \right\rangle$. Benfatto *et al.*[109] have shown how to calculate this configuration average for a N-atom cluster, provided that the N-dimensional

mass weighted instantaneous displacements $\mathbf{q} = \sqrt{m_j}\ \mathbf{u}_j$ follow a multivariate Gaussian distribution law, then:

$$\left\langle \chi^{\ell}_{(n)}(k) \right\rangle = \int d\mathbf{u}\, \frac{\exp\left[-\left(\mathbf{q}^{\dagger}\mathbf{M}^{-1}\mathbf{q}\right)/2\right]}{(2\pi)^{N/2}\det\left[(\mathbf{M})^{1/2}\right]} \times \left|A^{p,\ell}_{(n)}(k,\mathbf{q})\right| \sin\left[kR^{p}_{(n)}(\mathbf{q}) + \varphi^{p,\ell}_{(n)}(k,\mathbf{q})\right] \tag{74}$$

where $\mathbf{M}$ is the dynamical correlation matrix of the N-dimensional displacements. It is most convenient to switch from the mass weighted displacements $\mathbf{q}$ to the *normal coordinates* $\mathbf{Q} = \mathbf{A}^{-1}\mathbf{q}$ where $\mathbf{A}$ is some orthogonal matrix that will diagonalize the *dynamical matrix* $[\Phi]_{ij} = \frac{\partial^2 V}{\partial q_i \partial q_j}$. This defines 3N-6 normal modes of vibrations characterized by the eigenvalue ω_λ associated with the eigenvectors Q_λ. Starting from the averaged equilibrium configuration $\mathbf{Q}_0$ and retaining only the first order terms, the configuration average can now be rewritten:

$$\left\langle \chi^{\ell}_{(n)}(k) \right\rangle = \left|A^{p,\ell}_{(n)}(k,\mathbf{Q}_0)\right| \left[1 + D_1^2(k)\right]^{1/2} \exp\left[-D_2(k)\right] \times \sin\left[kR^{p}_{(n)}(\mathbf{Q}_0) + \varphi^{p,\ell}_{(n)}(k,\mathbf{Q}_0) + D_1(k)\right] \tag{75}$$

where:

$$D_1(k) = \sum_{\lambda}^{3N-6} [\mathbf{M}_Q]_{\lambda\lambda} \left[\frac{1}{\left|A^{p,\ell}_{(n)}(k,\mathbf{Q})\right|} \frac{\partial \left|A^{p,\ell}_{(n)}(k,\mathbf{Q})\right|}{\partial Q_\lambda} \frac{\partial \psi^{p}_{(n)}(k,\mathbf{Q})}{\partial Q_\lambda} \right]_{\mathbf{Q}_0}$$

$$D_2(k) = \frac{1}{2} \sum_{\lambda}^{3N-6} [\mathbf{M}_Q]_{\lambda\lambda} \left[\frac{\partial \psi^{p}_{(n)}(k,\mathbf{Q})}{\partial Q_\lambda} \right]^2_{\mathbf{Q}_0}$$

in which we have defined: $\psi^{p}_{(n)}(k,\mathbf{Q}) = kR^{p}_{(n)}(\mathbf{Q}) + \varphi^{p,\ell}_{(n)}(k,\mathbf{Q})$. Since we used the normal coordinates, the matrix $\mathbf{M}_Q$ is the diagonal vibrational correlation function whose elements are given by:

$$[\mathbf{M}_Q]_{\lambda\lambda} = \left\langle Q_\lambda^2 \right\rangle = \frac{\hbar}{2\omega_\lambda} \coth\left(\frac{\hbar\omega_\lambda}{2k_B T}\right) \tag{76}$$

where $k_B T$ is the usual Boltzmann scaling factor. This is mostly the exponential term $\exp\left[-D_2(k)\right]$ which is causing a strong damping of the EXAFS signals at large k values. In the single scattering EXAFS, *i.e.* for $n = 2$, the exponential term may reduce to a true Debye-Waller factor $\exp\left[-2\sigma_j^2 k^2\right]$ but *only* in the PW approximation because the phase-shifts are then fully independent of the cluster geometry. The corresponding Debye-Waller factor which is associated with the path length $R^p = R_{0j} + R_{j0} = 2R$ can alternatively be formulated:

$$[\sigma_j]^2 = \left\langle \left[\widehat{\mathbf{R}}_j.(\mathbf{u}_j - \mathbf{u}_0)\right]^2 \right\rangle = \sum_{\lambda} \widehat{\mathbf{R}}_j.(\mathbf{v}_j - \mathbf{v}_0) \left\langle Q_\lambda^2 \right\rangle / \mu_j \tag{77}$$

Here the vectors $\mathbf{v}_j = \widehat{\mathbf{R}}_j \left[\mu_j / m_j\right]^{1/2}$ are mass weighted *displacement fields* in the λ^{th} normal mode whereas $\mu_j = \left[[m_0]^{-1} + [m_j]^{-1}\right]^{-1}$. We want to stress

here that σ_j^2 is anyhow different from the Debye-Waller factors defined either in Mössbauer or in crystallography because the cross term $\langle \mathbf{u}_j.\mathbf{u}_0 \rangle$ cannot be neglected in EXAFS.

For higher order scattering paths ($n \geq 3$), there are two distinct terms which are expected to contribute to the $\exp[-D_2(k)]$ term: the first one arises again from fluctuations in the length of the scattering path R^p and the latter fluctuations are clearly affected by high frequency vibrational modes; the second contribution now arises from the change of the phase-shifts as a consequence of the fluctuating geometry of the cluster. Low frequency bending modes could now result in a non-Debye-Waller-like damping, *i.e.* in a damping that is not proportional to k^2. This second contribution may be suspected to become rapidly the dominant one for high order multiple scattering terms.

There are very few examples of multiple scattering EXAFS calculations where the damping of the multiple scattering signal is not treated as a freely adjustable or fitted parameter. Increasing the number of fitted parameters is obviously a strong handicap for those who are interested in evaluating the present limitations of the theory associated with a given choice of local effective potentials: it would be therefore highly desirable to calculate in a non-empirical way $D_1(k, Q_\lambda)$ and $D_2(k, Q_\lambda)$: this is only possible if one has access to the vibrational correlation functions $\mathbf{M}_Q$. Starting from reasonable guesses for a few local force constants, Poiarkova and Rehr[110] have used the equations of motions to calculate a projected vibrational density of states (VDOS) by Fourier transforming the time dependent correlation function of the normal displacements. Another option is to derive the vibrational correlation function directly from a separate experiment. Regarding organometallic complexes, the most rigorous results were obtained by Loeffen *et al.*[111,112] who used Inelastic Neutron Scattering (INS) to perform first a very detailed normal mode analysis of the zinc tetraimidazole complex and reinjected the results in a multiple scattering EXAFS calculation including manybody correlations up to the fourth order ($n = 4$). The partial derivatives $D_1(k, Q_\lambda)$ and $D_2(k, Q_\lambda)$ were obtained numerically for each one of the 105 normal modes that had been identified from INS: Loeffen and Pettifer[113] simply calculated the functions $A^\ell_{(n)}(k, Q_\lambda)$ and $\psi^p_{(n)}(k, Q_\lambda)$ for two different configurations, *i.e.* $[Q_\lambda]_0$ and $[Q_\lambda]_0 + \sigma[Q_\lambda]$ from which they approximated the relevant derivatives. They found that for most paths, the damping was essentially due to a small group of four modes assigned principally to the tetrahedral $Zn - N$ stretch modes of the complex. Unfortunately, no study of this type has ever been made for porphyrins or metalloproteins.

The theory has been extended by Benfatto *et al.*[109] to the case of anharmonic force fields by means of multidimensional cumulant expansion of the characteristic function of the probability distribution. A detailed account of anharmonic effects goes well beyond the scope of this review. We feel preferable to analyze in more detail the case of tri-atomic structures of nearly aligned atoms with the photoabsorber located on one side of the chain because this is the typical example where multiple scattering paths are known to have large contributions.[114] Without any loss of generality, one may parametrize the geometry of the system using two distance coordinates, *i.e.* R_1 which is the distance between the photoabsorber A and the atom B bonded to A, R_2 which is the distance between atoms B and C, and one angular coordinate ϑ close to 180° describing

the angles between A,B and C. If one assumes that there is no coupling between the angular mode and the stretching modes, one is led to a simple but realistic distribution function given by:

$$f(R_1, R_2, \vartheta) = \frac{\exp\left[-\frac{1}{2}(\mathbf{r}, \mathbf{M}^{-1}\mathbf{r})\right]}{2\pi \det \mathbf{M}} \frac{(180-\vartheta)}{\delta_\vartheta^2} \exp\left[-\frac{(180-\vartheta)^2}{2\delta_\vartheta^2}\right] \tag{78}$$

in which the bidimensional covariance matrix $\mathbf{M}$ can be rewritten:

$$\mathbf{M} = \begin{bmatrix} \sigma_{R_1}^2 & \rho_{12}\sqrt{\sigma_{R_1}^2 \sigma_{R_2}^2} \\ \rho_{12}\sqrt{\sigma_{R_1}^2 \sigma_{R_2}^2} & \sigma_{R_2}^2 \end{bmatrix} \tag{79}$$

where ρ is the bond - bond correlation factor. On the other hand, one implicitly assumes that ϑ is never fairly different from 180° so that the average angle $\overline{\vartheta}$ is given by: $\overline{\vartheta} = 180° - \sqrt{\pi/2}\delta_\vartheta$ with the variance: $\sigma_\vartheta^2 = (2 - \pi/2)\,\delta_\vartheta^2$. Therefore, the model distribution will depend on a total of six independent parameters which are respectively: $\overline{R}_1, \overline{R}_2, \sigma_{R_1}^2, \sigma_{R_2}^2, \rho_{12}, \delta_\vartheta$. Their determination by EXAFS is unfortunately not always possible due to strong correlations.[114]

C. Local Effective Potentials

1. Muffin-Tin Approximation

At this stage, we have a theory for XAS but we cannot really exploit it yet for *ab initio* simulations because we still do not know how to calculate the radial functions R_L or how to calculate the complex quantities t_ℓ^j . To perform such practical calculations, we need to go deeper into the construction of the molecular potential for a metalloporphyrin complex. The minimum size cluster which is required to describe a metalloporphyrin is already fairly large: it includes the complexed metal (M), the four nitrogen (4N) and sixteen carbons ($8C_\alpha$, $8C_\beta$) of the pyrrole rings, the four meso-bridging carbon atoms ($4C_{meso}$), very often the eight β substituents ($8X_\beta$) of the pyrrole rings or the four substituents of the meso-bridging carbons ($4Y_{meso}$), and indeed, whenever appropriate, all atoms (nZ) which define the axial ligands. One may usually forget the hydrogen atoms unless they critically affect the charge distribution very near the absorbing center which is, for practical convenience, always located at the origin (o). Each atom in the cluster is assumed to contribute essentially to a *local* potential $V_j(\mathbf{r}_j)$: a justification for this assumption is that the molecular potential is always dominated by strong local Coulomb singularities which extend only over very short distances (*i.e.* over distances of the order of the Bohr radius $a_0 \simeq 0.53$Å) whereas the interstitial potential is rather smooth and never very deep.

A convenient starting point is the so-called "*muffin-tin*" approximation and the construction of spherically averaged, local potentials with reference to a (slightly modified) prescription given a long time ago by Mattheiss[115]:

- Charge densities $\varrho_j(\mathbf{r}_j)$ can be obtained for neutral atoms from fully relativistic, self-consistent field (SCF) *atomic* calculations. Alternatively, in more advanced XANES programs, one can reinject in the present model

SCF *molecular charge densities* that can be obtained by running beforehand one of the several Quantum Chemistry programs or band structure calculations (*e.g.* LMTO-ASA-TB codes,[116] or FLAPW codes such as WIEN97[118]) which are now available.

- The atomic charge densities are placed on each atomic site of the chosen geometry and the superposed charge densities $\varrho(r) = \sum_j \varrho_j(|r - R_j|)$, or when available the SCF *molecular* charge densities, are *spherically averaged* about the atom whose local potential is required. The desired spherical average can be obtained, for example, using the Löwdin theorems on spherical expansion,[119] but restricted to $\ell = 0$. Finally, Poisson's equation is solved to derive the Coulomb part of the local potential. The whole procedure was largely inspired by the old Wigner-Seitz prescription to build a spherically averaged potential in crystals.

- When atomic charge densities are injected, the relaxation of the charge density around the core hole and the screening of this latter can be crudely accounted for by taking for the photoabsorber the charge density of the $Z+1$ atom with the corresponding core hole. This is usually not possible when external SCF molecular charge densities are used, especially when the charge densities are extracted from a band structure calculation. Ideally, one would like to have a self-consistent charge density of the system in the presence of the core hole and with the core electron promoted to an empty valence state: this is looking absolutely essential to simulate XMCD signals.

- The next step is to add the local exchange and correlation potentials.

2. *Local Density* Functional Theory:

A perennial question in quantum chemistry is how to calculate *exchange* and *correlation* in a many body problem. This is where two important theorems established in the early sixties by Hohenberg and Kohn[120] proved to be very productive: these authors demonstrated that all aspects of the electronic structure of a system in a non-degenerated ground state are completely determined by the *local* electron density $\varrho(\mathbf{r}) = \sum_k \psi_k^*(\mathbf{r})\,\psi_k(\mathbf{r})$ and they proposed a formal stationary expression of the energy as a functional of $\varrho(\mathbf{r})$. Slightly later, Kohn and Sham[121] extended these considerations to spin polarized systems by introducing the local density of electrons of spin $\sigma = 1/2\,(\uparrow)$ or $-1/2\,(\downarrow)$, *i.e.* $\varrho_\sigma(\mathbf{r}) = \sum_k f_\sigma \psi_{k\sigma}^*(\mathbf{r})\,\psi_{k\sigma}(\mathbf{r})$ where f_σ is the occupation number obeying Fermi statistics. Employing the energy variational principle, they finally derived a system of self-consistent, one-particle equations which can be written (in atomic units):

$$\left(-\frac{1}{2}\nabla^2 + v_{nuc}(\mathbf{r}) + u_{cb}\left[\varrho(\mathbf{r})\right] + v_{xc}^{\sigma}\left[\varrho_\uparrow(\mathbf{r}), \varrho_\downarrow(\mathbf{r})\right]\right)\psi_{k\sigma}(\mathbf{r}) = \epsilon_{k\sigma}\psi_{k\sigma}(\mathbf{r}) \tag{80}$$

where: $v_{nuc}(\mathbf{r})$ is the potential of the nuclei, $u_{cb}\left[\varrho(\mathbf{r})\right]$ is the so-called *direct* Coulomb electron-electron interaction and $v_{xc}^{\sigma}\left[\varrho_\uparrow(\mathbf{r}), \varrho_\downarrow(\mathbf{r})\right]$ is the exchange-correlation potential for spin σ. For an electron gas which is unpolarized,

$v_{xc}^{\sigma}\left[\varrho_{\uparrow}(\mathbf{r}),\varrho_{\downarrow}(\mathbf{r})\right]$ reduces to $v_{xc}[\rho]$. One should stress that the eigenvalues ϵ_k *do not correspond to elementary excitations*[87] and recall that, as yet, only their sum has significance as part of the expression of the energy of the ground state E_0: typically, Koopmans theorem relative to the removal of one electron is not satisfied by the Kohn-Sham eigenvalues ϵ_k. Concentrating first on unpolarized spin systems, it was found that, for a slowly varying density, the contribution to E_0 of the exchange-correlation energy E_{xc} is given by the density functional:

$$E_{xc}[\varrho(\mathbf{r})] \simeq \int \{\epsilon_{xc}[\varrho(\mathbf{r})]\}\,\varrho(\mathbf{r})\,d^3r \tag{81}$$

where ϵ_{xc} is the exchange-correlation energy *per electron* in a uniform electron gas with local density $\varrho(\mathbf{r})$. We may also express the corresponding potential as a functional derivative:

$$v_{xc}[\varrho(\mathbf{r})] \simeq \frac{d\{\varrho\epsilon_{xc}[\varrho]\}}{d\varrho} = \epsilon_{xc} + \varrho\frac{d\epsilon_{xc}}{d\varrho} \tag{82}$$

Similarly, for a spin polarized system, the correlation potential for spin σ would be given by:

$$v_c^{\sigma}(r_s,\xi) = \epsilon_c^{\sigma}(r_s,\xi) - \frac{r_s}{3}\frac{\partial\epsilon_c^{\sigma}(r_s,\xi)}{\partial r_s} - (\xi - sign(\sigma))\frac{\partial\epsilon_c^{\sigma}(r_s,\xi)}{\partial\xi} \tag{83}$$

where: $r_s = [3/(4\pi\varrho)]^{1/3}$ is the Seitz radius that characterizes the mean distance of interaction and $\xi = \left(\varrho_{\uparrow} - \varrho_{\downarrow}\right)/\left(\varrho_{\uparrow} + \varrho_{\downarrow}\right)$. We have listed in table 1 some of the local density functionals that are most frequently referred to in the literature either for v_{xc} or ϵ_{xc}.

Model # 1 : SLATER-JOHNSON Xα [122–124]

$$v_{xc\uparrow} = -6\alpha \left[(3/4\pi)\,\varrho^{\uparrow}(\mathbf{r})\right]^{1/3} \quad \text{with: } \alpha \simeq \tfrac{2}{3}$$

Model # 2 : GASPAR-KOHN-SHAM (exchange only)[125]

$$\epsilon_{x\uparrow} = -C_x \left[\rho_{\uparrow}(\mathbf{r})\right]^{4/3} \quad \text{with: } C_x = 0.9305$$

$$v_{x\uparrow} = -2/3 \left[(81/4\pi)\varrho_{\uparrow}(\mathbf{r})\right]^{1/3}$$

Model # 3 : THOMAS-FERMI-DIRAC-HARA[126]

$$\epsilon_{xc} = -C_{xc} \left[\rho(\mathbf{r})\right]^{4/3} \quad \text{with: } C_{xc} = 0.7386$$

Model # 4 : HEDIN & LUNDQVIST[86,87]

$$v_{xc} = \left[E_k - v_{nuc}(\mathbf{r}) - v_{cb}(\varrho) - (\hbar^2 p^2/2m)\right]$$

with: $p^2(r) = k^2 + k_F^2$ where: $k_F^2 = \left[3\pi^2 \varrho(r)\right]^{2/3}$ (local Fermi energy)

Model # 5 : GUNNARSSON & LUNDQVIST[127]

$$\epsilon_{xc}(r_s,\xi) = \epsilon_P(r_s) + \left[\epsilon_F(r_s) - \epsilon_P(r_s)\right] f(\xi)$$

$$f(\xi) = \left[(1+\xi)^{4/3} + (1-\xi)^{4/3} - 2\right] / \left[2^{4/3} - 2\right]$$

$$\epsilon_P = -3/2\pi\alpha r_s - c_P \left[\left(1 + x_P^3\right)\ln\left(1 + 1/x_P\right) + 1/2x_P - x_P^2 - 1/3\right]$$

$$\epsilon_F = -3/2\,(2)^{1/3}\,\pi\alpha r_s - c_F \left[\left(1 + x_F^3\right)\ln\left(1 + 1/x_F\right) + 1/2x_F - x_F^2 - 1/3\right]$$

where: $x_P = r_s/r_P$; $x_F = r_s/r_F$; $r_P = 11.4$; $r_F = 15.9$;

$$c_P = 0.0666\ ;\ c_F = 0.0406$$

Model # 6 : VOSKO-WILK-NUSAIR [128]

PERDEW-WANG[129]

$$\epsilon_c(r_s,\xi) = \epsilon_c^0(r_s,0) + \alpha_c(r_s)\left[f(\xi)/f''(0)\right]\left[1 - \xi^4\right] + \left[\epsilon_c^1(r_s,1) - \epsilon_c^0(r_s,0)\right]\xi^4 f(\xi)$$

$\epsilon_c^0(r_s)$; $\epsilon_c^0(r_s)$; $\alpha_c(r_s)$ are fitted to Monte-Carlo simulations

using a test function: $g(r_s) = -2A\left(1 + \alpha_1 r_s\right)$

$$\text{x} \ln\left\{1 + 1/\left[2A\left(\beta_1 r_s^{1/2} + \beta_2 r_s + \beta_3 r_s^{3/2} + ...\right)\right]\right\}$$

Table 1 : Density Functionals used for Exchange - Correlation

For a very long time, the most popular exchange-correlation potential has been the Slater Xα functional with the α values tabulated by Schwarz:[130] several calculations concerning the ground state properties of metalloporphyrins have been reported in the early eighties by Karplus and his co-workers[131–133] using such effective local potentials as a starting point for SCF calculations. The Gaspar-Kohn-Sham functional has also a number of adepts especially as a zero-order term for refined corrections detailed below. Since the early work of Lee and Beni,[134] nearly all EXAFS calculations have been performed using the Hedin & Lundqvist local self-energy: a strong argument for preferring this functional was that it has an imaginary part accounting for the life-time of the photoelectron. Beyond the Kohn-Sham "*Local Spin Density* " (LSD) approximation which is obviously a key step in defining local potentials, some additional refinements have been reviewed and carefully evaluated in the Quantum Chemistry literature: this is the case of the so-called "*Generalized Gradient*" (GG) approximation prescribed by Perdew *et al.*[135] :

$$E_{xc}^{GG} = \int \epsilon_{xc}^{GG}\left[\varrho_{\uparrow}(\mathbf{r}), \rho_{\downarrow}(\mathbf{r}); \nabla\varrho_{\uparrow}(\mathbf{r}), \nabla\varrho_{\downarrow}(\mathbf{r})\right]\rho(\mathbf{r})\,d^3r \tag{84}$$

Concentrating first on the exchange term, the function ϵ_x^{GG} could be written as:

$$\epsilon_x^{GG} = \epsilon_x^{LSD}\left[1+\kappa-\kappa/\left(1+\mu s^2/\kappa\right)\right] \tag{85}$$

where: $s = [\nabla\rho/(2\rho k_F)]$; $\kappa = 0.967$; $\mu = 0.235$. Similarly, for the correlation energy, Perdew *et al.* [135] suggested the following approximation:

$$\epsilon_c^{GG} = -m\left(e^4/\hbar^2\right)\gamma\left[\phi(\xi)\right]^3 \ln\left\{1+\frac{1}{\chi(s/\phi)^2\left[1+\chi(s/\phi)^2\right]}\right\} \tag{86}$$

where: $\varphi(\xi) = \left[(1+\xi)^{2/3}+(1-\xi)^{2/3}\right]/2$; $\chi \simeq 072161$; $\gamma \simeq 0.025$.

However, a fundamental prerequisite for gradient corrections to result in any significant improvement over the Kohn-Sham LSD approximation is to include *"Self-Interaction Corrections"* (SIC). Perdew and Zunger [136] have suggested that this was the price which one had to pay (i) to restore more accurate values of the total energy and produce realistic estimates of the gaps in band structure calculations of insulators; (ii) to obtain orbital eigenvalues consistent with Koopmans's theorem and possibly taking into account relaxation effects when an electron is removed; (iii) to restore a correct long-range behavior of the potential: far from the nucleus an electron which ventures out to large r distances will not "see" its own charge and so should experience the potential $-(Q+1)/r$ and not $-Q/r$ as it is the case in the LSD approximation. The whole question arises from the consideration that in any exact theory, the exchange-correlation energy of a single, fully occupied orbital (occupation number: $f_\sigma = 1$) must exactly cancel its self-direct Coulomb energy:

$$U[\rho_{k\sigma}] + E_{xc}[\rho_{k\sigma}] = 0 \tag{87}$$

This requirement is not satisfied rigorously by the Kohn-Sham LSD theory with the practical consequence that a correction has to be made to each one of the eigenvalues of equation (80):

$$\epsilon_{k\sigma}^{SIC} = \epsilon_{k\sigma}^{LSD} - 0.94\int \rho_{k\sigma}^{4/3}(\mathbf{r})\, d^3r \tag{88}$$

This has a cost in term of computing time since, for every eigenvalue, one has to perform this correction, solve the Schrödinger equation to obtain a new wavefunction and a new set of local densities and, possibly, iterate such a self-consistent procedure with a modified form of equation (80). Recent results have confirmed that for transition metal oxides, SIC improved drastically the band gaps compared to the local spin density approximation.[137,138] In practice, SIC seem to be most relevant for core states and localized excited states but should be negligible for continuum states, *e.g.* in the EXAFS regime. From the work of Perdew and Zunger,[136] one may anticipate that it should be possible to avoid self-consistent corrections by using orbitally averaged effective potentials. Along this line, the *"half-and-half "* approximation proposed by Becke[139] : $\epsilon_{xc} = 1/2\left[\epsilon_x + v_{cx}\right]$ may well be good enough in the pre-edge and edge region.

Such refinements are implemented in many advanced computing codes which are developed for quantum chemistry and are based on the theory of the local density functionals. We will try to explain below why such refinements have not been introduced in the codes available for simulating XANES or EXAFS spectra.

3. Many Body Green Functions and Self-Energy

The Green functions offer a powerful alternative approach to the many-body theory of electronic states.[64] Let us start with the quantity which has a physical meaning: the correlation of an electron with itself at another position and time. This is precisely the definition of one-particle Green's function in the time domain:

$$\widetilde{\mathbb{G}}\left(\mathbf{r},t;\mathbf{r}',t'\right) = -i\ \langle N|\ \mathbf{P}\ \left[\mathbf{\Psi}\left(\mathbf{r},t\right)\mathbf{\Psi}^{\dagger}\left(\mathbf{r}',t'\right)\right]|N\rangle \tag{89}$$

Here $|N\rangle$ is the manybody ground state and $\mathbf{P}$ is a time ordering operator that is re-ordering subsequent time dependent *operators* so that the latest event is always on the left. Note that $\mathbf{\Psi}\left(\mathbf{r},t\right)$ and $\mathbf{\Psi}^{\dagger}\left(\mathbf{r}',t'\right)$ *are not* wavefunctions but *field operators* which *subtract* or *add* an electron in a given spinorbital at the space-time argument $(\mathbf{r},t)$. For *non-interacting* electrons, the Fourier transform from the time domain to the energy domain would revert $\widetilde{\mathbb{G}}$ to the Green function given in equation (8). This is not anymore true for interacting electrons because the effective potential consists of two contributions: (i) the Hartree potential V_H (ii) the *self-energy* Σ which encompasses the effects of both exchange and correlation. In the time domain, the Green function is solution of a formal equation:

$$\left[i\frac{\partial}{\partial t} - H_0\left(\mathbf{r}\right) - V_H\left(\mathbf{r}\right)\right]\widetilde{\mathbb{G}}\left(\mathbf{r}\ t;\mathbf{r}'t'\right)$$

$$-\int d\mathbf{r}"dt"\widetilde{\Sigma}\left(\mathbf{r}\ t;\mathbf{r}"t"\right)\widetilde{\mathbb{G}}\left(\mathbf{r}"t";\mathbf{r}'t'\right) = \delta\left(\mathbf{r}-\mathbf{r}'\right)\delta\left(t-t'\right) \tag{90}$$

where $H_0\left(\mathbf{r}\right)$ is the one-electron Hamiltonian. This equation clearly shows that $\widetilde{\Sigma}$ is *non-local* , time correlated and in most cases complex.[140] In the energy domain, it reverts to the operator equation:

$$(E - H_0 - V_H)\mathbb{G}(E) - \Sigma\left(E\right)\mathbb{G}(E) = 1 \tag{91}$$

Suppose that the non-interacting equation (*i.e.* without Σ) has a known solution: $\mathbb{G}_H = [E - H_0 - V_H \pm i\epsilon]^{-1}$, then the general solution will satisfy : $[\mathbb{G}]^{-1} = [\mathbb{G}_H]^{-1} - \Sigma$ in analogy with an impedance problem. It also becomes obvious that the poles of $\mathbb{G}$ (or the zeros of $[\mathbb{G}]^{-1}$) will be moved in energy by the quantity $\Re\left(\Sigma\right)$ to the so-called *quasiparticle* energy. On the other hand, the lineshape will not be anymore a Dirac function as expected from (8): in the case of an homogeneous electron gas, $\mathrm{Im}(\mathbb{G})$ has at resonance the famous Fano (or Breit-Wigner) lineshape.[141] This is often termed as the *extrinsic* line broadening.

Equation (90) is completely useless regarding practical applications because nobody knows how to calculate the many-body ground state wave function $|N\rangle$. The breakthrough was obtained by Hedin[86,142] who derived a set of coupled equations involving $\widetilde{\mathbb{G}}\left(\mathbf{r}\ t;\mathbf{r}'t'\right)$ and Σ but not anymore $|N\rangle$, the price to be paid being the introduction of other time-correlated quantities such as the *screened Coulomb interactions W, a polarization propagator P and a vertex function* Γ. A detailed account of the whole theory and its of most recent developments would fall beyond the scope of the present review but we like to introduce the so-called "*GW Approximation*" *(GWA)*[142] which appears to be the latest

refinement to obtain a non-local self-energy in *ab initio* simulations of EXAFS spectra.[107,108] The underlying idea is that in molecules or in the solid, the screening is quite strong and results in weaker interactions so that it makes sense to expand Σ in series as: $\Sigma = \alpha_1 W + \alpha_2 W^2 + ...$the first order term corresponding to the GW approximation. This leads to the following equation:

$$\Sigma(\mathbf{r},\mathbf{r}';E) = \frac{1}{4\pi\hbar}\int \exp\left[iE\hbar^{-1}\epsilon\right] W(\mathbf{r},\mathbf{r}';E')\,\mathbb{G}(\mathbf{r},\mathbf{r}';E+E')\,dE' \qquad (92)$$

where the *screened* Coulomb interaction W is related to the *unscreened* Coulomb interaction v by: $W = \varepsilon^{-1}v$, ε being the frequency dependent dielectric function of the electron gas. What makes this approach attractive is that both W and $\mathbb{G}$ can be calculated to a reasonably good level of approximation using the *local density approximation* discussed in the previous subsection. For $\mathbb{G}$, this seems rather straightforward since one may replace in equation (8) the wavefunctions ψ_f by the LDA eigenvectors. For the dielectric function, one can make use of the general expression: $\varepsilon^{-1} = 1 + v\chi$ with $\chi = \chi_0\left[1 - \chi_0 v - \chi_0 K_{xc}\right]^{-1}$.[143] Here, χ_0 is the Alder-Wiser response function for independent electrons, *i.e.* the response function of Kohn-Sham electrons, whereas: $K_{xc}(\mathbf{r},\mathbf{r}') = \left[\partial^2 E_{xc}/\partial n(\mathbf{r})\,\partial n(\mathbf{r}')\right]$. Neglecting K_{xc}, this formulation of ε^{-1} reduces to the *Random Phase Approximation* (RPA) of the dielectric function which is a reasonable starting point to calculate Σ.[142] Note that one needs to determine the frequency dependence of the dielectric function to take into account the dynamical screening effects. The GW extension of the local density (LD) approximation can be summarized with another Dyson equation:

$$\mathbb{G}^{GW}(E) = \mathbb{G}^{LD}(E) + \mathbb{G}^{LD}(E)\left[\Sigma - V_{xc}^{LD}\right]\mathbb{G}^{GW}(E) \qquad (93)$$

which can be solved by a perturbation method to yield the quasiparticle energies E_f . A self-consistent approach, restricted in practice to a single iteration, is also required for Σ :

$$\langle\Sigma(E_f)\rangle = \langle\Sigma(E_f^{LD})\rangle + (E_f - E_f^{LD})\left\langle\frac{\partial\Sigma}{\partial E}\right\rangle_{E_f^{LD}} \qquad (94)$$

Recently, GW band structure calculations have been performed on NiO and other highly correlated systems for which LD methods were notoriously failing:[?,146] the GW results were much successful regarding the prediction of the band gap and of the magnetic moment. This tends to prove that in transition metal compounds where the d band is narrow the GW approximation is taking much better into account the strong $d-d$ interactions (U_{dd}) compared to previous local methods: this is precisely the failure of the LD methods that had accredited the superiority of the so-called *short-range* order methods (Hubbard or Anderson impurity model[147]) and of atomic multiplet models in the soft X-ray range.[19] There is a price to be paid for exploiting GW methods: this is again a huge increase in the computing time. In this context, one should fully exploit the natural separation of Σ into *core* and *valence* contributions as pointed out by Hedin and Lundqvist.[87] This has been done by Ankudinov and Rehr who produced the first EXAFS and XANES calculations performed with the GW approximation: the results proved to be slightly superior to the results

obtained with the Hedin-Lundqvist local self-energy but with a computing time multiplied by a factor 5.[107,108] This method should thus be restricted to cases which justify the corresponding need. A field of direct relevance is the simulation of L-edge XMCD spectra of rare-earth complexes in which the 4f band is also extremely localized and where the usual calculations often fail.

Another advantage of the many-body Green function approach is to treat on the same footing the photoelectron and the core hole: the difference is in the choice of the time-ordering operator. This has been an active field of research for physicists over decades. Recent theories show that, beyond the sudden approximation, there are two types of additional effects, often referred to as *intrinsic* and *interference losses*[148], which are both related to the dynamical screening of the core hole: they are not only responsible for the creation of *satellite* structures in the spectra (*shake-up, shake-off...*)[141,149,150] but also induce a subsequent broadening of the quasiparticle peak[148,151]. Bardyszewski and Hedin have established an interesting *theorem of cancellation* between extrinsic and intrinsic losses at some specific energy near threshold.[152] Its implications are still a matter of discussions among theoreticians and will not be considered in this review. The whole question has nevertheless a quite sensible practical importance because the calculation of accurate scattering amplitudes is ultimately necessary to extract reliable coordination numbers from EXAFS: this is the whole significance of the parameter $S^2(k) \neq 1$ which is traditionally introduced in the formulation of EXAFS and refers to the relative weight of the *main* many-body excitation channel. Indeed, the screening of the core hole is expected to be most effective in XANES: this is because the *time scale* of the screening is determined by the *plasmon frequencies* which are typically of the order of 10-20 eV. In other terms, for a photoelectron ejected in the quasi bound states near the Fermi level, the screening time is comparable with (or even shorter than) the time needed to promote the electron in the excited state.[141] Natoli and coworkers[153] have developed a formal *Multichannel* theory of Multiple Scattering that can be generalized to any arbitrary non-muffin-tin optical potential. If, for simplicity, we restrict ourself to the case of a muffin-tin potential, then the whole theory can be summarized with the following decomposition of the multichannel scattering path operator:

$$\left[\boldsymbol{\tau}^{-1}\right]_{LL'}^{ij\alpha\alpha'} = \left[T^{-1}\right]_{LL'}^{i\alpha\alpha} \delta_{ij} - \kappa_\alpha \left[H\right]_{LL'}^{ija} \delta_{\alpha\alpha'} - \left(1-\delta_{\alpha\alpha'}\right)\delta_{ij}\left[K^{-1}\right]_{LL'}^{i\alpha\alpha'} \quad (95)$$

where α, α' refer to the excitation channels and $\left[K^{-1}\right]$ is the inverse of the *reactance* matrix of the cluster and does control the cross over from the adiabatic to sudden regime. Note that $\kappa_{aa'}$ is now a tensor property of the system. Using again the simplifying operator notations, Natoli et al. have proposed the new series expansion:

$$\boldsymbol{\tau} = \left[\mathbf{1} - \boldsymbol{\tau}_c^\alpha \mathbf{K}^{-1}\right]\boldsymbol{\tau}_c^\alpha = \sum_{n=0}^{n} \left(\boldsymbol{\tau}_c^\alpha \mathbf{K}^{-1}\right)^n \boldsymbol{\tau}_c^\alpha \quad (96)$$

where $\boldsymbol{\tau}_c^\alpha$ would be a block-diagonal "scattering path operator" matrix characteristic of a pure channel α. The first order, *i.e.* $n = 0$, gives now the sudden approximation since the X-ray absorption cross section σ_0 is simply the sum over all contributions associated to diagonal channel indices. Equation (96) represents in a more concrete way the contribution of the interferences between intrinsic and extrinsic losses obtained by Bardyszewski and Hedin.[152]

4. Beyond the *Muffin-Tin* Approximation

Unfortunately, it has been our experience that neither the non-local refinement of the exchange-correlation potential nor even the use of self-consistent molecular charge densities can bring any spectacular improvement *unless* the constraint of using spherical local potentials can be relaxed in the theory of XAS. It has been known from the early days of the Xα method that the *muffin-tin* approximation was insufficient for open structures and for molecules with covalent bonds such as metalloporphyrins. In a very first attempt to take into account the reality of chemical bonding, Johnson and his collaborators,[154,155] introduced the clever concept of *overlapping spheres* which was codified later by Norman.[156] The latter author suggested that the ratio of the atomic spheres should be in the proportion of their atomic numbers and that the absolute value should satisfy the virial theorem. In real practice, the fraction of overlapping volume still remains a freely adjustable parameter which is typically of the order of 13-15% for the metal and the nitrogen atoms of metalloporphyrins.

In order to get rid of spherical potentials, modern approaches in band structure calculations or Quantum Chemistry systematically combine a re-expansion of the molecular orbitals on various bases together with *variational methods*: the spherical potentials merely serve to initiate a self-consistent calculation. This is not the case in the theory described in section II.A since spherical potentials are absolutely needed to integrate the Schrödinger equation and to calculate the phase-shifts and scattering amplitudes. In this respect, most of the advantages one would expect from exploiting self-consistent local charge densities obtained with any one of the modern quantum chemistry codes would be lost because the electron densities would have to be anyhow spheridized to be compatible with the theory of XAS. This has been confirmed by Foulis *et al.*[157] who tried to perform a non-muffin-tin simulation of the XANES spectrum of the chlorine molecule using the theory described below.

A formal MSW theory of XANES with *non-muffin-tin potentials* has been proposed for many years by Natoli *et al.*:[58,153,158] the only difference with respect to the theory developed in the previous sections concerns the propagation matrix $[H]^{ij}_{LL'}$ which is involved in the formulation of the scattering path operator in equation (42). The matrix $[H]^{ij}_{LL'}$ which initially depended only on the geometry of the cluster should be replaced by : $[H]^{ij}_{LL'} + [\Theta_{int}]^{ij}_{LL'}$ where $[\Theta_{int}]^{ij}_{LL'}$ will now depend on the *shape* of the non-constant potential introduced *in the interstitial region*. The generalized expression of the scattering path operator becomes:[153]

$$\boldsymbol{\tau}^{-1} = [T]^{-1} - \kappa\,[H] - [\Theta_{int}] \tag{97}$$

Under the (questionable) assumption that the Born approximation is valid, one may write:

$$[\Theta_{int}(E)]^{ij}_{LL'} \simeq \kappa^2 \int\int h^{+}_{-L}(\kappa r_i)\, V_{(II)}(\mathbf{r})\, h^{+}_{L'}(\kappa r_j)\, d\mathbf{r}d\mathbf{r}' \tag{98}$$

the difficulty being then to calculate these integrals by discrete numerical methods over the whole volume of the interstitial region (II). Unfortunately, the method rapidly turned out to be dissuasive or simply impracticable for large clusters such as metalloporphyrins because the computing time became rapidly

prohibitive and severe divergence problems had to be circumvented. Moreover, it was pointed out by Foulis *et al.*[157] that relaxing the muffin-tin potential is, in itself, insufficient: SCF charge densities had to be injected in the calculation in order to approach the experimental XANES spectrum of chlorine.

Since the need for spherical potentials has no other justification than the ultimate integration of the Schrödinger equation, one may question whether it would not be more efficient to look immediately for an alternative numerical method to the integration of the Schrödinger equation rather than to calculate numerically corrective terms. This is the very elegant strategy adopted by Joly who found feasible with modern computers to integrate the Schrödinger equation using a "*Finite-Difference Method* " (FDM):[159] with a carefully selected grid of points he was able to construct numerically the wave functions without any approximation in the interstitial zone and at the interface of the atomic spheres. The first results which are being published are very promising and show that it is possible to reproduce all the characteristic features of the XANES spectra of rutile (TiO_2) without any distortion of the energy scale.[160] If its potentiality is confirmed from many more studies, this method could become a very powerful tool to refine the analyses of XANES and pre-edge spectra of metalloporphyrins and hemoproteins.

5. Atomic EXAFS: *AXAFS*

This review would be incomplete if we were simply ignoring the (still) controversial question of the analysis of the so-called *Atomic EXAFS* (AXAFS). The EXAFS signal $\chi(k)$ is usually extracted by removing, using numerical procedures, some smooth background. How far this background is truly representative of the atomic absorption $\sigma_0(k)$ could be in itself a whole debate, especially when EXAFS spectra are recorded in the fluorescence excitation mode. Anyhow, in the late seventies, Holland *et al.*[161] already raised the strong point that the atomic contribution $\sigma_0(k)$ could be itself structured. Their original paper contained two interesting remarks well supported by the experience:

- Not only $\sigma_0(k)$ but implicitly the phase-shifts $\delta_\ell^0(k)$ are quite sensitive to the *shape* of the potential in the outer regions of the atomic potential: any artificial discontinuity in the potential or its first derivative (*e.g.* using a muffin-tin potential) will generate *unphysical* oscillations of the phase-shifts that extend over the whole range of the EXAFS spectra.

- In addition to multielectron excitations, Holland *et al.*[161] suspected the presence in $\sigma_0(k)$ of scattering resonances at positive energy. This led them to relate the atomic cross section $\sigma_0(k)$ to the so-called *Jost function* for angular momentum ℓ : $L_\ell(k) = |L_\ell(k)| \exp\left(-i\delta_\ell^0\right)$ and their final result was of the type: $\sigma_0(k) \propto |L_\ell(k)|^{-2}$. In the formal theory of collision phenomena,[63] the Jost function is the k-dependent renormalization factor that is required to match at the muffin-tin radius a_0 the *regular* solution of the partial ℓ-wave radial Schrödinger equation to the *asymptotic* solution. It has a remarkable mathematical property: if the scattering potential $V_0(\mathbf{r})$ is decaying faster than an exponential beyond the muffin-tin radius, *i.e.* for $r > a_0$ (...which is not the case for a Coulombian potential), then the Jost function has an *analytical* continuation in the whole complex k

plane which makes it possible to take into account poles associated with bound states or antibound states at negative energies as well as scattering resonances at positive energy. Starting from some arbitrary *modellization* of the Jost function proposed in the sixties by Newton,[162] Holland *et al.*[161] concluded that significant structural features at positive energies could only arise from the scattering resonance terms and should be detectable simultaneously in $\sigma_0(k), |L_\ell(k)|^{-2}$ and $\left[d\delta_\ell^0/dk\right]$. The latter point implies that any low frequency oscillating structure contaminating $\sigma_0(k)$ should *also* contaminate the EXAFS signals through $\delta_\ell^0(k)$. This is fully consistent with our own experience.

Recently, Rehr and his collaborators[163] have resurrected the whole AXAFS question and they proposed a slightly modified theory. It starts from the somewhat artificial postulate that the effective atomic potential could be split into two terms: a *free atom* potential $V_0^{fr}(\mathbf{r})$ -which is purely virtual- and a perturbation $\Delta V_0^{em}(\mathbf{r})$ describing the chemical interaction of the isolated atom with the nearest neighbors (*embedded atom* potential). The Green function should have an additional term: $G_0(\mathbf{r},\mathbf{r}') = G_0^{fr}(\mathbf{r},\mathbf{r}') + G_0^{fr}(\mathbf{r},\mathbf{r}')\,\Delta V_0^{em}(\mathbf{r})\,G_0^{fr}(\mathbf{r},\mathbf{r}')$. In complete analogy with EXAFS, the final result could be written:

$$\sigma_0(k) = \sigma_0^{fr}(k)\left[1+\chi_0^{em}(k)\right] \tag{99}$$

where $\chi_0^{em}(k)$ is the atomic EXAFS. A major difference with the previous model by Holland *et al.* is that we are not talking anymore of scattering resonances associated with singularities in the phase-shifts but of oscillations associated with a scattering potential that *has not anymore a spherical symmetry* since it depends strongly on the spatial distribution of the nearest neighbors. A crude approximation, still related to the muffin-tin model, is to describe $\Delta V_0^{em}(\mathbf{r})$ as a spherical potential centered on the absorbing site and which would reach its maximum at a distance $R_a \simeq a_0$ but would vanishes at the origin. Then, one would predict that the Fourier analysis of $\chi_0^{em}(k)$ should exhibit a (distorted) signal at a *virtual* interatomic distance $2R_a \simeq 2a_0 + \delta_0 + \delta^{em}$. This seems to be supported by the experience but the problem is, however, that one may often suspect this signal to be contaminated by experimental *artifacts* and additional physical processes. Nevertheless, provided that one could extract a clean Fourier Transformed AXAFS peak in a fully unambiguous way, then the latter signal would be an interesting new tool in XAS to detect small variations in the chemical bonding or in the charge delocalization of the absorbing atom surrounded by its nearest neighbors. Moreover, in magnetic dichroism experiments, $\chi_0^{em}(k)$ might also generate a specific contribution (*Magnetic* AXAFS) which may deserve further consideration.[164] At this stage, there is no real controversy on the issue that the shape of the potential is modified by the nearest neighbors and that it should affect $\sigma_0(k)$. However, a few warning messages have to be delivered here:

- In our opinion, it may be a very ambiguous exercise (Ramaker *et al.*[165]) to carry out so-called AXAFS simulations with a truncated potential $\Delta V_0^{em}(\mathbf{r})$ and a step-like discontinuity with respect to the interstitial potential V_{int} because, according to the early paper of Holland *et al.*,[161] this is well enough to generate *unphysical oscillations* of the phase-shifts and a fully artifactual AXAFS signal indeed sensitive to the chemical bonding.

- There should be a specific phase-shift $\delta^{em}(k)$ associated with the AXAFS and with the scattering potential $\Delta V_0^{em}(\mathbf{r})$ and the latter potential should also contaminate the normal EXAFS oscillations as predicted by Holland *et al.*[161]

- The muffin-tin approximation is an even more serious handicap in AXAFS than it is in EXAFS. We have seen in the previous section that, according to Natoli *et al.*,[158] the photoelectron transfer matrix $[H]^{ij}_{LL'}$ has to be replaced by: $[H]^{ij}_{LL'} + [T_{int}]^{ij}_{LL'}$ in the case of a non-muffin-tin potential. The latter effect is expected to induce a significant distortion of the peaks in the Fourier Transformed EXAFS spectra (*e.g.* structured tails) and one may fear that the conjugate effects of AXAFS and non-muffin-tin potentials will result in fairly complicate signals that will be difficult to interpret.

- From the experimental point of view, the reliability of the extracted AXAFS signals will always depend on the numerical procedures that are used. Moreover, it has been known for a long time that weak multielectron excitations can induce quite significant distortions of this atomic background.[166] There are many more experimental causes for background distortions such as the generation of polarized scattered radiation especially in fluorescence EXAFS experiments: this is particularly visible in dichroism experiments where the background distortions are strongly amplified.

For these various reasons, practical applications of AXAFS will unfortunately remain controversial for a while but the reality of the effect should be more firmly established when non-muffin-tin potentials will become routinely available.

D. Spin Dependent Effects

1. Dirac Equation and Relativistic Kohn-Sham Equation

A natural starting point for a rigorous theory of spin dependent effects is the relativistic Dirac equation which we may write in the compact form :

$$H_D \begin{pmatrix} \psi_u \\ \psi_v \end{pmatrix} = \begin{pmatrix} mc^2 + \mathbf{V}(\mathbf{r}) & c\mathbf{D} \\ c\mathbf{D} & -mc^2 + \mathbf{V}(\mathbf{r}) \end{pmatrix} \begin{pmatrix} \psi_u \\ \psi_v \end{pmatrix} \tag{100}$$

where ψ_u $(\uparrow;\downarrow)$ and ψ_v $(\uparrow;\downarrow)$ are respectively the *large* and the *small* bidimensional components of the Dirac spinor. These two components are associated with the eigenvalues: $W = E \pm mc^2$. The operator $\mathbf{D}$ is defined as: $\mathbf{D} = \boldsymbol{\sigma}.\boldsymbol{\pi} = \boldsymbol{\sigma}.(\mathbf{p} - \frac{e}{c}\mathbf{A})$ where $\boldsymbol{\sigma}$ denotes a 3 component vector associated with the Pauli operator matrices; $\mathbf{p} = -i\hbar\boldsymbol{\nabla}$ and $\mathbf{A}$ is the vector potential characterizing any interacting field. The scalar potential $\mathbf{V}(\mathbf{r})$ could be any type of 2x2 Hermitian matrix but, in local density theories, spin and space variables are uncoupled so that:

$$\mathbf{V}(\mathbf{r}) = \begin{pmatrix} V^{\uparrow}(\mathbf{r}) & 0 \\ 0 & V^{\downarrow}(\mathbf{r}) \end{pmatrix} \tag{101}$$

where the symmetric combination: $\frac{1}{2}\left[V^{\uparrow}(\mathbf{r})+V^{\downarrow}(\mathbf{r})\right]$ would be the spin non-restricted potential discussed in the previous section whereas the antisymmetric combination is associated with a magnetic field $\mathbf{B}$ oriented along the $\widehat{\mathbf{z}}$ axis:

$$\frac{1}{2}\left[V^{\uparrow}(\mathbf{r})-V^{\downarrow}(\mathbf{r})\right]\widehat{\mathbf{z}}=\frac{e\hbar^2}{2mc}\mathbf{B} \tag{102}$$

and also, according to classical electrodynamics, with a vector potential $\mathbf{A}$ since: $\mathbf{B}=\boldsymbol{\nabla}\times\mathbf{A}$. Indeed the latter vector potential *should* be included self-consistently in $\mathbf{D}$. We will see below that, in practice, this is not systematically done with the consequence that spin-orbit coupling may be not correctly treated.

There is no transformation that performs the *exact* diagonalization of H_D and, as a consequence, one cannot separate the strong and weak components. Switching on an external field such as the interaction with an x-ray photon will inevitably cause transitions between the positive and negative energy states associated with ψ_u and ψ_v. This is of more direct concern for inner shell spectroscopies because the deep core states are strongly relativistic: their weak component ψ_v should not be neglected since it may eventually cause transitions to ψ_u final states. This calls for a transposition of the whole MS theory in a fully relativistic frame using relativistic Green functions. Fortunately, valence electrons and electrons in quasi-bound excited states are slow so that the strong component should be enough to describe the final state: this is the common justification for the weakly-relativistic Pauli approximation which leads to a spin dependent Schrödinger-type equation. In this limit, it is assumed that H_D can be diagonalized using a variety of transformations (*e.g.* the Foldy-Wouthuysen or the Cini-Touschek transformations[63]). They have all in common to exploit the operator series expansion : $\Omega_F^{\pm}=1\pm\left(8mc^2\right)^{-1}[\boldsymbol{\sigma}.\boldsymbol{\pi}]^2$ ... for which only the unit term is kept. The weakly relativistic, Schrödinger equation then becomes :

$$H_D=H-\frac{\mathbf{p}^4}{8m^3c^2}+H_{Darwin}+H_{SO}+H_B+\left(H_{Spin-Spin}\right) \tag{103}$$

The spin-spin interaction can systematically be neglected in the X-ray range but the other additional terms may have to be considered. We have summarized below the formulation of these additional terms as one can find them in Quantum Mechanics textbooks[167] with the usual definition: $\boldsymbol{\sigma}_i=g_s\mathbf{s}_i$ where g_s is the Landé factor.

- $H_{SO}=-\sum_i\left(4m^2c^2\right)^{-1}\hbar e_i g_s\mathbf{s}_i.[\boldsymbol{\nabla}V_i\times\mathbf{p}_i]$
  is the familiar Spin-Orbit term which couples operators in the spin space *and* in the ordinary space: it is important because it *reduces the symmetry of the system*;

- $H_B=\sum_i(2mc)^{-1}\hbar e_i\left[\mathbf{L}_i+g_s\mathbf{s}_i\right].\mathbf{B}\ -\ \sum_i\left(8mc^2\right)^{-1}e_i^2\left[\mathbf{r}_i\times\mathbf{B}\right]^2$
  includes the paramagnetic + diamagnetic terms associated with the *effective* magnetic field $\mathbf{B}_{eff}$ that should include not only any external magnetic field but also internal exchange fields; the scaling factor of the paramagnetic term with respect to the diamagnetic term is $1:\alpha^2$ so that the diamagnetic term can be neglected in XAS. Note that the paramagnetic term H_B is odd with respect to the time-reversal operator.

- $H_{Darwin} = -\sum_i \left(8m^2c^2\right)^{-1} \hbar^2 e_i \Delta V_i$
  is known as the Darwin term. Since it does not change the symmetry of the system, it is not expected to split any band. The corresponding effects are then negligible except perhaps for electrons of s symmetry.

We refer again to textbooks of Quantum Mechanics to show that the validity of equation (103) is related to the approximation:[167]

$$\frac{2mc^2}{E + 2mc^2 - V(\mathbf{r})} \approx 1 - \frac{E - V(\mathbf{r})}{2mc^2}$$

which is certainly not legitimate if $V(\mathbf{r})$ becomes singular. This precisely causes problems in the derivation of weakly relativistic Green functions. Moreover, it is not a trivial exercise to establish the relativistic analog of the Kohn-Sham equation (80) for *a spin polarized multielectron system.* Following the theory by MacDonald and Vosko,[168] one would rewrite equation (100):

$$H_D = \begin{pmatrix} mc^2 + \mathbf{V}(\mathbf{r}) + \mathbf{V}_{spin}(\mathbf{r}) & c\mathbf{D} \\ c\mathbf{D} & -mc^2 + \mathbf{V}(\mathbf{r}) - \mathbf{V}_{spin}(\mathbf{r}) \end{pmatrix} \qquad (104)$$

with a decomposition: $\mathbf{V}(\mathbf{r}) = \mathbf{V}_0(\mathbf{r}) + \mathbf{V}_H(\mathbf{r}) + \mathbf{V}_{xc}(\mathbf{r})$ that would be fully consistent with our previous discussion. Note that the exchange-correlation energy $[E_{xc}]$ of the system now becomes a functional of *both* the charge density $\rho(\mathbf{r})$ *and* the spin magnetization density $m(\mathbf{r})$ which are defined as:[169]

$$\rho(\mathbf{r}) = \sum_i^{occ} \Psi_i^\dagger(\mathbf{r}) \Psi_i(\mathbf{r}) \quad \text{and} \quad m(\mathbf{r}) = \sum_i^{occ} \Psi_i^\dagger(\mathbf{r}) [\boldsymbol{\beta}.\boldsymbol{\sigma}] \Psi_i(\mathbf{r}) \qquad (105)$$

In the additional term responsible for spin polarization: $\mathbf{V}_{spin}(\mathbf{r}) = \boldsymbol{\sigma}.\mathbf{B}_{eff}(\mathbf{r})$, the magnetic exchange field is defined as:

$$\mathbf{B}_{eff} = \frac{e\hbar}{2mc} \frac{\partial [E_{xc}(\rho, |\mathbf{m}|)]}{\partial \mathbf{m}} \qquad (106)$$

Again $\mathbf{V}_{spin}(\mathbf{r})$ is odd with respect to the time-reversal operator and this is of fundamental importance for the observation of magnetic circular dichroism. However, strictly speaking, neither the theories by MacDonald and Vosko[168] nor by Strange *et al.*[169] *are fully relativistic regarding exchange* because one would have expected a vector potential $\mathbf{A}_{xc}$ to appear in the operator $\mathbf{D}$ as suggested by Vignale *et al.*[170,171] who pointed out that $\mathbf{A}_{xc}$ would require the addition of a *paramagnetic current* density functional. This is indeed why MacDonald and Vosko explicitly prefaced their theory of magnetism with the adjective "*spin-only*" because $\mathbf{V}_{spin}(\mathbf{r})$ *alone* does not allow any coupling between spin and orbital moments. Since there was the perception that something was probably missing in the theory of MacDonald and Vosko,[168] it has been proposed *quite empirically* by Brooks *et al.*[172] to add a mysterious "*Orbital Polarization*" term $\mathbf{V}_{op}(\mathbf{r})$ to the potential $\mathbf{V}(\mathbf{r})$: this new term was simply borrowed from atomic physics and was given the same formulation as a Spin-Orbit term. In band structure calculations,[173] $\mathbf{V}_{op}(\mathbf{r})$ has been found to improve significantly the

magnetic moments in systems with highly localized d and f electrons. However, recent works reported by Gasche *et al.*[174] and by Ebert[175,176] indicate that $\mathbf{V}_{op}(\mathbf{r})$ had only very little effect on the magneto-optical Kerr effect and probably on XMCD. Whether this is a partial or a general result remains still to be demonstrated.

In Quantum Chemistry, relativistic corrections to the self-energy are known to be small for systems which are *not spin-polarized nor spin oriented* : this is because valence electrons are *slow* electrons. Nevertheless corrections have been proposed which may improve the results for high Z elements such as the rare-earths, the 5d transition elements or the actinides as absorbing centers:

ELLIS CORRECTION:[177] $v_{xc}^{R} = v_{xc}\left[1 - \frac{\lambda}{9} - \frac{7\lambda^2}{180}\right]$ with: $\lambda = \left(1 + 1/c^2 k_F^2\right)^{-1}$

MACDONALD-VOSKO CORRECTION:[168]

$\epsilon_x^R = \epsilon_x\left[1 - \frac{3}{2}\frac{\beta\eta - \ln(\beta+\eta)}{\beta^2}\right]$ with: $\beta = v_F/c \quad \eta = \left(1+\beta^2\right)^{1/2}$

The problem of *spin polarized* system has been revisited later by MacDonald[178] who proposed different expressions. The latter corrections were anyhow neglected by Tyson in his recent theory of relativistic XAS spectra.[179]

2. Fully Relativistic Green Function

Green operators $G_D^{\pm}$ can still be defined by equation (6), the Hamiltonian H being simply replaced by H_D. The key quantity for spectroscopy is: $\mathrm{Im}\, G_D = \left[G_D^{+} - G_D^{-}\right]/2i$. The non-relativistic multiple scattering Green function defined by equation (31) can be transposed into a relativistic one:[169,175,176]

$$G_D(\mathbf{r}_i,\mathbf{r}_i';E) = \sum_{\Lambda\Lambda'} Z_\Lambda(\mathbf{r}_i,E)\,\tau_{\Lambda\Lambda'}^{ii}(E)\,Z_{\Lambda'}^{\dagger}(\mathbf{r}_i,E) - \sum_{\Lambda} Z_\Lambda(\mathbf{r}_{i<},E)\,J_\Lambda(\mathbf{r}_{i>},E) \tag{107}$$

Here, the functions $Z_\Lambda(\mathbf{r}_i,E)$ and $J_\Lambda(\mathbf{r}_{i>},E)$ are the *regular* and *irregular* solutions to the single site i Dirac equation. Usually, the second term does not contribute to the cross-section since it is real unless the energy has a complex part accounting for finite life-times as mentioned later. As a consequence of the introduction of $\mathbf{V}_{spin}(\mathbf{r})$, a Dirac spinor has no unique spin-angular character and should be written:[169]

$$Z_K(\mathbf{r},E) = \sum_{K'}\begin{pmatrix} g_{K'K}(\mathbf{r},E)\,\chi_K(\hat{\mathbf{r}}) \\ i\;f_{K'K}(\mathbf{r},E)\,\chi_{-K}(\hat{\mathbf{r}}) \end{pmatrix} \tag{108}$$

where the *radial* parts $g_{K'K}(\mathbf{r},E)$ and $f_{K'K}(\mathbf{r},E)$ are solutions of four coupled partial differential equations. The *spin-angular* part $\chi_K(\hat{\mathbf{r}})$ is defined as:

$$\chi_K(\hat{\mathbf{r}}) = \sum_{\sigma}(\ell\tfrac{1}{2}j\,|\mu-\sigma,\sigma)\,Y_\ell^{\mu-\sigma}(\hat{\mathbf{r}})\,X_{1/2}^{\sigma} \tag{109}$$

where $X_{1/2}^{\sigma}$ is the Pauli spin function. Perhaps less familiar is the introduction of the compact relativistic spin-orbit quantum number $K = (\pm\kappa,\mu)$ where $\kappa = \ell$ for $\ell = j - 1/2$ and $\kappa = -\ell - 1$ for $\ell = j + 1/2$, the magnetic quantum number μ being restricted to $-j \ldots +j$. A major complication with respect to the non-relativistic theory is that the scattering matrices $\left[T^i\right]_{\Lambda\Lambda'}$ and the scattering path operators $\tau_{\Lambda\Lambda'}^{ii}$ are acting in both the real space *and* the spin space. In the

spin space, one should envisage the contribution of off-diagonal terms, called "*spin-flip*" terms. The latter are not related to $\mathbf{V}_{spin}(\mathbf{r})$ but to the relativistic operator $\mathbf{D}$ which is responsible for *spin-orbit coupling* which makes possible transitions between states of different spin character σ. As for the orbital polarization discussed earlier, it seems justified to neglect the spin-flip terms in the XMCD calculations because they are, at least, one order of magnitude smaller than the diagonal terms.[180] Moreover, for a powdered sample, one is concerned with the trace of the spherical operators and spin-flip is certainly not relevant.

Once one knows how to calculate $G_D(\mathbf{r}_i, \mathbf{r}'_i\,; E)$, it becomes straightforward to calculate not only the x-ray absorption cross section but also other observables such as the density of states and the magnetic moment:[169]

$$N(E) = -\frac{1}{\pi}\,\mathrm{Im}\left[\int dr^3 Tr G_D(\mathbf{r},\mathbf{r}\,; E)\right] \tag{110}$$

$$M(\mathbf{r}) = -\frac{1}{\pi}\,\mathrm{Im}\left[\int_0^{E_f} dE\; Tr\boldsymbol{\beta}\boldsymbol{\sigma} G_D(\mathbf{r},\mathbf{r}\,; E)\right] \tag{111}$$

3. Semi Relativistic Green Function

Fully relativistic calculations are certainly safer but they suffer from the handicap that it is more difficult to identify a physical cause for what is measured experimentally. This is where the semi-relativistic theory of Brouder[180–183] proved itself to be complementary. In his approach, the key step is an equation which relates $G_D(\mathbf{r},\mathbf{r}'\,; E)$ to the non-relativistic, spin restricted Green functions $G_\uparrow(\mathbf{r},\mathbf{r}'\,; E)$ and $G_\downarrow(\mathbf{r},\mathbf{r}'\,; E)$ resulting in a diagonal 2x2 matrix $\mathbf{G}(\mathbf{r},\mathbf{r}', E)$ and finally:

$$G_D = [\mathbf{I} - \mathbb{T}]^{-1} \begin{pmatrix} \mathbf{G} & a\mathbf{GD} \\ a\mathbf{DG}^+ & a^2\left[\mathbf{DG}^+\mathbf{D} + 2m\mathbf{I}\right] \end{pmatrix} \tag{112}$$

with

$$\mathbb{T} = \begin{pmatrix} 0 & a\mathbf{GD}\left(\mathbf{W} - \kappa^2\mathbf{I}\right) \\ 0 & a^2\left[\mathbf{DGD} + 2m\mathbf{I}\right]\left(\mathbf{W} - \kappa^2\mathbf{I}\right) \end{pmatrix} \tag{113}$$

where $a = 1/2mc$ and $\mathbf{W}(\mathbf{r}) = \mathbf{V}(\mathbf{r}) + \mathbf{V}_{xc}(\mathbf{r}) + \mathbf{V}_{spin}(\mathbf{r})$. The interest of this fairly complicate formulation is that it can be expanded in series of c^{-n} with the advantage over the Foldy-Wouthuysen transformation that there is no divergent term, at least up to the fourth order. For the sake of simplicity, we have retained below only the two low order terms $\sigma^{(1)}$ and $\sigma^{(2)}$ which may contribute to XMCD:

$$\begin{aligned} \sigma(\widehat{\boldsymbol{\varepsilon}}) \;\simeq\; & -4\pi\alpha_0\hbar\omega \sum_K \langle [\psi_u^{core}]_K |\; \left[\widehat{\boldsymbol{\varepsilon}}^*.\mathbf{r}\right]\; \mathrm{Im}\left[\mathbf{G}\right]\left[\widehat{\boldsymbol{\varepsilon}}.\mathbf{r}'\right] | [\psi_u^{core}]_K \rangle \\ & -\frac{4\pi\alpha_0\hbar\omega}{(2mc)^2} \sum_K \langle [\psi_u^{core}]_K |\; \left[\widehat{\boldsymbol{\varepsilon}}^*.\mathbf{r}\right]\; \mathrm{Im}\left[\mathbf{GG}\right]\left[\widehat{\boldsymbol{\varepsilon}}.\mathbf{r}'\right] | [\psi_u^{core}]_K \rangle \end{aligned} \tag{114}$$

where $\mathbf{GG} = \mathbf{GD}\left(\mathbf{W} - \kappa^2\mathbf{I}\right)\mathbf{DG}$. These two terms involve only the *strong* components of the Dirac spinor for the core level.

4. XMCD and MEXAFS at $L_{II,III}$ Edges

The incident x-ray beam is left- (right-) circularly polarized if the helicity of the incoming x-ray photons is $-\hbar$ $(+\hbar)$ and the corresponding electric dipole interaction will be:[184] $\widehat{\boldsymbol{\varepsilon}}^{\pm}.\mathbf{r} = \mp\left[4\pi/3\right]^{1/2} rY_1^{\pm 1}\left(\widehat{\mathbf{r}}\right)$. The absorption cross sections for left and right circularly polarized x-ray photons are given by an equation of the type:

$$\sigma^{\pm} = -4\pi\alpha_0\hbar\omega \sum_{KK'} \kappa^2 \, \mathbf{M}_K^{\pm} \, \mathbf{M}_{K'}^{\pm} \, \mathrm{Im}\left[\boldsymbol{\tau}^{00}\right]_{KK'} \tag{115}$$

In the case of $L_{II,III}$ edges, the first term of equation (114) already implies that: $\Delta\sigma = \sigma^+ - \sigma^- \neq 0$. Circular dichroism is currently explained, at least for magnetic $3d$ metals, by the simultaneous conjunction of three effects:

(i) The core hole created in the highly relativistic $2p$ shell has a strong spin-orbit coupling which is known to be responsible for the large energy splitting between the $L_{II,III}$ edges and also causes the *spin-polarization* of the ejected photoelectron (Fano effect[185]).

(ii) **If** the magnetic exchange splitting associated with $\mathbf{V}_{spin}$ is turned on, the spin-dependent final states with d-like symmetry *are split.* In general, the spin degeneracy of the molecular orbitals can be lifted by the ligand field and/or by spin-orbit splitting of the valence band.[187]

(iii) Spin polarized photoelectrons with opposite helicity will not reach the same sublevels as a consequence of the electric dipole selection rules that are implicitly contained in the angular part of the matrix elements $\mathbf{M}_K^{\pm}$. The result can be made explicit in the following way: an absorbed photon that was left-circularly polarized can induce transitions only with $\Delta M_J = -1$, whereas an absorbed photon that was right-circularly polarized can induce transitions only with $\Delta M_J = +1$.

The first two effects (i and ii) are the classical ingredients of the so-called *two step model* of XMCD as proposed by Schütz *et al.*[164] but one has to realize that a separation in two steps is artificial since what makes sense is only the matrix elements. On the other hand, for the sake of clarity, we feel desirable to explicit a few conventions which may differ with the authors: we will assume hereafter that the magnetic field $\mathbf{B}$ is oriented parallel (or antiparallel) to the wavevector $\mathbf{k}$ of the x-ray photons:

- the photon helicity will be up $(+)$ for right circularly photons and down $(-)$ for left circularly polarized photons;
- the magnetic moment and the minority spins are always parallel to the magnetic field and reverse if the magnetic field is reversed.

At the time scale of the very short core hole life-time, one may first neglect the spin-orbit coupling in the 3d final states and the selection rules yield then very simple equations:

- At the L_{II} edge ($2p_{1/2}$ core state: $\ell_0 = 1$; $j_0 = \frac{1}{2} \Longrightarrow$ final states with d or s symmetry: $\ell = 2, 0$):

$$\sigma^+ = \sigma^{\uparrow}_{p\to d} + 3\sigma^{\downarrow}_{p\to d} + 2\sigma^{\uparrow}_{p\to s} \tag{116}$$

$$\sigma^- = 3\sigma^{\uparrow}_{p\to d} + \sigma^{\downarrow}_{p\to d} + 2\sigma^{\downarrow}_{p\to s}$$
$$\Delta\sigma = +2\left[\sigma^{\uparrow}_{p\to d} - \sigma^{\downarrow}_{p\to d}\right] - 2\left[\sigma^{\uparrow}_{p\to s} - \sigma^{\downarrow}_{p\to s}\right]$$
$$\sigma^+ + \sigma^- = +4\left[\sigma^{\uparrow}_{p\to d} + \sigma^{\downarrow}_{p\to d}\right] + 2\left[\sigma^{\uparrow}_{p\to s} + \sigma^{\downarrow}_{p\to s}\right]$$

- At the L_{III} edge ($2p_{3/2}$ core state: $\ell_0 = 1$; $j_0 = \frac{3}{2} \Longrightarrow$ final states with d or s symmetry: $\ell = 2, 0$):

$$\sigma^+ = 5\sigma^{\uparrow}_{p\to d} + 3\sigma^{\downarrow}_{p\to d} + \sigma^{\uparrow}_{p\to s} + 3\sigma^{\downarrow}_{p\to s} \qquad (117)$$
$$\sigma^- = 3\sigma^{\uparrow}_{p\to d} + 5\sigma^{\downarrow}_{p\to d} + 3\sigma^{\uparrow}_{p\to s} + \sigma^{\downarrow}_{p\to s}$$
$$\Delta\sigma = -2\left[\sigma^{\uparrow}_{p\to d} - \sigma^{\downarrow}_{p\to d}\right] + 2\left[\sigma^{\uparrow}_{p\to s} - \sigma^{\downarrow}_{p\to s}\right]$$
$$\sigma^+ + \sigma^- = +8\left[\sigma^{\uparrow}_{p\to d} + \sigma^{\downarrow}_{p\to d}\right] + 4\left[\sigma^{\uparrow}_{p\to s} + \sigma^{\downarrow}_{p\to s}\right]$$

These statistical equations let us expect a magnetic circular dichroism as soon as $\sigma^{\uparrow}_{p\to d} - \sigma^{\downarrow}_{p\to d} \neq 0$. They have been derived in a prophetic way by Erskine and Stern[186] when no intense source of circularly polarized X-rays was accessible. Note that they also predict that $\Delta\sigma$ should reverse its sign at the L_{II} and L_{III} edges. Usually, the nd band is narrow compared to the $(n+1)s$ band and it is a current approximation to neglect the dichroism associated with the weaker transition $2p \rightarrow (n+1)\,s$ so that the asymmetry ratio measured at the L_{II} and L_{III} edges should exhibit the following proportionality:

$$\left[\frac{\sigma^+ - \sigma^-}{\sigma^+ + \sigma^-}\right]_{L_{II}} \simeq -2\left[\frac{\sigma^+ - \sigma^-}{\sigma^+ + \sigma^-}\right]_{L_{III}} \qquad (118)$$

Moreover, the so-called *branching ratios* should also satisfy a statistical rule:

$$\frac{[\sigma^+ + \sigma^-]_{L_{II}}}{[\sigma^+ + \sigma^-]_{L_{III}}} \simeq \frac{1}{2} \quad \text{or} \quad \frac{[\sigma^+ + \sigma^-]_{L_{III}}}{[\sigma^+ + \sigma^-]_{L_{III}+L_{II}}} \simeq \frac{2}{3} \qquad (119)$$

It is now well documented that, for what concerns the L-edge spectra of $3d$ transition metals currently recorded in the soft x-ray range, neither equation (118) nor equation (119) are rigorously satisfied. This is usually interpreted as the experimental evidence that spin-orbit coupling cannot be neglected in the final $3d$ states. In a later subsection concerned with the magneto-optical sum rules, we will see that the theory can be corrected to account for this additional effect.

In our experience, equations (118) and (119) are *never* verified *in the near edge region* with non-metal rare-earth compounds. This is typically illustrated with the metalloporphyrin complex of gadolinium shown in the **Figures 2** of this chapter. It is our understanding that, since the $5d$ band is empty in the ground state, the exchange splitting is involving the very localized, magnetic 4f electrons which can spin-polarize not only the $5d$ final states as suggested by recent theories but also the deep $2p$ core hole which has a large radial overlap with the $4f$ band.[188–190] This is a major difference with the $3d$ transition metals where the spin polarization of the $2p$ levels by the magnetic $3d$ electrons is much smaller. On the other hand, the $4f$ valence electrons and the excited $5d$ orbitals

are expected to be highly sensitive to the ligand field which contributes to the energy splitting of the final state: this would in itself be enough to induce large deviations from the ideal branching ratio and from the statistical rule usually given for XMCD. These arguments call for a very careful use of these rules which are nevertheless very helpful for the $3d...5d$ transition metal series.

Equations (116) and (117) derive from symmetry considerations regarding the angular parts of the integrals represented by $\mathbf{M}_K^+ \mathbf{M}_{K'}^+$ and $\mathbf{M}_K^- \mathbf{M}_{K'}^-$. The next step which is to calculate the difference $\sigma_{p\to d}^{\uparrow} - \sigma_{p\to d}^{\downarrow}$ is more involving. An interesting question is to know whether XMCD is mostly an *atomic* property of the absorbing atom and to what extent it is influenced by the surrounding scatterers. We may return to the decomposition: $\boldsymbol{\tau} = \mathbf{T}_0 [\mathbf{I} + \mathbf{X}]$ where $\mathbf{X}$ is the "*cluster*" operator as opposed to $\mathbf{T}_0$ which characterizes the scattering process by the absorbing atom. This leads to the definition of the spin dependent cross sections:[182]

$$\sigma_0(k) = \frac{4\pi\alpha_0}{9}(E - E_{in})\, i\sqrt{E} \exp\left[i\delta_2^0(E)\right] D^H(E) \tag{120}$$

and for a powdered sample without orientational order:

$$\sigma_1(k) = \frac{4\pi\alpha_0}{9}(E - E_{in})\sqrt{E} \exp\left[i\delta_2^0(E)\right] [D(E)]^2 \frac{\widetilde{\mathbf{X}}^{00}(22;00;E)}{\sqrt{5}\sin\delta_2^0(E)} \tag{121}$$

In equation (121), $\widetilde{\mathbf{X}}^{00}(22;00;E)$ is the spherical tensor defined in section II.A.4. On the other hand, $D(E)$ combines the radial integrals of $\mathbf{M}_K^{\pm}\ \mathbf{M}_{K'}^{\pm}$:

$$D(E) = \int_0^\infty r^3 dr \psi_u^{core}(r)\, \underline{R}_2^0(r, E) \tag{122}$$

where ψ_u^{core} is the large component of the $2p_{j0}$ wavefunction. Similarly the radial integral $D^H(E)$ of equation (120) is defined by:

$$D^H(E) = \int_0^\infty r^3 dr \psi_u^{core}(r)\, F(r, E) \tag{123}$$

where:

$$F(r, E) = \int_0^\infty r'^3 dr \psi_u^{core}(r')\, R_2^0(r_<, E)\, H_2^0(r_>, E) \tag{124}$$

is an intermediary integral. As noted by Brouder,[180,181] simulations of spin resolved absorption cross section often meet with unexpected divergence problems, especially for large clusters or molecules and it is a good strategy to substitute E with *complex energies*: $e = E + i\Gamma$. We already mentioned in subsection II.C.2 that it was, for instance, essential to convolve the absorption spectra with the core hole life-time Γ_h. It is a nice mathematical property of the complex Green functions that such a convolution with a Lorentzian lineshape is trivial since all what one has to do is basically to replace $\mathrm{Im}\, G = [G^+ - G^-]/2i$ by: $\mathrm{Im}\, G = \left[G(e) - G\left(e^{\dagger}\right)\right]/2i$ where $e^{\dagger} = E - i\Gamma$. Another interesting refinement also explored by Brouder *et al.*[180] consists in taking into account the fact that the spinorbitals are occupied up to the Fermi level: this can be accounted for by a complex plane integration.

The observation of XMCD and MEXAFS implies that *both* $\sigma_0(k)$ and $\sigma_1(k)$ are different for spin-polarized $\uparrow$ or $\downarrow$ electrons. Equation (121) is obviously the

equation to be used for simulating the MEXAFS. Brouder and Hikkam[184] have simply developed (121) and established a rather simple decomposition of the MEXAFS signal:

$$\Delta\chi^{\ell}_{(2)}(\kappa) = \chi^{\uparrow}_{(2)}(\kappa) - \chi^{\downarrow}_{(2)}(\kappa) = \left[\Delta\chi^{\ell}_{(2)}(\kappa)\right]_{\cos} + \left[\Delta\chi^{\ell}_{(2)}(\kappa)\right]_{\sin} \tag{125}$$

In the PW approximation and assuming $\ell = 2$:

$$\begin{aligned}\left[\Delta\chi^{\ell}_{(2)}(\kappa)\right]_{\cos} &= \sum_{j} 2\left[\Delta\kappa R_j + \Delta\delta^{0}_{\ell}(\kappa)\right]\left|A^{j,\ell}_{(2)}(\kappa)\right| \\ &\quad \times \cos\left[2\kappa R_j + 2\delta^{0}_{\ell}(\kappa) + \phi^{j,\ell}_{(2)}(\kappa)\right]\end{aligned} \tag{126}$$

$$\begin{aligned}\left[\Delta\chi^{\ell}_{(2)}(\kappa)\right]_{\sin} &= \sum_{j}\sum_{\ell'} \frac{(-1)^{\ell'}(2\ell'+1)\,\Delta\delta^{j}_{\ell'}}{(\kappa R_j)^2} \\ &\quad \times \sin\left[2\kappa R_j + 2\delta^{0}_{\ell}(\kappa) + 2\delta^{j}_{\ell'}(\kappa)\right]\end{aligned} \tag{127}$$

- The first term exhibits a phase $\psi^{\ell}(\kappa)$ that is strictly *in quadrature* with respect to the spin averaged EXAFS: this term reflects principally the spin dependence of the central atom phase-shift and a possible spin dependence of the interstitial potential resulting in a change of the zero-energy. This term has been found to dominate the experimental MEXAFS spectrum of gadolinium metal in the ferromagnetic phase.[106,107,164,182] Since it carries strictly the same information as normal EXAFS, but with a poorer signal-to-noise ratio, its practical interest is very limited in chemistry.

- The second term is much more exciting because it carries information on the spin polarization *of the scattering atoms* labelled j : this second term has not the same phase as the spin averaged EXAFS signal, the phase-shift being slightly bigger than in EXAFS. This term *will vanish for scattering atoms which are not spin-polarized.* Thus, MEXAFS could be used to identify spin polarized scatterers and, for instance, to extract metal-metal internuclear distances: this is often difficult in a normal EXAFS spectrum because complicate interferences with non magnetic scatterers result rapidly in very uncertain assignments. This was the primary motivation of our XMCD study of the binuclear gadolinium complex with the bifacial porphyrinic ligand which we mentioned in the first section of this chapter: MEXAFS seems to indicate that there might be a *Gd...Gd* distance of the order of 4.2 Å but the long term stability of the compound under the beam seems to be limited. In a different context and for a different problem, MEXAFS did also provide us with the unique proof that chalcogen atoms could become spin polarized.[191]

5. XMCD and MEXAFS at K Edges

XMCD at the K-edge is typically one order of magnitude less intense than at the L_{II-III} edges and seldom exceeds 0.1% even in ferromagnetic metals

or alloys. Under such conditions, one will easily understand that recording reliable MEXAFS signals at the level of (peak-to-peak) 0.01% or less remains a formidable challenge for the instrumentation, even at third generation synchrotron radiation sources. On top of that, paramagnetic metalloporphyrins tend to align antiferromagnetically at very low temperature so that even XMCD is fairly difficult to measure. In this subsection, we want to show briefly that there are further complications arising from the theory itself. Indeed, the small amplitude of K-edge XMCD spectra stems from the lack of spin-orbit coupling in the $1s$ core state: the difference associated to the first term of equation (114) simply vanishes for spin-polarized $\uparrow$ or $\downarrow$ electrons. For spherical potentials, the second term can be rewritten in a more pedagogical form as a spin-orbit interaction:[180,181]

$$-\operatorname{Im}\left[\mathbf{GG}\right] = \frac{\alpha_0^2 a_0}{4}\frac{1}{r}\frac{\partial V}{\partial r}\left[\ell.\boldsymbol{\sigma}\right] = \xi\left(r\right)\left[\ell.\boldsymbol{\sigma}\right] \tag{128}$$

which does not vanish in the final state. As demonstrated by Brouder,[182] this term yields three distinct contributions to the absorption cross-section:

- an atomic contribution (Fano effect):

$$\sigma_0\left(k\right) = \frac{4\pi\alpha_0}{3}\left(E - E_{in}\right)E\exp\left[i\delta_1^0\left(E\right)\right]M^{HH} \tag{129}$$

- a contribution due to the spin polarization of the p states:

$$\sigma_{1p}\left(k\right) = \frac{4\pi\alpha_0}{3}\left(E - E_{in}\right)2iE\exp\left[i\delta_1^0\left(E\right)\right]\left[D.M^H\right]\frac{\widetilde{\mathbf{X}}^{00}\left(11;00;E\right)}{\sqrt{3}\sin\delta_1^0\left(E\right)} \tag{130}$$

- another contribution arising from the spin-orbit scattering by the local potentials:

$$\begin{aligned}\sigma_{1n}\left(k\right) = \frac{4\pi\alpha_0}{3}\left(E - E_{in}\right)E\left[D\left(E\right)\right]^2\sum_{j\ell'}\exp\left[i\delta_1^0\left(E\right) + i\delta_{\ell'}^j\left(E\right)\right].\zeta_{\ell'}^j \\ \times\sum_{a=\left|\ell'-1\right|}^{\ell'+1}\left[\left(\ell'-a\right)\left(\ell'+a+1\right)+2\right] \\ \times\sum_{\alpha}\left(-1\right)^{a-\alpha}\frac{\widetilde{\mathbf{X}}^{0j}\left(1\ell';a\alpha;E\right)\widetilde{\mathbf{X}}^{0j}\left(1\ell';a-\alpha;E\right)}{\sin\delta_1^0\left(E\right)\sin\delta_{\ell'}^j\left(E\right)}\end{aligned} \tag{131}$$

The latter equations requires the calculation of a few more spin-orbit related radial integrals:[180,181,183]

$$\begin{aligned}M^H\left(E\right) &= \int_0^\infty r^2 dr\xi\left(r\right)\underline{R}_1^0\left(r,E\right)F\left(r,E\right) \\ M^{HH}\left(E\right) &= \int_0^\infty r^2 dr\xi\left(r\right)\left[F\left(r,E\right)\right]^2 \\ \zeta_{\ell'}^j\left(E\right) &= \int_0^\infty r^2 dr\xi^j\left(r\right)\left[\underline{R}_{\ell'}^j\left(r,E\right)\right]^2\end{aligned}$$

(132)

whereas the radial integrals $D(E)$ and $F(E)$ which were defined in the previous subsection need to be implicitly rewritten with $\ell = 1$ instead of $\ell = 2$. To date, the only simulation which met with some success concerned the analysis of XMCD and MEXAFS of the iron metal foil: we are still very far from potential applications in organometallic and porphyrin chemistry but it is useful to learn from this example what may be the order of magnitude of each one of the three contributions described above. The atomic contribution has been found to be very weak. The spin polarization of the p-states seems to dominate at large κ values, *i.e.* in the energy range of MEXAFS but this is not true in the near edge region where the magnetic electrons in the d band were found to play a quite significant role.

The complexity of these results speaks from itself: XMCD and MEXAFS spectra are not only difficult to measure but their interpretation is hopeless without *ab initio* simulations requiring very sophisticated computing codes. Moreover, the present theory does not take into account the effects of multielectron excitations which are contributing to huge singularities in the MEXAFS spectra[192,193] and add to the difficulty of practical analyses .

6. Magneto-Optical Sum Rules

These rules are playing such a major role in the current applications of XMCD in magnetism that a review ignoring them would appear indecent. We feel even more important to stress what are the limits of their validity. We will restrict ourself to only three of the sum rules established by Carra *et al.*[16] , Thole *et al* [15] or Ankudinov:[107]

- At the L_{II-III} edges and for nd electrons:

$$\int \left[\Delta\sigma_{L_{III}}(E) + \Delta\sigma_{L_{II}}(E)\right] \frac{dE}{\hbar\omega} = \frac{-N}{2n_{hole}} \langle L_z \rangle_d \tag{133}$$

$$\int \left[\Delta\sigma_{L_{III}}(E) - 2\Delta\sigma_{L_{II}}(E)\right] \frac{dE}{\hbar\omega} = \frac{-N}{3n_{hole}} \left[2\langle S_z \rangle_d + 7\langle T_z \rangle_d\right] \tag{134}$$

where N is the sum of the polarization-averaged white line resonances extracted from the L_{II-III} near edge spectra:

$$N = \int \sum_{\lambda=0,\pm1} \left[\sigma_{L_{III}}(E) + \sigma_{L_{II}}(E)\right] \frac{dE}{\hbar\omega} \tag{135}$$

whereas $T_z = \left[\frac{1}{2}\boldsymbol{\sigma} - 3\hat{\mathbf{r}}.(\hat{\mathbf{r}}.\boldsymbol{\sigma})\right]$ would be the lowest order multipolar term measuring the asphericity of the spin magnetization.[175]

- At the K edge and for p electrons:

$$\frac{\int \Delta\sigma_K(E)\, dE}{\int \sigma_K(E)\, dE} = \frac{3}{n_{hole}} \langle L_z \rangle_p \tag{136}$$

These magneto-optical sum rules have the very appealing feature to connect separately the spin and orbital magnetic moments to the experimental XMCD spectra but one should never forget that their derivation requires questionable approximations which, in practice, seem to be acceptable for $3d, 4d$ and $5d$ transition metal compounds. It is well documented that the application of the sum rules yields erroneous conclusions in the more difficult case of the $L_{II,III}$ edges of rare-earth compounds. The following approximations may be incriminated:

- the electric quadrupole contribution is neglected;
- the $p \longrightarrow s$ transitions are neglected;
- the exchange splitting and the asphericity of the core levels are neglected;
- crystal field and spin-orbit splittings of the final d states are often neglected;
- the energy dependence of the matrix elements is neglected.

Another interesting question which deserves attention is the possible extension of the sum rules into the MEXAFS regime. Recent works by Gotsis and Strange,[194] Guo,[195,196] Ebert *et al.*[197–199] suggest that a better way to exploit the data is to make use of the *differential* formulation of the sum rules which could be rewritten:

$$[2\Delta\chi(\kappa)]_{L_{III}} + [\Delta\chi(\kappa)]_{L_{II}} = \frac{C}{2}\frac{\partial\langle L_z\rangle_d}{\partial\kappa}\frac{\partial\kappa}{\partial E} \tag{137}$$

$$[2\Delta\chi(\kappa)]_{L_{III}} - 2[\Delta\chi(\kappa)]_{L_{II}} = \frac{C}{3}\left[2\frac{\partial\langle S_z\rangle_d}{\partial\kappa} + 7\frac{\partial\langle T_z\rangle_d}{\partial\kappa}\right]\frac{\partial\kappa}{\partial E} \tag{138}$$

Very preliminary analyses of high quality MEXAFS spectra recorded at the ESRF on non-porphyrinic compounds suggest that the Fourier Transformed spectra of the left handside of equations (137) and (138) could give us access to the radial distribution of the spin and orbital components of the magnetic moments for a given symmetry.[200] Further work is in progress in order to evaluate whether or not this result is general.

7. Spin-Polarized, High Resolution Emission Spectra

In this section we are concerned with the splitting of fluorescence lines due to exchange interactions. A typical example is precisely the splitting of the K_β line of transition metals like iron or manganese: the outer $3p$ electrons involved in the K_β line emission have a very strong exchange interaction with the partly filled $3d$ shell and the splitting of the K_β line can be as large as 15 eV for high-spin iron. Neglecting the exchange with the deeper core states $(1s, 2s, 2p)$, the accepted interpretation is to assign the whole splitting of the K_β line to the dominant $\{3p, 3d\}$ exchange that should be also associated with a significant degree of spin polarization by the valence electrons. If the two split lines are well enough resolved, they should correspond to the relaxation of a core hole that is *spin-up* or *spin-down* relative to the spin state of the valence electrons of the absorbing

atom. This implies that one might have indirectly the capability to discriminate between the excitation processes creating photoelectrons with spin-up or spin-down relative to the spin of the central atom. Since the exchange interaction will make the energy of the $\{3p-up\}$ electrons lower than the energy of the $\{3p-down\}$ ones, the line with lower energy should correspond to the emission of photoelectrons with *spin-up*. This method has the considerable advantage over XMCD that it is applicable to study the *spin order in antiferromagnets as well as in ferromagnets* and does not require any (*circularly*) polarized light. The only requirement for it to work is that the exchange splitting has to be greater than its natural width or greater than the spin-orbit splitting if the latter is not negligible. Otherwise, the whole theory detailed in the previous sections for the calculation of spin dependent absorption cross sections should perfectly hold true.[107]

III. PRACTICE OF XAS

A. Standard Analyses of EXAFS

Numerous software packages have been developed to analyze EXAFS spectra. Detailed information concerning a limited selection of well identified codes is readily available through the WWW site of the International XAFS Society.[201] Many more programs do exist even though developers often feel reluctant to make public software products which are not mature enough or which are continuously evolving with the nature of the projects of current interest. Nearly all advanced data analysis packages are now systematically interfaced with *ab initio* simulation programs such as FEFFx,[103] MSXAS[99] and GNXAS,[100] or EXCURVE9x.[202] Our own "*amateurish*" package *XN* was initially developed at the University of Nancy (France) and has been interfaced with MSXAS since 1989.[203] It is still evolving to include new developments in XMCD, MEXAFS and XNCD that are going on at the ESRF.

1. Data Preparation

Typically, this includes:[204]

- *The correction of Fluorescence Detected spectra for self-absorption*: such a correction is mandatory for thick and concentrated samples because the intensity of the fluorescence signal $F(E)$ *is not proportional to the true absorption coefficient* $\mu(E)$.[205] Unfortunately, it is not realistic to look for a fully rigorous correction which would rapidly turn out to be fairly complicated. As a first approximation, Goulon *et al.* have proposed a so-called *homographic correction*[206,207] which is briefly outlined below and is valid only for very thick samples. The fluorescence signal $F(E)$ is first normalized with respect to the edge jump $F_0(E_j)$ and the normalized spectrum defined as: $Y(E) = F(E)[F_0(E_j)]^{-1}$ is next transformed according to:

$$S(E) = \frac{\beta_0 Y(E)}{1-\beta_0 Y(E)}[\mu_b(E) + \alpha_F \mu_F(E_F)] \simeq \mu(E) \qquad (139)$$

where:

$$\beta_0 = \frac{\mu_0(E_j)}{\mu_b(E_j) + \mu_0(E_j) + \alpha_F \mu_F(E_F)} \tag{140}$$

In the latter equations, E , E_j and E_F refer to the excitation energy (E), to the energy at which the edge jump is measured (E_j) and to the energy of the fluorescence photons (E_F). Since one is concerned here only with a correction, the absorption coefficients $\mu_b(E)$, $\mu_0(E)$ or $\mu_F(E_F)$ can be reasonably well approximated by using tables for atomic cross sections such as those published by McMaster *et al.*[208] In equations (139) and (140), α_F is a geometrical factor which depends on the arrangement of the fluorescence detectors and is unity only if the fluorescence emission is detected at 90° from the direction of the incident photons. A different renormalization algorithm has been developed by Waldo and Penner-Hahn.[209] Another strategy adopted by Tan *et al.*[210] is to correct for self-absorption the *apparent* EXAFS amplitudes and the Debye-Waller factors derived from a standard analysis: this method is however not suitable for *FD*-XANES nor for *FD*-XMCD studies.

- *The removal of the pre-edge background*: this can be done, for instance, by expanding the measured pre-edge signal $\mu_b(E)$ on a low order set of *orthogonal* Tchebycheff polynomials $T_n(x)$ where x is a reduced variable depending on the photon energy and n ≤ 3.[203]

- *The pre-normalization of each spectrum with respect to the edge-jump:* this is a key step to access to a reliable number density of scattering atoms in a given shell. One may exploit again a restricted set of orthogonal Tchebycheff polynomials $T_n(x)$ to fit $\mu(E)$ with an appropriate weighting factor of the high energy data. The fitted background $\mu_{0b}(E)$ is then extrapolated down to the edge region in order to define the edge jump $\mu_{jp} = \mu_{0b}(E_j)$.[203]

- *The self-consistent adjustment of the photoionization threshold* E_0 : this is mandatory in order to define the photoelectron wavevector $k = \left[(2m/\hbar^2)(E - E_0)\right]^{1/2}$. One has also to select the energy $E_{\min}$beyond which the EXAFS regime is reached. One should make clear that E_0 may have to be modified in an iterative way during the analysis in order to be fully consistent with a given choice of scattering phase-shifts.

- *The linearization of the data sampling in the k-space:* this is necessary as far as *Fast Fourier Transform* algorithms are used.

- *The extraction of the EXAFS oscillations* $\chi(k)$: for this rather delicate operation, one may exploit the following approximation:

$$S(k) = \chi(k) + \chi_{bg}(k) \simeq \frac{\mu(k)}{\mu_{jp}\left[1 - \frac{8}{3}\alpha^2 k^2\right]} \tag{141}$$

where the denominator is taken as a reasonable approximation for the *true* atomic background $\mu_0(k)$ at least for $k \leq 16\text{Å}^{-1}$.[205,211] In the past decade, a number of algorithms have been implemented in *XN* in order to extract $\chi(k)$ from the low frequency background $\chi_{bg}(k)$ but their careful

evaluation has shown that none can be certified to be fully reliable under any circumstances. A simple strategy is to decompose once again the normalized signal $S(k)$ on a restricted basis of *orthogonal* Tchebycheff polynomials $T_n(x_k)$:

$$S(k) = \chi(k) + \chi_{bg}(k) \simeq \sum_j \beta_j \chi_j(k) + \sum_{n=0}^{n=6} \alpha_n T_n(x_k) \qquad (142)$$

This makes sense:

- if the EXAFS signal has no low frequency components α_n;
- if the background $\chi_{bg}(k)$ does not contain high frequency components arising from Dirac or step like distortions such as normal or dispersive *"glitches"*, multielectron excitations[166] or the edge singularity of some contaminating element.

Even though such conditions are most often acceptable for EXAFS analyses, they are usually not met for reliable AXAFS studies. Equation (142) can also be solved as an *iterative* (*self-consistent*) linear problem once the dominant EXAFS signatures have been identified and pre-fitted,[212] the zero-order approximation being the direct fit of the data with all $\beta_j = 0$. The iterative approach reduces the amplitude of tiny artifactual polynomial wiggles that may arise near the end point of the fitting interval. Alternative options are well documented in the specialized EXAFS literature: they concern the use of *segmented* polynomials (*"splines"*) with the constraint that these polynomials and their first derivative have to be continuous at the *"knots"* where two consecutive polynomials meet. The selection of the *"knots"* and of their number (3 to 5) was initially left arbitrary but is now better codified. Cook and Sayers[213] and more recently Bauchspiess[214] have constrained the fit in order to minimize the local *curvature* of the splines. Bauchspiess[214] found even possible to incorporate in his algorithm the capability to damp sudden jumps associated to unwanted *"glitches"*. A number of examples have been produced which confirm that, very near the absorption threshold, the atomic background is structured, especially for high Z absorbers: this is where recent procedures elaborated by Li *et al.*[215,216] or by Newville *et al.*[217,218] seem to be more appropriate, especially if one wishes to extract reliable AXAFS signatures.

Even with the most sophisticated computer codes that are now available, none can honestly argue that his recipe to prepare the data is rigorous. The pre-processing of the data also affects the statistical and the spectral distribution of the experimental errors. There are hidden degrees of freedom associated with the background subtraction procedure but the latter are systematically obliterated when the authors come to a discussion of statistical tests used to validate curve fitting techniques in the momentum $k-$space. Our recommended criteria to select a given procedure is the *reproducibility* which is essential to minimize unwanted distortions in *difference* analyses described in section III.B

2. Fourier Transformed *Optical* Spectra

Sayers *et al.*[30] were the first to recognize that Fourier Transforming (FT) the XAFS oscillations $\chi(k)$ was a convenient way to display the whole structural content of an EXAFS experiment. Metalloporphyrins were rapidly identified as good illustrations of such FT spectra.[219] However, the *legibility* of standard FT-EXAFS spectra can be severely degraded by *the non-linear $k-$dependence of the phase-shifts because of the linear character of Fourier integrals.* Moreover, the lineshapes are often highly distorted due to the convolution of the expected Dirac peaks with the FT backscattering amplitude. Following Lee and Beni,[220] we found more efficient to display only *corrected* FT spectra which are sometimes referred to as *FT optical spectra* :

$$\widetilde{\chi}_j(R) = \int_0^\infty dk\, W(k)\, \frac{kR_j^{2p} \exp\left[2\sigma_j^2 k^2 - 2ikR - i\psi_j\left(k, \overline{R}_j\right)\right]}{F_j\left(k, \overline{R}_j\right) D^\ell\left(\overline{R}_j, \Gamma_t; k\right) S^2(k)}\, \chi(k) \quad (143)$$

where:

- $W(k)$ is a Kaiser-Bessel window function aimed at minimizing the side lobes of the observed signals[221] ;
- $\psi_j\left(k, \overline{R}_j\right) = 2\delta_0^\ell(k) + \phi_j^\ell\left(k, \overline{R}_j\right)$ is the phase-shift of any arbitrarily selected scattering path j;
- $F_j\left(k, \overline{R}_j\right) = \left(kR_j^2\right) A_j^\ell\left(k, \overline{R}_j\right)$ is the magnitude of the backscattered amplitude for path j;
- $\exp\left[-2\sigma_j^2 k^2\right]$ is the Debye-Waller factor associated with the scattering path j;
- $D^\ell\left(\overline{R}_j, \Gamma_t; k\right)$ is the damping function defined in equation (62);
- $S^2(k)$ is a semi-empirical correction accounting for the $k-$dependent losses briefly discussed in subsection II.C.3 dealing with the many-body problem.

Since $\widetilde{\chi}_j(R)$ is a complex function of R, it is a common practice to display either $\left|\widetilde{\chi}_j(R)\right|$ or $\mathrm{Im}\left[\widetilde{\chi}_j(R)\right]$. Regarding the applications of EXAFS to porphyrin chemistry, we recommend to display systematically $\mathrm{Im}\left[\widetilde{\chi}_j(R)\right]$ because:

(i) The *resolution* of the latter spectra is superior. This has, however, a price: since the peaks are convolved with $\widetilde{W}(R)$, *i.e.* the Fourier Transformed window function, the displayed signals usually exhibit two negative side lobes which should be symmetrical if the phase-shifts are properly corrected.

(ii) This representation preserves a *valuable phase information* that can be exploited to discriminate between scatterers of different types: *e.g.* $\{C, N, O\}$ *versus* $\{P, Cl, S\}$

(iii) As pointed out by Lee and Beni,[220] a simple criterion for adjusting E_0 for a specific shell j is to achieve the coincidence between the maxima of $\left|\widetilde{\chi}_j(R)\right|$ and $\mathrm{Im}\left[\widetilde{\chi}_j(R)\right]$. One may wonder why there is any need to adjust E_0. To justify this procedure, one has simply to remember that the calculation of the scattering phase-shifts requires the definition of the interstitial potential $\overline{V}_{int}$ which, within the muffin-tin approximation, offers only a very poor description

of chemical bonding. In the early days of the method, *i.e.* when tabulated phase-shifts were used, one had to shift E_0 well beyond the absorption threshold ($\Delta E_0 \geq 12$ eV). This is not anymore necessary with phase-shifts calculated with the new codes MSXAS or GNXAS since E_0 is systematically located at the onset of the absorption edge.

Obviously, a good reason for preferring *corrected* FT spectra as defined by equation (143) is that, at least for shell j, $\mathrm{Im}\left[\widetilde{\chi}_j\left(R\right)\right]$ should peak at the true interatomic distance $\overline{R}_j$ if the phase-shifts $\psi_j\left(k\right)$ injected in equation(143) are accurate enough. This appears to be the case when the phase-shifts $\psi_j\left(k\right)$ are generated with MSXAS, FEFFx, EXCURVE9x ... which calculate the phase-shifts and scattering amplitudes from first principles for each compound. On the other hand, one would expect the amplitude of the peak to be directly proportional to $N_j\ \widetilde{W}\left(R_j\right)$ if both the backscattering amplitudes $F_j\left(k,\overline{R}_j\right)$ and the damping functions $D^{\ell}\left(\overline{R}_j,\Gamma_t;k\right)S^2\left(k\right)$ were properly evaluated: this condition is, unfortunately, much harder to satisfy than for the phase correction. Note that the peak amplitudes suffer from systematic distortions for $i \neq j$ because the implicit scaling factor $\left(R_j^p/R_i\right)^2$ is not taken into account. In principle, the homogeneity of Eq. (143) would require to multiply the FT spectra not by $\left(R_j\right)^2$ but rather by R^2: this was scarcely done so far because the noise level was usually prohibitive at long distances and the current practice was rather to plot the FT spectra with $p = 0$.

For metalloporphyrins, it is convenient to select arbitrarily as shell j the characteristic contribution of the four pyrrolic nitrogen atoms. As an example, we have reproduced in **Figure 7** the corrected FT spectrum of the vanadyl porphyrin (TPP)VO that was obtained when the raw data shown in **Figure 3** were analyzed. Note that for low-Z scattering atoms (*i.e.* $C, N, O..$), the phase-shifts are not very different: this has the practical consequence that the various peaks which can be easily assigned to the vanadyl oxygen (O), to the four pyrrolic nitrogens ($4N$), and to the various carbons of the macrocycle: $8C_\alpha$, $4C_{meso}$, $8C_\beta$, are well in phase. In theory, the signals of shells $i \neq j$ *should not* peak exactly at the true interatomic distances R_i because, as discussed in section II.B.3, the phase-shifts do not depend simply on k but also on $\rho = kR$ in the curved-wave approximation. This argument looks at odds with the FT spectrum displayed in **Figure 7** which shows that neither the phase distortions for shells $i \neq j$ nor the differences between the observed peak positions and the true interatomic distances are radical as long as multiple scattering paths do not contribute. In reality, there is no contradiction with section II.B.3: one has simply to realize that equation (143) is more heavily weighting the experimental data recorded at high $k-$values for which the PW approximation is quite satisfactory.

Goulon *et al.*[222] found desirable to evaluate more accurately the influence of the curved-wave approximation on FT spectra. It has been shown,[207,222] that, under appropriate conditions ($kR \geq 1$), equation (143) could be replaced by a truncated series expansion:

$$\widetilde{\chi}_j\left(R\right) = \sum_{q=0}^{q=q'} \int_0^{\infty} dk\ W\left(k\right) \left[\frac{k\overline{R}_j^{2p} \exp\left[2\sigma_j^2 k^2 - 2ikR - i\psi_j^0(k)\right]}{F_j^0\left(k\right) D_{(2)}^{\ell}\left(\overline{R}_j,\Gamma_t;k\right) S^2\left(k\right)}\right] \quad (144)$$

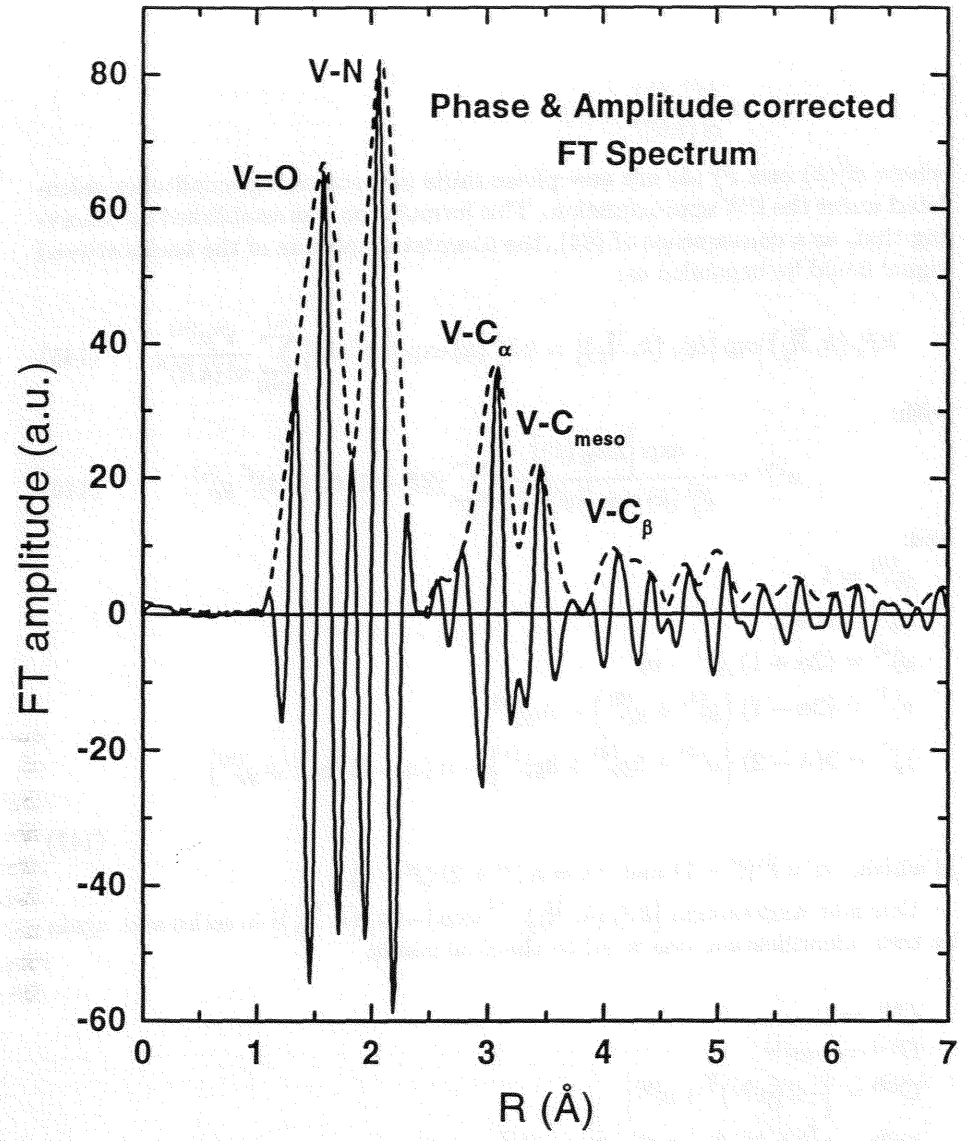

Figure 7: Complex FT *optical* EXAFS spectrum of (TPP)VO :

Imaginary part: Im [$\tilde{\chi}_j(R)$] *(full line)* ; Modulus : $|\tilde{\chi}_j(R)|$ *(dotted line)*.

These spectra were obtained by processing the data displayed in Figure 3 ($k_{max} \geq 21$ Å^{-1}).

$$\times \frac{kC_q(k)}{q!(kR)^q}\,\chi(k)$$

where $\psi_j^0(k)$ and $F_j^0(k)$ are now phase-shifts and scattering amplitudes calculated under the PW approximation. This formulation was established by observing that, as a consequence of (64), the complex amplitude of the backscattered signal could be expanded as:

$$kF_j\left(k,\overline{R}_j\right)\exp\left[i\psi_j\left(k,\overline{R}_j\right)\right] = kF_j^0(k)\exp\left[i\psi_j^0(k)\right]\sum_{n=0}^{n'}\frac{i^n a^{(n)}}{n!(kR)^n} \tag{145}$$

with:

$$a^{(n)} = \frac{\exp\left[2i\delta_0^\ell(k)\right]}{F_j^0(k)\exp\left[i\psi_j^0(k)\right]}\sum_{\ell'}(2\ell'+1)\,\mathbf{t}_{\ell'}^j\,(-1)^{\ell'}\,g_{\ell'}^{(n)} \tag{146}$$

and:

$$\begin{aligned}
g_{\ell'}^{(0)} &= 1\\
g_{\ell'}^{(1)} &= \alpha+2\\
g_{\ell'}^{(2)} &= (2\alpha+1)\,g_{\ell'}^{(1)} - m\\
g_{\ell'}^{(3)} &= (2\alpha-1)\left(g_{\ell'}^{(1)}+g_{\ell'}^{(2)}\right) - m g_{\ell'}^{(1)}\\
g_{\ell'}^{(4)} &= 2(\alpha-2)\left\{g_{\ell'}^{(3)}+3g_{\ell'}^{(2)}+3g_{\ell'}^{(1)}\right\} - \alpha(\alpha-2)\left[g_{\ell'}^{(1)}+g_{\ell'}^{(2)}\right]\\
&\ldots
\end{aligned} \tag{147}$$

in which: $\alpha = \ell'(\ell'+1)$ and $m = \alpha(\ell'+2)(\ell'-1)$

One may next expand $\left[kF_j\left(k,\overline{R}_j\right)\right]^{-1}\exp\left[-i\psi_j\left(k,\overline{R}_j\right)\right]$ in series and, again by term identification, one is led to the final result:

$$\begin{aligned}
C^{(0)} &= 1\\
C^{(1)} &= -ia^{(1)}\\
C^{(2)} &= \left[-2\left(a^{(1)}\right)^2 + a^{(2)}\right]\\
C^{(3)} &= i\left[6\left(a^{(1)}\right)^3 - 6a^{(1)}a^{(2)} + a^{(3)}\right]\\
C^{(4)} &= \left[24\left(a^{(1)}\right)^4 - 36\left(a^{(1)}\right)^2 a^{(2)} + 8a^{(1)}a^{(3)} + 6\left(a^{(2)}\right)^2 - a^{(4)}\right]\\
&\ldots
\end{aligned} \tag{148}$$

In all examples which were investigated so far, it was found that the FT series could be truncated for $q_{\max} = 4$, the higher order terms having little effect on the shape of the FT signals. The results[222] confirmed that the curved-wave propagation induced significant phase distortions *only for the shells located at very short distances* but had little or no effect when the explored Δk range was large enough. These results contributed to establish the reliability of corrected FT optical spectra which had been questioned in the past, especially when tabulated phase-shifts and backscattering amplitudes were used. In practice, it is much faster to use directly equation (143) rather than the FT series expansion which has nevertheless the advantage that the amplitude and phase corrections made for a given scatterer should remain valid for any $R \neq R_j$.

3. Autocorrelation Power Spectral Densities and Maximum Entropy Method

To display the whole structural information contained in EXAFS spectra, one may envisage another approach. EXAFS oscillations are most often analyzed as a *deterministic* signal buried in some random noise which is commonly assumed to be *stationary* and *ergodic. A priori*, one cannot refer directly to theories of adaptive filtering and signal processing because the deterministic signal *is not stationary.* According to a theorem established by Wold in 1938,[223] any deterministic signal can be transformed into a stationary random process by convolving it with a white noise of unit power spectral density: then adaptive filtering becomes possible. On the other hand, the primary goal of the spectroscopist is not to extract a clean EXAFS signal from noise: it is rather to extract from the data the radial distribution of the scattering atoms. This becomes far more challenging because one needs to transform the EXAFS oscillations into a *quasi stationary process in the momentum space.* In other terms, one would like the EXAFS *autocorrelation function:* $K_\chi(k_2, k_1)$ to be only a function of the difference $(k_2 - k_1)$. This would be the case for any exponentially damped periodic function but this is clearly wrong for a standard EXAFS signal because the phase-shifts $\psi_j\left(k, \overline{R}_j\right)$ are nonlinear functions of k and because the scattering amplitudes $F_j\left(k, \overline{R}_j\right)$ are not exponentially decaying functions. Phase and amplitude *corrected* signals, as generated in the previous section, should be more consistent with the latter definition of stationarity because one may expect the corrected EXAFS signal to be *reasonably well approximated* with a sum of complex exponential functions in the momentum space. This is, by construction, the case for shell j but one may question how far this approximation will hold true for the other shells. For metalloporphyrins, the spectra are often dominated by the EXAFS contributions of low Z scattering atoms of the macrocycle and therefore one may guess that the correction made for the four nitrogen shell $(j = 1)$ should, in a first approximation, be good enough to warrant the desired stationarity of the *whole* autocorrelation function. This does not hold true for binuclear complexes for which the analysis described below should fail. For a discrete, stationary stochastic signal, the autocorrelation function may be calculated from the standard definition:[224]

$$C_\chi^j(m) = \lim(N \to \infty) \frac{1}{2N+1} \sum_{n=-N}^{n=N} \chi_j(n)\chi_j^*(n-m) \qquad (149)$$

where N is the total number of data points that are available in the momentum space, n is the data point index and m characterizes a positive or negative incremental lag $m\Delta_k$ in the momentum space. Index j has been added to remind the reader that the EXAFS signal is corrected in phase and amplitude for shell j :

$$\chi_j(n\Delta_k) = FT^{-1}\left\{\left(\frac{R}{R_j}\right)^{2p} \widetilde{\chi}_j(R)\right\} \qquad (150)$$

where $k = n\Delta_k$. Since the data sequence is defined in a restricted momentum range $(n > 0)$, one will immediately notice that one can never access experimentally to the true autocorrelation function since N is finite. This has further implications if one is Fourier Transforming the experimental autocorrelation

function because $C_\chi^j(m\Delta_k)$ is also defined over a limited range of incremental lags in the momentum space and one needs again to introduce a Kaiser-Bessel window function if one wants to minimize the side lobes in the R-space. The corresponding FT spectrum $\widetilde{C}_\chi^j(R)$ *should not be confused* with $\widetilde{\chi}_j(R)$ because the two functions have a different origin. The link between the two functions is to be found in the Wiener-Kinchin theorem which, for a stationary process, implies that: $\left|\widetilde{C}_\chi^j(R)\right| \simeq \left|\widetilde{\chi}_j(R)\right|^2$ if $p = 0$. This is illustrated by **Figure 8** which displays both the calculated autocorrelation power spectral density for the vanadyl porphyrin (TPP)VO and the square of the modulus of the complex FT spectrum already displayed in **Figure 7.** It clearly appears from **Figure 8** that the Wiener-Khinchin theorem is well satisfied and this will hold true as long as one is using *corrected* EXAFS spectra. Note that the autocorrelation power spectral density $\widetilde{C}_\chi^j(R)$ has even a better resolution than the conventional FT power spectrum: this is natural because the autocorrelation function is defined over both positive and negative values of the phase lag $\pm m\Delta_k$. It is then somewhat surprising that, hitherto, the autocorrelation power spectral density of EXAFS signals has never been used nor displayed, even in the specialized literature. It is our guess that this may change in the future because the comparison of $\widetilde{C}_\chi^j(R)$ and $\widetilde{\chi}_j(R)$ could yield valuable additional information:

- Any decomposition of the sample under the very intense beams of third generation SR sources will result in a major distortion of the autocorrelation power spectral density because stationarity is lost.
- The presence of heavy scatterers should be easily detected because, again, the condition of quasi-stationarity cannot be satisfied.

Note that the definition of the autocorrelation function can be extended to *cross-correlation* functions which we found very useful to analyze noisy MEXAFS signals. On the other hand, stationary signals can be analyzed with the powerful resources of linear filtering by "*Maximum Entropy Methods*" (MEM).[224] For a *stationary, gaussian* random process, one would show that the rate of creation of the Shannon-Jaynes entropy is given by:

$$s = \frac{1}{4R_N}\int_{-R_N}^{R_M} \log\left[\widetilde{C}_\chi^j(R)\right] dR \tag{151}$$

where $R_N = [\Delta_k]^{-1}$ is the Nyquist radius of the random sequence. One may now raise the following question: is there any formulation of a spectral density $\widetilde{C}_\chi^j(R)$ that would be consistent with *a stationary rate of creation of entropy with respect* to *both the known* ***and*** *unknown correlations* ? The answer is in the affirmative and using the variational principle, it can be shown that the corresponding spectral density $\widetilde{C}_\chi^j(R)$ can be formulated:[224]

$$\widetilde{C}_\chi^j(R) = \frac{\Delta_k P_{M+1}}{\left|1 + \sum_{m=1}^{M} \gamma_m \exp(2i\Delta_k R)\right|^2} \tag{152}$$

where the coefficients γ_m define the response of a so-called *prediction-error filter*. The vector $\mathbf{\Gamma}_M(1, \gamma_1, ...\gamma_m, ...\gamma_M)$ is solution of the matrix equation:

$$\mathbf{T}_M \mathbf{\Gamma}_M = \mathbf{P}_{M+1} \tag{153}$$

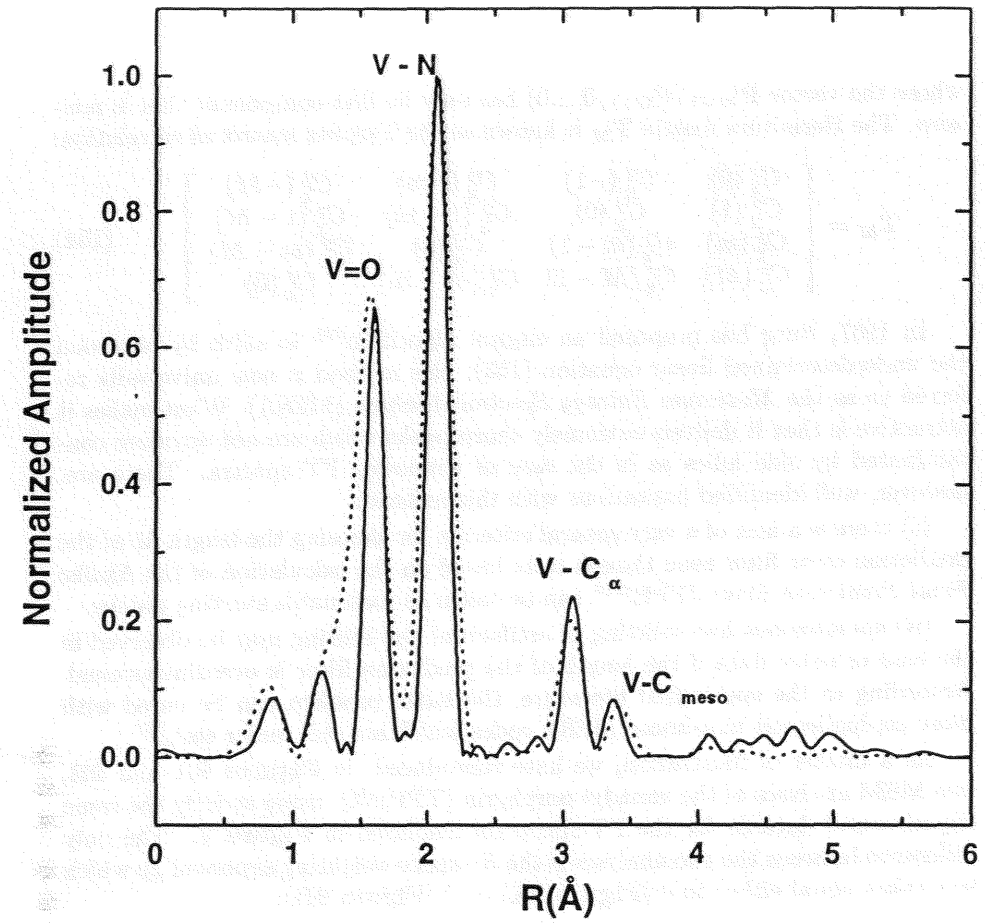

Figure 8: Self-consistent verification of the Wiener-Khinchin theorem:

(i) Power spectral density of the *quasi*-stationary autocorrelation function calculated for the corrected EXAFS signal of (TPP)VO (*full line*).

(ii) Squared modulus (*dotted line*) of the corrected FT spectrum calculated according to Eq. (142).

Note the enhanced spectral resolution of the autocorrelation power spectral density.

where the vector $\mathbf{P}_{M+1}\,(P_{M+1}, 0, ...0)$ has only its first component that is non-zero. The Hermitian matrix $\mathbf{T}_M$ is known as the Toeplitz matrix of correlation:

$$\mathbf{T}_M = \begin{bmatrix} C_\chi^j(0) & C_\chi^j(-1) & C_\chi^j(-m) & C_\chi^j(-M) \\ C_\chi^j(1) & C_\chi^j(0) & C_\chi^j(1-m) & C_\chi^j(1-M) \\ C_\chi^j(m) & C_\chi^j(m-1) & C_\chi^j(0) & C_\chi^j(m-M) \\ C_\chi^j(M) & C_\chi^j(M-1) & C_\chi^j(M-m) & C_\chi^j(0) \end{bmatrix} \qquad (154)$$

In 1967, Burg has proposed an elegant algorithm[225] to solve by recursion the underdetermined linear equation (153): this method is now universally referred to as the *Maximum Entropy Spectral Analysis* (MESA). What makes it attractive is that it delivers extremely sharp peaks which are not anymore contaminated by side lobes as in the case of windowed FT spectra. There are, however, well identified limitations with this method:

(*i*) there is a lack of a very general criterion for choosing the length M of the prediction error filter even though tests based on the calculation of the Akaike *Final Prediction Error* (FPE)[226] can be taken as reasonable starting points;

(*ii*) spontaneous line splitting or artifactual line shifting may be observed in the case of noisy data if the length of the prediction filter is overdimensioned. According to the specialized literature, the latter problem can be cured with more sophisticated *non-linear* MESA codes which are still under test.[227]

As a matter of illustration, we have reproduced in **Figures 9A** and **9B**, two MEM analyses of the vanadyl porphyrin (TPP)VO using strictly the same experimental data as for the FT spectrum displayed in **Figure 7.** The only difference between the two analyses is the R–space weighting exponent $2p$ which was taken equal either to 0 (**Figure 9A**) or 2 (**Figure 9B**):

- Indeed, the first option has to be preferred if one is interested in a tentative resolution of the signals originating from the coordination shells of the metal, under the restriction that they should have similar phase-shifts. Let us emphasize that the corrections for spherical wave propagation which were discussed in the previous section would be most relevant here.

- On the other hand, **Figure 9B** also shows that much information is still available at long path lengths using the MEM analysis: there is a fairly spectacular resolution of the signatures of the carbon atoms of the macrocycle: C_α, C_{meso} and C_β. Indeed, multiple scattering paths induce significant distortions of the signals observed at large distances but new options are being explored to exploit in a more quantitative way these signals that are very well above the noise level.

Recall that Maximum Entropy Spectral Analyses of EXAFS spectra were already pioneered by Labhardt and Yuen[228,229] in 1977. The method was revisited in these recent years by Matsubayashi *et al.* [230] who played with the EXAFS spectrum of a copper metal foil. Unfortunately, the experimental data used by Labhardt and Yuen were rather noisy and this may have caused the unmerited disqualification of the method. It should be also pointed out that these very first analyses inherently suffered from a *non-stationarity of the calculated correlations* because Labhardt and Yuen did not correct their EXAFS spectra for the non-linearity of the phase-shifts and for the non-exponentially decaying scattering amplitudes: in our experience, this may be enough to invalidate the method.

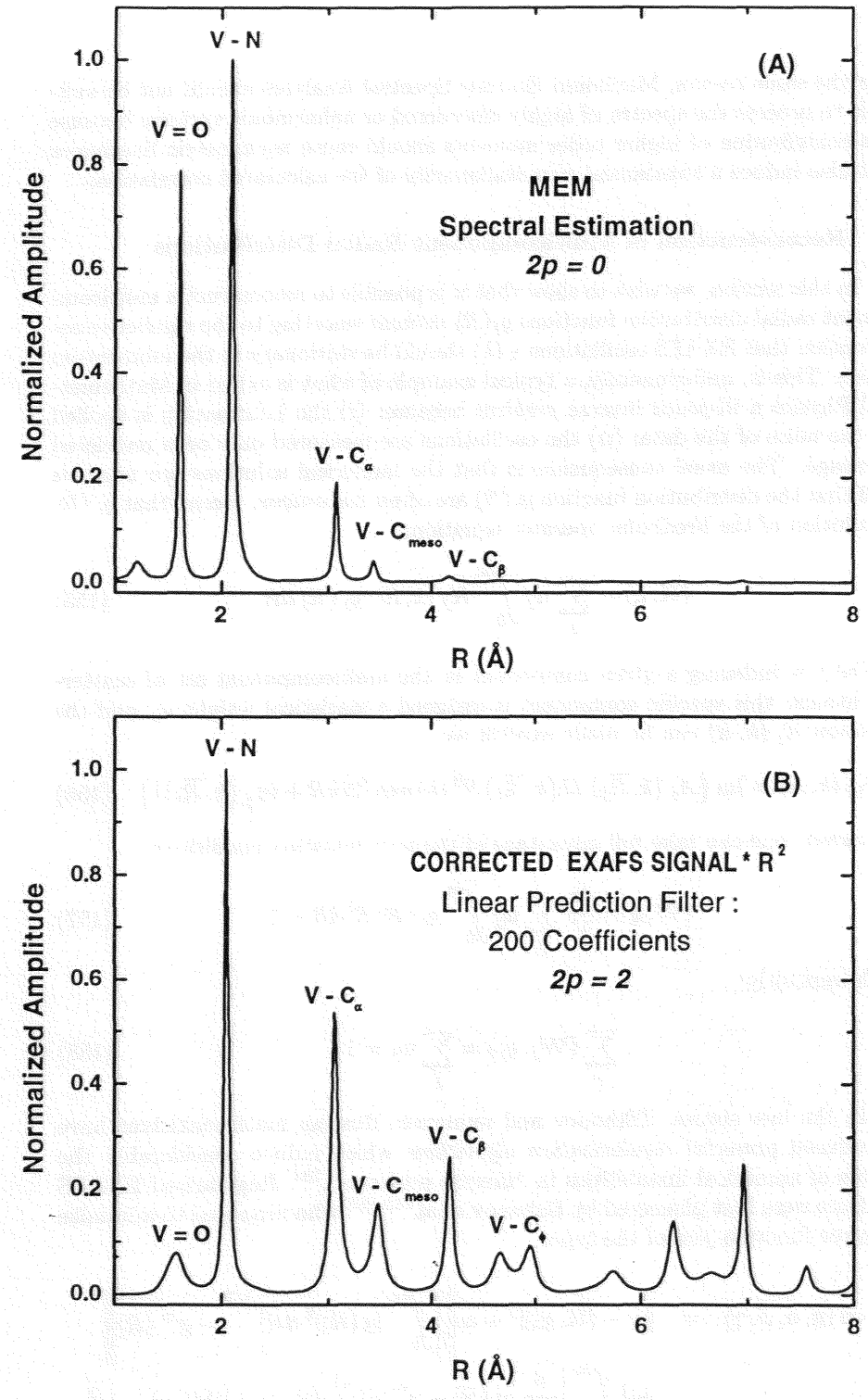

Figures 9: Maximum Entropy Spectral Analyses (MESA) of (TPP)VO obtained assuming a *quasi*-stationary autocorrelation of the EXAFS signal:

Figure 9A : R-space weighting corresponding to 2p=0 (*i.e.* conditions consistent with the usual FT spectra).

Figure 9B : R-space weighting corresponding to 2p=2 (*i.e.* favoring the long scattering paths).

For the same reason, Maximum Entropy Spectral Analyses should not be suitable to process the spectra of highly disordered or anharmonic systems because the contribution of higher order moments should cause asymmetric lineshapes but also induce a substantial *non-stationarity* of the calculated correlations.

4. Reconstruction of Multicomponent Radial Distributions

In this section, we wish to show that it is possible to reconstruct a multicomponent radial distribution functions $g_j(R)$ *without* resorting to the restrictive assumption that EXAFS oscillations $\chi(k)$ should be stationary in the momentum space. This is, unfortunately, a typical example of what is called in Mathematical Physics a *ill-posed inverse problem* because: (i) the information is spoiled by the noise of the data; (ii) the oscillations are measured only on a restricted $k-$range. The usual consequence is that the numerical solutions are *unstable* and that the distribution function $g_j(R)$ are often *not unique*. Recall that $g_j(R)$ is solution of the Fredholm operator equation:

$$(\mathbf{K},\mathbf{g}) = \sum_j w_j \int_0^\infty K_j(k,R)\ g_j(R)\, dR \tag{155}$$

where j is indexing a given component in the multicomponent set of scattering atoms: this specific component is assigned a statistical weight w_j and the function $K_j(k,R)$ can be made explicit as:

$$K_j(k,R) = \mathrm{Im}\left\{A_j\left(k,\overline{R}_j\right) D\left(k,\overline{R}_j\right) S^2(k) \exp\left[2ikR + i\psi_j\left(k,\overline{R}_j\right)\right]\right\} \tag{156}$$

Moreover, one can take full advantage of the normalization conditions:

$$(\mathbf{W},\mathbf{g}) = \frac{4\pi}{V}\sum_j w_j \int_0^\infty g_j(R)\, R^2 dR = 1 \tag{157}$$

with implicitly:

$$\sum_j (\mathbf{W}_j, g_j) = \sum_j w_j = 1 \tag{158}$$

In the late sixties, Tikhonov and numerous Russian mathematicians have introduced powerful *regularization algorithms* which reduce considerably the effects of numerical instabilities in "*inverse problems*".[231] Regularized EXAFS analyses were first pioneered by Babanov *et al.*[232–235] who proposed to minimize an error function fcn of the type:

$$\begin{aligned} fcn(\mathbf{g},\alpha,\beta,\gamma) \;=\; & \|\chi - (\mathbf{K},\mathbf{g})\|^2 + \alpha \left\| \left[\int_0^\infty |\mathbf{g}(R)|^2\, dR\right]^{1/2} - \mathbf{g}^{tr}(R) \right\|^2 \\ & + \beta \int_0^\infty \left| \frac{d}{dR}\left[\mathbf{g}(R) - \mathbf{g}^{tr}(R)\right] \right| dR \;\; + \gamma\, |(\mathbf{W},\mathbf{g}) - 1|^2 \end{aligned} \tag{159}$$

where α is the Tikhonov regularization parameter that imposes a penalty function to spurious solutions, β is a parameter which penalizes $g(R)$ solutions *which*

are not smooth and γ is a parameter restraining $g(R)$ to *positive* functions satisfying the normalization condition discussed above. Note that the regularization parameters α, β, γ are all positive and should, in principle, be very small if high quality data are available. In the above equation, $g^{tr}(R)$ may be either zero or some trial solution taking into account (unfortunately in a rather subjective way...) any additional *a priori* information regarding the system under investigation. There are three major steps towards a numerical solution of this problem:

- One has first to reformulate the error function using *discrete* variables: $\{R_m\}_{m=1}^{m=M}$ and $\{k_n\}_{n=1}^{n=N}$. Thus, the function to be minimized can be rewritten:

$$\sum_{n=1}^{N}\left\|\sum_{m=1}^{M}\sum_{j}\mathcal{A}_{n,mj}\mathcal{G}_{mj}-\mathcal{X}_n\right\|^2+\sum_{m=1}^{M}\sum_{j}\alpha_{mj}\left\|\mathcal{G}_{mj}-\mathcal{G}_{mj}^{tr}\right\|^2$$
$$+\sum_{m=1}^{M}\sum_{j}\beta_{mj}\left\|\frac{d}{dR}\left[\mathcal{G}_{mj}-\mathcal{G}_{mj}^{tr}\right]\right\|^2+\kappa_{mj}\left|(\mathcal{W}_{mj},\mathcal{G}_{mj})-w_j\right|^2 \tag{160}$$

  where $\mathcal{X}_n$ is a vector of dimension N, whereas $\mathcal{G}_{mj}$ and $\mathcal{W}_{mj}$ are vectors of dimensions $M \times j$. Similarly, matrix $\mathcal{A}_{n,mj}$ refers to the elements:

$$\mathcal{A}_{n,mj}=\int_{R_{m-1}}^{R_m}K_j\left(k_n,R\right)dR \tag{161}$$

- Next, it can be shown that the vector $\mathcal{G}_{mj}$ which minimizes the latter function is implicitly solution of a set of *linear equations*:

$$\left[\sum_{n+1}\mathcal{A}_{n,mj}^{t}\mathcal{A}_{n,mj}+\alpha\tau\mathcal{I}+\beta\mathcal{B}\right]\mathcal{G}_{mj}=\sum_{n}\mathcal{A}_{n,mj}^{t}\mathcal{X}_n \tag{162}$$

  where $\mathcal{I}$ is the unit matrix and $\mathcal{B}$ is a tridiagonal matrix of the type:[233]

$$\mathcal{B}=\begin{bmatrix}2\eta & -\eta & 0 & \ldots & 0\\ -\eta & 2\eta & -\eta & \ldots & 0\\ 0 & -\eta & 2\eta & \ldots & 0\\ \ldots & \ldots & \ldots & 2\eta & \ldots\\ 0 & 0 & 0 & \ldots & 2\eta\end{bmatrix} \tag{163}$$

  with: $\tau = \Delta R.\left[\Delta k\right]^{-1}$; $\eta = \left[\Delta R.\Delta k\right]^{-1}$. According to common notations, $\mathcal{A}_{n,mj}^{t}$ denotes the *transposed* matrix of $\mathcal{A}_{n,mj}$. In the left handside, the dimension is $n+1$ because the final result can be written in a more compact form if one defines the additional matrix element:[235]

$$\mathcal{A}_{n+1,mj}=W_{mj}\left[\frac{\gamma_{mj}}{\Delta k}\right]^{1/2} \tag{164}$$

  Anyhow, what is most important is that one is left with the resolution of a *linear* problem just as in the MEM approach described in the previous section although the philosophy is quite different.

- Finally, convergence to the *true* solution $\mathcal{G}_{mj}(\alpha,\beta,\gamma)$ of the inverse problem can be obtained only for an *optimal choice* of regularization parameters. How to choose the optimal parameters in dependence of the noise level is still a matter of debate between mathematicians.[236] The earlier approaches were based on "*a-posteriori-criteria*", *i.e.* on the minimization of the residual norms:

$$\|\chi - \mathbf{Ag}(\alpha,\beta,\gamma)\|^2 = \sigma^2_{noise} \quad (\textit{Morozov's discrepancy principle})$$

$$\|\chi - \mathbf{Ag}(\alpha,\beta,\gamma)\|^2 = \sigma^2_{noise}\alpha^{-1} \quad (\textit{Arcangeli's method})$$

A refined solution may also be obtained by a so-called *iterated* regularization procedure where the solution at order $\nu+1$ is given by:[235]

$$\left[\mathcal{A}^t\mathcal{A} + \alpha\tau\mathcal{I} + \beta\mathcal{B}\right]\mathcal{G}^{\nu+1}_{mj} = \left[\mathcal{A}^t_{n,mj}\mathcal{X}_n + \alpha_{mj}\mathcal{G}^{\nu}_{mj} + \kappa_{mj}\mathcal{W}^t_{mj}\right] \qquad (165)$$

As reported by Ageev *et al.*,[234] typical values found for the regularization parameters of EXAFS data were: $\alpha = 10^{-7}; \beta = 5.10^{-7}$ and $\gamma = 0.1$, convergence being assumed for $\nu = 3$. With third generation synchrotron radiation sources, the quality of the data should allow us to decrease α and β down to 10^{-10} and the regularization method should then converge without ambiguity towards the *true* radial distribution functions, especially for amorphous quasi-binary systems mixing high-Z and low-Z elements.

Although the regularization method was introduced in the early eighties, it has scarcely been used in western countries[237,238] mainly because the corresponding codes were not easily available and also because the calculations are time-consuming compared to the MEM approach which was described in the previous section. It has, however, the key advantage over the MEM approach that:

- it is *a priori* consistent with the presence of scattering atoms *of different nature* as underlined by Naumochkin and Kochubei[239] but only a discrimination between low Z *versus* high Z scatterers is realistic;
- the inclusion of spherical-wave effects is straightforward.

In its present version, the method cannot account for multiple scattering effects. Forgetting about the classical definition of $g_j(R)$, one might envisage to calculate a *scattering path distribution function* that would not be consistent anymore with the normalization condition clarified by equations (156): this implies that the algorithm should be deeply modified. As shown by Crozier,[237] the method apparently converges to a solution very similar to the FT optical spectrum if no normalization constraint is used ($\gamma \to 0$): this points up the advantage of constraining the inverse problem. There should be interesting perspectives regarding specific applications of the regularization method in porphyrin chemistry because one could fully exploit additional *structural* constraints.

5. Non-Linear Curve Fitting

Non-linear curve fitting techniques are most widely used to refine the EXAFS analyses. Looking at several papers published in high standard journals, it is, however, quite unfortunate that a number of basic criteria are ignored which are essential to make the conclusions fully reliable.

R-space Fourier Filtering: Since the pioneering work of Kincaid *et al.*,[240] it has been a common practice to filter out selected portions of the Fourier Transformed spectrum $\widetilde{\chi}_j(R)$, *e.g.* using a smooth Kaiser-Bessel filter function $KB(R).\widetilde{\chi}_j(R)$. It should be appreciated here that it is a major advantage of using *corrected* FT optical spectra as defined by equation (143): since corrected FT spectra do not suffer from the non-linearity of the phase-shift function $\psi_j(k)$, most of the structural information is really concentrated in the central peak and the truncation imposed by the filter is much less dramatic than in the case of *uncorrected* FT spectra which usually exhibit long tails on the low energy side of the peaks. The filtered spectra are next Fourier Transformed back into the momentum space. It is indeed mandatory to restore "*uncorrected spectra*" in the momentum space by removing all corrective factors introduced in equation (143):

$$\widetilde{KB}(k) * \chi(k) = \frac{F_j\left(k,\overline{R}_j\right) D^{\ell}\left(\overline{R}_j,\Gamma_t;k\right) S^2(k)}{k\overline{R}_j^{2n} \exp\left[2\sigma_j^2 k^2 - i\psi_j(k)\right]} \left[W(k)\right]^{-1} FT^{-1}\left\{KB.\widetilde{\chi}_j(R)\right\} \tag{166}$$

One should be aware that the Fourier Filtering technique is modifying the noise distribution and typically removes all high frequency noise. Even though the filtered data *may look completely free of noise*, in reality, noise is still there because the noise spectrum is (at best...) uniform. A now well established practice consists in sampling the high frequency noise, *e.g.* for 15Å $\leq R \leq$ 25Å where no EXAFS signature is expected to survive to the Debye-Waller damping, and then, assuming that this measured noise has a uniform distribution, one may transform its power spectrum back into the momentum space in order to obtain its autocorrelation function and its variance σ^2_{noise}: as discussed below, the derivation of the latter parameter σ^2_{noise} is important for assessing the reliability of a fit.

The parametrized EXAFS equations (60) and (61) can now be used to refine the scattering path length $\overline{R}_j$, the number density $\overline{N}_j$ of atoms in shell j, and the second moment σ_j^2 that characterizes the structural disorder of this shell. Unfortunately, there are many more *hidden* parameters:

- The scattering amplitudes $F_j\left(k,\overline{R}_j\right)$ and the phase-shifts $\psi_j\left(k,\overline{R}_j\right)$ are most often calculated from *ab initio* methods which have their own *degrees of freedom*: *e.g.* the choice of the muffin-tin radii, the choice between overlapping or non-overlapping spheres, the choice of the density functionals for the exchange-correlation energy and for the self-energy etc... Moreover, the calculated functions $F_j\left(k,\overline{R}_j\right)$ and $\psi_j\left(k,\overline{R}_j\right)$ are not the *true* functions and, for each data point in the momentum space, one has to admit the reality of systematic errors $\epsilon_F(k)$ and $\epsilon_\psi(k)$ which are quite tedious to estimate.

- The evaluation of $F_j\left(k,\overline{R}_j\right)$ and $\psi_j\left(k,\overline{R}_j\right)$ is getting questionable in the case of multiple scattering paths since we need to know the whole stereo-geometry of the cluster. Furthermore, as discussed in section II.B.4, the calculation of the configuration average also requires a detailed knowledge of the vibrational density of states or, at least, a detailed identification of the relevant normal modes.

- The correlation function $S^2(k)$ and the damping function $D^\ell(\overline{R}_j, \Gamma_t; k)$ suffer from the additional penalty that they are semi-empirical and certainly oversimplify the reality: this again increases the level of systematic errors through $\epsilon_{S^2}(k)$ and $\epsilon_D(k)$.

- The distribution of the interatomic distances R_j may not be Gaussian with the consequence that higher order moments than σ_j^2 may be needed to describe the system.

There is a price to be paid for freezing such hidden parameters even though this is never discussed in quoting error bars. Anyhow, since parameters like $\overline{R}_j$ or the second moments σ_j^2 have not a linear dependence, one has to resort to iterative fitting algorithms to minimize a "χ-square" error function (or a negative Log likelihood function) denoted hereafter $fcn(a_p)$ where a_p is a set of p parameters which have to be adjusted by fitting.

Fitting Software Packages : One of the authors (JG) has intensively used since 1976 the powerful and versatile minimization package *MINUIT* from CERN.[241] Basically, *MINUIT* combines the robust *SIMPLEX* algorithm with fast converging conjugated gradient techniques. Error analyses (*MINOS* option) are included assuming that the function $fcn(a_p)$ has a proper statistical meaning. The covariance (Hessian) matrix is available on printing request. *MINUIT* also offers the useful option (*CONTOUR* option) to map in two dimensions the lines of constant fcn values. Reasonably good results were also obtained with the *STEPT* package from the Quantum Chemistry Program Exchange (QCPE) library.[242] For well conditioned problems, convergence can be reached very fast using the Levenberg-Marquardt algorithm that exploits not only the gradient but also second derivatives with respect to the fitted parameters. In practice, *convergence speed is scarcely the key issue in EXAFS*: what is more important is that, in the iteration process, *MINUIT* offers the capability to *constrain* a given parameter in a selected range of physically relevant values. It is also a useful test to check whether or not different codes converge towards the same "*local minimum*" of fcn even though it cannot be taken for granted that this will be the "*true*" global minimum. If the fitting problem is not well conditioned, convergence may be obtained for various shallow local minima (or fine structures of the function fcn) and it is well known that the result may change for a different set of initial guesses a_p^0. In order to avoid that situation, it is mandatory to *minimize the correlations* between the parameters to be adjusted and to reduce the noise level.

Number of Shells to be Fitted : A fundamental question in fitting EXAFS spectra in the momentum space is to examine the physical significance of adding the new scattering shell $(j+1)$ to the previous j shells. Generating a better fit with too many parameters will be delusive because information will be lost in *correlations*. The natural attitude is to try to justify the addition of a new shell with statistical criteria. The first progress in this direction is to be credited to Joyner *et al.*[243] who proposed a so-called F-test, although they noted that such a test is rigorously applicable only to a *linear* fitting problem which is obviously not the case here. We propose below a slightly modified formulation of this test.

Errors estimations are most often based on the following formula :

$$\epsilon_\nu^2(j) = \frac{1}{\nu(j)} \frac{\sum_i w_i \left[\chi_i^{dat} - \chi_i^{the}(j)\right]^2}{\sum_i w_i \sigma_i^2} \tag{167}$$

where w_i is some appropriate weighting function of the data point χ_i^{dat} indexed i, χ_i^{the} is the corresponding modellized signal and σ_i^2 is the standard deviation of each data point due to statistical noise. It has already been suggested that σ_i^2 could be identified with σ_{noise}^2. Here ν is defined as:

$$\nu(j) = \frac{N^f - N^p(j) - 1}{N^f} > 0 \tag{168}$$

where N^f is the number of degrees of freedom of the system, *e.g.* the number of independent variables for a given data sampling, and $N^p(j)$ is the total number of adjusted parameters for j scattering shells. The difficulty is to define N^f. Information theory teaches us that, according to Brillouin:[244,245]

$$N^f = \frac{2}{\pi} \Delta R . \Delta k \tag{169}$$

$\Delta k = k_{\max} - k_{\min}$ is the length of the data set and ΔR is the corresponding filter bandwidth. If $\Delta R \simeq 1\text{Å}$ and $\Delta k \simeq 12\text{Å}^{-1}$, one obtains $N_{\max}^p = 6$ which immediately shows that how delusive it is to fit *more* than $j = 2$ shells with such a filtered signal since at least 3 parameters are required to define a single scattering shell. Equation (169) also clearly points out the futility of trying to fit filtered data with overcomplicated models when *shadowing* or multiple scattering paths are involved. It does not mean yet, unfortunately, that fitting the EXAFS signal with two shells is really sound. Ideally, $N^p(j)$ should include *all hidden* parameters discussed above and which are *arbitrarily* frozen. It has to be realized, for instance, that fitting a signal with two shells of *different* nature (*e.g.* $Fe...N_{eq} + Fe...S_{ax}$) or identical nature (*e.g.* $Fe...N_{eq} + Fe...N_{ax}$) should not cost the same price in numbers of degrees of freedom because one needs to introduce additional phase-shifts and amplitude parameters whenever the two shells are not identical. In practice, several parameters have anyhow to be frozen and the mathematical problem becomes that of *minimizing a constrained function*, with the practical consequence that all usual statistical tests become empirical. A simple *trick* is to forget about the frozen parameters in the calculation of $\nu(j)$ but, in compensation, to add to the statistical error σ_i^2 a *non-statistical term* $\sigma_i'^2$ accounting for the fact that a frozen parameter is assigned an approximate (incorrect) value. Anyone who will play scrupulously this game with EXAFS spectra will get depressed when he (she) will discover that $\sigma_i'^2$ is increasing faster than the statistical term. A more rigorous theory of the minimization of constrained functions is based on Lagrange multipliers (as illustrated in the previous section or in general applications of Maximum Entropy Methods) but the existence of the Lagrange multipliers is also subject to *constraint qualification tests* which are quite complicate and will not be discussed here.

In absence of any better option, it may be helpful to extend the significance test proposed by Joyner *et al.*[243] as:

$$\frac{\left[\nu\epsilon^2\right]^{(j+1)} - \left[\nu\epsilon^2\right]^{(j)}}{\left[\nu\epsilon^2\right]^{(j+1)}} > d \times \Delta N_j \times F(c, d, \Delta N_j)$$

where: $d = \nu\,(j+1)\,N^I$; ΔN_j is the number of parameters required to add a new shell; $F\,(c, d, \Delta N_j)$ are tabulated values of the statistical F-function for a significance criterion c. As compared to the original formulation by Joyner *et al.*,[243] we have simply replaced in the definition of d the total number of data points $NPTS$ by the number of independent degrees of freedom of the problem N^I in order to be more consistent with the previous discussion.

Recently, the concept of *multiple-edge fits* has been introduced as a practical way to increase the number of independent data points. This option is implemented as a standard feature of the computing code GNXAS. For example, this option makes it possible to fit simultaneously the correlated EXAFS spectra recorded at the L_{II}- and L_{III}-edges, a pre-requisite being to subtract the residual wiggles which are associated with the L_{III}-edge spectrum and contaminate the L_{II}-edge spectrum. One should never forget, however, that: (i) the noise level is fundamentally higher at the L_{II}-edge due to the larger background absorption; (ii) the number of *hidden* variables is doubled since the phase-shifts, the backscattering amplitudes and the definition of E_0 are fundamentally edge dependent. It is not completely clear that the gain in accuracy is so high as claimed by the promoters of this method.

Global Fitting, Global Mapping : In these recent years, the use of back-transformed Fourier Filtered data has been more and more criticized using the basic argument that statistical tests (which are essential in curve fitting techniques) require *independent data points*: this condition is not anymore satisfied whenever the data have been either "*smoothed* "or Fourier Filtered. This is why global fitting techniques (preferably including the atomic background!..) have more and more "*fans*", especially in U.K. Nevertheless, a practical limitation still arises from equation (169) which still holds true even though ΔR is increased by a factor of 10 or more. This calls still for a mandatory restriction of the number of adjustable parameters. Current strategies are listed below:

- One should analyze first the experimental spectra $\chi\,(k)$ of compounds for which the crystal structure is well known in order to adjust a variety of unknown parameters which are necessary to calculate the scattering amplitudes, the phase-shifts, the damping functions $D^{\ell}\left(\overline{R}_j, \Gamma_t; k\right)$ or $S^2\,(k)$. The corresponding parameters will then be kept frozen for the analysis of unknown compounds. Note that the level of information has been implicitly increased through the availability of the experimental spectra of model compounds of known structure.

- Parameters may be restricted by assuming that all atoms of similar type at similar distances have the same Debye-Waller factor and that the number densities $\overline{N}_j$ should be given *integer* values.

- Scattering paths which have a contribution lower than the statistical level may be neglected. The F-test discussed above can also be employed to discuss the statistical significance of an additional path.

- Groups of atoms comprising a well defined structural unit such as a pyrrole or an imidazole ring are refined *as a rigid unit* with a single distance coordinate and one or more angular parameters. Such a *group-constrained*

refinement technique (also referred to as *group fitting),* was first introduced by Hodgson *et al.*[246] in order to analyze the EXAFS spectra of biological samples. Simultaneously, it gives the means of including information extracted from other techniques such as X-ray diffraction. There are, however, several problems associated with this method:

(i) small but significant variations of the distances cannot be taken into account;

(ii) small angular changes can induce very significant changes in the amplitude of multiple scattering paths.

This led Binsted *et al.*[247] to introduce a *group-restrained* method in which small deviations from ideal distances are allowed and contribute to a modified error function $[fcn]_{Total}$:

$$[fcn]_{Total} = w_\chi [fcn\,(EXAFS)]_\chi + w_{Rg}\,[fcn]_{Rg} + w_{Ang}\;[fcn]_{Ang} \quad (170)$$

Here $[fcn]_{Rg}$ and $[fcn]_{Ang}$ are functions that are independent of the EXAFS data but compare the refined distances and the refined angles with "*ideal distances*" and "*ideal angles*" obtained from a crystal structure data base. Obviously, the parameters w_i are introduced to weight the relative significance of the contributions of the functions $[fcn]_{Rg}$ and $[fcn]_{Ang}$ with respect to the function $[fcn\,(EXAFS)]_\chi$ which compares the experimental EXAFS data with the simulated spectrum. Obviously, this method does not concur in this way to reduce the number of adjustable parameters which will remain most often strongly correlated but the choice is definitely made *to increase the number of constraints.*

- Whenever this is possible, one should try to *orthogonalize* the parameters to be fitted in order to minimize their correlations. For instance, this strategy is recommended if one wishes to include multiple scattering paths associated with a nearly colinear sequence of atoms A, B and C. Referring to equation (78), it has been pointed out by Filipponi [114] that the new variables $(R_1 \pm R_2)$ are usually only very weakly correlated and should be preferred to (R_1, R_2).

- Contour maps should be systematically used, as underlined by Joyner *et al.*,[243] in order to minimize the influence of the correlations between key parameters like R_j and E_{0j}. With the same concern, Chance *et al.*[248] are advocating what they call a "*global mapping* " of the error function with a fine 2-dimensional grid when the problem is to resolve two distances which are very close.

We like to point out that there is a possible alternative to Fourier Filtering: it consists in fitting simultaneously the data in *both* the momentum space and in the direct space with the important advantage that the information and the noise are not weighted in the same way in different spaces. Even with modern computers, this strategy remains very time-consuming but it stimulated Goulon and coworkers to elaborate the *Perturbed Difference* method which is described in section III.B and can be viewed as a specific alternative approach to the group fitting method discussed above.

Resolution limits : A perennial challenge for EXAFS is to resolve two distances $M(etal)...L\,(igand)_1$ and $M...L_2$ which are very close. Whenever two signals are not resolved in the FT spectrum, there is, *a priori*, very little hope to resolve them by *direct* curve-fitting in the momentum $k-$space especially if the spectra are truncated and do not permit to measure accurately the *beating half period* defined by the condition:

$$2k\Delta R + \Delta\psi\,(k) = n\pi \tag{171}$$

Thus, if the two scatterers are identical $\Delta\psi \equiv 0$, the condition for observing the first beating is $k_{\max} \geq \pi/2\Delta R$. Conversely, the best resolution being given by: $\Delta R_{\min} = \pi/2k_{\max}$, one will easily check that the prerequisite to decrease $\Delta R_{\min}$ down to 0.1 Å is to ensure that $k_{\max} \geq 16\text{Å}^{-1}$. In practice, the ultimate resolution will clearly depend upon the accuracy with which the beating minimum can be localized and typical resolution limits of $\Delta R_{\min} \simeq 0.15$-$0.20$ Å are probably more realistic. The situation is much worse for scatterers of different nature since $\Delta\psi \neq 0$. This is why considerable efforts are made at third generation synchrotron radiation source facilities in order to push $k_{\max}$ beyond 20-25 Å^{-1}. Even with the state-of-the-art instrumentation, this may turn out to be impossible in a number of cases. For instance, the sample may contain trace amounts of elements which have an absorption edge in the energy range over which the EXAFS signal is measured: then *any* analysis (in the R-space or in the momentum space) will be spoiled by the contaminating edge signal which is usually more intense that the weak, heavily damped EXAFS oscillations which one would like to extract from noise.

Below the ultimate resolution limit $\Delta R_{\min}$, one is left with the possibility to perform a single shell fit but with a *structural disorder* characterized by successive moments:

$$\overline{N}_j\sigma_s^{(n)} = \sum_i N_i\left(R_i - \overline{R}_j\right)^n \tag{172}$$

One may, for instance, use the approximate formulation:

$$\begin{aligned}\chi_j^{\ell}(k) \;=\; & \overline{N}_j\left|A_{(2)}^{\ell}\left(k,\overline{R}_j\right)\right| D_{(2)}^{\ell}\left(\overline{R}_j,\Gamma_t;k\right) S^2(k)\exp\left[-2\sigma_i^2k^2\right] \\ & \times\left[A_s - iB_s\right]\mathrm{Im}\left\{\exp i\left[2k\overline{R}_j + \psi_j\left(k,\overline{R}_j\right)\right]\right\}\end{aligned} \tag{173}$$

where:

$$A_s \simeq 1 + \frac{3\sigma_s^{(2)}}{\overline{R}_j^2} - 2k^2\sigma_s^{(2)} + \frac{4\sigma_s^{(3)}}{\overline{R}_j^3} + \frac{4\sigma_s^{(3)}k^2}{\overline{R}_j} + ...$$

$$B_s \simeq \frac{4k\sigma_s^{(2)}}{\overline{R}_j}\left[1 - \frac{3\sigma_s^{(3)}}{2\sigma_s^{(2)}\overline{R}_j}\right] + \frac{4}{3}\sigma_s^{(3)}k^3 + ...$$

Notice that the phase correction due to a spread in distances is of the order of $\sigma_s^{(3)}k^3$ and so, for data collected over a limited range in k, a small distribution σ_s produces only a very small effect on the phase.

6. Phase-Shifts and Scattering Amplitudes

It has hitherto been implicitly assumed that scattering amplitudes $F_j\left(k,\overline{R}_j\right)$ and phase-shifts $\psi_j\left(k,\overline{R}_j\right)$ were obtained by running codes like FEFFx, MSXAS / GNXAS or EXCURVE9x. As discussed in section II, there is a continuous refinement of *ab initio* methods which grows obsolete to use tabulated phase-shifts such as those compiled by Teo and Lee[249,250] or by McKale *et al.*[251] which were widely used in the eighties. Initially, we thought that the superiority of FEFF, MSXAS or EXCURVE would rest essentially on the possibility to take into account spherical wave corrections and to include multiple scattering paths. Vaarkamp *et al.*[252] have compared several theoretical standards and went to the conclusion that, even for single scattering paths, the quality of the experimental EXAFS spectra is getting high enough to discriminate between different types of potentials. The number density of scattering atoms predicted with FEFF6 is significantly improved with respect to previous methods exploiting Teo and Lee tables which were known to be incorrect.[253]

We wish to draw attention, however, onto some difficulties which are ignored by those who trust too much theoretical calculations: the muffin-tin discontinuities can cause very weak but still undesirable low frequency oscillations of the calculated functions $F_j\left(k,\overline{R}_j\right)$ and $\psi_j\left(k,\overline{R}_j\right)$. Indeed such oscillations do not exist in the experimental data and their artifactual nature become sensible when the calculated functions $F_j\left(k,\overline{R}_j\right)$ and $\psi_j\left(k,\overline{R}_j\right)$ are tentatively used to display *corrected FT spectra* as discussed in section III.A.2: instead of obtaining clean peaks, one may detect unphysical side lobes which do not exist either in simulated FT spectra or in spectra corrected with parametrized amplitude & phase-shifts.[249] This seems to be most sensible in organometallic chemistry when the scattering atoms are low-Z elements with a weak scattering amplitude: a first illustration of this difficulty was reported Ruiz *et al.*[254] who investigated the weak multiple scattering signatures of ferrocene. Similar effects were observed with various metalloporphyrins and imidazole complexes for which MSXAS was used to generate $F_j\left(k,\overline{R}_j\right)$ and $\psi_j\left(k,\overline{R}_j\right)$. One way to get rid of these undesirable effects is to resort to numerical filtering techniques. Of course, "*normal*" FT spectra, *i.e. uncorrected* FT spectra, are inherently insensitive to this problem. Weak low frequency oscillations of the calculated functions $F_j\left(k,\overline{R}_j\right)$ and $\psi_j\left(k,\overline{R}_j\right)$ may not affect substantially the results of the curve fitting technique but one should be aware that they would contribute to increase the level of undesirable correlation between the parameters of different shells.

B. Difference EXAFS Analyses

1. Ill-Conditioned Problems

In practice, one is quite often facing complex structural problems where standard analyses fail to give the desired information. This may happen:

- *Whenever* destructive interferences develop between two scattering paths featuring nearly the same length but opposed phase-shifts: the practical consequence is a loss of information with the net result that fitting techniques become ill-conditioned and unstable.

- *Whenever* the radial distributions associated with *two different ligands* exhibit a strong overlap, *e.g.* for the coordination shell. Porphyrin chemistry offers a great deal of illustrations of that particular situation because the axial $M\,(etal)...N_{ax}$,O_{ax} bond lengths can hardly be very different from the equatorial $M...N_{eq}$ interatomic distances. In the previous sections, we strongly insisted that there was very little, or even no hope to resolve such close lying signals using standard analyses.
- *Whenever* the system under investigation is evolving with time so that a fraction of the initial compound is still coexisting with reacted species. Due to the lack of site selectivity of EXAFS, there is again no hope to resolve the contributions of each species.

Such ill-conditioned problems clearly suffer from a degeneracy of the structural information which can be partly lifted by *difference analyses.* To begin with a simple example, we have reproduced in **Figure 10A** the FT spectra of (OEP)VO and (OEP)VS, *i.e.* the oxo- and the thio-vanadyl-2,3,7,8,12,13,17,18-octaethylporphyrinato complexes considered in references[255–257]. Recall that the corresponding EXAFS spectra were recorded at a *first generation* Synchrotron Radiation source and neither the quality nor the resolution of the FT-spectra are as good as for the FT spectrum of (OEP)VO displayed in **Figure 7.** Nevertheless, the signatures of the carbons of the macrocycle, *i.e.* $8C_{\alpha}$, $4C_{meso}$, $8C_{\beta}$, can still be easily identified and look perfectly superimposed for the two compounds. Quite contrarily, there is a dramatic distortion of the signal of the four nitrogen atoms of (OEP)VS . The latter distortion was explained by a *destructive interference* of the EXAFS oscillations of the $V...N$ and $V...S$ shells which are nearly equidistant while the phase-shifts of nitrogen and sulfur differ by *ca.* π. This interpretation can be supported by Fourier Transforming the *difference spectrum*: $\Delta\chi\,(k)\{$(OEP)VS-(OEP)VO$\}$. As illustrated by **Figure 10B** which reproduces the difference spectrum $\Delta\widetilde{\chi}_j\,(R)$, the characteristic signatures of a porphyrin macrocyle, *i.e.* $8C_{\alpha}, 4C_{meso}$, $8C_{\beta}$, cancel out in a first approximation and one is left with the differential contribution of the axial ligands: $(V...S) - (V...O)$. Note that the spectrum exhibits two *negative* peaks at distances which match approximately the expected bond lengths for $V = O$ and $V = S$. The negative sign of *both* signatures is indeed fully consistent with the interpretation that the phase-shifts of nitrogen and sulfur differ by *ca* π. A refinement of the corresponding bond lengths by curve fitting in the momentum space led to the refined results: $R\,(V...S) = 2.06 \pm 0.02$ Å and $R\,(V...O) = 1.62 \pm 0.02$ Å in good agreement with the crystal structure data of relevant compounds.[257]

2. Difference Analyses with Structural Perturbation

Direct difference analyses of EXAFS spectra were first performed by Cramer *et al.*[258] who tried to detect the contribution of the unbound oxygen in the oxy-picket fence model of oxyhemoglobin by comparing the spectra of the oxy- and deoxy- complexes. Cramer *et al.* perfectly identified the fatal limitation of *direct* differences: if the axial displacement of the metal is neglected, it becomes impossible to achieve a perfect cancellation of the signatures of the porphyrin macrocycle and misleading residual signatures are generated. These difficulties can be circumvented if the FT spectrum $\widetilde{\chi}_j\,(R)$ of the reference compound

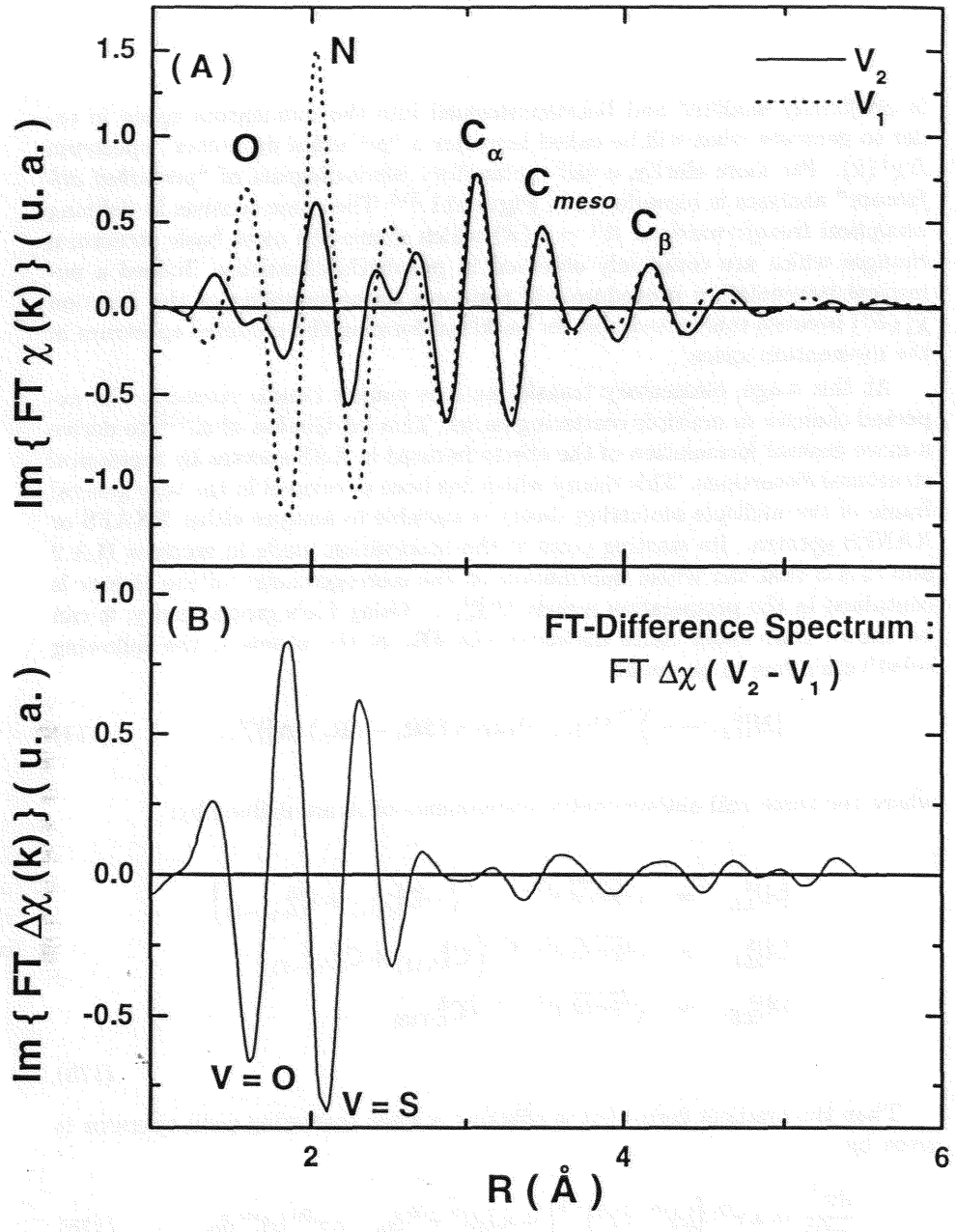

Figures 10:

Figure 10A: FT optical spectra Im [$\tilde{\chi}_1(R)$] of the V_1 = (OEP)VO *(dotted line)* and V_2 = (OEP)VS *(full line). Note the strong distortion of the V...N signal in the spectrum of V_2 as compared to V_1.*

Figure 10B: FT optical spectrum Im [$\Delta\tilde{\chi}_1(R)$] of the difference signal:

$\Delta\chi(k) = \chi_{V_2}(k) - \chi_{V_1}(k)$. *Note the inverted phase of sulfur explaining the destructive interference observed in Figure 10A.*

is *artificially modified* and backtransformed into the momentum space in order to generate what will be called hereafter a "*perturbed difference*" spectrum $\Delta\chi^{\dagger}(k)$. For more clarity, a self explanatory block-diagram of "*perturbed difference*" analyses is reproduced in **Figure11**.[253] The game consists in defining *analytical transformations* $R'^{\dagger} = f(R)$ which mimic the most basic structural changes which are commonly observed in porphyrin chemistry. Indeed a numerical interpolation procedure will restore a linear sampling of the function $\widetilde{\chi}_j^{\dagger}(R')$ because this is desirable for backtransforming the modified spectrum in the momentum space.

At this stage, elementary transformations cannot handle correctly the expected changes in multiple scattering paths. This led Goulon *et al.*[259] to derive a more general formulation of the effects induced in XAS spectra by *topological* structural distortions. This theory which has been developed in the very general frame of the multiple scattering theory is suitable to analyze either EXAFS or XANES spectra. Its starting point is the observation made in sections II.A.2 and II.A.3 that the whole information on the stereogeometry of the cluster is contained in the propagation matrix $[H]^{ij}_{LL'}$. Using Lie's group theory, it can be shown that under finite displacements $\delta\mathbf{R}_i$ of the atoms i, the following substitution has to be made:

$$[H]^{ij}_{LL'} \longrightarrow \sum_{L''} [H]^{ij}_{LL''} \left\{\exp\left[\kappa\left(\delta\mathbf{R}_i - \delta\mathbf{R}_j\right).\mathbf{A}\right]\right\}^{ij}_{L''L'} \tag{174}$$

where the three real antisymmetric components of $\mathbf{A}$ are defined by:

$$\begin{aligned}
[A]^{x}_{LL'} &= \sqrt{2\pi/3}\; i^{(\ell-\ell'+1)} \left\{-\mathbb{C}^{L}_{L'(11)} + \mathbb{C}^{L}_{L'(1-1)}\right\} \\
[A]^{y}_{LL'} &= \sqrt{2\pi/3}\; i^{(\ell-\ell')} \left\{\mathbb{C}^{L}_{L'(11)} + \mathbb{C}^{L}_{L'(1-1)}\right\} \\
[A]^{z}_{LL'} &= \sqrt{2\pi/3}\; i^{(\ell-\ell'+1)} \mathbb{C}^{L}_{L'(10)}
\end{aligned} \tag{175}$$

Then the gradient term that is affecting a given scattering path operator is given by:

$$\frac{d\boldsymbol{\tau}^{00}}{dR_i^{\alpha}} = \kappa\boldsymbol{\tau}^{0i}\left[[A]^{\alpha}, \left[T^i\right]^{-1}\right] + \kappa\,[A]^{\alpha}\,\boldsymbol{\tau}^{00}\delta_{0i} - \kappa\boldsymbol{\tau}^{00}\,[A]^{\alpha}\,\delta_{0i} \tag{176}$$

with $\alpha = x, y, z$. This provides us with firm theoretical bases for a generalization of the concept of "*perturbation*" in the momentum k-space. Unfortunately, there is still no code yet available to fully exploit this approach. Moreover, preliminary tests carried out by Loos[207] have indicated that higher order corrections than the gradient would be needed to reproduce the measured changes with an accuracy of 0.01Å. It may then be faster to calculate the perturbation $\Delta\boldsymbol{\tau}_{(n)}$ from the basic definition: $\Delta\boldsymbol{\tau}_{(n)} = \left[\boldsymbol{\tau}^{00}\right]^{\dagger}_{(n)} - \left[\boldsymbol{\tau}^{00}\right]_{(n)}$ where $\left[\boldsymbol{\tau}^{00}\right]^{\dagger}_{(n)}$ would refer to a "*perturbed cluster*". This practical consideration is not modifying the basic philosophy of the method.

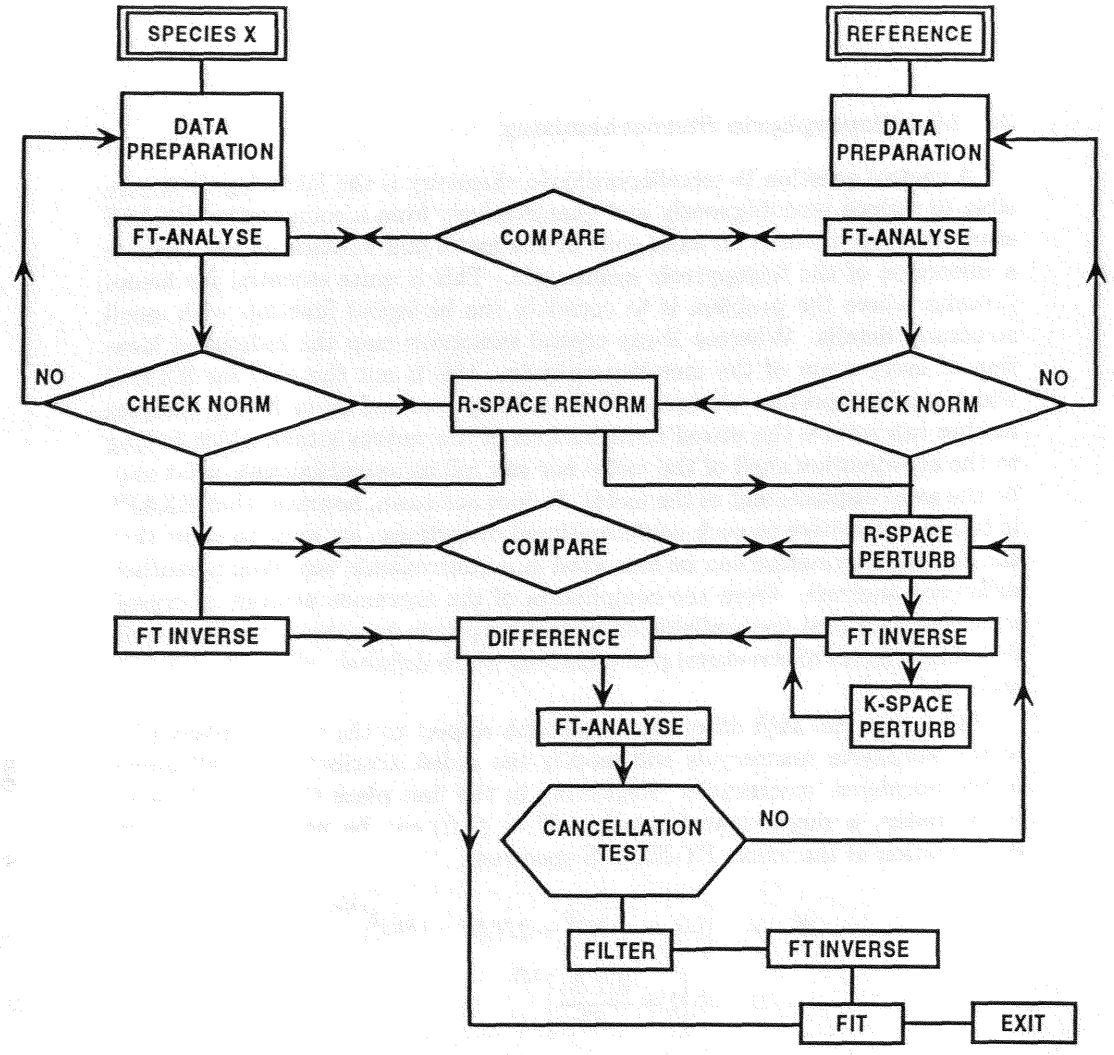

Figure 11: Block-diagram introducing the concept of *Perturbed Difference* analyse

3. Metalloporphyrin Stereochemistry

A central question in metalloporphyrin chemistry is the following: is it possible to deduce unambiguously and quantitatively from a comparative EXAFS study whether there is an axial shift of the metal and whether or not there is a distortion of the tetrapyrrole macrocycle. This is quite essential for hemoproteins where the problem is to correlate the biological function with small structural details. Whereas X-ray crystal structures map the individual location of every atom of the metalloporphyrin, this is not the case for EXAFS which is a local probe technique. FT-EXAFS spectra and curve fitting analyses neither can resolve the mixed contributions of the various atoms which belong to the coordination shell of the metal nor can tell us *unambiguously* what may be the axial displacement of the metal. It does not mean, however, that EXAFS is totally insensitive to such conformational distortions: we want to show that the desired information can be extracted in a quite reliable way from perturbed difference analyses. From the compilation of the enormous amount of crystal structure data that are available on metalloporphyrin complexes, we have codified three classes of structural perturbations which definitely affect the EXAFS spectra:

(1): *An axial shift* δh of the metal with respect to the average plane (P_c) of the porphyrin macrocycle will modify the radial distribution of *all* atoms of the porphyrin macrocycle. Neglecting in the first place the multiple scattering paths, a simple transformation $R' = f(R)$ can be used to model the perturbation of the whole FT-EXAFS spectrum:

$$\begin{aligned} R' &= \left[(R_{CT}+H)^2 + 2H.\delta h + (\delta h)^2\right]^{1/2} \\ &\simeq R\left[1+\frac{2H.\delta h}{R^2}\right]^{1/2} \end{aligned} \tag{177}$$

where H is the absolute value of the axial displacement of the metal *in the reference compound* whereas R_{CT} would be the radial distribution of the atoms of the porphyrin if the center of the macrocyclic cavity is selected as origin of the coordinate system. If H is known from the crystal structure of the reference compound, then careful difference EXAFS studies should allow us to determine δh for the compound of interest.

(2): *An apparent variation of the macrocyclic cavity radius* Δ_{cav} is usually associated with *ruffled* conformations of the porphyrin macrocycle. As pointed out a long time ago by Hoard,[260] small amplitude rotations ϕ of the pyrrole subunits around the $M\,(etal)...N_{eq}$ axes are possible in accordance with the S_4 symmetry provided that the bond parameters are satisfying the condition:

$$a_N + b\cos\frac{\alpha}{2} - c\sin\psi = \left(b\sin\frac{\alpha}{2} + c\cos\psi\right)\cos\phi \tag{178}$$

The notations are clarified in **Figure 12A**. The adjustments in bond parameters are most often taken into account by the $M...N_{eq}$ bonds so that an *apparent* contraction (expansion) of the macrocyclic cavity radius is observed.

(A)

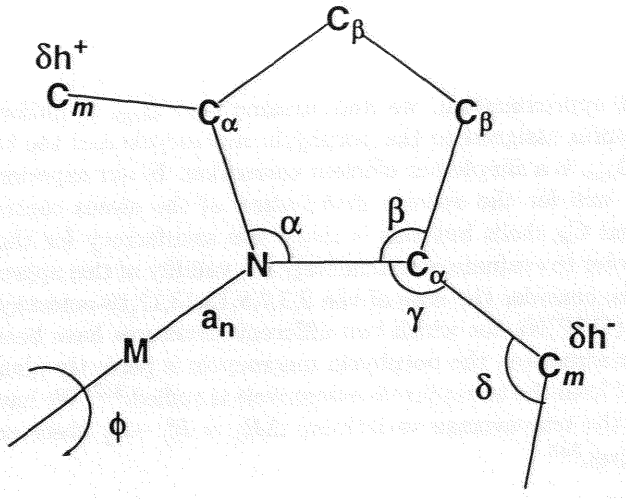

(B)

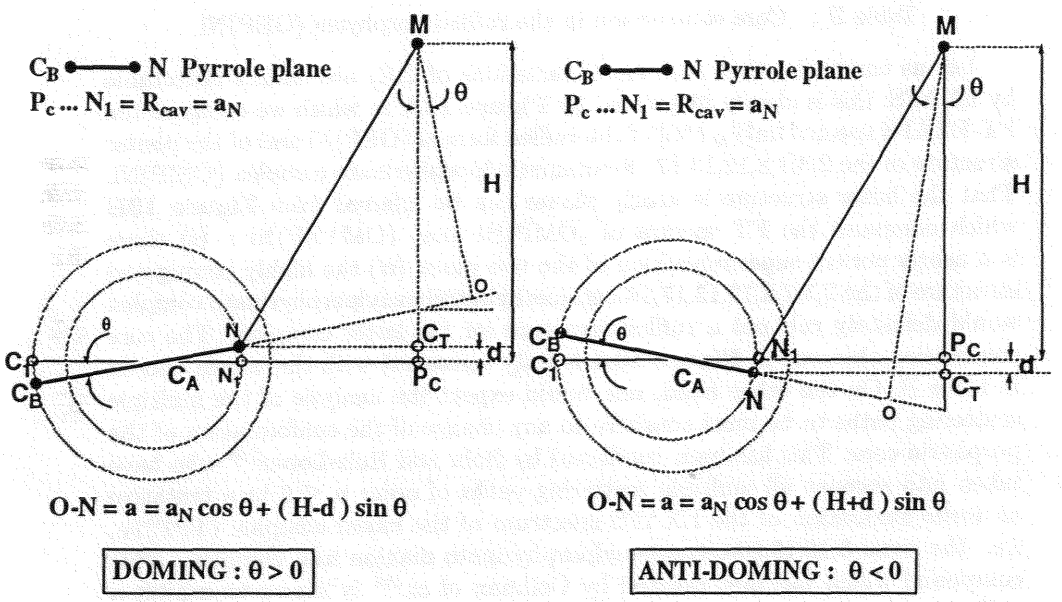

Figures 12: Geometrical distortions of the porphyrin macrocycle:

Figure 12A: Ruffled core distortion according to Hoard.

Figure 12B: Doming (A), *anti*doming (B) or saddle-shaped distortions ($A_{1,3}+B_{2,4}$)

In the first approximation, we may assume that Δ_{cav} is uniform for all EXAFS signatures assigned to the porphyrin macrocycle and the transformation: $R' = R + \Delta_{cav}$ is a simple but efficient correction. In our experience, this works reasonably well for the *average distribution* of the atoms contributing to the N_{eq}, C_α and C_β shells but this is much less satisfactory for the C_{meso} signatures. In order to evaluate quantitatively the validity of this approximation, it is attractive to consider the case of the 2,3,7,8,12,13,17,18-octaethylporphyrinato complexes (OEP)Ni for which two different structures have been reported: in the triclinic structure, the porphyrin macrocycle is perfectly planar[261] while in the trigonal form the tetrapyrrole macrocycle is ruffled.[262] We have summarized in table II the true average variations: $\Delta R_j = R'_j - R_j$ observed between the two structures:[253]

Shells j	$Ni...N_{eq}$	$Ni...C_\alpha$	$Ni...C_{meso}$	$Ni...C_\beta$
ΔR_j (Å)	0.026	0.024	0.0105	0.028

Table II : Core contraction in the ruffled porphyrin (OEP)Ni

Let us emphasize that such small variations of ΔR_j are readily detectable by EXAFS: this is clearly illustrated by **Figure 13A** in which we compare the FT-EXAFS spectra $\mathrm{Im}[\widetilde{\chi}_N(R)]$ of the ruffled form of (OEP)Ni and of the planar structure of the 2,3,7,8,12,13,17,18-octamethylporphyrinato complex (OMP)Ni. That the latter structure is nearly planar can be inferred from **Figure 13B** which compares the FT spectra of (OMP)Ni and (OMTBP)Ni : (*i*) there is a nearly perfect superimposition of the two plots; (*ii*) the highly conjugated structure of the 2,3,7,8,12,13,17,18-octamethyltetrabenzylporphyrinato complex would definitely rule out a ruffled structure for the latter complex. The core contraction observed in **Figure 13A** is fully consistent with the values quoted in table II. On the other hand, one would expect the analysis of the multiple scattering paths to be most sensitive to any change of the conformation of the porphyrin core. This has been confirmed by Bohr and Ruiz-Lopez[263] who have taken into account all multiple scattering paths of order $n \leq 6$ in a tentative *ab initio* simulation of the EXAFS spectrum of the naked complex (TPP)Fe, *i.e.* the *meso*-5,10,15,20-tetraphenylporphyrinato dianion iron complex. This compound which was first isolated by Collman *et al.*[264] is known to exhibit a ruffled macrocycle.

(3): *Doming, antidoming and saddle shaped conformations*[265] can be generated by tilting the pyrrole ring around axes which are perpendicular to the $Metal...N_{eq}$ bonds (**Figure 12B**). Such deformations are frequently observed in dodecasubstituted porphyrins.[266] Doming conformations of the porphyrin core make it possible to keep short $Metal...N_{eq}$ bond lengths while allowing a quite substantial displacement of the metal above the average plane of the porphyrin. The most convenient geometrical parameters that are needed to describe these conformations are: (*i*) the distance d separating the four N_{eq} plane from the mean plane of the porphyrin skeleton and (*ii*) the tilt angle ϑ (*See* **Figure 12B**). Then, the transformation that is relevant for the EXAFS spectrum is given by:

$$R' \simeq R\left[1 + \frac{(H'^2 - H^2)}{R^2} + 2\frac{(a'_N - a_N)}{R}\left(1 - \frac{H^2}{2R^2}\right) + \frac{(a'_N - a_N)^2}{R^2}\right]^{1/2} \quad (179)$$

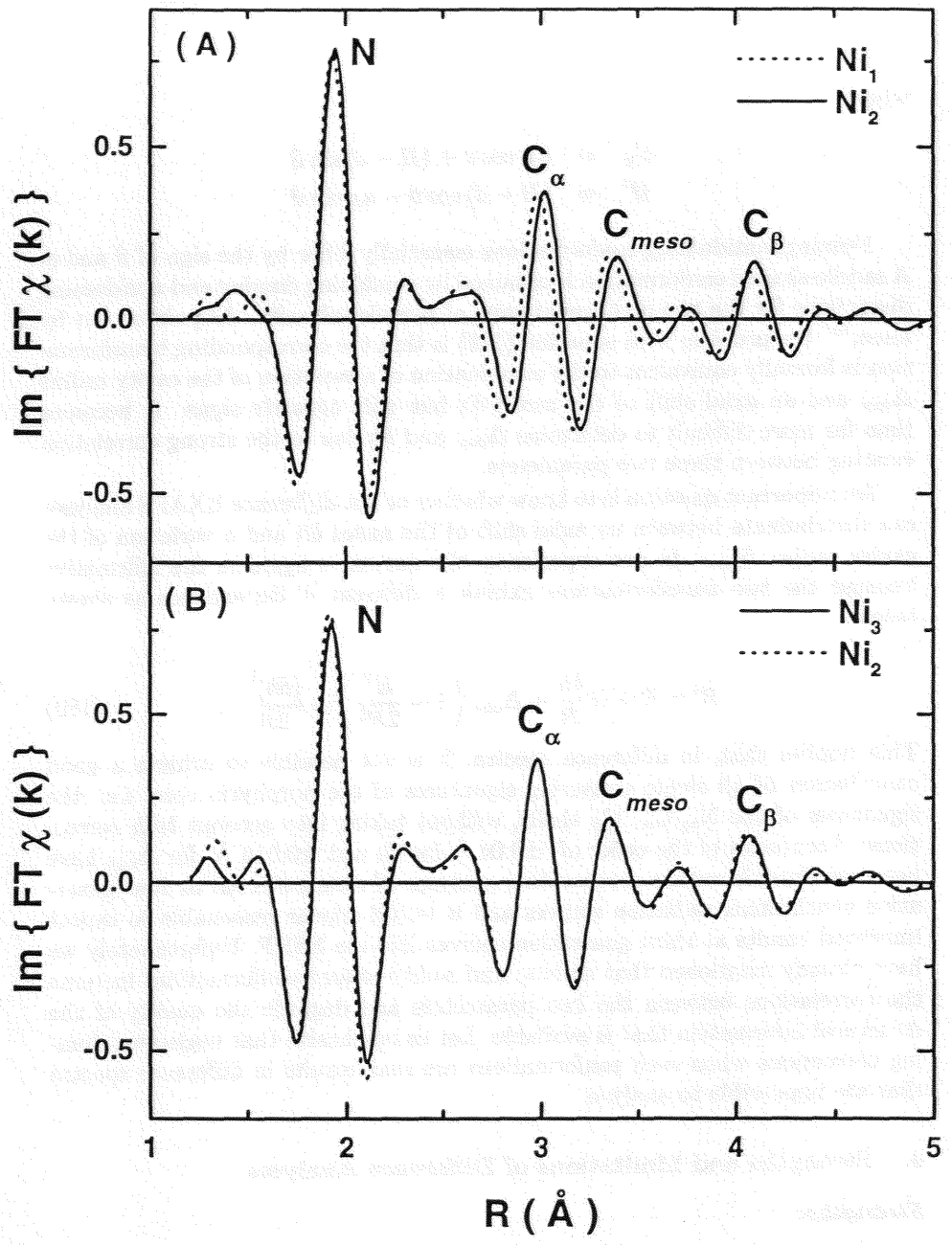

Figures 13: Sensitivity of EXAFS spectra to a *ruffling* of the porphyrin macrocycle:

Figure 13A : FT- EXAFS spectra Im [$\tilde{\chi}_1(R)$] of a ruffled species: Ni_1= (OEP)Ni and a non-ruffled species: Ni_2 = (OMP)Ni .

Figure 13B : FT-EXAFS spectra Im [$\tilde{\chi}_1(R)$] of two complexes with a nearly planar macrocycle Ni_3 = (OMTBP)Ni and Ni_2 = (OMP)Ni .

where:

$$\begin{aligned} a'_N &= a_N \cos\vartheta + (H-d)\sin\vartheta \\ H' &= (H-d)\cos\vartheta - a_N \sin\vartheta \end{aligned}$$

Doming, antidoming conformations essentially differ by the sign of ϑ and d. A saddle-shaped conformation is obtained by combining doming and *anti*doming distortions for the two orthogonal pairs of pyrrole subunits. As pointed out by Loos,[207] the problem with equation (179) is that the corresponding transformation is formally equivalent to the combination of a variation of the cavity radius Δ_{cav} and an axial shift of the metal δh but *with opposite signs*. It becomes then far more difficult to determine Δ_{cav} and δh due to the strong correlation existing between these two parameters.

An important question is to know whether or not *difference* EXAFS analyses can discriminate between an axial shift of the metal δh and a variation of the cavity radius Δ_{cav}. In our experience, the answer is again in the affirmative because the two transformations exhibit a different R dependence as shown below:

$$R' \simeq R + H\frac{\delta h}{R} + \Delta_{cav}\left(1 - \frac{H^2}{2R^2}\right) + \frac{(\delta h)^2}{2R} \qquad (180)$$

This implies that, in difference spectra, it is not possible to achieve a good cancellation of all single scattering signatures of the porphyrin core, *i.e.* the signatures of the N_{eq},C_α, C_β shells, without taking into account *both* corrections. Accuracies of the order of ± 0.04 Å for δh and ± 0.015 Å for Δ_{cav} have been obtained in rather conservative analyses of data collected at first generation synchrotron radiation sources and it would appear reasonable to expect improved results at third generation sources like the ESRF. Unfortunately we have already mentioned that *doming* and *saddle-shaped* conformations increase the correlations between the two parameters and degrade the quality of the structural information that is available. Let us emphasize that neglecting doming corrections when such conformations are real, results in difference spectra that are impossible to analyze.

4. Strengths and Limitations of Difference Analyses

***Strengths*:**

- In ideal analyses, the signatures that are characteristic of the porphyrin macrocycle should *cancel out in the difference* and therefore, FT difference EXAFS spectra of metalloporphyrins should be *dominated by the contribution of the axial ligand(s)*. The spectral resolution limits which hold true for a single spectrum analysis can be transgressed in difference analyses because additional, independent structural information is injected. For the same reason, one may recover the structural information lost in destructive interferences involving the porphyrin macrocycle. Some indication regarding the nature of the axial ligands may still be obtained by considering the phase of the signatures which dominate the difference spectrum. Spherical wave corrections are fully transparent in the cancellation procedure.

- *Cancellation tests are highly discriminant* with the practical consequence that minor structural distortions are easily detected. Note that cancellation tests have a "*concrete*" physical content whereas curve fitting techniques are essentially based on the minimization of statistical error functions. Difference spectra can also be refined using iterative algorithms just as in non linear curve fitting techniques with the practical advantages:

  - to speed up the cancellation tests and make error assessments less empirical;

  - to fit separately the signatures of the axial ligands with the benefit of a considerable reduction of the number of parameters and of the correlations.

- In perturbed difference analyses, the axial shift δh *is not calculated by triangulation* with respect to only the distance $C_t...N_{eq}$, but results from an *optimized geometrical transformation* which affects *all atoms* of the macrocycle: $4N_{eq}, 8C_\alpha, 4C_{meso}, 8C_\beta$... As discussed in section IV, this is necessary to remove undesirable ambiguities.

- One would gain in exploiting both the *sum* and the *difference* of the individual spectra. In practice, the perturbed difference method should be viewed as an attempt to define a new set of variables decoupling the two problems which are of central interest in the chemistry of metalloporphyrins: (*i*) the identification of the axial ligands; (*ii*) the detection of significant structural distortions of the macrocyclic cluster. This is just another strategy to minimize correlations in the EXAFS analyses.

***Limitations*:**

- Difference analyses become attractive as soon as two compounds have at least *one identical component* contributing to the ligand field. This happens in porphyrin or phthalocyanin chemistry but this is, unfortunately, not general. For instance, difference analyses cannot be used in *ex nihilo* studies of metalloproteins, *i.e.* when nothing is known regarding the nature of the active site. At this stage, intuition combined with a deep knowledge of structural organometallic chemistry are and will ever remain most determinant to identify relevant model compounds.

- The synthesis, the purification or the chemical stability of the model compounds used as reference, *e.g.* naked iron porphyrins such as (TPP)Fe , may cause additional troubles. Furthermore, the charge on the metal site may be different and can explain subtle structural changes.

- Difference methods, like MEXAFS, are most demanding from the signal-to-noise ratio of the experimental data. The reliability of the procedures used to extract the background and to pre-normalize the spectra are also very critical. There is finally a need to develop more sophisticated difference analyses taking into account the perturbation of the multiple scattering paths.

5. Selected Examples

Over the past decade, Goulon and coworkers reported several successful applications of difference analyses in porphyrin chemistry.[253,267–270,272–274] Since this method is still in infancy and has not benefitted from a wide diffusion, we will try to illustrate briefly below the potentiality and the limitations of this method with a few selected examples. All corresponding experimental spectra were still recorded at a first generation synchrotron radiation source (LURE-Orsay, France) in the mid-eighties and higher quality data could now be recorded at the ESRF.

Dichlorocarbene: It has been shown by Mansuy *et al.*[275–277] that the reaction of iron(III) porphyrins with polyhalomethanes in the presence of a large excess of reductant produces a wide variety of iron-bonded carbene porphyrinato species. A typical example is the dichlorocarbene **1** = (TPP)FeC(Cl)$_2$ which can be prepared by reaction of the naked iron porphyrin **2** = (TPP)Fe with carbon tetrachloride.[277] Obviously, species **2** was the most appropriate choice as reference to carry out a *perturbed difference analysis* from which it was rather easy to establish that, in the dichlorocarbene complex **1**:

(*i*) the metal is unambiguously shifted out of the mean porphyrin plane with: $\Delta h = 0.30 \pm 0.03$ Å;

(*ii*) there is a tiny increase of the macrocycle cavity radius: $\Delta_{cav} = +0.015$ Å.

The resulting FT-Difference spectrum is reproduced in **Figure 14.** Since the phase-shifts of the *Fe...N* pair were systematically used to display the unperturbed optical FT spectra of species **1** and **2** and the intermediary results of our iterative cancellation procedure, we found more consistent to keep the same corrections to display also the difference spectrum reproduced in **Figure 14** even though we do not expect any *Fe...N* shell to contribute anymore to it. The difference spectrum exhibits only two well resolved peaks which are the signatures of the dichlorocarbene ligand: the first peak is to be assigned to the *Fe...C* single scattering signal and the second to the dominant *Fe...C...Cl* multiple scattering path. At this stage, curve fitting procedures combined with *ab initio* simulations carried out with the MSXAS code led us to the refined interatomic distances: $R(Fe = C) = 1.70 \pm 0.02$ Å ; $R(Fe...Cl) = 3.08 \pm 0.03$ Å. The result of the fit is also displayed in **Figure14**. By reference to known crystal structure data, we constrained the *C-Cl* bond length to remain within the acceptable range: 1.81 ± 0.03 Å and by trial and error, we found that the most probable [*Fe-C-Cl*] bond angle was $122° \pm 2°$. It should be noticed that the low frequency bending modes of the bent sequence [*Fe...C...Cl*] are expected to result in a strong damping of the *direct* single scattering path *Fe...Cl* with the practical consequence that the observed signature is largely dominated by the multiple scattering contribution. It is quite noteworthy that in this pentacoordinated complex, the *Fe=C* bond length deduced from the present EXAFS study is much shorter than in the hexacoordinated species **3** = (TPP)FeC(Cl)$_2$(H$_2$O) for which the crystal structure is known:[278] this result is fully consistent with the fact that complex **1** was carefully prepared in perfectly anhydrous, non coordinating solvents.[270,271]

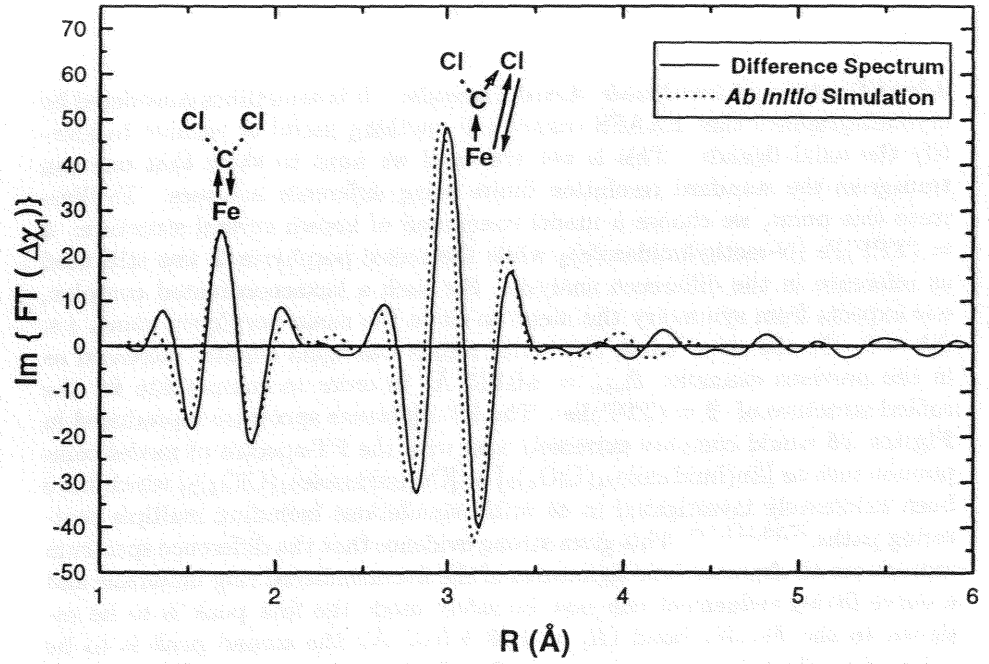

Figure 14: FT optical spectrum Im $[\Delta\tilde{\chi}_1(R)]$ *(full line)* of the difference signal: $\Delta\chi(k) = \chi_1(k) - [\chi_2(k)]^{\dagger}$ where: $\chi_1(k)$ is the *unperturbed* EXAFS signal of the dichlorocarbene complex **1** = (TPP)FeC(Cl)$_2$ whereas $[\chi_2(k)]^{\dagger}$ is the spectrum of the naked porphyrin **2** = (TPP)Fe after perturbation (Δ_{cav} = +0.015 Å ; δh=0.30 ± 0.03 Å). The two parameters characterizing the perturbation were iterated in order to minimize the residual signatures of the porphyrin macrocycle. A simulated FT spectrum *(dotted line)* generated with MSXAS and including all multiple scattering paths for the Fe=C(Cl)$_2$ axial moiety is also displayed.

Identification of Imidazole Axial Ligands: It is sometimes considered by crystallographers that EXAFS cannot tell anything useful or reliable to identify the axial ligands. This is not true and we want to show that one can transgress the standard resolution limits using *difference* analyses. To illustrate this point, we choose a model compound of known crystal structure: **4** = (TPP)Fe (N-methylimidazole)$_2$ while the naked porphyrin **2** was still used as reference in the difference analysis. For such a hexacoordinated complex, one expects from symmetry the metal to sit in the mean porphyrin plane, *i.e.* $\Delta h = 0$. On the other hand, the cavity radius was again slightly increased as in the previous example: $\Delta_{cav} = +0.015$ Å in order to compensate for the ruffled structure of **2** = (TPP)Fe . The FT-*difference* spectrum reproduced in **Figure 15** would compare extremely well with the FT-spectra of model compounds such as [Zn(imidazole)$_4$(ClO_4)$_2$] or [Cu(imidazole)$_4$(ClO_4)$_2$] which have been extensively investigated in *ab initio* simulations including multiple scattering paths.[97,98,111,112] This gives strong evidence that the difference spectrum reproduces all characteristic signatures of the five-membered ring imidazole and a curve fitting refinement can now be safely used: the first peak is to be assigned to the $Fe...N_1$ bond ($R_1 = 1.98 \pm 0.02$ Å); the second peak is to be assigned to the single scattering path $Fe...C_\alpha$ ($R_2 = 2.99 \pm 0.02$ Å); the third peak ($R_3 = 4.02 \pm 0.02$ Å) is well known to be enhanced by a focusing effect resulting from several unresolved multiple scattering paths:

- $[Fe...N_1...C_\beta...Fe]$, $[Fe...N...N_\beta...Fe]$,
- $[Fe...N_1...C_\beta...N_1...Fe]$, $[Fe...N_1...N_\beta...N_1...Fe]$

A tentative refinement of the multiple scattering paths gave an average distance $Fe...\{C_\beta, N_\beta\}$ of 4.1 Å. At this stage, it is worth emphasizing that the difference spectrum shown in **Figure 15** is notably different from the usual pattern of a porphyrin macrocycle: the signature of the *meso* carbons has vanished and the relative amplitude of the second and third peaks is well characteristic of the imidazole ring.

Nitrosoalkane-Hemoglobin Complexes: The next problem to be considered here is one of the most difficult ones if one sticks to conventional curve fitting analyses. We are concerned here with hexacoordinated iron-porphyrin complexes in which the two axial ligands are *non symmetrically* bonded to iron. The motivation behind the present study is to be found in the isoelectronic character of the *NO* group of nitrosoalkanes with respect to molecular oxygen O_2: this has the predictable consequence that nitrosoalkanes which may form during the oxidative metabolism of hydroxylamines and amines should inhibit the normal function of Hemoglobin (Hb).[279] The strategy employed to tackle this problem was to record under the same experimental conditions the EXAFS spectra of both the active complex : **5** = Hb(RNO) and a model compound: **6** = (TPP)Fe(N-methylimidazole)(RNO) the exact structure of which is unfortunately not known. In the present study, R was the bulky isopropyl group (i-Pr). The basic idea was to compare two *difference* spectra: $\Delta\chi_1\left[(\mathbf{5}) - (\mathbf{2})^\dagger\right]$ *versus* $\Delta\chi_2\left[(\mathbf{6}) - (\mathbf{2})^\dagger\right]$. We are indeed keen to prove that the difference method can be extended to the analysis of *dilute* biological samples in aqueous solutions.

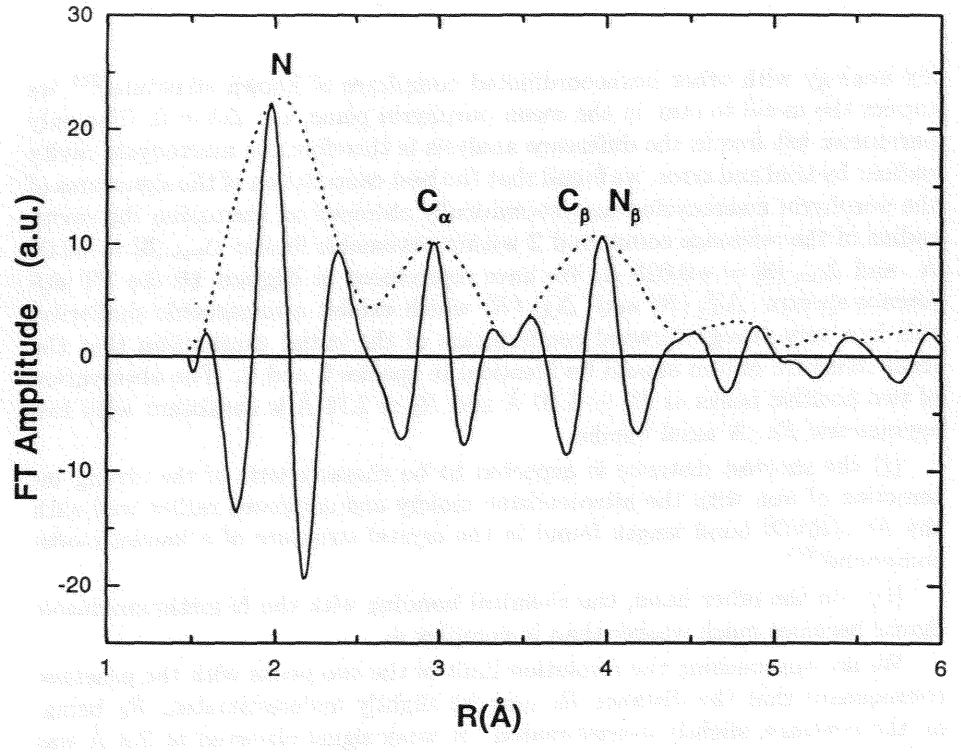

Figure 15: FT optical spectrum $\mathrm{Im}[\Delta\tilde{\chi}_1(R)]$ of the difference signal: $\Delta\chi(k)=\chi_3(k)-[\chi_2(k)]^{\dagger}$ where: $\chi_3(k)$ is the *unperturbed* EXAFS signal of the complex **3** = (TPP)Fe(N-MeIm)$_2$ and $[\chi_2(k)]^{\dagger}$ is deduced from the experimental spectrum of the naked porphyrin **2** = (TPP)Fe by taking into account only a small change of the cavity radius: Δ_{cav} = +0.015 Å since, by symmetry, δh=0. Note that the difference spectrum is dominated by the characteristic single and multiple scattering signatures of the five membered ring imidazole.

By analogy with other hexacoordinated complexes of known structure,[279] we expect the metal to stay in the mean porphyrin plane, *i.e.* $\Delta h = 0$. The only parameter left free in the difference analysis is therefore the macrocycle cavity radius: by trial and error, we found that the best cancellation of the signatures of the porphyrin macrocycle was systematically obtained on *increasing* the cavity radius of the reference compound **2** within reasonable limits: Δ_{cav} [**5**] = +0.04 Å and Δ_{cav} [**6**] = +0.025 Å. We have reproduced in **Figure 16** the FT *difference* spectra $\Delta\widetilde{\chi}_1(R)$ and $\Delta\widetilde{\chi}_2(R)$ which exhibit a remarkable similarity: this is a very straightforward confirmation of the initial *assumption* that the local structure of iron should be identical in species **5** and **6.** The observation of two positive peaks at $R_1 \simeq 1.80$ Å and $R_2 \simeq 2.12$ Å is consistent with two asymmetric *Fe...N* axial bonds:

(*i*) the shortest distance is expected to be characteristic of the strong interaction of iron with the nitrosoalkane moiety and compares rather well with the *Fe...(RNO)* bond length found in the crystal structure of a known model compound;[279]

(*ii*) on the other hand, the chemical bonding with the N-methylimidazole ligand becomes much weaker than in complex **4.**

We are approaching the resolution limit of the two peaks with the practical consequence that the distance R_1 may be slightly underestimated, R_2 being, on the contrary, slightly overestimated. A weak signal observed at 2.8 Å was tentatively assigned to the oxygen atom of the nitrosoalkane functional group. Clearly, it would have been desirable to collect experimental data with a better signal-to-noise ratio over a wider momentum range: this was impossible by the time these experiments were performed at LURE.[271]

C. Analyses of XANES Spectra

In the past decades, XANES spectra recorded at high energy, *e.g.* at the *K*-edges of transition metals, have most often been used as "*fingerprints*" of given cluster geometries without any very deep analysis of the spectra. Some valuable attempts were made to correlate in a more systematic way the observation or simply the enhancement of a specific shape resonance with structural changes or with the spin state of the absorbing atom.[280–282] In the soft X-ray range where EXAFS oscillations are of fairly limited interest due to the presence of many overlapping edges, atomic & molecular physicists have invested much more time and efforts in the identification and in the quantitative analysis of the pre-edge and shape resonances.[3,6] Today, the interests of the two communities are merging together and concur to the development of more sophisticated analyses.

1. Deconvolution of XANES Spectra

One serious difficulty which refrained many people from refining the analyses of pre-edge or XANES spectra arises from the discouraging fact that the resonances have such a broad lineshape at high energy that all attempts to identify the excited states are frustrated. The origin of the problem is well understood:[283]

- The ultra-short life-time of the deep core hole is resulting in a dramatic broadening of the corresponding energy level which is smearing out all

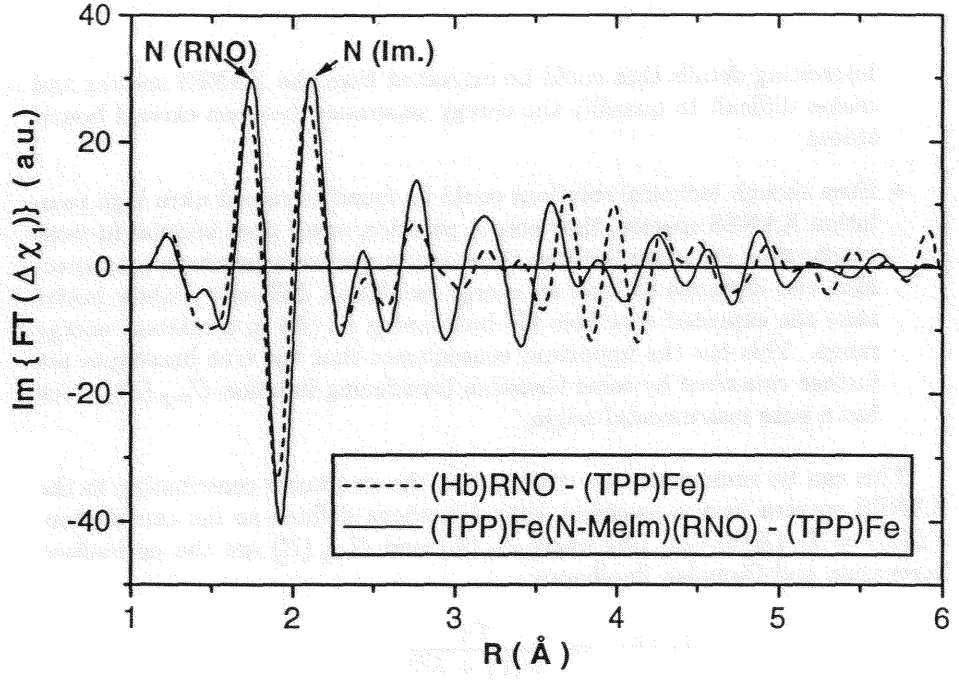

Figure 16: *Optical* FT spectra Im [$\Delta\tilde{\chi}_1(R)$] of the difference signals $\Delta\chi(k) = \chi_4(k) - [\chi_2(k)]^{\ddagger}$ *(full line)* and $\Delta\chi(k) = \chi_5(k) - [\chi_2(k)]^{\ddagger}$ *(dotted line)* where $\chi_4(k)$ and $\chi_5(k)$ are unperturbed experimental spectra of species **4** = (Hb)(RNO) and **5** = (TPP)Fe(N-MeIm)(RNO) . $[\chi_2(k)]^{\ddagger}$ is deduced from the experimental spectrum **2** = (TPP)Fe with: $\Delta_{cav}(\mathbf{4})$ = +0.04 Å ; $\Delta_{cav}(\mathbf{5})$ = +0.025 Å . The short Fe...N distance is assigned to the nitrosoalkane and the long one to imidazole.

interesting details that could be extracted from the XANES spectra and makes difficult to quantify the energy separation between excited bound states.

- Even though technical solutions could be found to record ultra high resolution XANES spectra, they are, in practice, never used because in most synchrotron radiation facilities the existing spectrometers have been specified and designed to have an energy resolution ΔE only slightly better than the expected core hole life broadening $\Gamma_h(E)$ in a relevant energy range. This has the important consequence that the true lineshapes are further *convolved* by some Gaussian broadening function $G_{\exp}(E)$ which has a pure instrumental origin.

This can be summarized by writing that the structures contributing to the XANES spectra have a so-called *Voigt-Lineshape* defined as the convolution: $VL(E) = L_h(E) \otimes G_{\exp}(E)$ where $L_h(E)$ and $G_{\exp}(E)$ are the normalized Lorentzian and Gaussian lineshapes:

$$\begin{aligned} L_h(E) &= \frac{\Gamma_h}{\pi(\Gamma_h^2 + E^2)} \\ G_{\exp}(E) &= \frac{1}{\sigma_{\exp}\sqrt{2\pi}} \exp\left[-\frac{E^2}{2\sigma_{\exp}^2}\right] \end{aligned} \tag{181}$$

that are commonly characterized by their *Full Width at Half Maximum* ($FWHM$): $w_L = 2\Gamma_h$; $w_G = (2\sigma \ln 4)^{1/2}$. This formalism can be extended to the description of the absorption threshold by calculating the primitive of the Voigt lineshape:

$$TV(E) = \int_{-\infty}^{E} VL(u)du \tag{182}$$

Recall that the primitive of the Lorentzian function is an arctangent function whereas the primitive of the Gaussian function is the error function, which for most programming languages is a built-in function. This implies that fitting an absorption edge with a simple arctangent function should be restricted only to a situation where the instrumental broadening is negligible: this is certainly not the case if one wishes to analyze the K-edge XANES spectra of argon, chlorine, sulfur... As regards numerical applications, the convolution product that appears in the definition of the Voigt lineshape is a major handicap in the development of efficient curve fitting procedures. Recently, Teodorescu *et al.*[283] have proposed an interesting numerical approximation for a Voigt profile at resonance energy E_i:

$$VL(E, E_i) = \frac{1}{2\pi}\frac{\Gamma_h}{\sigma_{\exp}^2} F\left[\frac{\Gamma_h}{\sqrt{2}\sigma_{\exp}}, \frac{E - E_i}{\sqrt{2}\sigma_{\exp}}\right] = aF(\gamma_h, e) \tag{183}$$

where the function $F(\gamma_h, e)$ is of the type:

$$F(\gamma_h, e) = c_0 \exp\left[-e^2/2c_1^2\right] + \frac{c_2}{c_3^2 + e^2} \tag{184}$$

c_0, c_1, c_2, c_3 being parametrized functions of the reduced quantity γ_h. For some applications, it might be more appropriate to use a generalized *Fano-Voigt* lineshape with: $c_2' \simeq c_2 [1 + \delta e/c_2]^2$. In the latter mathematical model, the Lorentzian term ($\delta = 0$) becomes a Fano function whenever $\delta = 1$.

An alternative approach which looks very attractive has recently been pioneered by Loeffen *et al.*[284]: it consists in deconvolving numerically the experimental XANES spectra in order to produce some artificial narrowing of the resonance lines. One should stress immediately that, according to elementary information theory, such a numerical procedure makes sense *only if the quality of the experimental data is very high* because the initial signal-to-noise ratio S_0/N_0 will be spoiled by the numerical deconvolution:

$$\frac{S}{N} \simeq \left[\frac{S_0}{N_0}\right]^{\eta} \quad \text{with: } \eta \rightarrow 0 \tag{185}$$

where η is the reduction factor of the actual spectral bandwidth. For example, if we assume a pure Lorentzian lineshape: $\eta = \delta\Gamma_h \,/\, \Gamma_h$. This implies that one has to pay for an increase in energy resolution with a reduction in the signal-to-noise ratio: as a consequence, a deconvolution should never be pushed to the ultimate limit, *e.g.* $\delta\Gamma_h \rightarrow 0$. As confirmed by several analyses performed at the ESRF, this technique is becoming particularly attractive to analyze XANES spectra recorded at third generation sources where signal-to-noise ratio in excess of 10^8 can easily be obtained on concentrated species. In practice, the code which we developed for industrial applications of XANES spectra[285,286] is slightly different from the original procedure used by Loeffen *et al.*:[284]

- Starting from the second derivative XANES spectra which can be calculated with very efficient algorithms, the first derivative is readily obtained by a straightforward numerical integration. It was found preferable to perform the deconvolution as well as curve fitting procedures using systematically the first derivative XANES spectra because there is no step function to be taken into account and because the structures to be fitted are much better resolved.

- The first derivative XANES spectrum can be Fourier Transformed in the time space using standard FFT algorithms and an optimum Kaiser-Bessel window function. Partial deconvolution is performed in the time-space in which the FT expression of the Voigt function $\widetilde{VF}(t)$ and of its first derivative can be calculated *without any approximation* using well known properties of Fourier Transformed functions. The information entropy is also evaluated.

- The deconvolved spectrum is next transformed back into the energy domain and the window function is removed. The deconvolved, first derivative XANES spectrum is integrated numerically to yield the displayed XANES spectra after a suitable renormalization procedure.

- Under favorable circumstances, the *deconvolved* XANES spectrum can be decomposed into a sum of resolved resonances plus a non-structured absorption edge. It becomes then attractive to make the analysis more quantitative by fitting the deconvolved spectrum with a sum of discrete

Fano-Voigt lines described by equations (183) and (184) and which add up to some absorption threshold described by equation (182). In practice, it was found easier to perform such a curve fitting using directly the deconvolved first derivative XANES spectrum: analytical derivatives of the Fano-Voigt lineshapes can be easily obtained to approximate the discrete resonances while a standard Voigt lineshape can be used to approximate the derivative of the absorption threshold. A non-linear curve fitting procedure has been made possible *via* a specific interface to the code MINUIT which is also used to refine the EXAFS analyses. The present analysis can accommodate up to 4 discrete resonances. Following Outka and Stöhr,[287] this model has been extended to include an asymmetric Gaussian lineshape as an option. The quality of the fits can be again estimated with reference to standard statistical criteria.

What makes the deconvolution technique most attractive is the possibility to enhance considerably the energy resolution of the *pre-edge* structures. This is nicely illustrated by **Figure 17A** which reproduces the tin L_{III}-edge XANES spectrum of (OEP)$SnCl_2$ while **Figure 17B** displays the chlorine K-edge of the same compound. The very sharp pre-edge resonances shown in **Figures 17** are of obvious interest if one wishes to refine the energy diagram of the empty molecular orbitals in this compound.[32] Loeffen *et al.*[284] were the first to use the deconvolution technique at the L_{II-III} edges of rare-earth compounds and noted that it was quite possible to resolve the contribution of the weak electric quadrupole transitions ($E2$) associated with the transitions from the $2p_{3/2}, 2p_{1/2}$ inner levels to the strongly localized but partially empty $4f$ shell: the investigation of such transitions proved to be particularly useful to simulate the electronic and the magnetic properties of rare-earth oxides. We have reproduced respectively in **Figure 18A** and **Figure 18B** the *deconvolved* XANES spectra of (DPA)[Gd(OH)]$_2$ at the gadolinium L_{III}- and L_{II}-edges measured in the aligned paramagnetic phase. The weak prepeaks assigned to the quadrupolar transitions ($E2$) are clearly apparent but, even more important, the ligand field splitting of the $5d$ excited states (< 3 eV) is well resolved: spin-orbit coupling in the final state is also shown to play an important role because the *branching ratios* of the two split peaks are not identical as indicated by the comparison of the spectra recorded at the gadolinium L_{III}- and L_{II}-edges. This is indeed consistent with the observation of a strong XMCD signal for this compound.

2. *Ab initio* Simulations XANES Analyses

Trends: Much progresses have been made in *ab initio* simulations of XANES spectra following the initial impulses given by Natoli *et al.*[288] and by Durham.[289] Several recent versions of "*Full Multiple Scattering*" computing codes are available and test examples of calculated XANES spectra have been reported in the specialized literature.[290,291] As discussed in sections II.C.3 and II.C.4, there is still a need for much more advanced *ab initio* calculations performed with upgraded models of the self-energy and "*Non-Muffin-Tin*" local potentials: such advanced codes are under development at several places.[107,160] Given the strong spin-structure correlations well illustrated by the porphyrin chemistry, it would be attractive to perform systematically *spin-resolved ab initio* calculations of the XANES spectra as reported recently by Della Longa *et al.*[347]. Indeed, it would

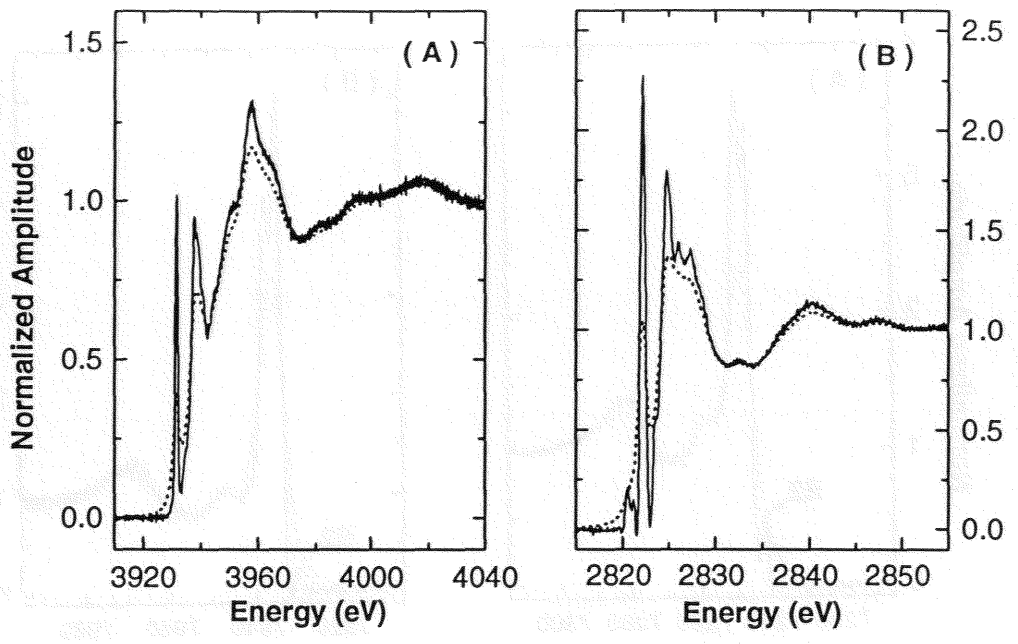

Figure 17: Deconvolved XANES spectra of $(OEP)SnCl_2$ *(full lines) versus* original spectra *(dotted lines).*

Figure 17A: Deconvolved XANES spectrum recorded at the Sn L_{III}-edge with $\sigma_{exp} \approx 0.25$ eV and $\Gamma_h \approx 0.9$ eV.

Figure 17B: Deconvolved XANES spectrum recorded at the Cl K-edge with $\sigma_{exp} \approx 0.21$ eV and $\Gamma_h \approx 0.3$ eV.

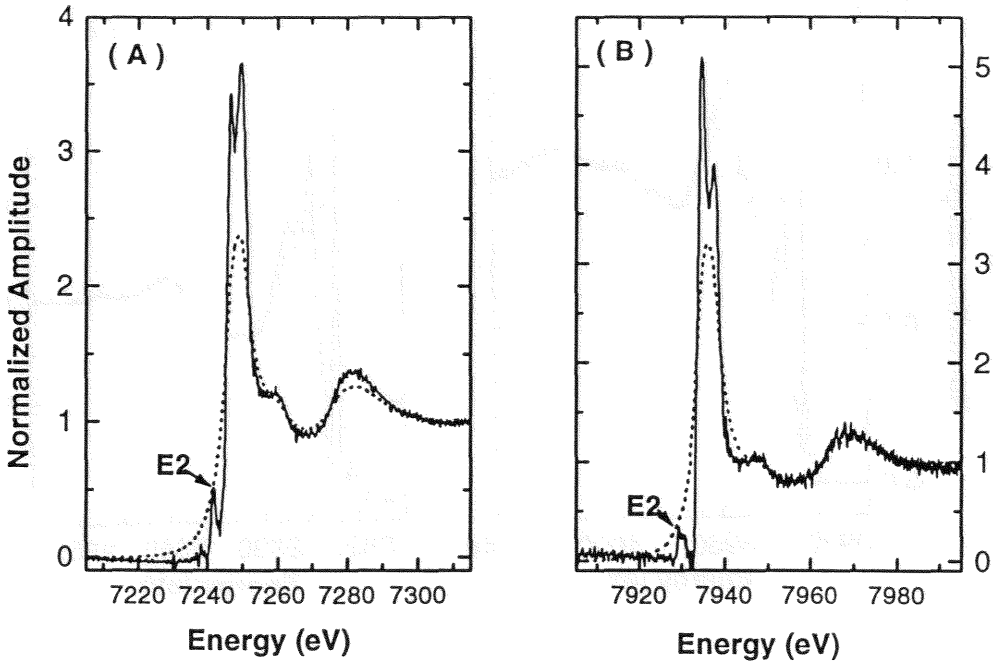

Figure 18: Deconvolved XANES spectra of (DPA)[Gd(OH)]$_2$ *(full lines) versus* original spectra *(dotted lines).*

Figure 18A: Deconvolved XANES spectrum recorded at the Gd L_{III}-edge with $\sigma_{exp} \approx 0.50$ eV and $\Gamma_h \approx 2.0$ eV.

Figure 18B: Deconvolved XANES spectrum recorded at the Gd L_{II}-edge with $\sigma_{exp} \approx 0.56$ eV and $\Gamma_h \approx 2.0$ eV.

Note the well resolved prepeak assigned to quadrupolar (E2) transitions towards the 4f shell.

be highly desirable to calculate as well *spin-polarized potentials* in order to be able to simulate the XANES and XMCD spectra of spin polarized paramagnetic complexes aligned in strong magnetic fields. In this section, we want essentially to illustrate with a few selected examples how remarkably sensitive "*Extended Continuum*" calculations of XANES spectra can be to structural and electronic properties of metalloporphyrins. As explained in section II.B.1, one may speak of "*Extended Continuum*" calculations whenever the final states with energies greater than the interstitial potential $\overline{V}_{int}$ are treated artificially as *continuum* resonances although the $\overline{V}_{int} < E < 0$ levels typically correspond to bound states. The spectra which are reproduced below were all obtained by running the latest version of the code "*CONTINUUM* " which has been upgraded over several decades by Natoli and his collaborators.[292]

Linear Dichroism of XANES spectra: A number of applications of XANES spectra in biology *indirectly* exploits the extreme sensitivity of XANES spectra to *linear* dichroism effects. This sensitivity is illustrated by **Figures 19-21** which reproduce the polarization resolved "*extended continuum*" MSW simulations of the XANES spectra of (TPP)VO. The polarization vector $\mathbf{e}$ was taken either parallel or perpendicular to the C_4 axis of the porphyrin macrocycle and therefore should have been associated with the irreducible representations $a_1\left(\mathbf{e}_{\parallel}\right)$ and $e\left(\mathbf{e}_{\perp}\right)$ of the group C_{4v}. In reality, there are several examples in the literature which indicate that the porphin macrocycle is scarcely planar and can suffer distortions, such as the saddle-shape conformation, which will lower the symmetry and lift the degeneracy of the $(\mathbf{e}_{\perp}^{\mathbf{x}}, \mathbf{e}_{\perp}^{\mathbf{y}})$ representation. The cluster used for these simulations consisted of 50 atoms but one is facing here the commonplace difficulty that the *exact* structure of (TPP)VO is unknown: this implies that one has to probe different macrocycle geometries which are inspired by known crystal structures:

(*i*) For the calculations displayed in **Figures 19,** we have retained the model of a strongly distorted macrocycle directly extrapolated from the structure of (TPP)CrO in which a vanadyl group was substituted for the chromyl group. The $V...O$ distance was deduced from the EXAFS spectrum. The displacement of the metal with respect to the average plane of the pyrrole nitrogen was kept unchanged $C_t...MO \simeq 0.47$ Å.

(*ii*) For the calculations displayed in **Figures 20** and **Figures 21,** we have considered a less distorted, ruffled porphin structure but the vanadyl group was shifted along the C_4 axis so that $C_t...MO \simeq 0.6$ Å in the simulations reproduced in **Figure 20** while $C_t...MO \simeq 0.3$ Å in the simulations reproduced in **Figure 21**.

The overlap between the muffin-tin spheres of vanadium and oxygen is a rather fuzzy parameter which has, nevertheless, a strong influence on the respective intensities of the various shape resonances: it was finally frozen to 15% by trial and error. Let us insist that, at such an early stage of the XANES analysis, the goal is *not to match perfectly the shape of the experimental spectra* but merely *to identify the main shape resonances* contributing to the XANES spectrum. This is why we found always quite instructive to start *ab initio* simulations with Xα calculations performed under the unrealistic assumption that the core hole life-time could be made infinitely long: in such spectra, all contributing resonances are *ideally* resolved and one may have more chance

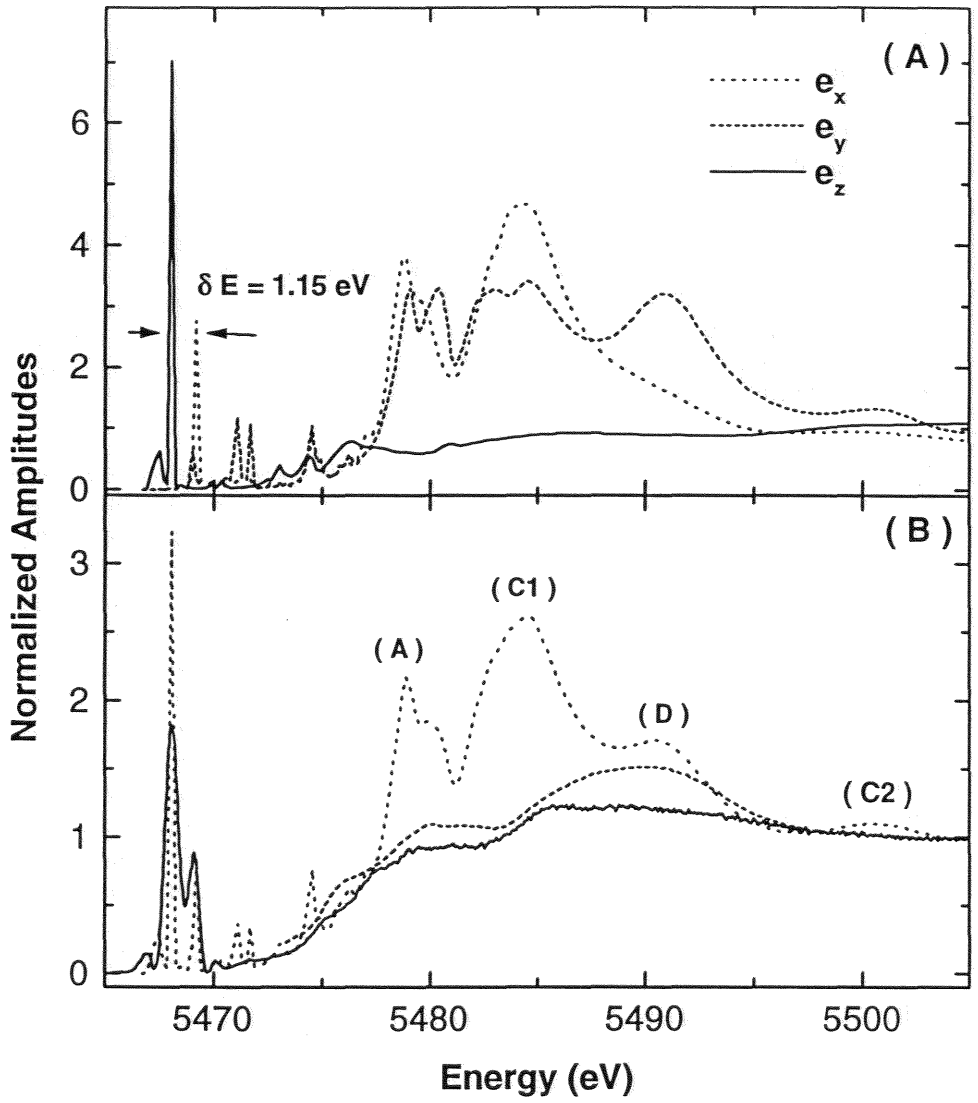

Figures 19: "*Extended continuum*" MSW - XANES spectra of (TPP)VO simulated for a 50 atom cluster assuming a saddle-shaped distorted macrocycle as observed in (TPP)CrO and δh=0.47 Å.

Figure 19A : MSW-Xα spectra simulated with the polarization vector either parallel: $\mathbf{e}^{z}_{//}$ *(full line)* or perpendicular: $\mathbf{e}^{x}_{\perp}$ *(dotted line)*, $\mathbf{e}^{y}_{\perp}$ *(dashed line)* to the *pseudo* C_4 axis **Oz**. Note that the degeneracy is lifted by the distortion of the macrocycle. An infinite core hole life-time is assumed in order to enhance the resolution.

Figure 19B : Deconvolved experimental XANES spectrum *(full line)*; Polarization averaged MSW-XANES spectra with Xα exchange correlation potential *(dashed line)* or Hedin Lundqvist potential *(dotted line)*.

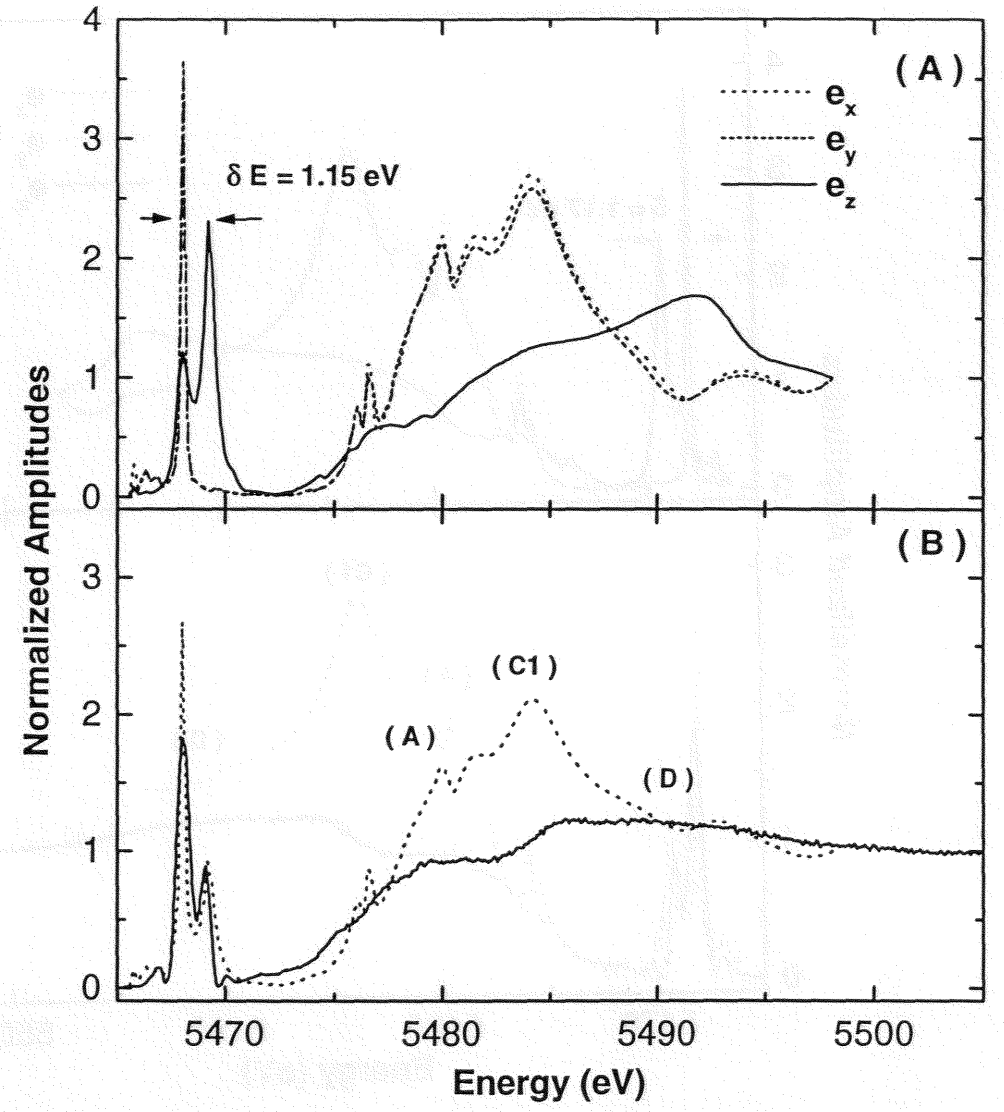

Figure 20: "*Extended continuum*" MSW-XANES spectra of (TPP)VO simulated for a 50 atom cluster assuming a *ruffled* macrocycle and δh=0.6 Å.

Figure 20A: MSW-Xα spectra simulated with the polarization vector either parallel: $\mathbf{e}^{z}_{//}$ *(full line)* or perpendicular: $\mathbf{e}^{x}_{\perp}$ *(dotted line)*, $\mathbf{e}^{y}_{\perp}$ *(dashed line)* to the *pseudo* C_4 axis **Oz** . An infinite core hole life time is assumed in order to enhance the resolution.

Figure 20B : Deconvolved experimental XANES spectrum *(full line)*; Polarization averaged MSW-XANES spectra with Xα exchange correlation potential *(dotted line)*.

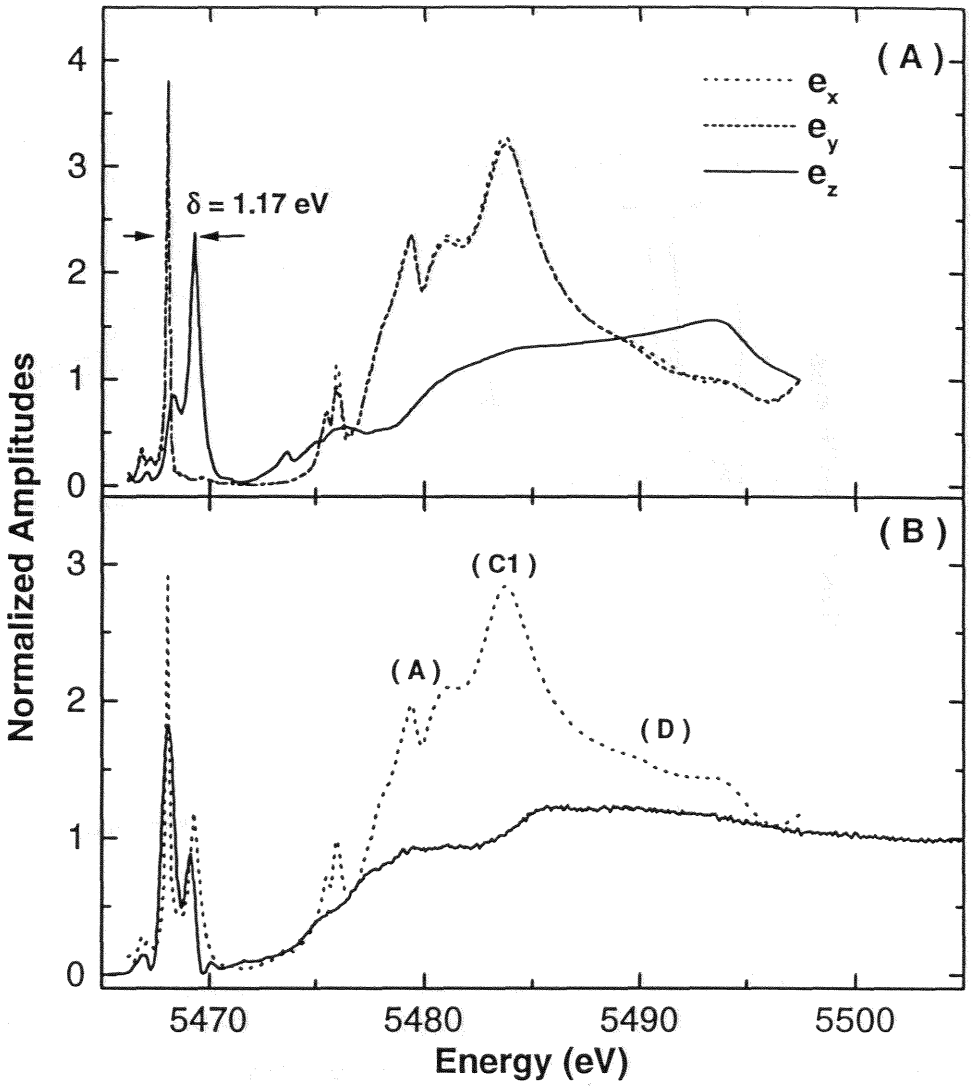

Figure 21: "*Extended continuum*" MSW-XANES spectra of (TPP)VO simulated for a 50 atom cluster assuming a *ruffled* macrocycle and δh=0.3 Å.

Figure 21A: MSW-Xα spectra simulated with the polarization vector either parallel: : $\mathbf{e}^{z}_{//}$ *(full line)* or perpendicular: $\mathbf{e}^{x}_{\perp}$ *(dotted line)*, $\mathbf{e}^{y}_{\perp}$ *(dashed line)* to the *pseudo* C_4 axis **Oz** . An infinite core hole life time is assumed in order to enhance the resolution.

Figure 21B : Deconvolved experimental XANES spectrum *(full line)*; Polarization averaged MSW-XANES spectra with Xα exchange correlation potential *(dotted line)*.

to correlate the intensity of a specific resonance with a structural property of the unknown complex. Polarization resolved spectra are displayed in **Figures 19A, 20A** and **21A** whereas the polarization averaged spectra are compared in **Figures 19B, 20B** and **21B** with the experimental spectrum which was deconvolved according to the prescription of the previous section with $\sigma_{\mathrm{exp}} \simeq 0.36$ eV and $\Gamma \simeq 0.45$ eV. Recall that the experimental XANES spectrum of (TPP)VO was recorded at low temperature (T=10 K) in the Fluorescence Detection mode using a thick pellet diluted with boron nitride (BN), *i.e.* a material which has a good thermal conductivity. The data were corrected for reabsorption losses using the procedure described in section III.A.1 and the signal-to-noise ratio was better than 10^8. It is worth noting that the spectrum was recorded with incremental steps in energy δE much smaller than the true energy resolution ΔE of the monochromator: $\delta E \leq 5meV \ll \Delta E = 0.84$ eV.

Several interesting conclusions can be drawn from the various simulations reproduced in **Figures 19-21**:

- All spectra reproduced in **Figures 19B-21B** reveal a characteristic splitting of the pre-edge *"white line"* in a polarization averaged XANES spectrum because the energies of the sharp pre-edge resonances differ by *ca.* 1.15 eV in the $a_1\left(\mathbf{e}_{\|}\right)$ and $e\left(\mathbf{e}_{\perp}^{\mathbf{x}}, \mathbf{e}_{\perp}^{\mathbf{y}}\right)$ spectra. Simulations including the finite life-time of the core hole ($2\Gamma_h \simeq 1.01$ eV) would show that *there is absolutely no chance* to detect this splitting directly with the experimental spectrum without the numerical deconvolution introduced in the previous section. It is, however, quite remarkable that the *sign* of the dichroism associated with the prepeak *is reverted* if one compares the polarization resolved spectra displayed in **Figure 19A** and **Figure 20A** (or **21A**): this implies that the linear dichroism is indirectly probing the distortion of the macrocycle. The energy splitting of the prepeak has a weak correlation with the axial shift of the metal: this conclusion is at odds with that of earlier XANES simulations on (OEP)VX molecules by Ruiz-Lopez and Natoli[85] but unfortunately restricted to small prototypical clusters ($_4N$)VO.

- As illustrated by **Figures 19A,B,** there is also a fairly characteristic splitting of the $1s \rightarrow 4p$ resonances, and more specifically a splitting of the $e\left(\mathbf{e}_{\perp}^{\mathbf{x}}, \mathbf{e}_{\perp}^{\mathbf{y}}\right)$ spectra, into three resonances which were labelled $(A), (C_1), (D)$ by analogy with the existing literature. It appears immediately that resonance (D) is strongly enhanced for a saddle-shape (or domed) porphin macrocycle as compared to a ruffled macrocycle. This is consistent with earlier studies by Bianconi *et al.* on hemes.[280] What is however noteworthy is that resonance (C_1) is *predominantly polarized in the plane of the porphyrin* rather than along the pseudo C_4 axis: this is again at odds with earlier assignments based on calculations performed with too small size clusters. This is a clear message that it may be very risky to assign some weakly resolved resonance without detailed simulations. XANES spectra are clearly shown to be very sensitive to the geometry of the macrocycle: (i) a shift of the metal out of the porphyrin plane is enhancing resonance (C_1); (ii) doming or saddle-shaped distortions are enhancing resonances (D). In the specific case of (TPP)VO, a comparison of **Figures 19B**, **20B** and **21B** suggests that the porphyrin macrocycle is effectively dis-

torted with a saddle-shape geometry and the metal is certainly shifted out of the porphyrin plane. Note that nearly all small resonances found in the deconvolved spectrum are present in the simulated XANES spectrum of **Figure 19B**. For the sake of comparison, we have included in **Figure 19B** a simulation of the XANES spectrum performed with the Hedin-Lundqvist potential but still without any core hole life-time broadening: it clearly shows that the imaginary part of the potential already induces a significant broadening of the various resonances so that the simulated XANES spectrum bears a stronger resemblance to the experiment than in the case of the Xα calculation.

Recall that the early calculations published by Penner-Hahn *et al.* [11] for (TpTP)CrO and (TpTP)CrN did not reveal any polarization dependent *energy splitting* of the prepeak. In order to clarify this point, we found attractive to reproduce in **Figure 22-B** a deconvolved experimental spectrum of (TPP)CrN : the latter does not exhibit any line splitting of the prepeak comparable to what was observed for (TPP)VO but only a weak satellite at low energy. This result is rather consistent with the polarization averaged *ab initio* simulations of the XANES spectrum shown in **Figure 22-A** and which were obtained either with the Xα or Hedin-Lundqvist exchange-correlation potentials. The stereogeometry of the 50 atom cluster used for these *ab initio* simulations, was directly inspired from the known crystal structure of this compound. One would discover substantial differences if one compares the simulated XANES spectra shown in **Figure 22A** with the earlier simulations reported by Penner-Hahn *et al.* in reference[11] and which concerned only a 6 atom cluster*:* the degeneracy of the e spectra is clearly lifted by the saddle-shaped distortion of macrocycle with the important consequence that a significant contribution of the prepeak is recovered for the $\mathbf{e}_\perp$ polarization. The new simulations explain very well the presence of a large residual signature for the latter polarization in the experimental spectra reported by Penner-Hahn *et al.*[11]

Another lesson to be learned from the comparisons of **Figures 19-22A** with the **Figures 19-22B** is that the polarized spectra $a_1\left(\mathbf{e}_\parallel\right)$ and $e\left(\mathbf{e}_\perp^{\mathbf{x}}, \mathbf{e}_\perp^{\mathbf{y}}\right)$ are so different that some of the resonances that are characteristic of a given polarization can still be perfectly identified in the *polarization averaged spectrum.* In other terms, dichroism effects could be investigated without having to resort to painful experiments with single crystals. This consideration was the starting point of the extensive activity of Bianconi and his coworkers on various hemoproteins like hemoglobins and carboxymyoglobins in the mid-eighties. Recently, they developed a new application of the XANES studies : the procedure called *Temperature Derivative X-ray Absorption Spectroscopy* (TDXAS) allowed them to probe the conformational landscape of carboxymyoglobin in trehalose or sucrose glassy media. Starting with a temperature quenched photodissociated sample of carboxymyoglobin, they used *one characteristic resonance* of the XANES spectrum which is most sensitive to the *Fe...CO* bonding to monitor the derivative with temperature of the intensity of this signal when the sample is allowed to warm up. By analogy with similar experiments carried out with other spectroscopies, the analysis of the derivative spectra is expected to give access to the distribution function $g\left(H_b\right)$ of activation enthalpy barriers H_b relative to the recombination process.[293] This technique might develop as a very promising extension of XANES spectroscopy.

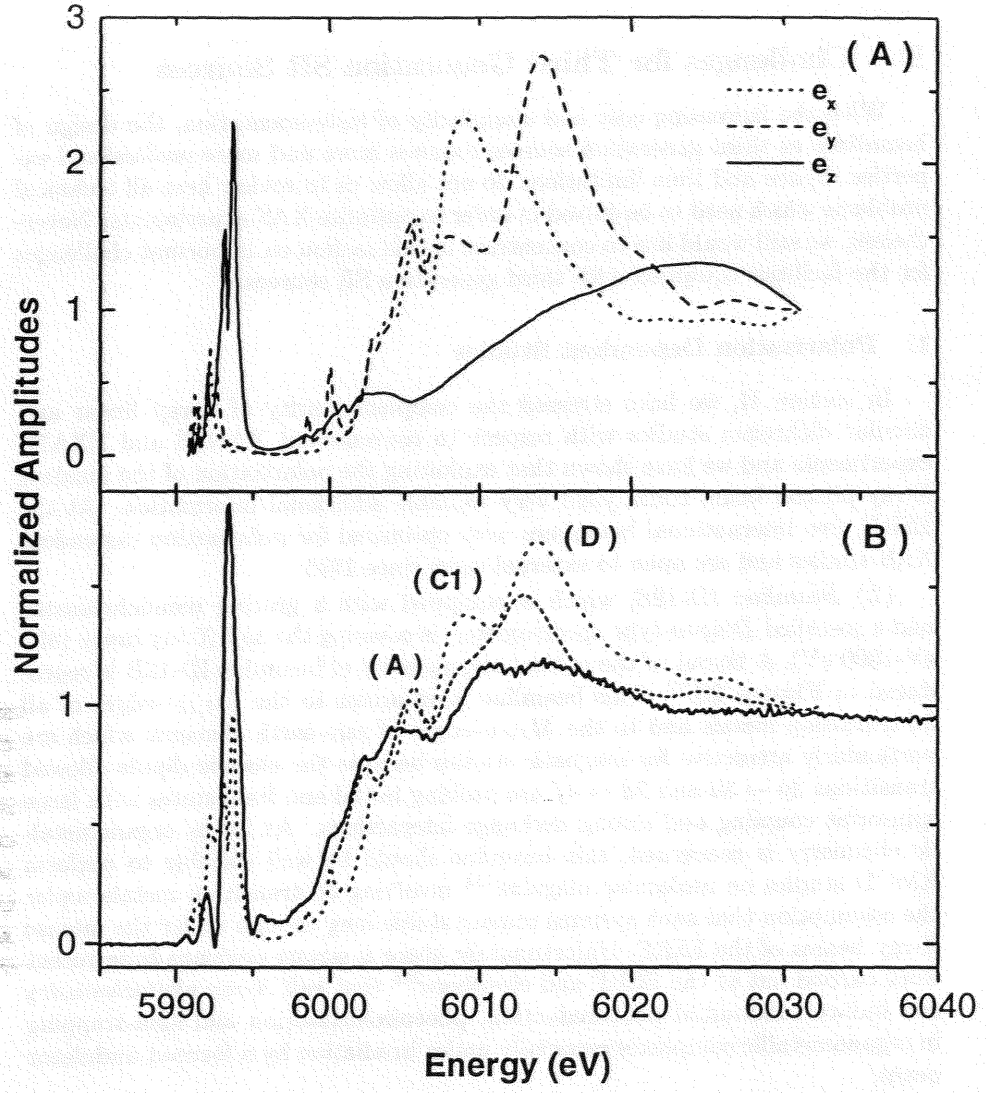

Figure 22: *"Extended continuum"* MSW-XANES spectra of (TPP)CrN simulated for a 50 atom cluster assuming a saddle-shaped distorted macrocycle and δh=0.42 Å.

Figure 22A : MSW-Xα spectra simulated with the polarization vector either parallel: $\mathbf{e}_{//}^{z}$ *(full line)* or perpendicular: $\mathbf{e}_{\perp}^{x}$ *(dotted line)*, $\mathbf{e}_{\perp}^{y}$ *(dashed line)* to the *pseudo* C_4 axis **Oz**. Note that the degeneracy is lifted by the distortion of the macrocycle. An infinite core hole life-time is assumed in order to enhance the resolution.

Figure 22B : Deconvolved experimental XANES spectrum *(full line);* Polarization averaged MSW-XANES spectra with Xα exchange correlation potential *(dashed line)* or Hedin Lundqvist potential *(dotted line)*

D. Challenges for Third Generation SR Sources

With the increasing cost and complexity of instrumentation, the design of beamlines at third generation sources requires more and more professional expertise. Space and time limitations do not allow us to review here all technical problems which need to be solved in order to optimize XAS experiments. Nevertheless, we still would like to concentrate in this section on important challenges for the facilities equipped with third generation SR sources.

1. Polarization Dependent Studies

In section II, we have stressed the complementarity of X-ray linear and circular dichroism studies with respect to conventional XANES and EXAFS experiments and we have shown that exploiting the polarization of the incident X-ray photon beam could yield very valuable additional information. At the ESRF, two international beamlines were optimized for polarization dependent XAS studies and are open to external users since 1995:

(1) *Beamline ID-12B*, which is equipped with a grating monochromator and a so-called *Dragon*-type spectrometer, is covering the *soft X-ray range* (400 eV-1800 eV). A layout of the optical arrangement of beamline ID-12B is reproduced in **Figure 23**.[52] This beamline gives access to the $L_{II,III}$-edges of all $3d$ transition metals and to the $M_{IV,V}$-edges of rare-earth elements which are particularly attractive for magnetic studies because the electric dipole allowed transitions $2p \rightarrow 3d$ and $3d \rightarrow 4f$ are probing initial and final states with large spin-orbit coupling and strong exchange interactions. As far as organometallic chemistry is concerned, this beamline should be well suitable to perform XMCD studies on molecular magnets[294] involving $3d$ transition metals under the assumption that such systems remain stable long enough under the intense X-ray beams of the ESRF. Unfortunately, there is strong evidence from recent work carried out at the ESRF and elsewhere[295] that *soft X-ray photochemistry* can induce substantial photoreduction, photoisomerization and spin-trapping in organometallic complexes especially under irradiation by a focused undulator beam.

(2) *Beamline ID-12A* which is equipped with a double crystal Bragg monochromator has been designed to cover the higher energy range: 1.5-20 keV which is of more direct interest for EXAFS. The corresponding layout is reproduced in **Figure 24**. A detailed description of this beamline and of its performances can be found elsewhere.[53] High quality reflective optics is used to minimize the contamination of the monochromatic X-ray beam by spurious harmonics and to refocus it at the sample location with a spot size which can be made as small as $25\mu m$ (vertical) $\times$ $300\mu m$ (horizontal). The stability of the rocking curve of the cryogenically cooled monochromator was measured to be better than 0.14 arcsec over periods of several hours. Photodiodes which offer the advantages of a better detection linearity over a very large dynamic range, a fast response, a good efficiency and the desirable UHV compatibility are replacing the gas ion chambers which are still very popular in many other facilities. The ultra-low noise readout electronics has been designed to compensate automatically for the dark current of the photodiodes down to 0.5 pA and is, under normal operating conditions, coupled to a powerful *digital lockin* system which takes full benefit of the modulation of the X-ray beam at some intermediary frequency (*e.g.* 68

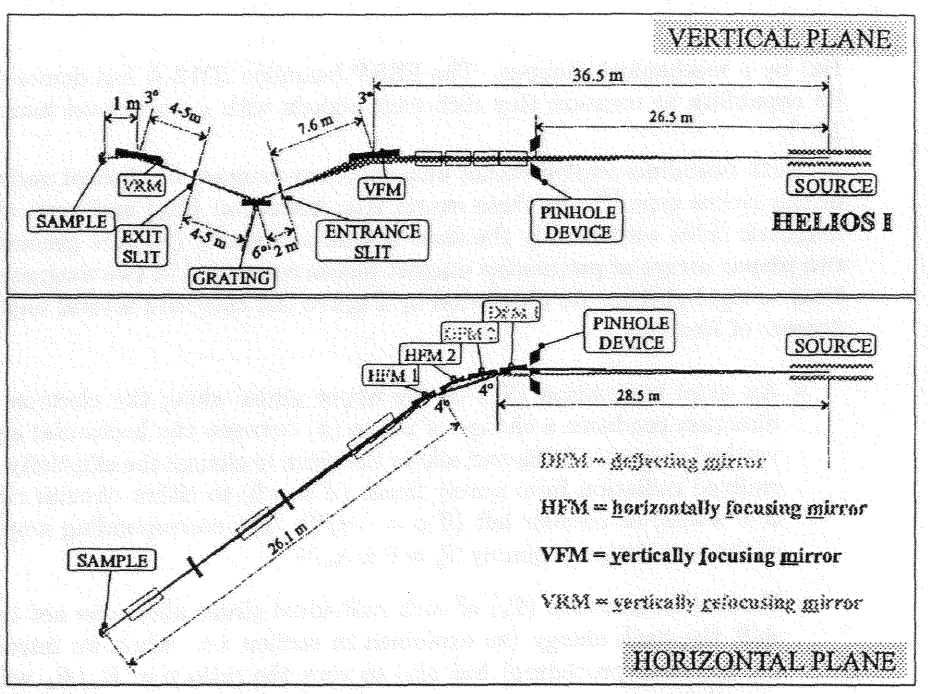

Figure 23: Layout of the "Double-Head Dragon" spectrometer of the ESRF beamline ID-12B dedicated to polarization dependent XAS studies in the soft X-ray range (400 eV - 1800 eV).

Hz) by a mechanical chopper. The ESRF beamline ID12-A has demonstrated its capability to measure tiny dichroism signals with a noise level lower than 10^{-4}.

Both beamlines exploit rather unusual X-ray sources, *i.e.* helical undulators of the Helios type.[296] In these exotic IDs, horizontal (B_x) and vertical (B_z) magnetic fields with strictly the same spatial periodicity (λ_u) are generated by two planar arrays of permanent magnet blocks assembled in two magnetic jaws fixed to rigid girders. As illustrated by **Figure 25**, there are several important degrees of freedom:

- An axial translation (T_y) of the upper girder along the electron beam direction produces a change of phase (ϕ) between the horizontal and the vertical magnetic fields and allows the users to change the ellipticity of the emitted radiation from purely linear (if $\phi = 0$) to either circular right (if $\phi = +\pi/2$) or circular left (if $\phi = -\pi/2$). The corresponding amplitude of the translation is simply $T_y = 0 \pm \lambda_u/4$

- Vertical translations (T_z) of each individual girder allow one not only to shift the peak energy (as explained in section *i.e.* when we introduced the gap-scan procedure) but also to vary the ratio $\rho = B_x/B_z$ which is essential to generate circular ($\rho = 1$) or elliptic ($\rho < 1$) polarization and control the relative intensities of emitted odd harmonics.[297]

Alternative designs have also been proposed.[298] There is a noticeable peculiarity associated with Helios-I which has been split into two segments:[296] a "*magnetic chicane*" slightly perturbs the direction of injection of the electrons in both segments with the practical consequence that the undulator emits two slightly divergent X-ray beams deflected in a symmetric way with respect to the direction of the incoming electron beam which also coincides with the direction of emission of the second undulator Helios-II. Since the two segments of Helios-I have been designed to be out of phase, the first beam denoted Helios-IA is *left* (right) circularly polarized while the second beam Helios-IB is *right* (left) circularly polarized and *vice-versa*. One beam or the other can be alternatively selected by a fast mechanical chopper which also delivers a time reference to a phase sensitive readout electronics (digital lockin system): a fast modulation of the polarization is particularly suitable to minimize the undesirable effects of source instabilities. Although the deflection angle induced by the magnetic chicane is as small as $200 - 340\ \mu rad$, this is enough to allow the *three* beams, *i.e.* Helios-IA, Helios-II, Helios-IB to be fully separated at 26.5 m from the source, *i.e.* at the frontend of the beamline. As illustrated by **Figure 23**, two mirrors (DFM-1 + DFM-2) deflect the two beams Helios-IA + Helios-IB towards the side branch beamline ID-12B whereas the central beam emitted by Helios-II is used independently and simultaneously by the straight branch beamline ID-12A which is operated in parallel.[53] Note that the mirrors intercepting the direct undulator beams are made of CVD-silicon carbide in order to accept a huge heat load without suffering any significant deformation. The mirrors have been polished to a microroughness of 3 Å (*RMS*) and their measured slope errors were below 1 arcsecond. Recently, a third helical undulator has been installed on the same straight section of the storage ring and its direction of emission strictly coincides with the axis of Helios-II. This new device has been designed

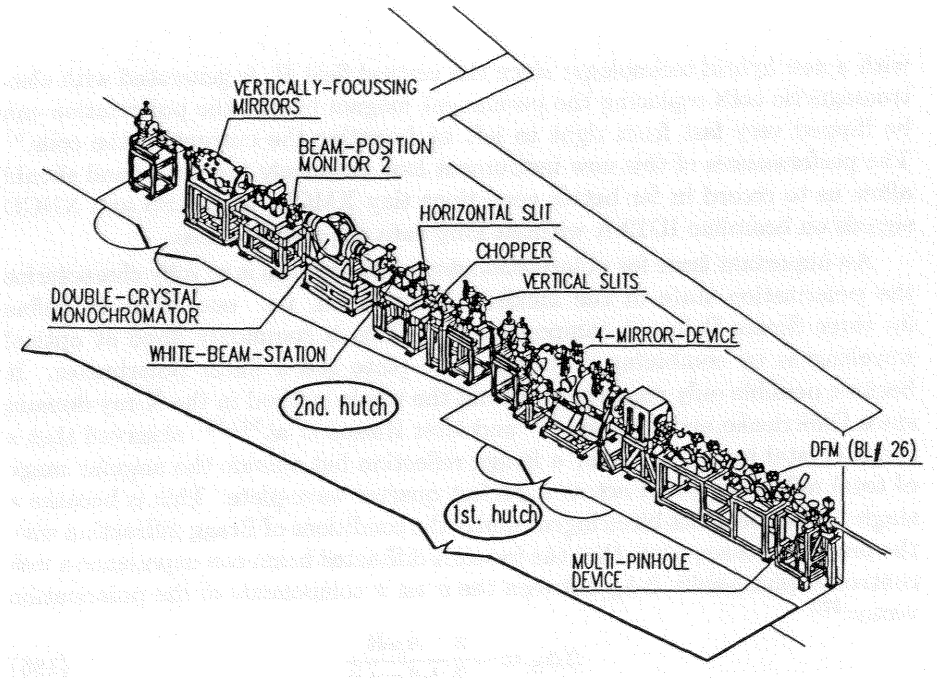

Figure 24: Layout of the ESRF beamline ID-12A dedicated to polarization dependent XAS studies at higher energies (1.5 keV - 15 keV).

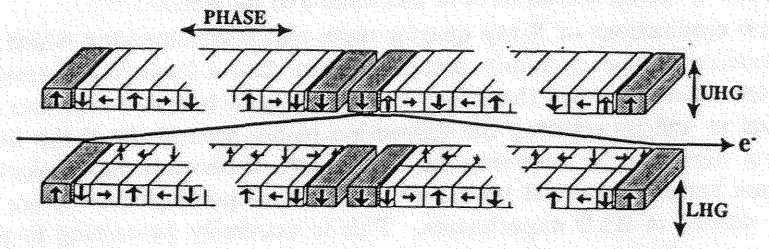

Figure 25: Magnetic design of the helical undulator Helios-I. The shaded magnets make up the magnetic chicane producing two slightly divergent X-ray beams of opposite polarization. UHG and LHG refer to vertical translation modifying the upper and lower half-gaps respectively. PHASE is an axial translation controlling the polarization state of the emitted radiation.

with a new hybrid technology: since the vertical field B_z is generated with electromagnetic coils replacing the permanent magnet blocks, the polarization can be flipped very fast from right to left by inverting the current in the coils.[51] The performances of this new instrument look extremely promising and should allow us to record in far better conditions tiny XMCD, MEXAFS and XNCD signals on beamline ID12-A without long data acquisition times.

An important issue for polarization dependent studies is to fully characterize the polarization state of the incident X-ray beam, *i.e.* one needs to define its three Stokes-Poincaré components P_j. This is commonly done at optical wavelengths by combining a quarter-wave plate and a linear polarimeter. It became possible only recently to extend the whole method in the X-ray domain since Dmitrienko and Belyakov[299] and later Hirano *et al.*[300,301] observed that a single crystal tuned very near a Bragg reflection but outside the angular range of total reflection, could act as a perfect quarter wave-plate. This is because a single crystal becomes birefringent under the conditions of Bragg diffraction with the practical consequence that the forward-diffracted beam can experience a well controlled phase-shift $\Delta\phi_B$ between the σ an π components of the polarization vector:[302]

$$\Delta\phi_B = -\frac{\pi}{2}\frac{A_B \delta t}{\Delta\vartheta \cos\psi} \tag{186}$$

In the latter equation, δt is the crystal thickness; ψ is the angle between the incident beam wavevector and the normal to the crystal; $\Delta\vartheta$ is the angular offset (defined as the difference between the true angle of incidence ϑ_B and the Bragg angle ϑ_B^0 at the middle of the reflection profile) and A_B is a factor which depends on energy and on the nature of the crystal. For $\Delta\phi_B = \pm\pi/2$ a circularly polarized beam is thus transformed into a linearly polarized beam just as with a quarter-wave plate. Diamond crystals or ultra-thin silicon crystals featuring a reasonably good transmissivity have been used as quarter-wave plates in the energy range of beamline ID-12A.[53,303] Coupled to various types of linear polarimeters, these devices made it possible to measure the circular polarization rates P_3 of both helical undulators Helios-I and Helios-II: typically, a circular polarization rate in excess of 97% was measured for Helios-I.[303]

New applications of X-ray quarter wave plates are emerging which exploit the conversion of a circularly polarized beam into a linearly polarized beam with the advantage that the orientation of the polarization vector can now be selected at will by rotating the diffraction planes around the X-ray beam direction. Moreover, by reverting the sign of $\Delta\vartheta$, it becomes straightforward to generate linearly polarized beams with orthogonal polarization vectors as precisely desired in XLD experiments. This is extremely interesting in practice because one does not need any longer to rotate the sample, which often turns out to be difficult if the latter is inserted in a vacuum chamber, a bulky cryostat or between the poles of a heavy magnet. For instance, this technique made it possible to detect very small signals of X-ray Magnetic Linear Dichroism with an unsurpassed sensitivity in the range of 10^{-4} using a magnetically oriented sample located in a 7T superconducting magnet.[53,304] We expect further developments of this technique in the near future, especially for organometallic complexes oriented in aligned liquid crystals[305] or for hemoproteins in oriented membranes.[306,307]

2. Time-Resolved Studies

What is to be measured ? From a phenomenological point of view, there are four distinct classes of systems evolving with time:

- The most common class (A) concerns systems which suffer some *irreversible* transformation after a single shot excitation, a chemical reaction ...or time dependent radiation damages under the very intense X-ray beam. For such systems, one is most often interested in catching any structural information of a short living species.

- Another class (B) concerns systems for which *cyclically repetitive excitations* can be carried out with the same sample which is supposed to return reversibly into its initial state. Many types of excitations can be used: photoexcitation, electrical or mechanical excitations, Temperature jumps, Pressure jumps *etc...* The sampling time during which X-ray data are accumulated has implicitly to be kept short with respect to the relaxation time of the system but the statistics is recovered by reproducing the experiment as many times as possible. If two species have very different time-response and coexist in a mixture, one may try to exploit such cyclic excitation to create artificially the conditions of a *dynamical discrimination, e.g.* by properly delaying in time the data acquisition.

- It is sometimes possible to define experimental conditions which make it possible to investigate a time evolving system *in a quasi-stationary state.* Such systems define class (C). By extension, the investigation of quenched meta-stable states are regrouped in this category.

- The last category (D) concerns systems *fluctuating* with time: the problem is then to measure the time-correlation function of the corresponding random process which can be connected with various dynamical properties such as a diffusion rate or a chemical relaxation rate.

A priori, one may think of using XAS to characterize these various classes of time-evolving systems. It is however essential to realize, as an important preamble, that part of the structural information which one would like to find in EXAFS spectra may unfortunately vanish in an excited or reactive state. This is because the transformation of species **I** into a structurally different species **J** can be modelled as a sort of diffusional process with random jumps along a specific internal (or chemical path) coordinate, this process being typically hindered by a weak enthalpy barrier. As discussed in section II.B.4, the only quantity that has a physical meaning is the configuration average of the absorption cross section: we have therefore to consider the potential surface associated with the internal chemical coordinate with the practical result that there will be *an additional Debye-Waller damping factor* σ^2_{chem} which may have a quite dramatic effect on the EXAFS oscillations if the low frequency vibrational levels are populated. In the worst cases, the EXAFS signal may vanish. A typical illustration of that situation has been reported by Goulon *et al.*[308] when they tried to analyze the EXAFS spectra of the dinitrosyl-dicarbonyl iron complex $Fe\,(NO)_2\,(CO)_2$ dissolved in tetrahydrofuran (THF) or acetonitrile (MeCN) : while the contribution of the dinitrosyl ligands was easily identified, it turned

out to be impossible to detect any EXAFS signal from the carbonyl ligands.[69,308] The clue to this puzzling result was found later when it was discovered by labelling the carbonyl groups with ^{14}C that there was a rapid exchange taking place in solution between free and bound ligands. It has also been found that this dynamical exchange process affected indirectly the multiple scattering paths of the more rigidly bound dinitrosyl moiety $Fe(NO)_2$.[69] A similar warning message concerning a dynamical damping of the EXAFS oscillations in systems which are subject to *fast* chemical exchanges had already been passed in the early eighties by Sham *et al.*[309]

***Irreversible Processes*:** As far as class (A) is concerned, the most obvious strategy is to shorten the data acquisition time. This can be done without a too severe penalty in terms of signal-to-noise ratio with the intense undulator sources available at third generation SR facilities. Again two complementary technical options can be envisaged:

- **Quick-scan Technique**:

This method has been pioneered at HASYLAB (Hamburg-Germany) for several years by Frahm[310,311] and also at LURE (Orsay-France) by Lagarde *et al.*[312] It consists in scanning *continuously* the Bragg angle which selects the energy of a double crystal monochromator. As underlined by Dobson *et al.* from the SERC (Daresbury-U.K.), this technique offers the major advantage that it is compatible with a Fluorescence Detection scheme.[313–315] At the ESRF beamline ID-26 which is dedicated to XAS studies on dilute samples, the continuous scan of the double crystal monochromator can be synchronized with a continuous scan of the magnetic gap(s) of either a single undulator or of two phased undulators.[316] As illustrated by **Figure 26**, it turned out to be possible to record XANES and EXAFS spectra of reasonably good quality for a solution of carboxy-myoglobin at a concentration of 7 mM in very short times: $\Delta t_{XANES} = 3$ s and $\Delta t_{EXAFS} = 10$ s *i.e.* with a data acquisition time of less than 10 ms per data point. This result looks particularly promising because the probability for developing severe radiation damages over such short data collection times is dramatically reduced.

- **Energy Dispersive Spectrometry**

Energy Dispersive Monochromators (EDM) offer the decisive advantage for time-resolved studies that the entire spectrum is recorded *simultaneously*. This is a fairly old concept in the X-ray range: such an EDM was used by Cauchois *et al.*[317] to record on a photographic plate the very first X-ray absorption spectrum measured in Europe with a Synchrotron Radiation source. Typically, the double crystal monochromator is replaced with an energy dispersing crystal operated either in Bragg or Laue geometry at a fixed angle of incidence and which refocus the beam at the sample location. A position sensitive detector makes it possible to recover the Intensity-Energy correlation which is necessary to yield the absorption spectrum. The EDM concept was resurrected in the early eighties by Matsushita *et al.*[318,319] who replaced the photographic plate by a photodiode array with modern readout electronics. Matsushita *et al.*[320] were also the first

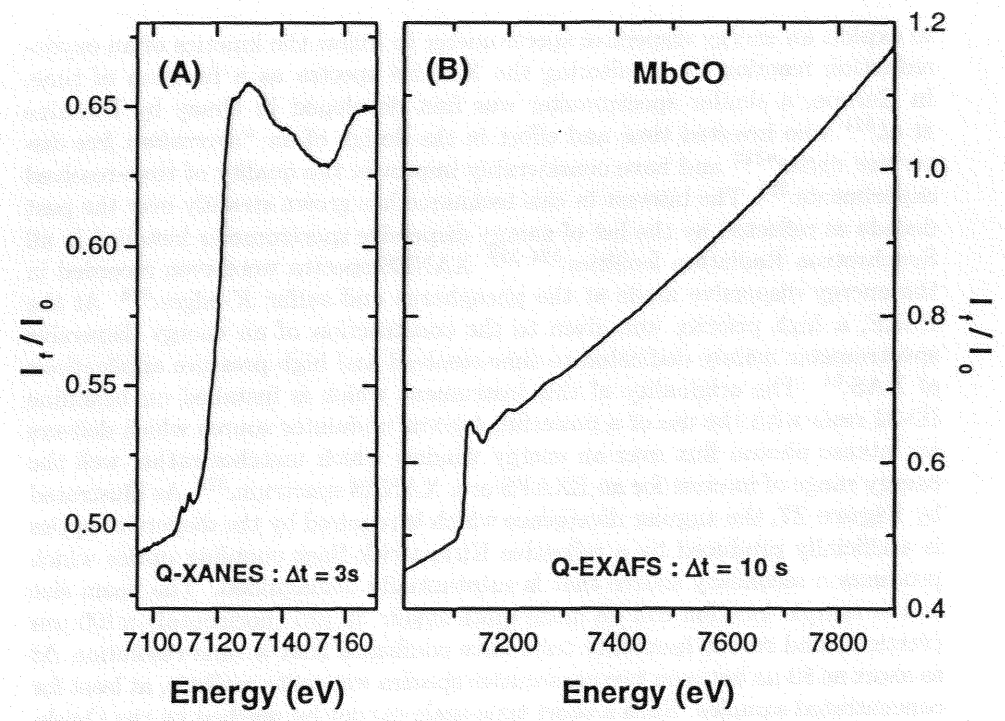

Figures 26: Quick Gap-scan at the ESRF beamline ID-26:

Figure 26A : XANES spectrum of an aqueous solution of MbCO (7mM) recorded in a total integrated time $\Delta t \leq 3s$.

Figure 26B : Full EXAFS spectrum of the same solution recorded in a total integrated time $\Delta t \leq 10$ s.

to exploit an energy dispersive spectrometer to follow the kinetics of an oxydo-reduction reaction by monitoring the XANES spectra as a function of time. In Europe, a similar spectrometer was first developed in Orsay by Fontaine *et al.*[321] who invested time and effort in the design of an "*aberration free dispersive optics*"[322] and have considerably improved the quality of time-resolved experiments.[323] The interest in this technique has grown steadily over the past decade as reflected by the list of energy dispersive spectrometer installed in all Synchrotron Radiation facilities.[324–328] XANES spectra were even recorded in the energy dispersive mode at the phosphorus and sulfur K-edges.[326] At the ESRF, a high priority was given to the construction of an energy dispersive spectrometer mainly dedicated to time-resolved and high pressure applications of XAS.[54] The originality of this instrument which is installed on beamline ID-24 rests with the use of a powerful, *tapered* undulator source which delivers an intense photon flux over an energy window which matches rather well the energy range of interest for an EXAFS or a XANES spectrum.[329] As illustrated by **Figure 27**, the angular divergence which is required by the dispersive optics is artificially produced by a reflective Kirkpatrick-Baez coupling optics which produces a secondary source that is substantially demagnified. The beam size at the sample location can be made quite small: 30 μm (horizontal) $\times 100$ μm (vertical) and recent feasibility tests have confirmed that a time resolution Δt as short as 50 μs between two consecutive spectra was quite realistic, at least for concentrated samples. Such a short time-scale cannot be reached by the Quick-scan technique. Unfortunately, energy dispersive spectrometry still suffers from well identified limitations:[329,330]

(*i*) The method is hardly compatible with Fluorescence Detection as long as a parallel detection of the whole spectrum is required. Some potentiality for Fluorescence Detection can be recovered in the so-called *Turbo-Scan* technique which consists in moving very fast a thin slit in the energy dispersed beam but the price to be paid is the loss of detection parallelism, a loss of intensity by three orders of magnitude and a much longer overall data acquisition. Nevertheless, there are experiments which can perfectly accommodate such degraded experimental conditions.

(*ii*) For powdered mixtures, the local inhomogeneities and the large scattered intensity concur to spoil the space-energy correlation and to degrade the quality of the spectra.

(*iii*) The difficulty to design suitable spatially resolved I_0 beam intensity monitors let the experiments be more sensitive to the time-dependent source instabilities.

(*iv*) The spectral range of an energy dispersive EXAFS spectrum is somewhat restricted compared to a conventional EXAFS and the data reduction requires a more delicate energy calibration procedure.

Nevertheless, in spite of these technical difficulties, energy dispersive spectrometry keeps an unequalled potentiality for time-resolved studies in the millisecond time scale, with numerous potential applications in electrochemistry.

Cyclically Repetitive Processes : The feasibility of *time-resolved photolysis XAS experiments* with 100μs time resolution was first demonstrated by Huang in 1983.[331–333] The flash photolysis of carbonmonoxy-myoglobin was selected as a test example. The concept of the experiment looks rather simple: for every

Beamline ID24 at ESRF

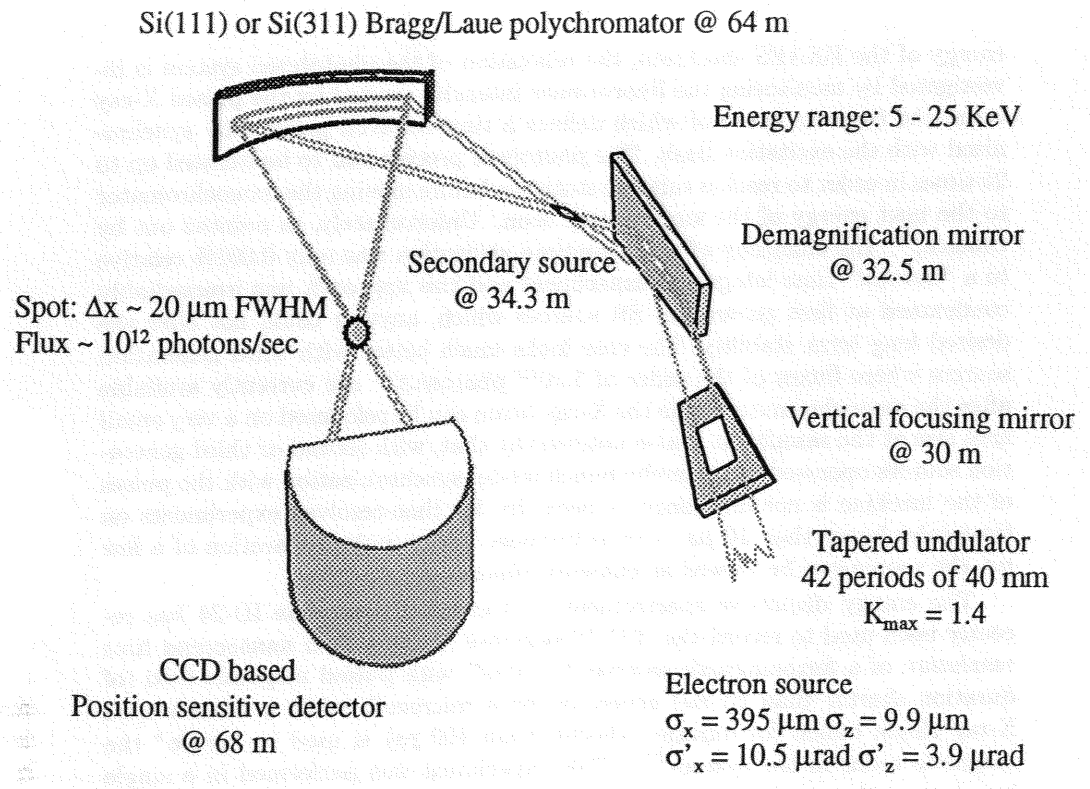

Figure 27: Schematic optical layout of the energy dispersive spectrometer of the ESRF beamline ID-24 dedicated to time-resolved studies. Full XANES or EXAFS spectra can be recorded within a time-scale $\Delta t \geq 100$ μs.

energy of the EXAFS spectrum, the relaxation of the photolyzed system is investigated by monitoring the fluorescence intensity excited by the pulsed X-ray beam the time structure of which defines a time-resolved probe fully synchronized with the excitation flash. The photolysis process had to be iterated up to 25 times in order to reach a suitable statistics before moving the monochromator to the next energy of the step by step scan. Unfortunately, as pointed out by Chance,[334] the efficiency of the beamtime utilization was only 0.001% relative to a *"normal"* time integrated experiment and this approach was irremediably condemned at first generation SR sources which, anyway could not offer the desired long term stability. The case looks much better with third generation sources where fluxes of the order of 5.10^{12} photons.s^{-1} are currently available after the monochromator while the X-ray beam can be refocused on a very small spot size at the sample. It is also noteworthy that, with second or third generation sources operated in the multi-bunch mode, synchronization with the pulses of the machine is not any longer a necessity for time-resolved experiments on timescales larger than 10 μs : this is because, with a pulse separation of a few ns, the source can be viewed as *quasi-continuous.*

The energy dispersive spectrometer of the ESRF beamline ID-24 has recently been used to record the *XMCD response function with nanosecond time resolution* of a ferromagnetic sample *"pumped"* with pulsed magnetic field (of duration shorter than 23 ns) generated by a microcoil, while a time-delayed X-ray single bunch (of duration shorter than 100 ps) is used to *"probe"* the magnetic order in the system.[335] This experiment was performed in a single bunch operation mode of the machine, *i.e.* with a repetition rate of ~355 kHz: typically 6×10^7 X-ray pulses are needed to generate a full XMCD spectrum with a decent statistics in *ca.* 3 minutes.

At the ESRF beamline ID-12A, *a sub-nanosecond time-resolved experiment* directly related to porphyrin chemistry has been performed: it concerned the detection of the decay curve of the Q-band luminescence ($\lambda_{max} = 690\ nm$) of a powdered sample of (TPP)Zn under X-ray excitation.[336] The time-resolved X-ray Excited Optical Luminescence (XEOL) signal was detected with a so-called *dissector* tube[337] which was synchronized with the electron bunch repetition rate and had an instrumental time resolution better than 10 ps. As illustrated by **Figure 28-A**, the kinetics of the XEOL decay is characterized by two different relaxation times: $\tau_1 \leq 15\ ps$ and $\tau_2 \simeq 650\ ps$. By using an appropriate time window, it was possible to isolate the contribution of the fast decaying component for every X-ray excitation energy and to record a XANES spectrum which is *site selective of the fast decaying species.* The latter XANES spectrum is reproduced in **Figure 28-B.** Recall that Goulon *et al.*[338] had already demonstrated in the past that the integrated XEOL emission could be used to record the XANES and EXAFS spectra of several *regular* porphyrins such as: (TPP)Zn ; (TBP)Zn ; (OMP)GaOH or (OEP)$SnCl_2$. The interest in XEOL excitation spectra was stimulated by the discovery that *site selective* EXAFS spectra could be obtained in the case of macroscopic *mixtures* of two samples containing the same absorbing element: this was established by Goulon and coworkers[339] who used a mixture of ZnO + (TPP)Zn to demonstrate this potentiality. Time-resolved XEOL spectroscopy should be a powerful extension of this technique and could help to discriminate between different excitation processes or different species.

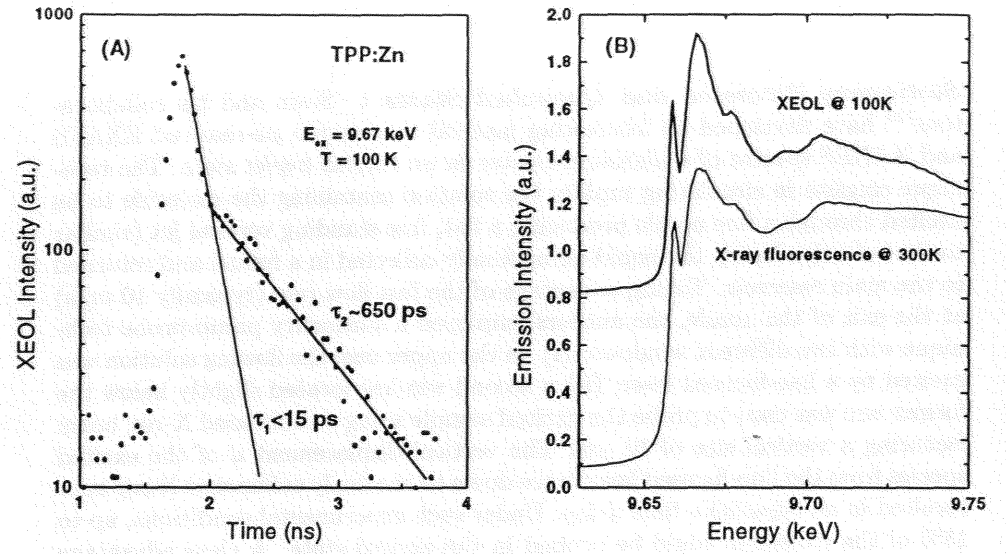

Figures 28: Sub-nanosecond time-resolved X-ray Excited Optical Luminescence (XEOL) spectra of (TPP)Zn recorded at the zinc K-edge at the ESRF beamline ID-12A:

Figure 28A: Time resolved decay of the XEOL intensity revealing two fast relaxation channels characterized with the respective decay times: $\tau_1 \leq 15$ ps and $\tau_2 \approx 650$ ps.

Figure 28B: Zn K-edge XANES spectra of (TPP)Zn recorded by monitoring:

i) the total X-ray fluorescence yield at 300 K ;

ii) *only* the fast decaying XEOL component that is characteristic of an ultra-short living excited state.

(Note that the XEOL intensity was collected within a short time window: $\Delta t \leq 1$ ns).

Stationary Processes and Quenched States : Stern and his collaborators[340] have developed an interesting method to measure μs-resolved EXAFS and XANES spectra of a platinum cluster *in an excited triplet state.* The technique consists in circulating rapidly the solution containing the molecule to be excited through a fine nozzle producing a flat, free standing vertical jet (similar to that of a dye laser), the liquid being finally collected in a funnel and returned to the main reservoir. Taking advantage of the fast flow rate (typically 10 m/s) at the exit of the nozzle, the authors employed a stationary pump-probe technique with two different windows: (*i*) in the upper one, the flowing solution was excited by a line-focused laser; (*ii*) a second window located slightly below the former one was used to probe the excited sample using a collimated X-ray beam featuring a vertical size of 10 μm. The vertical displacement d of the excited species from the line-focused laser trace down to the finely collimated X-ray spot resulted in an *adjustable time delay.* Under such experimental conditions, up to 18% of the molecules could be probed in the excited state. A clear advantage of this technique is that it is fully compatible with Fluorescence Detection. The only restriction seems to be that photolysis *has to be fast*, the latter handicap being compensated by the fact that a great deal of laser power can be used without heating the sample by more than a fraction of a degree.

Reactive intermediates in fast enzymatic reactions could also be investigated using Bray's rapid freeze technique:[341] after fast mixing, the solution is ejected again very fast from a nozzle into a cold isopentane bath. The quenching time is much longer, *i.e.* typically of the order of 5 *ms.* This method has been used by Saigo *et al.*[342,343] to record EXAFS and XANES of various reactive intermediates formed with hemoproteins. The same technique was exploited by George *et al.*[344] for different applications.

Fluctuation Correlation Techniques : A new technique called *X-ray Fluorescence Correlation Spectroscopy* (XFCS) has been proposed in 1991 by Goulon *et al.*[345] to investigate systems fluctuating with time. It was suggested that this technique might be appropriate to study *very slow* diffusional processes such as the lateral diffusion of hemoproteins or ionophores in a biological membrane. If the primary exciting X-ray beam can be focused on a very small volume, the number density of dilute absorption centers will fluctuate with time as a consequence of random diffusional processes and the autocorrelation function of the radiated X-ray fluorescence intensity should give access to the diffusion rates of the competing diffusion processes. In 1998, Shina and coworkers have reported the first experience confirming the remarkable potentiality of this technique in molecular dynamics.[346]

References

1. Azaroff, L.V., Ed. *X-ray Spectroscopy*; McGraw-Hill, Inc.: New York, 1974.

2. Koningsberger, D.C., Prins, R. Eds *X-Ray Absorption: Principles, Applications, Techniques of EXAFS, SEXAFS and XANES*; Chemical Analysis Series, 92, John Wiley & Sons (Wiley-Interscience Publication): New York, 1987.

3. Stöhr, J. *NEXAFS Spectroscopy*; Springer Series in Surface Sciences, *25*, Ertl,G., Gomer R., Mills, D.L., Eds.; Springer-Verlag: Berlin, First Edition 1992; Corr. 2nd Printing 1996.

4. Iwasawa, Y., Ed. *X-ray Absorption Fine Structure for Catalysts and Surfaces*; Series on Synchrotron Radiation Techniques and Applications, Vol.2; World Scientific: Singapore, New Jersey, London, Hong Kong, 1996.

5. Durham, P.J. *Theory of XANES;* In *X-Ray Absorption: Principles, Applications, Techniques of EXAFS, SEXAFS and XANES*; Koningsberger, D.C., Prins, R., Eds.; Chemical Analysis Series, 92; John Wiley & Sons (Wiley-Interscience Publication): New York, 1987; Chapter 2, pp. 53-84.

6. Bianconi, A. *XANES Spectroscopy*; In *X-Ray Absorption: Principles, Applications, Techniques of EXAFS, SEXAFS and XANES*; Koningsberger, D.C., Prins, R., Eds; Chemical Analysis Series, 92; John Wiley & Sons (Wiley-Interscience Publication): New York, 1987; Chapter 11, pp. 573-662.

7. Bianconi, A.; Garcia, J.; Benfatto, M. *XANES in Condensed Systems*; In *Topics in Current Chemistry*; Springer-Verlag: Berlin, Heidelberg, New-York, 1988; Vol. 145, pp 30-67.

8. Azaroff, L.V.; Pease, D.M. *X-ray Absorption Spectra;* In *X-ray Spectroscopy*; Azaroff, L.V., Ed.; McGraw-Hill, Inc.: New York, 1974; Chapter 6, pp. 284-337.

9. Wong, J.; Lytle, F.W.; Messmer, R.P.; Maylotte, D.J. *Phys. Rev. B* **1984**, *30*, 5596-5610

10. Brouder, Ch. *J. Phys. Condens. Matter* **1990**, *2*, 701-738.

11. Penner-Hahn; J. E.; Benfatto; M.; Hedman, B.; Takahashi, T.; Doniach, S.; Groves, J. T.; Hodgson, K. O. *Inorg. Chem.* **1986**, *25*, 2255-2259.

12. Schütz, G.; Wagner, W.; Wilhelm, W.; Kienle, P.; Zeller, R.; Frahm, R.; Materlick, G. *Phys. Rev. Lett.* **1987**, *58*, 737-740.

13. Chen, C.T.; Sette, F.; Ma, Y.; Modesti, S. *Phys. Rev. B* **1990**, *42*, 7262-7265.

14. Chen, C.T.; Smith, N.V.; Sette, F. *Phys. Rev. B* **1991**, *43*, 6785-6787.

15. Thole, B.T.; Carra, P.; Sette F.; Van der Laan, G. *Phys. Rev. Lett.* **1992**, *68*, 1943-1946.

16. Carra, P.; Thole, B.T.; Altarelli, M.; Wang, X.D. *Phys. Rev. Lett.* **1993**, *70*, 694-697.

17. Stöhr, J.; Wu, Y. *X-Ray Magnetic Circular Dichroism: Basic Concepts and Theory for 3d Transition Metal Atoms*; In *Synchrotron Radiation Sources*; Schlachter, A. S., Wuilleumier, F. J., Eds.; Kluwer Academic, Dordrecht: Dordrecht, 1994; Vol. 254, pp 221-252.

18. Stöhr, J.; Nakajima R. *J. Phys. IV France* **1997**, *7-C2*, 47-57.

19. De Groot, F. M. F. *J. Electron Spectrosc. Relat. Phenom.* **1994**, *67*, 529-622.

20. Arrio, M.-A.; Sainctavit, Ph.; Brouder, Ch.; Deudon, C. *Physica B* **1995**, *208 & 209*, 27-28.

21. Ralston, C.Y.; Chen, J.; Peng, G.; George, S.J.; Van Elp, J.; Cramer, S.P. *Physica B* **1995**, *208 & 209*, 203-208.

22. Van Elp, J.; Peng, G.; Zhou, Z.H.; Mukund, S.; Adams, M.W.W. *Phys. Rev. B* **1996**, *53*, 2523-2527.

23. Peng, G.; Van Elp, J.; Jang, H.; Que Jr., L.; Armstrong, W.H.; Cramer, S.P. *J. Am. Chem. Soc.* **1995**, *117*, 2515-2519.

24. Goulon, J.; Goulon-Ginet, C.; Rogalev, A.; Gotte, V.; Malgrange, C.; Brouder, Ch. *J. Chem. Phys.* **1998**, *108*, 6394-6403.

25. Natoli, C.R.; Brouder, Ch.; Sainctavit, Ph.; Goulon, J.; Goulon-Ginet, C.; Rogalev, A. *Eur. Phys. J. B* **1998**, *4*, 1-11.

26. Guilard, R.; Lopez, M.A.; Tabard, A.; Richard, P.; Lecomte, C.; Brandès, S.; Hutchinson, J.E.; Collman, J.P. *J. Am. Chem. Soc.* **1992**, *114*, 9877-9889.

27. Lachkar, M.; Tabard, A.; Brandès, S.; Guilard, R.; Atmani, A.; De Cian, A.; Fischer, J.; Weiss, R. *Inorg. Chem.* **1997**, *36*, 4141-4146.

28. Kronig, R. de L. *Z. Physik* **1931**, *70*, 317-323; *Z. Physik* **1932**, *75*, 191-210; *Z. Physik* **1932**, *75*, 468-475.

29. Stern, E.A. *Phys. Rev. B* **1974**, *10*, 3027.

30. Stern, E.A.; Sayers, D.E.; Lytle, F.W. *Phys. Rev. B* **1975**, *11*, 4838

31. Natoli, C. R. *Physica B* **1995**, *208 & 209*, 5-10.

32. Gotte, V. Ph.D. Thesis, Université Henri Poincaré de Nancy-I, France, 1999.

33. Jaklevic, J.; Kirby, J.; Klein, M.P., Robertson, A.S.; Brown, G.S; Eisenberger, P. *Solid State Commun.* **1977**, *23*, 679.

34. Goulon, J.; Goulon-Ginet, C.; Cortès, R.; Dubois, J.-M. *J. Phys. France* **1982**, *43*, 539-548.

35. Stojanoff, V.; Hämäläinen, K.; Siddons, D.P.; Hasting, J.B.; Berman, L.E.; Cramer, S.P.; Smith, G. *Rev. Sci. Instrum.* **1992**, *63*, 1125-1127.

36. Masciovecchio, C.; Bergmann, U.; Krisch, M.; Ruocco, G.; Sette, F.; Verbeni, R. *Nucl. Instrum. Meth. B* **1996**, *111*, 181-186.

37. Wang, Xin; Grush, M.; Froeschner, A.G.; Cramer, S.P. *J. Synchrotron Rad.* **1997**, *4*, 236-242.

38. Bergmann, U.; Cramer, S.P. *Proc. SPIE* **1999**, in press.

39. Hämäläinen, K.; Siddons, D.P.; Hasting, J.B.; Berman, L.E. *Phys. Rev. Lett.* **1991**, *67*, 2850-2853.

40. Tsutsumi, K. *J. Phys. Soc. Japan* **1959**, *14*, 1418.

41. Tsutsumi, K.; Nakamori, H.; Ishikawa, K. *Phys. Rev. B* **1976**, *13*, 929.

42. Hämäläinen, K.; Kao, C.C.; Hasting, J.B.; K., Siddons, D.P.; Berman, L.E.; Stojanoff, V.; Cramer, S.P. *Phys. Rev. B* **1992**, *46*, 14274.

43. Wang, X.; Randall, C.; Peng, G.; Cramer, S.P. *Chem. Phys. Lett.* **1995**, *243*, 469-473.

44. Wang, X.; De Groot, F. M. F.; Cramer, S. P. *Phys. Rev. B* **1997**, *56*, 4553-4564.

45. Wang, X; Cramer, S.P. *J. Phys. IV France* **1997**, *7-C2*, 361-363.

46. Goulon, J.; Rogalev, A.; Krisch, M.; Sette, F.; Gotte, V.; Goulon-Ginet, C.; Barbe, J.-M.; Guilard, R.; Gauthier, Ch. To be published.

47. Grush, M. M.; Christou, G.; Hämäläinen, K.; Cramer, S.P. *J. Am. Chem. Soc.* **1995**, *117*, 5895-96.

48. Bergman, U.; Grush, M.M.; Horne, C.R.; DeMarois, P.; Penner-Hahn, J.E.; Yocum, C.F.; Wright, D.W.; Dubé, C.E.; Armstrong, W.H.; Christou, G.; Eppley, H.J.; Cramer, S.J. *J. Phys. Chem. B* **1998**, *102*, 8350-8352

49. Heald, S.M. *EXAFS with Synchrotron Radiation*; In *X-Ray Absorption: Principles, Applications, Techniques of EXAFS, SEXAFS and XANES*; Koningsberger, D.C., Prins, R., Eds.; Chemical Analysis Series, 92; John Wiley & Sons (Wiley-Interscience Publication): New York, 1987; Chapter 4, pp. 119-161.

50. Krinsky, S.; Perlman, M.L.; Watson, R.E. *Characteristics of Synchrotron Radiation and its Sources;* In *Handbook of Synchrotron Radiation;* Eastman, D.E., Farge, Y., Eds.; Vol.Ia; Koch, E.E., Ed.; North-Holland Publishing Company.: Amsterdam, 1983; Chapter 2, pp. 65-171.

51. Chavanne, J.; Elleaume, P.; Van Vaerenbergh, P. *J. Synchrotron Rad.* **1998**, *5*, 196-201.

52. Goulon, J.; Brookes, N.B.; Gauthier, Ch.; Goedkoop, J.; Goulon-Ginet, C., Hagelstein, M.; Rogalev, A. *Physica B* **1995**, *208 & 209*, 199-202.

53. Goulon, J.; Rogalev, A.; Gauthier, Ch.; Goulon-Ginet C.; Pasté, S.; Signorato, R.; Neumann, C.; Varga, L.; Malgrange, C. *J. Synchrotron Rad.* **1998**, *5*, 232-238.

54. Hagelstein, M.; San Miguel, A.; Fontaine, A.; Goulon, J. *J. Phys. IV France* **1997**, *7-C2*, 303-308.

55. Gauthier, Ch.; Solé, V.A.; Signorato, R.; Moguiline, E.; Goulon, J. *J. Synchrotron Rad.* **1999**, *7*, in press.

56. Rogalev, A.; Gotte, V.; Goulon, J.; Gauthier, Ch.; Chavanne, J.; Elleaume, P. *J. Synchrotron Rad.* **1998**, *5*, 989-991.

57. Natoli, C.R.; Benfatto, M. *J. Phys. France* **1986**, *47-C8*, 11-35.

58. Natoli, C. R.; Benfatto, M.; Doniach, S. *Phys. Rev. B* **1986**, *34*, 4682-4694.

59. Lee, P.A.; Pendry, J.B. *Phys. Rev. B* **1975**, *11*, 2795-2811.

60. Vedrinskii, R.; Novakovich, A.A. *Phys. Met. Metallogr.* **1975**, *39*, 1-8.

61. Ashley, C.A.; Doniach, S. *Phys. Rev. B* **1975**, *11*, 1279-1288.

62. Lloyd, P.; Smith, P.V. *Adv. Phys.* **1972**, *21*, 69-142

63. Roman, P. *Advanced Quantum Theory;* Addison-Wesley Series in Advanced Physics; Hamermesh, M., Ed.; Addison-Wesley Publishing Co., Inc.: Reading, MA, 1965.

64. Inkson, J.C. *Many-Body Theory of Solids: An Introduction*; Plenum Press: New-York, London, 1984; 2nd Printing 1986.

65. Brouder, Ch.: *Multiple Scattering Theory*; In *Magnetism and Synchrotron Radiation*; Beaurepaire, E., Carrière, B., Kappler, J.-P., Eds.; Les Editions de Physique France: 1997; Chapter 3, pp. 33-54.

66. Cabaret, D. Ph.D. Thesis, Université P. & M. Curie de Paris VI, France, 1997.

67. Gyorffy, B.L. *Phys. Rev.B* **1972**, *5*, 2382-84.

68. Gyorffy, B. L.; Stott, M.J. In *Band Structure Spectroscopy of Metals and Alloys*; Fabian, D.J., Watson, L.M., Eds; Academic Press: London, 1973; pp. 385-403; see also: *J. Solid State Comm.* **1971**, *9*, 613-617.

69. Bohr, F. Ph.D. Thesis, Université H. Poincaré de Nancy-I, France, 1993.

70. Dill, D.; Dehmer, J.L. *J. Chem. Phys.* **1974**, *61*, 692-699.

71. Brouder, Ch.; Alouani, M.; Bennemann, K. H. *Phys. Rev. B* **1996**, *54*, 7334-7349.

72. Brouder, Ch.; Ruiz-Lopez, M. F.; Pettifer, R. F.; Benfatto, M.; Natoli, C. R. *Phys. Rev. B* **1989**, *39*, 1488-1500.

73. Schaich, W.L., *Phys. Rev. B* **1984**, *29*, 6513-6519.

74. Gurman, S. J.; Binsted, N.; Ross, I. *J. Phys. C: Solid State Phys.* **1984**, *17*, 143-151.

75. Gurman, S. J.; Binsted, N.; Ross, I. *J. Phys. C: Solid State Phys.* **1986**, *19*, 1845-1861.

76. Gurman, S. J. In *Synchrotron Radiation and Biophysics*; Hasnain, S. S., Ed.; Ellis Horwood: New York, Chichester, 1990; pp. 9-42.

77. Vedrinskii, R. V.; Bugaev, L. A.; Levin, I. G. *Phys. Stat. Sol.* **1988**, *150*, 307-314.

78. Dehmer, J.L.; Dill, D. *J. Chem. Phys.* **1976**, *65*, 5327-5329.

79. Natoli, C.R. In *EXAFS and Near Edge Structure II*; Bianconi, A., Incoccia, L., Stipcich, S., Eds.; Springer Series in Chemical Physics; Springer-Verlag: Berlin, 1983; Vol.*27*, pp. 43-56.

80. Müller, J.E.; Wilkins, J.W. *Phys. Rev. B* **1984**, *29*, 4331-4348.

81. Natoli, C.R. In *EXAFS and Near Edge Structure III*; Hodgson, K.O., Hedman, B., Penner-Hahn, J.E., Eds.; Springer Proceedings in Physics; Springer-Verlag: 1984; Vol.*2*, pp. 38-42.

82. Sette, F.; Stöhr, J.; Hitchcock, A.P. *J. Chem. Phys.* **1984**, *81*, 4906.

83. Stöhr, J.; Sette, F.; Johnson, A.L. *Phys. Rev. Lett.* **1984**, *53*, 1684.

84. Ruiz-Lopez, M. F.; Rinaldi, D.; Esselin, C.; Goulon, J.; Poncet, J. L.; Guilard, R. *J. Phys. France* **1986**, *47-C8*, 637-640.

85. Ruiz-Lopez, M. F.; Natoli, C. R. *J. Chim. Phys.* **1989**, *86*, 905-910.

86. Hedin, L.; Lundqvist, B. I. *Solid State Physics*, Ehrenreich, H.; Seitz, F.; Turnbull, D., Eds.; Academic Press: 1969; Vol. *23*, pp. 1-181.

87. Hedin, L.; Lundqvist, B. I. *J. Phys. C: Solid State Phys.* **1971**, *4*, 2064-2083.

88. Ekardt, W.; Tran Thoai, D. B. *Solid State Commun.* **1981**, *40*, 939-942.

89. Lee, P.A.; Citrin, P.H.; Eisenberger, P.; Kincaid, B.M. *Rev. Mod. Phys.* **1981**, *53*, 769-806.

90. Teo, B.K. *J. Am. Chem. Soc.* **1981**, *103*, 3990-4001.

91. Boland, J.J.; Crane, S.E.; Baldeschwieler, J.D. *J. Chem. Phys.* **1982**, *77*, 142-153.

92. Co, M.S.; Hendrickson, W.A.; Hodgson, K.O.; Doniach, S. *J. Am. Chem. Soc.* **1983**, *105*, 1144-1150.

93. Alberding, N.; Crozier, E.D. *Phys. Rev. B* **1983**, *27*, 3374-3382.

94. Cramer, S.P.; Hodgson, K.O.; Steifel, E.I.; Newton, W.E. *J. Am. Chem. Soc.* **1978**, *100*, 2748-2761.

95. Ruiz-Lopez, M.F.; Loos, M.; Goulon, J.; Natoli, C.R.; Ballivet-Tkatchenko, D. *Physica B* **1989**,*158*, 231-233

96. Westre, T.E.; Di Cicco, A.; Filipponi, A.; Natoli, C.R.; Hedman, B.; Solomon, E.I.; Hodgson, K.O. *J. Am. Chem. Soc.* **1994**, *116*, 6757-6768.

97. Pettifer, R.; Foulis, D.L.; Hermes, C. *J. Phys. France* **1986**, *47-C8*, 545-550.

98. Strange, R.W.; Hasnain, S.S.; Blackburn, N.J.; Knowles, P.F. *J. Phys. France* **1986**, *47-C8*, 593-596.

99. Ruiz-Lopez, M.F.; Bohr, F.; Filipponi, A.; Di Cicco, A.; Tyson, T.; Benfatto, M.; Natoli, C.R. In *X-Ray Absorption Fine Structure;* Hasnain, S.S., Ed.; Ellis Horwood: New York, Chichester, 1991; pp.75-77.

100. Westre, T.E.; Di Cicco, A.; Filipponi, A.; Natoli, C.R.; Hedman, B.; Solomon, E.I.; Hodgson, K.O. *J. Am. Chem. Soc.* **1995**, *117*, 1566-1583.

101. Rehr, J. J.; Albers, R. C.; Natoli, C. R.; Stern, E. A. *Phys. Rev. B* **1986**, *34*, 4350-4353.

102. Rehr, J. J.; Albers, R. C. *Phys. Rev. B* **1990**, *41*, 8139-8149.

103. Rehr, J.J.; Mustre de Leon, J.; Zabinsky, S.I.; Albers, R.C. *J. Am. Chem. Soc.* **1991**, *113*, 5135-5140.

104. Mustre de Leon, J.; Rehr, J.J.; Zabinsky, S.I.; Albers, R.C. *Phys. Rev. B* **1991**, *44*, 4146-4156.

105. Zabinsky, S.I.; Rehr, J.; Ankudinov, A.; Albers, R.C.; Eller, M.J. *Phys. Rev. B* **1995**, *52*, 2995-3009.

106. Ankudinov, A.; Rehr J. *Phys. Rev. B* **1995**, *52*, 10214-10220.

107. Ankudinov, A. Ph.D. Thesis, University of Washington, U.S.A., 1996

108. Ankudinov, A. L.; Rehr, J. J. *J. Phys. IV France* **1997**, *7-C2*, 121-124.

109. Benfatto, M.; Natoli, C. R.; Filipponi, A. *Phys. Rev. B* **1989**, *40*, 9626-9635.

110. Poiarkova, A. V.; Rehr, J. J. *Phys. Rev. B* **1999**, submitted.

111. Loeffen, P. W.; Pettifer, R. F.; Fillaux, F.; Kearley, G. J. *J. Chem. Phys.* **1995**, *103*, 8444-8455.

112. Loeffen, P. W.; Pettifer, R. F.; Tomkinson, J. *Chem. Phys.* **1996**, *208*, 403-420.

113. Loeffen, P. W.; Pettifer, R. F. *Phys. Rev. Lett.* **1996**, *76*, 636-639.

114. Filipponi, A. *J. Phys.: Condens. Matter* **1995**, *7*, 9343-9356.

115. Mattheiss, L. F. *Phys. Rev.* **1964**, *133*, A1399-A1403; *Ibid.* **1964**, *134*, A970-A973.

116. Andersen, O. K.; Jepsen, O. *Phys. Rev. Lett.* **1984**, *53*, 2571-2574.

117. Jepsen, O.; Andersen, O.K. *Z. Phys. B* **1995**, *97*, 35-47.

118. Blaha, P.; Schwarz, K.; Luitz, J. Program "WIEN*97*", University of Wien, 1997.

119. Löwdin, P.O. *Adv. Phys.*, **1956**, *5*, 96.

120. Hohenberg, P.; Kohn, W. *Phys. Rev. B* **1964**, *136*, 864-871.

121. Kohn, W.; Sham, L.J. *Phys. Rev. A* **1965**, *140*, 1133-1138.

122. Slater, J.C. *Phys. Rev.* **1951**, *81*, 381

123. Slater, J. C.; Johnson, K. H. *Phys. Rev. B* **1972**, *5*, 844-853.

124. Slater, J. C. *The Self-Consistent Field for Molecules and Solids*; In *Quantum Theory of Molecules and Solids*; Mc Graw-Hill: New York, 1974; Vol. IV.

125. Gaspar, R. *Acta Phys. Acad. Sci. Hung.* **1954**, 3.

126. Hara, S. *J. Phys. Soc. Japan* **1967**, *22*, 710.

127. Gunnarsson, O.; Lundqvist, B. I. *Phys. Rev. B* **1976**, *13*, 4274-4298.

128. Vosko, S. H.; Wilk, L.; Nusair, M. *Can. J. Phys.* **1980**, *58*, 1200-1211.

129. Perdew, J. P.; Wang, Y. *Phys. Rev. B* **1992**, *45*, 13244-13249.

130. Schwarz, K. *Phys. Rev. B* **1972**, *5*, 2466-2468.

131. Case, D. A.; Karplus, M. *J. Am. Chem. Soc.* **1977**, *99*, 6182-6194.

132. Sontum, S., F.; Case, D. A. *J. Phys. Chem.* **1982**, *86*, 1596-1606.

133. Sontum, S. F.; Case, D. A.; Karplus, M. *J. Chem. Phys.* **1983**, *79*, 2881-2892.

134. Lee, P. A.; Beni, G. *Phys. Rev. B* **1977**, *15*, 2862-2883.

135. Perdew, J. P.; Burke, K.; Ernzerhof, M. *Phys. Rev. Lett.* **1996**, *77*, 3865-3868.

136. Perdew, J. P.; Zunger, A. *Phys. Rev. B* **1981**, *23*, 5048-5079.

137. Svane, A.; Gunnarsson, O. *Phys. Rev. Lett.* **1990**, *65*, 1148-1151.

138. Szotek, Z.; Temmernan, W. M.; Winter, H. *Phys. Rev. B* **1993**, *47*, 4029-4032.

139. Becke, A. *J. Chem. Phys.* **1993**, *98*, 1372-1377.

140. Godby, R. W. *Exchange and Correlation in Solids* In: *Unoccupied Electronic States*; Fuggle, J. C., Inglesfield, J. E., Eds.; Springer-Verlag: Berlin, Heidelberg, New York, 1992; Vol. 69, pp. 51-88.

141. Hedin, L. *Many-Body Effects;* In *X-ray Spectroscopy*; Azaroff, L.V., Ed.; Mc Graw-Hill, Inc.: New York, 1974; Chapter 5, pp. 226-283.

142. Hedin, L. *Phys. Rev. A* **1965**, 796.

143. Singhal, P., Callaway, J. *Phys. Rev. B* **1974**, *14*, 2347.

144. Godby, R. W.; Schlüter, M.; Sham, L. J. *Phys. Rev. B* **1988**, *37*, 10159-10175.

145. Aryasetiawan, F.; Gunnarsson, O. *Phys. Rev. Lett.* **1995**, *74*, 3221-3224.

146. Aryasetiawan, F.; Gunnarsson, O. *Rep. Prog. Phys.* **1998**, *61*, 237-312.

147. Anisimov, V. I.; Zaanen, J.; Andersen, O. K. *Phys. Rev. B* **1991**, *44*, 943-954.

148. Lu, D.; Rehr, J.J. *Phys. Rev. B* **1988**, *37*, 6126-6133.

149. Bair, R.A.; Goddard III, W.A. *Phys.Rev. B* **1980**, *22*, 2767-2776.

150. Stern, E.A. *Phys. Rev. Lett.* **1982**, *49*, 1353-1356.

151. Rehr, J.J.; Bardyszewski, W.; Hedin, L. *J. Phys. IV France* **1997**, *7-C2*, 97-98.

152. Bardyszewski, W.; Hedin, L. *Phys. Scripta* **1985**, *32*, 439; *J. Phys. IV France* **1987**, *C9*, 1101.

153. Natoli, C. R.; Benfatto, M.; Brouder, Ch.; Ruiz-Lopez, M. F.; Foulis, D. L. *Phys. Rev. B* **1990**, *42*, 1944-1968.

154. Johnson, K. H. *Scattered-Wave Theory of the Chemical Bond*; Academic Press, Inc.: New York, 1973; Vol. 7, pp 143-185.

155. Johnson, K. H. *Quantum Chemistry, Annual Reviews* **1975**, *26*, 39-57.

156. Norman, J. G. *J. Mol. Phys.* **1976**, *31*, 1191-1198.

157. Foulis, D. L.; Pettifer, R. F.; Sherwood, P. *Europhys. Lett.* **1995**, *28*, 647-652.

158. Foulis, D. L.; Pettifer, R. F.; Natoli, C. R.; Benfatto, M. *Phys. Rev. A* **1990**, *41*, 6922-6927.

159. Joly, Y. *Phys. Rev. B* **1996**, *53*, 13029-13037.

160. Joly, Y. *J. Phys. IV France* **1997**, *7-C2*, 111-115.

161. Holland, B.W.; Pendry, J.B.; Pettifer, R.F.; Bordas, J. *J. Phys. C: Solid State Phys.* **1978**, 633-642.

162. Newton, R.G. *Scattering Theory of Waves and Particles,* McGraw-Hill: New York, 1966, 2nd Edition, 1982.

163. Rehr, J. J.; Booth, C. H.; Bridges, F.; Zabinsky, S. I. *Phys. Rev. B* **1994**, *49*, 12347-12350.

164. Schütz, G.; Ahlers, D. *Magnetic EXAFS;* In *Spin-Orbit Influenced Spectroscopies of Magnetic Solids*; Proceedings of an International Workshop held at Herrsching, Germany in 1995; Ebert, H., Schütz, G., Eds.; Springer Verlag: Heidelberg, Berlin, 1996; Vol. 466, pp. 229-257.

165. Ramaker, D.E.; Mojet, B.; Koningsberger, D.C.; Grady, W.E. *J. Phys.: Condens. Matter* ***1999,*** in press.

166. Filipponi, A. *Physica B* **1995**, *208 & 209,* 29-32.

167. Weissbluth, M. *Atoms and Molecules,* Academic Press Inc.: New York, 1978; Chapter 15.

168. MacDonald, A. H.; Vosko, S. H. *J. Phys. C: Solid State Phys.* **1979**, *12*, 2977-2990.

169. Strange, P.; Ebert, H.; Staunton, J. B.; Gyorffy, B. L. *J. Phys. Condens. Matter* **1989**, *1*, 2959-2975.

170. Vignale, G.; Rasolt, M. *Phys. Rev. B* **1988**, *37*, 10685-10696.

171. Vignale, G.; Skudlarski, P. *Phys. Rev. B* **1992**, *46*, 10232-10238.

172. Brooks, M. S. S.; Johansson, B. *Spin-Orbit Interaction, Orbital Magnetism and Spectroscopic Properties;* In *Spin-Orbit Influenced Spectroscopies of Magnetic Solids*; Proceedings of an International Workshop held at Herrsching, Germany, in 1995; Ebert, H., Schütz, G., Eds.; Springer Verlag: Berlin, Heidelberg, New York, 1996; Vol. 466; pp. 211-228.

173. Norman, M.R. *Phys. Rev. Lett.* **1990**, *64*, 1162-1165; *Ibid.* (*errata*) 2466.

174. Gasche, T.; Brooks, M. S. S.; Johansson, B. *Phys. Rev. B* **1996**, *53*, 296-301.

175. Ebert, H. *Rep. Prog. Phys.* **1996**, *59*, 1665-1735.

176. Ebert, H. *Circular Magnetic X-ray Dichroism in Transition Metal Systems*; In *Spin-Orbit Influenced Spectroscopies of Magnetic Solids*; Proceedings of an International Workshop held at Herrsching, Germany, 1995; Ebert, H., Schütz, G., Eds.; Springer Verlag: Berlin, Heidelberg, New York, 1996; Vol. 466, pp. 159-177.

177. Ellis, D. E. *J. Phys. B: Atom. Molec. Phys.* **1977**, *10*, 1-5.

178. MacDonald, A. H. *J. Phys. C: Solid State Phys.* **1983**, *16*, 3869-3876.

179. Tyson, T. A. *Phys. Rev. B* **1994**, *49*, 12578-12589.

180. Brouder, Ch.; Alouani, M.; Bennemann, K.H. *Phys. Rev. B* **1996**, *54*, 7334-7349.

181. Brouder, Ch. *Multiple Scattering Theory of X-ray Magnetic Circular Dichroism*; In *Magnetism and Synchrotron Radiation*; Beaurepaire, E., Carrière, B., Kappler, J.-P., Eds.; Les Editions de Physique France, 1997; pp. 55-64.

182. Brouder, Ch.; Alouani, M.; Giorgetti, Ch.; Dartyge, E.; Baudelet, F. *Multiple Scattering Approach to Magnetic EXAFS*; In *Spin-Orbit-Influenced Spectroscopies of Magnetic Solids*; Proceedings of an International Workshop held at Herrsching, Germany, 1995; Ebert, H., Schütz, G., Eds.; Springer Verlag: Berlin, Heidelberg, New York, 1996; Vol. 466, pp. 259-274.

183. Brouder, Ch. *J. Phys. IV France* **1997**, *7-C2*, 377-381.

184. Brouder, Ch.; Hikkam, M. *Phys. Rev. B* **1991**, *43*, 3809-3820.

185. Fano, U. *Phys. Rev.* **1969**, *178*, 131-136; *Ibid.* (*erratum & addendum*) *184*, 250-251.

186. Erskine, J.L.; Stern, E.A. *Phys. Rev.* **1975**, *12*, 5016-5024.

187. Thole, B. T.; Van Der Laan, G. *Europhys. Lett.* **1987**, *4*, 1083-1086.

188. Van Veenendaal, M.; Goedkoop, J.; Thole, B.T. *Phys. Rev. Lett.* **1997**, *78*, 1162-65.

189. Jo, T.; Imada, S. *J. Phys. Soc. Japan* **1993**, *62*, 3721-3727.

190. Harmon, B.N.; Freeman, A.J. *Phys. Rev. B* **1974**, *10,* 1979-1993.

191. Rogalev, A.; Goedkoop, J.B.; Rogaleva, M.; Gotte, J.; Goulon, J. *J. Phys. IV France* **1997**, *7-C2*, 425-426.

192. Dartyge, E.; Baudelet, F.; Fontaine, A.; Giorgetti, Ch.; Pizzini, S.; Kappler, J.P.; Krill, G.; Brouder, Ch. *Phys. Rev. B* **1992**, *46*, 3155-3158.

193. Dartyge, E.; Baudelet, F.; Brouder, Ch.; Fontaine, A.; Giorgetti, Ch.; Kappler, J.P.; Krill, G.; Lopez, M.F.; Pizzini, S. *Physica B* **1995**, *208 & 209,* 751-54.

194. Gotsis, H. J.; Strange, P. *J. Phys. : Condens. Matter* **1994**, *6*, 4109-1416.

195. Guo, G. Y. *J. Phys. : Condens. Matter* **1996**, *8*, L747-752.

196. Guo, G. Y. *Phys. Rev. B* **1998**, *57*, 10295-10298.

197. Ebert, H.; Popescu, V.; Ahlers, D.; Schütz, G.; Lemke, L.; Wende, H.; Shrivastava, P.; Baberschke, K. *Europhys. Lett.* **1998**, *42*, 295-300.

198. Ahlers, D.; Schütz, G.; Popescu, V.; Ebert, H. *J. Appl. Phys.* **1998**, *83*, 7082-7084.

199. Ebert, H.; Popescu, V.; Ahlers, D. *J. Synchrotron Rad.* **1999**, *7*, in press.

200. Rogalev, A., Goulon, J.; Brouder, Ch. *J. Phys. : Condens. Matter* **1999**, *11*, 1115-1121.

201. International XAFS Society, Standards & Criteria Committee, http://ixs.csrri.iit.edu/IXS.

202. Binsted, N.; Gurman, S.J.; Campbell, J.W., Stephenson, P. EXCURVE: Daresbury Laboratory Program, 1982, CCLRC, Daresbury Laboratory, Warrington, WA4 4AD, Chelshire, U.K.

203. Goulon, J. XN: A FORTRAN Package for EXAFS, XANES, XMCD, XNCD Analyses and Simulations; 1rst version coupled to the fitting package MINUIT from CERN: 1978; Difference EXAFS analyses: 1986; coupling to MSXAS in 1989; restructuration in progress since 1996 to incorporate specialized options for dichroism; unpublished.

204. Sayers, D.E.; Bunker, B.A. *Data Analysis*; In *X-Ray Absorption: Principles, Applications, Techniques of EXAFS, SEXAFS and XANES*; Koningsberger, D.C., Prins, R., Eds.; Chemical Analysis Series, 92; John Wiley & Sons (Wiley-Interscience Publication): New York, 1987, Chapter 6, pp. 211-253.

205. Goulon, J.; Goulon-Ginet, C.; Cortès, R.; Dubois, J.-M. *J. Phys. France* **1982**, *43*, 539-548

206. Loos, M.; Ascone, I.; Goulon-Ginet, C.; Goulon, J.; Guillard, C.; Lacroix, M.; Breysse, M.; Faure, D.; Descourières, T. *Physica B* **1989**, *158*, 145-148.

207. Loos, M. Ph.D. Thesis, University of Nancy-I, France, 1990.

208. McMaster, W.H.; Kerr del Grande, N.; Mallett, J.H.; Hubbell, J.H. In *Compilation of X-ray Cross Sections;* 1969, UCRL-50174 Sec. II, rev.*1*, N.T.I.S. (U.S. Dept. of Commerce) , 5285 Port Royal Road, Springfield, VA 22151.

209. Waldo, G.S., Penner-Hahn, J.E. Poster at the XAFS-V Conference in Seattle, 1988.

210. Tan Z.; Budnick, J.; Heald, S.M. *Rev. Sci. Instrum.* **1989**, *60*, 1021-1025.

211. Lengeler, B.; Eisenberger, P. *Phys. Rev. B* **1980**, *21*, 4507-4520.

212. Goulon-Ginet, C. Ph.D Thesis, University of Nancy-I, France, 1979.

213. Cook, J. W.; Sayers, D. A. *J. Appl. Phys.* **1981**, *52*, 5024-5031.

214. Bauchspiess, K. R. *Physica B* **1995**, *208 & 209*, 183-184.

215. Li, G.G.; Bridges, F.; Brown G.S. *Phys. Rev. Lett.* **1992**, *68*, 1609-1612.

216. Li, G. G.; Bridges, F.; Booth, C. H. *Phys. Rev. B* **1995**, *52*, 6332-6348.

217. Newville, M.; Livins, P.; Yacoby, Y.; Rehr, J.; Stern, E. A. *Jpn. J. Appl. Phys.* **1992**, *32*, 125-127; *Phys. Rev. B* **1993**, *47*, 14126-14131.

218. Stern, E. A.; Newville, M.; Ravel, B.; Yacoby, Y.; Haskel, D. *Physica B* **1995**, *208 & 209*, 117-120.

219. Sayers, D. E.; Lytle, F. W.; Weissbluth, M.; Pianetta, P. *J. Chem. Phys.* **1975**, *62*, 2514-2515.

220. Lee, P.A.; Beni, G. *Phys. Rev. B* **1977**, *15*, 2862-2883.

221. Harris, F. J. *Proc. IEEE* **1978**, *66*, 51-83.

222. Loos, M.; Brouder, Ch.; Goulon, J. *Physica B* **1989**, *158*, 276-278.

223. Wold, H. Ph.D. Thesis, University of Stockholm (2nd Edition by Almqvist & Wiksell: Uppsala, 1954)

224. Smylie, D.E; Clarke, G.K.C.; Ulrych, T.J. *Analysis of Irregularities in Earth's Rotation;* In *Methods in Computational Physics*; Academic Press: New York, 1973; Vol. 13, pp. 391-430.

225. Burg, J.P. *A New Analysis Technique for Time Series Data;* Lecture at the Advanced Study Institute on Signal Processing, NATO: Entschede, Netherlands, 1968.

226. Akaike, H. *Ann. Inst. Statist. Math.* ***1969,*** *21,* 243-247*; Ibid.* 407-419*; Ibid.* **1970**, *22,* 203-217.

227. Gotte, V.; Goulon, J.; Goulon-Ginet, C.; Rogalev, A.; Benayoun, G. Preliminary results to be published.

228. Yuen, C.; Weissbluth, M.; Labhardt, A. SSRL Report N°77/06, 1977.

229. Labhardt, A.; Yuen, C. *Nature (London)* **1979**, *277*, 150-151.

230. Matsubayashi, N.; Shimada, H.; Imamura, M.; Yoshimura, Y.; Sato, T.; Nishijima, A. *Jpn. J. Appl. Phys.* **1993**, *Suppl. 32-2*, 122-124.

231. Tikhonov, A.; Arsenin, V. *Méthodes de Résolution de Problèmes mal Posés*; Editions MIR: Moscou (French Edition), 1976.

232. Babanov, Yu. A.; Vasin, V.V.; Ageev, A.L.; Ershov, N.V. *Phys. Stat. Sol. B* **1981**, *105,* 747-754.

233. Ershov, N.V.; Ageev, A.L.; Vasin, V.V.; Babanov, Yu. A. *Phys. Stat. Sol. B* **1981**, *108,* 103-111.

234. Ageev, A.L.; Babanov, Yu. A.; Vasin, V.V.; Ershov, N.V.; Serikov, A.V. *Phys. Stat. Sol. B* **1983**, *117,* 345-350.

235. Babanov, Yu. A.; Ershov, N.V.; Shvetsov, V.R.; Ageev, A.L.; Vasin, V.V. *J. Non-Crystalline Sol.* **1986**, *79,* 1-17.

236. Engl, H.W.; Neubauer, A. *Optimal Parameter Choice for Ordinary and Iterated Tikhonov Regularization;* In *Inverse and Ill-Posed Problems;* Engl, H.W.; Groetch, C.W. Eds, Notes and Reports in Mathematics, in Science and Engineering; Academic Press Inc.: London, 1987; Vol.4, pp.97-125.

237. Crozier, E.D. *Physica B* **1989**, *158*, 14-18.

238. Yang, D. S.; Bunker, G. *Phys. Rev. B* **1996**, *54*, 3169-3172.

239. Naumochkin, A.N.; Kochubei, D.I. *Nucl. Instrum. Meth. A* **1987**, *261*, 163-165.

240. Shulman, R.G.; Eisenberger, P.; Kincaid, B. *Ann. Rev. Biophys. Bioeng.* **1978**, *7*, 559-578.

241. James, F.; Roos, M. MINUIT: A System for Minimizing a Function of n Parameters and Computing the Errors and Correlations; CERN Computer Center Program Library: Genova, 1974, D506-516.

242. Chandler, J. P. STEPT: A Family of Routines for Optimization and the Fitting of Data; Program N°307, Quantum Chemistry Program Exchange (QCPE) Library, Chemistry Department, Indiana University: Stillwater, 1975.

243. Joyner, R.W.; Martin K.J.; Meehan, P. *J. Phys. C: Solid State Phys.* **1987**, *20*, 4005-4012.

244. Brillouin, L. In *Science and Information Theory*; Academic Press: New York, 1962, 2nd Edition.

245. Lytle, F.W.; Sayers, D.E.; Stern, E.A. *Physica B*, **1989**, *158*, 701-722.

246. Co, M. S.; Scott, R. A.; Hodgson, K. O. *J. Am. Chem. Soc.* **1981**, *103*, 986-988.

247. Binsted, N.; Strange, R. W.; Hasnain, S. S. *Biochemistry* **1992**, *31*, 12117-12125.

248. Chance, M.; Miller, L.M.; Fischetti, R.F.; Scheuring, E.; Huang, W.X.; Sclavi, B.; Hai, Y.; Sullivan, M. *Biochemistry*, **1996**, *35*, 9014-9023.

249. Teo, B.-K.; Lee, P. A.; Simmons A.L.; Eisenberger, P., Kincaid, B.M. *J. Am. Chem. Soc.* **1977**, *99*, 3854-55; Teo, B.-K.; Lee, P. A.; Simmons A.L. *Ibid*, **1977**, *99*, 3856-57.

250. Teo, B.-K.; Lee, P. A. *J. Am. Chem. Soc.* **1979**, *101*, 2815-2832.

251. McKale, A.G.; Knapp, G.S.; Chan, S.K. *Phys. Rev. B* **1986**, *33*, 841.

252. Vaarkamp, M.; Dring, I.; Oldman, R.J.; Stern, E.A.; Koningsberger, D.C. *Phys. Rev. B* **1994**, *50*, 7872-7883

253. Goulon, J.; Loos, M.; Friant, P.; Ruiz-Lopez, M. F. *Structural Applications of X-ray Absorption Spectroscopy (EXAFS and XANES) in Coordination Chemistry;* In *Chemical Crystallography with Pulsed Neutrons and Synchrotrons X-Rays;* Carrondo, M. A., Jeffrey, G. A., Eds.; Dordrecht Reidel Publishing Company: Dordrecht, 1988; Vol. 221, pp. 247-293.

254. Ruiz-Lopez, M.F.; Loos, M.; Goulon, J.; Benfatto, M.; Natoli, C.R. *Chem. Phys.* **1988**, *121*, 419-437.

255. Goulon, J.; Goulon-Ginet, C.; Friant, P.; Poncet, J. L.; Guilard, R.; Battioni, J. P.; Mansuy, D. In *Proceedings 4th Int. Conf. Org. Chem. of Selenium & Tellurium*; Berry, F.J., McWhinnie, R., Eds.; Univ. Aston: Birmingham,U.K., 1983; pp. 379-390.

256. Goulon, J.; Friant, P.; Poncet, J. L.; Guilard, R.; Fischer, J.; Ricard, L. In *EXAFS and Near Edge Structure*; Bianconi A., Incoccia L., Stipcich S. Eds.; Springer Ser. Chem. Phys.; Springer Verlag, 1983; Vol.27, pp. 100-102.

257. Poncet, J. L.; Guilard, R.; Friant, P.; Goulon-Ginet, C.; Goulon, J. *Nouv. J. Chim.* **1984**, *8*, 583-90.

258. Cramer, S.P.; Eccles, T.K.; Kutzler, F.; Hodgson, K.O., Doniach, S. *J. Am. Chem. Soc.* **1976**, *98*, 8059-8069.

259. Brouder, Ch.; Goulon, J. *Physica B* **1989**, *158*, 351-354.

260. Hoard, J.L. *Ann. N.Y. Acad. Sci.* **1973**, *206,* 18.

261. Cullen, D.L.; Meyer Jr., E.F. *J. Am. Chem. Soc.* **1974**, *96*, 2095-2102.

262. Meyer Jr., M.F. *Acta Cryst. B* **1972**, *28*, 2162-2167.

263. Bohr, F.; Ruiz-Lopez, M. F. *Chem. Phys.* **1991**, *156*, 55-61.

264. Collman, J.P.; Hoard, J.L.; Kim, N.; Lang, G.; Reed, C.A. *J. Am. Chem. Soc.* **1975**, *97*, 2676-2681.

265. Jentzen, W.; Hobbs, J.D.; Simpson, M.C.; Taylor, K.K.; Ema. T.; Nelson, N.Y.; Medforth, C.J.; Smith, K.M.; Veyrat, M.; Mazzanti, M.; Ramasseul, R.; Marchon, J.-C.; Goddard, W.A. III, Shelnutt, J.A. *J. Am. Chem. Soc.* **1995**, *117*, 11085-11097.

266. Nurco, D.J.; Medford, C.J.; Forsyth, T.P.; Olmstead, M.M.; Smith, K.M. *J. Am. Chem. Soc.* **1996,** *118*, 10918-10919.

267. Goulon, J.; Friant, P.; Goulon-Ginet, C.; Coutsolelos, A.; Guilard, R. *Chem. Phys.* **1984**, *83*, 367-375.

268. Friant, P.; Goulon, J.; Fischer, J.; Ricard, L.; Schappacher, M.; Weiss, R.; Momenteau, M. *New J. Chem.* **1985**, *9*, 33-40.

269. Bortolini, O. ; Ricci, M.; Meunier, B.; Friant, P.; Ascone, I.; Goulon, J. *New J. Chem.* **1986**, *10*, 39-49.

270. Goulon, J.; Loos, J.; Ascone, I.; Goulon-Ginet, C.; Battioni, P.; Battioni, J.P.; Mahy, J.P.; Mansuy, D.; Meunier, B. In *Biophysics and Synchrotron Radiation;* Springer Series in Biophysics; Bianconi, A., Congiu-Castellano, A., Eds; Springer-Verlag: Berlin, Heidelberg, New-York, 1987; Vol.2, pp. 191-200.

271. Ascone, I.; Loos, M.; Goulon, J.; Battioni, J.P.; Battioni, P.; Mahy, J.P.; Bedi, G.; Mansuy, D.: *Structural Characterization using Difference EXAFS Spectroscopy of Hemoprotein and Related Biomimetic Porphyrin Complexes*", in the Proceedings of the 2nd International Conference *Biophysics and Synchrotron Radiation-II,* Chester, 4-8 July 1988.

272. Loos, M.; Friant, P.; Ascone, I.; Goulon, J.; Barbe, J.-M.; Coutsolelos, P. A.; Guilard, R. *J. Phys. France* **1986**, *47-C8*, 641-644.

273. Loos, M.; Goulon, J.; Barbe, J.-M.; Guilard, R. *J. Phys. France* **1986**, *47-C8*, 633-636.

274. Marchon, J. C.; Latour, J. M.; Grand, A.; Belakhovsky, M.; Loos, M.; Goulon, J. *Inorg. Chem.* **1990**, *29*, 57-67.

275. Mansuy, D.; Battioni, J.P.; Chottard, J.C.; Ullrich, V. *J. Am. Chem. Soc.* **1979**, *101*, 3971-3973.

276. Mansuy, D.; Lange, M.; Chottard, J.C. *J. Am. Chem. Soc.* **1978**, *100*, 3213-3214.

277. Mansuy, D.; Lange, M.; Chottard, J.C.; Morliere, P.; Brault, D. *J. Chem. Soc., Chem. Comm.* **1977**, 648-649.

278. Mansuy, D.; Lange, M.; Chottard, J.C.; Bartoli, J.F.; Chevrier, B.; Weiss, R. *Angew. Chem., Int. Ed. Eng.* **1978**, *17*, 781.

279. Mansuy, D.; Battioni, P.; Chottard, J.C.; Riche, C.; Chiaroni, A. *J. Am. Chem. Soc.* **1983**, *105*, 455-463.

280. Bianconi, A.; Congiu-Castellano, A.; Dell'Arricia, M.; Giovannelli, A.; Morante, S. *FEBS Letters* **1985**, *191*, 241-244.

281. Oyanagi, H; Iizuka, T.; Matsushita, T.; Saigo, S.; Makino, R.; Ishimura, Y. In *Biophysics and Synchrotron Radiation;* Springer Series in Biophysics; Bianconi, A., Congiu-Castellano, A., Eds.; Springer-Verlag: Berlin, Heidelberg, New-York, 1987; Vol.2, pp. 99-106.

282. Morante, S.; Congiu-Castellano, A.; Dell'Arricia, M.; Durham, P.J.; Giovanelli, A.; Burattini E.; Bianconi, A. In *Biophysics and Synchrotron Radiation;* Springer Series in Biophysics; Bianconi, A., Congiu-Castellano, A., Eds.; Springer-Verlag: Berlin, Heidelberg, New-York, 1987; Vol.2, pp. 107-113.

283. Teodorescu, C. M.; Esteva, J.M.; Karnatak, R.C.; El Afif, A. *Nucl. Instr. Meth. Phys. Res. A* **1994**, *345*, 141-147.

284. Loeffen, P. W.; Pettifer, R. F.; Müllender, S.; Van Veenendaal, M. A.; Röhler, J.; Sivia, D. S. *Phys. Rev. B* **1996**, *54*, 14877-14880.

285. Pasté, S.; Gotte, V.; Goulon-Ginet, C.; Rogalev, A.; Goulon, J.; Georget, P.; Marcilloux, J. *J. Phys. IV France* **1997**, *7-C2*, 665-666.

286. Gotte, V.; Rogalev, A.; Goulon, J.; Goulon-Ginet, C.; Michon, L.; Guilard, R. *J. Phys. IV France* **1997**, *7-C2*, 667-668.

287. Outka, D.A.; Stöhr, J. *J. Chem. Phys.* **1988**, *88*, 3539-3554.

288. Natoli, C. R.; Misemer, D. K.; Doniach, S.; Kutzler, F. W. *Phys. Rev. A* **1980**, *22*, 1104-1108.

289. Durham, P. J.; Pendry, J. B. *Computer Phys. Comm.* **1982**, *25*, 193-205.

290. Della Longa, S.; Soldatov, A.; Pompa, M.; Bianconi, A. *Computational Material Science* **1995**, *4*, 199-210.

291. Binsted, N.; Hasnain, S. S. *J. Synchrotron Rad.* **1996**, *3*, 185-196.

292. Natoli, C.R. **1998**, unpublished code.

293. Bianconi, A.; Natali, F.; Alosi, M.L.; Grande, S.; Lanzara, A.; Saini, S.L. *J. Synchrotron Rad.* **1999**, *7*, in press.

294. Miller, J.S.; Epstein, E.J. *Chem. & Engineer. News* **1995**, 30-41.

295. Collison, D.; Garner, C.D.; McGrath, C.M.; Mosselmans, F.W.; Pidcock, E.; Roper, M.D.; Searle, B.G.; Seddon, J. M.W.; Sinn, E.; Young, N.A. *J. Chem. Soc., Dalton Trans.* **1998**, 4179-4186.

296. Elleaume, P. *J. Synchrotron Rad.* **1994**, *1*, 19-26.

297. Elleaume, P.; Chavanne, J.; Maréchal, X.; Goulon, J.; Braicovich, L.; Malgrange, C.; Emerich, H.; Marot, G.; Susini, J. *Nucl. Instrum. Meth. A* **1991**, *308*, 382-389.

298. Sasaki, S.; Kakuno, K.; Takada, T.; Shimada, T.; Yanagida, K.; Miyahara, Y. *Nucl. Instrum. Meth. A* **1993**, *331*, 763-767.

299. Dmitrienko, V.E.; Belyakov, V.A. *Pis'ma Zh. Tekh. Fiz.* **1980**, *6*, 1440-1441.

300. Hirano, K.; Ishikawa, T.; Annaka, S.; Kikuta, S. *Jpn J. Appl. Phys. Lett.* **1991**, *30*, L407-L410.

301. Hirano, K.; Kanzaki, K.; Mikami, M.; Miura, M.; Tamasaku, K.; Ishikawa, T.; Annaka, S.; Kikuta, S. *J. Appl. Cryst.* **1992**, *25*, 531-535.

302. Gilès, C.; Malgrange, C.; Goulon, J.; De Bergevin, F.; Vettier, Ch.; Dartyge, E.; Fontaine, A.; Giorgetti, C.; Pizzini, S. *J. Appl. Cryst.* **1992**, *27*, 232-240.

303. Goulon, J.; Malgrange, C.; Gilès, C.; Neumann, C.; Rogalev, A.; Moguiline, E.; De Bergevin, F.; Vettier, Ch. *J. Synchrotron Rad.* **1996**, *3*, 272-281.

304. Varga, L. Ph.D. Thesis, Université Pierre & Marie Curie Paris VI, France, 1999.

305. Goulon, J.; Sette, F.; Moise, C.; Fontaine, A.; Perey, D.; Rudolf, P.; Baudelet, F. *Jpn. J. Appl. Phys.* **1993**, *Suppl. 32-2*, 284-289.

306. George, G.; Prince, R.C.; Frey, T.G.; Cramer, S.P. *Physica B* **1989**, *158*, 81-83.

307. Dittmer, J.; Dau, H. *J. Phys. Chem. B* **1998**, *102*, 8196-8200.

308. Ruiz-Lopez, M.F.; Loos, M.; Goulon, J.; Natoli, C.R.; Ballivet-Tkatchenko, D. *Physica,* **1989**, *158*, 200-202.

309. Sham, T.K.; Hastings, J.B.; Perlman, M.L. *J. Am. Chem. Soc.* **1980**, *102*, 5904-5906; *Chem. Phys. Lett.* **1981**, *83*, 391-396.

310. Frahm, R. *Nucl. Instrum. Meth. A* **1988**, *270*, 578-581; *Rev. Sci. Instrum.* **1989**, *60*, 2515-2518

311. Frahm, R.; Wong, J. *Jpn. J. Appl. Phys.* **1993**, *Suppl. 32-2*, 188-191.

312. Lagarde, P.; Lemonnier, M.; Dexpert, H. *Physica B* **1989**, *158*, 337-339.

313. Dobson, B.R.; Hasnain, S.S.; Neu, M.; Ramsdale, Ch. A.; Murphy, L.M. *Jpn. J. Appl. Phys.* **1993**, *Suppl. 32-2*, 192-194.

314. Dobson, B.R. *Synchrotron Radiation News* **1994,** *7*, 21-24.

315. Murphy, L.; Dobson, B.R.; Neu, M.; Ramsdale, Ch.A.; Strange, R.W.; Hasnain, S.S. *J. Synchrotron Rad.* **1995**, *2*, 64-69.

316. Solé, V.A.; Gauthier, Ch.; Goulon, J.; Natali, F. *J. Synchrotron Rad.* **1999**, *7*, in press.

317. Cauchois, Y.; Bonnelle, C.; Missoni, G. *C.R. Acad. Sci. (Paris)* **1963**, *257*, 409-411.

318. Kaminaga, U.; Matsushita, T.; Kohra, K. *Jpn J. Appl. Phys.* **1981**, *20*, 355-358.

319. Phizackerley, R.P.; Rek, Z.U.; Stephenson, G.B.; Conradson, S.D.; Hodgson, K.O.; Matsushita, T.; Oyanagi, H. *J. Appl. Cryst.* **1983**, *16*, 220-232.

320. Matsushita, T.; Oyanagi, H.; Saigo, S.; Kihara, H.; Kaminaga, U. In *EXAFS and Near Edge Structure III ;* Hodgson, K.O., Hedman, B., Penner-Hahn, J.E., Eds.; Springer Proceedings in Physics, Springer Verlag, 1984; Vol.2, pp. 476-478.

321. Dartyge, E.; Depautex, C.; Dubuisson, J.M.; Fontaine, A.; Jucha, A.; Leboucher, P.; Tourillon, G. *Nucl. Instrum. Meth. A* **1986**, *246*, 452-460.

322. Tolentino, H.; Dartyge, E.; Fontaine, A.; Tourillon, G. *J. Appl. Cryst.* **1988**, *21*, 15-21

323. Fontaine, A.; Baudelet, F.; Dartyge, E.; Guay, D.; Tolentino, H; Tourillon, G. *Time resolved X-ray Absorption Spectroscopy;* In *Synchrotron Radiation and Dynamic Phenomena;* Beswick, A. Ed.*;* Particles and Fields Series *49;* American Institute of Physics: New York, 1992, AIP Conference Proceedings; Vol. 258, pp. 496-514.

324. Allinson, N.M.; Baker, G.; Greaves, G.N.; Nicoll, J.K. *Nucl. Instrum. Meth. A* **1988**, *266*, 592-597.

325. Hagelstein, M.; Cunis, S.; Frahm, R.; Rabe, P. *Rev. Sci. Instrum.* **1992**, *63*, 911-913.

326. Blank, H.; Neff, B.; Steil, St.; Hormes, J. *Rev. Sci. Instrum.* **1992**, *63*, 1334-37.

327. Allen, P.G.; Conradson, S.D.; Penner-Hahn, J.E. *Synchrotron Radiation News* **1992**, *5*, 16-24.

328. Lee, P.L.; Beno, M.A., Jennings, G.; Ramanathan, M.; Knapp, G.S.; Bai, J.; Montano, P.A.; Huang, K.G. *Rev. Sci. Instrum.* **1994**, *65*, 1-6.

329. Hagelstein, M.; Fontaine, A.; Goulon, J. *Jpn. J. Appl. Phys.* **1993**, *Suppl. 32-2*, 240-242.

330. Pascarelli, S.; Neisius, T.; De Panfilis, S.; Bonfim, M.; Pizzini, S.; Mackay, K.; David, S.; Fontaine, A.; San Miguel, A.; Itie, J.P.; Gauthier, M.; Polian, A. *J. Synchrotron Rad.* **1999**, *7*, in press.

331. Huang, H.W.; Liu, W.H.; Teng, T.Y.; Wang, X.F. *Rev. Sci. Instrum.* **1983**, *54*, 1488-1491.

332. Liu, W.H.; Wang, X.F.; Teng, T.Y.; Huang, H.W. *Rev. Sci. Instrum.* **1983**, *54*, 1653-1656.

333. Huang H.W. In *EXAFS and Near Edge Structure III* ; Hodgson, K.O., Hedman, B., Penner-Hahn, J.E., Eds.; Springer Proceedings in Physics; Springer Verlag, 1984, Vol.2, pp. 158-163.

334. Chance, B. In *EXAFS and Near Edge Structure III* ; Hodgson, K.O., Hedman, B., Penner-Hahn, J.E., Eds.; Springer Proceedings in Physics; Springer Verlag, 1984, Vol.2, pp. 154-157.

335. Bonfim, M.; Mackay, K.; Pizzini, S.; San Miguel, A.; Tolentino, H.; Gilès, C.; Neisius, T.; Hagelstein, M.; Baudelet, F.; Malgrange, C.; Fontaine, A. *J. Synchrotron Rad.* **1998**, *5*, 750-752.

336. Rogalev, A.; Goulon, J. *J. Phys. IV France* **1997**, *7-C2*, 565-568.

337. Zinin, E.I. *Nucl. Instrum. Meth.* **1983**, *208*, 439-441.

338. Goulon, J.; Tola, P.; Brochon, J.C.; Lemonnier, M.; Dexpert-Ghys, J.; Guilard, R. In *EXAFS and Near Edge Structure III* ; Hodgson, K.O., Hedman, B., Penner-Hahn, J.E., Eds.; Springer Proceedings in Physics; Springer Verlag, 1984, Vol.2, pp. 490-495.

339. Goulon, J.; Tola, P.; Lemonnier, M.; Dexpert-Ghys, J., *Chem. Phys.* **1983**, 78, 347-356.

340. Livins, P.; Thiel, D.; Stern, E.; Lewis, A. *Jpn. J. Appl. Phys.* **1993**, *Suppl.32-2*, 195-197.

341. Bray, R.C. *Biochem. J.* **1961**, *81*, 189-93.

342. Saigo, S.; Sone, N.; Nagamura, T.; Oyanagi, H.; Iizuka, T.; Kusunoki, M.; Matsushita, T. In *Biophysics and Synchrotron Radiation;* Bianconi, A.; Congiu-Castellano, A., Eds; Springer Series in Biophysics; Springer-Verlag: Berlin, Heidelberg, New-York, 1987; Vol.2, pp. 130-135.

343. Saigo, S.; Hashimoto, H.; Shibayama, N.; Nomura, M.; Nagamura, T. *Jpn. J. Appl. Phys.* **1993**, *Suppl. 32-2*, 538-540.

344. George, G.N.; Bray, R.C.; Cramer, S.P. *Biochem. Soc. Trans.* **1986**, *14*, 651

345. Goulon, J.; Goulon, C.; Gauthier, Ch.; Emerich, H. In *Synchrotron Radiation and Dynamic Phenomena;* Beswick, A. Ed.*;* Particles and Fields Series *49;* American Institute of Physics: New York, 1992; AIP Conference Proceedings Vol. 258, pp. 419-427.

346. Wang, J.; Sood, A.K.; Satyam, P.V.; Feng, Y.; Wu, X.-Z.; Cai, Z.; Yun, W.; Sinha, S.K. *Phys. Rev. Lett.* **1998**, *80*, 1110-1113.

347. Della Longa, S.; Bianconi, A.; Congiu Castellano, A.; Girasole, M.; Kovtun, A. P.; Soldatov, A. V. *J. Phys. France IV* **1997**, *7-C2*, 631-632.

Deuxième partie

Etude des interactions entre gaz rares et diverses espèces moléculaires actives ou complexantes.

2.1 Etudes structurales des intermédiaires formés par réaction de l'ozone avec des dérivés halogéno-dodécaphénylporphyrinato-manganèse(III).

2.1.1 Introduction

Depuis des années, l'ozone est utilisée, en chimie organique, comme puissant agent d'oxydation des oléfines, des hydrocarbures aromatiques et autres espèces riches en électrons. La structure dipolaire de la molécule d'ozone et la formation d'un intermédiaire de type ozonide lors cette attaque sont les deux caractéristiques principales de cette réaction. Ce puissant agent d'oxydation remplace maintenant le chlore dans le traitement des effluents puisque les sous-produits chlorés sont extrêmement toxiques et leur concentration dans l'eau est strictement réglementée. Les dérivés organiques contenant des groupes électro-attracteurs ne sont pas oxydés de manière efficace par l'ozone seul; aussi un *Advanced Oxidation Process* (AOP)[1] a été développé afin de permettre la dégradation de ce type de composé. Ce processus met en oeuvre de l'ozone sous irradiation UV ou de l'ozone et du peroxyde d'hydrogène. Durant ce processus, l'ozone se décompose pour donner des radicaux hydroxylés. Cette espèce hautement réactive mais non sélective permet d'obtenir une élimination plus efficace des micro-polluants comme les dérivés chlorés ou les pesticides tels que le DDT[2].

De nos jours, le traitement industriel des eaux usées met l'accent sur les processus d'activation de l'ozone par des composés organométalliques ou inorganiques permettant non seulement d'éliminer efficacement les hydrocarbures saturés et les oléfines, mais aussi de réduire la consommation d'ozone. Les métalloporphyrines synthétiques sont de bonnes candidates pour être des catalyseurs de ces réactions d'oxydation. Elles constituent de remarquables modèles de systèmes biologiques, d'enzymes tels que le cytochrome P-450 mono-oxygénase[3], qui catalyse de nombreuses réactions d'oxydation *in vivo*. En outre, les porphyrines présentent l'avantage de pouvoir être coordinées à de nombreux métaux et les diverses substitutions pouvant intervenir sur le motif de base permettent d'en moduler les propriétés. Ainsi, il est bien établi que les porphyrines de fer ou de manganèse peuvent activer le dioxygène et catalyser de nombreuses réactions d'oxydation sélectives dans des conditions non extrêmes.

B. Meunier et ses collaborateurs[4] ont montré que de telles porphyrines de fer ou de manganèse pouvaient être utilisées efficacement dans le traitement des eaux usées et sont de bons catalyseurs de la dégradation de composés peu réactifs tels que les poly-chlorophénols. Ces macrocycles porphyriniques doivent être eux-mêmes protégés contre les agents d'oxydations tels que l'ozone. La substitution des carbones en position β-pyrroliques par des groupes électro-attracteurs, par exemple le brome ou

---

[1] Glaze,W.H.;Kang,J.W;Chopin, D.H. *Ozone:Sci. Eng* **1987**, *9*, 335-352.
[2] Reynolds,G. *Ozone:Sci. Eng.* **1989**, *11*, 339-382.
[3] Ullrich, V. *Topics in Current Chemistry* **1979**, *83*, 67-104.
[4] Meunier B., *Chem. Rev.* (Washington D.C.) **1992**, 92, 1411-1456

des groupes phényles, permettent de prévenir une telle oxydation. La substitution des sites β-pyrroliques implique une distorsion non-plane de la conformation du macrocycle comme l'ont montré Smith et coll.[5], et Takeda[6]. La résistance à l'oxydation peut être encore améliorée par la substitution des carbones en position *meso* par des groupements pentafluorophényl. Cette substitution a, en outre, l'avantage de minimiser la formation de complexe binucléaire μ-oxo ne présentant pas d'activité catalytique[7].

C'est pourquoi, R. Guilard et son équipe du LIMSAG (UMR 5633 CNRS-AIR LIQUIDE-Université de Dijon) ont été conduits à synthétiser une série de dérivés dodécaphénylporphyrinato de manganèse. Ces dérivés ont été caractérisés par des analyses électrochimiques et spectrochimiques[8]. Une structure crystallographique a été obtenue pour le chloro(meso - 5,10,15,20 - tetrakis - pentafluorophenyl - 2,3,7,8,12,13,17,18 - octakis - phenylporphyrinato) de manganèse (III) dénommé dès à présent $DPPF_{20}MnCl$. Elle montre que le macrocycle adopte une conformation hydride *saddle/ruffle*.[9] Il a aussi été démontré[8] que ce dérivé mis en présence d'ozone en solution forme un complexe stable de manganèse (IV) qui ne présente pas d'activité catalytique. En revanche, l'action de l'ozone sur $DPPF_{20}MnCl$ en présence d'un large excès de pyridine conduit à un complexe présentant une activité catalytique. Un bullage de dioxygène dans la solution de complexe de manganèse (IV) régénère le dérivé de manganese (III) de départ. Ces deux complexes de manganèse (IV) sont stables en phase solide. Ce travail de synthèse et de caractérisation a été accompli lors de la thèse de K. Périé au LIMSAG de Dijon.

Le but de notre travail a été de tenter de clarifier la nature et de proposer une structure pour les espèces qui se forment lors de la réaction d'ozonation des composés halogéno-dodécaphénylporphyrinato de manganèse, en combinant les études EXAFS et XANES non seulement au seuil K du manganèse mais aussi au seuil K du chlore. Nous avons utilisé la méthode d'analyse de différence des spectres EXAFS avec perturbations structurales décrite dans la première partie de ce manuscrit, qui permet d'obtenir des informations structurales fiables quand on choisit des composés modèles appropriés. Nous avons, en outre, effectué des simulations *ab initio* des spectres XANES enregistrés au seuil K du chlore afin de proposer une structure pour les complexes formés.

Les résultats, détaillés dans les deux publications reproduites dans les paragraphes 2.1.2 et 2.1.3, ont conduit aux conclusions suivantes:

Les spectres EXAFS au seuil K du manganèse prouvent que la réaction de l'ozone avec les dérivés chloro- ou bromo-porphyrinato Mn(III) mène strictement aux mêmes intermédiaires dans lequel l'atome de métal est dans un état formellement tétravalent. Le schéma de coordination inclut les quatre atomes d'azote pyrroliques équatoriaux et deux molécules d'ozone arrangées dans des configurations symétriques par rapport au noyau porphyrinique. Cette géométrie implique que l'atome de métal soit déplacé vers le plan moyen des azotes de la porphyrine. La coordination du manganèse avec chaque molécule d'ozone donne deux distances manganèse-oxygène non équivalentes : $R(Mn...O_1) = 2.09 \pm 0.02Å$; $R(Mn...O_2) = 2.49 \pm 0.05Å$. La deuxième liaison est plus

---

[5] Medforth,C.J.; Smith, K.M. *Tetrahedron Lett.* **1990**, *31*, 5583-5586.

[6] Takeda,J.; Sato, M. *Tetrahedron Lett.* **1994**, *35* , 3565-3568.

[7] Chank, C.K.;Ebina, F. *J.Chem.Soc. Chem. Commun.* **1981**, 778-779.

[8] Périé, K; Thèse, Université de Bourgogne, Dijon (France),**1996**.

[9] Guilard R.;Périé K.;Barbe, J.-M.;Nurco, D.J.;Smith K.M.;Van Caemelbecke, E.;Kadish, K.M. *Inorg Chem* **1998**, *37*, 973-981.

faible avec une distribution asymétrique (anharmonique) des distances ($Mn...O_2$). Tandis que ces intermédiaires n'ont que peu ou pas d'activité catalytique dans l'époxydation des oléfines, l'espèce présentant une activité catalytique est obtenue quand l'ozone réagit avec le même précurseur dans un large excès de pyridine. Dans l'espèce catalytiquement active, le signal ($Mn...O_1$) n'est pas affecté par la présence de la pyridine, tandis que le signal ($Mn...O_2$) est diminué d'au moins un facteur deux. Il n'y a pas de preuve que la pyridine soit coordinée à l'atome de manganèse. D'importantes informations ont été obtenues à partir des études XAS faites au seuil K du chlore sur les espèces chlorées traitées avec l'ozone. La formation d'anions chlorates ou hypochlorites peut être exclue tandis que l'interprétation des spectres XANES et EXAFS supporte la formation de clusters moléculaires covalents comme Cl-O-O-O ou le dimère O-O-O-Cl-O-O-O qui contribuent à deux distances caractéristiques $R(Cl...O_1) = 1.70 \pm 0.02$ Å; $R(Cl...O_2) = 2.22 \pm 0.02$ Å. Les spectres XANES montrent un doublet caractéristique dans la zone de pré-seuil qui semble être la signature de ces clusters selon la terminologie usuelle des simulations dites "Extended Continuum MSW".

2.1.2 Publication

Structural Studies using X-ray Absorption Spectroscopy of intermediates formed by reaction of Ozone with Halogeno-Dodecaphenylporphyrinato-Manganese (III) derivatives

by

Vincent Gotte[1], José Goulon[1], Chantal Goulon-Ginet[1,2], Andrei Rogalev[1], Calogero R. Natoli[3], Karine Perié[4], Jean-Michel Barbe[4] and Roger Guilard[4]

[1] *European Synchrotron Radiation Facility (ESRF), Boite Postale 220, F-38043 Grenoble Cedex, France*

[2] *Université Joseph Fourier, Faculté de Pharmacie, F-38706 La Tronche, France*

[3] Laboratori Nazionali di Frascati dell'Istituto Nazionale di Fisica Nucleare, P.O. Box 13, I-00044 Frascati, Italy

[4] *Laboratoire d'Ingéniérie Moléculaire pour la Séparation et les Applications des Gaz (LIMSAG), UMR 5633 CNRS-AIR LIQUIDE, Université de Bourgogne, Faculté des Sciences Gabriel, Boulevard Gabriel, F- 21100 Dijon, France*

(*Revised Draft: October 11th, 1999*)

Abstract:

Difference EXAFS and XANES studies at the Mn K-edge are reported which shed light on the mechanisms of activation of the title compounds by ozone. The reaction of ozone with either the chloro- or bromo- porphyrinato Mn(III) derivatives yields the same intermediate in which the metal is in a formally tetravalent (IV) state. The coordination scheme includes the four equatorial pyrrolic nitrogen atoms of the porphyrin plus two ozone molecules arranged in a symmetrical configuration with respect to the porphyrin core. This geometry implies that the metal is shifted back into the mean plane of the porphyrin nitrogens. The Mn coordination with each ozone molecule results in two non equivalent Mn...O distances: R(Mn...O_1) = 2.09 ± 0.02 Å; R(Mn...O_2) = 2.49 ± 0.05 Å. The second signal is assigned to a much weaker bond with an asymmetric (anharmonic) distribution of the (Mn...O_2) distances. Whereas these intermediates have little or no catalytic activity regarding the epoxidation of olefins, catalytically active species were obtained when ozone reacts with the same precursors in an excess of pyridine. In the catalytically active species, the (Mn...O_1) signal remains unaffected by the presence of pyridine whereas the (Mn...O_2) signal is decreased by a factor two. Since there is no evidence of pyridine being coordinated to Mn, we suspect that pyridine is mediating a partial decomposition of one bound ozone molecule to release an active radical species. From Cl K-edge XAS studies performed on the chlorinated species treated with ozone and model compounds, we can definitely rule out the formation of chlorates or hypochlorite anions but both the XANES and EXAFS spectra show that Cl is oxidized during its substitution by ozone at the Mn site and could yield with ozone a covalent moiety Cl–O–O–O similar to the one which is presumed to form in the stratosphere by reaction of chlorine radicals with ozone. Some more speculative would be the formation of dimeric species in which a single Cl atom could bridge two ozone molecules. The radial distribution around Cl would then consist of two oxygen nearest neighbors at R(Cl...O_1) = 1.69 ± 0.03 Å and four oxygen atoms at R(Cl...O_2) = 2.20 ± 0.02 Å. This model is supported by *ab initio* MSW simulations of the XANES as well as by the EXAFS spectra.

Introduction

Ozone is a key component in industrial processes developed for recycling wastewater. Due to its electrophilic character, molecular ozone oxidizes preferentially olefins, aromatic hydrocarbons and other electron rich species[1-3]. Advanced oxidation processes (AOP's) [4-6] combining ozone, hydrogen peroxide and (or) UV irradiation to produce highly reactive hydroxyl radicals are currently used to eliminate organic pollutants containing electron-withdrawing groups such as chlorinated hydrocarbons or pesticides like DDT [7]. Today, interest is concentrating on the catalytic activation of ozone by inorganic or organometallic compounds [8,9]: such catalytic processes are less sensitive to radical trapping and could be optimized in order to minimize the ozone consumption. Moreover, it should be possible to increase the efficiency of secondary reactions of degradation of organic pollutants and to eliminate saturated hydrocarbons as well as olefins. In this perspective, synthetic metalloporphyrins are attractive compounds since it is well established that iron or manganese porphyrins can activate dioxygen and catalyze a variety of selective oxidation reactions under mild conditions [10-12]. Meunier *et al.* [12-14] have shown that supported manganese and iron porphyrins could be used in the treatment of wastewater, more specifically for the degradation of poorly reactive organic pollutants such as polychlorophenols [14]. The substitution of the β-pyrrole sites with electron-withdrawing bromine or phenyl groups [15,16] is required to avoid the electrophilic attack by ozone and prevent the oxidation of the porphyrin macrocycle itself. Usually, such a substitution of the β-pyrrole sites with bulky groups result in distorted, non-planar (ruffled and saddle-shaped) conformations of the macrocyclic ligand as investigated for several years by Smith *et al.* [17-23] or others [24]. The resistance to the electrophilic attack can also be further enhanced by replacing the four *meso* substitutents -which are phenyl groups in the popular tetraphenylporphyrins (TPP)- by pentachlorophenyl (C_6Cl_5 -) or pentafluorophenyl (C_6F_5 -) groups which act again as electron-withdrawing substitutents[25,26] and were recognized to minimize the formation of inactive μ-oxo binuclear complexes [27,28].

These considerations led us to synthesize series of dodecaphenylporphyrinato derivatives of iron (III) and manganese (III) which were first characterized by electrochemical and spectrochemical methods[16,29]. A crystal structure[29] was solved for the chloro- (meso-5,10,15,20 tetrakis-pentafluorophenyl- 2,3,7,8,12,13,17,18 octakis-phenylporphyrinato) Manganese (III) complex (hereafter denoted: **1** = ($DPPF_{20}$)MnCl) and confirmed the expected saddle-shaped conformation of the porphyrin macrocycle. It was found that **1** was not decomposed by ozone but formed in solution a well defined Mn (IV) compound **2**, the structure of which was unknown. Species **2** had itself no catalytic activity regarding the epoxidation of olefins but it was found that the action of ozone on the same precursor **1** in presence of a large excess of pyridine produced a different species **3** which presented a significant catalytic activity.

It is the aim of the present paper to unravel structural information on these compounds by combined EXAFS and XANES studies carried out at both the Mn and Cl K-edges. Our strategy will be based mostly on difference EXAFS analyses [30,31] which already allowed us to rule out [32] the formation of an oxo-manganese compound with a short Metal...O bond as found, for example, in the ferryl compounds which were identified as key intermediates in the catalytic cycle of cytochrome P450 [31]. On the other hand, the EXAFS and XANES spectra recorded at the Cl K-edge will be used to show that ozone is not only reacting at the Mn sites but is also oxidizing the former chlorine ligand.

Materials and Methods

MATERIALS:

All complexes were synthesized, purified and characterized following already described experimental procedures[16,29]. The X-ray absorption spectra of the following complexes were investigated:

1 = $(DPPF_{20})Mn^{III}Cl$; **2** = $[(DPPF_{20})MnCl + O_3]$; **3** = $[(DPPF_{20})MnCl + O_3 + Pyridine]$;
4 = $(DPPF_{20})Mn^{III}Br$; **5** = $[(DPPF_{20})MnBr + O_3]$;
6 = $(DPPF_{20})Mn^{III}N_3$; **7** = $(DPPF_{20})Mn^{V}N$.

Here, $(DPPF_{20})$ refers to the (meso- 5,10,15,20 tetrakis-pentafluorophenyl- 2,3,7,8,12,13,17,18 octakis-phenylporphyrinato) macrocyclic dianion the structure of which is shown in Scheme 1. In discussing the Cl K-edge EXAFS or XANES spectra, we will refer to additional reference systems:

8 = $[Mn(ClO_4)_2 , 6\ H_2O]$; **9** = $KClO_3$; **10** = $[NaOCl / H_2O]$.

Compounds **8** and **9** were purchased from Aldrich Chemical Company Inc. (purity grade: 99%) and were used without any purification. Regarding the aqueous solution **10**, the concentration in ClO^- anions was 12% by weight. With the exception of the latter solution which required us to design vacuum tight liquid cells, all other samples were prepared and investigated as thick powdered pellets (carefully mixed with dried BN or cellulose) suitable for fluorescence yield (FY) detection.

EXAFS & XANES SPECTRA:

The EXAFS and XANES spectra were recorded at the European Synchrotron Radiation Facility (ESRF) beamline ID12-A which is a UHV, windowless beamline thus most suitable for EXAFS studies at the chlorine K-edge. Since a detailed description of this beamline can be found elsewhere[33] , we will retain here only a few points which are of direct relevance for the present study. It should be kept in mind that the X-ray source is an helical undulator and that the spectral bandwidth of an undulator peak is typically large enough to cover the XANES region but is much too narrow to record a full EXAFS spectrum over 1000-1500 eV. This led us to pioneer the so-called "gap-scan" technique[34] which consists in optimizing the magnetic gap of the undulator so that the energy of the monochromator always matches the peak intensity of the undulator spectrum. A pair of SiC mirrors were inserted upstream with respect to the monochromator in order to keep the level of unwanted harmonics 5 orders of magnitude below the fundamental. The monochromator was equipped with a pair of Si (111) crystals cooled down to 152K and previous tests have established that the energy resolution was very close to theoretical limits, *i.e.* $\Delta E \approx 1.0$ eV at the Mn K-edge; $\Delta E \approx 0.5$ eV at the Cl K-edge with a reproducibility between two consecutive spectra better than 10 meV. All spectra discussed in the present paper were recorded using the Fluorescence Yield (FY) detection mode. The samples were inserted in a high vacuum fluorescence chamber which was equipped with 4 large area, low noise photodiodes arranged in the backscattering geometry, each photodiode bearing a 12 μm thick Cr filter for the experiments carried out at the Mn K-edge. The incident beam was chopped at *ca.* 67 Hz and the a.c. modulated analog signal was processed by a multichannel digital lock-in readout electronics [35].

DATA ANALYSES

The basic EXAFS analyses followed standard procedures detailed elsewhere[31]. Since the spectra were recorded in FY detection mode, the data were carefully corrected for saturation & self absorption [36,37]. Throughout the present paper, we never display the k^n weighted FT spectra but, following a suggestion made by Lee and Beni [38] , we exploit phase and amplitude corrected "optical" FT spectra defined [31] by:

$$\tilde{\chi}_j(R) = \int_0^{\infty} dk\ W(k)\ \frac{k\bar{R}_j^{2p}\exp\left[2\sigma_j^2k^2 - 2ikR - i\psi_j\left(k;\ \bar{R}_j\right)\right]}{F_j\left(k;\ \bar{R}_j\right)D^{\ell}\left(\bar{R}_j\ ;\ \Gamma_t\ ;k\right)S_0^2(k)}\ \chi(k) \qquad (1)$$

where:

- W(*k*) is a Kaiser-Bessel window function aimed at minimizing the side lobes of the observed signals;
- $\psi_j\left(k;\bar{R}_j\right) = 2\delta_0^{\ell}(k) + \phi_j^{\ell}\left(k;\bar{R}_j\right)$ is the phase-shift associated with the selected scattering path indexed j with the, configuration averaged, path length $2\bar{R}_j$;
- $F_j\left(k;\bar{R}_j\right) = \left(k\bar{R}_j^2\right)A_j^{\ell}\left(k;\bar{R}_j\right)$ is the magnitude of the backscattering amplitude for the selected path j ;
- $\exp\left[-2\sigma_j^2k^2\right]$ is the Debye-Waller factor of the scattering path j ;
- $D^{\ell}\left(\bar{R}_j;\Gamma_t;\ k\right)$ is a damping function taking into account the finite energy resolution of the monochromator as well as the core hole life-time ;
- $S_0^2(k)$ is a semi-empirical correction accounting for the *k*-dependent losses in the general many-body problem.

For applications concerning porphyrin chemistry, it is most convenient to display $\Im\left[\tilde{\chi}_j(R)\right]$ spectra because: (*i*) the resolution is better; (*ii*) a valuable phase information is preserved that can be exploited to discriminate between scattering atoms of very different nature; (*iii*) as pointed out by Lee and Beni [38], a simple criterion for adjusting E_0, is to let coincide the maxima of $\Im\left[\tilde{\chi}_j(R)\right]$ and $\left|\tilde{\chi}_j(R)\right|$ for a well resolved shell j. Phase shifts and backscattering amplitudes required to exploit equation (1) can now be generated with well established codes: MSXAS[39], EXCURVE[40], FEFF7[41]... Throughout the present paper, the phase-shifts and backscattering amplitudes injected into equation (1) were those of the most intense signature of the FT-spectrum, *i.e* .the Mn...$N_{pyrrole}$ shell and were calculated with MSXAS.

Perturbed Difference EXAFS analyses play a central role in the present study. Such analyses have already been successfully used to solve in a reliable way a number of ill-conditioned problems in porphyrin chemistry [30,31,42-52]. For the sake of brevity, we will only refer here to a recent review in which the method is discussed and illustrated with specific applications. Nevertheless, one should be aware that the method has practical implications regarding the selection of the reference compounds:

- Comparison should be made between metalloporphyrins featuring the same macrocyclic ligand in order to minimize the effects of structural distortions: this is why compounds **1-7** were all prepared with the ligand $DPPF_{20}$.
- Ideally, the reference compound should have no axial ligand. This is clearly not possible with Mn porphyrins in a high oxidation state but the pentacoordinated species **7** could be retained as a suitable reference because the short distance Mn-N did not interfere with the signatures of the axial ligands in the unknown species **2-5**. Unfortunately, no crystal structure of species **7** was available and it was therefore a prerequisite of the method to refine first the relevant structural parameters of species **7** by comparison with species **2** for which we had a crystal structure.
- As far as EXAFS studies are concerned, it is always a good idea, at least in our opinion, to check for the self consistency of the results obtained over a whole series of model

compounds. This is true for any type of data analysis but is particularly recommended for difference analyses. This is why compound **6** was also included in the present study.

One limitation in XANES studies stems from the broad line shape of the pre-edge resonances which result from the convoluted effects of a very short core hole lifetime and a finite energy resolution of the monochromator. A very attractive approach to circumvent this difficulty was proposed by Loeffen *et al.* [48] : it consists in deconvoluting numerically the experimental XANES spectra in order to recover narrower resonance lines. We have developed our own deconvolution algorithms following procedures detailed elsewhere[31]. The key parameters characterizing the Lorentzian lineshape and Gaussian instrumental broadening functions are their full widths at half maximum (fwhm):

$$w_L = 2\Gamma_h; \quad w_G = 2\sigma_{exp}(\ln 4)^{1/2}$$

Deconvoluted spectra are particularly useful to compare experimental spectra with *ab initio* simulations of the XANES spectra. In the present study, full multiple scattering simulations of the XANES spectra were performed with the code "*CONTINUUM*" developed by Natoli and co-workers[49]. Due to the finite mean free path of the photoelectron in the excited state, it is reasonable in such calculations to restrict the radial distribution of the scattering atoms around the photoabsorber to a single metalloporphyrin cluster of 121 atoms ($R \leq 9$Å). The Mattheiss prescription [50] was used to build up the cluster electronic density by superposition of neutral atomic charge densities obtained from the Clementi-Roetti tables[51] while the Coulomb part of the potential was obtained by a superposition of the atomic potentials. The muffin-tin radii were chosen according to the Norman criterion[52] allowing a 15% overlap between contiguous spheres to simulate the *axial* atomic bonds but only 5% for the chemical bonds within the porphyrin macrocycle. For the exchange-correlation part of the potential, we deliberately decided to stay with the standard Xα functional density in order to preserve as narrow resonance lineshapes as possible. A better agreement with the experimental spectra would have been obtained with the energy-dependent complex Hedin-Lundqvist self energy which takes into account extrinsic losses of the photoelectron[53]. In the present study, we were merely interested in reproducing the energy splitting of the various pre-edge resonances (or shape resonances) contributing to a XANES spectrum and which are sensitive finger-prints of a given stereo-geometrical conformation of a given cluster.

Results and discussion

DIFFERENCE EXAFS ANALYSES AT THE Mn K-EDGE

The optical FT spectra of species: **1** = $(DPPF_{20})Mn^{III}Cl$ and **2** = $[(DPPF_{20})MnCl + O_3]$ are compared respectively in Figures 1a and 2a with the "perturbed" FT spectrum of the reference compound, *i.e.* the nitrido complex: **7** = $(DPPF_{20})MnN$. It is noteworthy that the most characteristic signatures of the porphyrin macrocycle: 4 $N_{pyrrole}$; 8 C_α; 4 C_{meso} ; 8 C_β ; (see scheme 1b for notations) have nearly the same phase. This is not true for the signature of the first carbons ($C_{1\phi}$) of the four meso-substituting phenyl groups which exhibit a nearly "inverted" phase whereas their intensity is significantly enhanced: this is a clear indication that the multiple scattering paths Mn → C_{meso} → $C_{1\phi}$ → Mn are dominant due to the nearly colinear arrangement of the metal, of the methine carbons C_{meso} and the carbons $C_{1\phi}$. Similarly, the "in-phase" C_β signals are most often peaking at distances that are too short to be assigned to a pure single scattering signal and exhibit amplitudes which vary significantly with the planarity of the macrocycle.

A careful investigation of the FT spectra reproduced in Figures 1a and 2a would reveal a small (but well reproducible) contraction of the distances Mn...C_j that are characteristic of the porphyrin core in both species **1** and **2** with respect to the unperturbed reference compound

7. The amplitude of this contraction is much larger in the case of sample **2**, *i.e.* the sample treated with ozone. It is our interpretation that such a contraction is associated with a different shift (H) of the metal with respect to the mean plane of the pyrrole nitrogens and with a correlated change in the conformation of the macrocycle. These effects were taken into account in the "perturbed" FT spectra of species **7** reproduced in Figures 1a /2a the criteria retained being to achieve the most effective cancellation of the signatures of the porphyrin macrocycle in the difference spectra which are shown in Figures 1b and 2b. Similar analyses were performed with the various pairs of spectra obtained with samples **3-6**. For the sake of comparison, we have regrouped in Figures 4a and 4b the FT difference spectra obtained respectively for compounds **4** and **6** using perturbed spectra of species **7** as reference. The assignment of the signatures of the axial ligands is now getting straightforward:

- The method let us expect first a *negative* contribution of the nitrogen atom of the nitrido species **7**. This signal is rather well resolved. It should be kept in mind that its peak position is slightly modified as a consequence of the perturbation method but a straightforward analytical correction can be used to recover the exact Mn...N distance.
- Most characteristic are the inverted signatures of the chlorine and bromine atoms which have opposite scattering phase shifts. Fitting techniques applied to the difference spectra in the momentum space made it easy to correct for the different phase shifts and scattering amplitudes in order to recover the exact interatomic distances and determine the corresponding Debye-Waller factors.
- In the case of the azido derivative **6**, only the assignment of the signature of the first nitrogen atom is unambiguous and can yield an accurate Mn...N_1 distance. Weaker signals associated with the Mn...N_2 and Mn...N_3 single scattering paths are expected to contribute to the difference spectrum but their assignment remains tentative although the signals look quite consistent with simulations including multiple scattering paths.

We have regrouped in table 1 the characteristic interatomic distances and related structural parameters deduced from the difference analyses after appropriate numerical refinements. The nitrido complex **7** will play a key role in this study as the most suitable reference for the structural investigation of the complexes treated with ozone. This is because species **7** is contributing to a single negative peak (at *ca.* 1.51 Å) in the FT difference spectra, outside the range of interest to identify the axial ligands in species **2-5**. Perturbed Difference EXAFS Analyses *per se* cannot yield absolute values, neither for the axial shift H of the metal nor for the radius of the macrocyclic cavity but the known crystal structure of species **1** allowed us to recover absolute structural parameters for species **7**. As summarized in table 1, we found that, in species **7**, the metal is shifted away from the mean plane of the pyrrole nitrogens by: H = 0.38 ± 0.02 Å whereas this shift is 0.24 Å in species **1**. The difference ΔH = 0.14 Å as well as the short distance Mn...N (1.51 ± 0.01 Å) which were deduced from the difference analysis are fully consistent with the known crystal structure of another nitrido-Mn^V complexes [54]. We also noted a significant increase in the macrocyclic cavity radius: ΔR_{cav} = ½ Δ_{cav} = + 0.02 Å which is consistent with a non-planar structure of the macrocycle. On the other hand, the saddle-shaped conformation would be more consistent with: $0.00 \leq d \leq +0.04$ Å whereas the crystal structure of species **1** gave: d = -0.04 Å. The latter value has, however, to be considered as a trend because Difference Analyses are insensitive to the first order to the combined doming + antidoming distortions describing a porphyrin with a saddle-shaped conformation. Regarding the Mn^{III} species **4** and **6**, we found a conformation of the porphyrin macrocycle fairly similar to the conformation of compound **1**: this is reflected by the refined distances of the metal from the mean pyrrole nitrogen: H(**4**) = 0.20 ± 0.02 Å; H(**6**) = 0.26 ± 0.02 Å. The axial distances: R (Mn...Br) = 2.51 ± 0.01Å in species **4** and R (Mn...N_{azido}) =

2.05 ± 0.01Å in species **6**, are in excellent agreement either with earlier EXAFS measurements[44] or with known crystal structures of other porphyrinic compounds [55]. In the case of the azido complex, a refined analysis taking into account multiple scattering paths allowed us to refine the assignment of the three nitrogen atoms of the azido ligand and indicated that the MnN_1N_2 angle should be close to 130°.

Having collected reliable structural information concerning the reference species **7**, we can now turn to a discussion of the structure of the complexes formed with ozone. The following remarks can be made immediately:

(i) Even though species **2** and **5** were prepared with fairly different precursors (*i.e.* species **1** and **4**), the Mn atoms have strictly the same structural environment. This becomes obvious if one simply looks at Figures 4 which compare either the optical FT spectra of species **2** and **5** (Fig. 4a) or their FT difference spectra (Fig. 4b) with respect to species **7**: In both cases, there is a striking similarity of the spectra that are compared. It will be shown in a subsequent section that their XANES spectra also look pretty much identical. This result rules totally out the presence of either chlorine or bromine atoms in the coordination sphere of the metal.

(ii) The difference analyses tell us next that the Mn atom is, in both cases, systematically shifted back into the average plane of the $N_{pyrrole}$ ligands : this is *a priori* consistent with a model in which the Mn atom would be coordinated with two ozone molecules arranged in a *symmetric* configuration with respect to the porphyrin core. Persevering with this interpretation, we found that the FT difference spectra shown in Figure 4b can be analyzed reasonably well in terms of a negative contribution of a single nitrogen atom assigned to the nitrido species **7**, plus the positive contributions of two sets of oxygen atoms :

- two oxygen atoms O_1 located at a well defined distance: R (Mn...O_1) = 2.09 ± 0.02 Å ;
- two oxygen atoms O_2 located at a somewhat longer distance: R (Mn...O_2) = 2.49 ± 0.05 Å with a much bigger structural disorder and a fairly asymmetric distribution implying the contribution of higher order correlations and a phase distortion.

We have compared in Figure 5 the spectra obtained by Fourier-Transforming the perturbed difference $\Delta\chi(k) = \left\{ [\chi(k)]_2 - [\chi(k)]_7^* \right\}$ and a simulated difference spectrum $\Delta\chi_{sim}(k)$ generated as the best fit to our structural model. For more consistency, we also added the contributions of the relevant multiple scattering paths: Mn → O_1 → O_2 → Mn ; Mn → O_2 → O_1 → Mn and Mn → O_1 → O_2 → O_1 → Mn assuming that the Mn O_1O_2 angle could be of the order of 100° (cf. scheme 2). As shown by Fig. 5, the agreement between the simulated and experimental data is good enough to establish the credibility of our interpretation. Unfortunately, the problem with such a fit is that the level of correlations between the parameters used to describe the second oxygen shell is quite high so that the proposed structure cannot be given as unique and remains tentative. That one cannot detect any signal associated with the third oxygen O_3 is not really surprising since we expect the ozone molecule (O_1-O_2-O_3) bound to Mn to be bent, the $O_1O_2O_3$ angle being typically of the order 116°. In such a bent geometry, any rotation of the fragment O_2O_3 around the O_1O_2 axis would induce a broad distribution of the long Mn...O_3 distances with the consequence that no EXAFS signal could survive to such a structural disorder. Recall that EXAFS cannot discriminate *a priori* between two structural models in which the Mn atom would be bound either to two ozone molecules or two oxygen molecules unless the distances R (Mn...O_1) and R (Mn...O_2) are different in these two options.

We have compared in Figure 6 the FT difference spectra obtained respectively with sample **3** and sample **2** using species **7** as a common reference with strictly the same perturbation in both analyses. Let us recall that species **2** = [($DPPF_{20}$)MnCl + O_3] has no

catalytic activity regarding the epoxidation of olefins whereas species **3** = [$(DPPF_{20})MnCl + O_3$ + Pyridine] has a catalytic activity. Clearly, the structural environment of Mn is not identical in samples **2** and **3**: whereas the first signal assigned to two oxygen atoms at R (Mn...O_1) = 2.09 ± 0.02 Å is fairly similar in both compounds, the second signal tentatively assigned to two oxygen atoms at R (Mn...O_2) = 2.49 ± 0.05 Å has a much lower intensity in species **3**, the reduction factor being >2. This means that, for a large number of absorbing sites, either oxygen O_2 is not there anymore or the distribution of the distances R (Mn...O_2) is becoming so broad that the EXAFS signal can no longer be detected. One would expect this situation to happen, for instance, if part of the ozone molecules bound to Mn was decomposed to release a single oxygen radical O_1. still bound to Mn. An important point which may support this interpretation is that the difference spectrum of species **3** does not reveal any subtle evidence that pyridine would replace ozone as axial ligand:

- Let us start with the experimental result that we observe a decrease of only the second signal Mn...O_2. Thus, if pyridine was exchanged with one ozone molecule bound to Mn, then, our spectra would imply that the Mn...$N_{pyridine}$ distance should also be as short as 2.09 Å. This is, however, extremely unlikely, especially for hexa (or hepta) coordinated porphyrinic complexes. As far as metalloporphyrin chemistry is concerned, the interaction with pyridine solvent molecules is usually found very weak and contributes to only fairly long metal...nitrogen distances: illustrating this argument is the long distance R(Mn...$N_{pyridine}$) ~ 2.45 Å found in hexacoordinated Mn (III) compounds such as (TPP)MnCl(Pyridine) [56]. Jorgensen[57] has considered the case of the interaction of pyridine with oxo derivatives such as (Porphyrin):Mn=O and concluded that this interaction involved antibonding orbitals weakening the chemical bond with pyridine.

- Nevertheless, if one would accept that the Mn...Pyridine interaction could be as strong as with an imidazole ligand, then, we should have been able to detect in the difference EXAFS spectrum the characteristic pattern of the carbons of the pyridine ring: $2C_\alpha + 2C_\beta + 1C_\gamma$ all enhanced by multiple scattering. It is our experience that the relevant contributions from a bound imidazole ring are well detectable due to the high sensitivity of difference analyses. In contrast, in the present study, there is no evidence of any residual signature which could be assigned, for example, to the ortho- carbons (C_α) of the pyridine ring.

The absence of pyridine in the immediate environment of the Mn site implies that the activation of species **3** is only indirectly mediated by pyridine.

Mn K-EDGE XANES SPECTRA

In comparative studies where small details are becoming essential, it is more convenient to display the first derivative of the XANES spectra with respect to the energy of the incident photons (the original spectra being available as supplementary materials). This led us to compare the first derivative XANES spectrum of species **2** = [$(DPPF_{20})MnCl + O_3$] with successively the first derivative XANES spectra of samples **1** = $(DPPF_{20})MnCl$ (Fig. 7a), **5** = [$(DPPF_{20})MnBr + O_3$] (Fig. 7b) and **3** = [$(DPPF_{20})MnCl + O_3$ + Pyridine] (Fig. 7c). Figure 7a confirms that the local environment of the Mn atom is different in species **1** and **2** as reflected by the modified morphology of the distribution of the shape resonances at high energy. Particularly noteworthy is the low amplitude of the pre-edge structure in species **2** as compared with sample **1**: this can be well understood if one remembers that electric dipole transitions 1s → (A_1, E) are allowed in a ligand field with approximatively C_{4v} symmetry whereas there is no dipole allowed transition to 3d orbitals in a ligand field with symmetry D_{4h} or D_{2h} . This result supports our interpretation that, in species **2**, the metal is shifted back to the mean plane of the porphyrin as a consequence of its coordination with two ozone molecules arranged in a symmetric way with respect to the equatorial porphyrin plane. On the other hand, we learned from other spectroscopies (*e.g.* EPR) that, in solution, the oxidation state of Mn is formally

(IV) in species **2** but only (III) in species **1**. The XANES spectra recorded from powdered samples in the solid state are fully consistent with this conclusion. However, Figure 7a illustrates very well the point that interpretations based solely on XANES studies can be misleading since, in the case of species **2**, the pre-edge resonance is shifted down to lower energies whereas the edge and the most intense shape resonances are shifted up to higher energies. On the other hand, figures 7b,7c show that species **2**, **3**, and **5** should share the same local environment of the metal since all pre-edge or shape resonances exhibit the same peak energy with nearly the same relative intensity. The only significant difference concerns the relative intensity of a weak shoulder in the edge (marked with an arrow in Fig. 7b,7c). Recall that such a shoulder is most often found in the first derivative XANES spectra of many iron porphyrins or hemoproteins and that it was recognized to be sensitive to the spin state of the metal [32,58]. The small difference that we observe in the XANES spectra of species **2** and **3** could thus be correlated with the results of EPR studies[16] carried out on the same compounds and which revealed that the EPR spectra were also different. Although species **2** is paramagnetic with a large magnetic moment (4.34 μ_B), we failed to detect any XMCD signal even when the sample was cooled down to 12 K and inserted in a high magnetic field (6T): this negative result is supporting the conclusion that the spins are ordering antiferromagnetically at low temperature[16].

We found attractive to check whether or not the structural model proposed in the previous section (*i.e.* scheme 2) could be supported further by *ab initio* MSW simulations of the XANES spectra. The XANES spectrum of species **1** was first simulated using a cluster containing 118 atoms and a stereo-geometrical arrangement directly deduced from the known crystal structure[29]. In Figure 8a, a polarization averaged, simulated XANES spectrum is compared with a numerically deconvoluted experimental spectrum for which the core hole life-time broadening was not fully compensated. Even though the shape resonances are still severely damped in the experimental spectrum (as a consequence of the residual core hole life-time broadening + the inelastic losses of the photoelectron...), we found rather encouraging that nearly all resonances predicted by the calculation were basically detectable in the deconvoluted experimental spectrum even though neither the relative amplitudes nor the exact resonance energy can yet be perfectly reproduced. The same sort of simulation was also attempted for species **7** = ($DPPF_{20}$)Mn N : we used a cluster containing again 118 atoms but with a stereo-geometry now postulated from our perturbed difference analysis of the EXAFS spectra. Again, all the resonances predicted by the calculation could be identified in the deconvoluted experimental spectrum. It was qualitatively confirmed that the intensity of the prepeak was correlated with the shift of the metal out of the plane of the porphyrin and that the most intense shape resonance was a good finger print for the saddle-shape distortion of the macrocycle.

Finally, we tried to simulate the XANES spectra of sample **2** = [($DPPF_{20}$)MnCl + O_3] using a cluster containing 121 atoms in a stereo-geometrical arrangement largely inspired by the known structure of species **1**, the latter structure being however modified in order to make it consistent with the coordination scheme 2. As illustrated by Figure 8b, the results are encouraging regarding the consistency of our interpretation. Unfortunately, the quality of the experimental data did not allowed us to push the deconvolution technique to its limit and the experimental spectrum reproduced in Figure 8b still suffers from a severe broadening. Nevertheless, it is already remarkable that the low intensity, splitted structure of the pre-edge resonances look consistent with our calculation. The calculation also suggested that the intensity of the strongest resonance found near 6570 eV should be particularly sensitive to the saddle-shaped configuration of the porphyrin macrocycle.

CL K-EDGE XANES:

In the previous sections, we have produced strong arguments supporting the lack of coordination of chlorine (in species **2** and **3**) and bromine (in species **5**) to manganese. It was attractive to check independently this conclusion by investigating directly the Cl K-edge XAS spectra of samples **1**, **2** and **3**. On the other hand, it is well documented that Br^- anions are oxidized by molecular ozone to yield BrO^- ; BrO_2^- and BrO_3^- anions [59-61], the formation of carcinogen bromates[62] being precisely an undesirable by-product in the desinfection of water by ozone. Since nothing as clear was ever reported regarding the eventual formation of hypochlorite ClO^- and/or chlorate ClO_3^- anions, this prompted us to record the XANES spectra of the following references: **8** = [Mn $(ClO_4)_2$, 6 H_2O]; **9** = $KClO_3$ and the aqueous solution **10** = [NaOCl / H_2O]. The corresponding XANES spectra are compared in Figure 9a. The latter spectra were deconvoluted numerically using the following parameters: $w_L = 0.6$ eV; w_G = 0.5 eV and the corresponding spectra are also displayed in Figure 9b. The energy resolution of the experimental spectra reproduced in Fig. 9a compares very favourably with the previous Cl K-edge XANES of chlorates or perchlorates [63-65] whereas additional details are revealed by Figure 9b. No XANES spectrum has yet been reported for NaOCl aqueous solutions. All spectra exhibit resonant structures which peak at energies increasing with the oxidation state of the chlorine: E_{P1}(**8**) = 2833.9 eV for ClO_4^- in **8** ; E_{P1}(**9**) = 2829.9 eV for ClO_3^- in **9**. It is noteworthy that the XANES spectrum of the aqueous hypochlorite solution **10** looks like the superposition of a sharp contribution due to chlorate anions at E_{P3}(**10**) = 2829.9 eV plus two non-identified resonances (or edge ?) at much lower energies: E_{P1}(**10**) = 2821.3 eV and E_{P2}(**10**) = 2823.7 eV. This result may explain why anhydrous hypochlorite anions have never been isolated in the solid state: hydrated OCl^- anions may are obviously partially oxidized into ClO_3^- anions whereas the existence of solvated Cl^- anions cannot be completely ruled out. The present result certainly calls for a more systematic study of such aqueous solutions at various pHs.

On the other hand, the XANES spectra of samples **1**, **2**, **3** are compared in Figure 10a whereas deconvoluted spectra of species **1** and **2** are also displayed in Figure 10b. For the sake of consistency, we kept the same broadening parameters as for the analysis of the reference systems **8**-**10**. It is obvious from Figure 10a that the XANES spectra of samples **2** and **3** are different from the XANES spectrum of the precursor **1**. Most characteristic in the XANES spectra of samples **2** and **3** is the pre-edge doublet which is observed at fairly low energies: E_{P1}(**2**) = 2818.6 eV and E_{P2}(**3**) = 2820.5 eV whereas the edge of sample **2** is unambiguously shifted towards higher energy by more than 1eV and is overlapping with the range where the characteristic resonances / edge of solution 10 were observed. Indeed, as far as species **2** and **3** are concerned, the chlorine atoms are certainly not in a high oxidation state and the direct formation of chlorate or perchlorate anions can be definitely ruled out. We are, however, in the ambiguous (but frequent) situation where the edge and the pre-edge resonances shift in opposite directions with the practical consequence that the information regarding the charge carried by the absorbing atom is getting confused. The reason for this is to be found in the so-called Natoli's rule: $\Delta E.R$ = Cst. This rule, which is extensively used in the soft X-ray range, reminds us that, whenever the energy separation ΔE between the pre-edge resonances and the edge is increased, then the interatomic distance R with the nearest neighbor should decrease. If we apply very tentatively this rule to the XANES spectra of species **1** and **2**, then we are led to the conclusion that the nearest neighbor distance in species **2** should be 1.65 ± 0.05 Å. Interestingly, this is precisely the order of magnitude of the short Cl...O bond lengths predicted either for ClO^- or for Cl-Ozone molecular clusters. This consideration is therefore consistent with the admitted view that chlorine should be oxidized by ozone. By the way, the Natoli's rule would also definitely rule out the formation of chloride ions interacting with ozone or "somewhere" with the porphyrin because the bulky chloride anion with its electronic

structure close to Ar could only be compatible with large Cl^-...X ionic distances, typically in excess of 3.1 Å.

CL K-EDGE EXAFS:

We have also recorded the Cl K-edge EXAFS spectra of species **1** and **2** and we have reproduced in Figures 11a and 11b the corresponding optical FT EXAFS spectra. The quality of the spectra $k^3.\chi(k)$ (available as supplementary material) is very similar for both compounds: the signal-to-noise ratio is certainly not as good as in the case of the spectra recorded at the Mn K-edge but it is well compatible with FT analyses over a fairly reasonable momentum range [2-15 $Å^{-1}$]. The optical FT spectrum of species **1** was corrected for the dominant shell, *i.e.* for the Cl...Mn scattering path, the additional signatures of the Cl...N and Cl...C_α being not properly resolved. The refined distance R(Cl...Mn)= 2.35 ± 0.02 Å which was obtained by fitting the latter data was found in reasonable agreement with the (slightly better) distance R(Mn...Cl) = 2.37 ± 0.01 Å deduced from the difference EXAFS analyses performed at the Mn K-edge. The optical FT spectrum of species **2** shown in Figure 11b was tentatively corrected for Cl...O scattering paths: it seems to be dominated by two signals provisionally assigned to oxygen scatterers and which are peaking at R(Cl...$O_{(1)}$) = 1.69 ± 0.03 Å and R(Cl...$O_{(2)}$) = 2.20 ± 0.02 Å respectively. The FT spectrum is thus nicely supporting the indication given by the Natoli's rule regarding the first neighbor distance R(Cl...$O_{(1)}$). On the other hand, the FT spectrum of species **2** is ruling out the formation of a simple ClO^- anion because we have a well defined structural order beyond the first neighbor. Of particular interest is the second shell peaking at 2.20 Å which is more intense than the first one and would be compatible with a model containing twice more oxygens as second neighbors. Interestingly, the two distances R(Cl...$O_{(1)}$) and R(Cl...$O_{(2)}$) would then match perfectly the postulated chemical structure of the molecular species $\mathbf{S_3}$= [Cl-O-O-O] which is presumed to form in the stratosphere[66] as a result of the interaction of ozone with Cl. radicals. Since such hypothetical molecular species were never isolated, their geometries have been tentatively optimized from *ab initio* calculations which also made it possible to evaluate the heat of formation of such species [67,68]. In this perspective, Rathmann and Schindler[67] have compared the ground state geometry of three isomers:

$\mathbf{S_1}$ (C_{3v}) = Sym [ClO_3] ; $\mathbf{S_2}$ =[O-Cl-O-O]; $\mathbf{S_3}$= [Cl-O-O-O]

and have shown that $\mathbf{S_1}$ (48 kcal/mol) and $\mathbf{S_3}$ (41 kcal/mol) had the lowest heats of formation. In our case, the formation of a species like $\mathbf{S_1}$ can certainly be ruled out by the EXAFS spectrum because symmetry would require all Cl...O bond lengths to be identical and much shorter than what we observe (R = 1.48 Å). Regarding species $\mathbf{S_3}$, the radial distribution of the nearest neighbors deduced from the geometry optimized by Rathman and Shindler[67] would give one oxygen at 1.71 Å and 2 oxygen atoms at 2.20 Å with bond angles Cl-$O_{(1)}$-$O_{(2)}$ and $O_{(1)}$-$O_{(2)}$-$O_{(3)}$ respectively equal to 109.5° and 109.3°. It is our tentative interpretation that a similar cluster (or molecular moiety) could form during the substitution of one chlorine atom by ozone at the Mn site. At this stage, one could perfectly envisage that the ozone molecule interacting with chlorine could be the same as the one bound to the Mn site as discussed in the previous section of this paper. This could perhaps explain why the FT EXAFS spectrum exhibits some long range order beyond 3.2 Å even though any interpretation of the corresponding signatures would be, at this stage, very speculative. Another problem which we left behind in the present discussion concerns the rather large amplitude of the EXAFS spectrum of species **2**: from the optical FT spectra displayed in Fig. 11a,11b for species **1** and species **2** (which are compensated for different scattering amplitude), and also from more accurate fits, it appears most probable that the environment of chlorine should rather consist of two oxygens at short distance R(Cl...$O_{(1)}$) and four oxygens at long distance R(Cl...$O_{(2)}$). One is led therefore to formulate the hypothesis that in species **2**, a single chlorine atom could

perhaps bridge two ozone molecules. We will produce below an additional argument supporting this hypothesis.

TENTATIVE AB INITIO SIMULATIONS OF THE CL XANES SPECTRA:

Inspired by the consideration that a XANES spectrum is a characteristic finger print of the stereo-geometrical arrangement of the atoms in a molecular cluster, we found very attractive to investigate how close one would be able to reproduce the XANES spectrum of species **2** using *ab initio* MSW calculations and the structural information deduced from the EXAFS spectrum. As far as the interpretation developed in the previous section is correct, then one should be able to reproduce the XANES spectrum with only a small cluster of oxygen atoms in the immediate vicinity of the absorbing chlorine atom and we could use as a reasonable starting point the stereo-geometry of the molecular species $\mathbf{S_3}$= [Cl-O-O-O] which was optimized by Rathman and Shindler [67]. Of course, in our simulation, the charge localized on the chlorine is one parameter and there is absolutely no chance that such calculation can tell us (directly) anything about the oxidation state of chlorine compared to other compounds like the chlorate anions. Nevertheless, if the model is correct, we should be able to reproduce more or less accurately the splitting of the pre-edge resonances and the profile of the shape resonances near the edge. A simulation of the XANES spectrum of species $\mathbf{S_3}$= [Cl-O-O-O] is reproduced in Figure 12a and is compared with the deconvoluted spectrum of sample 2. It is fairly encouraging that the "extended *continuum*" spectrum reproduces nearly perfectly the characteristic splitting of the pre-edge resonances in the experimental spectrum: we tried to simulate in the same way many other clusters such as ClO^-; $\mathbf{S_1}$ (C_{3v}) = Sym [ClO_3] ; $\mathbf{S_2}$ =[O-Cl-O-O]; etc... but none of the simulated spectra did ever exhibit any splitting. Unfortunately, with the cluster $\mathbf{S_3}$, the shape resonances in the edge and beyond the edge do not agree at all with the experimental spectrum. This led us to re-envisage once again the dimeric model ($\mathbf{S_6}$) in which a single chlorine would now bridge two ozone molecules. The simulated XANES spectrum of this somewhat artificial cluster is displayed in Figure 12b: whereas a splitting of the pre-edge structures is still apparent, the profile of the edge clearly reproduces much more closely the measured spectrum. It is not in our intention to argue yet that cluster $\mathbf{S_6}$ is truly existing: its geometry and its stability are not supported by any *ab initio* optimization, as opposed to cluster $\mathbf{S_3}$. We simply wish to produce this result as an indication that this model should be a better approximation of the local geometrical arrangement of the atomic potentials around chlorine in species **2**, independently of the true charge distribution. It is indeed much more compatible with the large intensity of the EXAFS spectrum.

Conclusion

Complementary X-ray Absorption Spectroscopy studies have been reported which shed light on the complex mechanisms of activation of dodecaphenylporphyrinato- halogeno-Manganese (III) derivatives by ozone. Combining difference EXAFS analyses and XANES spectra at the Mn K-edge, we have established first that the reaction of ozone with the chloro- or the bromo- precursors **1** or **4** resulted in the formation of strictly the same intermediate in which the Mn atom was in a formally tetravalent (IV) state. In species **2** or **5**, the metal ligand field should include the four equatorial pyrrolic nitrogen atoms of the porphyrin plus two ozone molecules arranged in a rather symmetrical configuration with respect to the macrocycle. We found that the interaction of Mn with each ozone molecule resulted in two asymmetric Mn...oxygen distances: R(Mn...O_1) = 2.09 ± 0.02 Å; R(Mn...O_2) = 2.49 ± 0.05 Å. The second signal was given as characteristic of a much weaker bonding with an asymmetric (anharmonic) distribution of the (Mn...O_2) distances. This geometry would be consistent with several arguments suggesting that the metal was shifted back into the mean plane of the pyrrolic nitrogen atoms. The chlorine or bromine atoms do not contribute to any detectable signal in the Mn K-edge EXAFS spectra of species **2** or **5**. MSW simulations of the XANES

spectra have been performed which confirmed that the porphyrin core was clearly non-planar in whole series. For what concerns species **2**, such *ab initio* calculations offered an additional test regarding the consistency of the geometry deduced from difference EXAFS analyses.

Species **2** and **5** do not exhibit any catalytic activity in the epoxidation of olefins. In contrast, species **3** which was obtained by reaction of ozone with the same precursor **1** but in presence of a large excess of pyridine has a remarkable catalytic activity. Difference EXAFS analyses as well as the comparison of their XANES spectra have confirmed that the structures of species **2** and **3** should be slightly (but unambiguously) different:

(i) the signal of the short Mn...Oxygen distances: R(Mn...O_1) remains more or less unaffected by the presence of pyridine whereas the long distance signal at R(Mn...O_2) is decreased by at least a factor 2 or more. There is however no indication that pyridine could be coordinated to manganese.

(ii) the Mn K-edge XANES spectra of species **2** and **3** suggest that the spin state of the metal may not be strictly the same in these two compounds as also indicated by a comparison of their EPR spectra.

A simple picture compatible with these results would be that pyridine is mediating a partial disruption of the ozone molecules bound to Mn with the formation of active radical species.

Valuable additional information was also extracted from the XANES and EXAFS studies carried out at the Cl K-edge on samples **1**, **2** and **3**. The comparison of the XANES spectra of the latter species and of the model systems **8**, **9** and **10** definitively ruled out the formation of chlorates or unstable ClO^- anions. From a simple comparison of the XANES spectra of species **2** and its precursor **1**, we pointed out, by resorting to the well known Natoli's rule, that the chlorine atom was most probably oxidized with a nearest oxygen neighbor at *ca.* 1.65 ± 0.05 Å. This result was confirmed by the analysis of the Cl K-edge EXAFS spectrum of species **2** which exhibits two characteristic Cl...oxygen distances: R(Cl...$O_{(1)}$) = 1.69± 0.03 Å; R(Cl...$O_{(2)}$) = 2.20 ± 0.02 Å with a probable site population: $N_{(2)}/N_{(1)} \sim 2$. The EXAFS spectrum thus definitely ruled out the formation of ClO^- anions but suggested that, during the substitution of the chlorine atom by one ozone molecule, chlorine could interact with ozone to produce a species similar to the molecular species $\mathbf{S_3}$ = [Cl–$O_{(1)}$–$O_{(2)}$–$O_{(3)}$] that is presumed to form in the stratosphere as a result of the interaction of ozone with Cl. radicals. The EXAFS spectrum would agree remarkably well with the postulated geometry of $\mathbf{S_3}$. Persevering with this interpretation, we have used extended *continuum* MSW calculations to simulate the XANES spectrum of species $\mathbf{S_3}$ and we found that this cluster was also the only one which was reproducing the characteristic splitting of the pre-edge resonances in the XANES spectrum of species **2**. Moving to a somewhat more speculative model in which a chlorine atom would bridge two ozone molecules, we found possible to generate a XANES spectrum reproducing even more closely the main features of the deconvoluted experimental XANES spectrum of species **2**. This model would also be much more consistent with the amplitude of the EXAFS spectrum of species **2**.

At this stage, we would like to emphasize that the present study is producing the very first evidence of a coordination of ozone to manganese. The structures which we propose for species **2**, **3** or **5** are different from what was initially guessed: the present study rules out definitely the formation in the solid state of a high valent manganese oxo compound as the one which was first isolated and characterized using EXAFS by Schappacher and Weiss[69] and others[70] at very low temperature. It is also quite remarkable that the Mn...Oxygen distances: R(Mn...O_1) = 2.09 Å which we report for species **2**, **3** and **5** are much longer than the Mn...Oxygen distance R(Mn...O_1) = 1.8 Å found by Bortolini *et al.*[44] for their "oxo-like" Mn (IV) species obtained by direct oxidation of (TMP)MnCl with NaOCl in aqueous solution.

Such a difference is not really surprising if one accepts that two ozone molecules, and more precisely two oxygen atoms per ozone molecule, are coordinated symmetrically to the metal in species **2**, **3** or **5** whereas the metal had only two axial oxygen ligands in the high valent complex of Bortolini *et al.*[44].

Acknowledgments: This work is part of a joint collaboration supported financially by the French company AIR-LIQUIDE, the French C.N.R.S and the European Synchrotron Radiation Laboratory (ESRF) in partial fulfillment of the ESRF contract CL066. The authors are particularly grateful to Dr. P. Cocolios (AIR-LIQUIDE) for having initiated this project.

References

[1] Bailey, P.S. in: *Ozonation in Organic Chemistry,* Wasserman, H. H. Ed.; Academic Press: New York, 1982; Vol. 2 pp.3-422

[2] Criegee, R. in *Peroxide Reaction Mechanisms*, Edwards, J. O. Ed. ; Wiley Interscience: New York, 1962

[3] Bablon, G.; Bellamy, W.D.; Bourbigot, M.M; Daniel, F.B.; Doré, M.; Gordon, E. F. G.; Langlais, B.; Laplanche, A.; Ventresque, B. in *Ozone in Water Treatment* ; Langlais, B.; Reckow, A.; Brink, D.R. Eds. ; Lewis Publishers: New York, 1991; pp.11-132

[4] Glaze, W.H.; Kang, J.W.; Chopin, D.H. *Ozone : Sci. Eng.* **1987**, *9*, 335-352

[5] Peyton, G.R.; Glaze, W.H. *Environ. Sci. Techn.* **1988**, *22*, 761-767

[6] Hoigné, J.; Bader, H. *Proceedings of the 12th World Congress of the International Ozone Association, Lille (France)*, **1995**, *Vol.1*, pp.27-30

[7] Reynolds, G. *Ozone : Sci. Eng.* **1989**, *11*, 339-382

[8] Al-Hayek, N.; Legube, B.; Doré, M. *Environ. Techn. Lett.* **1989**, *10*, 415-426

[9] Gracia, R.; Aragues, J.L.; Cortès, S.; Ovelleiro, J.L. *Proceedings of the 12th World Congress of the International Ozone Association, Lille (France)*, **1995**, *Vol.1*, pp.75-86

[10] Mansuy, D. *Coord. Chem. Rev.* **1993**, *125*, 129-142

[11] Montanari, F.; Banfi, S.; Pozzi, G.; Quici, S. in *Metalloporphyrins Catalyzed Oxidations*; Montanari, F.; Casella, L. Eds ; Kluwer Academic Publishers: Dordrecht, 1994; pp. 149-173

[12] Meunier, B. *Chem. Rev.* (Washington D.C.) **1992**, *92*, 1411-1456

[13] Meunier, B.; Labat, G.; Seris, J.L. WO 91/08985, 1991

[14] Sorokin, A.; Seris, J.-L.; Meunier, B. *Science*, **1995**, *268*, 1163-1166

[15] Campestrini, S.; Robert, A.; Meunier, B. *J. Org. Chem.* **1991**, *56*, 3725-3727

[16] a) Périé, K.; Barbe, J.M.; Cocolios, P.; Guilard, R. *Bull. Soc. Chim. Fr.* **1996**, *133*, 697-702
b) Périé, K. *Ph.D.* Thesis, Université de Bourgogne, Dijon (France), **1996**

[17] Medforth, C.J.; Smith, K.M. *Tetrahedron Lett.* **1990**, *31*, 5583-86

[18] Shelnutt, J.A.; Medforth, C.J.; Berber, M.D.; Barkigia, K.M.; Smith, K.M.
J. Am. Chem. Soc. **1991**, *113*, 4077-4087

[19] Medforth, C.J.; Senge, M.O.; Smith, K.M.; Barkigia, K.M.; Sparks, L.D.; Shelnutt, J.A.
J. Am. Chem. Soc. **1992**, *114*, 9859-9869

[20] Barkigia, K.M.; Renner, M.W.; Furenlid, L.R.; Medforth, C.J.; Smith, K.M.; Fajer, J.
J. Am. Chem. Soc. **1993**, *115*, 3627-3635

[21] Gentemann, S.; Medforth, C.J.; Forsyth, T.P.; Nurco, D.J.; Smith, K.M.
J. Am. Chem. Soc. **1994**, *116*, 7363-7368

[22] Senge, M.O.; Forsyth, T.P.; Nurco, D.J.; Smith, K.M.
Angew. Chem. (Int. Ed. Eng.) **1994**, *33*, 2485-2487

[23] Nurco, D.J.; Medforth, C.J.; Forsyth, T.P.; Olmstead, M.; Smith K.M.
J. Am. Chem. Soc. **1996**, *118*, 10918-10919

[24] Ochsenbein, P.; Ayougou, K.; Mandon, D.; Fischer, J.; Weiss, R.; Austin, R. N.; Jayaraj, K.; Gold, A.; Terner, J.; Fajer, J. *Angew. Chem. Int. Ed. Eng.* **1994**, *33*, 348-350

[25] Tsuchiya, S. *Chem. Phys. Lett.* **1990**, *169*, 608-610

[26] Takeda, J.; Sato, M. *Chem. Pharm. Bull.* **1994**, *42*, 1005-1007

[27] Chang, C.K.; Ebina, F. *J. Chem. Soc. Chem. Commun.* **1981**, 778-779

[28] Traylor, P.S.; Dolphin, D.; Traylor, T.G. *J. Chem. Soc. Chem. Commun.* **1984**, 279-280

[29] Guilard, R.; Périé, K.; Barbe, J.-M.; Nurco, D.J.; Smith, K.M.;
Van Caemelbecke, E.; Kadish, K.M. *Inorg. Chem.* **1998**, *37*, 973-981

[30] Goulon, J.; Loos, M.; Ascone, I.; Goulon-Ginet, C.; Battioni, P.; Battioni, J.P.; Mahy, J.P.; Mansuy, D.; Meunier, B. *Structural Investigation of Biomimetic Complexes of Cytochrome P-450 by Difference EXAFS Spectroscopy* in: *Biophysics and Synchrotron Radiation*, Bianconi, A.; Congiu-Castellano, A. Eds., Springer Series in Biophysics; Springer-Verlag: Berlin, Heidelberg, Vol.2, **1987**, 191-200

[31] Goulon, J.; Goulon-Ginet, C.; Gotte, V. *X-ray Absorption Spectroscopy Applied to Porphyrin Chemistry* in: Handbook of Porphyrin Chemistry, Kadish, K.M.; Smith, K.M.; Guilard, R. Eds, Academic Press: New-York, (1999) *in press.*

[32] Gotte, V.; Goulon, J.; Rogalev, A.; Goulon-Ginet, C.; Perié, K.; Barbe J.-M.; Guilard, R.; Cocolios, P. *J. Phys. (France)* **1997**, *7-Colloque C2*, 663-664

[33] Goulon, J.; Rogalev, A.; Gauthier, Ch.; Goulon-Ginet, C.; Pasté, S.; Signorato, R.; Neumann, C.; Varga, L.; Malgrange, C. *J. Synchrotron Rad.* **1998**, *5*, 232-238.

[34] Rogalev, A.; Gotte, V.; Goulon, J.; Gauthier, Ch.; Chavanne, J.; Elleaume, P. *J. Synchrotron Rad.* **1998**, *5*, 989-991

[35] Gauthier, Ch.; Goujon, G.; Feite, S.; Moguiline, E.; Braicovich, L.; Brookes, N.B.; Goulon, J. *Physica B* **1995**, *208-209*, 232-234

[36] Goulon, J.; Goulon-Ginet, Ch.; Cortès, R.; Dubois, J.-M. *J. Phys. (France)* **1982**, *43*, 539-548

[37] Loos, M. ; Ascone, I.; Goulon-Ginet C.; Goulon, J.; Guillard, C.; Lacroix, M.; Breysse, M.; Faure, D.; Descourières, T. *Physica B* **1989**, *158*, 145-148

[38] Lee, P.; Beni, G *Phys. Rev. B* **1977**, *15*, 2862-2883

[39] Ruiz-Lopez, M.; Bohr, F.; Filipponi, A.; Di Cicco, A.; Tyson, T.; Benfatto, M.; Natoli, C.R. *MSXAS: A system of programs for X-ray Absorption Spectra calculations using the multiple scattering approach* in: X-ray Absorption Fine Structure VII ; Hasnain, S.S. Ed.; Ellis-Horwood: London; 1991, pp. 75-77

[40] a) Gurman, S.J.; Binsted, N.; Ross, I.
J. Phys. C: Solid State Phys. **1984**, *17*, 143-151
b) Binsted, N.; Hasnain, S.S. *J. Synchrotron Rad.* **1996**, *3*, 185-196

[41] a) Rehr, J.J.; Mustre de Leon, J.; Zabinsky, S.I.; Albers, R.C.
J. Am. Chem. Soc. **1991**, *113* , 5135-5140
b) Ankudinov, A.L.; Rehr, J.J. *J. Phys. IV (France)* **1997**, *7-C2*, 121-124

[42] Goulon, J.; Friant, P.; Goulon-Ginet, C. ; Coutsolelos, P. A.; Guilard, R. *Chem. Phys.* **1984**, *83*, 367-375

[43] Friant, P.; Goulon, J.; Fischer, J.; Ricard, L.; Schappacher, M.; Weiss, R.; Momenteau, M. *New J. Chem.* **1985**, *9*, 33-40

[44] Bortolini, O.; Ricci, M.; Meunier, B.; Friant, P.; Ascone, I.; Goulon, J.
New J. Chem. **1986**, *10*, 39-49

[45] Loos, M.; Friant, P.; Ascone, I.; Goulon, J.; Barbe, J.-M.; Coutsolelos, P. A.; Guilard, R. *J. Phys.(France)* **1986**, *47-C8*, 641-644

[46] Loos, M.; Goulon, J.; Barbe, J.-M.; Guilard, R. *J. Phys.(France)* **1986**, *47-C8*, 633-636

[47] Marchon, J.-C.; Latour, J.-M.; Grand, A.; Belakhovsky, M.; Loos, M.; Goulon, J. *Inorg. Chem.* **1990**, *29*, 57-67

[48] Loeffen, P.W.; Pettifer, R.F.; Müllender, S.; Van Veenendaal, M.A., Röhler, J.; Sivia, D.S. *Phys. Rev. B* **1996**, *54*, 14877-14880

[49] Natoli, C.R., Benfatto, M. and Doniach, S. *Phys. Rev. A,* **1986**, *34*, 4682-4694

[50] Mattheis, L. *Phys. Rev. A* **1964**, *134*, 970-73

[51] Clementi, E.; Roetti, C. *Atom. Data Nucl. Data Tables* **1974**, *14*, 177-478

[52] Norman, J.G. Jr. *Mol. Phys.* **1976**, *31*, 1191-1198

[53] Hedin, L.; Lundqvist, B.I. *J. Phys. C: Solid St. Phys.* **1971**, *4*, 2064-2083

[54] Hill, C.G.; Hollander, F.J. *J. Am. Chem. Soc.* **1982**, *104*, 7318-7319

[55] Day, V.W.; Stults, B.R.; Tasset, E.L.; Marianelli, R.S.; Boucher, L.J. *Inorg. Nucl. Chem. Lett.* **1975**, *11*, 505-509

[56] Kirner, J.F.; Scheidt, W.R. *Inorg. Chem.* **1975**, *14*, 2081-2086

[57] Jorgensen, K.A., *Theoretical Studies of Oxometalloporphyrins and their Reactions with Organic Substrates* in:*Metalloporphyrins in Catalytic Oxidations,* Sheldon, R.A. Ed., Marcel Dekkers, Inc.: New York, Basel, Hong Kong, **1994**, 69-97

[58] Oyanagi, H.; Izuka, T.; Matsushita, T.; Saigo, S.; Makino, R.; Ishimura, Y. *Local Structure of Haem-Iron Studied by High Resolution XANES: Thermal Spin Equilibrium in Myoglobin* in: *Biophysics and Synchrotron Radiation,* Bianconi, A.; Congiu-Castellano, A. Eds., Springer Series in Biophysics; Springer-Verlag: Berlin, Heidelberg, Vol.2, **1987**, 99-106

[59] Haag, W.R.; Hoigne, J. *Environ. Sci. Technol.* **1983**, *17*, 261-267

[60] Croue, J.P.; Koudjonou, B.K.; Legube, B. *Proceedings of the 12th World Congress of the International Ozone Association, Lille (France)*, **1995**, *Vol.1*, pp. 223-235

[61] Siddiqi, M.; Amy, G. *Proceedings of the 12th World Congress of the International Ozone Association, Lille (France)*, **1995**, *Vol.1*, pp. 237-250

[62] Kurokawa, Y.; Maekawa, A.; Takahashi, M.; Hayashi,Y *Environ. Health Perspectives* **1990**, *87*, 309-335

[63] Filipponi, A.; Tyson T.A.; Hodgson, K.O.; Mobilio, S. *Phys. Rev. A* **1993**, *48*, 1328-1338

[64] Shadle, S.E.; Hedman, B.; Hodgson, K.O.; Solomon, E.I. *Inorg. Chem.* **1994**, *33*, 4235-4244

[65] Wu, Z.Y.; Tyson, T.A.; Natoli, C.R. *Physica B* **1995**, *208-209*, 611-613

[66] Prasad, S.S. *Nature* **1980**, *285*, 152

[67] Rathmann, T.; Schindler, R.N. *Chem. Phys. Lett.* **1992**, *190*, 539-542

[68] Workman, M.A.; Francisco, J.S. *Chem. Phys. Lett.* **1997**, *279*, 158-164

[69] Schappacher, M.; Weiss, R. *Inorg. Chem.* **1987**, *26*, 1189-90

[70] Ayougou, K.; Bill, E.; Charnock, J.M.; Garner, C.D.; Mandon, D.; Trautwein, A.X.; Weiss, R.; Winckler, H. *Angew. Chem. (Int. Ed. Eng.)* **1995**, *34*, 343-346

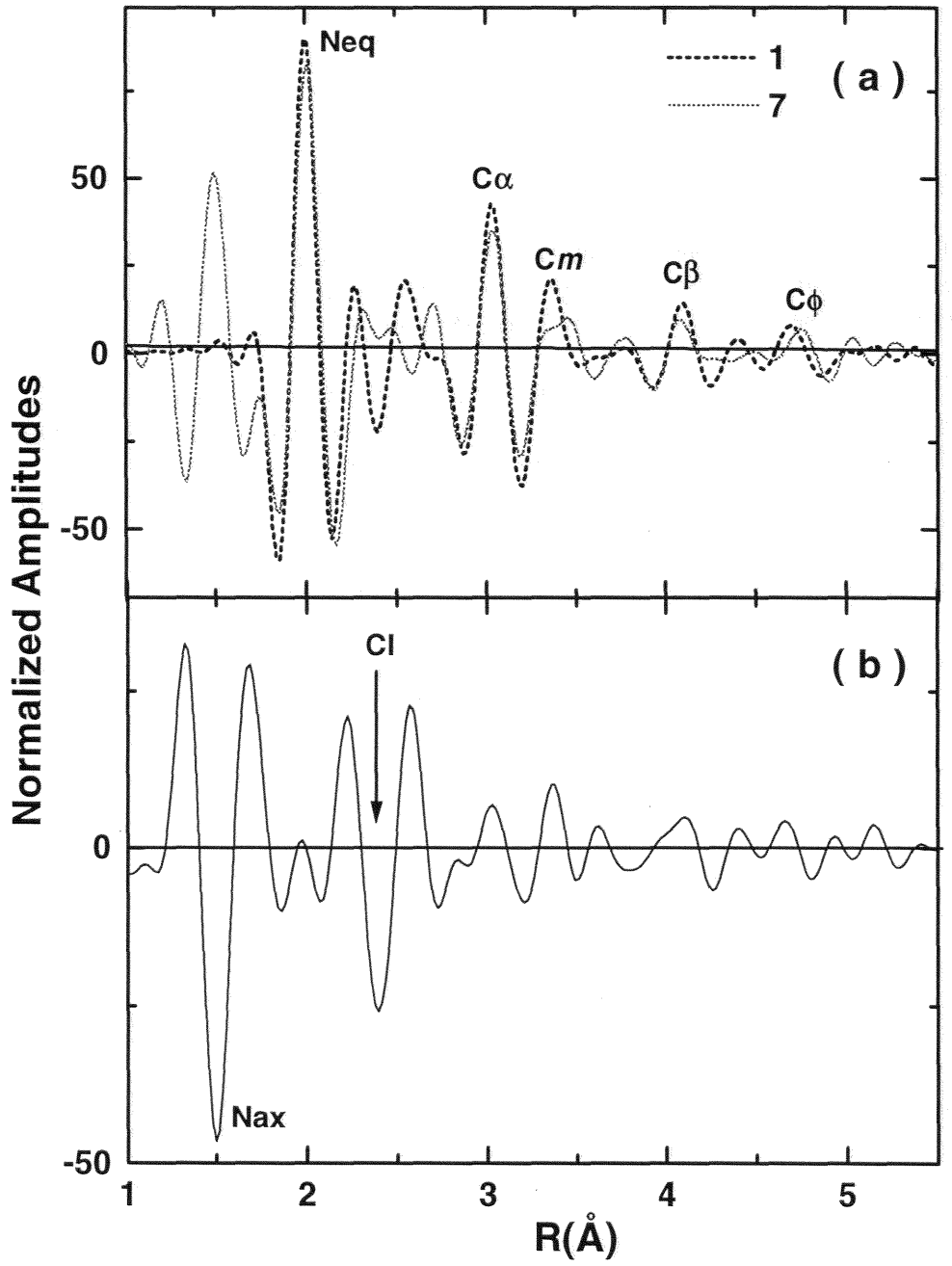

Figures 1:

Figure 1a: Comparison of the optical FT spectrum of species **1** = $(DPPF_{20})Mn\,Cl$ (dashed line) with a modified (*) optical FT spectrum of species **7** = $(DPPF_{20})Mn^{V}\,N$ (full line) taking into account a small structural perturbation: $\Delta H(7) = -0.14$ Å ; $\Delta R_{cav}(7) = -0.020$ Å; $\Delta d\,(7) = -0.06$ Å.

Figure 1b: Optical FT spectrum of the difference: $\Delta\chi(k) = \left\{ [\chi(k)]_1 - [\chi(k)]_7^* \right\}$.

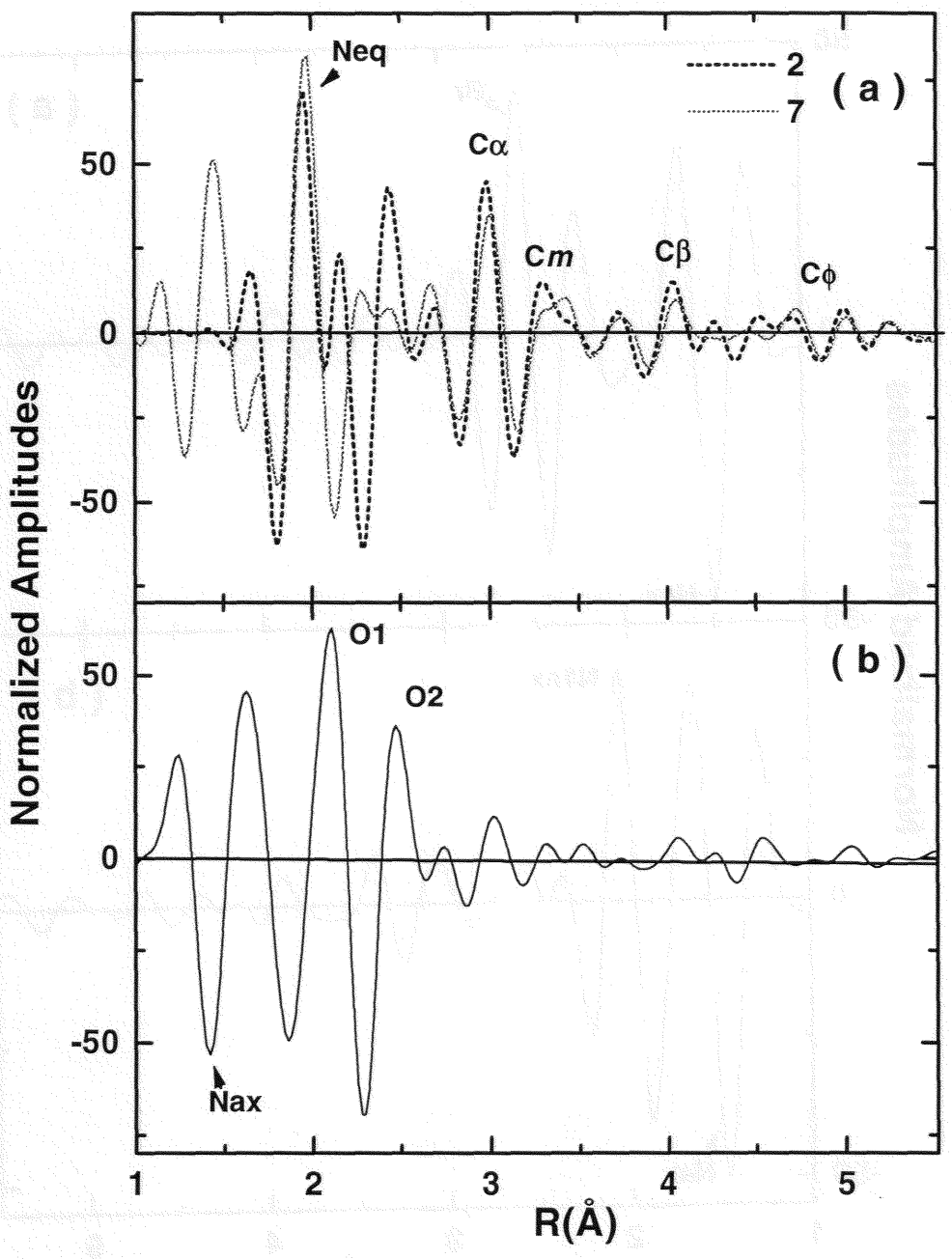

Figures 2:

Figure 2a: Comparison of the optical FT spectrum of the unknown species **2** = $[(DPPF_{20})MnCl + O_3]$ (dashed line) with a modified optical FT spectrum of species **7** = $(DPPF_{20})Mn^{V}N$ (full line) taking into account the optimized structural perturbation: $\Delta H(\mathbf{7}) = -0.38$Å ; $\Delta R_{cav}(\mathbf{7}) = -0.025$ Å ; $\Delta d(\mathbf{7}) = -0.06$ Å

Figure 2b: Optical FT spectrum of the difference $\Delta\chi(k) = \left\{ [\chi(k)]_2 - [\chi(k)]_7^* \right\}$.

Note the overlapping contributions of two oxygen shells, *i.e.* $(Mn\ldots O_1)$ and $(Mn\ldots O_2)$.

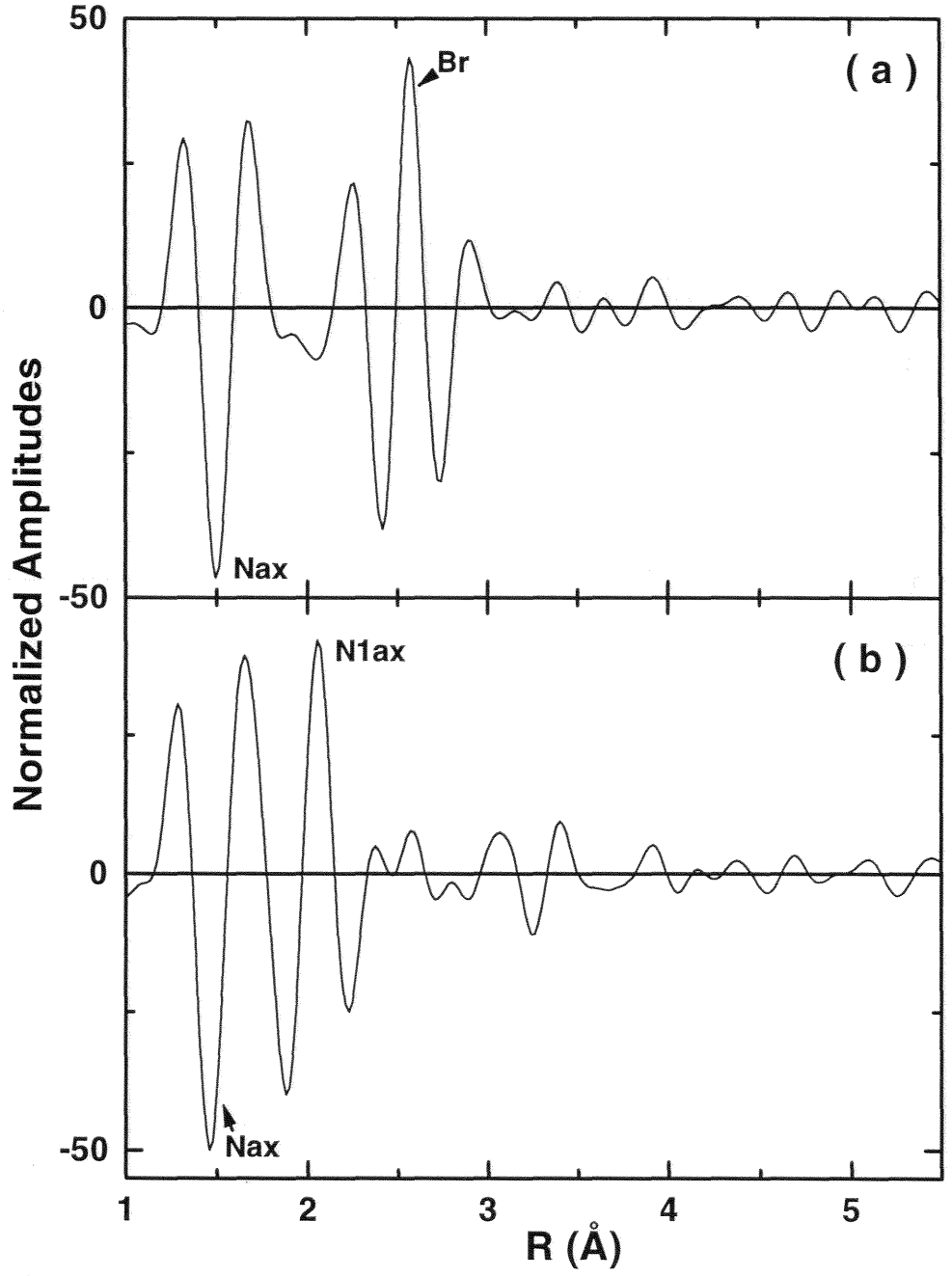

Figures 3: Difference EXAFS analyses of model compounds: **4** = ($DPPF_{20}$)Mn Br and **6** = ($DPPF_{20}$)Mn (N_3) using a spectrum of species **7** = ($DPPF_{20}$)Mn^{V} N modified according to the structural data of table 1.

Figure 3a: Optical FT of the difference: $\Delta\chi(k)=\left\{[\chi(k)]_4-[\chi(k)]_7^*\right\}$

Figure 3b: Optical FT of the difference spectrum: $\Delta\chi(k)=\left\{[\chi(k)]_6-[\chi(k)]_7^*\right\}$.

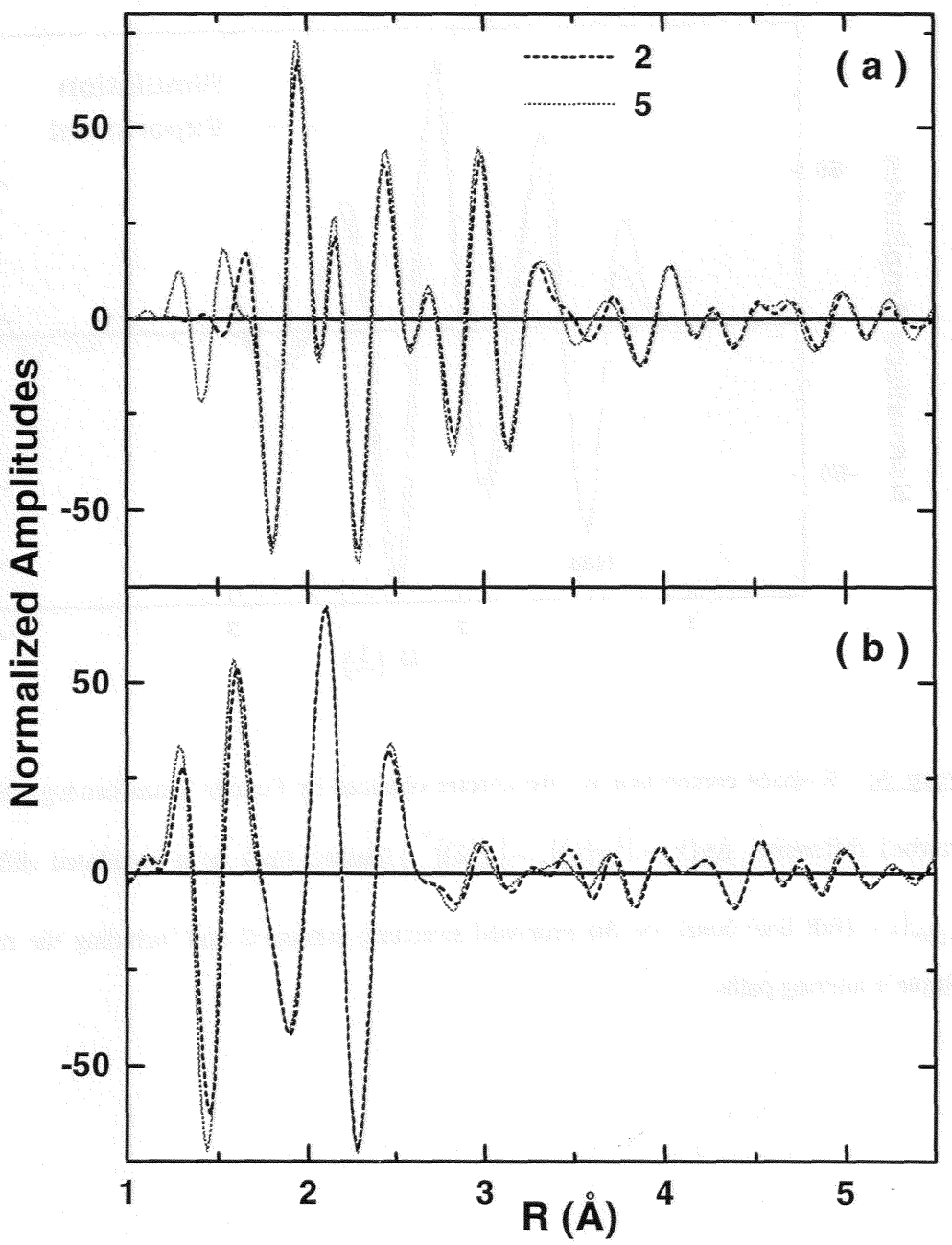

Figures 4:

Figure 4a: Comparison of the optical FT spectra of species **2** = [($DPPF_{20}$)MnCl + O_3] (dashed line) and **5** = [($DPPF_{20}$)MnBr + O_3] (full line)

Figure 4b: Comparison of the optical FT spectra calculated from the differences:

$$\Delta\chi(k)=\left\{\left[\chi(k)\right]_5-\left[\chi(k)\right]_7^*\right\} \text{ and } \Delta\chi(k)=\left\{\left[\chi(k)\right]_2-\left[\chi(k)\right]_7^*\right\}$$

Note the remarkable superposition of the two plots.

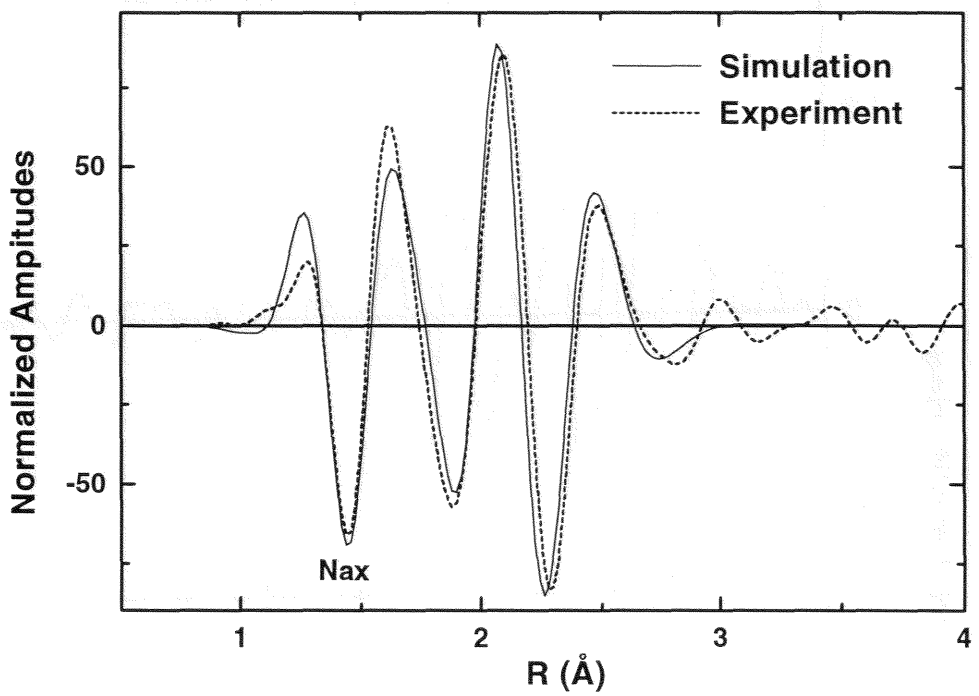

Figure 5: R-space comparison of the spectra obtained by Fourier Transforming either the perturbed difference $\Delta\chi(k)=\left\{\left[\chi(k)\right]_2-\left[\chi(k)\right]_7^*\right\}$ (dashed line) or a simulated difference $\Delta\chi_{sim}(k)$ (full line) based on the proposed structural scheme 2 and including the relevant multiple scattering paths.

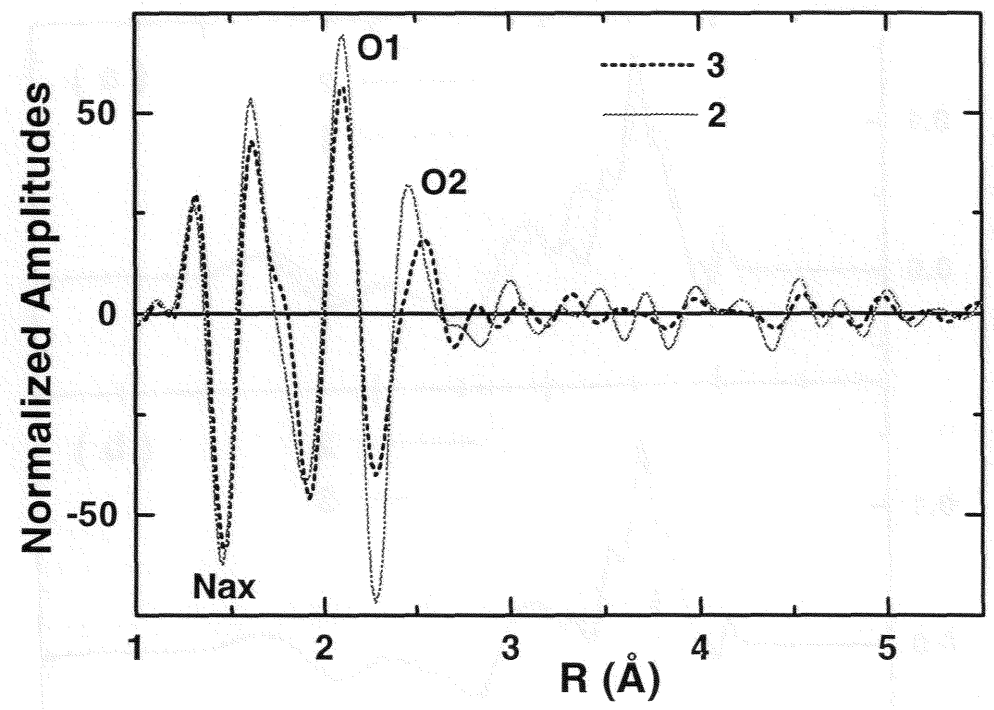

Figure 6: Comparison of the optical FT spectra calculated from the differences: $\Delta\chi(k)=\left\{[\chi(k)]_3-[\chi(k)]_7^*\right\}$ (dashed line) and $\Delta\chi(k)=\left\{[\chi(k)]_2-[\chi(k)]_7^*\right\}$ (full line) refering to the same perturbed reference.

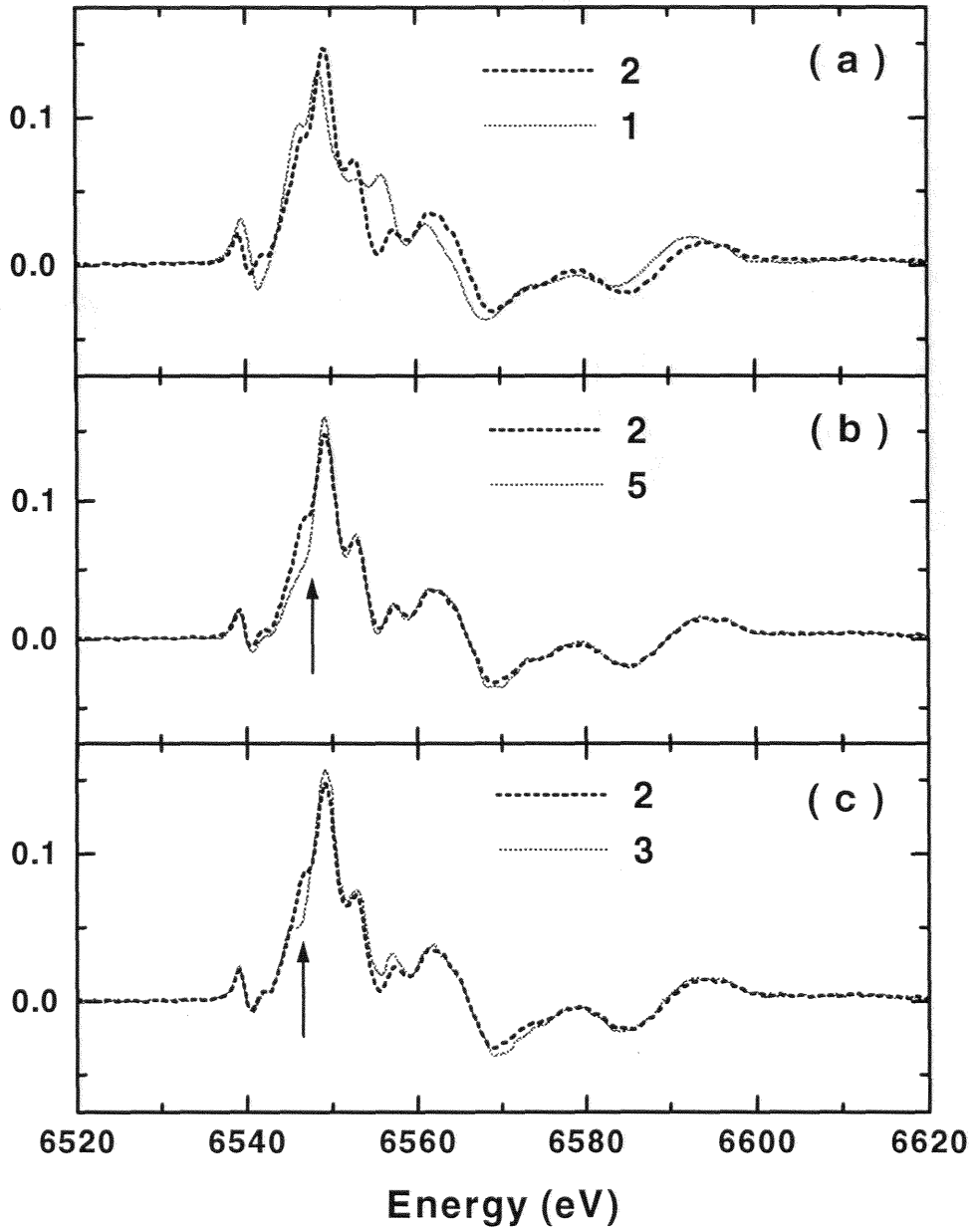

Figures 7: 1rst derivatives of the Mn - K-edge XANES spectra:

Figure 7a: Sample **2** = [$(DPPF_{20})$MnCl + O_3] (dashed line) *versus* sample **1** = $(DPPF_{20})$MnCl (full line)

Figure 7b: Sample **2** = [$(DPPF_{20})$MnCl + O_3] (dashed line) *versus* sample **5** = [$(DPPF_{20})$MnBr + O_3] (full line)

Figure 7c: Sample **2** = [$(DPPF_{20})$MnCl + O_3] (dashed line) *versus* sample **3** = [$(DPPF_{20})$MnCl + O_3 + Pyridine]

Arrows point to the small differences that are detectable in Figures 7b and 7c.

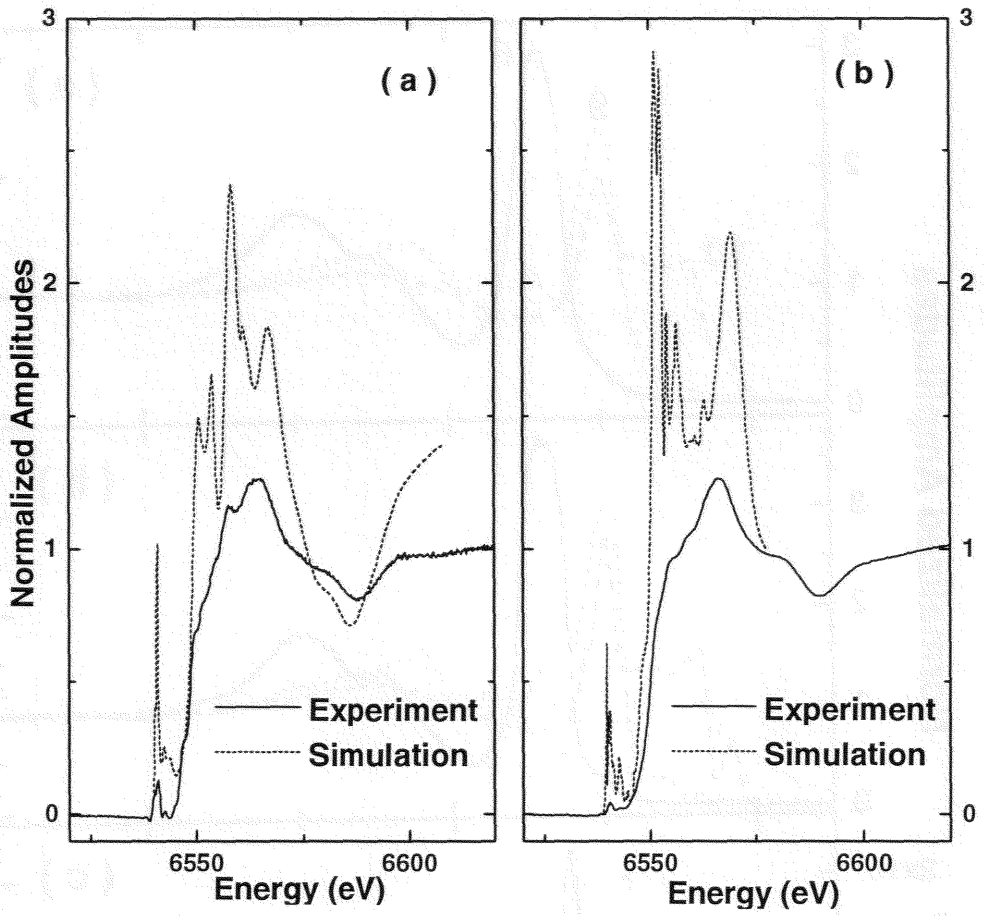

Figures 8: MSW simulations of the Mn K-edge XANES spectra:

Figure 8a: Polarization averaged simulated XANES spectrum (dashed line) of species **1** = $(DPPF_{20})MnCl$ calculated for a molecular cluster containing 118 atoms in a stereo-geometrical arrangement deduced from the known crystal structure. For the sake of comparison we have reproduced on the same plot a partially deconvoluted experimental spectrum (full line).

Figure 8b: Polarization averaged simulated XANES spectrum (dashed line) of species **2** = $[(DPPF_{20})MnCl + O_3]$ calculated for a molecular cluster containing 121 atoms in a stereo-geometrical arrangement deduced from the crystal structure of species **1** but modified in order to be consistent with the conclusions of the difference EXAFS study. For the sake of comparison we have again reproduced on the same plot a partially deconvoluted experimental spectrum (full line).

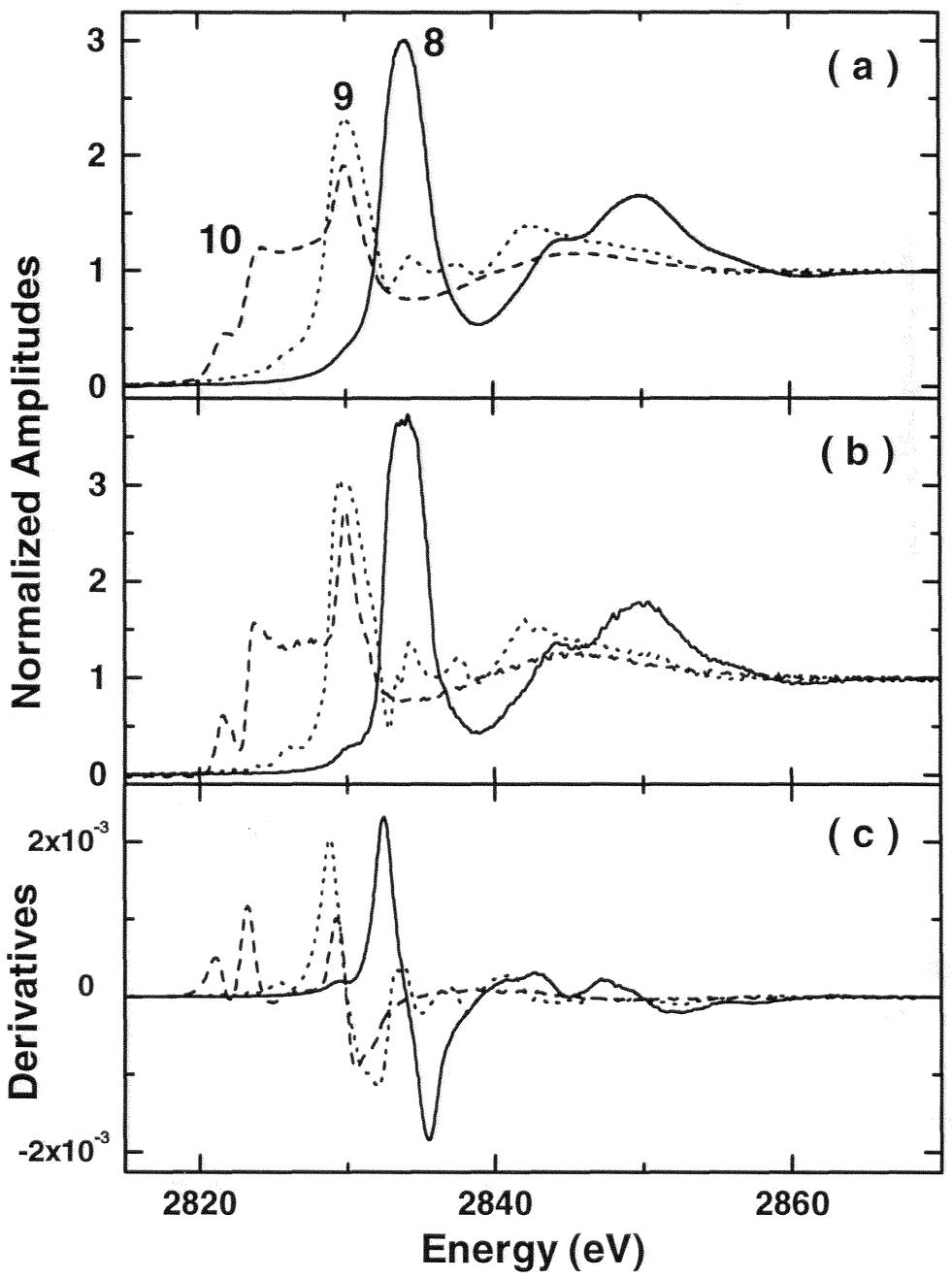

Figures 9: Cl K-edge XANES spectra of sample **8** = [Mn $(ClO_4)_2$, 6 H_2O] (full line); **9** = $KClO_3$ (dotted line) and solution **10** = [NaOCl / H_2O] (dashed line):

Figure 9a: Comparison of their XANES spectra

Figure 9b: Comparison of numerically deconvoluted XANES spectra

Figure 9c: Comparison of the first derivative spectra.

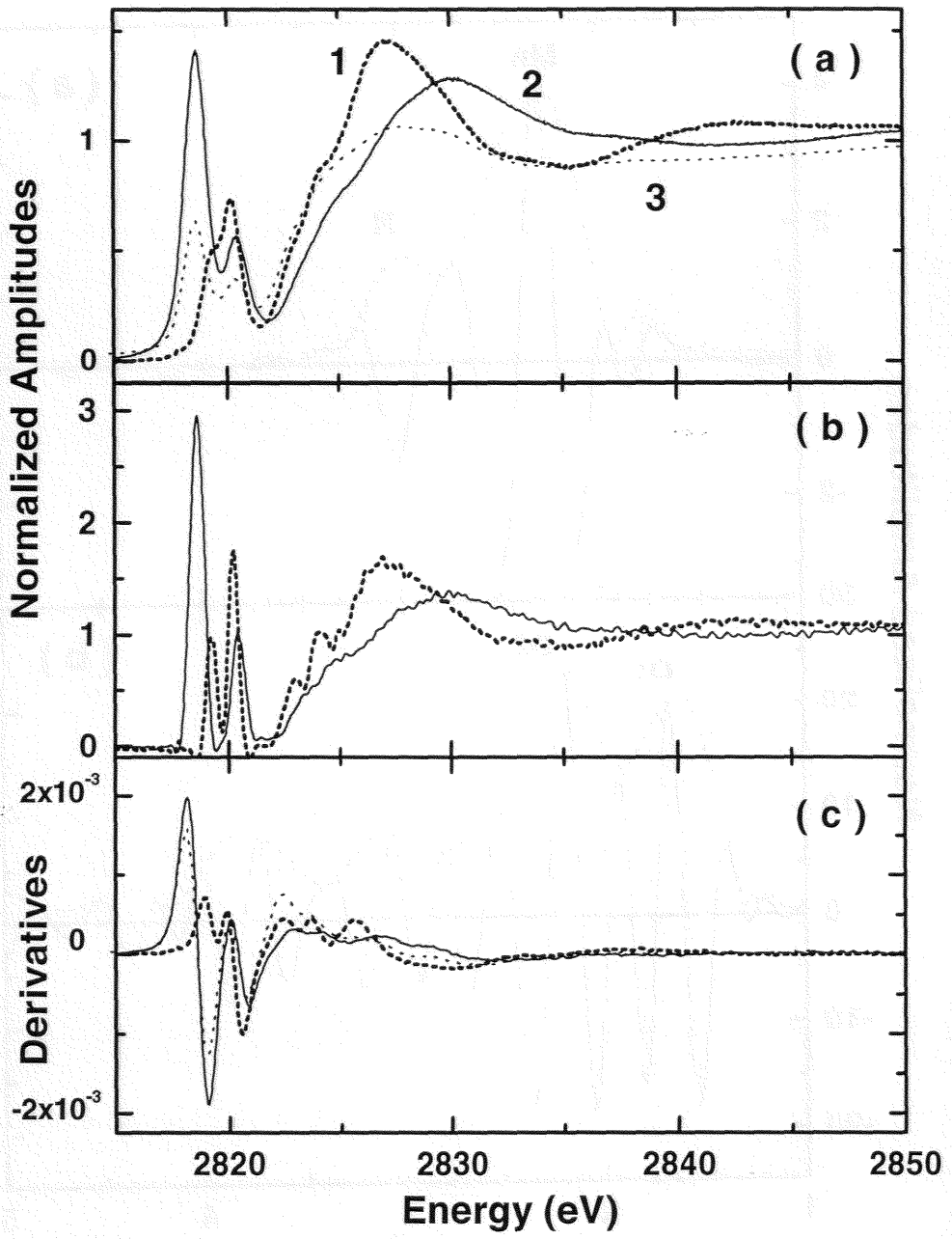

Figures 10: Cl K-edge XANES spectra of species **1** = ($DPPF_{20}$)MnCl (dashed line); **2** = [($DPPF_{20}$)MnCl + O_3] (full line) and the active sample **3** = [($DPPF_{20}$)MnCl + O_3 + Pyridine] (dotted line)

Figure 10a: Comparison of the rough XANES spectra;

Figure 10b: Comparison of numerically deconvoluted spectra;

Figure 10c: Comparison of the first derivatives.

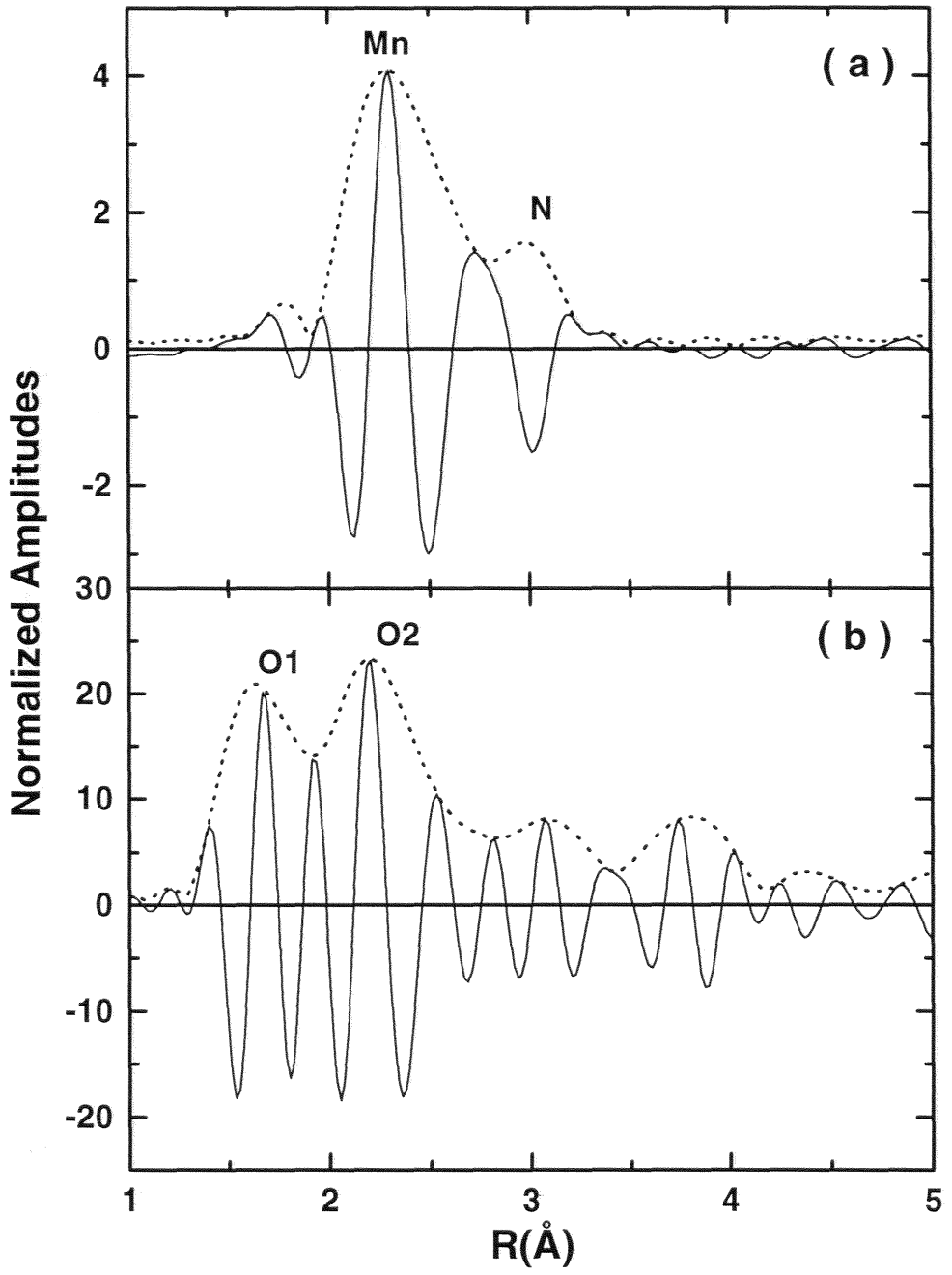

Figures 11:

Figure 11a: FT spectra $\Im\left[\tilde{\chi}_1(R)\right]$ (full line) and $\left|\tilde{\chi}_1(R)\right|$ (dotted line) of species **1** = ($DPPF_{20}$)Mn Cl corrected for the scattering phase shifts and amplitude of the shortest single scattering path: Cl...Mn .

Figure 11b: FT spectra $\Im\left[\tilde{\chi}_1(R)\right]$ (full line) and $\left|\tilde{\chi}_1(R)\right|$ (dotted line) of species **2** = [($DPPF_{20}$)MnCl + O_3] corrected for the scattering phase shifts and amplitude of the shortest Cl...O single scattering path.

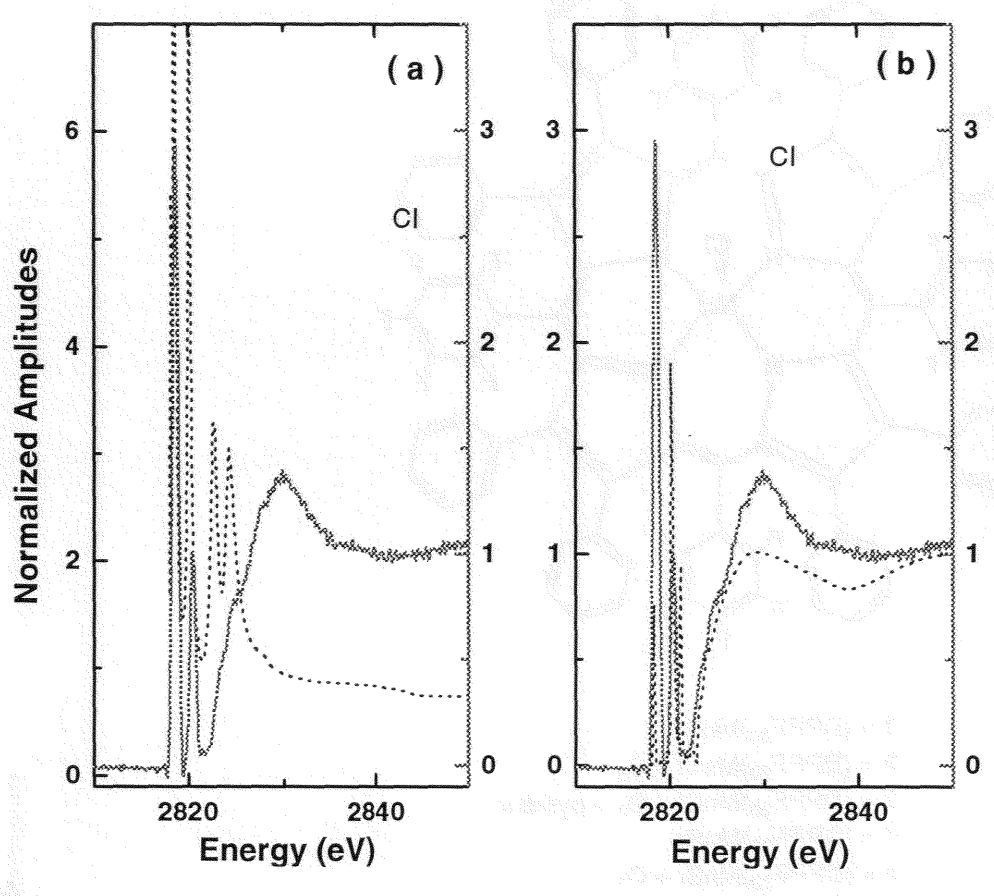

Figures 12:

Figure 12a: Simulated Cl K-edge XANES spectrum of $\mathbf{S_3}$ = [Cl–$O_{(1)}$–$O_{(2)}$–$O_{(3)}$] (dotted line) compared to the numerically deconvoluted experimental spectrum of species **2**. Note the remarkable splitting of the pre-edge structures.

Figure 12b: Simulated Cl K-edge XANES spectrum of an hypothetical cluster in which a chlorine atom would bridge two ozone molecules (dotted line) compared again to the numerically deconvoluted experimental spectrum of species **2**. Note the improved agreement in the near edge region.

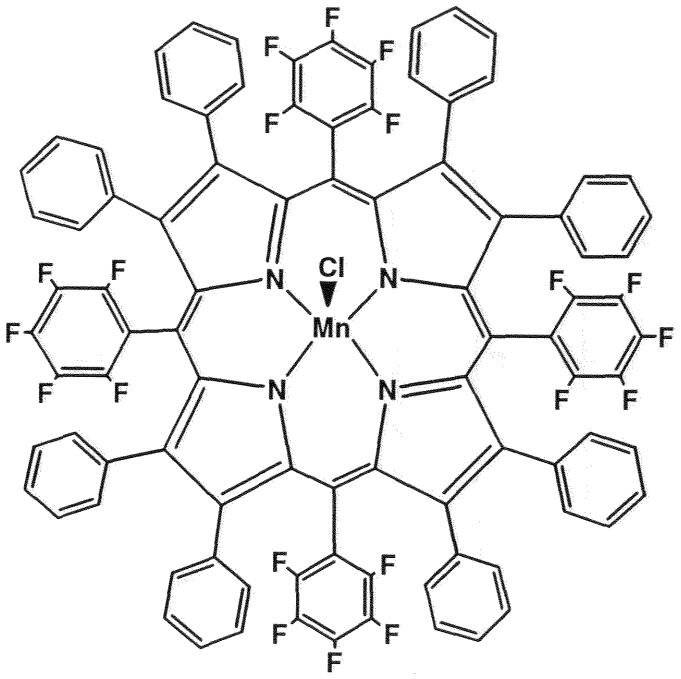

1 = $(DPPF_{20})MnCl$
2 = $(DPPF_{20})MnCl + O_3$
3 = $(DPPF_{20})MnCl + O_3$ + pyridine
4 = $(DPPF_{20})MnBr$
5 = $(DPPF_{20})MnBr + O_3$
6 = $(DPPF_{20})MnN_3$
7 = $(DPPF_{20})Mn^{V}N$

Scheme 1: Developed chemical formula of the ($DPPF_{20}$) porphyrinato dianion

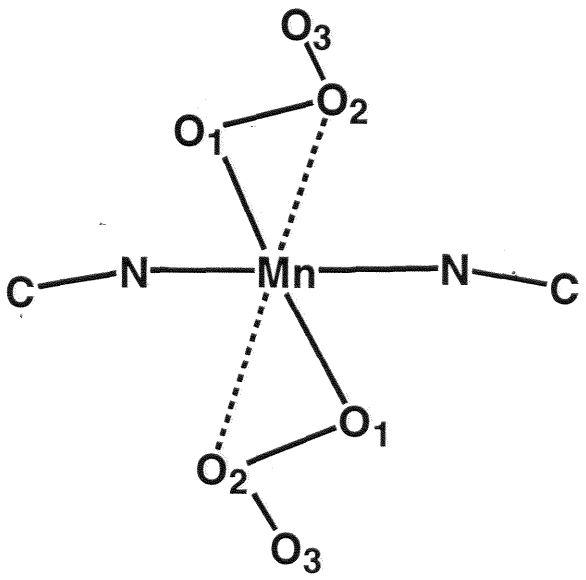

Scheme 2: Proposed coordination of Mn in species **2** and **5**

Table 1: Interatomic distances (in Å) and relevant structural parameters deduced from Difference EXAFS analyses .

1 = $(DPPF_{20})$Mn Cl				
R(Mn...Cl)	R(Mn...N_{eq})	ΔR_{cav}*	H*	d*
2.37 ± 0.01	2.00 ± 0.01	(0.00 ± 0.00)	(0.24)	(-0.02)
4 = $(DPPF_{20})$Mn Br				
R(Mn...Br)	R(Mn...N_{eq})	ΔR_{cav}	H	d
2.51 ± 0.01	2.00 ± 0.01	-0.005 ± 0.005	0.20 ± 0.02	- 0.02 ± 0.02
6 = $(DPPF_{20})$Mn N_3				
R(Mn...N_1)	R(Mn...N_{eq})	ΔR_{cav}	H	d
2.05 ± 0.01	2.00 ± 0.01	0.000 ± 0.005	0.24 ± 0.02	- 0.02 ± 0.02
R(Mn...N_2) ?	R(Mn...N_3) ?	Mn-N_1-N_2 ?		
3.15 ± 0.02	4.05 ± 0.05	134 ± 1°		
7 = $(DPPF_{20})$Mn N				
R(Mn...N_{ax})	R(Mn...N_{eq})	ΔR_{cav}	H	d
1.51 ± 0.01	2.01 ± 0.01	-0.025 ± 0.005	0.38 ± 0.02	+ 0.04 ± 0.02
2 = [$(DPPF_{20})$MnCl + O_3] or **5** = [$(DPPF_{20})$MnBr + O_3]:				
R(Mn...O_1)	R(Mn...N_{eq})	ΔR_{cav}	H	d
2.09 ± 0.02	2.00 ± 0.01	0.000 ± 0.005	0.00 ± 0.02	- 0.02 ± 0.02
R(Mn...O_2)	Mn-O_1-O_2	σ^2(Mn...O_1)	σ^2(Mn...O_2)	σ^3(Mn...O_2)
2.49 ± 0.05	100 ± 1°	0.0048±0.0009	0.0140±0.0025	0.0055±0.0010
Negative reference signal of **7** :		R(Mn...N_{ax})	σ^2(Mn...N_{ax})	
(*Perturbed distance*)		1.49 ± 0.01	0.0025±0.0004	

* ΔR_{cav} differences or absolute values for H and d refer to the known crystal structure of species **1** .
Errors bars are deduced from the cancellation test in difference analyses.
Question marks (?) are for tentative assignments of weak signals.

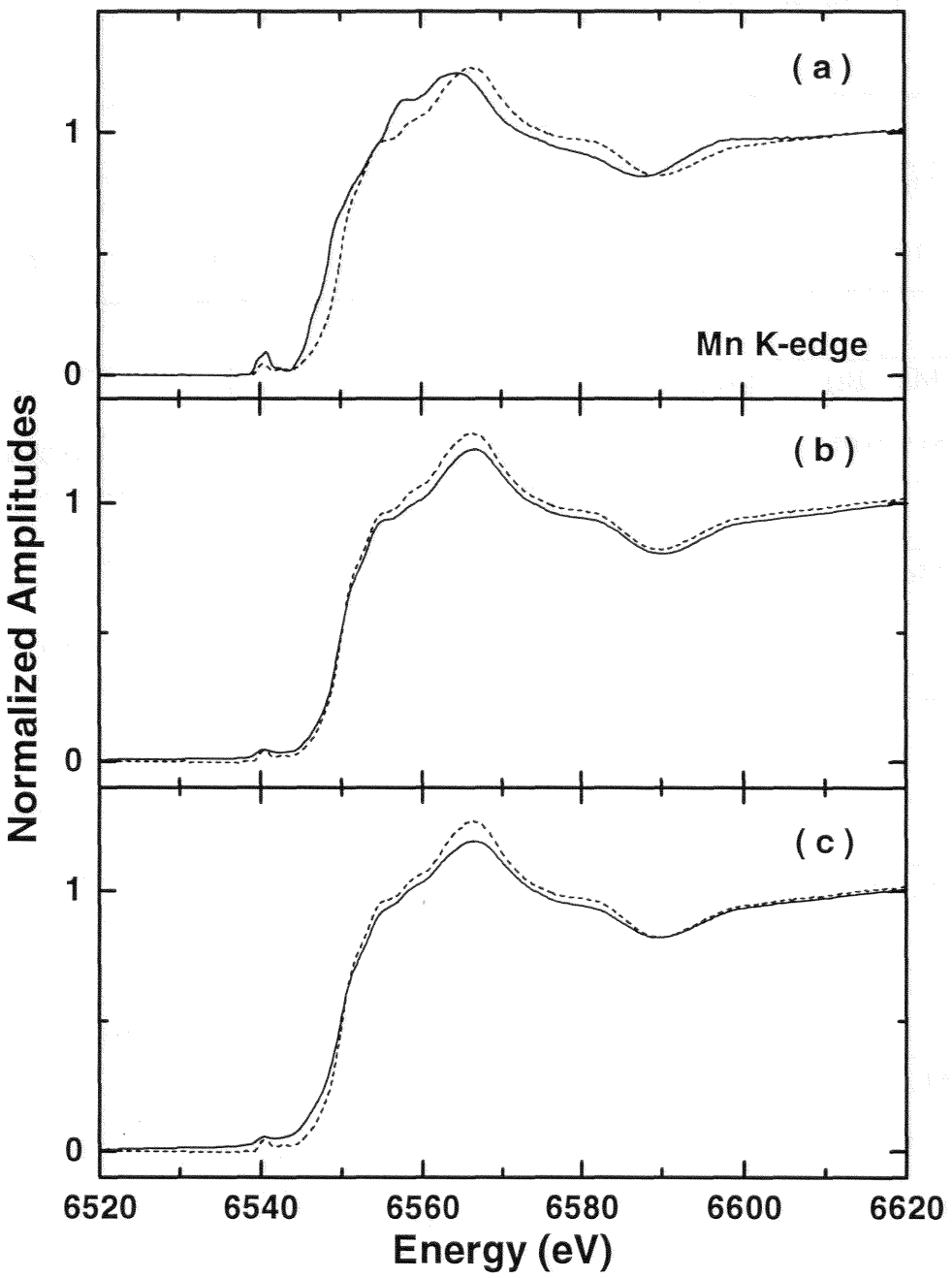

Figures SM-1: Mn - K edge XANES spèctra

Figure SM-1a: Sample **2** = [$(DPPF_{20})MnCl + O_3$] (dashed line)
versus sample **1** = $(DPPF_{20})MnCl$ (full line)

Figure SM-1b: Sample **2** = [$(DPPF_{20})MnCl + O_3$] (dashed line)
versus sample **5** = [$(DPPF_{20})MnBr + O_3$] (full line)

Figure SM-1c: Sample **2** = [$(DPPF_{20})MnCl + O_3$] (dashed line)
versus sample **3** = [$(DPPF_{20})MnCl + O_3$ + Pyridine]

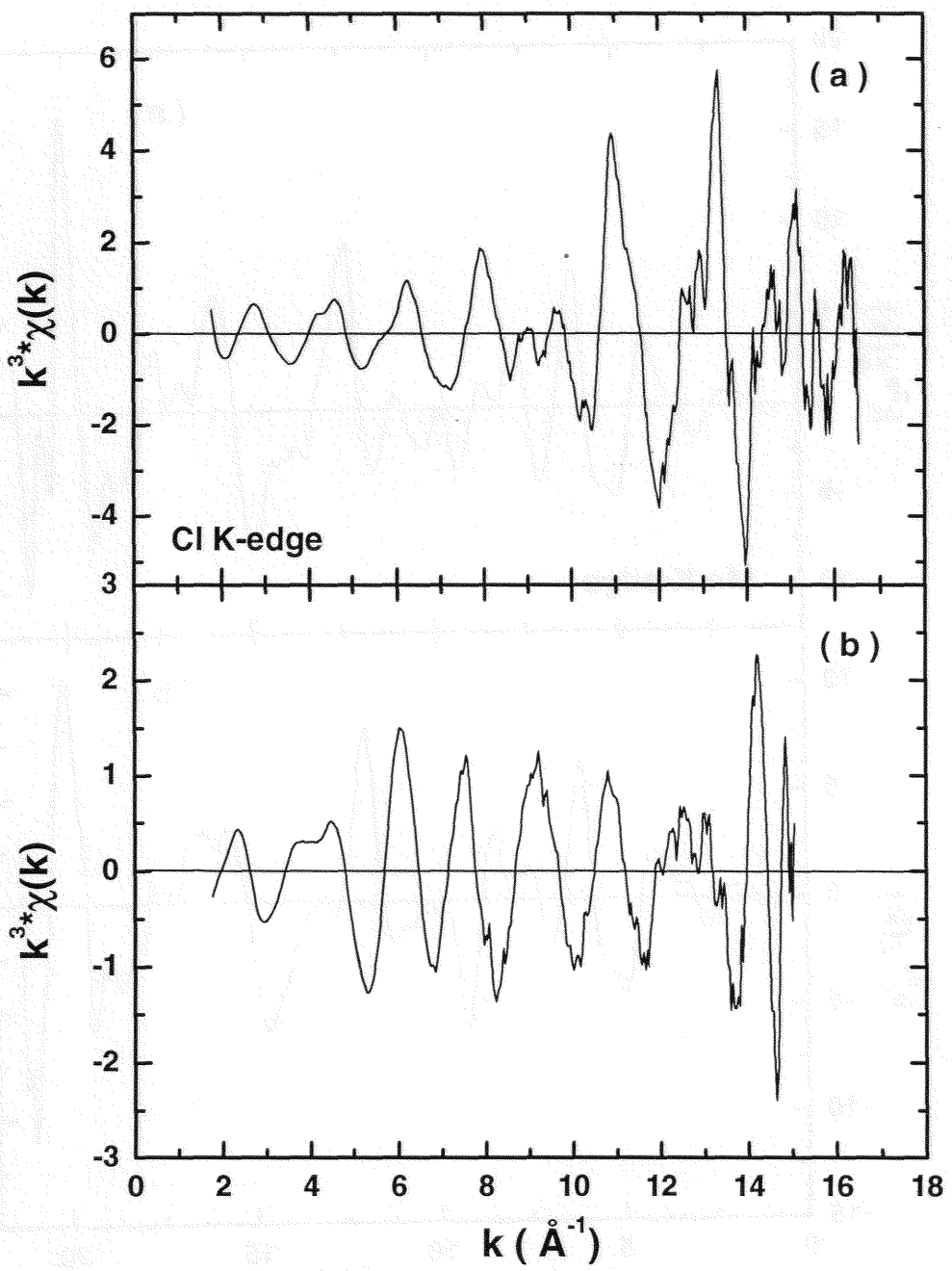

Figures SM-2: Cl - K edge EXAFS data $k^3.\chi(k)$

Figure SM-2a: Sample **2** = [$(DPPF_{20})MnCl + O_3$] : Single scan 39 (10-06-96)

Figure SM-2b: Sample **1** = $(DPPF_{20})MnCl$: Single scan 12 (10-06-96)

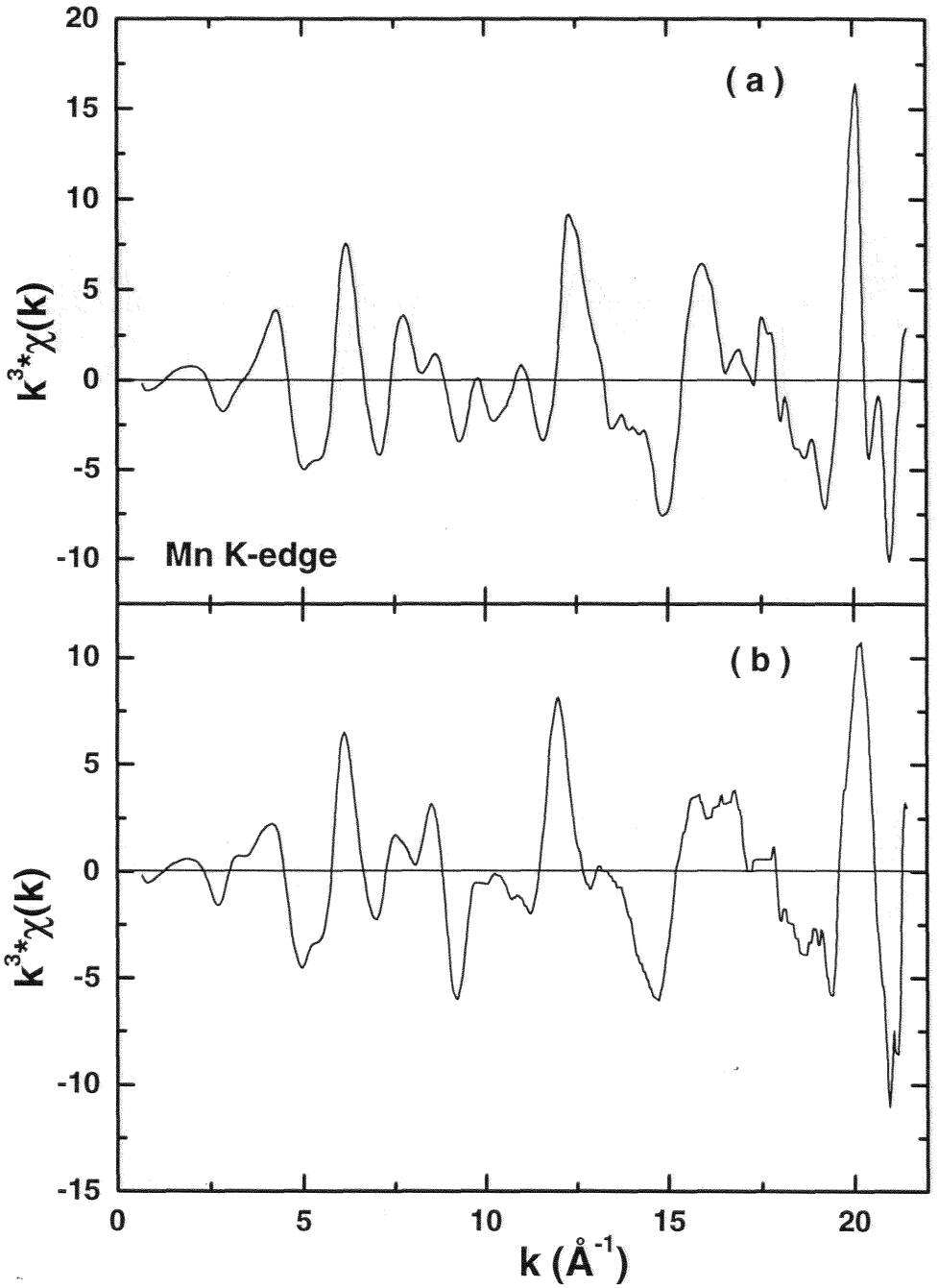

Figures SM-3: Mn - K edge EXAFS data $k^3.\chi(k)$

Figure SM-3a: Sample **2** = [$(DPPF_{20})MnCl + O_3$] : Averaged data (08-10-96)

Figure SM-3b: Sample **1** = $(DPPF_{20})MnCl$: Averaged data (08-10-96)

2.1.3 Acte de congrès

J. PHYS. IV FRANCE 7 (1997)
Colloque C2, Supplément au Journal de Physique III d'avril 1997 C2-663

XAFS Studies of High-Valent Porphyrinato Manganese Complexes with Ozone

V. Gotte*, J. Goulon*, A. Rogalev*, C. Goulon-Ginet*,**, K. Perié***, J.M. Barbe***, R. Guilard*** and P. Cocolios****

* *ESRF, BP. 220, 38043 Grenoble, France*
** *Université Joseph-Fourier, Faculté de Pharmacie, 38706 La Tronche, France*
*** *LIMSAG (UMR 9953), Université de Bourgogne, 6 boulevard Gabriel, 21100 Dijon, France*
**** *Centre de Recherche Air Liquide, BP. 126, Les Loges-en-Josas, 78350 Jouy-en-Josas, France*

Abstract. We produce strong evidence of the interaction of ozone with a series of Manganese (III) porphyrinato complexes to form a well defined reactive intermediate. In the latter species, the Manganese atom which is formally in a tetravalent (IV) state, is (at least) hexacoordinated with the metal unambiguously lying in the basal plane of the four pyrrolic nitrogens of the porphyrin macrocycle. Substitution of Bromine or Chlorine axial ligands by ozonids is most likely to happen. This conclusion is also supported by XANES and EXAFS spectra recorded at the Chlorine K-edge which suggest that ozone may even form with chlorine a complex anion.

1. MOTIVATIONS

Reactions involving ozone are well known in organic chemistry, especially with olefines and dienes. There are, in contrast, very few applications of ozone in organometallic chemistry and catalysis. Meunier *et al.* [1] have reported the epoxidation of olefines by ozone in presence of a Mn (III) porphyrinato complex. It was never proved experimentally that the reactive intermediate could be a high valent Mn (V) oxo complex [2]. It is the aim of this project to investigate whether or not molecular ozone can form well defined reactive intermediates with metalloporphyrins.

2. EXPERIMENTAL SECTION

Ozone is a very powerful oxidizing agent and all common metalloporphyrins are destroyed by reaction with ozone. Such a destruction can be prevented by using β-substituted pyrrol rings [1] and a variety of ozone resistant ligands has been synthesized at the LIMSAG in Dijon. It was agreed to concentrate the present XAFS study on a new family of Mn (III) dodecaphenyl-porphyrinato complexes with perfluorinated protective groups on the meso bridging carbons : [DPP-F_{20}] : Mn - (X)(Y) where X and Y are axial ligands. The following reactive intermediates were isolated : **1**: {[DPP-F_{20}] : Mn - Cl + O_3} ; **2**: {[DPP-F_{20}] : Mn - (Cl)(Pyridine) + O_3} ; **3**: {[DPP-F_{20}] : Mn - Br + O_3}. Additional reference compounds used for difference analyses included : **4**: [DPP-F_{20}] : Mn ≡ N ; **5**: [DPP-F_{20}] : Mn – Cl ; **6**: [DPP-F_{20}] : Mn – Br

All data were collected at the windowless ESRF beamline ID12A. The "undulator gap scan" technique was required to record Cl K-edge EXAFS spectra whereas the natural bandwidth of the second harmonics proved to be wide enough to collect excellent EXAFS spectra at the Mn K-edge over 1500 eV or more. Reflective optics allowed us to keep the level of unwanted harmonics at least 5 orders of magnitude below the fundamental. X-ray fluorescence excitation spectra carefully corrected for fluorescence re-absorption [3] were systematically used.

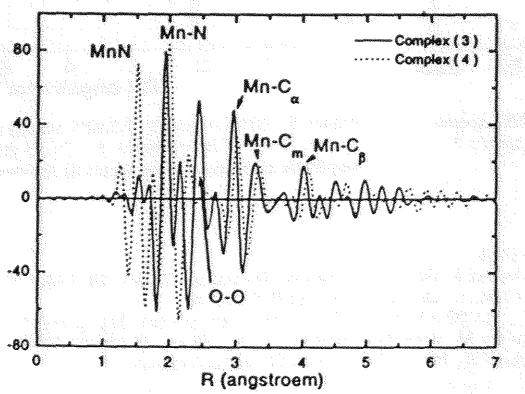

Figure 1. Mn K-edge FT-EXAFS spectra of species **3** and of the nitrido complex **4**. Phase shifts and amplitude corrections refer to the Mn*...N shell of the porphyrin.

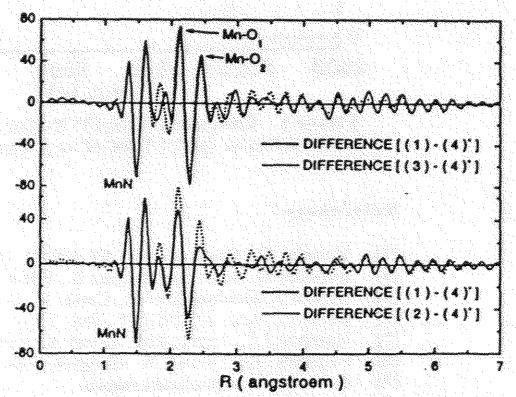

Figure 2 "Perturbed" Difference Analyses used to identify the axial ligands. Complex **4** of known structure was used as reference to cancel out the porphyrin signatures.

3. RESULTS

The quality of the EXAFS spectra recorded at the Mn K-edge stimulated us to perform the FT over a wide k range, *i.e.* $k \leq 19$ Å^{-1} in order to benefit of a high resolution in the R space. As illustrated by Fig. 1 which compares the FT spectra of the unknown species **3** and of the nitrido complex **4**, we found that the complexes activated with ozone all exhibit the same additional signature at *ca.* R = 2.4 Å which we assigned intuitively to ozonid ligands. More detailed structural information on these axial ligands were extracted from *Perturbed Difference Analyses* pioneered a long time ago by Goulon *et al.* [2,3-5]. We simply tried to "perturb" the experimental EXAFS spectrum of the nitrido complex **4** until we obtained a reasonably good cancellation of all characteristic signatures of the porphyrin macrocyle in difference spectra. Special algorithms were developed to mimic an axial shift of the metal and secondary changes in the shape of the macrocycle: ruffling, doming etc... All difference spectra reproduced in Fig. 2 exhibit the same pattern : a negative signal associated with the Mn ≡ N short distance in **4** and positive signatures which may consist of two Mn*...O shells at *ca.* 2.1 and 2.4 Å for the ozonids. Note that we had essentially to shift the metal back to the basal plane of the four pyrrolic nitrogen of the porphyrin macrocycle (Δh = -0.4 ± 0.05 Å). This is a very strong indication that two ozonid ligands should be coordinated to each Mn atom (See Fig.3).

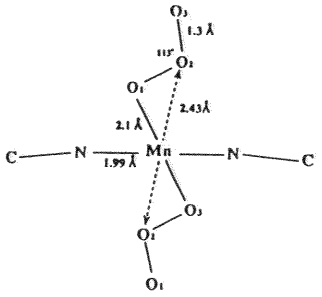

Figure 3 Tentative model consistent with the coordination of two ozonid ligands to the manganese atom.

The Mn K-edge XANES spectra of the reactive species formed with ozone do not exhibit any intense preedge structure : this is clearly another argument supporting the hexacoordination of the Mn atom. On the other hand, the very high similarity of the difference spectra obtained for species **1** and species **3** is implicitely ruling out any residual coordination of chlorine or bromine ligands to the metal since their contributions should show up in Fig. 2 and should be quite different. This prompted us to record the XANES and EXAFS spectra of samples **1** and **2** at the Cl* K-edge. As illustrated by Fig. 4, the interaction with ozone induces a dramatic change in the Cl* XANES spectrum which, however, looks fairly different from the characteristic spectra of ClO_2^-, ClO_3^- or ClO_4^- anions [6]. It is our interpretation that a complex anion $[Cl\text{-}O_3]^-$ has been formed. We have reproduced in Fig. 5 the FT EXAFS spectra of the unknown complex **1** and its precursor **5**. For the sake of comparison, we applied strictly the same phase shift & amplitude corrections to both spectra. For species **5**, the Cl*... Mn signature is peaking at the expected distance (2.34 Å) but the Cl*...N signature shows an unusual phase. The FT spectrum of the unknown species **1** is clearly different : the most intense signature peaking at 2.24 Å was tentatively assigned to a short Cl*...O distance which looks consistent with the result of a calculation carried out with the MSI molecular simulation package [7].

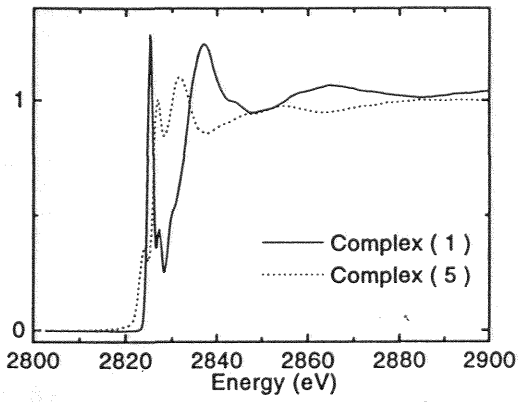

Figure 4 Comparison of the Cl* K-edge XANES spectra of the unknown species **1** and of its precursor species **5**.

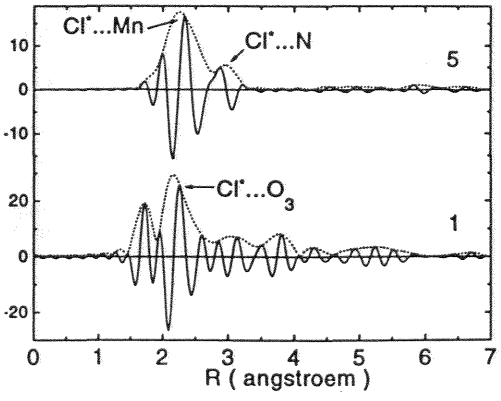

Figure 5 Cl* K-edge FT EXAFS spectra of the unknown species **1** and of its precursor **5**. Phase-shift & scattering amplitude corrections were identical for comparison.

References

[1] Meunier B., *Chem. Review* **92** (1992) 1411-1456.
[2] Bortolini O., Ricci M., Meunier B., Friant P., Ascone I., Goulon J., *Nouveau Journal de Chimie* **10** (1986) 39-49.
[3] Goulon J., Goulon-Ginet C., Cortès R., Dubois J.M., *J. de Physique* **43** (1982) 539-48.
[4] Goulon J., Loos M., Friant P., Ruiz-Lopez M.F., NATO ASI Series C (D. Reidel, Dordrecht) **221** (1988) 247-293.
[5] Marchon J.C., Latour J.M., Grand A., Belakhovsky M., Loos M., Goulon J., *Inorg. Chem.* **29** (1990) 57-67.
[6] Filipponi A., Tyson T.A., Hodgson K.O., Mobilio S., *Physical Review* **A48** (1993) 1328-48.
[7] Pullumbi P., unpublished results.

2.2 Etude des complexes d'inclusion de l'argon dans les solvants organiques.

Nous présentons ici les résultats obtenus lors de l'étude des complexes d'inclusion de l'argon dans les solvants organiques. Cette étude n'a pas fait l'objet d'une publication dans la presse spécialisée mais seulement d'un rapport interne à ESRF.

Motivations

Les gaz rares sont connus pour se lier aux protéines (par exemple la myoglobine) avec une certaine sélectivité de site: le krypton ou le xénon sont souvent utilisés comme sonde pour la détermination de la phase en cristallographie des protéines par rayons X. Des interactions spécifiques existent aussi avec des molécules organiques de type cage (éthers-couronnes, cyclodextrines...)[1] et le but de ce projet était d'étudier la nature de cette interaction "*host-guest*". Pour le xénon, des informations exploitables ont pu être extraites de spectres RMN du ^{129}Xe. De telles informations manquent dans le cas de l'argon. Celui-ci pourrait avoir un domaine d'application plus large. Ceci nous a conduit à vérifier si les spectres XAFS enregistrés au seuil K de l'argon pouvaient être sensibles aux interactions "*host-guest*".

Experience

Une série de molécules cages a été synthétisée au LIMSAG de Dijon. Le critère de sélection a été le suivant : (i) une augmentation de la solubilité de l'argon dans un solvant donné, (ii) l'existence d'intéractions avec le xénon prouvée par la RMN du ^{129}Xe. Ce dernier argument peut se révéler fallacieux étant donné les différences de taille et de polarisabilité de Xe et de Ar. Finalement, nous avons commencé nos tests avec les solutions suivantes : (1) une solution d'argon dans le pentane qui a été utilisée comme témoin; (2) une solution Argon/[Kryptofix (222):MeOH]; (3) une solution Argon/[cryptophane A : dioxanne]. La concentration de l'argon est de l'ordre de 50 à 200 ppm. Toute l'étude a été faite à température ambiante.

Les spectres XANES ont été enregistrés au seuil K de l'argon dans le mode fluorescence. Les expériences furent difficiles à cause de : (i) la haute dilution de l'élément absorbant, (ii) le faible rendement de fluorescence de l'argon (5%), (iii) la forte réabsorption du solvant, (iv) le manque de filtres pour discriminer la fluorescence du diffusé. La ligne ID12A est une ligne sans fenêtre et fonctionne sous ultra-haut-vide; ainsi la première difficulté fut de concevoir une cellule résistant au vide, pouvant contenir une solution, avec une fenêtre de kapton de 12 µm d'épaisseur, et ayant un grand angle solide pour pouvoir détecter la fluorescence. Cette cellule a été utilisée pour enregistrer le spectre de l'argon gazeux qui nous a servi à calibrer l'énergie.

---

[1] Branda, N.; Grotzfield, R.; Valdès, C.; Rebek, J.; Control of self-assembly and reversible encapsulation of Xenon in a self-assembling dimer by acid-base chemistry", *J.Am.Chem.Soc,* **1995**, *111*, 85-88.

Résultats

Comme illustré par les Fig.1 et 2, des spectres d'une qualité sans précédent ont été enregistrés pour l'argon gaz. Les excitations multiélectroniques bien résolues prennent place dans un domaine de 15 à 30 eV après le seuil de photoionisation. Ces structures sont en accord avec les calculs théoriques de Deslattes et coll[2].. L'échantillonnage en énergie de 10 meV et la bonne statistique ont permis de déconvoluer le spectre avec un profil de Voigt. Grâce à cette déconvolution, nous avons été en mesure d'assigner sans ambiguité les résonnances atomiques 1s4p, 1s5p, 1s6p et d'assigner l'énergie du seuil à 3206.35 eV, c'est-à-dire 0.8 eV au dessus de la résonnance 1s6p comme prévu par la théorie[3]. Avec une résolution du monochromateur proche de la limite théorique de 0.46 eV, la largeur à mi-hauteur de la résonnance 1s4p montre un élargissement dû à la durée de vie du trou profond de 0.68±0.01 eV, en parfait accord avec la théorie.
Les spectres XANES des solutions (1) à (3) sont présentés sur la Fig.3. Les larges résonnances apparaissant au-delà du pic 1s4p ont été assignées à la polarisabilité induite par la matrice. Puisqu'elles apparaissent déjà dans le spectre de la solution Ar/pentane, elles ne peuvent pas être utilisées pour discriminer les interactions *"host-guest"* des effets de solvant. Les oscillations EXAFS, si elles existent, sont plus faibles que les excitations multiélectroniques KM. Un tel amortissement des oscillations EXAFS pourrait indiquer que l'argon n'est pas emprisonné dans la cage du macrocycle du kryptofix ou du cryptophane A: la durée de vie de ces espèces complexées est trop courte et les modes vibrationnels "basse fréquence" sont aisément excités.

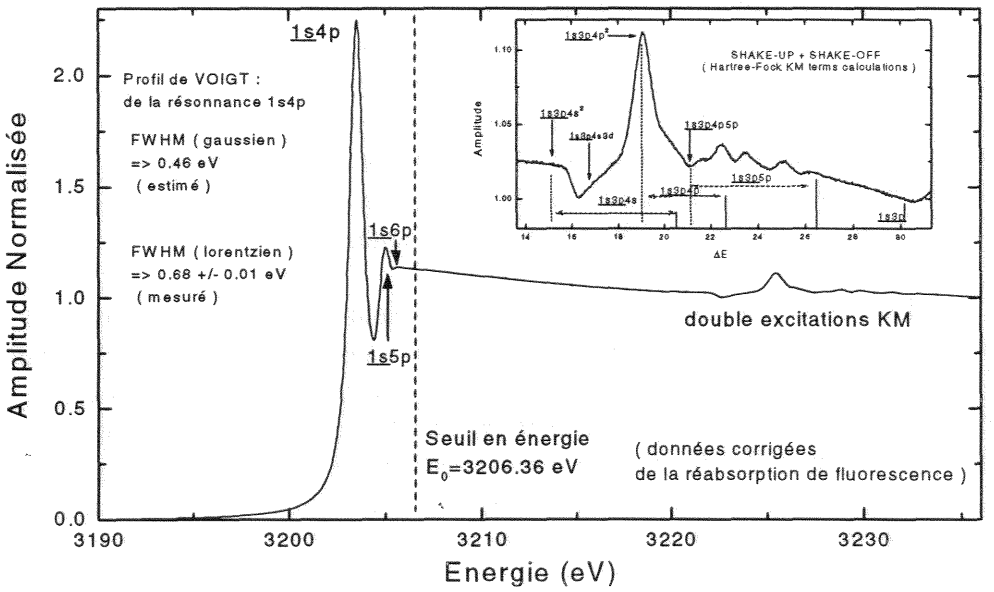

Fig 1 : Spectre XANES de l'argon gaz au seuil K, avec les excitations multiélectroniques KM .

---

[2] Deslattes, R.D.; Lavilla, R.E.; Cowan, P.L.; Henins, A.; *Phys. Rev*, **1983**, A27, 923-33.
[3] Teodorescu, C.M.; Karnatak, R.C.; Esteva, J.M.; El Alif, A.; Connerade, J.P.; J. Phys. B: *At. Mol. Opt. Phys.* , **1993**, *26*, 4019.

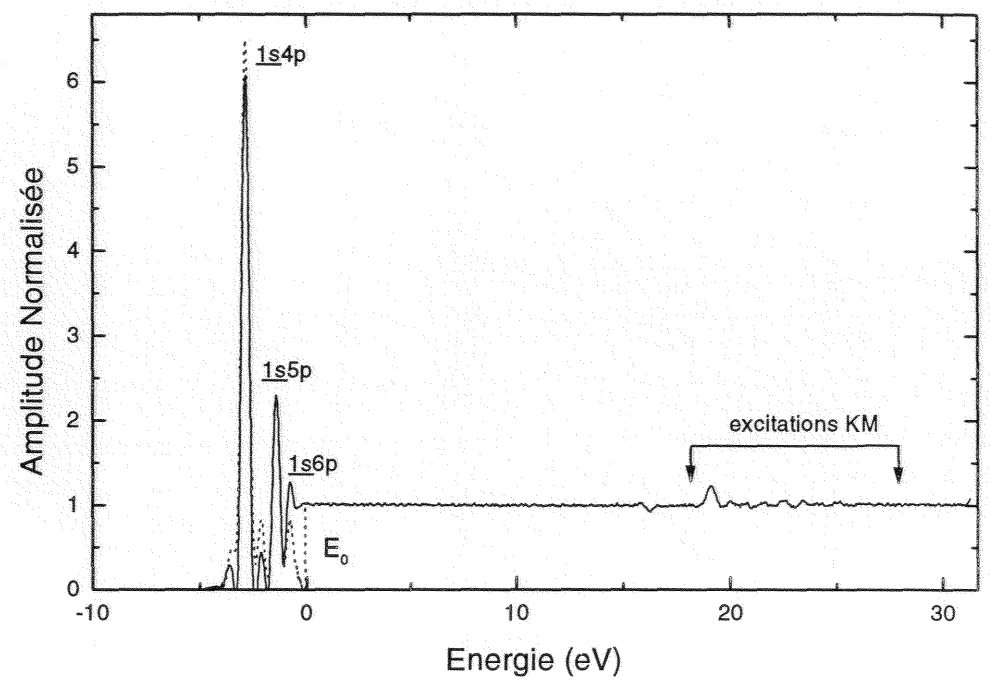

Fig. 2 : Spectre XANES de l'argon gaz avec une plus grande résolution en énergie.

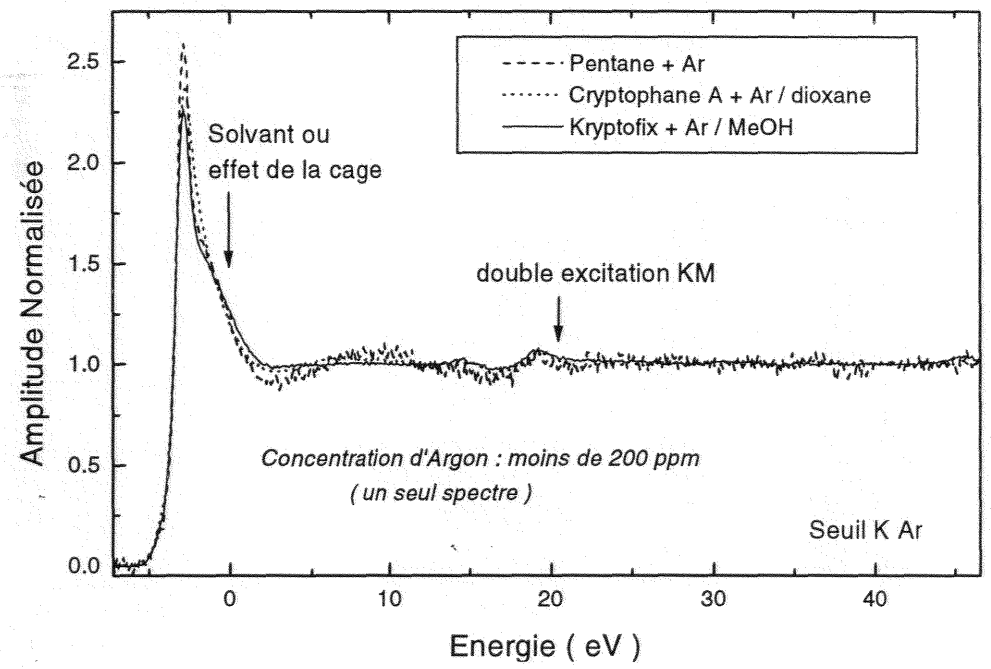

Fig. 3 : Spectres XANES des solutions (1), (2) et (3).

Troisième partie

Le dichroïsme circulaire "naturel" dans le domaine des rayons X

3.1 Introduction

Dans cette troisième partie, nous rapportons les premiers résultats qui ont été obtenus dans un projet de recherche propre à l'équipe ID-12A et consacré à la mise en évidence du dichroïsme circulaire "naturel" dans le domaine des rayons X (XNCD).Nous avons, bien entendu, participé à ce projet. Bien que les mesures de dichroïsme circulaire soient couramment utilisées, dans le domaine UV-visible, en particulier par les biologistes, pour caractériser des espèces chirales, ce phénomène n'avait encore jamais été détecté dans le domaine des rayons X.
La première raison est qu'il fallait disposer d'une source de lumière polarisée circulairement dont on puisse modifier facilement l'état de polarisation circulaire droite ou gauche. Il a fallu attendre la construction des sources de rayonnement de 3ième génération avec la mise en oeuvre des onduleurs hélicoïdaux, tels HELIOS-II implanté sur ID-12A, qui sont capables de délivrer un grand flux de photons à polarisation variable.
La deuxième raison est que l'origine du dichroïsme circulaire n'est pas la même dans la gamme des rayons X ou dans le domaine UV-visible. Dans les publications reproduites dans les paragraphes suivants, il a été démontré que, dans le domaine des rayons X, les signaux de dichroïsme circulaire résultaient de termes d'interférence E1.E2 entre les éléments de matrice de transition dipôle électrique-quadrupôle électrique, alors que dans le domaine UV-visible, le dichroïsme circulaire est dû essentiellement au couplage E1.M1 (force rotatoire de Rosenfeld-Condon) des éléments de matrice de transition dipôle électrique-dipôle magnétique. Malheureusement, cette origine du XNCD implique qu'il ne peut être détecté que là où des termes d'interférences dipôle électrique-quadrupôle électrique existent c'est-à-dire dans les monocristaux gyrotropes ou tout au moins dans des systèmes qui présentent un ordre orientationnel partiel. Quand on peut l'observer, le spectre XNCD est sensible à la configuration absolue du site absorbeur chiral et contient aussi une information sur le mélange des orbitales de parité pair ou impair à ce site.

Parmi les 21 classes de cristaux non-centrosymétriques, il a été montré que seulement 13 classes vont présenter du dichroïsme circulaire X. Ainsi, pour nos études, nous avons sélectionnés :

- le cristal uniaxe d'iodate de lithium (α-LiO_3) qui cristallise avec 2 molécules par cellule dans le groupe énantiomorphe $P6_3$ et qui est doué d'une rotativité spécifique importante,
- le cristal biaxial de $KTiOPO_4$ (KTP) qui appartient à la classe non enantiomorphe mm2.

Ces deux cristaux ont en commun de présenter une susceptibilité non linéaire très grande dans le domaine UV-visible.

Le problème de la mesure du dichroïsme circulaire X reste le même que dans les autres domaines optiques où il faut éviter les effets simultanés de la biréfringence ou du dichroïsme linéaire qui masquent les signaux de dichroïsme circulaire plus faibles .

Pour les cristaux uniaxes, les mesures sont relativement plus simples lorsque le faisceau incident est parallèle à l'axe optique du cristal comme le montrent les résultats des mesures effectuées aux seuils L_1, L_2 et L_3 de l'iode sur le cristal d'iodate de lithium reproduits dans la publication du paragraphe 3.2.

Les mesures sur les cristaux biaxes sont beaucoup plus difficiles en raison de la superposition des effets de dichroïsme linéaire. En effet, même si la source de lumière Helios-II a été optimisée pour émettre un faisceau incident ayant un taux de polarisation circulaire élevé (92% à 97 %) dont l'hélicité peut être inversée aisément, il faut également connaitre la fonction de transfert du monochromateur à deux cristaux qui va dégrader ce taux de polarisation, au voisinage de 45°. Le faisceau à la sortie du monochromateur est donc un faisceau polarisé dont le taux résiduel de polarisation circulaire dépend de l'angle de Bragg du faisceau sur le monochromateur. Ainsi, quand on inverse le signe de l'hélicité, les composantes de polarisation circulaire (P3) et linéaire (P2) du faisceau peuvent être modifiées de manière non négligeable pour des valeurs élevées de l'angle de Bragg. Ainsi s'explique le fort signal de dichroïsme linéaire obtenu pour KTP quand on calcule la différence entre les spectres d'absorption enregistrés au seuil K du titane avec des hélicités inversées (Publication 3.3). Une étude de la dépendance angulaire du signal quand on fait tourner le cristal autour l'axe du faisceau permet de séparer les contributions respectives du dichroïsme linéaire dont la valeur moyenne s'annule au cours d'une rotation de 180 degrés et du dichroïsme circulaire qui lui, reste invariant quel que soit l'angle.

Tous les spectres XNCD ont été enregistrés dans le mode fluorescence en raison de la trop grande absorption des cristaux en transmission. Dans la publication 3.4 qui étudie comment varient les caractéristiques de polarisation d'un faisceau X polarisé à l'intérieur d'un cristal gyrotrope, il est montré que, dans le cas d'un cristal uniaxe, les spectres XNCD enregistrés dans le mode transmission ou dans le mode fluorescence sont strictement proportionnels. Dans le cas des cristaux biaxes, cette proportionnalité n'est valable qu'au premier ordre, des effets du second ordre devant être pris en considération.

Enfin, il est essentiel de noter que, comme dans les études d'absorption des rayons X classiques, les résultats que nous avons obtenus en dichroïsme circulaire naturel ont pu être expliqués grâce à un effort parallèle sur le plan théorique qui n'aurait pu être mené à bien sans la collaboration amicale de C.R. Natoli et de Ch. Brouder.

3.2 Publication

JOURNAL OF CHEMICAL PHYSICS VOLUME 108, NUMBER 15 15 APRIL 1998

X-ray natural circular dichroism in a uniaxial gyrotropic single crystal of $LiIO_3$

José Goulon,[a] Chantal Goulon-Ginet,[b] Andrei Rogalev, and Vincent Gotte
European Synchrotron Radiation Facility, B.P. 220, F-38043, Grenoble Cedex, France

Cécile Malgrange and Christian Brouder
Laboratoire de Minéralogie Cristallographie, CNRS URA9, Universités de Paris VI et Paris VII, Tour 16, 4 place Jussieu F-75252, Paris Cedex 05, France

Calogero R. Natoli
Laboratori Nazionali di Frascati dell'Istituto di Fisica Nucleare, P.O. Box 13, I-00044 Frascati, Italy

(Received 1 August 1997; accepted 16 January 1998)

We produce the first experimental evidence of x-ray natural circular dichroism (XNCD) in a uniaxial gyrotropic crystal of α-$LiIO_3$ that is known to crystallize with space group $P6_3$ and to exhibit a very strong nonlinear susceptibility. For the sake of simplicity, the optical axis was set colinear to the direction of the exciting x-ray beam in order to get rid of undesirable birefringence and linear dichroism effects. The nicely structured XNCD spectra recorded at the L_{I}, L_{II}, and L_{III} edges of iodine are assigned to the electric dipole–electric quadrupole (E1.E2) interference terms which do not vanish in gyrotropic crystals but contribute to a second order polarizability. Our interpretation is consistent with a band structure calculation and is fully supported by *ab initio* multiple scattering simulations. The signatures recorded at the L_{II} and L_{III} edges are similar and have the same sign. This is in contrast to x-ray magnetic circular dichroism (XMCD) spectra which usually exhibit opposite signs at the L_{II} and L_{III} edges: while the exchange and spin-orbit interactions are the driving terms in XMCD, this is not the case in XNCD. The XNCD signal detected at the L_{I} edge is found to be relatively more intense and has the opposite sign. These results leave very little space for a contribution of the electric dipole–magnetic dipole (E1.M1) interference terms which are usually dominant at optical wavelengths but should be barely detectable in the x-ray range. © *1998 American Institute of Physics.* [S0021-9606(98)03715-5]

I. INTRODUCTION

The natural optical activity of crystals has fascinated successive generations of physicists since the discovery by Arago in 1811 that crystalline quartz had a remarkable optical activity on natural light.[1] More than one century later, the first theory of crystal gyrotropy was introduced, in the early thirties, by Hylleraas.[2] It took, however, another 30 years of development to refine macroscopic theories derived from the *Constitutive Equations* which include spatial dispersion in classical electrodynamics.[3–10] These theories are currently used for modeling optical activity in crystals and for ray tracing in anisotropic media.[11] Indeed, the crystal symmetry has to be taken into account in the representation of the optical activity by a rank-3 tensor:[12–14] among the 21 noncentrosymmetric crystal classes, only a subset of 18 classes (excluding: T_d, D_{3h}, C_{3h}) are *optically active.*[13] Moreover, looking for Cartesian representations that are invariant under all operations of the O group, it can be shown that the optical activity tensor can be decomposed into three irreducible representations:[13,14] (i) a pseudoscalar, (ii) a vector, and (iii) a rank-2 pseudodeviator. Since only the pseudoscalar and the pseudodeviator parts contribute to the gyration tensor responsible for the rotatory power and natural circular dichroism, we are left with the usual 15 gyrotropic crystal classes.[12] Only crystal classes compatible with chiral enantiomorphism have a nonzero pseudoscalar part. On the other hand, gyrotropic crystals featuring a large pseudodeviator part are most often showing a large nonlinear susceptibility at optical wavelengths. More important for the present study is the link between the *macroscopic* gyration tensor and the *microscopic* multipolar polarizability tensors: Buckingham and Barron[15–18] were the first to point out that the electric dipole (E1)–electric quadrupole (E2) interference terms were contributing to the pseudodeviator part of the optical activity tensor but not to the pseudoscalar part which could be identified with the pure electric dipole (E1)–magnetic dipole (M1) coupling.

There are very few gyrotropic crystals for which the optical activity tensor is fully characterized at optical wavelengths. In biaxial crystals, optical activity and birefringence occur together and the optical effects of birefringence usually swamp completely those of gyrotropy so that sophisticated techniques are required to unravel what is really due to gyrotropy. There is also a wide variety of mechanisms contributing to optical activity[19,20] and their identification is not a trivial task. A natural trend is to extend such experimental studies into different energy ranges in order to have access to

[a]Author to whom correspondence should be addressed. Electronic mail: goulon@esrf.fr
[b]Also at: The Université de Grenoble I-Faculté de Pharmacie, F-38706 La Tronche, France.

complementary information. Inner shell x-ray absorption or emission spectroscopies are particularly attractive because they are element specific.[21] At present, there are clearly renewed perspectives for x-ray polarimetry boosted by the tremendous development of third generation synchrotron radiation sources[22] and the recent availability of undulators that offer a full control of the polarization state of the emitted x-ray photons.[23] Unfortunately, all previous attempts to observe x-ray natural circular dichroism (XNCD) on various chiral organometallic complexes were inconclusive or at best ambiguous.[24] In contrast, x-ray ellipsometry was performed at the cobalt K-edge on powdered samples of the enantiomeric complexes of [tris (1,2-diaminoethane) $Co^{(III)}$] Br_3H_2O and revealed a subtle rotation of the plane of polarization of the incident x-rays at an energy characteristic of a weak prepeak.[25] Since optical rotatory dispersion and circular dichroism are related *via* a Kramers–Kronig transformation, the latter experiment implies that XNCD should also be detectable experimentally. For a *nonoriented powder*, optical activity should stem essentially from the Rosenfeld–Condon rotatory strength (R_0), i.e., from the *pseudoscalar* term:

$$R_0 \propto \mathrm{Im}\{\langle i|E1|f\rangle.\langle f|M1|i\rangle\}. \tag{1}$$

The problem with the transposition of Eq. (1) to the x-ray range is triplex. For transitions from core states, the initial state sum over all the spin-orbital projections of the core electron gives rise to a sort of Rosenfeld–Condon sum rule (i.e., the equivalent of the optical sum rule!) so that the total net dichroism would be systematically zero. Second, even for oriented crystals, the magnetic dipole transition matrix element (TME) would be zero at zeroth order approximation due to the radial orthogonality of the core and valence orbitals ($\Delta n=0$ selection rule). Even though correlation and many-body effects can make this selection rule less restrictive, there is still the problem that no magnetic dipole transition is allowed from a *pure* $1s$ (or $2s$) atomic state and that the energy separation between deep core levels makes the $\{1s,2p\}$ hybridization highly improbable, except (perhaps) in the very soft energy range, i.e., for K or L_1 edges of low Z elements.[26–28] Since the experiment of Siddons *et al.*[25] was performed at the cobalt K-edge, one is led to the conclusion that the observed optical activity can hardly be explained by the pseudoscalar rotatory strength R_0.

For oriented single crystals, the difference is that one may now expect a substantial contribution of the E1.E2 pseudodeviator part of the optical activity tensor. The corresponding absorption cross section should be given by:

$$\sigma^{\mathrm{E1.E2}}=4\pi^2\alpha_0.[h\omega/2\pi].P_3k\sum_j \sum_{\alpha,\beta,\gamma,\lambda} \varepsilon_{\alpha\beta\lambda}\hat{k}_\lambda\hat{k}_\gamma \times\langle i|r_\alpha|j\rangle.\langle j|r_\beta r_\gamma|i\rangle.\delta(E_j-E_i+[h\omega/2\pi]), \tag{2}$$

where α_0 is the fine structure constant, P_3 is the circular polarization rate, and $\hat{k}_\lambda$ are the components of the unit wave vector. We also made use in Eq. (2) of the usual notation of the Levi–Civita alternating tensor $\varepsilon_{\alpha\beta\gamma}$. Let us underline that $\langle\sigma^{\mathrm{E1.E2}}\rangle$ will vanish for a nonoriented powdered sample since: $\langle\hat{k}_\lambda\hat{k}_\gamma\rangle=1/3\,\delta_{\lambda\gamma}$.

Only 13 crystal classes out of the 15 gyrotropic crystal classes will contribute to a nonzero E1.E2 interference term: C_1, C_{1h}, C_2, C_{2v}, D_2, D_{2d}, C_3, D_3, C_4, D_4, S_4, C_6, D_6. This is because the crystal classes for which the optical activity tensor is only a *pseudo*scalar have to be excluded. The $\sigma^{\mathrm{E1.E2}}$ cross term has not yet been observed experimentally in the x-ray range. It is, however, well documented that electric quadrupole transitions contribute to x-ray absorption spectra,[29–31] to x-ray magnetic circular dichroism (XMCD),[32–34] and also to diffraction processes.[35–36] Templeton and Templeton[37] pointed out recently that the E1.E2 interference terms could explain the tetrahedral anisotropy of x-ray anomalous scattering in noncentrosymmetric crystals for weak or forbidden Bragg reflections. This situation prompted us to initiate two parallel projects concentrating on the experimental detection of XNCD *in oriented single crystals:*

(i) The first project dealt with stereogenic *organometallic* complexes in which the absorbing metal center (e.g., a rare earth element) is *itself* in a chiral ligand field. The strategy was to grow single crystals in which the (+) or (−) enantiomers are perfectly resolved. The first results were recently reported elsewhere.[38,39]

(ii) The second project was concerned with *inorganic* gyrotropic crystals which may or may not belong to crystal classes compatible with enantiomorphism but which all exhibit *very strong nonlinear effects* at optical wavelengths.

The present paper is the first report concerning the second subject. For simplicity, we choose a uniaxial crystal of α-$LiIO_3$ which is known to exhibit a large specific rotativity,[13,40] together with a very strong nonlinear susceptibility in the visible range:[41–44] Lithium iodate crystals are commonly used to frequency double various lasers such as the [Ti: sapphire], the alexandrite, or the [Cr:$LiSrAlF_6$] lasers. As pointed out by Machavariani,[45] experiments with biaxial crystals are far more difficult to interpret because the anisotropy of the permittivity tensor can give rise to other effects in crystal optics which are not related to gyrotropy.

With intense x-ray sources and high resolution crystal analyzers, one may try to detect optical asymmetry in x-ray emission spectra. A molecular field theory has recently been proposed for XNCD in the soft x-ray resonant raman regime:[46] Surprisingly, circular dichroism (CD) was predicted to exist for *achiral* molecules in a pure electric dipole E1 approximation under the restriction that, again, a strong delocalization of the core orbitals may be envisaged. The existence of such CD has still to be confirmed experimentally. In the resonant inelastic x-ray scattering (RIXS) regime, the parity conserving selection rule is $\Delta 1=0, \pm 2$ (Ref. 47) and the problem is different. Nevertheless, in another experiment to be reported elsewhere,[48] we have already confirmed that optical asymmetry can be detected in high resolution x-ray emission spectra: in fact, this independent experiment gave us an indirect proof of the results discussed below.

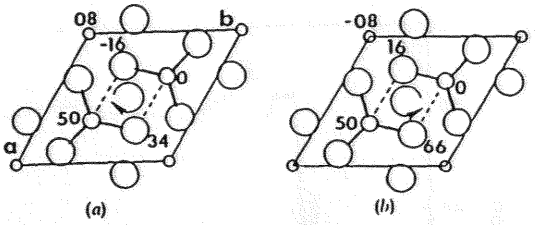

FIG. 1. Projections on (001) of a *left*-handed helical structure (a) and a *right*-handed helical structure (b) for α-$LiIO_3$ reproduced from Ref. 55. Small circles: Li; medium-sized circles: I; large circles: O.

II. EXPERIMENT

A. α-$LiIO_3$ single crystal

We ordered from CASIX Inc. a 1-mm thick slice (5×5 mm) of α-$LiIO_3$ single crystal cut normal to the optical axis. This crystal (reference FUJIAN CX LiIO3: 551), which was of very high optical quality, was kept carefully either in a sealed bag under argon or in a vacuum vessel. From previous crystal structure studies,[49–55] it is known that α-$LiIO_3$ crystallizes with two molecules *per* cell in space group $P6_3$. As already noted by Templeton and Templeton,[56] this is a suitable material for observation of dichroism because the threefold axes of the two achiral iodate ions are parallel: this is the relative disposition of the IO_3 groups that generates a chiral helical structure in which iodine and oxygen atoms alternate (Fig. 1). Since the space group $P6_3$ is compatible with enantiomorphism, it should be possible to grow crystals with opposite chirality. Furthermore, α-$LiIO_3$ crystals are *polar*, i.e., the morphology of each crystal and the sign of the piezo- and pyroelectric coefficients change with the orientation of the helical axis **c** that is characterized by the orientation of the apices of the IO_3 groups. As discussed by Stadnicka *et al.*,[54] the absolute configuration of the crystal can be resolved using anomalous scattering effects on a number of Bijvoet pairs: 001 reflections can be used to determine the direction of +**c** and those with $h,k \neq 0$ can be used to determine the crystal handedness. At the present stage of the project, the determination of the absolute configuration of our crystal was not essential and was not undertaken.

B. Instrumental aspects

The experiments reported in this paper were carried out at the ESRF beamline ID12A. The performances of the beamline are described elsewhere.[57] In the present experiment, the source was the helical undulator "Helios-II," which is best suited to cover the energy range of interest. The first optical component intercepting the undulator beam was a pair of CVD-SiC mirrors located upstream with respect to the monochromator and acting essentially as low pass filters to reduce the heat load on the most critical component, which is the monochromator itself. Since these mirrors are deflecting the beam horizontally they do not affect the energy resolution. The fixed exit, two crystal monochromator was equipped with a pair of (111) Si crystals cryogenically cooled down to 133 K. Given the extremely low emittance of the source, the energy resolution was found to agree quite well with theoretical predictions for perfect Si crystals: 0.66 at the iodine L_{III} edge; 0.70 at the iodine L_{II} edge; 0.75 eV at the iodine L_I edge. In all cases the instrumental resolution was far better than the respective atomic natural widths:[58] 3.08; 3.25; 3.46 eV. Since the stability of the rocking curve between two consecutive scans is better than 0.65 μrad, the residual drift in the energy scale is $\leqslant$8.5 meV: the quality of XNCD spectra is then entirely limited by the source instabilities.

Unfortunately, we cannot make a full use of the high circular polarization rate of the source because the polarization transfer function of the monochromator is getting more and more unfavorable at the energy of the iodine L_{II} or L_{III} absorption edges. This point is illustrated by Table I, in which we have summarized the estimated values of the Stokes–Poincaré components P_1, P_2, P_3 of the monochromatic beam. Note that throughout the paper, we use the same convention as Barron in Ref. 18: P_3 is taken positive for an excess intensity of right circularly polarized photons (i.e., for an excess of photons with *negative* helicity!). From earlier polarimetry experiments,[57] we found it reasonable to assume that the x-ray beam emitted by the undulator Helios-II could be characterized with a circular polarization component $P_3 = \pm 0.92$.[57] Let us underline that reversing the phase of the undulator and therefore the helicity of the emitted photons does not imply that the helicity of the monochromatic x-ray photons has been *exactly* reversed, especially whenever there is a residual P_2 component in the incident beam.

Since the α-$LiIO_3$ single crystal was much too thick to be used in the transmission mode, all spectra discussed in the present paper were collected in the integrated x-ray fluorescence mode. At the time of the experiment, the fluorescence chamber was equipped with four photodiodes in a symmetric arrangement with respect to the vertical plane. The "backscattering" detector geometry is particularly attractive since it makes it possible to keep the optical axis of the crystal

TABLE I. Estimated polarization state components of the monochromatic beam at the L_{III}, L_{II}, and L_I absorption edges of iodine. The polarization state of the undulator beam itself was estimated to be $P_{3+} = +0.92$ and $P_{3-} = -0.92$. In Eq. (2), P_3 follows the standard convention: it is positive for an excess intensity of right circularly polarized light (i.e., photons with *negative* helicity).

Iodine L_{III} edge:	Iodine L_{II} edge:	Iodine L_I edge:
$E = 4562$ eV	$E = 4857$ eV	$E = 5193$ eV
Bragg angle: 25.56 deg	Bragg angle: 23.86 deg	Bragg angle: 22.38 deg
$P_{1+} = 0.60$ $P_{1-} = 0.60$	$P_{1+} = 0.55$ $P_{1-} = 0.55$	$P_{1+} = 0.51$ $P_{1-} = 0.51$
$P_{2+} = 0.09$ $P_{2-} = 0.27$	$P_{2+} = 0.11$ $P_{2-} = 0.28$	$P_{2+} = 0.13$ $P_{2-} = 0.29$
$P_{3+} = 0.63$ $P_{3-} = -0.58$	$P_{3+} = 0.68$ $P_{3-} = -0.63$	$P_{3+} = 0.73$ $P_{3-} = -0.70$

colinear with the incident x-ray beam. The α-$LiIO_3$ single crystal was mounted on a linear translator (T_y) which was itself fixed onto a differentially pumped "high" precision rotary drive (DRF-55 from VG Instruments): this allowed us to rotate the crystal around its optical axis. Since we had also the possibility to translate the crystal along the beam direction, we were able to optimize the solid angle in which the detectors were collecting the fluorescence photons and to minimize the crystal diffraction peaks in the energy range of interest.

Due to well known saturation/self-absorption effects, fluorescence yield (FY) spectra are not related *in a linear way* to x-ray absorption spectra.[59] A rather simple homographic transform of the fluorescence data[60] was systematically used to restore spectra proportional to the absorption coefficient. This correction is essential to measure reliable intensities for white lines. All dichroism spectra were processed with an "in-house" FORTRAN code ("dichro") which has been carefully debugged and evaluated by processing a number of x-ray magnetic circular dichroism (XMCD) data. A great deal of attention has been paid to detect (derivative-like) artifacts which may be caused by very small angular drifts of the source: we found it possible to minimize such undesirable effects by correlating carefully optimized sequences of scans. Under the conditions of the present experiment, the level of reproducibility of an independent series of XNCD spectra was in the range of 2.10^{-4} or 3.10^{-4}.

III. RESULTS AND DISCUSSION

A. XANES and EXAFS spectra

We have compared in Figs. 2(a) and 2(b) the XANES spectra recorded at the various L-edges with the same crystal orientation, i.e., with the **c** axis parallel to the beam direction. For the sake of comparison, the XANES spectra were systematically renormalized with respect to the edge jump and relative energy scales were used. The choice of consistent energy offsets [i.e., ΔE (L_{III})=4560.7 eV; ΔE (L_{II})=4855.6 eV] was a trivial exercise for the L_{II-III} edge XANES spectra which look very similar [see Fig. 2(a)]: the spectra were simply shifted so as to let the inflexion point of the pre-edge signatures coincide. Even though there are subtle differences in the relative intensities of some resonances, globally speaking, we are approaching the 2:1 statistical limit for the L_{III}/L_{II} branching ratio. This is not too surprising since, as discussed by de Groot,[61] we are looking here at a system where the $2p$ core-hole spin-orbit splitting is large (295 eV) and the $5d$ band is empty so that there are no G_{dd} Slater integrals to be taken into account.

The L_I edge XANES spectrum reproduced in Fig. 2(b) is dominated by a huge white line with a peak-to-(atomic)background ratio of ~5:1. A slightly less intense white line (with a peak-to-background ratio of only 4:1) had already been reported for the L_I edge absorption spectrum of KIO_3 in a powdered sample.[62] In the K-edge XANES spectra reported by Templeton and Templeton for their α-$LiIO_3$ single crystal,[56] there appears clearly to be also a white line but, as emphasized by the authors in their paper, the convolution with the fairly large spectral width of the core hole

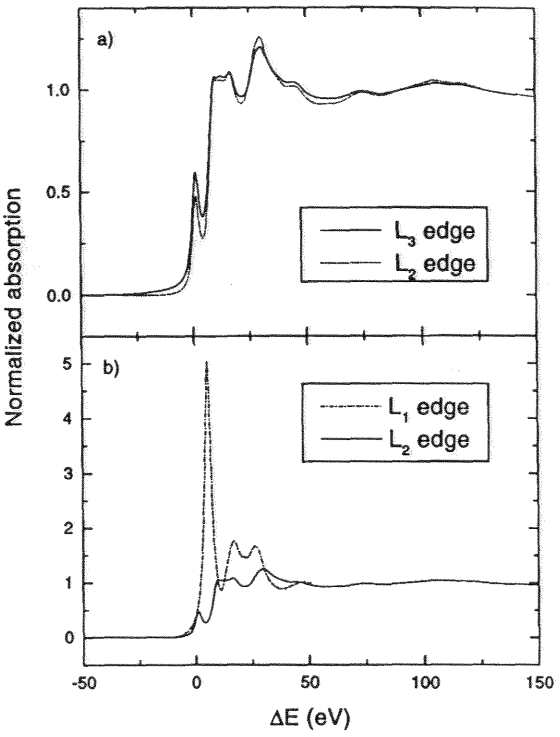

FIG. 2. Comparative display of the FY-XANES spectra of -$\alpha$$LiIO_3$ recorded at the $L_{I-II-III}$ edges of iodine with an elliptically polarized incident beam. The crystal **c** axis was aligned with the direction of the incident beam. All spectra are corrected for self-absorption and renormalized with respect to the edge jump. (a): comparison of the L_{II-III} edges: (b): comparison of the L_{I-II} edges. Note the strong white line at the L_I edge and the large intensity of the next two "shape" resonances at higher energy.

(10.6 eV[59]) and the poor instrumental resolution (2.8 eV) results in a broader peak with a lower intensity. The spectra displayed in Fig. 2(b) were tentatively rescaled in energy by phase-matching the EXAFS oscillations. For this purpose, we have compared in Figs. 3(a) and 3(b) the Fourier transformed (FT) EXAFS spectra recorded, respectively, at the L_I and L_{II} edges and *corrected* for the first I–O shell according to:[63]

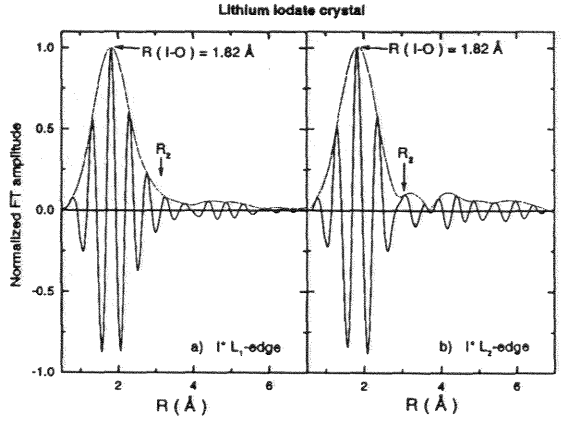

FIG. 3. (a): Corrected FT-EXAFS spectrum using data collected at the L_I edge. (b): Corrected FT-EXAFS spectrum using data collected at the L_{II} edge. Note that the EXAFS spectrum had to be truncated only 290 eV above the edge due to the discontinuity associated with the L_I edge. Following the criterion of Lee–Beni, E_0 was adjusted in both cases so as to make the maxima of $|\tilde{\chi}(R)|$ and $\mathrm{Im}\{\tilde{\chi}(R)\}$ coincide.

$$\tilde{\chi}_{I\text{-}O}(R)=\int_0^\infty dk\cdot w(k)\cdot\chi(k)\cdot\frac{k\cdot\bar{R}_{I\text{-}O}^{2l}\cdot\exp\{+2\sigma_{I\text{-}O}^2k^2-2ikR-i\psi_{I\text{-}O}(k)\}}{|f_2^l(\pi,k,\bar{R}_{I\text{-}O})|\cdot D_2^1(k,\Gamma,\bar{R}_{I\text{-}O})\cdot S^2(k)},\quad(3)$$

where: $\chi(k)$ is the standard notation for the EXAFS modulation; $w(k)$ is a Kaiser–Bessel window function minimizing the truncation side lobes; $|f_2^1(\pi,k,\bar{R}_{I\text{-}O})|$ is the backscattering amplitude of the nearest oxygen shell; $\psi_{I\text{-}O}(k)=2\delta_{0,\ \text{absorber}}^l(k)+\phi_{2,\ \text{scatterer}}^l(k)$ is the total scattering phase-shift; $D_2^1(k,\Gamma,\bar{R}_{I\text{-}O})$ and $S^2(k)$ are damping functions accounting for inelastic losses; $\sigma_{I\text{-}O}^2$ is the usual Debye–Waller factor.

Both FT spectra reproduced in Figs. 3(a) and 3(b) are dominated by the signature of the three oxygen atoms directly bound to iodine to form the IO_3^- anion: the two spectra yield exactly the same interatomic distance R_1 (I–O)=1.82 ±0.01 Å. From the crystal structure, one would expect the coordination polyhedron of iodine to consist of six oxygens with two unequal I–O interatomic distances:[52] $R_1=1.806$ and $R_2=2.91$ Å. That there is only a very weak, poorly resolved second shell is not too surprising, since x-ray diffraction data[53] also revealed that the distance R_2 had a fairly large temperature dependence implying a large Debye–Waller factor. A perennial question in EXAFS is how to refine the E_0 value: here we made use of the Lee and Beni criterion[63,64] which (inherently) depends on the theoretical model used to calculate the phase shifts. This was, however, a rather marginal problem here because we were mostly interested in a crude evaluation of the energy difference ΔE_0 needed to display on the same plot the L_{II} and the L_I edge XANES spectra with consistent energy scales: the relative energy shifts used to plot the spectra reproduced in Fig. 2(b) were thus, respectively, ΔE (L_I)=5187.6 eV; ΔE (L_{II}) =4855.6 eV.

The outcome of this useful exercise is that the intense white line observed at the L_I edge *has a poor overlap* with the shape resonances of the L_{II} edge. This observation will be of direct interest in the discussion of the XNCD spectra in the next section. It is also very apparent from Fig. 2(b) that the multiple scattering resonances contributing to the L_I edge XANES spectrum are systematically more intense than those contributing to the L_{II} edge XANES spectrum. Since both spectra were recorded in the FY mode, one could argue that either the fluorescence yields or the branching ratios between radiative, Auger, and Coster–Kronig channels are fairly different.[65] However, similar trends also exist in a number of L_{III} and L_I edge spectra recorded in the *transmission* mode (see, for instance, Ref. 66 or 67).

B. XNCD spectra

We have reproduced in Figs. 4(a) and 4(b) the difference spectra $[\sigma^L-\sigma^R]$ obtained, respectively, at the L_{III} and L_{II} edges. For the sake of comparison, the spectral differences were renormalized with respect to the relevant edge jump and we decided to keep the same relative energy scales as in Fig. 2. Note that the signal-to-noise ratio cannot be as good at the L_{II} edge as at the L_{III} edge since there is a large background level resulting from all fluorescence channels opened by the L_{III} edge photoionization. There is nevertheless a striking similarity between the two difference spectra which have the same spectral "morphology" and the same negative sign. The most intense signatures are found in an energy range of ~60 eV above the edges with a peak amplitude of ~0.6% at the $L_{II\text{-}III}$ edges. On correcting these figures for the circular polarization transfer of the monochromator (see Sec. II B), the order of magnitude of the measured effect slightly exceeds 1%. We found it useful to check that a rotation of the crystal around the beam direction did not change significantly the shape nor the intensity of the L_{III} XNCD spectra: This is illustrated by Fig. 5, in which we display for five different crystal orientations the difference spectra $[\sigma^L-\sigma^R]$. We should underline here that the spectra shown in Fig. 5 are direct difference between only two consecutive scans. The observed invariance of the XNCD spectra is fully consistent with Eq. (2) if we identify $[\sigma^L-\sigma^R]=-\sigma^{E1.E2}$. It would be straightforward to show that $\sigma^{E1.E2}$ remains unchanged in a rotation by 90 or 180° around the direction of the incident beam. This is indeed fully consistent with the general result established by Barron in Ref. 18 regarding natural CD in uniaxial crystals.

We have reproduced in Fig. 6 the spectral difference $[\sigma^L-\sigma^R]$ measured at the iodine L_I edge. This experiment was much more demanding because: (i) the *absolute differences* in the fluorescence intensity were smaller (0.3%) than

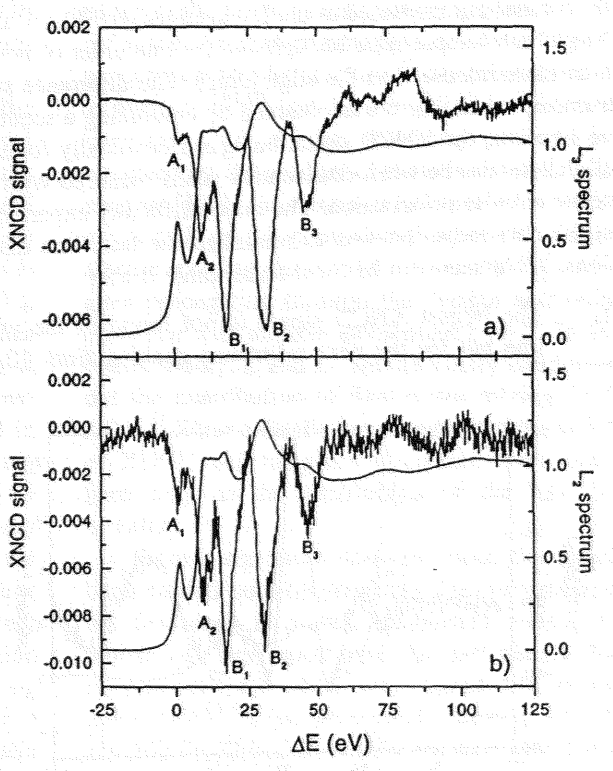

FIG. 4. Normalized XNCD spectral differences $[\sigma^L-\sigma^R]$ at the L_{III} and L_{II} edges. The spectra are not corrected for the polarization transfer function of the monochromator. The relative energy scale is the same as in Fig. 2(a). The polarization averaged XANES spectra are also displayed for the sake of comparison. Note the striking similarity in the morphology of the two XNCD spectra which both have the same negative sign. (a): L_{III} edge XNCD spectrum; (b): L_{II} edge XNCD spectrum.

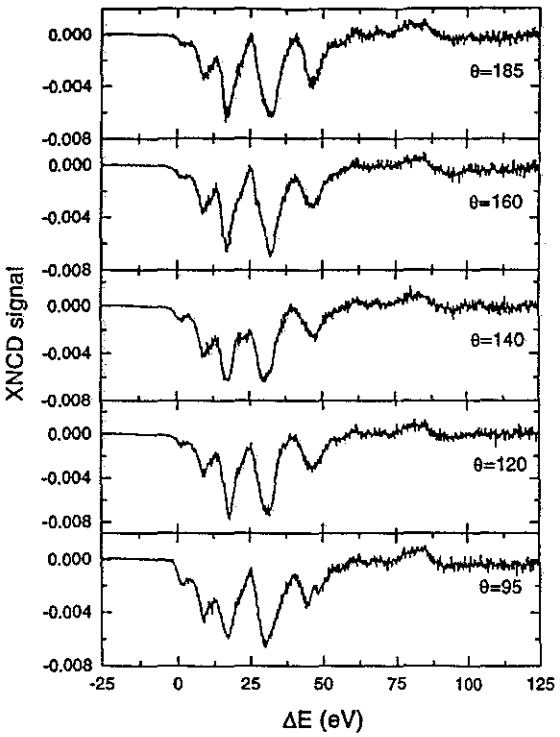

FIG. 5. Comparison of XNCD spectra recorded at the L_{III} edge for discrete crystal orientations which differ by a rotation around the c axis (i.e., around the beam direction): $\Delta\Theta$=95; 120; 140; 160; 185. Note that each plot is a direct difference between only two consecutive scans recorded with opposite circular polarization.

the differences measured at the L_{II-III} edges (0.6%); (ii) there was an intense pre-edge background (~ one order of magnitude more intense than the edge jump). The difference spectrum shown in Fig. 6 was obtained by combining a sequence of 40 scans, the XNCD signal being systematically found in all differences between consecutive scans recorded with opposite circular polarization. The major difficulty experienced in the data reduction was to minimize the base line distortions. What seems to be most remarkable is that:

(i) The largest XNCD signal is not found in the white line but for the next resonance peaking from 12 eV toward higher energy; the latter peak also coincides with a maximum in the L_{II-III} edge XANES spectra [see Fig. 2(b)];

(ii) The sign of the most intense signals is positive as opposed to the spectral differences measured at the L_{II-III} edges;

(iii) The L_I-XNCD spectrum has a remarkably flat base line;

(iv) The pre-edge subtraction and the renormalization with respect to a small edge jump result in a relative amplitude of the main peak which is unexpectedly large: ~4.0% if we refer to the raw data and ~5.5% if we take into account the polarization transfer of the monochromator.

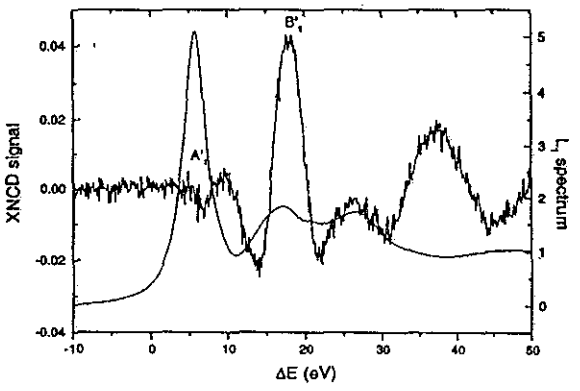

FIG. 6. Normalized XNCD spectral differences $[\sigma^L-\sigma^R]$ measured at the L_I edge. The relative energy scale is the same as in Fig. 2b. The polarization averaged XANES spectrum is also displayed for the sake of comparison. Observe the absence of any strong signature at the energy of the white line. Note the positive sign of the main peak.

IV. SIMULATIONS OF XNCD SPECTRA

A. Selection rules and symmetry of the final states

This seems to be an appropriate point at which to recall first what the relevant selection rules are that are associated with Eq. (2). In full conformity with "atomiclike" selection rules we have: $\Delta l=\pm 1$ for E1 transitions; $\Delta l=0$, ± 2 for E2 transitions with: $\Delta l\neq 0$ if $l_0=0$. This has very clear implications: at the L_I edge, the final states $|j\rangle$ should mix atomic orbitals (AO's) with p and d-type symmetry for the E1 and E2 transitions; at the L_{II-III} edges, the final states should mix AO's with d- or s-symmetry for the E1 transitions and either p- or f-symmetry for the E2 transitions. Note that the crystal geometry may restrict the choice of m values. Typically, our experimental configuration is only consistent with final states which mix $\{p,d\}$ and $\{d,f\}$ AO's. We cannot yet rule out final states mixing $\{s,f\}$ and $\{s,p\}$ AO's in the XNCD spectra recorded at the L_{II-III} edges. For sure, the key difference between the L_I and L_{II-III} edges XNCD spectra arises from the absence at the L_I edge of any contribution mixing $\{d,f\}$ AO's.

B. Band structure calculations

In a first attempt to support our interpretation, we have performed a band structure calculation relying on a tight binding (TB) version of the linear muffin-tin orbital (LMTO) method in the atomic sphere approximation (ASA). We used the TB-LMTO-ASA code developed by Andersen and Jepsen[68] and the crystal structure of α-$LiIO_3$ reported in Ref. 52. We found that the gap between the filled valence band and the empty conduction band was ~5 eV, in good agreement with the known optical absorption spectrum of α-$LiIO_3$ crystals. We have reproduced in Figs. 7(a) and 7(b) the local density of states (DOS—*per* unit cell and eV) of projected p, d, and f symmetries in the iodine Wigner–Seitz sphere. A prerequisite for XNCD to be detected at the L_{II-III} edges is that in the conduction band, d-projected DOS should overlap with either p- or f-projected DOS. We see from Fig. 7(a) that there is a clear overlap $\{d,p\}$ DOS at energies ranging from 5 up to 20 eV above the Fermi level set as the origin of the energy scale. Similarly, Fig. 7(b) makes us expect an even stronger overlap of $\{d,f\}$ DOS at energies ranging from 20 up to 40 eV above the Fermi level (and at higher energy).

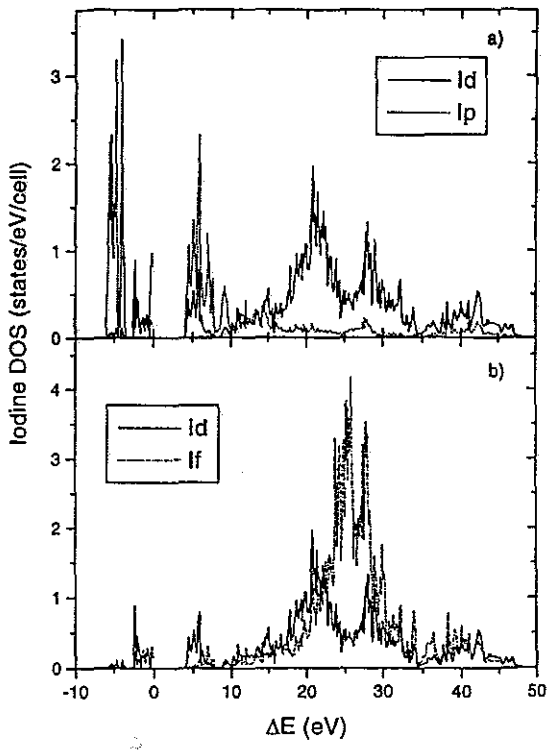

FIG. 7. Local DOS (per unit cell and eV) for p, d, and f symmetries in the iodine Wigner–Seitz sphere calculated with the Andersen–Jepsen TB-LMTO-ASA code of Ref. 68. (a): Overlap of the $\{p,d\}$ DOS; (b): Overlap of the $\{f,d\}$ DOS.

For iodine, we found only a minor contribution of s-DOS very near the bottom of the conduction band but no significant overlap with the f-projected DOS.

Focusing again on the XNCD spectra recorded at the L_{II-III} edges, an interesting point brought out by the band structure calculations is that the small peaks found near the edge (marked A_1, A_2 in Fig. 4; $\Delta E \leqslant 12.5$ eV) might well refer to final states mixing $\{d,p\}$ AO's, whereas the intense peaks found at higher energy (marked B_1, B_2, B_3; $\Delta E \geqslant 17.5$ eV) should involve final states mixing $\{d,f\}$ AO's. Indeed, it does not make sense to correlate *directly* the peaks observed in the XNCD spectra with characteristic maxima of the overlapping DOS. On the other hand, we wish to draw attention to the fact that the intense white line observed in the L_I XANES spectrum cannot be explained by considering only the p-projected DOS at the iodine site. As illustrated by Fig. 8, we found that the p-projected DOS is quite large very near the bottom of the conduction band at the sites of the three tightly bound oxygen atoms: this may well cause a strong resonance characteristic of the IO_3^- anion, possibly with the creation of an excitonlike state. Since the IO_3^- anion is not itself chiral, there is no reason to expect a very strong contribution of $\sigma^{E1.E2}$ in the L_I white line since XNCD is mostly due to the overlap in the iodine Wigner–Seitz sphere of $\{d,p\}$ DOS [see Fig. 7(a)], which also explains the weak XNCD at L_{II-III} edges. Further inspection of the projected p-type DOS of the oxygen atoms *in the valence band* also confirmed the expected hybridization of $\{p,d\}$ AO's of iodine with $2p$ AO's of oxygen: this could be a favorable circumstance for an efficient screening of the core hole.[69]

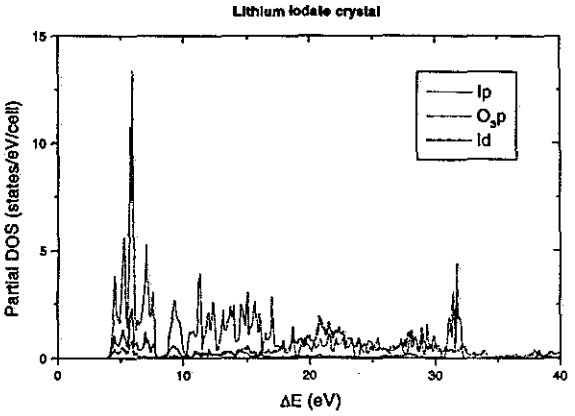

FIG. 8. Comparison of partial DOS: continuous line: local DOS (per unit cell and eV) of p symmetry at the bound oxygen sites; dashed line: local DOS (per unit cell and eV) of p symmetry at the iodine site; dotted line: local DOS (per unit cell and eV) of d symmetry at the iodine site.

C. Multiple scattering simulations

There are well known limitations in the use of band structure calculations in x-ray absorption spectroscopy: (i) the perturbation induced by the core hole cannot be easily taken into account even with the definition of supercells, and most calculations implicitly assume that the multielectron system is relaxed; (ii) the LMTO method can hardly yield a reliable picture of the electronic structure at high energy, e.g., for $E \geqslant 40$ eV. It is indeed preferable to carry out multiple scattering (MS) calculations in the *direct* space as opposed to the previous calculations performed in the *reciprocal* space. As another consequence of the "optical theorem" generalized by Natoli *et al.*,[70] the cross section for natural dichroism $\sigma^{E1.E2}$ can be shown to be proportional to the imaginary part of the scattering path operator $[\tau_{LL'}]^{00}$ weighted by the product of the atomic electric dipole matrix element $[E1]_L$ for creating a photoelectron with angular momentum L at the photoabsorbing site 0 multiplied by the electric quadrupole matrix element $[E2]_{L'}$ to annihilate it after propagating through the system and returning to the same site with angular momentum $L' \neq L$. In the framework of MS theory, L and L' should satisfy conditions which rule out the contribution of final states mixing $\{s,f\}$ and $\{s,p\}$ AO's.[71] Since a detailed presentation of the whole MS theory of XNCD will be given elsewhere,[71] we will concentrate here only on the simulations of the XNCD spectra for α-$LiIO_3$.

From a technical point of view, the simulations have been carried out *independently* with two different codes: (i) the first code is a well established code ("Continuum") which was developed over the past decade by Natoli and co-workers[72] and which was upgraded to include the calculation of $\sigma^{E1.E2}$; (ii) the second code was written by Brouder initially for XMCD but could be transformed to simulate also XNCD spectra.[73] "Continuum" generates energy dependent complex potentials according to the Hedin–Lundqvist prescription[74] and takes into account the presence of the core hole at the absorbing site. The second code is running essentially with real potentials but offered us the additional possibility to reinject in the MS calculations the self-consistent

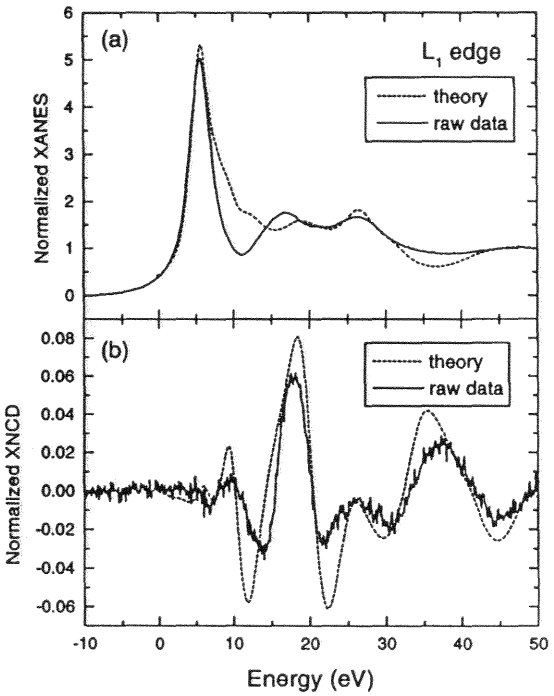

FIG. 9. Comparison of the experimental and the simulated XANES and XNCD spectra at the L_{I} absorption edge. MS calculations were performed according to the theory of Ref. 71, using the self-consistent Andersen–Jepsen potentials and the code of Ref. 73. (a): XANES spectra; (b): XNCD spectra; the experimental XNCD spectrum was corrected for the polarization transfer function of the monochromator.

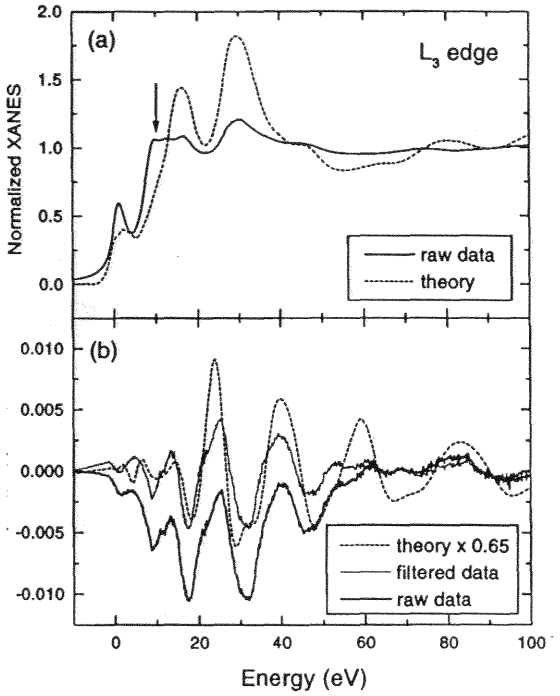

FIG. 10. Comparison of the experimental and the simulated XANES and XNCD spectra at the L_{III} absorption edge. MS calculations were performed according to the theory of Ref. 71, using the self-consistent Andersen–Jepsen potentials and the code of Ref. 73. (a): XANES spectra; the arrow indicates where the multiexcitation channels should contribute. (b): XNCD spectra; the experimental spectrum ("raw data") was corrected for the polarization transfer function of the monochromator; also displayed in Fig. 10(b) is a filtered spectrum ("filtered data") in which the base line distortion has been removed by a numerical procedure.

potentials extracted from the previous LMTO calculations carried out in the reciprocal space.[69] In practice, the second code turned out to be better at reproducing the relative intensity and shapes of the edge resonances, while "Continuum" is better at reproducing the damping of the XANES and XNCD spectra due to inelastic effects. Both calculations were performed with the same cluster: we used a cluster of 40 atoms matching in a sphere of diameter 10 Å, the radius of the latter sphere being of the same order of magnitude as the photoelectron mean free path. A detailed comparison of the results obtained with the two codes will be discussed elsewhere:[71] we produce here only the spectra simulated with the self-consistent "Andersen–Jepsen" local potentials.

As illustrated by Fig. 9, there is a quite remarkable agreement between the theory and the experiment for the XANES and XNCD spectra recorded at the L_{I} edge. Even though the experimental XNCD spectrum was corrected for the polarization transfer of the monochromator, the theory still predicts a slightly more intense XNCD signal than what was measured experimentally: this is not too surprising since the inelastic and the vibrational effects are not properly taken into account in the present MS calculation. Neither the experimental XNCD spectrum nor the simulated one exhibit any strong signature in the energy range of the white line: this agrees very well with the discussion of the previous section. A careful examination of Fig. 9 would reveal some significant discrepancies at ~12 eV from the Fermi level: we will come back later to this point.

We also compare in Fig. 10 the XANES and XNCD spectra recorded at the L_{III} edge and the corresponding MS simulations. Even though the most intense signatures are still rather well reproduced by the theory, the general agreement is not as good as for the L_{I} edge:

(i) The experimental XNCD spectrum exhibits some sort of low frequency "base line distortion" which does not exist at the L_{I} edge and which is not predicted by the theory: this led us to generate numerically a "filtered" spectrum and to display it also in Fig. 10 in order to refine the comparison with theory;

(ii) The amplitude of the experimental XNCD spectrum is not as large as in the simulated spectrum;

(iii) At ~12 eV from the Fermi level, there is again some discrepancy between experiment and theory not only in the XNCD spectrum but clearly also in the XANES: there seems to be some contribution missing in the theory and there was no improvement found in running "Continuum."

Regarding the latter point (iii), it is our interpretation that the origin of the observed discrepancies is to be found in *multielectron excitations* which are not included in our MS simulations. Typically, multielectron excitations involving $[2s5p] \rightarrow \{6p^2, 5d^2\}$ hybridized AO's and $[2p5p] \rightarrow [6p5d]$ transitions can be predicted to occur precisely at ~12 eV above the relevant absorption edges. The systematic investigation and identification of multielectron excitations (e.g., shake-up processes) in L-edge XANES spectra is now a fairly well documented subject.[75–79] It should be also borne

in mind that intense multielectron excitations were recently discovered in the L-edge XMCD spectra of several rare earth compounds.[80,81] There is no doubt that the extension of the existing codes in order to calculate XANES and XNCD in the framework of a multichannel MS theory would be highly desirable: this may, unfortunately, require more time and effort.

That the experimental XNCD spectrum seems to be systematically less intense at the L_{III} edge than the MS simulations is puzzling: A similar observation was already made in the case of the chiral organometallic complex reported in Ref. 39. It is also noteworthy that the MS codes do not reproduce correctly the amplitude of the resonances in the XANES spectrum. Therefore one cannot conclude that the incorrect amplitude of the simulated XNCD is a specific failure of the one-electron theory of XNCD:[71] Even with Hedin–Lundqvist potentials, we are clearly not yet able to give a correct representation of all inelastic effects at the L_{III} edge of iodine. A further complication with the interpretation of XNCD spectra at the L_{III} edge is that the theory predicts *destructive interferences* at low energy between oscillating XNCD structures, respectively, associated with $\{d,f\}$ and $\{d,p\}$ final states:[71] There is no hope to reproduce correctly this sort of interference if we have not a very accurate model for the amplitude of each component.

Quite ambiguous is the origin of the base line distortion (i) which is systematically observed at the L_{II-III} edges for any orientation of the crystal. Since there is anyhow a large discrepancy between theory and experience regarding the amplitude of the XNCD spectrum, we cannot yet rule out that this base line distortion might have a true spectroscopic origin. It is our view that (i) could have more to do with the experiment itself. An imperfect renormalization of two consecutive scans could well generate this sort of base line problem: this might be the case if the fluorescence signal is contaminated by energy dispersive diffraction peaks ("glitches") or by any intense elastic scattering background. Note that the base line distortion is observed when the polarization transfer of the monochromator is poor: one might then also suspect a contamination by some residual linear dichroism, especially if there is a small misalignment of the crystal off axis.

V. CONCLUSION

The present paper produces the first experimental evidence of x-ray natural circular dichroism in a gyrotropic crystal of α-$LiIO_3$ commonly used for second harmonic generation (SHG) at optical wavelengths. Once the data are corrected for the polarization transfer of the monochromator, we are left with large effects since, at the L_{II-III} edge $[\sigma^L-\sigma^R] \approx 1\%$ whereas $[\sigma^L-\sigma^R] \approx 5.5\%$ at the L_I edge. The origin of XNCD is ascribed to the electric dipole (E1)–electric quadrupole (E2) interference terms which are much larger in the x-ray range than in the visible range. This interpretation is supported by band structure and MS calculations. It is remarkable that the signatures recorded at the L_{II} and L_{III} edges are identical and have the same sign, whereas the signal measured at the L_I edge has the opposite sign and is, relatively, far more intense. This is in contrast with x-ray magnetic circular dichroism (XMCD): while the exchange and spin-orbit interactions are the driving terms in XMCD, this is clearly not the case in XNCD. The present study also leaves very little space for a contribution of the electric dipole–magnetic dipole (E1.M1) interference terms which are usually dominant at optical wavelengths but should hardly be detectable in the x-ray range. Given the various restrictions discussed earlier in the paper, one expects in any case the M1 transition matrix element to be at least one order of magnitude smaller than the E2 matrix element. Another factor depressing the importance of the E1.M1 interference term with respect to the E1.E2 contribution discussed in the present paper is to be found in the fact that the E1.E2 term is proportional to the magnitude of the photon wave vector (hence to the transition energy): the E1.E2 contribution thus benefits from a quite substantial multiplicative factor in the x-ray range.

Finally, there is another key difference between XNCD and XMCD: whereas XMCD spectra may still be reproduced with some success near the absorption edge using the *atomic model*, this would fail for XNCD spectra which are entirely due to *molecular or crystal field effects* and call for much more refined descriptions of the hybridization of atomic orbitals. From the present study, one may anticipate that XNCD could become a useful tool to study the *electronic structure* of a variety of crystals which are of interest for nonlinear optics or as ferroelectrics. Indeed, experiments will be restricted to situations where: $\langle \sigma^{E1.E2} \rangle \neq 0$. Applications concerning chiral surfaces could be envisaged if good enough signal-to-noise ratio can be obtained. Given the rather convincing agreement found between our MS simulations and the experiments, one may really think of using XNCD to determine the absolute configuration of a chiral center in enantiomorphous crystal classes.

ACKNOWLEDGMENTS

Acknowledgments are due to O. K. Andersen and O. Jepsen (MPI-Stuttgart) for the authorization to make use of their TB-LMTO-ASA code. J.G. is grateful to F. Sette and Y. Petroff for their friendly support in the recent years.

[1] D.-F.-M. Arago, Mém. de l'Institut de France **12**, Part 1, 93 (1811).
[2] E. Hylleraas, Z. Phys. **44**, 871 (1927).
[3] E. U. Condon, Rev. Mod. Phys. **9**, 432 (1937).
[4] M. Born and M. Goeppert-Mayer, *Solid State Theory* (1938).
[5] M. Born and K. Huang, *Dynamical Theory of Crystal Lattices* (Clarendon, Oxford, 1954).
[6] F. I. Fedorov, Opt. Spektrosk. **6**, 49 (1959).
[7] L. D. Landau and E. M. Lifshitz, *Electrodynamics of Continuous Media* (Pergamon, New York, 1960).
[8] V. M. Agranovich and V. L. Ginzburg, *Spatial Dispersion in Crystal Optics and Theory of Excitons* (Wiley-Interscience, London, 1966).
[9] E. J. Post, *Formal Structure of Electromagnetics* (North-Holland, Amsterdam, 1962).
[10] A. Yariv and P. Yeh, *Optical Waves in Crystals* (Wiley, New York, 1984).
[11] S. C. McClain, L. W. Hillman, and R. A. Chipman, J. Opt. Soc. Am. A **10**, 2371 (1993); **10**, 2383 (1993).
[12] J. F. Nye, *Physical Properties of Crystals* (Oxford University Press, New York, 1957).
[13] J. Jerphagnon and D. S. Chemla, J. Chem. Phys. **65**, 1522 (1976).
[14] J. Jerphagnon, D. S. Chemla, and R. Bonneville, Adv. Phys. **27**, 609 (1978).
[15] A. D. Buckingham, Adv. Chem. Phys. **12**, 107 (1967).

[16] A. D. Buckingham and M. B. Dunn, J. Chem. Soc. A , 1988 (1971).
[17] L. D. Barron, Mol. Phys. **21**, 241 (1971).
[18] L. D. Barron, *Molecular Light Scattering and Optical Activity* (Cambridge University Press, Cambridge, 1982).
[19] V. A. Kizel, Yu. I. Krasilov, and V. I. Burkov, Sov. Phys. Usp. **17**, 745 (1975).
[20] E. Charney, *Molecular Basis of Optical Activity* (Wiley-Interscience, New York, 1979).
[21] J. Goulon, in *Rayonnement synchrotron polarisé. Electrons polarisés et Magnétisme*, Proceedings of the 1st Winter school held in Mittelwihr/ France, 1989, pp. 333–386.
[22] M. Hart, in *Resonant Anomalous Scattering—Theory and Applications*, edited by G. Materlik, C. J. Sparks, and K. Fisher (Elsevier Science, New York, 1994).
[23] P. Elleaume, J. Synchrotron Radiat. **1**, 19 (1994).
[24] J. Goulon, F. Sette, C. Moise, A. Fontaine, D. Perey, P. Rudolf, and F. Baudelet, Jpn. J. Appl. Phys., Suppl. **32**, 284 (1993).
[25] D. P. Siddons, M. Hart, Y. Amemiya, and J. B. Hastings, Phys. Rev. Lett. **64**, 1967 (1990).
[26] B. Stewart, J. Phys. IV **4**, 179 (1994).
[27] L. Alagna, S. Di Fonzo, T. Prosperi, S. Turchini, P. Lazzeretti, M. Malagoli, R. Zanasi, C. R. Natoli, and P. J. Stephens, Chem. Phys. Lett. **223**, 402 (1994).
[28] O. Vahtras, H. Ågren, and V. Carravetta, J. Phys. B **30**, 1493 (1997).
[29] C. Brouder, J. Phys.: Condens. Matter **2**, 701 (1990).
[30] J. E. Penner-Hahn, R. A. Scott, K. O. Hodgson, S. Doniach, S. R. Desjardins, and E. I. Solomon, Chem. Phys. Lett. **88**, 595 (1982).
[31] G. Dräger, R. Frahm, G. Materlick, and O. Brümmer, Phys. Status Solidi B **146**, 287 (1988).
[32] J. C. Lang, G. Srajer, C. Detlefs, A. I. Goldman, H. König, Xindong Wang, B. N. Harmon, and R. W. McCallum, Phys. Rev. Lett. **74**, 4935 (1995).
[33] C. Giorgetti, E. Dartyge, C. Brouder, F. Baudelet, C. Meyer, S. Pizzini, A. Fontaine, and R. M. Galéra, Phys. Rev. Lett. **75**, 3186 (1995).
[34] M. H. Krisch, C. C. Kao, F. Sette, W. A. Caliebe, K. Hämäläinen, and J. Hastings, Phys. Rev. Lett. **74**, 4931 (1995).
[35] H. Wagenfeld, Phys. Rev. **144**, 216 (1966).
[36] K. D. Finkelstein, Q. Shen, and S. Shastri, Phys. Rev. Lett. **69**, 1612 (1992).
[37] D. H. Templeton and L. K. Templeton, Phys. Rev. B **49**, 14850 (1994).
[38] B. Stewart, R. D. Peacock, T. Prosperi, L. Alagna, S. Turchini, J. Goulon, C. Goulon-Ginet, and A. Rogalev, J. Phys. (France) IV, **7**, 463 (1997).
[39] L. Alagna, T. Prosperi, S. Turchini, J. Goulon, A. Rogalev, C. Goulon-Ginet, C. R. Natoli, B. Stewart, and R. D. Peacock, Phys. Rev. Lett. (submitted).
[40] O. G. Vlokh, L. A. Laz'ko, and I. S. Zheludev, Sov. Phys. Crystallogr. **20**, 401 (1975).
[41] S. K. Kurtz, T. T. Perry, and J. G. Bergman, Appl. Phys. Lett. **12**, 186 (1968).
[42] G. Nath and S. Haussühl, Appl. Phys. Lett. **14**, 154 (1969).
[43] F. R. Nash, J. G. Bergman, G. D. Boyd, and E. H. Turner, J. Appl. Phys. **40**, 5201 (1969).
[44] J. Jerphagnon, Appl. Phys. Lett. **16**, 298 (1970).
[45] V. Sh. Machavariani, J. Phys.: Condens. Matter **7**, 5151 (1995); R. V. Vedrinski (personal communication).
[46] Yi Luo, O. Vahtras, F. Gel'mukhanov, and H. Ågren, Phys. Rev. A **55**, 2716 (1997).
[47] J. H. Guo, P. Glans, P. Skytt, N. Wassdahl, J. Nordgren, Yi Luo, H. Ågren, Y. Ma, T. Warwick, P. Heinmann, E. Rotenberg, and J. D. Denlinger, Phys. Rev. B **52**, 10681 (1995).
[48] C. Dallera, M. Krisch, A. Rogalev, J. Goulon, and F. Sette, Chem. Phys. Lett. (submitted).
[49] A. Rosenzweig and B. Morosin, Acta Crystallogr. **20**, 758 (1966).
[50] J. L. De Boer, F. Van Bolhuis, R. Olthof-Hazekamp, and A. Vos, Acta Crystallogr. **21**, 841 (1966).
[51] I. D. Campbell, A. Mathieson, and M. F. Mackay, Acta Crystallogr., Sect. B: Struct. Crystallogr. Cryst. Chem. **25**, 1214 (1969).
[52] C. Svensson, J. Albertsson, R. Liminga, Å. Kvick, and S. C. Abrahams, J. Chem. Phys. **78**, 7343 (1983).
[53] E. Coquet, J. M. Crettez, J. Pannetier, J. Bouillot, and J. C. Damien, Acta Crystallogr., Sect. B: Struct. Sci. **39**, 408 (1983).
[54] K. Stadnicka, A. M. Glazer, and J. R. L. Moxon, J. Appl. Crystallogr. **18**, 237 (1985).
[55] Hua-Guang Yang, Dao-Fan Zhang, Wan-Chun Chen, and Yin-Yuan Li, J. Appl. Crystallogr. **22**, 144 (1989).
[56] D. H. Templeton and L. K. Templeton, Acta Crystallogr., Sect. A: Found. Crystallogr. **45**, 39 (1989).
[57] J. Goulon, A. Rogalev, C. Gauthier, C. Goulon-Ginet, S. Pasté, R. Signorato, C. Neumann, L. Varga, and C. Malgrange, J. Synchrotron Rad. (in press).
[58] M. O. Krause and J. H. Oliver, J. Phys. Chem. Ref. Data **8**, 329 (1979).
[59] J. Goulon, C. Goulon-Ginet, R. Cortès, and J. M. Dubois, J. Phys. (Paris) **43**, 539 (1982).
[60] M. Loos, I. Ascone, C. Goulon-Ginet, J. Goulon, G. Guilard, M. Lacroix, M. Breysse, D. Faure, and T. Descourières, Physica B **158**, 145 (1989).
[61] F. M. F. de Groot, J. Electron Spectrosc. Relat. Phenom. **67**, 529 (1994).
[62] G. Liang, A. Sahiner, M. Croft, Wei Xu, X.-D. Xiang, D. Badresingh, Weiguang Li, J. Chen, J. Peng, A. Zettl, and F. Lu, Phys. Rev. B **47**, 1029 (1993).
[63] J. Goulon, M. Loos, P. Friant, and M. Ruiz-Lopez, NATO ASI Ser. C **221**, 247–293 (1988).
[64] P. A. Lee and G. Beni, Phys. Rev. B **15**, 2862 (1977).
[65] F. M. F de Groot, M. A. Arrio, Ph. Sainctavit, Ch. Cartier, and C. T. Chen, Solid State Commun. **92**, 991 (1995).
[66] S. M. Angeretti, G. Dalba, P. Fornasini, M. Benfatto, and F. Rocca, Phys. Rev. B **44**, 11569 (1991).
[67] J. Chaboy, J. Garcia, A. Marcelli, and T. A. Tyson, Jpn. J. Appl. Phys., Part 1 **32**, 107 (1992).
[68] O. K. Andersen and O. Jepsen, Phys. Rev. Lett. **53**, 2571 (1984).
[69] D. Cabaret, Ph.D. Thesis, University of Paris VI, 1997.
[70] C. R. Natoli, M. Benfatto, and S. Doniach, Phys. Rev. A **34**, 4682 (1986).
[71] C. R. Natoli, Ch. Brouder, Ph. Sainctavit, J. Goulon, C. Goulon-Ginet, and A. Rogalev, Eur. Phys. J. (in press).
[72] C. R. Natoli, M. Benfatto, and T. Tyson, unpublished code; see also, T. A. Tyson, K. Hodgson, C. R. Natoli, and M. Benfatto, Phys. Rev. B **46**, 5997 (1992).
[73] Ch. Brouder, unpublished code; see also, Ch. Brouder, M. Alouani, K. H. Bennemann, Phys. Rev. B **54**, 7334 (1996).
[74] L. Hedin and B. I. Lundqvist, Solid State Phys. **23**, 1 (1969); J. Phys. C **4**, 2064 (1971).
[75] K. Zhang, E. A. Stern, J. J. Rehr, and F. Ellis, Phys. Rev. B **44**, 2030 (1991).
[76] I. Arcon, A. Kodre, M. Stuhec, D. Glavic-Cindro, and W. Drube, Phys. Rev. A **51**, 147 (1995).
[77] T. Tochio, Y. Ito, T. Mukoyama, M. Takahashi, and S. Emura, J. Phys. France IV **7**, 1263 (1997).
[78] M. A. McDonald, S. H. Southworth, J. C. Levin, A. Henins, R. D. Deslattes, T. LeBrun, Y. Azuma, P. L. Cowan, and B. A. Karlin, Phys. Rev. A **51**, 3598 (1995).
[79] V. Gotte, A. Rogalev, and J. Goulon (unpublished spectra).
[80] E. Dartyge, A. Fontaine, C. Giorgetti, S. Pizzini, F. Baudelet, G. Krill, C. Brouder, and J. P. Kappler, Phys. Rev. B **46**, 3155 (1992).
[81] E. Dartyge, F. Baudelet, C. Brouder, A. Fontaine, C. Giorgetti, J. P. Kappler, G. Krill, M. F. Lopez, and S. Pizzini, Physica B **208–209**, 751 (1995).

3.3 Publication

J. Synchrotron Rad. (1999). **6**, 673–675

X-ray natural circular dichroism of gyrotropic crystals

José Goulon,[a]* Chantal Goulon-Ginet,[a,b] Andrei Rogalev,[a] Vincent Gotte,[a] Cécile Malgrange[c] and Christian Brouder[c]

[a]European Synchrotron Radiation Facility, B.P. 220, F-38043 Grenoble Cedex, France, [b]Faculté de Pharmacie, Université Joseph Fourier, Domaine de la Merci, F-38700 La Tronche, France, [c]Laboratoire de Minéralogie Cristallographie, Universités Paris VI et VII, Case 115, 4 Place Jussieu, F-75252 Paris Cedex 05, France. Email:goulon@esrf.fr

We review the conditions under which Natural Circular Dichroism can be observed in the X-ray range for either uniaxial or biaxial gyrotropic single crystals.

Keywords: optical activity, circular dichroism, X-ray absorption spectra

1. Introduction

Over one century after the discovery of X-rays (Röntgen, 1895) and the discovery of circular dichroism (CD) in absorption bands (Cotton, 1895), we have produced the first experimental evidence of *Natural* CD in the X-ray range (Goulon *et al.*, 1998; Alagna *et al.*, 1998). Such experiments became possible with the third generation Synchrotron Radiation sources and, more specifically, with the development of powerful helical undulators which can produce intense fluxes of X-rays with a full control of their polarization state (Elleaume, 1994). Whereas X-ray Magnetic Circular Dichroism (XMCD) spectra are most easily recorded by reversing the direction of the applied magnetic field (Schütz *et al.*, 1987), it is essential in X-ray Natural Circular Dichroism (XNCD) experiments to reverse the sign of the Stokes-Poincaré component P_3 : this is where our helical undulator Helios-II is particularly appropriate. The recent development of X-ray quarter-wave plates made it also possible to measure accurately the polarization rates of the incident X-ray beam (Goulon *et al.*, 1996) whereas the polarization transfer function of Bragg monochromators can now be predicted very accurately. On the other hand, there was rather little motivation to look for natural optical activity in the X-ray range because the Rosenfeld rotatory strength is expected to vanish in inner shell spectroscopies. There are several reasons for that : (i) Magnetic Dipole (M1) transitions are forbidden due to the orthogonality of the core and valence orbitals ($\Delta n = 0$ selection rule); this is even more restrictive for spectra recorded at K (or L_1) edges because no magnetic dipole transition is allowed from a pure 1s (or 2s) atomic state while the energy separation between deep core levels makes 1s,2p hybridization quite improbable; (ii) the sum over all spin orbital projections of the core electrons results in a kind of internal optical sum rule so that the measured dichroism should systematically yield zero. We realized that natural circular dichroism could nevertheless be observed with gyrotropic single crystals due to the substantial contribution in the X-ray range of the Electric Dipole-Electric Quadrupole (E1.E2) interference terms first investigated by Barron at optical wavelengths (Barron, 1971). We will discuss first which crystal class is appropriate to detect XNCD and we will give a general formulation of the XNCD cross sections σ (E1.E2).

2. X-ray gyrotropy in non-centrosymmetrical crystals

Looking for the rotational invariants in O_3^+ of the rank-3 optical activity tensor γ_{ijk} , one is led to a decomposition including a scalar, a vector and a rank-2 pseudodeviator parts.

Table 1
Rotational invariants of γ_{ijk} for the 21 non-centrosymmetrical crystal classes.

Crystal classes	Point groups	Enantiomorphism		XNCD
		Pseudoscalar	Vector	Pseudodeviator
$\bar{4}3m\ \bar{6}m\ \bar{6}$	$T_d\ D_{3h}\ C_{3h}$	no	no	no
432 23	$O\ T$	yes	no	no
622 32 422	$D_6\ D_3\ D_4$	yes	no	yes
$6mm\ 3m\ 4mm$	$C_{6v}\ C_{3v}\ C_{4v}$	no	yes	no
6 3 4	$C_6\ C_3\ C_4$	yes	yes	yes
$\bar{4}2m$	D_{2d}	no	no	yes
$\bar{4}$	S_4	no	no	yes
$mm2$	C_{2v}	no	yes	yes
222	D_2	yes	no	yes
2	C_2	yes	yes	yes
m	C_s	no	yes	yes
1	C_1	yes	yes	yes

At optical wavelengths, both the scalar and the pseudodeviator parts contribute to detectable optical activity whereas, in the X-ray range, *only the pseudodeviator part* induces natural optical activity. Following Jerphagnon and Chemla (1976), we have summarized in table 1 which ones of the 21 non-centrosymmetrical crystal classes are compatible with XNCD. Note that there are only two crystal classes (432 ; 23) which have a non zero pseudoscalar part but no pseudodeviator term: such crystals are optically active in the visible but will not exhibit any XNCD. Thus, only 13 crystal classes will exhibit XNCD. Hereafter, we will consider two crystals which both exhibit a large non-linear susceptibility at optical wavelengths: α-$LiIO_3$ is uniaxial (class 3) and belongs to an enantiomorphous crystal class whereas $KTiOPO_4$ (KTP) belongs to the biaxial non-enantiomorphous crystal class *mm2*.

The X-ray absorption cross section associated with the E1.E2 interference term can be written :

$$\sigma_{NCD} = (4\pi)^2 \alpha_0 \hbar\omega\, k\, P_3 \sum_f \varepsilon_{\alpha\beta\lambda} \kappa_\lambda \kappa_\gamma \langle g|r_\alpha|f\rangle\langle f|r_\beta r_\gamma|g\rangle \times \delta(E_f - E_g - \hbar\omega)$$

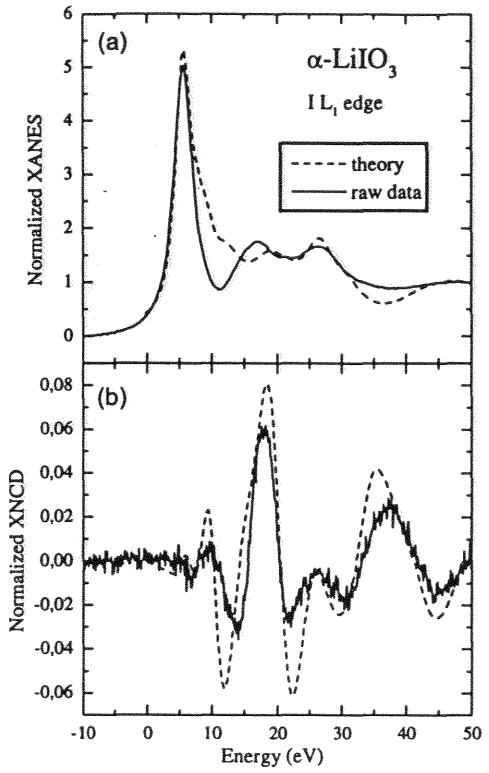

Figure 1
a) Comparison of the experimental and simulated L_1 edge XANES spectra of α-$LiIO_3$.
b) Comparison of the experimental and simulated L_1 edge XNCD spectra of α-$LiIO_3$.

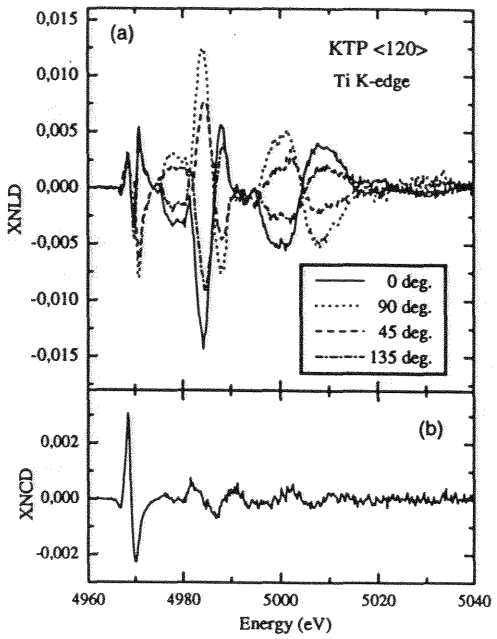

Figure 2
a) Linear dichroism contaminating the measured CD spectra of KTP <1,2,0>.
b) Extracted XNCD signal.

where α_0 is the fine structure constant, $\varepsilon_{\alpha\beta\lambda}$ is the Levi-Civita alternating tensor and the κ_λ are the components of the unit wavevector. For a powder or a solution, the orientational average: $<\sigma_{NCD}>=0$ and there is no XNCD. This is due to the fact that the Wigner rotation matrices respectively associated with E1 and E2 are orthogonal.

3. Results

The *Fluorescence Detected* X-ray absorption near edge spectrum (XANES) of α-$LiIO_3$ measured at the L_1 edge of iodine is reproduced in Fig.1a whereas the corresponding XNCD signal $[\sigma_L - \sigma_R]$ is displayed in Fig.1b. The largest XNCD signal is not found in the white line but for the next resonance peaking from 12 eV toward higher energy. The amplitude of the XNCD signal is rather large: up to 5.5 % after proper correction for the polarization transfer of the monochromator. Note that there is a fairly encouraging agreement between the experimental XANES or XNCD data and the spectra simulated using *ab initio* calculations performed within the framework of the Multiple Scattering theory. On the other hand, the XNCD spectra recorded at the L_2 and L_3 edges have the same sign and are looking very similar (Goulon *et al.*, 1998): this is in contrast with XMCD spectra which, most often, exhibit opposite sign. While the exchange and spin-orbit interactions are the driving terms in XMCD, this is not the case in XNCD and our data leave very little or no hope to detect any contribution of the scalar E1.M1 interference term.

As illustrated by Fig.2a, the case of biaxial crystals is far more complicate because the tiny effects of X-ray gyrotropy are swamped by large linear dichroism signals (XNLD) mostly due to the imperfect polarization transfer of Bragg monochromators (Goulon *et al.*, 1999). Since the contribution of gyrotropy is invariant in a rotation around the wavevector of the incident beam, the true XNCD signal can be extracted from the angular dependence of the spectra (Fig.2b). There is another complication: light propagating inside a biaxial crystal does not keep a constant polarization state. This can be taken into account using the differential equation (Goulon *et al.*, 1999):

$$\frac{\partial}{\partial z}|S\rangle = a\mathbf{M}|S\rangle \quad \text{with} \quad \mathbf{M} = \begin{bmatrix} t' & u' & -v' & w \\ u' & t' & -w' & v \\ -v' & w' & t' & u \\ w & -v & -u & t' \end{bmatrix}$$

where $|S\rangle$ is the Stokes vector for a penetration depth z whereas **M** is a 4x4 differential Müller matrix in which the coefficients u, u', v, v', w and w' can be related to the anisotropic components of the multipolar polarizability tensors at the absorbing site (Goulon *et al.*, 1999). It should be underlined that $\{w,w'\}$ are the only terms that contain any information on the time-even,

antisymmetric part of the microscopic gyrotropy tensor, whereas $\{u,u'\}$ and $\{v,v'\}$ describe the anisotropy of the electric dipole (E1.E1) and electric quadrupole (E2.E2) terms in non-magnetic crystals. One is led to the following expression of the *Fluorescence-Detected* XNCD spectra :

$$S_0^3 = -2P_3^0 S_0^0 \Gamma_{00}^F(\varphi)\{w\mu + [wt'+(u'v - v'u)]\mu^2 + \varepsilon(\mu^3)\}$$

where: $S_3^0 = P_3^0 S_0^0$ is the circular Stokes component of the incident X-ray beam, $\Gamma_{00}^F(\varphi)$ is the quantum yield of X-ray fluorescence emitted in a direction characterized by the wavevector $\mathbf{k}_F$ that can be deduced from the wavevector $\mathbf{k}$ of the incident beam by a rotation φ in the scattering plane. On the other hand, μ refers to the usual correction for reabsorption with : $1/\mu = -(t'+t'_F)$ where at' and at'_F stand for the isotropic absorption cross sections at the energies of the incident photons and fluorescence photons respectively. We wish to emphasize that there are certainly biaxial crystals for which $uv'-vu' \neq 0$ *i.e.* the anisotropy of the dipolar electric polarizability may contribute to a second order circular dichroism that is not related to gyrotropy. We found, however, that this additional dichroism, first predicted by Born and Huang (1954), should be small in *Fluorescence-Detected* XNCD experiments.

References

Alagna, L., Prosperi, T., Turchini, S., Goulon, J., Rogalev, A., Goulon-Ginet, C., Natoli, C.R., Stewart, B. & Peacock, R.D. (1998). *Phys. Rev. Lett.* **80**, 4799-4802.

Barron, L.D. (1971). *Molecular Physics* **21**, 241-246.

Born, M. & Huang, K. (1954). In *Dynamical Theory of Crystal Lattices*, Clarendon-Oxford, pp. 336-38.

Cotton, A. (1895). *C. R. Acad. Sci. (Paris)* **120**, 989-1044.

Elleaume, P. (1994). *J. Synchrotron Rad.* **1**, 19-26.

Goulon, J., Malgrange, C., Gilès, C., Neumann, C., Rogalev, A., Moguiline, E., De Bergevin F. & Vettier, C. (1996). *J. Synchrotron Rad.* **3**, 272-281.

Goulon, J., Goulon-Ginet, C., Rogalev, A., Gotte, V., Malgrange,C., Brouder, Ch. & Natoli, C.R. (1998). *J. Chem. Phys.* **108**, 6394-6403.

Goulon, J., Goulon-Ginet, C., Rogalev, A., Gotte, V., Brouder, Ch. & Malgrange, C. (1999). *Submitted to J. Opt. Soc. Am. B.*

Jerphagnon, J. & Chemla, D.S. (1976). *J. Chem. Phys.* **65**, 1522-1529.

Röntgen, W.C. (1895). Communication to the Würtzburg Physical & Medical Society.

Schütz, G., Wagner, W., Wilhelm, W., Kienle, P., Zeller, R., Frahm, R. & Materlik, G. (1987). *Phys. Rev. Lett.* **58**, 737-740.

(Received 10 August 1998; accepted 3 December 1998)

3.4 Publication

Eur. Phys. J. B **12**, 373–385 (1999)

THE EUROPEAN PHYSICAL JOURNAL B
EDP Sciences

X-ray dichroism in biaxial gyrotropic media: Differential absorption and fluorescence excitation spectra

J. Goulon[1,a], C. Goulon-Ginet[1,b], A. Rogalev[1], V. Gotte[1], C. Brouder[2], and C. Malgrange[2]

[1] European Synchrotron Radiation Facility, B.P. 220, 38043 Grenoble Cedex, France
[2] Laboratoire de Minéralogie Cristallographie[c], Universités Paris VI & VII, Tour 16, 4 place Jussieu, 75252 Paris Cedex 05, France

Received 3 March 1999

Abstract. The differential absorption and the differential change in the polarization state of an X-ray beam propagating inside a gyrotropic crystal are described using a 4×4 Müller matrix, the 16 elements of which are related to the anisotropic components of the multipolar polarizability tensors at the absorbing site. Analytical expressions are given up to third order for X-ray linear and circular dichroism, X-ray optical rotation and X-ray circular polarimetry in transmission. The same formalism is extended to discuss *Fluorescence detected dichroism* spectra with or without polarization analysis of the fluorescence. *Fluorescence detected dichroism* is strictly proportional to dichroism measured in the transmission geometry only for uniaxial crystals. In biaxial crystals, the tiny effects of X-ray gyrotropy are swamped by large linear dichroism signals due to the imperfect polarization transfer function of Bragg monochromators. Second order effects should also be taken into consideration. Our general formulation of linear and circular dichroism includes terms of *odd parity* with respect to the action of the time reversal operator: such terms cannot contribute to *natural* dichroism but can be activated by a magnetic field. The terms responsible for X-ray magnetic circular dichroism are well known but *non-reciprocal* X-ray gyrotropy effects are also predicted in magnetic crystals of appropriate symmetry.

PACS. 33.55.Ad Optical activity, optical rotation; circular dichroism – 41.50.+h X-ray beams and X-ray optics – 78.70.Dm X-ray absorption spectra

1 Introduction

We have produced recently the very first unambiguous experimental evidence [1] of **F**luorescence **d**etected **X**-ray **N**atural **C**ircular **D**ichroism (Fd-XNCD) in a uniaxial gyrotropic crystal of lithium iodate ($\alpha - LiIO_3$), *i.e.* a crystal known to exhibit a large specific rotativity together with a very strong non-linear susceptibility in the visible range. With such thick and heavily absorbing crystals, dichroism experiments can hardly be performed in transmission and it is much simpler to record differential X-ray fluorescence excitation spectra using an incident X-ray beam which is either right - or left - circularly polarized. Of course, in the case of a uniaxial crystal such as $\alpha - LiIO_3$, it is preferable to keep the direction of the incident X-ray beam colinear with the optical axis of the crystal. The same geometry was retained to detect Fd-XNCD in a pair of enantiomeric crystals of a stereogenic organometallic complex in which the absorbing metal center was sitting in a chiral ligand field [2]. In both experiments, the origin of XNCD was assigned to electric dipole - electric quadrupole ($E_1.E_2$) interference terms which contribute to the pseudodeviator part of the optical activity tensor. A theory of XNCD has been developed in the framework of multiple scattering (MS) and has been published in a previous issue of the same journal [3].

Unfortunately, one is running into serious complications as soon as the isotropy is lost in a plane perpendicular to the direction of propagation of the incident X-ray beam. It is well documented from classical optics that optical activity, linear dichroism and birefringence may occur all together in biaxial crystals and that the last two effects usually swamp completely those of gyrotropy: very sophisticated experimental techniques are then required to disentangle what is truly due to gyrotropy in a CD experiment. On the other hand, light propagating inside a biaxial crystal does not keep a constant polarization state [4]. Since this point was systematically neglected in all previous X-ray studies on oriented crystals [5,6], we found attractive to analyze carefully what is really measured when a polarized X-ray beam propagates inside a biaxial, gyrotropic crystal. Recall that a somewhat mysterious "*X-ray crystal optics effect*" was predicted to

[a] e-mail: goulon@esrf.fr
[b] *also:* Université de Grenoble-I, Faculté de Pharmacie, 38706 La Tronche, France
[c] CNRS URA9

occur in all biaxial crystals [7]: the origin of this second order effect will become fully transparent from our analysis. It has also the practical consequence that *fluorescence detected* dichroism spectra cannot be anymore rigorously equivalent to dichroism spectra recorded in a transmission geometry. Nevertheless, we like to point out that complementary information could be extracted from a detailed analysis of the polarization components of the X-ray fluorescence photons emitted in a given direction.

The organization of the paper is the following: in Section 2, the differential absorption and the differential change in the polarization state of the X-ray beam are described using a 4×4 Müller matrix, the 16 elements of which are related to the anisotropic components of the multipolar polarizability tensors at the absorbing site. We propose analytical expressions of the Stokes components at any point along the propagation axis of the X-ray beam inside the crystal. In Section 3, we derive general formula for X-ray Circular Dichroism (XCD), X-ray Linear Dichroism (XLD), X-ray Optical Rotation (XOR), X-ray Circular Polarimetry (XCP) for a transmission geometry. In Section 4, the same formalism is extended to calculate Fd-XCD spectra with (or without) polarization analysis. Finally, we discuss in Section 5 the consistency of all our results with respect to symmetry, rotational invariance and time reversality properties and we briefly review what are the implications regarding magnetic crystals.

2 Stokes vector in anisotropic absorbing media

Let us consider a quasi monochromatic X-ray beam propagating along the z direction through a crystal plate of finite thickness d and which is infinitely wide in the $\{x, y\}$ plane. As a first step, we wish to describe the differential absorption and the differential change of polarization induced by a thin layer of infinitesimal thickness $\mathrm{d}z$.

2.1 Differential Müller equation

We found most convenient to extend into the X-ray range the theory of refringent scattering which was elaborated by Buckingham *et al.* [8–10] for optical spectroscopy. Recall that an important implication of this theory is that all modes propagating inside the crystal should be parallel to the wave vector of the incident beam: this requirement is quite acceptable in the X-ray range where the real part of the refractive index $n = 1 - \delta$ is very close to unity $(\delta \leq 10^{-5})$ with the practical consequence that critical angles for X-ray reflection $\theta_c = \sqrt{2\delta}$ are in the range of a few mrad. Thus, for a transverse polarized wave propagating along the direction $\mathbf{n}$, the complex *scattering tensor* $a^*_{\alpha\beta}$ can reasonably be expanded as:

$$a^*_{\alpha\beta} = \alpha^*_{\alpha\beta} + \zeta^*_{\alpha\beta\gamma}\mathbf{n}_\gamma + \mathrm{Q}^*_{\alpha\gamma\gamma\beta}\left[\mathbf{n}^2_\gamma\right] + \ldots \quad (1)$$

where: $\alpha, \beta \neq \gamma$. In equation (1), $\alpha^*_{\alpha\beta}$ and $\mathrm{Q}^*_{\alpha\gamma\gamma\beta}$ are respectively the complex *electric dipole* polarizability tensor and the complex *electric quadrupole* polarizability tensor, the detailed expressions of which are given in Appendix A1. There have been ample experimental evidence produced in these recent years [5,11–15] that X-ray absorption spectroscopy is sensitive to the electric quadrupole $(E_2.E_2)$ cross sections: this implies that the last term of equation (1) should not be neglected in the X-ray range. It is precisely the aim of this paper to show that the complex *Gyrotropy* tensor $\zeta^*_{\alpha\beta\gamma}$, which is written in full detail in Appendix A1, can also play a significant role in X-ray absorption or excitation spectroscopies.

For biaxial crystals which are anisotropic in a plane perpendicular to the direction of propagation $(0, 0, 1)$, it is most appropriate to introduce the following complex tensors:

$$\begin{aligned} t^* &= t - \mathrm{i}t' \\ &= \left[\alpha^*_{xx} + \alpha^*_{yy}\right] + \left[\zeta^*_{xxz} + \zeta^*_{yyz}\right] + \left[Q^*_{xzzx} + Q^*_{yzzy}\right] \end{aligned} \quad (2)$$

$$\begin{aligned} u^* &= u - \mathrm{i}u' \\ &= \left[\alpha^*_{xx} - \alpha^*_{yy}\right] + \left[\zeta^*_{xxz} - \zeta^*_{yyz}\right] + \left[Q^*_{xzzx} - Q^*_{yzzy}\right] \end{aligned} \quad (3)$$

$$\begin{aligned} v^* &= v - \mathrm{i}v' \\ &= \left[\alpha^*_{xy} + \alpha^*_{yx}\right] + \left[\zeta^*_{xyz} + \zeta^*_{yxz}\right] + \left[Q^*_{xzzy} + Q^*_{yzzx}\right] \end{aligned} \quad (4)$$

$$\begin{aligned} w^* &= w - \mathrm{i}w' \\ &= \left[\alpha^*_{xy} - \alpha^*_{yx}\right] + \left[\zeta^*_{xyz} - \zeta^*_{yxz}\right] + \left[Q^*_{xzzy} - Q^*_{yzzx}\right] \end{aligned} \quad (5)$$

and by direct identification, one obtains:

$$\begin{aligned} t = &+ \left[\alpha_{xx}(f) + \alpha_{yy}(f)\right] + \left[\zeta_{xxz}(f) + \zeta_{yyz}(f)\right] \\ &+ \left[Q_{xzzx}(f) + Q_{yzzy}(f)\right] \end{aligned} \quad (6)$$

$$\begin{aligned} t' = &- \left[\alpha_{xx}(g) + \alpha_{yy}(g)\right] - \left[\zeta_{xxz}(g) + \zeta_{yyz}(g)\right] \\ &- \left[Q_{xzzx}(g) + Q_{yzzy}(g)\right] \end{aligned} \quad (7)$$

$$\begin{aligned} u = &+ \left[\alpha_{xx}(f) - \alpha_{yy}(f)\right] + \left[\zeta_{xxz}(f) - \zeta_{yyz}(f)\right] \\ &+ \left[Q_{xzzx}(f) - Q_{yzzy}(f)\right] \end{aligned} \quad (8)$$

$$\begin{aligned} u' = &- \left[\alpha_{xx}(g) - \alpha_{yy}(g)\right] - \left[\zeta_{xxz}(g) - \zeta_{yyz}(g)\right] \\ &- \left[Q_{xzzx}(g) - Q_{yzzy}(g)\right] \end{aligned} \quad (9)$$

$$v = +2\left[\alpha_{xy}(f) + \zeta_{xyz}(f) + Q_{xzzy}(f)\right] \quad (10)$$

$$v' = -2\left[\alpha_{xy}(g) + \zeta_{xyz}(g) + Q_{xzzy}(g)\right] \quad (11)$$

$$w = +2\left[\alpha'_{xy}(g) + \zeta'_{xyz}(g) + Q'_{xzzy}(g)\right] \quad (12)$$

$$w' = -2\left[\alpha'_{xy}(f) + \zeta'_{xyz}(f) + Q'_{xzzy}(f)\right]. \quad (13)$$

As detailed in Appendix A1, f and g refer to the *dispersive* and *absorptive* lineshapes respectively. It will appear in the following sections that, for biaxial crystals, the quantity $[uv' - vu']$ will play an important role. It could be easily checked on starting from the various definitions found in Appendix A1 that, due to the summation over all excited states, we have *a priori*: $[uv' - vu'] \neq 0$.

Barron [4] has clearly established that the variation of the Stokes vector $|\mathbf{S}(z)\rangle$ of any incident beam as a function of its penetration depth z is given by a linear differential

equation of the type:

$$\frac{\partial}{\partial z}\left|\mathbf{S}\left(z\right)\right\rangle = a\left[\mathbf{M}\right].\left|\mathbf{S}\left(z\right)\right\rangle \tag{14}$$

in which: $a = (1/2)\omega N\mu_0 c$, μ_0 being the permeability of free space and N the number density of absorbing centers [4]. The matrix [M] can be identified with a *differential* Müller matrix to be written:

$$[\mathbf{M}] = \begin{bmatrix} t' & u' & -v' & w \\ u' & t' & -w' & v \\ -v' & w' & t' & u \\ w & -v & -u & t' \end{bmatrix}. \tag{15}$$

This is the point at which we deviate from the earlier analysis by Barron [4] since he converted immediately the four Stokes parameters into physically relevant quantities, *i.e.* the beam intensity I, the azimuth ϑ, the ellipticity η and the degree of polarization P_d using classical definitions:

$$I = \frac{1}{2}\left[\frac{\varepsilon\varepsilon_0}{\mu\mu_0}\right]^{1/2} S_0 \tag{16}$$

$$\vartheta = \frac{1}{2}\arctan\left[\frac{S_2}{S_1}\right] \tag{17}$$

$$\eta = \frac{1}{2}\arctan\left[\frac{S_3}{\sqrt{S_1^2 + S_2^2}}\right] \tag{18}$$

$$P_d = \frac{\left[S_1^2 + S_2^2 + S_3^2\right]^{1/2}}{S_0}. \tag{19}$$

The problem with the latter transformation is that the set of coupled differential equations replacing equation (14) is not anymore linear and the integration becomes intractable except for uniaxial crystals. Our own strategy was to integrate first equation (14).

2.2 Integrated Müller matrix [Φ (z)]

2.2.1 Uniaxial gyrotropic crystals

For a uniaxial gyrotropic crystal aligned in such a way that the optical axis coincides with the direction of propagation of the X-ray beam, the differential Müller matrix (15) simplifies a lot since $u = u' = v = v' = 0$:

$$[\mathbf{M}] = \begin{bmatrix} t' & 0 & 0 & w \\ 0 & t' & -w' & 0 \\ 0 & w' & t' & 0 \\ w & 0 & 0 & t' \end{bmatrix}. \tag{20}$$

The secular equation has the following roots:

$$\lambda_1 = t' - w;\ \lambda_2 = t' + w;\ \lambda_3 = t' - \mathrm{i}w';\ \lambda_4 = t' + \mathrm{i}w'$$

and admits the following eigenvectors:

$$\rho_1 = \begin{bmatrix} 1/\sqrt{2} \\ 0 \\ 0 \\ -1/\sqrt{2} \end{bmatrix} \quad \rho_2 = \begin{bmatrix} 1/\sqrt{2} \\ 0 \\ 0 \\ +1/\sqrt{2} \end{bmatrix}$$

$$\rho_3 = \begin{bmatrix} 0 \\ 1/\sqrt{2} \\ \mathrm{i}/\sqrt{2} \\ 0 \end{bmatrix} \quad \rho_4 = \begin{bmatrix} 0 \\ \mathrm{i}/\sqrt{2} \\ 1/\sqrt{2} \\ 0 \end{bmatrix}. \tag{21}$$

A general solution to the differential equation (14) is:

$$\left|\mathbf{S}\left(z\right)\right\rangle = \left[\mathbf{R}_v\right]\left[\mathbf{D}_\lambda\right]\left[\mathbf{R}_v^{-1}\right]\left|\mathbf{S}^0\right\rangle \tag{22}$$

with the following definitions:

$$\left[\mathbf{R}_v\right] = \left[\rho_1\ \rho_2\ \rho_3\ \rho_4\right];\quad \left|\mathbf{S}^0\right\rangle = \left|\mathbf{S}\left(z=0\right)\right\rangle;$$
$$\left[\mathbf{D}_\lambda\right]_{ij} = \delta_{ij}\exp\left(a\lambda_i z\right)$$

δ_{ij} being the Kronecker symbol. Finally, the Stokes vector $\left|\mathbf{S}\left(z\right)\right\rangle = \left[\Phi\left(z\right)\right]\left|\mathbf{S}^0\right\rangle$ can be written:

$$\begin{bmatrix} S_0(z) \\ S_1(z) \\ S_2(z) \\ S_3(z) \end{bmatrix} = \exp\left(at'z\right) \times \begin{bmatrix} \cosh\left(awz\right) & 0 & 0 & \sinh\left(awz\right) \\ 0 & \cos\left(aw'z\right) & -\sin\left(aw'z\right) & 0 \\ 0 & \sin\left(aw'z\right) & \cos\left(aw'z\right) & 0 \\ \sinh\left(awz\right) & 0 & 0 & \cosh\left(awz\right) \end{bmatrix} \begin{bmatrix} S_0^0 \\ S_1^0 \\ S_2^0 \\ S_3^0 \end{bmatrix}. \tag{23}$$

2.2.2 Biaxial gyrotropic crystals

The first step is to solve a biquadratic secular equation of matrix [M]:

$$\left[\lambda - t'\right]^4 + P\left[\lambda - t'\right]^2 - Q^2 = 0 \tag{24}$$

with:

$$P = \left[u^2 - u'^2\right] + \left[v^2 - v'^2\right] - \left[w^2 - w'^2\right]$$
$$Q = uu' + vv' - ww'.$$

The eigenvalues of equation (24) can again be written:

$$\lambda_1 = t' - B';\ \lambda_2 = t' + B';\ \lambda_3 = t' - \mathrm{i}A';\ \lambda_4 = t' + \mathrm{i}A'$$

but analytical expressions for A' and B' are getting rather cumbersome. A solution to the differential equation (14) can still be given by equation (22) provided that one is able to develop analytically the eigenvector matrix $\left[\mathbf{R}_v\right]$ and its inverse $\left[\mathbf{R}_v^{-1}\right]$. Note that the final result can still be written:

$$\left|\mathbf{S}\left(z\right)\right\rangle = \left[\Phi\left(z\right)\right]\left|\mathbf{S}^0\right\rangle \tag{25}$$

with matrix elements $\varphi_{ij}(z)$ that have all the same functional form:

$$\varphi_{ij}(z) = \exp\left(at'z\right) \times \left\{ \begin{array}{c} \left[\frac{1}{2}\delta_{ij} + \beta''_{ij}\right]\cos\left(aA'z\right) - \left[\gamma'_{ij} + \gamma''_{ij}\right]\sin\left(aA'z\right) \\ +\left[\frac{1}{2}\delta_{ij} - \beta''_{ij}\right]\cosh\left(aB'z\right) + \left[\gamma'_{ij} - \gamma''_{ij}\right]\sinh\left(aB'z\right) \end{array} \right\}. \quad (26)$$

For practical applications, we need analytical expressions of the individual functions $\varphi_{ij}(z)$. As detailed in Appendix A2, one can save much algebra by defining complex matrices: $[\mathrm{M}^{\pm}] = \left[\mathrm{M}'\right] \pm \mathrm{i}\left[\mathrm{M}''\right]$ where $\left[\mathrm{M}'\right]$ and $\left[\mathrm{M}''\right]$ are traceless matrices. Matrix $[\Phi]$ can then be easily expanded as a series of successive powers in z.

3 X-ray dichroism and polarimetry in transmission

3.1 Circular dichroism

3.1.1 Formulation

Circular dichroism is the difference in the absorption cross sections measured during two consecutive experiments carried out with an incident light that is respectively left- and right-handed circularly polarized. For each experiment, the polarization state is characterized by the Stokes-Poincaré's ratios defined according to the following convention [4]:

$$P_1^0 = \frac{S_1^0}{S_0^0} = \frac{I_0^{0°} - I_0^{90°}}{I_0^{0°} + I_0^{90°}}; \quad P_2^0 = \frac{S_2^0}{S_0^0} = \frac{I_0^{45°} - I_0^{135°}}{I_0^{45°} + I_0^{135°}}$$

$$P_3^0 = \frac{S_3^0}{S_0^0} = \frac{I_0^R - I_0^L}{I_0^R + I_0^L}.$$

Of course, one would like to have two monochromatic beams of strictly opposite polarization state, *i.e.* I_0 $\left\{P_1^0 = P_2^0 = 0;\ P_3^0 = \pm 1\right\}$ and therefore:

$$\left[\sigma^{\mathrm{L}} - \sigma^{\mathrm{R}}\right] = \ln\left(\frac{\left[I^{\mathrm{R}}/I_0^{\mathrm{R}}\right]}{\left[I^{\mathrm{L}}/I_0^{\mathrm{L}}\right]}\right) = \ln\left(\frac{\phi_{00}(z) + \phi_{03}(z)}{\phi_{00}(z) - \phi_{03}(z)}\right)$$

$$= \ln\left(1 + \frac{2\xi_{03}(z)}{1 - \xi_{03}(z)}\right) \simeq 2\xi_{03} \quad (27)$$

where: $\xi_{0j}(z) = \phi_{0j}(z)/\phi_{00}(z)$. Unfortunately, such "*ideal conditions*" are never met in the X-ray range: even with a nearly perfect helical undulator source [16], one has still to worry about the polarization transfer function of the two-crystal monochromator which is getting very poor when the Bragg angle approaches 45° with the practical consequence that $P_1^0 \neq 0$ and is rapidly increasing [17]. Furthermore, flipping the helicity of the photons emitted by the source does not imply that the circular polarization rate of the monochromatic X-ray beam is reversed since what is monitored downstream with respect to a two crystal monochromator is a complicated change of polarization state [1]:

$$\left\{P_1^{\mathrm{h}}, P_2^{\mathrm{h}}, +P_3^{\mathrm{h}}\right\}_{\mathrm{Source}} \Longleftrightarrow \left\{P_1^{\mathrm{h}}, P_2^{\mathrm{h}}, -P_3^{\mathrm{h}}\right\}_{\mathrm{Source}}$$

$$\Downarrow \ [\mathrm{Monochromator}]$$

$$\left\{P_1^0, P_2^0, +P_3^0\right\} \Longleftrightarrow \left\{P_1^0, P_2^0(1-\varepsilon_2), -P_3^0(1-\varepsilon_3)\right\}$$

where $\varepsilon_{2,3}$ become significant as soon as $P_2^0 \neq 0$ (which is most often the case...). Neglecting again the non linear terms with respect to ξ_{03}, the *apparent* circular dichroism has, in practice, to be reformulated as:

$$\left[\sigma^{\mathrm{L}} - \sigma^{\mathrm{R}}\right] \approx \frac{2\xi_{03}P_3^0(1-\varepsilon_3)}{1 + \xi_{01}P_1^0 + \xi_{02}P_2^0} + \frac{\xi_{02}\varepsilon_2 P_2^0}{1 + \xi_{01}P_1^0 + \xi_{02}P_2^0}. \quad (28)$$

Thus, in biaxial crystals, the *measured* circular dichroism is most often contaminated with unwanted *linear* dichroism due to the second term in equation (28). The latter is usually large enough to swamp completely the tiny contribution of gyrotropy. Note that the denominator may also induce a second order correction if the experiments are carried out with elliptically polarized photons.

3.1.2 Uniaxial crystals with the beam propagating along the optical axis

Since: $\phi_{01}(z) = \phi_{02}(z) = 0$, we have $\xi_{01}(z) = \xi_{02}(z) = 0$. As a consequence, *there cannot be any contamination by linear dichroism.* Furthermore, one directly obtains from (23): $\xi_{03}(z) = \tanh(awz)$ and, in full agreement with reference [4], the XCD signal is given by:

$$\left[\sigma^{\mathrm{L}} - \sigma^{\mathrm{R}}\right] \approx 2(awd)P_3^0(1 - \varepsilon_3/2) \quad (29)$$

where d is the crystal thickness.

3.1.3 Biaxial crystals

Let us first restrict our analysis to the simplest case of experiments performed under ideal conditions ($P_1^0 = P_2^0 = 0$; $P_3^0 = \pm 1$). Direct substitution of equation (27) with the series expansion detailed in Appendix A2 yields up to the third order:

$$\left[\sigma^{\mathrm{L}} - \sigma^{\mathrm{R}}\right] \approx \left\{ \begin{array}{c} 2(awd) - (ad)^2\left[uv' - vu'\right] \\ -\frac{1}{3}(ad)^3\left[w\left(u^2 + v^2 + 2u'^2 + 2v'^2\right) + w'\left(uu' + vv'\right)\right] \end{array} \right\}. \quad (30)$$

The first order term of equation (30) is the same as for uniaxial crystals and characterizes the crystal gyrotropy. However, even under ideal conditions, *i.e. in the absence of unwanted linear dichroism*, there is a second order term

$$\Delta\vartheta(z) \approx \left\{ \begin{array}{c} -\frac{1}{2}ad(v'-w') + \frac{1}{4}(ad)^2[u'(v'-w')-u(v-w)] \\ +\frac{1}{12}(ad)^3\left[\begin{array}{c} v'(u^2-u'^2-v^2+v'^2-w^2+w'^2)+2v(uu'-vv'-ww') \\ -w'(u^2-u'^2-2v^2+2v'^2)-2w(uu'-2vv') \end{array}\right] \end{array} \right\}. \quad (36)$$

proportional to $[uv' - vu']$ which can generate XCD *even in the case of non-gyrotropic crystals:* we may identify this term with the "*crystal optics effect*" predicted by Machavariani [7] using a different formalism. It is also noteworthy that the "*absorptive*" (w) and "*dispersive*" (w') parts of the gyrotropy tensor start to mix up in the third order term. What is however most striking in equation (30) is the decomposition into terms of *odd parity* related to gyrotropy, and terms of *even parity* which are independent of gyrotropy. One could envisage to separate experimentally the two contributions with a piezoelectric, gyrotropic crystal: let one assume that the crystal is electrically excited at some modulation frequency ω_M; then the linear and quadratic terms could be discriminated by analyzing the dichroism response either at ω_M or $2\omega_M$. This is unfortunately unrealistic in the X-ray range.

3.2 Linear Dichroism in biaxial crystals

As already emphasized in the previous section, linear dichroism is expected to contaminate all XCD experiments performed on biaxial crystals as soon as the Poincaré component P_2 of the source is not strictly equal to zero. We want to point out here that standard XLD spectra also contain hidden information on gyrotropy. Let us first transpose equation (27) for linear dichroism:

$$\left[\sigma^{90°} - \sigma^{0°}\right] = \ln\left(\frac{\varphi_{00}(z)+\phi_{01}(z)}{\varphi_{00}(z)-\phi_{01}(z)}\right) = \ln\left(1+\frac{2\xi_{01}(z)}{1-\xi_{01}(z)}\right) \quad (31)$$

$$\left[\sigma^{135°} - \sigma^{45°}\right] = \ln\left(\frac{\varphi_{00}(z)+\phi_{02}(z)}{\varphi_{00}(z)-\phi_{02}(z)}\right) = \ln\left(1+\frac{2\xi_{02}(z)}{1-\xi_{02}(z)}\right) \quad (32)$$

where: $|\xi_{0j}| \leq 1$. To the same order of approximation as in the previous section, one obtains:

$$\left[\sigma^{90°} - \sigma^{0°}\right] \approx \left\{ \begin{array}{c} 2au'd-(ad)^2[vw+v'w'] \\ -\frac{1}{3}(ad)^3[u'(v^2+w'^2+2v'^2+2w^2)-u(vv'+ww')] \end{array} \right\} \quad (33)$$

$$\left[\sigma^{135°} - \sigma^{45°}\right] \approx \left\{ \begin{array}{c} -2av'd-(ad)^2[uw+u'w'] \\ +\frac{1}{3}(ad)^3[v'(u^2+w'^2+2u'^2+2w^2)-v(uu'+ww')] \end{array} \right\}. \quad (34)$$

It would be erroneous to believe that Linear Dichroism is totally insensitive to crystal gyrotropy: the second order terms in equations (33, 34) are involving both w and w'. It is quite noteworthy that, exactly as in the case of XCD, the second order term involves the product of a dispersive lineshape (f) by an absorptive lineshape (g). As regards the third order term, let us observe that the terms in $\{w^2, w'^2, ww'\}$ are small in comparison with the terms of same order referring to the anisotropy of dipolar polarizability $\{u^2, u'^2, uu'\}$ or $\{v^2, v'^2, vv'\}$ so that the former can be neglected. Anyhow, no reliable information on gyrotropy can be extracted from XLD experiments unless the anisotropy in the first order polarizability is known with a very high accuracy.

3.3 Rotatory power

Optical rotation is a very weak effect in the X-ray range [18,19], at least for uniaxial crystals. It is therefore desirable to carry out such a delicate experiment with an X-ray beam featuring a "*pure*" polarization state such as $\{P_1^0 = 1;\ P_2^0 = P_3^0 = 0\}$. Typically, in the experiment reported by Siddons *et al.* [20], the polarization state of the incident beam was: $P_1^0 = 1 - \varepsilon$ with ε of the order of 10^{-8}. It results from equation (17) that the optical rotation $\Delta\vartheta(z)$ is given by:

$$\Delta\vartheta(z) = \frac{1}{2}\arctan\left(\frac{\phi_{20}(z)+\phi_{21}(z)P_1^0}{\phi_{10}(z)+\phi_{11}(z)P_1^0}\right). \quad (35)$$

To the same level of approximation as before, one obtains:

see equation (36) *above*

The latter expression simplifies a lot in the case a uniaxial crystal with the beam propagating along the direction of the optical axis because $u = u' = v = v' = 0$:

$$\Delta\vartheta(z) \approx \frac{1}{2}aw'd. \quad (37)$$

The latter result is perfectly consistent with equation (23). Note that it is also fully consistent with a well known result of classical optics in the visible range: linear dichroism will induce a significant optical rotation in non-gyrotropic

crystals ($w = w' = 0$) as soon as the absorption is not isotropic in the plane perpendicular to the direction of propagation of the incident beam. In view of the complexity of (36), it appears practically hopeless to sort out the contribution of gyrotropy in the case of biaxial crystals and CD experiments look preferable.

3.4 Circular polarimetry

It may be tempting to analyze directly the polarization state of a transmitted beam in order to access to the individual components $S_j(d)$. With the recent availability of X-ray quarter-wave plates [21–25], circularly polarized X-ray photons can be converted with a good efficiency into linearly polarized ones with a polarization vector oriented in any desired direction: the latter component can then be selected with a linear polarimeter exploiting either coherent (*i.e.* Bragg diffraction at 45°) or incoherent scattering at 90°. As discussed elsewhere, circular polarimetry can be performed either upstream or downstream with respect to the monochromator: in the former case, one may get rid of the poor polarization transfer of the monochromator and fully exploit the high circular polarization rate of helical undulator sources [25]. As far as X-ray gyrotropy is concerned, the quantity of interest turns out to be the *inverse* of the circular asymmetry ratio denoted hereafter $\rho_3(z)$:

$$\frac{1}{\rho_3(z)} = \frac{S_3^{\mathrm{R}}(z) + S_3^{\mathrm{L}}(z)}{S_3^{\mathrm{R}}(z) - S_3^{\mathrm{L}}(z)} = \frac{\varphi_{30}(z) + \varphi_{31}(z) P_1^0 + \varphi_{32}(z) P_2^0 (1-\varepsilon_2)}{\varphi_{33}(z) P_3^0 (1-\varepsilon_3) + \varphi_{32}(z) \varepsilon_2 P_2^0} \quad (38)$$

or to some degree of approximation:

$$\frac{1}{\rho_3(z)} \approx \frac{1}{P_3^0}\xi_{30}\left(1+\varepsilon_3-\varepsilon_2 P_2^0 \xi_{32}\right) + \xi_{31}\frac{P_1^0}{P_3^0} + \xi_{32}\frac{P_2^0}{P_3^0}(1-\varepsilon_2). \quad (39)$$

Thus, under ideal conditions $\left(P_1^0 = P_2^0 = 0;\ P_3^0 = 1\right)$, one obtains:

$$\frac{1}{\rho_3(z)} \approx \left\{ \begin{array}{c} a w d - \frac{1}{2}(ad)^2[u'v - uv'] \\ + \frac{1}{6}(ad)^3[w(2u^2+2v^2+u'^2+v'^2) - w'(uu'+vv') - 2w^3] \end{array} \right\}. \quad (40)$$

Up to the second order, the information content of circular polarimetry is then, within a factor 1/2, strictly equivalent to the information currently available from XCD experiments and there is no valuable additional information to be extracted from the third order term.

4 Fluorescence detected dichroism

The backscattering geometry of the experiment reported in [1] is illustrated with Figure 1. The wavevector of the incident X-ray beam $\mathbf{k}$ $[0,0,1]$ is defined with respect to the laboratory coordinate axes $\{x,y,z\}^{(1)}$ whereas the wavevector of the emitted X-ray fluorescence photons $\mathbf{k_F}$ $[0,0,1]$ is defined with respect to another coordinate system $\{x',y',z'\}^{(2)}$. The two coordinate systems transform into one another by a rotation $R(\phi)$ around the normal to the scattering plane $\{\mathbf{k},\mathbf{k_F}\}$. This is the appropriate point at which to recall that a tensor component $T_{\alpha\beta\gamma}$ will transform in rotation R as:

$$T_{\lambda\mu\nu}(x',y',z') = L_{\lambda\alpha}(R) L_{\mu\beta}(R) L_{\nu\gamma}(R) T_{\alpha\beta\gamma}(x,y,z) \quad (41)$$

where the factors $L_{\mu\beta}(R)$ are the direction cosines which specify the orientation of the new set of axes with respect to the old ones. We will use extensively equation (41) below.

4.1 Formulation of the fluorescence signal

We will restrict our analysis to the case of a spontaneous X-ray fluorescence emission associated with a radiative decay of the core hole created by the primary absorption of a polarized incident X-ray photon. Anisotropic Resonant Inelastic X-ray Scattering (RIXS) processes would require a specific theoretical framework and will be considered elsewhere. Thus, the fluorescence emitted by an ultrathin slice of crystal of thickness Δz and corresponding to a penetration depth z will be characterized by a Stokes vector $|\mathbf{S_F}\rangle$ satisfying the differential equation:

$$\frac{\partial}{\partial z}|\mathbf{S_F}(z'=0)\rangle = \left[\Gamma^{\mathrm{F}}\right]\frac{\partial}{\partial z}\left|\mathbf{S}^{(1)}(z)\right\rangle = a\left[\Gamma^{\mathrm{F}}\right]\left[\mathbf{M}^{(1)}\right]\left|\mathbf{S}^{(1)}(z)\right\rangle \quad (42)$$

where, the superscripts $^{(1)}$ or $^{(2)}$ refer to the coordinate systems $\{x,y,z\}^{(1)}$ or $\{x',y',z'\}^{(2)}$. Here $\left[\Gamma^{\mathrm{F}}\right]$ is a diagonal 4×4 matrix describing the quantum yield of polarized fluorescence emission and will be defined in more detail in the next section and in Appendix A3. We need to describe the reabsorption of the *fluorescence photons* inside the crystal: this requires us to introduce *another* Müller matrix $[\Phi^{(2)}]$ so that:

$$\frac{\partial}{\partial z}|\mathbf{S_F}(z')\rangle = \frac{1}{L_{z'z}}\left[\Phi^{(2)}(z')\right]\frac{\partial}{\partial z}|\mathbf{S_F}(z'=0)\rangle = \frac{a}{L_{z'z}}\left[\Phi^{(2)}(z')\right]\left[\Gamma^{\mathrm{F}}\right]\left[\mathbf{M}^{(1)}\right]\left|\mathbf{S}^{(1)}(z)\right\rangle \quad (43)$$

or:

$$\frac{\partial}{\partial z}|S_{\mathrm{F}j}(z')\rangle = \frac{a}{L_{z'z}}\sum_{i=0}^{3}\phi_{j\beta}^{(2)}(z')\,\Gamma_{\beta\beta}^{\mathrm{F}} m_{\beta\alpha}^{(1)}\phi_{\alpha i}^{(1)}(z)\left[P_i^0 S_0^0\right]^{(1)}. \quad (44)$$

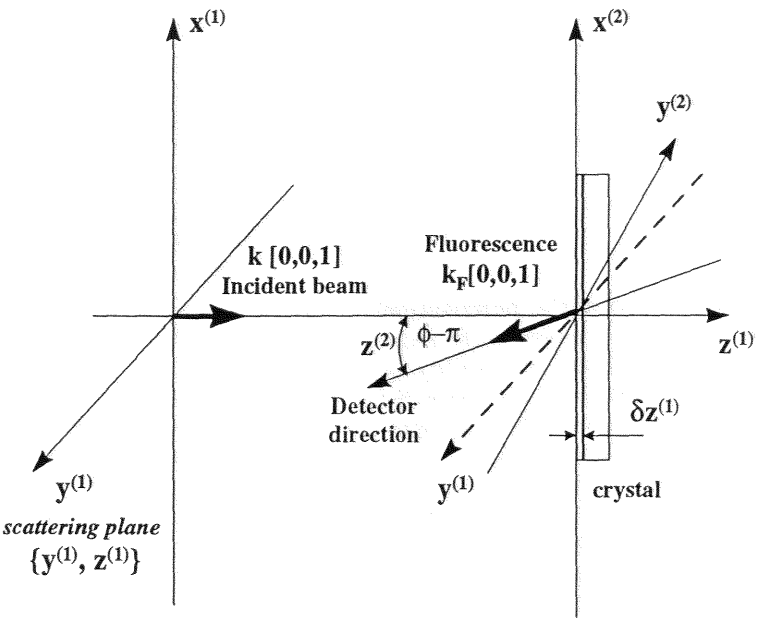

Fig. 1. Geometry for Fluorescence detected X-ray Natural Circular Dichroism (Fd-XNCD) experiments. Note that the optical axis of the crystal is colinear with the wavevector k [0, 0, 1] of the incident beam defined with respect to the laboratory coordinate system $\{x, y, z\}^{(1)}$, whereas the wavevector $\mathbf{k}_F$ [0, 0, 1] relative to the X-ray fluorescence photons is defined with respect to the secondary coordinate system$\{x, y, z\}^{(2)}$.

As long as the polarization of the fluorescence emission is not analyzed, only the $j = 0$ component is retained and the fluorescence signal is given by:

$$I_F = \frac{a\left[S_0^0\right]^{(1)}}{L_{z'z}} \int_0^d \mathrm{d}z \sum_{i=0}^{3} \phi_{0\beta}^{(2)}(z)\, \Gamma_{\beta\beta}^F m_{\beta\alpha}^{(1)} \phi_{\alpha i}^{(1)}(z) \left[P_i^0\right]^{(1)}. \tag{45}$$

The main difficulty is thus to calculate 16 integrals of the type:

$$\Psi_{\alpha\beta\gamma} = \int_0^d \mathrm{d}z \left[\phi_{0\gamma}^{(2)}(z)\, \phi_{\beta\alpha}^{(1)}(z)\right]. \tag{46}$$

Fortunately, in most practical cases, the *reabsorption process can be taken as isotropic* and matrix $[\mathbf{M}^{(2)}]$ reduces to the scalar term $t'^{(2)}$ whereas $\phi_{0\gamma}^{(2)} = \delta_{0\gamma} \exp\left(azt'^{(2)}\right)$: this is because a strongly anisotropic absorption can hardly be observed outside the typical energy range of X-ray Absorption Near Edge (XANES) spectra whereas the energy E_F of all *fluorescence* emission lines is systematically lower than the energy of the corresponding excitation edge. One might certainly find examples where a fluorescence line is interfering with *another* absorption edge at lower energy but such a complicated situation will not be considered here. Let us also keep in mind that isotropic reabsorption may not hold true in the case of RIXS.

4.2 Polarization of the emitted fluorescence photons

The emitted fluorescence photons may have a significant degree of polarization: this implies that $[\Gamma^F]$ is not a scalar but is a tensor property of the crystal. As shown by equation (45), we are interested here only in the four diagonal matrix elements: Γ_{jj}^F which are proportional to the four components of a *coherence vector* as defined by Born and Wolf [26,27]:

$$\Gamma_{00}^F = \gamma_0 \left\langle E_{x'}^F E_{x'}^{F*} + E_{y'}^F E_{y'}^{F*} \right\rangle = \gamma_0 \beta_F \left\langle -t'_F(g) \right\rangle^{(1)} \tag{47}$$

$$\Gamma_{11}^F = \gamma_1 \left\langle E_{x'}^F E_{x'}^{F*} - E_{y'}^F E_{y'}^{F*} \right\rangle \Gamma_{11}^F = \gamma_1 \beta_F \left\langle -u'_F(g) \right\rangle^{(1)} \tag{48}$$

$$\Gamma_{22}^F = \gamma_2 \left\langle -\left[E_{x'}^F E_{y'}^{F*} + E_{y'}^F E_{x'}^{F*}\right] \right\rangle \Gamma_{22}^F = -\gamma_2 \beta_F \left\langle -v'_F(g) \right\rangle^{(1)} \tag{49}$$

$$\Gamma_{33}^F = \gamma_3 \left\langle -\mathrm{i}\left[E_{x'}^F E_{y'}^{F*} - E_{y'}^F E_{x'}^{F*}\right] \right\rangle \Gamma_{33}^F = \gamma_3 \beta_F \left\langle w_F(g) \right\rangle^{(1)} \tag{50}$$

where the brackets remind us that a configuration average has to be taken over all emitting sites. Equivalently, the matrix elements Γ_{jj}^F can be expressed in terms of the absorptive components $t'_F(g)$, $u'_F(g)$, $v'_F(g)$ and $w_F(g)$ of the complex tensors $\{t_F^*, u_F^*, v_F^*, w_F^*,\}$ characterizing now the emission process itself. Detailed expressions of $t'_F(g)$,

Table 1. Extended Stokes components in emission geometry without polarization analysis

Fluorescence detected XCD

$$\mathbb{S}_0^3 \approx -\frac{2I_0 P_3^0 \Gamma_{00}^{\mathrm{F}}}{\cos\phi} \left\{ \begin{array}{c} w\mu + \left[t'w + u'v - uv'\right]\mu^2 \\ + \left[t'\left(u'v - uv'\right) + w\left(u'^2 - u^2 + v'^2 - v^2 + w^2\right) - w'\left(uu' + vv'\right)\right]\mu^3 \end{array} \right\} \tag{57}$$

Fluorescence detected XLD

$$\mathbb{S}_0^1 \approx -\frac{2I_0 P_1^0 \Gamma_{00}^{\mathrm{F}}}{\cos\phi} \left\{ \begin{array}{c} u'\mu + \left[t'u' - \left(vw + v'w'\right)\right]\mu^2 \\ - \left[t'\left(vw + v'w'\right) - u'\left(v'^2 - v^2 + u'^2 + w^2 - w'^2\right) - u\left(vv' - ww'\right)\right]\mu^3 \end{array} \right\} \tag{58}$$

$$\mathbb{S}_0^2 \approx -\frac{2I_0 P_2^0 \Gamma_{00}^{\mathrm{F}}}{\cos\phi} \left\{ \begin{array}{c} -v'\mu - \left[t'v' + uw + u'w'\right]\mu^2 \\ - \left[t'\left(uw + u'w'\right) + v'\left(u'^2 - u^2 + v'^2 + w^2 - w'^2\right) + v\left(uu' - ww'\right)\right]\mu^3 \end{array} \right\}. \tag{59}$$

$u'_{\mathrm{F}}(g)$, $v'_{\mathrm{F}}(g)$ and $w_{\mathrm{F}}(g)$ are given in Appendix A3. Note that equation (50) would predict the existence of *X-ray gyrotropic emission* in addition to *X-ray gyrotropic absorption*. Such a gyrotropic emission is still unknown in the X-ray range: it would be the X-ray analog of the so-called *Circularly Polarized Luminescence* (CPL) which is a well established chiroptical spectroscopy in the visible range [28–30]. Unfortunately, the only terms which might contribute to a gyrotropic emission in the X-ray range are again electric dipole-electric quadrupole interference terms $(E_1.E_2)$ which vanish in powder or solutions. Moreover, since the $(E_1.E_2)$ interference terms probe the overlap in energy of states of different parity [3], there is very little or no hope to detect any gyrotropic emission for fluorescence lines involving only transitions between deep atomic core levels (*e.g.* the K_α lines). Gyrotropic emission could then be detectable only in very few cases: (*i*) for fluorescence lines associated with transitions in which a deep core hole is filled by valence electrons; (*ii*) for RIXS processes which fall out of the scope of the present paper. Let us recall that a quite significant degree of circular polarization has already been measured in *X-ray Excited Optical Luminescence* (XEOL) spectra [31].

4.3 Fluorescence detected dichroism spectra

In this section, we will concentrate first on fluorescence detected dichroism spectra recorded *without polarization analysis* because such experiments have already been performed. For the sake of clarity, it is most convenient to define "*extended*" Stokes components $\mathbb{S}_{\mathrm{F}(j)}^{\mathrm{I}(i)}$ with two indices: the lower index would characterize the emitted fluorescence beam and the upper one would refer to the incident beam. As long as we do not analyze the polarization states of the emitted photons, we are concerned only with the three components:

$$\mathbb{S}_0^1 = S_{\mathrm{F}(0)}^{\mathrm{I}(90°)} - S_{\mathrm{F}(0)}^{\mathrm{I}(0°)} \tag{51}$$

$$\mathbb{S}_0^2 = S_{\mathrm{F}(0)}^{\mathrm{I}(135°)} - S_{\mathrm{F}(0)}^{\mathrm{I}(45°)} \tag{52}$$

$$\mathbb{S}_0^3 = S_{\mathrm{F}(0)}^{\mathrm{I(L)}} - S_{\mathrm{F}(0)}^{\mathrm{I(R)}}. \tag{53}$$

For infinitely thick samples, one would show that:

$$\mathbb{S}_0^i = -\frac{2aI_0 P_i^0 \Gamma_{00}^{\mathrm{F}}}{L_{z'z}} \int_0^\infty \mathrm{d}z \exp\left(-az/\mu\right) \left[\mathrm{M}\Phi\right]_{0i} \tag{54}$$

where we have introduced the simplifying notation: $1/\mu = -\left[t'^{(1)} + t'^{(2)}\right]$. Combining the following identities:

$$\int_0^\infty \mathrm{d}z \exp\left(-az/\mu\right)\cos\left(az\lambda\right) = \frac{\mu}{a\left(1+\lambda^2\mu^2\right)} \tag{55}$$

$$\int_0^\infty \mathrm{d}z \exp\left(-az/\mu\right)\sin\left(az\lambda\right) = \frac{\lambda\mu^2}{a\left(1+\lambda^2\mu^2\right)} \tag{56}$$

with the series expansion of $[\Phi(z)]$ developed in Appendix A2, one is led to the final results listed in Table 1 (Eqs. (57-59)).

By comparing equation (57) with equation (30), it will immediately appear that Fd-CD is strictly proportional to transmission circular dichroism in the case of uniaxial crystals when the incident beam propagates along the direction of the optical axis. In the case of biaxial crystals, this proportionality still holds true for the first order term with respect to μ. Regarding the second and third order terms, it appears again that non-gyrotropic crystals with $w = w' = 0$ should exhibit non-zero Fd-XCD spectra if $(u'v - v'u) \neq 0$: this was precisely the condition discussed

earlier in Section 3 to observe the so-called "*crystal optics effect*" of Machavariani [7]. It is however quite remarkable that in the case of gyrotropic crystals, the leading second order term of $\mathbb{S}_0^3$ should be $wt'\mu^2$ (which is proportional to the isotropic absorption t') rather than $(u'v - v'u)\mu^2$. This additional term $wt'\mu^2$ does not exist in transmission CD experiments but it makes the analyses far more comfortable if one is interested in sorting out clean gyrotropy spectra: in other terms, Fd-XCD offers the significant advantage over XCD to depress the relative contribution of the unwanted "crystal optics effects". Of course, one could draw symmetrical conclusions if one compares the analytical expressions derived for Fd-XLD and transmission linear dichroism experiments.

The previous discussion concerned "*ideal experimental conditions*", *e.g.* $P_1^0 = P_2^0 = 0; P_3^0 = \pm 1$. Indeed, Fd-XCD spectra of biaxial crystals are, under real experimental conditions, also systematically contaminated by unwanted linear dichroism signatures:

$$\left[\mathbb{S}_0^3\right]_{\text{apparent}} = (1 - \varepsilon_3/2)\,\mathbb{S}_0^3 + \varepsilon_2 \mathbb{S}_0^2. \tag{60}$$

4.4 Polarization analysis of emission spectra

We may investigate next whether new information could be extracted from a careful analysis of the polarization state of the fluorescence photons. The following integrals have now to be calculated:

$$\mathbb{S}_j^i = -\frac{2aI_0 P_i^0 \Gamma_{jj}^{\mathrm{F}}}{L_{z'z}} \int_0^\infty \mathrm{d}z \exp\left(-az/\mu\right) [\mathrm{M}\Phi]_{ji} \tag{61}$$

and, to the same level of approximation as before, one would derive the following results:

4.4.1 Incident X-ray beam circularly polarized

$$\mathbb{S}_1^3 \approx -\frac{2I_0 P_3^0 \Gamma_{11}^{\mathrm{F}}}{\cos\phi} \left\{v\mu + \left[t'v + u'w - uw'\right]\mu^2\right\} \tag{62}$$

$$\mathbb{S}_2^3 \approx -\frac{2I_0 P_3^0 \Gamma_{22}^{\mathrm{F}}}{\cos\phi} \left\{u\mu + \left[t'u - v'w + vw'\right]\mu^2\right\} \tag{63}$$

$$\mathbb{S}_3^3 \approx -\frac{2I_0 P_3^0 \Gamma_{33}^{\mathrm{F}}}{\cos\phi} \left\{t'\mu - \left[u^2 + v^2 - w^2\right]\mu^2\right\}. \tag{64}$$

4.4.2 Incident X-ray beam linearly polarized (90°–0°)

$$\mathbb{S}_1^1 \approx -\frac{2I_0 P_1^0 \Gamma_{11}^{\mathrm{F}}}{\cos\phi} \left\{t'\mu + \left[u'^2 - v^2 - w'^2\right]\mu^2\right\} \tag{65}$$

$$\mathbb{S}_2^1 \approx -\frac{2I_0 P_1^0 \Gamma_{22}^{\mathrm{F}}}{\cos\phi} \left\{w'\mu + \left[t'w' - u'v' - uv\right]\mu^2\right\} \tag{66}$$

$$\mathbb{S}_3^1 \approx -\frac{2I_0 P_1^0 \Gamma_{33}^{\mathrm{F}}}{\cos\phi} \left\{-v\mu - \left[t'v - u'w + uw'\right]\mu^2\right\}. \tag{67}$$

Table 2. Electric polarizability tensors contributing to the first order inμ in the absorption and emission processes. Let us recall that t', u', v' and w refer to absorptive parts and u, v and w' to dispersive parts. Do not confuse $t'^{(2)}$ and t'_{F} which refer to different matrix elements: the former is describing the reabsorption of the fluorescence photons at energy E_{F} whereas the latter describes the spontaneous emission process.

j\i	$i=1$	$i=2$	$i=3$	Γ_{jj}^{F}
$j=0$	u'	$-v'$	w	$-t'_{\mathrm{F}}$
$j=1$	t'	w'	$-v$	$-u'_{\mathrm{F}}$
$j=2$	$-w'$	t'	$-u$	$-v'_{\mathrm{F}}$
$j=3$	v	u	t'	w_{F}

4.4.3 Incident X-ray beam linearly polarized (135°–45°)

$$\mathbb{S}_1^2 \approx -\frac{2I_0 P_2^0 \Gamma_{11}^{\mathrm{F}}}{\cos\phi} \left\{-w'\mu - \left[t'w' + u'v' + uv\right]\mu^2\right\} \tag{68}$$

$$\mathbb{S}_2^2 \approx -\frac{2I_0 P_2^0 \Gamma_{22}^{\mathrm{F}}}{\cos\phi} \left\{t'\mu + \left[v'^2 - u^2 - w'^2\right]\mu^2\right\} \tag{69}$$

$$\mathbb{S}_3^2 \approx -\frac{2I_0 P_2^0 \Gamma_{33}^{\mathrm{F}}}{\cos\phi} \left\{-u\mu - \left[t'u + v'w - vw'\right]\mu^2\right\}. \tag{70}$$

Indeed, the 12 extended Stokes components $\mathbb{S}_j^i$ listed above will again simplify a lot in the case of uniaxial crystals since only the first order terms with respect to μ will survive. We have regrouped in Table 2 the polarizability tensors contributing to the first order terms for the various combinations of indices i and j.

Note that in the case of uniaxial crystals, $u = u' = 0$ and $v = v' = 0$ for what concerns the primary absorption process but $\Gamma_{11}^{\mathrm{F}} \neq 0$, $\Gamma_{22}^{\mathrm{F}} \neq 0$ since, in a gyrotropic crystal, the components of the polarizability tensor are different in directions respectively parallel or perpendicular to the optical axis. One could use a linearly polarized incident beam (selecting for instance: $i = 2$) and analyze the relevant linearly polarized components of the emitted photons (*e.g.* $j = 1$ if $i = 2$): this experiment should give access to $w'(f)$, *i.e.* the *dispersive* part of the gyrotropy tensor. The information available from the latter experiment is then strictly equivalent to what can be learned from *optical rotation measurements in transmission*. A considerable advantage of such "*Fluorescence detected X-ray Optical Rotation*" (Fd-XOR) experiments is indeed the possibility to exploit this technique even *with thick crystals* for which conventional XOR measurements are impossible. Actually, what would be measured in Fd-XOR is not $w'(f)$ but the product $\Gamma_{11}^{\mathrm{F}} w'(f)$ which may also depend on the anisotropy of the emission process. One could circumvent the latter complication by performing the same polarization analysis with both $i = 1$ and $i = 2$ since the ratio: $\left[\mathbb{S}_1^2/\mathbb{S}_1^1\right] \simeq w'(f)/t'(g)$ would be independent of the anisotropy of the emission process.

Even though the case of biaxial crystals looks inherently far more complicated, it might still be attractive to try to measure the three components $\mathbb{S}_3^i$. The last

one, (*i.e.* $i = 3$) would give us a unique, unambiguous access to gyrotropy in the emission channel. On the other hand, one might envisage to disentangle the contribution of the so-called "*crystal optics effect*" because: $[\mathbb{S}_3^1\mathbb{S}_0^1 + \mathbb{S}_3^2\mathbb{S}_0^2]\,/\mathbb{S}_3^3 \simeq -[u'v - v'u]\,\Gamma_{00}^{F}/t'$. Unfortunately, at the present stage of the technique, X-ray fluorescence emission with polarization analysis looks like an experimental *tour de force*, especially in terms of signal-to-noise ratio, and it remains to be proved that one can really measure this second order contribution.

5 Discussion

It is well known from general quantum mechanics that absorption processes are truly measurable only if they are associated with anti-hermitian, time-even tensor properties. Since this condition has to be satisfied by all tensor properties contributing to linear or circular dichroism, we feel essential to cross-check the consistency of our results.

5.1 Antisymmetric character of dichroism tensors

As illustrated by equation (30), the tensor property responsible for circular dichroism is to the first order $w(g)$ which, according to equation (12), is the sum of 3 antisymmetric tensors. One may easily establish the antisymmetric character of all higher order terms: typically the quantity $[u(g)v'(f) - v(g)u'(f)]$ will change its sign on exchanging x and y because this term is, by definition, the cross product of symmetric tensors $\{v, v'\}$ by antisymmetric ones $\{u, u'\}$. The same sort of consideration can be extended to the various terms contributing to linear dichroism: *e.g.* $\{u, u'\}$ reverse their sign on exchanging x and y and are thus antisymmetric. On the contrary, $\{v, v'\}$ which are symmetrical tensors cannot contribute to any measurable linear dichroism unless the polarization vector is rotated by $\pm 45°$ so that the roles of $\{u, u'\}$ and $\{v, v'\}$ are finally exchanged.

5.2 Rotational invariance of circular dichroism around the incident beam direction

This is a well known property and a common argument used to reject possible instrumental artifacts. Using equation (41), it is straightforward to show that $w(g)$, $w'(f)$ and $[u(g)v'(f) - v(g)u'(f)]$ are invariant in any rotation around the direction of the wavevector $\mathbf{k}$. Thus, there is absolutely no hope to discriminate between $w(g)$ and $[u(g)v'(f) - v(g)u'(f)]$ by simply rotating the crystal around the direction of the incident beam. This result is indeed comforting our interpretation that the cross term $[u(g)v'(f) - v(g)u'(f)]$ is to be identified with the dispersion term derived by Born and Huang in a dielectric crystal [32]: as pointed out only very recently by Nelson [33], this second order term was the only one found by Born and Huang because they neglected in their theory the interaction of electric dipoles with either magnetic dipoles or electric quadrupoles.

5.3 Time-reversality

As emphasized by Barron [4] and others [35,36], the tensors $\{\alpha_{\alpha\beta};\ \zeta'_{\alpha\beta\gamma};\ Q_{\alpha\gamma\gamma\beta}\}$ have *time even parity* with respect to the action of the time-reversal operator: $\{\alpha_{\alpha\beta};\ Q_{\alpha\gamma\gamma\beta}\}$ are then responsible for *natural* linear dichroism whereas $\{\zeta'_{\alpha\beta\gamma}\}$ contributing to w is responsible for *natural* circular dichroism. In contrast, $\{\alpha'_{\alpha\beta};\ \zeta_{\alpha\beta\gamma};\ Q'_{\alpha\gamma\gamma\beta}\}$ have *time odd parity* with respect to the action of the time-reversal operator and cannot contribute to any dichroism unless another time-odd perturbation is present: this may be the case of an external magnetic field or of an internal exchange field. In other words, $\{\alpha'_{\alpha\beta};\ \zeta_{\alpha\beta\gamma};\ Q'_{\alpha\gamma\gamma\beta}\}$ will induce magnetic linear (or magnetic circular) dichroisms provided that there is a magnetic field oriented along the direction of propagation of the incident beam. It is precisely well documented that $\alpha'_{\alpha\beta}$ and $Q'_{\alpha\gamma\gamma\beta}$ are contributing to X-ray magnetic circular dichroism. It has also been suggested a long time ago by Brown *et al.* [34] and by other groups [4,35,36] that the symmetrical part of the gyrotropy tensor $\zeta_{\alpha\beta\gamma}$ could be responsible for "*non-reciprocal*" birefringence in antiferromagnetic crystals which have a non-zero magnetoelectric tensor. The reality of this effect was confirmed only quite recently at optical wavelengths [37]. Since $\zeta_{\alpha\beta\gamma}$ contributes to the definition of the anisotropy tensor u' in equation (9), our analysis would predict that the "*non-reciprocal*" gyrotropy should generate a *non-reciprocal X-ray magnetic linear dichroism*. Even though the "*non-reciprocal*" gyrotropy tensor cannot contribute to any first order X-ray circular dichroism, we think that circular dichroism could still arise through the second order cross term $[uv' - vu']$ which combines products of the type: $\zeta_{xyz}(f)\alpha_{xx}(g)$; $\zeta_{xyz}(f)\ \alpha_{yy}(g)$; $\zeta_{xxz}(g)\ \alpha_{xy}(f)$; $\zeta_{yyz}(g)\ \alpha_{xy}(f)$; $\zeta_{xyz}(g)\ \alpha_{xx}(f)$; $\zeta_{xyz}(g)\ \alpha_{yy}(f)$; $\zeta_{xxz}(f)\ \alpha_{xy}(g)$; $\zeta_{yyz}(f)\ \alpha_{xy}(g)$ and in which the dipolar contribution associated with $\alpha_{\alpha\beta}\,(g)$ may be large.

6 Conclusion

For the first time, we have proposed a unified formulation of the differential absorption and differential change of polarization state of a polarized X-ray beam propagating inside a biaxial gyrotropic crystal. The starting point of this analysis is a 4×4 differential Müller matrix, the 16 elements of which are related to the anisotropic components of the multipolar polarizability tensors at the absorbing site. Our primary goal was to derive analytical expressions for X-ray linear and circular dichroism, optical rotation and circular polarimetry in a transmission configuration. The same formalism has been extended to encompass the case of Fluorescence detected X-ray dichroism, which is a technique of much more practical interest. Analytical expressions have been obtained for the "*extended*" Stokes components $\mathbb{S}_j^i$ of the emitted photons: our results confirm that more information could be obtained if one could analyze –*at least*– the linear polarization components of the X-ray fluorescence emitted in a specific direction.

In the case of biaxial crystals, we face serious problems since the tiny effects of X-ray gyrotropy in circular dichroism may be completely swamped out by large linear dichroism signals mostly due to the imperfect polarization transfer of X-ray monochromators. It is shown that Fd-XCD spectra are not anymore strictly proportional to transmission XCD spectra. As far as circular dichroism is concerned, one has also to take into account a possible contribution of second order terms: even in the case of non-gyrotropic crystals, one should record non-zero XCD spectra whenever the condition: $[u(g)v'(f) - v(g)u'(f)] \neq 0$ is satisfied. Since this contribution is also invariant in any rotation around the direction of the incident beam, it appears *a priori* fairly difficult to discriminate normal gyrotropy effects from the latter "*crystal optics effect*" the existence of which was predicted by Machavariani [7]. Interestingly, the relative importance of this contribution has been found to be depressed in Fd-XCD spectra.

Last but not least, we checked the consistency of our results with respect to antisymmetry and time reversal properties. Our formulation of linear and circular dichroism in gyrotropic crystals includes terms of odd parity with respect to the action of the time reversal operator: the terms responsible for X-ray magnetic circular dichroism in anisotropic crystals are well identified but we obtain additional terms which cannot contribute to any natural X-ray linear nor circular dichroism but may well cause *non-reciprocal* X-ray gyrotropy effects in antiferromagnetic crystals.

Appendix A1

Following Buckingham [10], one may define at the absorbing site a variety of multipolar polarizability tensor components:

$$\alpha_{\alpha\beta}(f^*) = +\alpha_{\beta\alpha}(f^*) = \frac{2}{\hbar}\sum_j f^*\omega_{ij}^* \,\mathrm{Re}\{\langle i|E_{1\alpha}|j\rangle\langle j|E_{1\beta}|i\rangle\} \quad (71)$$

$$\alpha'_{\alpha\beta}(f^*) = -\alpha'_{\beta\alpha}(f^*) = -\frac{2}{\hbar}\sum_j f^*\omega \,\mathrm{Im}\{\langle i|E_{1\alpha}|j\rangle\langle j|E_{1_\beta}|i\rangle\} \quad (72)$$

$$A_{\alpha\beta\gamma}(f^*) = +A_{\alpha\gamma\beta}(f^*) = \frac{2}{\hbar}\sum_j f^*\omega_{ij}^* \,\mathrm{Re}\{\langle i|E_{1_\alpha}|j\rangle\langle j|E_{2_\beta\gamma}|i\rangle\} \quad (73)$$

$$A'_{\alpha\beta\gamma}(f^*) = +A'_{\alpha\gamma\beta}(f^*) = -\frac{2}{\hbar}\sum_j f^*\omega \,\mathrm{Im}\{\langle i|E_{1\alpha}|j\rangle\langle j|E_{2\beta\gamma}|i\rangle\} \quad (74)$$

$$G_{\alpha\beta}(f^*) = \frac{2}{\hbar}\sum_j f^*\omega_{ij}^* \,\mathrm{Re}\{\langle i|E_{1\alpha}|j\rangle\langle j|M_{1\beta}|i\rangle\} \quad (75)$$

$$G'_{\alpha\beta}(f^*) = -\frac{2}{\hbar}\sum_j f^*\omega \,\mathrm{Im}\{\langle i|E_{1\alpha}|j\rangle\langle j|M_{1\beta}|i\rangle\} \quad (76)$$

$$C_{\alpha\beta\gamma\delta}(f^*) = +C_{\gamma\delta\alpha\beta}(f^*) = \frac{2}{3\hbar}\sum_j f^*\omega_{ij}^* \,\mathrm{Re}\{\langle i|E_{2\alpha\beta}|j\rangle\langle j|E_{2\gamma\delta}|i\rangle\} \quad (77)$$

$$C'_{\alpha\beta\gamma\delta}(f^*) = -C'_{\gamma\delta\alpha\beta}(f^*) = \frac{2}{3\hbar}\sum_j f^*\omega \,\mathrm{Im}\{\langle i|E_{2\alpha\beta}|j\rangle\langle j|E_{2\gamma\delta}|i\rangle\} \quad (78)$$

where E_1, M_1 and E_2 refer to the electric dipole, magnetic dipole and electric quadrupole operators. In the case of mixed multipole components (73, 74; 75, 76), there is no direct separation into symmetric / antisymmetric parts with respect to the exchange of the first two indices and it is therefore much convenient to generate two additional tensors which are *symmetric* or *antisymmetric* with respect to the exchange of these indices:

$$\zeta_{\alpha\beta\gamma} = +\zeta_{\beta\alpha\gamma} = +\frac{1}{c}\left\{\frac{\omega}{3}\left[A'_{\alpha\beta\gamma}+A'_{\beta\alpha\gamma}\right]+\epsilon_{\delta\gamma\alpha}G_{\beta\delta}+\epsilon_{\delta\gamma\beta}G_{\alpha\delta}\right\} \quad (79)$$

$$\zeta'_{\alpha\beta\gamma} = -\zeta'_{\beta\alpha\gamma} = -\frac{1}{c}\left\{\frac{\omega}{3}\left[A_{\alpha\beta\gamma}-A_{\beta\alpha\gamma}\right]+\epsilon_{\delta\gamma\alpha}G'_{\beta\delta}-\epsilon_{\delta\gamma\beta}G'_{\alpha\delta}\right\} \quad (80)$$

where c is the velocity of light and $\epsilon_{\alpha\beta\gamma}$ is the Levi-Civita alternating tensor. The tensor (80) is to be identified with a microscopic gyrotropy tensor whereas the tensor (79) may be called "*non-reciprocal gyrotropy tensor*" for reasons which are discussed in Section 5. In equations (71–80), the complex function f^* is defined by:

$$f^* = f + \mathrm{i}g = \frac{(\omega_{ij})^2-\omega^2}{\left[(\omega_{ij})^2-\omega^2\right]^2+[\omega\Gamma_j]^2} + \mathrm{i}\frac{\omega\Gamma_j}{\left[(\omega_{ij})^2-\omega^2\right]^2+[\omega\Gamma_j]^2} \quad (81)$$

where f and g are the well known dispersive and absorptive lineshapes. One may also define the complex transition energy: $\omega_{ij}^* = \omega_{ij} - \mathrm{i}\Gamma_j/2$, where Γ_j is the full width at half maximum (fwhm) of a Lorentzian lineshape and, as far as X-ray absorption spectroscopy is concerned, the latter parameter refers to the life time of the deep core hole in the excited state. As discussed elsewhere [1,5], the magnetic dipole (M_1) transition matrix elements (TME) are expected to be very small in the X-ray range but we decided to maintain the terms (75, 76) for the sake of completeness of the final results which may then be more easily extrapolated into other energy ranges. On the other hand, there is ample experimental evidence [5,11–15] that X-ray absorption spectroscopy is sensitive to the pure electric quadrupole ($E_2.E_2$) cross sections: this implies that the terms (77, 78) cannot be neglected in the X-ray range.

In the theory of refringent scattering developed by Buckingham [10] or Barron [4], it is finally most convenient to introduce the following *complex* multipolar

polarizability tensors $\alpha^*_{\alpha\beta}$, $C^*_{\alpha\beta\gamma\delta}$ and $\zeta^*_{\alpha\beta\gamma}$ respectively defined as:

$$\alpha^*_{\alpha\beta} = \left[\alpha_{\alpha\beta}(f) + \alpha'_{\alpha\beta}(g)\right] + \mathrm{i}\left[\alpha_{\alpha\beta}(g) - \alpha'_{\alpha\beta}(f)\right] \quad (82)$$

$$C^*_{\alpha\beta\gamma\delta} = \left[C_{\alpha\beta\gamma\delta}(f) + C'_{\alpha\beta\gamma\delta}(g)\right] + \mathrm{i}\left[C_{\alpha\beta\gamma\delta}(g) - C'_{\alpha\beta\gamma\delta}(f)\right] \quad (83)$$

$$\zeta^*_{\alpha\beta\gamma} = \left[\zeta_{\alpha\beta\gamma}(f) + \zeta'_{\alpha\beta\gamma}(g)\right] + \mathrm{i}\left[\zeta_{\alpha\beta}(g) - \zeta'_{\alpha\beta}(f)\right]. \quad (84)$$

For the sake of simplifying the notations, it was found preferable to replace $C^*_{\alpha\gamma\gamma\beta}$ in equation (1) with:

$$Q^*_{\alpha\gamma\gamma\beta} = \frac{(\omega)^2}{3c^2} C^*_{\alpha\gamma\gamma\beta}.$$

Appendix A2

Let us define the matrix [M′], which is the differential Müller matrix [M] of equation (15) but *without the diagonal elements*, and its associated matrix [M"] such as:

$$[\mathrm{M}'] = \begin{bmatrix} 0 & u' & -v' & w \\ u' & 0 & -w' & v \\ -v' & w' & 0 & u \\ w & -v & -u & 0 \end{bmatrix} \quad [\mathrm{M}''] = \begin{bmatrix} 0 & -u & v & w' \\ -u & 0 & w & v' \\ v & -w & 0 & u' \\ w' & -v' & -u' & 0 \end{bmatrix}. \quad (85)$$

We may next define two conjugated complex matrices such as: $[\mathrm{M}^+] = [\mathrm{M}'] + \mathrm{i}\,[\mathrm{M}'']$ and $[\mathrm{M}^-] = [\mathrm{M}'] - \mathrm{i}\,[\mathrm{M}'']$. It is then easy to check that the latter two matrices have the remarkable properties:

$$[\mathrm{M}^+]^2 = -\Delta^2\,[\mathrm{I}_d] \qquad [\mathrm{M}^-]^2 = -\Delta^{*2}\,[\mathrm{I}_d] \quad (86)$$

where: $\Delta^2 = (u+\mathrm{i}u')^2 + (v+\mathrm{i}v')^2 - (w+\mathrm{i}w')^2$ and where Δ^* is the complex conjugate of Δ. Therefore, any exponential matrix of $\lambda\,[\mathrm{M}^\pm]$ can be decomposed as the sum of a term proportional to the identity matrix $[\mathrm{I}_d]$, plus a term proportional to $[\mathrm{M}^\pm]$. More precisely, we have:

$$\exp\left(\lambda\,[\mathrm{M}^+]\right) = \cos\left(\lambda\Delta\right)[\mathrm{I}_d] + \frac{1}{\Delta}\sin\left(\lambda\Delta\right)[\mathrm{M}^+] \quad (87)$$

$$\exp\left(\lambda\,[\mathrm{M}^-]\right) = \cos\left(\lambda\Delta^*\right)[\mathrm{I}_d] + \frac{1}{\Delta^*}\sin\left(\lambda\Delta^*\right)[\mathrm{M}^-] \quad (88)$$

Since $[\mathrm{M}^+]$ and $[\mathrm{M}^-]$ commute, it is straightforward to show that a more convenient analytical formulation of the integrated Müller matrix $[\Phi'(z)] = \exp\left(az\,[\mathrm{M}']\right) = \exp\left(\frac{1}{2}az\,[\mathrm{M}^+ + \mathrm{M}^-]\right)$ is:

$$[\Phi'(z)] = \left\{\cos\left(az\Delta/2\right)[\mathrm{I}_d] + \frac{1}{\Delta}\sin\left(az\Delta/2\right)[\mathrm{M}^+]\right\} \times \left\{\cos\left(az\Delta^*/2\right)[\mathrm{I}_d] + \frac{1}{\Delta^*}\sin\left(az\Delta^*/2\right)[\mathrm{M}^-]\right\}. \quad (89)$$

Indeed, the diagonal element of [M] can be reintroduced in the final result by simply multiplying $[\Phi'(z)]$ by the exponential factor $\exp\left(azt'\right)$:

$$[\Phi(z)] = \exp\left(azt'\right)[\Phi'(z)]. \quad (90)$$

The analytical formula derived in this paper are then based on the fairly usual series expansions of the complex functions: $\cos\left(az\Delta/2\right)$; $\cos\left(az\Delta^*/2\right)$; $\sin\left(az\Delta/2\right)$ and $\sin\left(az\Delta^*/2\right)$.

Appendix A3

Our goal in this appendix is to make explicit the matrix elements Γ^{F}_{jj}. Starting with the definition of the *coherence vector* by Born and Wolf [26,27], the four diagonal matrix elements can be expressed in the crystal coordinate system as:

$$\Gamma^{\mathrm{F}}_{00} = \gamma_0 \left\langle \left[E^{\mathrm{F}}_x E^{\mathrm{F}*}_x + E^{\mathrm{F}}_y E^{\mathrm{F}*}_y\right] - \left[E^{\mathrm{F}}_y E^{\mathrm{F}*}_y - E^{\mathrm{F}}_z E^{\mathrm{F}*}_z\right]\sin^2\phi + \left[E^{\mathrm{F}}_y E^{\mathrm{F}*}_z + E^{\mathrm{F}}_z E^{\mathrm{F}*}_y\right]\sin\phi\cos\phi \right\rangle \quad (91)$$

$$\Gamma^{\mathrm{F}}_{11} = \gamma_1 \left\langle \left[E^{\mathrm{F}}_x E^{\mathrm{F}*}_x - E^{\mathrm{F}}_y E^{\mathrm{F}*}_y\right] + \left[E^{\mathrm{F}}_y E^{\mathrm{F}*}_y - E^{\mathrm{F}}_z E^{\mathrm{F}*}_z\right]\sin^2\phi + \left[E^{\mathrm{F}}_y E^{\mathrm{F}*}_z - E^{\mathrm{F}}_z E^{\mathrm{F}*}_y\right]\sin\phi\cos\phi \right\rangle \quad (92)$$

$$\Gamma^{\mathrm{F}}_{22} = \gamma_2 \left\langle -\left[E^{\mathrm{F}}_x E^{\mathrm{F}*}_y + E^{\mathrm{F}}_y E^{\mathrm{F}*}_x\right]\cos\phi - \left[E^{\mathrm{F}}_x E^{\mathrm{F}*}_z + E^{\mathrm{F}}_z E^{\mathrm{F}*}_x\right]\sin\phi \right\rangle \quad (93)$$

$$\Gamma^{\mathrm{F}}_{33} = \gamma_3 \left\langle -\mathrm{i}\left[E^{\mathrm{F}}_x E^{\mathrm{F}*}_y - E^{\mathrm{F}}_y E^{\mathrm{F}*}_x\right]\cos\phi - \mathrm{i}\left[E^{\mathrm{F}}_x E^{\mathrm{F}*}_z - E^{\mathrm{F}}_z E^{\mathrm{F}*}_x\right]\sin\phi \right\rangle \quad (94)$$

where the scalar factors γ_i $(\delta\Omega/4\pi)$ are the quantum yields of anisotropic fluorescence in a solid angle $\delta\Omega/4\pi$. The latter solid angle is defined either by the angular acceptance of the detector or by the acceptance of the crystal analyzer when energy resolved emission spectra are recorded. Since the *coherent* fluorescence intensities $\left\langle E^{\mathrm{F}}_\alpha E^{\mathrm{F}*}_\beta \right\rangle$ are proportional to the anisotropic transition probabilities, one may write:

$$\Gamma^{\mathrm{F}}_{00} = \gamma_0\beta_{\mathrm{F}} \left\langle -t'_{\mathrm{F}}(g)\right\rangle^{(1)} \quad (95)$$

$$\Gamma^{\mathrm{F}}_{11} = \gamma_1\beta_{\mathrm{F}} \left\langle -u'_{\mathrm{F}}(g)\right\rangle^{(1)} \quad (96)$$

$$\Gamma^{\mathrm{F}}_{22} = -\gamma_2\beta_{\mathrm{F}} \left\langle -v'_{\mathrm{F}}(g)\right\rangle^{(1)} \quad (97)$$

$$\Gamma^{\mathrm{F}}_{33} = \gamma_3\beta_{\mathrm{F}} \left\langle w_{\mathrm{F}}(g)\right\rangle^{(1)} \quad (98)$$

where $\beta_{\mathrm{F}} \propto \omega^2_{\mathrm{F}}$ is a conversion factor which is proportional to the square of the fluorescence energy. By analogy with equations (7–13), one may then write:

$$-t'_{\mathrm{F}} = \left\langle \begin{array}{c} \left[\alpha^{\mathrm{F}}_{xx} + \alpha^{\mathrm{F}}_{yy}\right] - \left[\alpha^{\mathrm{F}}_{yy} - \alpha^{\mathrm{F}}_{zz}\right]\sin^2\phi + \left[\alpha^{\mathrm{F}}_{yz} + \alpha^{\mathrm{F}}_{zy}\right]\sin\phi\cos\phi \\ + \left[\zeta^{\mathrm{F}}_{xxz} + \zeta^{\mathrm{F}}_{yyz}\right] n_z\cos^2\phi - \left[\zeta^{\mathrm{F}}_{yyz} - \zeta^{\mathrm{F}}_{zzz}\right] n_z\cos^2\phi\sin^2\phi \\ + \left[\zeta^{\mathrm{F}}_{xxy} + \zeta^{\mathrm{F}}_{yyy}\right] n_y\sin^2\phi - \left[\zeta^{\mathrm{F}}_{yyy} - \zeta^{\mathrm{F}}_{zzy}\right] n_y\sin^4\phi \end{array} \right\rangle + 2\left[\zeta^{\mathrm{F}}_{yzz}\sin\phi\cos\phi\right] n_z\cos^2\phi + 2\left[\zeta^{\mathrm{F}}_{yzy}\sin\phi\cos\phi\right] n_y\sin^2\phi \quad (99)$$

$$-u'_{\mathrm{F}} = \left\langle \begin{array}{c} \left[\alpha^{\mathrm{F}}_{xx} - \alpha^{\mathrm{F}}_{yy}\right] + \left[\alpha^{\mathrm{F}}_{yy} - \alpha^{\mathrm{F}}_{zz}\right]\sin^2\phi - \left[\alpha^{\mathrm{F}}_{yz} + \alpha^{\mathrm{F}}_{zy}\right]\sin\phi\cos\phi \\ + \left[\zeta^{\mathrm{F}}_{xxz} - \zeta^{\mathrm{F}}_{yyz}\right] n_z\cos^2\phi + \left[\zeta^{\mathrm{F}}_{yyz} - \zeta^{\mathrm{F}}_{zzz}\right] n_z\cos^2\phi\sin^2\phi \\ + \left[\zeta^{\mathrm{F}}_{xxy} - \zeta^{\mathrm{F}}_{yyy}\right] n_y\sin^2\phi + \left[\zeta^{\mathrm{F}}_{yyy} - \zeta^{\mathrm{F}}_{zzy}\right] n_y\sin^4\phi \end{array} \right\rangle - 2\left[\zeta^{\mathrm{F}}_{yzz}\sin\phi\cos\phi\right] n_z\cos^2\phi - 2\left[\zeta^{\mathrm{F}}_{yzy}\sin\phi\cos\phi\right] n_y\sin^2\phi \quad (100)$$

$$-v'_{\mathrm{F}} = \left\langle \begin{array}{c} 2\alpha^{\mathrm{F}}_{xy}\cos\phi + 2\alpha^{\mathrm{F}}_{xz}\sin\phi \\ +2\left[\zeta^{\mathrm{F}}_{xyz}\cos\phi + \zeta^{\mathrm{F}}_{xzz}\sin\phi\right] n_z\cos^2\phi \\ +2\left[\zeta^{\mathrm{F}}_{xyy}\cos\phi + \zeta^{\mathrm{F}}_{xzy}\sin\phi\right] n_y\sin^2\phi \end{array} \right\rangle \quad (101)$$

$$w_{\mathrm{F}} = \left\langle \begin{array}{c} 2\alpha'^{\mathrm{F}}_{xy}\cos\phi + 2\alpha'^{\mathrm{F}}_{xz}\sin\phi \\ +2\left[\zeta'^{\mathrm{F}}_{xyz}\cos\phi + \zeta'^{\mathrm{F}}_{xzz}\sin\phi\right] n_z\cos^2\phi \\ +2\left[\zeta'^{\mathrm{F}}_{xyy}\cos\phi + \zeta'^{\mathrm{F}}_{xzy}\sin\phi\right] n_y\sin^2\phi \end{array} \right\rangle . \quad (102)$$

For simplicity, the "*pure*" electric quadrupole ($E_2.E_2$) transition matrix elements have been deliberately omitted in the latter equations. The brackets imply that one has to take a configuration average over all emitting atoms: anisotropic emission can thus only be observed in oriented single crystals but certainly not in powders nor in solution.

References

1. J. Goulon, C. Goulon-Ginet, A. Rogalev, V. Gotte, C. Malgrange, Ch. Brouder, C.R. Natoli, J. Chem. Phys. **108**, 6394 (1998).
2. L. Alagna, T. Prosperi, S. Turchini, J. Goulon, A. Rogalev, C. Goulon-Ginet, C.R. Natoli, B. Stewart, R.D. Peacock, Phys. Rev. Lett. **80**, 4799 (1998).
3. C.R. Natoli, Ch. Brouder, Ph. Sainctavit, J. Goulon, C. Goulon-Ginet, A. Rogalev, Eur. Phys. J. B **4**, 1 (1998).
4. L.D. Barron, *Molecular Light Scattering and Optical Activity* (Cambridge University Press, 1982).
5. Ch. Brouder, J. Phys.-Cond. Matter **2**, 701 (1990).
6. T. Lippmann, A. Kirfel, K. Fischer, J. Appl. Cryst. **29**, 186 (1996).
7. V.Sh. Machavariani, J. Phys.-Cond. Matter **7**, 5151 (1995).
8. L.D. Barron, A.D. Buckingham, Mol. Phys. **20**, 1111 (1971).
9. A.D. Buckingham, R.E. Raab, Proc. R. Soc. London A **345**, 365 (1975).
10. A.D. Buckingham, Adv. Chem. Phys. **12**, 107 (1968).
11. J.E. Penner-Hahn, R.A. Scott, K.O. Hodgson, S. Doniach, S.R. Desjardins, E.I. Solomon, Chem. Phys. Lett. **88**, 595 (1982).
12. G. Dräger, R. Frahm, G. Materlick, O. Brümmer, Phys. Stat. Sol. B **146**, 287 (1988).
13. J.C. Lang, G. Strajer, C. Detlefs, A.I. Goldman, H. König, Xindong Wang, B.N. Harmon, R.W. McCallum, Phys. Rev. Lett. **74**, 4935 (1995).
14. C. Giorgetti, E. Dartyge, Ch. Brouder, F. Baudelet, C. Meyer, S. Pizzini, A. Fontaine, R.M. Galera, Phys. Rev. Lett. **75**, 3186 (1995).
15. M.H. Krisch, C.C. Kao, F. Sette, W.A. Caliebe, K. Hämäläinen, J. Hastings, Phys. Rev. Lett. **74**, 4931 (1995).
16. P. Elleaume, J. Synchrotron Rad. **1**, 19 (1994).
17. C. Malgrange, C. Carvahlo, L. Braicovich, J. Goulon, Nucl. Instrum. Methods A **308**, 390 (1991).
18. M. Hart, Philos. Mag. B **38**, 41 (1978).
19. M. Sauvage, C. Malgrange, J.F. Petroff, J. Appl. Cryst. **16**, 14 (1983).
20. D.P. Siddons, M. Hart, Y. Amemiya, J.B. Hastings, Phys. Rev. Lett. **64**, 1967 (1990).
21. V.E. Dmitrienko, V.A. Belyakov, Pis'ma Zh. Tekh. Fiz. **6**, 1440 (1980); Sov. Tech. Phys. Lett. **6**, 621 (1980).
22. T. Ishikawa, K. Hirano, S. Kikuta, J. Appl. Cryst. **24**, 982 (1991).
23. T. Ishikawa, K. Hirano, K. Kanzaki, S. Kikuta, Rev. Sci. Instrum. **66**, 1540 (1995).
24. C. Gilès, C. Malgrange, J. Goulon, C. Vettier, F. De Bergevin, A. Freund, P. Elleaume, E. Dartyge, A. Fontaine, C. Giorgetti, S. Pizzini, Proc. SPIE **2010**, 136 (1993).
25. J. Goulon, C. Malgrange, C. Gilès, C. Neumann, A. Rogalev, E. Moguiline, F. De Bergevin, C. Vettier, J. Synchrotron Rad. **3**, 272 (1996); Phys. Rev. B **52**, 10681 (1995).
26. M. Born, E. Wolf, *Principles of Optics*, 6th edn. (Pergamon Press, 1985), pp. 546-547.
27. R.M.A. Azzam, N.M. Bashara, *Ellipsometry and Polarized Light* (North Holland Personal Library, Elsevier Science Publishers, B.V., 1989), pp. 62-63.
28. C.A. Emeis, L.J. Oosterhoff, Chem. Phys. Lett. **1**, 129 (1967).
29. J.P. Riehl, F. Richardson, Chem. Rev. **86**, 1 (1986).
30. J.P. Riehl, F. Richardson, J. Chem. Phys. **65**, 1011 (1976).
31. C. Gauthier, I. Ascone, J. Goulon, R. Cortès, J.M. Barbe, R. Guilard, Chem. Phys. Lett. **147**, 165 (1990).
32. M. Born, K. Huang, *Dynamical Theory of Crystal Lattices* (Clarendon, Oxford, 1954), pp. 336-338.
33. D.F. Nelson, J. Opt. Soc. Am. **B6**, 1110 (1989).
34. W.F. Brown, S. Shtrikman, D. Treves, J. Appl. Phys., 1233 (1963).
35. R.R. Birss, R.G. Shrubsall, Philos. Mag. **15**, 687 (1967).
36. R.M. Hornreich, S. Shtrikman, Phys. Rev. **171**, 1065 (1968).
37. B.B. Kritchetsov, V.V. Pavlov, R.V. Pisarev, V.N. Gridnev, J. Phys.-Cond. Matter **5**, 8223 (1993).

Quatrième partie

Contribution aux développements méthodologiques sur la ligne de lumière ID-12A

4.1 Introduction

Dans cette partie, nous présentons les quatre publications qui se rapportent aux développements méthodologiques sur la ligne ID-12A auxquels nous avons participé.

4.1.1 Enregistrement de spectres EXAFS et M-EXAFS avec la technique dite "undulator gap-scan"

La technique "undulator gap-scan" a été développée car il est difficile d'enregistrer un spectre EXAFS sur un domaine de 1000 à 1500 eV avec un onduleur. En effet, le spectre d'émission d'un onduleur est caractérisé par une série de pics discrets, d'une faible bande passante en énergie. La largeur à mi-hauteur du premier harmonique spectral impair de l'onduleur Helios-II est de 90 eV, tandis que celle du second harmonique spectral pair est de 500 eV. L'utilisation de l'harmonique pair large est limitée par le fait que l'intensité du pic est plus faible. Une meilleure solution consiste à corréler la variation de l'entrefer de l'onduleur avec la rotation du cristal du monochromateur afin de garder constant le flux de photons transmis par celui-ci ainsi que le taux de polarisation circulaire. Il devient alors possible d'enregistrer les spectres EXAFS sur un large domaine d'énergie.
C'est grâce à cette technique que nous avons pu enregistrer les spectres EXAFS aux seuils K du manganèse et du chlore, présentés dans la deuxième partie de ce mémoire.

4.1.2 Spectroscopie d' absorption X au seuil K du soufre

La technique "gap-scan" a été aussi utilisée pour deux projets industriels concernant divers échantillons soufrés pour lesquels les spectres au seuil K du soufre ont pu être enregistrés sur 1300 eV.

La première de ces études, effectuée en collaboration avec le centre de recherche HUTCHINSON, avait pour but d'estimer la quantité de composés polysulfurés contenus dans des vulcanisats. En effet, les caractéristiques mécaniques des caoutchoucs sont directement corrélées à la stabilité des liaisons soufre-soufre.
Les spectres XANES déconvolués ont permis d'assigner sans ambiguité les résonances de pré-seuil caractéristiques des liaisons σ^*(S-S), π^*(S-S) et σ^*(S-C) des divers échantillons. L'analyse des spectres EXAFS a montré que les différents vulcanisats contenaient un taux variable de liaisons pontantes soufre-soufre et de sulfure de zinc.

La seconde étude a été réalisée en collaboration avec le LIMSAG (UMR 5633) de Dijon et le centre de recherche ELF-Solaize. Il s'agissait de déterminer le taux de groupes fonctionnels sulfone ou sulfoxyde formés par oxydation thermique de sulfures aliphatiques dans les bitumes artificiels. La méthode d'analyse retenue est l'analyse différentielle des spectres XANES, utilisée par Huggins et coll.[1], que nous avons étendue aux spectres de dérivés premières. Par comparaison des spectres de différence de dérivées premières des espèces oxydées et non-oxydées avec ceux de composés modèles, il est possible d'estimer, d'une part, la composition relative en poids des espèces sulfidiques par rapport à la somme des espèces sulfidiques et thiophéniques, et

[1] Huggins, F.E.;Vaidya S.V.; Huffman, G.; Mill, T.; Youtcheff, J.; *Proc. Am. Chem. Soc. Meeting - Division of fuel chemistry*, **1992**, 1376-1382.

d'autre part, le taux de groupes fonctionnels sulfone et/ou sulfoxyde formés par oxydation des sulfures aliphatiques. La faible concentration en sulfoxydes dans les espèces oxydées est corroborée par l'étude des spectres EXAFS où la signature typique de la liaison soufre-oxygène n'est pas observée.

4.1.3 Spectres XMCD et spectres EXAFS polarisés en spin

En utilisant le second harmonique spectral de l'onduleur Helios-II, nous avons enregistré les spectres XMCD aux seuils L_{II} et L_{III} de l'europium, ainsi que les spectres EXAFS polarisés en spin, pour les deux phases ferromagnétique (T=50 K, B=6,5 T) et paramagnétique (T=2 K, B=1,5 T) d'un échantillon de sulfure d'europium. Seule l'intensité des spectres XMCD est modifiée lorsque le sulfure d'europium passe d'une phase à l'autre. La comparaison entre les distributions radiales des spectres EXAFS classiques et des spectres EXAFS polarisés en spin suggère que les soufres portent un moment magnétique induit par interaction d'échange avec les europiums voisins. Notre contribution à cette étude s'est limitée à la mise en oeuvre des logiciels pour analyser les spectres.

4.2 Acte de congrès

Spectroscopy

J. Synchrotron Rad. (1998). **5**, 989–991

XAFS and X-MCD spectroscopies with undulator gap scan

Andrei Rogalev,* Vincent Gotte, José Goulon, Christophe Gauthier, Joel Chavanne and Pascal Elleaume

European Synchrotron Radiation Facility, BP 220, F-38043 Grenoble CEDEX, France. E-mail: rogalev@esrf.fr

(*Received 4 August 1997; accepted 27 October 1997*)

The first experimental applications of the undulator gap-scan technique in X-ray absorption spectroscopy are reported. The key advantage of this method is that during EXAFS scans the undulator is permanently tuned to the maximum of its emission peak in order to maximize the photon statistics. In X-MCD or spin-polarized EXAFS studies with a helical undulator of the Helios type, the polarization rate can also be kept almost constant over a wide energy range.

Keywords: EXAFS; X-MCD; spin-polarized EXAFS; undulator sources.

1. Introduction

Undulator sources are very attractive for X-ray absorption spectroscopy because they offer an unprecedented spectral brilliance together with the possibility to minimize the heat load on the optics. Unfortunately, the spectral bandwidth of odd harmonics, which are most intense, may be large enough to cover the XANES region but is much too narrow to record a full EXAFS spectrum which extends over 1000–1500 eV. Moreover, since the photon flux varies dramatically when the monochromator is scanned across the undulator peak, the dynamic range of the detection system has to be large. Tapering the undulator gap results in a broadening of the spectral distribution but at the expense of a reduced source brilliance and a lower peak intensity: this was the strategy retained for the ESRF beamline ID24 (Hagelstein *et al.*, 1997). Alternatively, one may exploit even harmonics which exhibit a much wider bandwidth but again a lower peak intensity. A far better option is to move the undulator gap (or the half-gaps of a helical undulator) so that the energy of the X-ray monochromator always matches the maximum of the undulator peak. This technique, hereafter called 'undulator gap scan', is most attractive since it preserves the undulator brightness and keeps the intensity of the incoming beam almost constant over the whole EXAFS scan. Whenever a helical undulator is used, this technique offers the valuable advantage of also keeping the polarization state of the X-ray beam constant over a wide energy range.

The aim of this paper is to establish the practicability of the undulator gap-scan technique which is now routinely used at the ESRF ID12A beamline. Two examples were selected to illustrate the merits of this technique in X-ray absorption spectroscopies: the first concerns an EXAFS study of [*d*,*l*] cystine at the sulfur *K*-edge; the second concerns spin-polarized XAFS spectra of EuS recorded at the Eu $L_{II,III}$-edges in the ferromagnetic phase. A major concern in these experiments is the stability of the electron beam in the machine: the case of high-energy machines, such as ESRF, APS or SPring-8, is most favourable since the sensitivity of a machine to external perturbations scales as E^{-2}, where E is the electron beam energy. Considerable efforts have been made (*e.g.* with proper magnetic shimming of all insertion devices) to minimize such instabilities. Another difficulty is to design detectors that are fully insensitive to tiny beam displacements.

2. Experimental

Since a complete layout of the ESRF beamline ID12A is presented elsewhere in the same issue (Goulon *et al.*, 1998), together with a discussion of the performances of the optical components of the beamline, we will concentrate here only on the characteristics of the source and on the gap-scan procedure. Note that all spectra reproduced in the following section were recorded by monitoring the fluorescence (FY) of the sample as a function of the energy of the incident photons. All fluorescence detectors, intensity monitors or position monitors installed at beamline ID12A are (single- or multi-anode) silicon photodiodes associated with digital lock-ins exploiting a square-wave-modulated X-ray beam (Gauthier *et al.*, 1995).

2.1. *Helios-II undulator source*

The source most commonly used at the ESRF beamline ID12A is the helical undulator Helios-II which has 31 magnetic periods (Elleaume, 1994). Horizontal (B_x) and vertical (B_z) magnetic field distributions featuring the same spatial periodicity (λ_u = 52 mm) are generated by two planar arrays of permanent magnets assembled in two magnetic jaws fixed to rigid girders. The users have access to three independent translations: an axial translation (T_y) of the upper girder induces a variation of the 'phase' (φ) between the horizontal and vertical fields and is commonly used to select right-handed ($\varphi = \pi/2$; $T_y = \lambda_u/4$), left-handed ($\varphi = -\pi/2$; $T_y = -\lambda_u/4$) or linear ($\varphi = 0$; $T_y = 0$) polarizations; vertical translations (T_z) of each individual girder are used not only to shift the undulator peak energy but also to vary the ratio $\rho = B_x/B_z$, which is critical to maximize the circular polarization rate ($\rho = 1$). Note that for elliptical polarizations ($\rho \neq 1$), varying ρ will rotate the long axis, change the ellipticity and modify the relative intensities of high-order harmonics (Elleaume *et al.*, 1991). A critical adjustment of the two half-gaps is thus quite essential. For any undulator setting, the field integral can be kept below 30 μTm thanks to a very efficient multipole shimming technique (Chavanne *et al.*, 1992).

2.2. *Undulator gap-scan procedure*

One needs first to build up a lock-up table which correlates (for any desired polarization state) the displacements $T_z(B_x)$ and $T_z(B_z)$, or the corresponding 'half-gaps' values, with the energy of the maximum of the undulator peak. Let us start with the simplest case where only one half-gap is varied during an energy scan. We use a second-order polynomial fit of the data stored in the lock-up table to calculate the optimized values of the translation $T_z(B_x)$ or $T_z(B_z)$ for any energy (or Bragg angle) of the

monochromator. A flow chart (Fig. 1) summarizes the whole procedure programmed under *SPEC* (Certified Scientific Software, Cambridge, MA, USA): the input parameters include the values of A, B and C (fitted from the data stored in the lock-up table), the starting (E_{min}) and final (E_{max}) energies of the scan and the number of data points (Npts). For every energy, the optimized gap is calculated and is compared with the previous setting. If the difference exceeds 2.5 μm (minimum step size authorized) then the gap is moved to its optimum value. Depending on the absolute half-gap settings, the undulator peak may shift by 2–5 eV.

Moving only one single half-gap is not acceptable for circular dichroism experiments since the ellipticity of the X-ray beam would change during the scan. A modified procedure (hereafter called 'double' gap-scan) has thus been elaborated where both half-gaps are changed simultaneously in a correlated way according to the equation

$$[\text{half-gap } B_z] = 1.7641 + 1.2489^*[\text{half-gap } B_x], \qquad (1)$$

so that the horizontal and vertical magnetic fields are kept strictly equal ($\rho = 1$).

3. Results

3.1. *Sulfur K-edge EXAFS of [d,l] cystine*

In the perspective of further EXAFS studies on low-Z elements, we tried first to evaluate the performances of the 'gap-scan' technique by recording the EXAFS spectrum of a pellet of [*d,l*] cystine at the sulfur K-edge. This was a rather demanding test because (i) the EXAFS signal is expected to be very weak (especially at room temperature) since this compound has a very low symmetry, and (ii) high-quality data over a large energy range are required to have a chance of resolving the close-lying S···C and S···S signatures expected at 1.8 and 2.03 Å, respectively. For this experiment, the half-gap B_x was completely open so that the undulator radiation was linearly polarized with the polarization vector in the horizontal plane. The only chance to record an EXAFS spectrum over a wide energy range (*i.e.* 2400–3800 eV) was therefore by scanning the half-gap B_z. As illustrated by Fig. 2(*a*), the EXAFS oscillations $k\chi(k)$ clearly extend over more than 18 Å^{-1} with still a very high signal-to-noise ratio, while the experimental cut-off of earlier data recorded at the sulfur K-edge hardly exceeded 10 or 12 Å^{-1}. We have reproduced in Fig. 2(*b*) the Fourier-transformed spectrum corrected for the phase shifts and the backscattering amplitude of the [$S_1\cdots C_{1\gamma}$] absorber–scatterer pair. Note that the signatures of the first two shells are well resolved and that the first few interatomic distances [R_1 ($S_1{}^*-C_{1\gamma}$) = 1.8, R_2 ($S_1{}^*-S_2$) = 2.03, R_3 ($S_1{}^*-C_{2\beta}$) = 2.84 and R_4 ($S_2{}^*-C_{1\gamma}$) = 3.03 Å] agree perfectly with the crystal structure data (Chaney & Steinrauf, 1974).

3.2. *Spin-polarized EXAFS spectra of EuS at the Eu L-edges*

The 'double' gap-scan technique was used to record spin-polarized EXAFS spectra over a wide energy range encompassing both the L_{II}- and L_{III}-edges of rare-earth absorbers: here the key advantage is that the polarization rate of the X-ray photons can be kept almost constant over the whole energy range so that the signatures measured at both edges can be directly compared without correction. Ferromagnetic EuS (T_C = 16.3 K) was selected as a test compound since it was known to exhibit a quite intense X-ray magnetic circular dichroism (X-MCD) signal at the Eu L-edges (Rogalev *et al.*, 1997). The sample (*i.e.* a pellet of EuS diluted in BN) was mounted onto the cold finger of a liquid-helium cryostat (T = 2 K) located between the poles of a

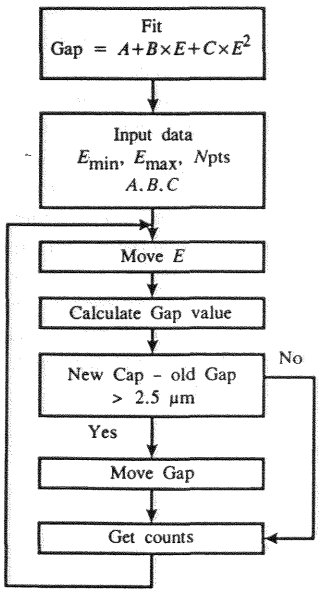

Figure 1
Flow chart of the gap-scan procedure.

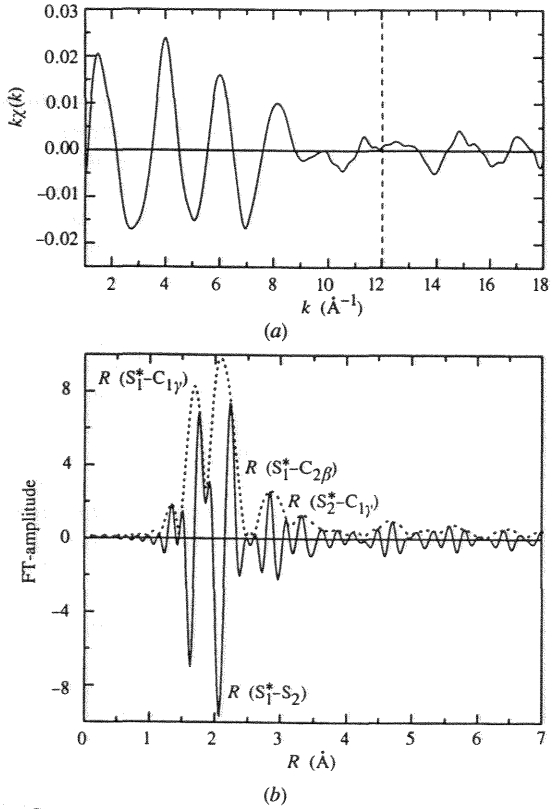

Figure 2
(*a*) Normalized $k\chi(k)$ EXAFS spectrum of [*d,l*] cystine recorded at the sulfur K-edge. The dotted line at 12 Å^{-1} refers to the typical cut-off of earlier data at the sulfur K-edge. (*b*) FT-EXAFS spectrum of [*d,l*] cystine corrected for the phase shifts and backscattering amplitude of the $S_1\cdots C_{1\gamma}$ pair.

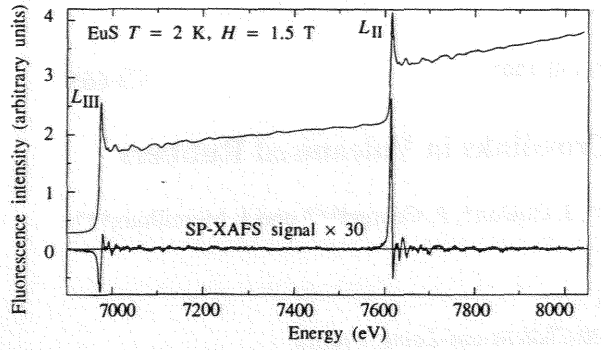

Figure 3
Spin-averaged and spin-polarized XAFS spectra of EuS at the Eu $L_{II,III}$-edges in the ferromagnetic phase. The SP-XAFS spectrum is a direct difference of two consecutive scans recorded with opposite photon helicity.

superconducting electromagnet (B = 1.5 T). We have reproduced in Fig. 3 the spin-polarized differential EXAFS spectrum, *i.e.* the difference between two consecutive spectra recorded with opposite helicities of the incident X-ray photons, and the spin-averaged EXAFS spectrum. The data were collected over more than 1000 eV on readjusting simultaneously the half-gaps B_x and B_z. A detailed analysis of these experiments is to be published elsewhere (Rogalev *et al.*, 1998). In the latter spin-polarized difference spectrum, there is no perceptible discontinuity that might be correlated to a gap change, even on the scale of tiny spin-polarized EXAFS signatures. We would also like to mention that strictly the same gap scan has been repeated on replacing the sample by a beam-position monitor (Gauthier *et al.*, 1995): we failed to detect any displacement greater than 5 μm of the baricentric location of the monochromatic X-ray beam during a change of gap.

4. Conclusions

Two 'gap-scan' procedures are available: (i) the standard procedure keeps the undulator permanently tuned to its peak intensity during an EXAFS scan and may be used either with planar or helical undulators; (ii) in the case of helical undulators of the Helios type, the 'double gap-scan' technique also keeps the polarization rate almost constant over a wide energy range. As reflected by the excellent quality of the spectra produced in Fig. 2 and Fig. 3, both techniques were found to be perfectly reliable.

We are grateful to A. Götz, J. Klora and V. Rey Bakaikoa for their help in developing and debugging the gap-scan software.

References

Chaney, M. O. & Steinrauf, L. K. (1974). *Acta Cryst.* B**30**, 711–716.
Chavanne, J., Chinchio, E., Diot, M., Elleaume, P., Frachon, D., Marechal, X., Mariaggi, C. & Revol, F. (1992). *Rev. Sci. Instrum.* **63**(1), 317–320.
Elleaume, P. (1994). *J. Synchrotron Rad.* **1**, 19–26.
Elleaume, P., Chavanne, J., Marechal, X., Goulon, J., Braicovich, L., Malgrange, C., Emerich, H., Marot, G. & Susini, J. (1991). *Nucl. Instrum. Methods*, A**308**, 382–389.
Gauthier, C., Goujon, G., Feite, S., Moguiline, E., Braicovich, L., Brookes, N. B. & Goulon, J. (1995). *Physica*, B**208/209**, 232–234.
Goulon, J., Rogalev, A., Gauthier, C., Goulon-Ginet, C., Paste, S., Signorato, R., Neumann, C., Varga, L. & Malgrange, C. (1998). *J. Synchrotron Rad.* **5**, 232–238.
Hagelstein, M., San Miguel, A., Fontaine, A. & Goulon, J. (1997). *J. Phys. IV*, **7**(C2), 303–308.
Rogalev, A., Goedkoop, J. B., Rogaleva, M., Gotte, V. & Goulon, J. (1997). *J. Phys. IV*, **7**(C2), 465–466.
Rogalev, A., Neumann, C., Gotte, V. & Goulon, J. (1998). *Phys. Rev. Lett.* Submitted.

4.3 Acte de congrès

J. PHYS IV FRANCE 7 (1997)
Colloque C2, Supplément au Journal de Physique III d'avril 1997 C2-665

Sulfur K-Edge XAS Study of Sulfidic Crosslinks in Vulcanised Rubbers

S. Pasté*, V. Gotte*, C. Goulon-Ginet*,**, A. Rogalev*, J. Goulon*, P. Georget*** and J. Marcilloux***

* *ESRF, BP. 220, 38043 Grenoble, France*
** *Université Joseph Fourier, 38043 Grenoble, France*
*** *Centre de Recherche HUTCHINSON, BP. 31, 45120 Châlette-sur-Loing, France*

Abstract This feasibility study allowed us to establish three main results : (i) With high quality XANES spectra, it becomes quite possible to resolve the characteristic σ*(S-S), π*(S-S) and σ*(S-C) resonances; (ii) The "undulator gap scan" technique can yield excellent EXAFS spectra at the sulfur K-edge over more than 1300 eV; (iii) S K-edge EXAFS spectra made it possible to discriminate between vulcanizates with variable amounts of sulfur crosslinks and zinc sulfide.

1. MOTIVATIONS

Quantifying the polysulfidic content in vulcanizates is of direct interest to rubber industry because strength and fatigue properties of rubber are directly related to the stability of the sulfur crosslinks. Recent XANES studies carried out at the sulfur K-edge by Chauvistré *et al.* [1-2] pointed out that valuable information could be obtained by fitting the σ*(S-S) and σ*(S-C) resonances. It will be shown below that it is even more attractive to try to correlate the information that can be extracted from both XANES & EXAFS spectra.

2. EXPERIMENTAL

The ESRF windowless beamline ID12A (formerly BL6) was found most appropriate to carry out these experiments at low excitation energy even though the fwhm energy bandwidth of the undulator peak is only 95 eV for Helios-II : this is good enough to scan XANES but not EXAFS spectra. We produce here the first EXAFS spectra recorded at the ESRF using the "undulator gap scan" technique.

The so-called 4-Mirror device located upstream with respect to the monochromator was initially designed to steer the two beams of Helios-I [3]. We used only one channel (*i.e.* mirrors 1B + 2A) and, for more simplicity, we did not try to refocus the X-ray beam in the horizontal plane. At 8 mrad incidence, each mirror had a reflectivity of *ca.* 83%.and we have checked that the level of residual harmonics in the reflected beam was at least 5 orders of magnitude below the fundamental. The fixed exit monochromator was equipped with a pair of Si [111] crystals cooled down to 140 K in order to minimize the thermomechanical deformation of the first crystal under heat load.

For such highly absorbing samples, we found preferable to record X-ray fluorescence excitation spectra . The detectors were PNN^+ photodiodes operated in the photovoltaic mode. A digital lock-in exploiting a square wave modulation of the X-ray beam was used to get rid of residual dark currents and possible drifts in the readout electronics [4]. All spectra were carefully corrected for fluorescence re-absorption [5].

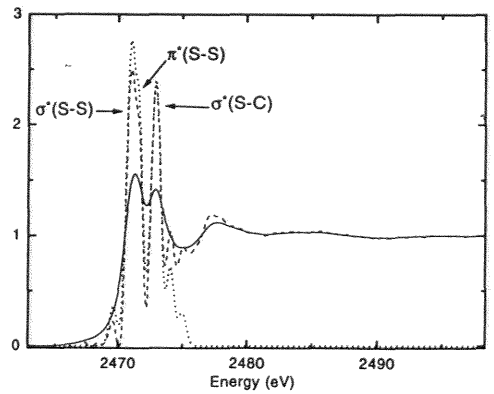

Figure 1 S K-edge XANES spectra of [d,l] cystine. Raw data (---) . Deconvolved spectrum (- - - -) . Fitted preedge resonances (.....) .

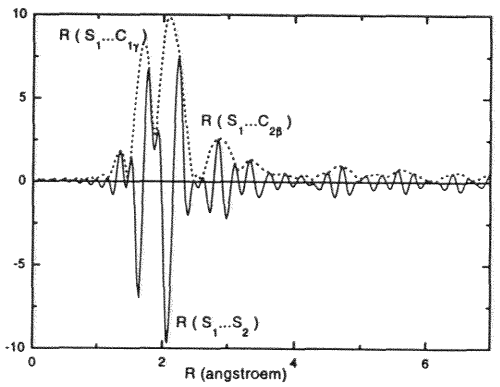

Figure 2 FT EXAFS spectrum of [d,l] cystine corrected for the phase shifts & backscattering amplitude of the S*...C_1 shell. Note the inverted phase of the S*...S shell.

3. RESULTS

[d,l] cystine was selected as reference compound. The XANES spectrum shown in Fig.1 has been recorded with a step size of 44 meV. The high quality of the data allowed us to deconvolve numerically the experimental spectrum with a Voigt I lineshape (2Γ = 0.6 eV [6] ; 2.35σ = 0.8 eV) as pioneered at the ESRF by Loeffen *et al.* [7]. Most spectacular is the resolution of the σ^* (S-S) + π^*(S-S), and σ^*(S-C) resonances. *Ab initio* molecular simulations are underway to identify the exact nature of the lowest excited states which are of direct interest for the present problem.

By correlating the changes of the undulator gap with the rotation of the double crystal monochromator, we have recorded the EXAFS spectrum over 1300 eV. With EXAFS oscillations extending over 18 $Å^{-1}$, the close lying S*-C and S*-S signatures are well resolved in the FT spectrum reproduced in Fig.2. : the first distances $R_1(S_1^*\text{-}C_{1\gamma})$ = 1.80 Å ; $R_2(S_1^*\text{-}S_2)$ = 2.03 Å ; $R_3(S_1^*\text{-}C_{2\beta})$ = 2.84 Å. ; $R_4(S_2^*\text{-}C_{1\gamma})$ = 3.03 Å. are in perfect agreement with the crystal structure [9].

We compare in Fig. 3 the XANES spectra of two vulcanizates (samples A & C). Although the quality of the data is not as good as for the [d,l] cystine, the numerical deconvolution again improved the resolution of the σ^* (S-S) and σ^*(S-C) resonances at the expense of enhanced noise. As opposed to sample A, sample C shows a substantial contribution of sulfur crosslinks, as reflected by the large amplitude of the σ^*(S-S) pre-edge resonance. The presence of trace amounts of chlorine revealed by a small edge jump at *ca.* 2826 eV made the reduction of the EXAFS data far more delicate than for [d,l] cystine. We had to develop a specific algorithm to minimize the perturbation induced by the chlorine fluorescence : this allowed us to analyze our data over 15 $Å^{-1}$. We compare in Fig. 4 the FT EXAFS spectra of samples A and C both corrected tentatively with the phase-shifts and scattering amplitudes of a S*-C pair. One may again identify unambiguously in the spectrum of species C the characteristic pattern of the polysulfidic crosslinks : $R_1(S_1^*\text{-}C_1)$ = 1.79 Å ; $R_2(S_1^*\text{-}S_2)$ = 2.03 Å ; $R_3(S_1^*\text{-}C_2)$ = 2.79 Å. The FT spectrum of species A shows a much smaller contribution of polysulfidic crosslinks but exhibits an intense signature at a larger R distance : this signal was tentatively assigned to the presence of larger amounts of ZnS which are produced during the vulcanization process [2]. This interpretation is supported by the lower trace of Fig.4 which reproduces the same FT spectrum of species A but now corrected for a S*-Zn pair : this spectrum contains all characteristic signatures of the FT spectrum of ZnS, as published in ref. [10]. Characteristic distances are : $R_1(S_1^*\text{-Zn})$ = 2.31 Å ; $R_2(S_1^*\text{-}S_2)$ = 3.0 Å.

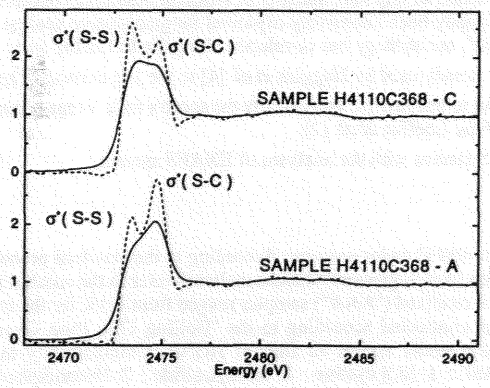

Figure 3. S K-edge XANES spectra of two vulcanizates (A & C) produced at Hutchinson Research Center. Raw data (---) . Deconvolved spectrum (- - - -) .

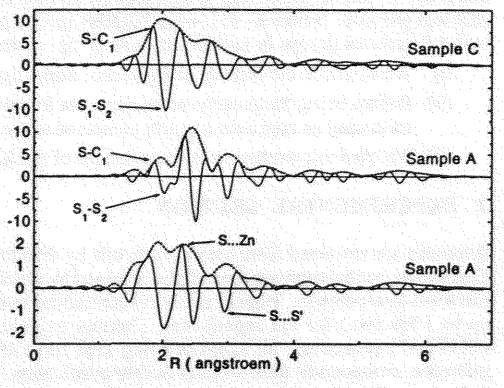

Figure 4. FT EXAFS spectra of samples A & C. Traces **a** & **b** were corrected for a S*...C shell. Trace **c** was corrected for a S*...Zn shell.

References

[1] Chauvistré R., Hormès J., Brück D., Sommer K., Engels H.W., *Kautschuk + Gummi Kunstoffe* **45** (1992) 808-813.
[2] Chauvistré R., Hormès J., Sommer K., *Kautschuk + Gummi Kunstoffe* **47** (1994) 481-484.
[3] Elleaume P., *J. Synchrotron Radiation* **1** (1994) 19-26.
[4] Gauthier C., Goujon G., Feite S., Moguiline E., Braicovich L., Brookes N.B., Goulon J., *Physica* **B208-209** (1995) 232-234.
[5] Loos M., Ascone I., Goulon-Ginet C., Goulon J., Guillard C., Lacroix M., Breysse M., Faure D., Descourières T., *Physica* **B158** (1989) 145-148.
[6] Krause M.O., Oliver J.H., *J. Phys.*, Chem. Ref. Data, **8** (1979) 307-38.
[7] Loeffen P.W., Pettifer R., Müllender S., Van Veenendaal M.A., Röhler J., Sivia D.S., *these Proceedings* (1996).
[8] Teodorescu C.M., Esteva J.M., Karnatak R.C., El Afif A., *N.I.M.* **A345** (1994) 141-147.
[9] Chaney M.O., Steinrauf L.K., *Acta Cryst.* **B30** (1974) 711-16.
[10] Goulon J., Cortès R., Retournard A., Georges A., Battioni J.P., Frety R., Morawek B., *EXAFS and Near Edge Structure III - Springer Proceedings in Physics* **2** (1984) 449-51.

4.4 Acte de congrès

J. PHYS. IV FRANCE 7 (1997)
Colloque C2, Supplément au Journal de Physique III d'avril 1997 C2-667

A Study Using Sulfur K-Edge XAS of Bitumens, Asphaltenes, Maltenes and their Oxidation Products by Comparison with Model Compounds

V. Gotte*, A. Rogalev*, J. Goulon*, C. Goulon-Ginet*,**, L. Michon***, R. Guilard***
and D. Martin****

* *ESRF, BP. 220, 38043 Grenoble, France*
** *Université Joseph-Fourier, Faculté de Pharmacie, 38706 La Tronche, France*
*** *LIMSAG (UMR 9953), Université de Bourgogne, 6 boulevard Gabriel, 21100 Dijon, France*
**** *Centre de Recherche ELF - Solaize, BP. 22, 69360 Saint Symphorien d'Ozon, France*

Abstract High resolution Sulfur K-edge XANES spectra have been recorded at the ESRF on "test" samples of bitumen, asphaltene and maltene fractions and various model compounds. All these fractions were found to have a low content of sulfidic species as opposed to thiophenic species and it is therefore not surprising that thermally oxidized samples (RTFOT) had also a low content (1%) of sulfoxides. This is indeed consistent with the absence of any detectable S=O signature in the EXAFS spectra which were recorded over more than 1300 eV using the "undulator gap scan" technique.

1. MOTIVATIONS

Oxidative aging of bitumens is a problem of high economic value. This is why we got interested in quantifying the amount of sulfoxide or sulfone functional groups formed on thermal oxidation of aliphatic sulfides in artificial bitumens conditioned for research purpose. Sulfur K- & L-edge XANES spectra have already been intensively exploited for quantitative analyses of the sulfur functional groups in asphalts or coals [1-6]. At the ESRF, our strategy has developed along the following lines :

(i) We extended the concept of *Difference Xanes Spectra* already used by Huggins *et al.* [4] to the 1rst derivative spectra .

(ii) Before fitting the preedge resonances, we found helpful to deconvolve numerically the spectra for a Voigt-I lineshape following an approach recently pioneered at the ESRF by Loeffen *et al.* [7].

(iii) We tried to corroborate the conclusions of the XANES studies with the analyses of EXAFS spectra.

2. EXPERIMENTAL SECTION

Bitumens are extracted from heavy crude oils by distillation at 400°C under vacuum. According to the standard procedure of Corbett [8], asphaltenes are the residua obtained by precipitation from n-pentane whereas maltenes refer to the soluble fraction extracted in n-pentane. Typical sulfur concentrations in the non-oxidized ("AAA") samples ranged from 4.3% for the maltenes up to 7.5% (wt.) for the asphaltenes. Thermal oxidation was conducted according to the "Rolling Thin Film Oven Test" ("RTFOT") procedure, all samples being kept for 150 minutes under an hot air flow at 163°C. Commercially available reference compounds used without further purification included : **1**: [d,l] cystine ; **2**: Benzylsulfide ; **3**: Benzodiphenylene ; **4**: Benzylsulfoxide ; **5**: Benzylsulfone ; **6**: Diphenylsulfone.

All spectra were recorded at the ESRF windowless beamline ID12A (formerly BL6). The fwhm energy bandwidth of the undulator peak being only 95 eV for Helios-II, the "undulator gap scan" technique had to be used to record EXAFS spectra over 1300 eV. Reflective optics are used to keep the level of unwanted harmonics at least 5 orders of magnitude below the fundamental. For such highly absorbing samples, we found preferable to record X-ray fluorescence excitation spectra which were carefully corrected for fluorescence re-absorption [9].

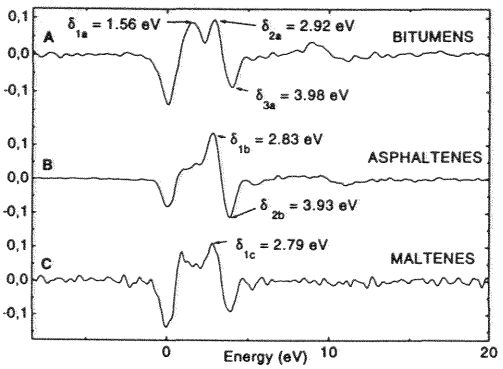

Figure 1. S K-edge 1rst Derivative Difference Spectra {[RTFOT] - [AAA]} calculated for the various fractions.

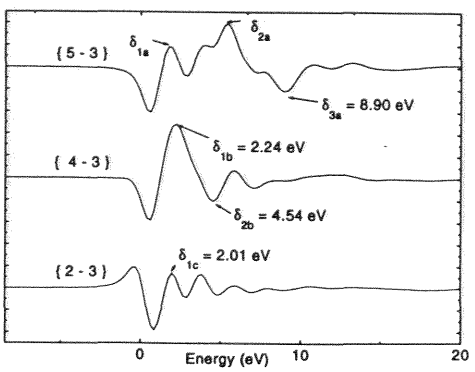

Figure 2. S K-edge 1rst Derivative Difference Spectra for the following couples : {5 - 3}, {4 - 3}, {2 - 3}

3. RESULTS

A convenient way to display the tiny differences between oxidized [RTFOT] and non-oxidized [AAA] fractions is to plot the corresponding 1rst Derivative Difference Spectra reproduced in Fig.1. A comparison with the difference spectra of model compounds also shown in Fig. 2 immediately confirmed that the thermal oxidation resulted in the formation of sulfoxide functional groups at the expense of the sulfidic species. However, edge differences are much smaller than in reference [5] and suggest that only 6% of the sulfidic species may be oxidized.

The next step concerned the evaluation of the respective proportions of sulfidic and thiophenic species in the various [AAA] fractions. We improved quite significantly the reliability of the fits by pre-deconvolving numerically the raw spectra with an optimized Voigt - I lineshape ($2\Gamma = 0.6$ eV [6] ; $2.35\sigma = 0.5$ eV). A typical illustration of the quality of the fits which were generated is given with Fig.3 which concerns the bitumen [AAA] fraction. From similar analyses carried out on normalized spectra, we were led to the following estimation of the relative wt percentage of sulfidic species *vs* the sum of sulfidic + thiophenic species:

- Bitumen fraction [AAA] : 16%
- Asphaltene fraction [AAA] : 17%
- Maltene fraction [AAA] : 22%

It is a straigthforward consequence of the latter figures that the amount of sulfoxide formed during thermal oxidation (RTFOT) should not exceed 1.3% of the total sulfur content : this is extremely low...

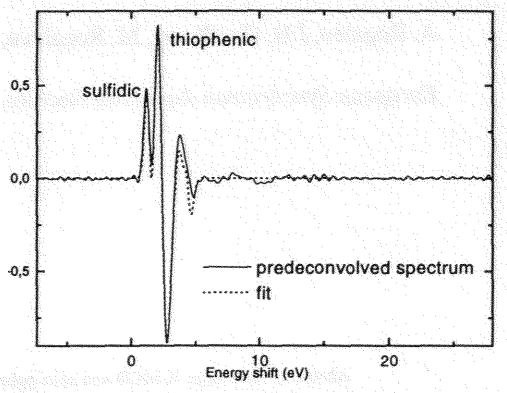

Figure 3 Fit of the first derivative of the predeconvolved spectrum of the bitumen [AAA] fraction. Notice that the typical splitting due to sulfidic and thiophenic species is well reproduced.

This interpretation is well supported by the EXAFS study. As illustrated by Fig. 4 which reproduces the FT EXAFS spectrum of species **6**, sulfones and sulfoxides have a typical FT pattern associated with the imperfectly resolved S*...O and S*...C_1 signatures. Such a signature cannot be detected in the FT spectra of species **3** and of the RTFOT maltene fraction.

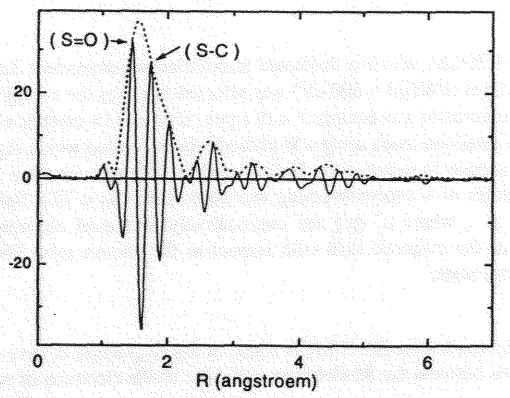

Figure 4. FT EXAFS spectrum of **6** corrected for the phase shifts & scattering amplitude of a S*...C pair. R_1(S*=O) = 1.43 Å ; R_2(S*-C) = 1.76 Å ;

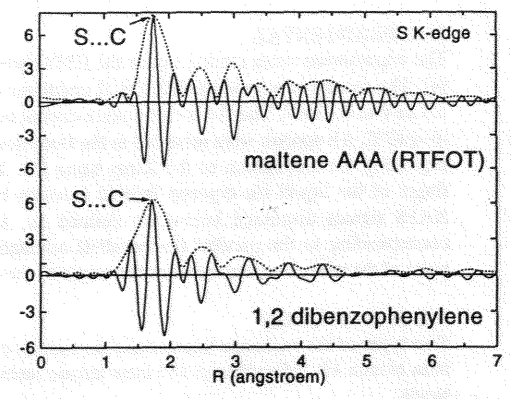

Figure 5. FT EXAFS spectra of the maltene RTFOT fraction and of species **3** with the same corrections.

References

[1] Green J.B., Yu S.K.T., Pearson C.D., Reynolds J.W., *Energy & Fuel* **7** (1993) 119-126.
[2] George G.N., Gorbaty M.L., *J. Am. Chem. Soc.* **111** (1989) 3182-86.
[3] Taghiei M.M., Huggins F.E., Shah N., Huffman G., *Energy & Fuel* **6** (1992) 293-300.
[4] Huggins F.E., Vaidya S.V., Huffman G., Mill T., Youtcheff J., *Proc. Am. Chem. Soc. Meeting - Division of Fuel Chemistry* (1992) 1376-1382.
[5] Waldo G.S., Mullins O.C., Penner-Hahn J.E., Cramer S.P., *Fuel* **71** (1992) 53-57.
[6] Kasrai M., Bancroft G.M., Brunner R., Jonasson R.G., Brown J.R., Tan K.H., Feng X., *Geochimica et Cosmochimica Acta* **58** (1994) 2865-287.
[7] Loeffen P.W., Pettifer R., Müllender S., Van Veenendaal M.A., Röhler J., Sivia D.S., *These Proceedings* (1996).
[8] Corbett L.W., *Analytical Chemistry* **41** (1969) 576.
[9] Goulon J., Goulon-Ginet C., Cortès R., Dubois J.M., *J. de Physique* **43** (1982) 539-48.

4.5 Acte de congrès

J. PHYS. IV FRANCE 7 (1997)
Colloque C2, Supplément au Journal de Physique III d'avril 1997 C2-465

Spin Polarised XAFS of EuS in Ferromagnetic and Paramagnetic Phases

A. Rogalev, J.B. Goedkoop, M. Rogaleva, V. Gotte and J. Goulon

European Synchrotron Radiation Facility, BP. 220, 38043 Grenoble cedex, France

Abstract. Near edge X-MCD and spin polarised EXAFS spectra have been recorded at the $L_{2,3}$-edges of Eu in EuS. Only the intensity but not the shape of the X-MCD spectrum is altered when EuS evolves from the ferromagnetic to the paramagnetic phase, i.e. above 20 K. Spin polarised EXAFS spectra confirm that the sulfur 3p valence band electrons are the mediators of the antiferromagnetic coupling between next-nearest Eu neighbours.

1. INTRODUCTION

Europium sulfide is a ferromagnetic semiconductor with a Curie temperature of 16.7 K. It is a representative example of isotropic Heisenberg ferromagnet [1]. Most interesting, there are two types of magnetic interactions in EuS: ferromagnetic between the nearest Eu^{2+} ions and antiferromagnetic between the Eu ions separated by sulfur atom [2]. This antiferromagnetic coupling has been interpreted as resulting from an indirect exchange mediated by sulfur 3p valence band electrons which are magnetically polarised by the quasi-localised Eu 4f electrons [3].

2. EXPERIMENTAL

The experiments were carried out at the ESRF beamline ID12A which is dedicated to polarisation dependent XAFS studies [4]. The second harmonic of HELIOS-II undulator spectrum (FWHM ≈ 500 eV) was selected to cover the energy range from 6.9 keV to 8.1 keV. The fixed-exit double-crystal monochromator was equipped with a pair of Si <111> crystals cooled down to -140°C. All spectra were recorded in the fluorescence detection mode using a Si photodiode associated with a digital lock-in exploiting the modulation of the X-ray beam [5]. The sample (a pellet of the EuS diluted in BN) was mounted on the cold finger of the liquid He cryostat located between the poles of a superconducting electro-magnet (B_0 < 7T). Spin-polarised XAFS signals discussed below are defined as $\mu^+ - \mu^-$, where μ^+ (μ^-) are consecutively measured absorption spectra corresponding to the parallel (antiparallel) orientation of the magnetic field with respect to the photon spin. The inflection point of the white line was taken as the origin of the energy scale.

3. X-MCD STUDIES

Two types of the exchange interactions are usually considered to describe X-MCD signal at the $L_{II,III}$-edges of rare-earth atoms: intra atomic 4f - 5d exchange and inter atomic interaction between the 5d electrons and outer shells electrons of neighbouring atoms.

Figure 1 reproduces the XANES spectra recorded with reversed polarisation and the corresponding dichroic signals at the L_3 and L_2 edges of Eu in the ferromagnetic phase (T=2K and B=1.5T). The X-MCD spectra have nearly the same dispersive shape but opposite signs. The amplitude ratio of the dichroic signals at the L_3 and L_2 edges is equal to -4, which is twice larger

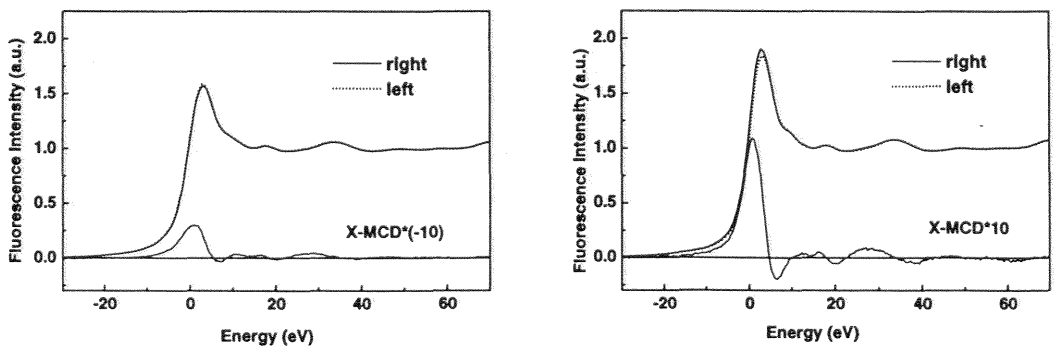

Figure1: XANES and X-MCD spectra at the L3 (left panel) and L2 (right panel) edges of Eu.

than for Gd^{3+} ions [6] which have the same atomic configuration (Xe^{2+} with a half-filled 4f shell; spectroscopic ground state $^8S_{7/2}$). A strong deviation of the branching ratio of the X-MCD signals at the L_{II} and L_{III} edges from the statistical value is expected due to the presence of an orbital magnetic moment carried by the 5d electrons of Eu.

Due to its relatively low Curie temperature EuS appears to be a good system to compare X-MCD in ferromagnetic and paramagnetic states. X-MCD spectra at the L_2 edge of Eu in ferromagnetic (T=2K, B_0=1.5 T) and paramagnetic (T=50K, B_0= 6.5 T) states are shown in fig. 2. One may observe that the shape of the signal does not change although its amplitude decreases dramatically. This suggests that the X-MCD signal is mainly due to the intra atomic 4f - 5d exchange interaction and is practically not affected by the inter atomic interactions.

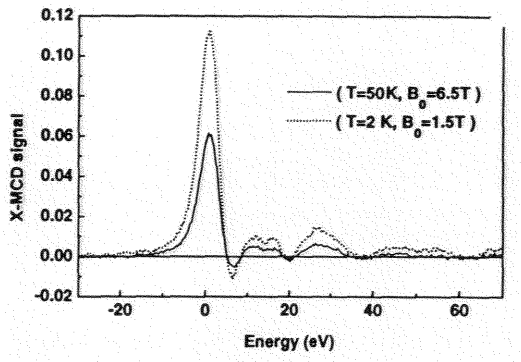

Figure 2: X-MCD spectra at the Eu L_2-edge in ferromagnetic and paramagnetic phases of EuS.

4. SPIN-POLARISED EXAFS STUDIES

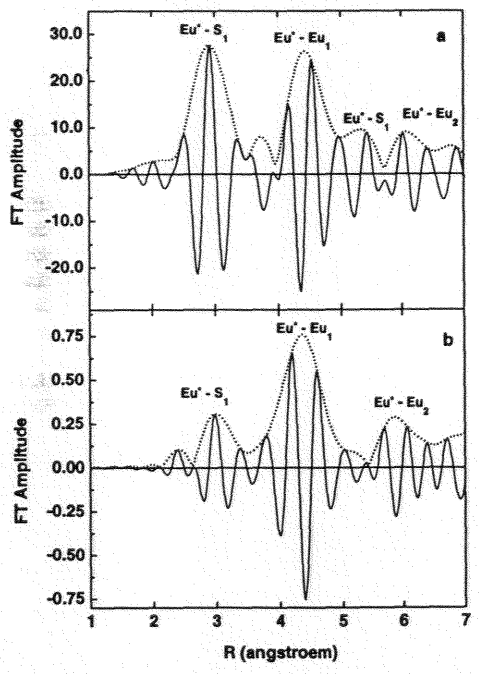

Figure 3: FT spectra of "classical" (panel a) and spin-polarised EXAFS (panel b) recorded at the Eu L_3- edge (T=2K, B_0=1.5 T).

The spin-polarised EXAFS spectra of EuS in a ferromagnetic state (T = 2K, B_0 = 1.5T) have been recorded at the L_{II} and L_{III} edges of Eu. The amplitude of the spin-polarised EXAFS oscillations at the L_2-edge is twice larger compared to the signal at the L_3-edge which has an opposite sign. It corresponds to the difference in the effective photoelectron polarisation (-0.5 for the L_{II}-edge and +0.25 for the L_{III} edge) despite of the strong deviation observed for the X-MCD spectra. It implies that the effect of the orbital polarisation is practically negligible in the EXAFS region at least for EuS. We did not observe in the spectra the multiple excitations expected *ca.* 130 eV above the absorption edge. The analysis of the spin-polarised EXAFS spectra has been performed using the standard procedure. We compare in Fig. 3 the Fourier transform spectra of the "classical" EXAFS and its spin-polarised counterpart recorded at the L_3 edge. Both FT spectra are corrected with the phase-shifts and scattering amplitudes of a Eu^*- S_1 pair calculated with the FEFF6 code [7]. Assignment of the peaks in both spectra is indicated in fig. 3. As expected the most intense peak in the spin-polarised FT spectrum is due to the Eu^*- Eu_1 signature which has a distorted phase. Surprisingly the signal corresponding to the first coordination shell formed by 6 sulfur atoms does not vanish in the spin-polarised EXAFS spectrum although its amplitude is significantly reduced. This suggests that sulfur ions are carrying a magnetic moment induced by exchange interaction with Eu neighbours.

Acknowledgements

We thank Dr. O.Leupold (Hamburg University, Germany) for providing us with the polycrystalline europium sulfide.

References

[1]. Wachter P., Handbook on Phys. and Chem. of Rare Earth, Ed. K.A.Gschneider and L.Eyring, North Holland Publ. Co., 1979, Chap. 19.
[2]. Zinn W., *J. Magn. Magn. Mater.*, **3** (1976) 23.
[3]. Liu L., *Solid State Comm*, **46** (1983) 83.
[4]. Goulon J., Brookes N.B., Gauthier C., Goedkoop J., Goulon-Ginet C., Hagelstein M., Rogalev A., *Physica* **B 208&209** (1995) 199.
[5]. Gauthier C., Goujon G., Feite S., Moguiline E., Braicovich L., Brookes N.B., Goulon J., *Physica* **B 208&209** (1995) 232.
[6]. Goedkoop J., Rogalev A., Neumann C., Goulon J., *These Proc.* (1996).
[7]. Mustre de Leon J., Rehr J.J., Zabinsky S.I., and Albers R.C., *Phys. Rev.* **B44** (1991) 4146.

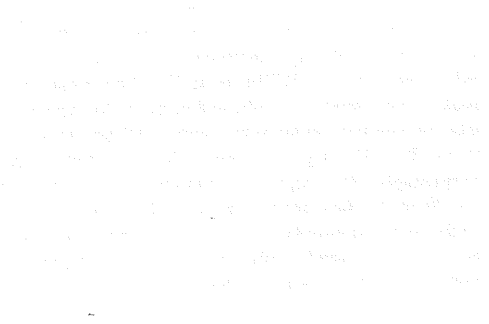

Conclusion générale

Un résultat important de ce travail aura été de tenter de clarifier la nature des espèces qui se forment lors de l'ozonation de composés halogénés de manganèse(III) dans lesquels le métal est complexé par divers macrocycles porphyriniques dodéca-substitué en position β. Pour cela nous avons tenté de combiner des études EXAFS et XANES, voire XMCD. La méthode d'analyse différentielle avec perturbation structurale, appliquée aux spectres EXAFS enregistrés au seuil K du manganèse, s'est révélée être un outil puissant, car elle permet d'obtenir des informations structurales fiables, inaccessibles par l'analyse directe des spectres. L'étude des spectres XANES, enregistrés au seuil K du chlore, combinées aux simulations *ab initio*, nous a aidé à proposer une structure pour les clusters moléculaires covalents formés par l'action de l'ozone sur le chlore.
Ce travail constitue, à notre connaissance, la première mise en évidence de l'existence d'une chimie de coordination entre le manganèse et l'ozone.
En particulier nous avons participé aux projets de recherche de l'équipe en charge de la ligne ID-12A, qui était consacré à la mise en évidence du dichroïsme circulaire naturel dans le domaine de rayons X. Il a été démontré que ces signaux résultaient des termes d'interférence E1.E2 entre les éléments de matrice de transition dipôle électrique-quadrupôle électrique. L'origine même du XNCD implique qu'il ne peut être détecté que dans les cristaux gyrotropes ou des systèmes présentant un ordre orientationnel partiel. Son intérêt est que le spectre XNCD est sensible à la configuration absolue du site absorbeur chiral et contient aussi une information sur le mélange des orbitales de parité pair ou impair de ce site. Des spectres ont été enregistrés sur des cristaux uniaxes (α-$LiIO_3$), au seuils L_1 L_2 et L_3 de l'iode, et sur des cristaux biaxes ($KTiOPO_4$) au seuil K du titane, pour lequel les mesures ont été beaucoup plus difficiles, en raison de la superposition du signal de dichroïsme linéaire et de la biréfringeance.

L'analyse des spectres a été une part importante de notre travail. De ce point de vue nous avons participé à l'écriture de plusieurs logiciels spécialisés dans l'analyse de spectres XANES et EXAFS. Ils ont été écrits de facon évolutive, afin de pouvoir mieux les adapter aux nécessités expérimentales. L'une d'elle était d'avoir la possibilité d'analyser des spectres dès que le dernier point a été enregistré, afin de pouvoir juger de la qualité des données.

Enfin, l'une des tâches qui m'avait été assignée a été de concevoir une cellule liquide utilisée pour l'enregistrement d'espèces en solution et utilisable dans un environnement ultra-haut-vide. Ce fut une tâche longue et minutieuse, bien que cela ne transparesse pas dans ce mémoire.

Il est important de souligner que ce travail a été réalisé à l'ESRF qui dispose d'un anneau de stockage fonctionnant à une haute énergie (6 GeV) et constitue une source de rayonnement synchrotron de troisième génération douée d'une brillance spectrale exceptionnelle. Toutes les expériences décrites dans ce travail ont été réalisées en utilisant le rayonnement d'un onduleur hélicoïdal qui n'a pas, pour l'instant, d'équivalent dans aucun autre centre de rayonnement synchrotron existant. Avec cette source, les spectroscopistes ont, non seulement une source de très haute brillance spectrale, mais aussi un contrôle presque parfait de l'état de polarisation du rayonnement émis. C'est cet outil qui nous a permis de résoudre un problème vieux de plus d'une centaine d'années: la mise en évidence de l'activité optique naturelle dans le domaine spectral des rayons X. Nous avons pu apprécier, cependant, qu'il faut une instrumentation de trés haute qualité et de trés haute fiabilité pour pouvoir vraiment tirer parti des qualités d'une telle source: les instruments mis au point dans le groupe de spectroscopie d'absorption X de l'ESRF sont clairement à la hauteur de ces enjeux.

Le prix à payer est cependant dans la complexité des réglages qui requièrent une expertise qui ne s'improvise pas. A ce stade, nous avons eu la chance de bénéficier de l'aide des scientifiques en charge de la ligne de lumière ID-12A. Un autre problème dont nous avons pris conscience au cours de ce travail de Thèse est celui des dommages causés aux échantillons soumis à des flux aussi intenses: ces problèmes constituent, à l'évidence une limite incontournable pour les applications futures.

université HENRI POINCARÉ
NANCY 1

FACULTÉ DES SCIENCES

Monsieur **GOTTE Vincent**

DOCTORAT de l'UNIVERSITE HENRI POINCARE, NANCY-I

en CHIMIE INFORMATIQUE & THEORIQUE

VU, APPROUVÉ ET PERMIS D'IMPRIMER

Nancy, le 22 NOV 1999 n°293

Le Président de l'Université

UNIVERSITÉ HENRI POINCARÉ, NANCY 1
LE PRÉSIDENT
Cl. BURLET

3C-F9

Un objectif majeur de ce travail aura été de démontrer que la spectroscopie d'absorption X permettait d'accéder à des informations structurales précieuses sur les complexes qui se forment lors de l'activation de l'ozone par divers composés halogénés du manganèse (III) dans lesquels le métal est complexé par des macrocycles porphyriniques dodécaphénylsubstitués. L'analyse des spectres EXAFS et XANES, enregistrés au seuil K du manganèse montre que, dans les intermédiaires formés en présence d'ozone, le métal est formellement tétravalent et son schéma de coordination inclut les 4 atomes d'azote pyrrolique du noyau porphyrinique dans le plan équatorial, plus, sur l'axe, deux molécules d'ozone disposées symétriquement par rapport au noyau macrocyclique. L'étude des spectres EXAFS et XANES, enregistrés au seuil K du chlore, et leurs simulations par des méthodes *ab initio*, mettent en évidence l'existence d'entités moléculaires Cl-O-O-O voire O-O-O-Cl-O-O-O. Nous avons été beaucoup moins heureux dans notre tentative de caractérisation des complexes d'inclusion de l'argon par le cryptophane A et le kryptofix(222) dans les solvants organiques. Nous précisons les difficultés expérimentales rencontrées dans ce dernier projet.Nous avons par ailleurs contribué à mettre en évidence pour la première fois, le dichroïsme circulaire naturel (XNCD) dans le domaine des rayons X. L'origine de ce phénomène est lié aux termes tensoriels d'interférences dipôle électrique-quadrupôle électrique (E1.E2) qui existent uniquement dans les cristaux gyrotropes uniaxiaux et biaxiaux. Les premiers resultats obtenus concernaient les seuils L de l'iode dans un monocristal de iodate de lithium appartenant à une classe de cristaux énantiomorphes. Enfin, notre contribution à divers développements méthodologiques sur la ligne de lumière ID-12A est attestée par le fait que nous avons été associé aux publications correspondantes.

Mots clés :

Manganèse - Chlore - Porphyrine - EXAFS - XANES - XNCD.